ELECTROCHEMISTRY OF SILICON AND ITS OXIDE

XIAOGE GREGORY ZHANG

Electrochemistry of Silicon and Its Oxide

This page intentionally left blank

Electrochemistry of Silicon and Its Oxide

Xiaoge Gregory Zhang

Cominco Ltd.
Mississauga, Ontario, Canada
and
McMaster University
Hamilton, Ontario, Canada

KLUWER ACADEMIC PUBLISHERS
NEW YORK, BOSTON, DORDRECHT, LONDON, MOSCOW

eBook ISBN: 0-306-47921-4
Print ISBN: 0-306-46541-8

Created in the United States of America

Visit Kluwer Online at: http://kluweronline.com
and Kluwer's eBookstore at: http://ebooks.kluweronline.com

To the people who assisted,
encouraged, and inspired me

This page intentionally left blank

There is an expanding frontier of ignorance
Richard P. Feynman

This page intentionally left blank

Foreword

It may be argued that silicon, carbon, hydrogen, oxygen, and iron are among the most important elements on our planet, because of their involvement in geological, biological, and technological processes and phenomena. All of these elements have been studied exhaustively, and voluminous material is available on their properties. Included in this material are numerous accounts of their electrochemical properties, ranging from reviews to extensive monographs to encyclopedic discourses. This is certainly true for C, H, O, and Fe, but it is true to a much lesser extent for Si, except for the specific topic of semiconductor electrochemistry. Indeed, given the importance of the electrochemical processing of silicon and the use of silicon in electrochemical devices (e.g., sensors and photoelectrochemical cells), the lack of a comprehensive account of the electrochemistry of silicon in aqueous solution at the fundamental level is surprising and somewhat troubling. It is troubling in the sense that the non-photoelectrochemistry of silicon seems "to have fallen through the cracks," with the result that some of the electrochemical properties of this element are not as well known as might be warranted by its importance in a modern technological society.

Dr. Zhang's book, *Electrochemical Properties of Silicon and Its Oxide,* will go a long way toward addressing this shortcoming. As with his earlier book on the electrochemistry of zinc, the present book provides a comprehensive account of the electrochemistry of silicon in aqueous solution. The topics covered are mostly fundamental in nature and include comprehensive accounts of the silicon/electrolyte interface, anodic oxidation, etching, photoeffects, cathodic reactions and redox couples, porous silicon, and photoelectrochemistry. The book starts with a discussion of basic semiconductor electrochemistry that sets the stage for the discussion of specific phenomena (e.g., anodic oxidation) in later chapters. Careful attention has been paid to the accurate definition of terms and to identifying what is unique about silicon with regard to its electrochemical properties. The level of the book renders it suitable as an introduction to the field of silicon electrochemistry, with its value being greatly enhanced by inclusion of material that is not related to photoeffects, which has been covered extensively elsewhere.

As with any book, the material that is presented reflects the interests of the author and this book is no exception. However, Dr. Zhang has stepped back and taken a new look at a field that for so long has been dominated by one particular aspect of the subject. Accordingly, it is my fervent hope that the book will spark a renewed interest in the general electrochemistry of one of the most important and remarkable of elements, silicon.

State College, Pennsylvania D.D. Macdonald

This page intentionally left blank

Preface

The importance of electrochemistry in silicon technology has spurred intense research activity in the last five decades, resulting in a tremendous amount of experimental data and theoretical information on the silicon/electrolyte interfaces. This book is a comprehensive compilation and digestion of this body of information.

The aim of this book is to serve as a centralized information source for anyone who is interested in the surface and electrochemical properties of silicon and its oxides. It will be most useful to the scientists who study the surface phenomena of silicon and to the engineers who design and fabricate silicon-based electronic devices. It can also serve as a general reference for researchers working in the fields of semiconductor electrochemistry and surface science, in which silicon is commonly used as a model material. In addition, it can be useful to the geologists who study rock–water interactions and to the people who work on etching and surface treatment of glasses.

My fascination with the electrode behavior of silicon began some fourteen years ago when I was a postdoctoral research fellow at MIT investigating the formation mechanism of porous silicon.[2,8,9] The decision to write this book came shortly after the publication of my first book entitled "Corrosion and Electrochemistry of Zinc" in 1996.[970] I recognized then: "From the viewpoint of material users and researchers, it is most beneficial that all the relevant information, theoretical and practical on all aspects of electrochemistry of one element be systematically organized in a single source." Compiling and digesting the results from all discrete studies provide a collective and holistic perspective in evaluating the validity and difference in the data and theories resulting from individual studies, and allow a more complete characterization of each specific phenomenon. Also, writing a book of this nature is itself a research process, through which new data and new insights that are not clear in individual studies, can be generated. As a result, about 100 new tables, figures and illustrations of synthesized information are generated and presented here for the first time.

Two general considerations have been taken in the selection of the information from the literature. The first is the emphasis on the information pertaining to silicon as a single crystalline material and not that pertaining to alloys and structures made or transformed from silicon. This emphasis is essential in warranting a sufficient focus and space for such an extensively studied material as silicon. The second is the emphasis on details and specificity of data because the diverse electrochemical phenomena observed on silicon electrodes are governed by specific conditions and are differentiated only in detail. In practice, it is the condition-phenomenon specific information

rather than the generalized information that is most useful to the people who work on concrete problems.

Each phenomenon is dealt with by a systematic characterization first based on a collective body of experimental data followed by a comprehensive discussion on the underlying mechanisms. It is believed that while the experimental data generally remains true and therefore valuable over time, theories and mathematical formulations tend to vary with individual studies, and their usefulness, with a few exceptions, are limited to its time. This is because the former is the measurement of facts whereas the latter is the interpretation of the measurement.

In discussing mechanisms, the focus is on physical schemes rather than mathematical formulations. This is because many details of the phenomena observed in the complex system of silicon/electrolyte interface are still not understood and mathematical formulations are not really meaningful without a clear understanding of the physical schemes. Thus, for each phenomenon, the concepts and theories on the physical schemes proposed in different studies are compared against the collective body of data. Generalization is provided when a coherence exists in the data and the theories. When it does not exist, effort is made to provide a comprehensive analysis with new hypotheses that is more consistent with the collective body of data from a global perspective. Generally, for a complex system a collective view is more accurate and more complete than individual ones.

The information in the book is organized in nine chapters comprising roughly of two parts: The first part, consisting of Chapters 1 to 4, deals with the conditions of silicon/electrolyte interface and second part, of Chapters 5 to 8, deals with the phenomena of silicon electrodes. The first chapter provides an overview on the basic concepts and theories of semiconductor electrochemistry to serve as a reference base on which the electrochemical properties of silicon are described. Chapter 2 covers the information on the surface conditions of silicon and the characteristics of silicon/electrolyte interfaces. The information related to properties of silicon oxides in general and to those of anodic oxides in specific are presented in Chapters 3 and 4. Chapter 5 deals with the anodic behavior of silicon electrodes with respect to the chemical nature of the reactions and the kinetic processes. Chapter 6 summarizes research findings on the various cathodic reactions and the reactions of redox couples. Chapter 7 is devoted to the etching of silicon by compiling the data on etch rate and morphology of etched surfaces, and by discussing the etching mechanisms in different solutions. Chapter 8, the largest chapter, deals with the formation and morphology of porous silicon, and the complex mechanistic aspects, utilizing all information presented in the earlier chapters. The last chapter, Chapter 9, provides a summary on the book from six different respects that connect the information in different chapters, and an indication on the areas of interest for future research.

ACKNOWLEDGMENTS

A book such as this is the result of labor for many years, during which I have received assistance, encouragement, and inspiration in various forms from many people.

I wish, first of all, to express my immense gratitude to my wife Li and my son Kevin for their understanding and support in my undertaking such a time and energy-consuming endeavor.

I am specially grateful to D.D. Macdonald of the Pennsylvania State University for his reviewing the manuscript and writing a foreword for this book. My sincere thank is due to a number of people who reviewed the different chapters: J. Bardwell of The National Research Council of Canada, T.D. Burleigh of University of Pittsburgh, J.J. Kelly of University of Utrecht, and E.S. Kooij of University of Twente. I would also like to acknowledge M. Christopherson and H. Föll of Christian-Albrechts University for providing photographs on porous silicon.

I would like particularly to thank K. Howell of Kluwer Academic/Plenum Publishers, the editor of this book; his enthusiastic engagement and critical reading of the entire book have been especially important. I am also grateful to X. Gu, J. Jin, M.C. Zhang, and A.Q. Xing who helped in various tasks such as literature search, copying, and typing and so on, which are invisible but essential in the development of a book.

I would also take this opportunity to express my gratitude to S.L. Smith of University of California at Davis, and R.M. Latanision and S.D. Senturia of MIT for providing me the opportunity many years ago to study the electrochemistry of silicon, from which I gained the knowledge and developed a lasting fascination with silicon.

Finally, I wish that this book can be a tribute to the authors, whose research work contributed to the huge knowledge base on silicon that made this book possible.

Xiaoge Gregory Zhang
Toronto, Canada
xgzhang@interlog.com

This page intentionally left blank

Contents

CHAPTER 2. Silicon/Electrolyte Interface

CHAPTER 3. Anodic Oxide

CHAPTER 6. Cathodic Behavior and Redox Couples

CHAPTER 7. Etching of Silicon

CHAPTER 8. Porous Silicon

This page intentionally left blank

List of Symbols

Symbols	Definition	Section
a	lattice constant	2.1
a_{ox}, a_{red}	activities of oxidized and reduced species	1.1
$a_{n,s}$, $a_{p,s}$	capture coefficients for electrons and holes at the surface	1.4
B	Tafel slope	5.8
C	capacitance	1.1
	concentration of electrolyte	2.2
C_{ss}	surface states capacitance	1.1
d, d_0	thickness of oxide film	3.4, 5.13
D_{red}, D_{ox}	densities of occupied and empty states in the electrolyte	1.1
D^0_{red}, D^0_{ox}	normalizing factors	1.1
D_L	intrinsic Debye length	2.1
D_n	diffusion coefficient of electrons	2.1
D_p	diffusion coefficient of holes	2.1
e	electron charge	1.1
E	energy level	1.1
	field	3.4, 5.10
E_0	energy at which there is zero surface state charge	1.2
E_{bd}	breakdown field	2.1
E_{ox}, E_{red}	energy levels of the oxidized and reduced species	1.1
E_{cs}, E_{vs}	conduction and valence band edges at the surface	1.1
E_{redox}	redox potential	1.2
E_{corr}	corrosion potential	1.5
E_g	width of band gap	1.1
E_s	surface field	1.2
ΔE	activation energy	4.1
f	frequency of current oscillation	5.10
f_D	Fermi-Dirac distribution function	1.1
f_M	Maxwell-Boltzmann distribution function	1.1
f_{ss}	non-equilibrium occupancy of surface levels	1.4
g	density of allowed states	1.1
	rate of photo carrier generation	1.4
g_{ss}	degeneracy of the energy level	1.2
i_a, i_c	anodic and cathodic currents	1.3

Symbols	Definition	Section
i_0, i_{ex}, i_{00}	exchange current densities	1.3, 5.6
i_p^{lim}	limiting current due to hole diffusion in the bulk	5.6
i_{dl}, i_b	photo currents generated in the double layer and in the bulk	1.4
i_{ph}	photo current	1.4
i^c, i^v	conduction band and valence band currents	1.3
i_a^c, i_a^v	anodic currents via the conduction band and valence band	1.3
i_c^c, i_c^v	cathodic currents via conduction band and valence band	1.3
i_0^c, i_0^v	exchange current densities via conduction band and valence band	1.3
i_i, i_e	ionic and electronic currents	3.4
i_p	hole diffusion current	1.4
	passivation current	5.2
i_{net}	net current density	1.5
i_{corr}	corrosion current density	1.5
i_s, i_t, i_b	current densities at pore bottom, pore tip and pore wall	8.6
I_0	light intensity	1.4
J_1, J_2, J_3, J_4	peak and valley current values of I–V curve in HF	5.2
J_c, J_v	flux of electrons and holes from/into the conduction and valence bands	1.4
ω	light frequency	1.4
k	Boltzmann's constant	1.1
	rate constant	4.4
K, K_a, K_i, K_{sF}	equilibrium constants	2.2, 4.4
L_p	hole diffusion length	1.4
M	atomic weight	2.1
	molar concentration per liter	2.2
n	effective dissolution valence	5.4
N_0	atomic density	2.1
N_v	effective density of states in the valance band	1.1
N_a, N_d	acceptor and donor concentrations	1.1
N_{em}, N_{oc}	densities of empty states and occupied states	1.3
n_i	intrinsic carrier density	1.1
	anionic concentration	3.4
n_1	captured electron density in the surface states	1.4
n_s^0, p_s^0	surface electron and hole concentrations at equilibrium	1.3
n_0	electron concentration at equilibrium	1.2
p_0	hole concentration at equilibrium	1.3
p	density of holes in the valence band	1.1
p_1	captured holes in the surface states	1.4
q	charge	1.1
Q_H	charge in the Helmholtz double layer	1.2
Q_{soln}	charge in the solution	1.2
r	radius of curvature	2.2
	rate of particle movement	5.11
	etch rate	7.3
r_0	radius of atoms	2.1
R	rate of dissolution, etching, etc.	4.2, 7.2

Symbols	Definition	Section
R_s	rate of recombination via surface states	1.4
$R_{n,s}$, $R_{p,s}$	recombination rates of electrons and holes via surface states	1.4
s	surface recombination velocity	1.4
t	time	
	oxide thickness	9.3
V	electrode potential	1.1
	volume	2.2
V_{fb}	flatbandpotential	1.1
V_p	possivation potential	5.2
T_m	melting temperature	2.1
V_{app}	applied potential	1.2
V_{ex}	excess voltage	3.4
V_{oc}	open circuit photo potential	1.4
V_s^0	potential across the space charge layer at equilibrium	1.3
V_m	measured potential	1.1
ΔV	potential drop, overpotential	1.3, 8.6
x_d	width of space change layer	1.3
Y	quantum efficiency	1.4
ε	relative permittivity	1.1
ε_0	permittivity of vacuum	1.1
Φ	Schotteky barrier height	1.2
ϕ_0	standard electrode potential	2.2
λ	reorientation energy	1.1
	number of holes involved in reaction	5.11
σ	surface free energy	2.2
μ	$E_c - E_F$	1.1
τ_p	life time of hole	1.3
μ_e, μ_h	chemical potentials of electrons and holes	1.1
μ_e, μ_p	mobility of electrons and holes	2.1
μ_i	ionic mobility	3.4
θ	fraction of surface coverage	4.4
	angle of the side pore from the main pore	8.6
ρ	density	2.1
	resistivity	8.6
η	power efficiency of photo cell	1.4
η_a	anodic overpotential	1.3
η_e	concentration overpotential in electrolyte	1.3
η_{sc}	$V_s - V_s^0$, space charge layer over potential	1.3
η_{H2}	efficiency of hydrogen evolution	5.5
κ	transition coefficient	1.3
v	velocity of electrons in oxide film	3.4
χ	electron affinity	1.1
$\gamma_{integral}$	partitioning coefficient of potential	1.2
γ_{differ}	partitioning coefficient of potential change	1.2
ASTM	American Society of Testing and Materials	7.8
BHF	buffered HF solution	4.2
CE	current efficiency	3.2

Symbols	Definition	Section
CVD	chemical vapor deposition	3.2
EDP	etching solution mixed with ethylenediamine, pyrocatechol and water	7.4
IPA	isopropyl alcohol	7.7
LPD	liquid phase deposition	3.2
MOS	metal-oxide-semiconductor	3.2
NMA	N-Methylacetamine	3.3
MeCN	Acetonitrile	8.2
ACN	Acetonitrile	6.7
PS	porous silicon	8.1
LDCVD	low pressure chemical vapor deposition	4.3
pzc	potential of zero charge	1.1
OCP	open circuit potential	1.5
SCE	potential of saturated calomel electrode	2.7
SHE	standard potential of hydrogen electrode	2.2
TMAH	tetramethyl ammonium hydroxide, etching solution	7.4
r.d.s.	rate determining step	5.12
rpm	number of rotations per minute	5.1
UV	ultra violet light	2.4

1

Basic Theories of Semiconductor Electrochemistry

1.1. INTRODUCTION

Silicon, due to its importance in the electronics industry, is perhaps the most investigated electrode material in the field of semiconductor electrochemistry. A wide range of electrode phenomena, from electropolishing to formation of porous silicon as well as from current multiplication to current oscillation, can occur on silicon electrodes. As will be seen in later chapters, many details of these phenomena are not directly explicable by the existing theories of semiconductor electrochemistry. This is perhaps related to the fact that the basic theories deal with idealized situations, but the electrode behavior of a specific system almost always deviates from the ideal situations in different ways. Also, the rich details of each large-scale phenomenon, e.g., formation of porous silicone are determined by a set of reactions that are intrinsically complex at the atomic scale such that the rich details are lost when simplifications are made in a theory. However, the basic concepts and theories can still be useful in describing the electrode processes at certain temporal and spatial scales and the large-scale phenomena can be understood by taking into account the different aspects and scales of these processes.

This chapter provides an overview of the various aspects of semiconductor electrochemistry, which will be useful in describing the specific phenomena on silicon electrodes in later chapters. Also, this systematic description of the basic theories is intended to be used as a reference base, on which the details of electrode behavior in different situations are characterized and organized. To avoid unnecessary detail and use of space, the descriptions in this chapter are limited to the basic concepts, the physical schemes, and the essential quantities and equations that are required to understand these concepts and schemes. More detailed treatment of the various aspects of semiconductor electrochemistry can be found in the literature.[1,44,86,270,962]

1.2. ENERGETICS OF SEMICONDUCTOR/ELECTROLYTE INTERFACE

The energy spectrum of electrons in an ideal crystal consists of two different types of energy bands: those with filled energy levels (allowed bands) and those with no energy levels (band gaps). For a semiconductor the upper unfilled band is called the conduction band and the lower almost filled band is called the valence band as shown in Fig. 1.1. The energy levels in a semiconductor are characterized by the conduction band edge E_c and valence band edge E_v and by the Fermi level E_F. The Fermi level describes the equilibrium distribution of carriers in the bands and is the chemical potential of electrons in the semiconductor. The width of the band gap, $E_g = E_v - E_c$, depends on the strength of the chemical bonds. For silicon at 300K the band gap is 1.12eV. The effective band gap is reduced by heavy doping, larger than $10^{18}/cm^3$. For silicon, a band gap reduction of more than 100mV is associated with a dopant concentration of $10^{19}/cm^3$.[45]

The electronic conductivity of semiconductors, as expected from the band structure, can be generated by electrons of atoms of the basic substance in the crystal (intrinsic conductivity) as well as by electrons of impurity atoms or by the presence of defects (extrinsic conductivity). In intrinsic semiconductors at $T \gg 0\,K$, the generation of current carriers occurs as a result of the thermal excitation of some electrons from the valence band to the conduction band, with the corresponding thermal rupture of some chemical bonds. Simultaneously, an equal number of positively charged holes are created in the valence band. In an electric field, these holes behave like particles possessing a positive charge equal in absolute value to the charge of the electron. For extrinsic semiconductors, impurities and defects (which have energy levels located in the band gap) are classified as either donors or acceptors as shown in Fig. 1.1. Donors, usually located at energy levels slightly below the conduction band, give up excess electrons to the conduction band, thereby creating electron conductivity (*n*-type semiconductors). Acceptors, located at energy levels slightly above the valence band, capture valence electrons from atoms of the basic substance, producing hole conductivity (*p*-type semiconductors).

Similar to E_F for the energy levels in semiconductors, the energy levels of electrons in electrolytes associated with ions are characterized by the redox potential, E_{redox}. The redox potential describes the tendency of the species to give up or accept electrons and can be considered as the effective Fermi level of the solution.

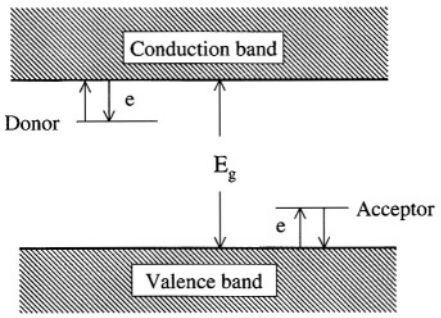

FIGURE 1.1. The energy band diagram for a semiconductor showing the lower edge of the conduction band (E_c), a donor level and an acceptor level within the forbidden gap (E_g), the Fermi level (E_F), and the top of the valence band (E_v).

When a semiconductor is brought into contact with an electrolyte, equilibrium is attained when the Fermi levels in the two phases become equal, that is, $E_F = E_{redox}$. In the case shown in Fig. 1.2 for an *n*-type semiconductor, where E_F of the semiconductor is higher than that in solution, electrons will flow from the semiconductor to the solution phase. The resulting excess charge in the solid semiconductor does not reside at the surface as it would in a metal, but instead is distributed in a region near the surface called the space charge region. The resulting electric field in the space charge region is shown by a bending of the bands. In the case of Fig. 1.2 where the semiconductor is positively charged with respect to the solution, the bands are bent upward (with respect to the level in the bulk semiconductor). On the other hand, an ionic layer on the solution side establishes an electric double layer between the solid surface and solution.

Thus, several charged layers exist at the interface of a semiconductor and an electrolyte. Figure 1.3 illustrates the different charged layers in the semiconductor/electrolyte region. On the semiconductor side there is the space charge layer associated with a band bending of V_s. The ionic layer on the solution side can be further divided. The charged layer lies between the solid and the plane at the position of the closest approach of mobile ions, called the outer Helmholtz plane (ohp). The Helmholtz layer is formed by ions attracted to the electrode surface by the excess charge in the space charge layer and also by the polar water molecules. In particular, the adsorption of H^+ and OH^- is an important process that determines the potential drop in the Helmholtz layer of many semiconductors. Between the outer Helmholtz plane and the solid surface there is also a layer (not illustrated in the diagram) containing solvent molecules and sometimes other specifically adsorbed species.[44] The locus of the specifically adsorbed ions is called the inner Helmholtz plane. The charge layer that extends from the outer Helmholtz layer into the bulk, called the Gouy–Chapman layer, is a region of solution with excess ions of one sign and its thickness depends on the electrolyte concentration. In concentrated electrolytes (>0.1 M) the contribution of the Gouy–Chapman layer is negligible and the potential drop on the solution side of the double layer can be expressed by the potential drop in the Helmholtz layer, V_H.

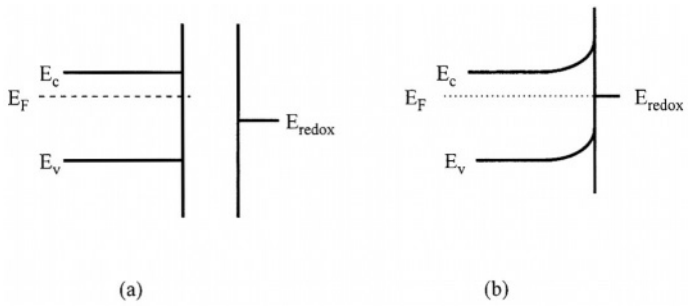

FIGURE 1.2. Representation of the formation of a semiconductor/electrolyte interface in the dark: (a) before the contact; (b) after the contact and electrostatic equilibration when the Fermi level in the semiconductor and the redox potential of the solution become equal.

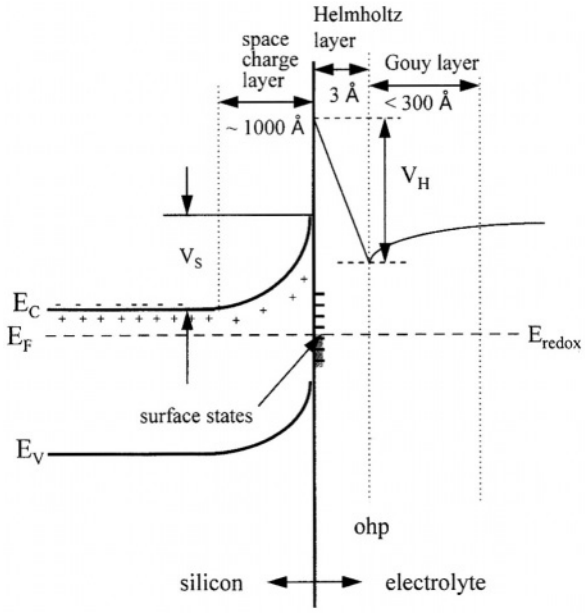

FIGURE 1.3. Schematic illustration of the double layers in the semiconductor/electrolyte interface at an equilibrium condition. V_s is the potential drop across the space charge layer and V_H is the potential drop across the Helmholtz double layer. After Morrison.[44]

The typical thickness of each of these three layers is indicated in Fig. 1.3. The actual thickness of these layers of the interface depends on the specific conditions in the system such as doping level of the semiconductor, electrolyte concentration, and bias condition. In many situations the presence of surface states due to adsorbates or surface defects is also important in determining the distribution of charge in the depletion region. Sometimes, electrode reaction processes can result in the formation of a solid surface phase such as oxides. Depending on its thickness and degree of homogeneity, it can drastically affect the electrical properties of the interface. As will be seen in the rest of this book, formation of oxide on silicon plays a critical role in many phenomena observed on silicon electrodes.

1.2.1. Energy Levels in Semiconductor

For a semiconductor at $T > 0\,\mathrm{K}$ a dynamic process exists: Electrons are constantly thermally excited from the valence band to the conduction band, corresponding to electron–hole generation. At the same time, some electrons are losing energy and falling back to the valence band, corresponding to electron–hole recombination. At equilibrium, there is a constant density of electrons in the excited states, the rate of generation equaling the rate of recombination.

The distribution of the electrons among the allowed energy states in the semiconductor crystal at thermal equilibrium is described by the Fermi–Dirac distribution function.[45] It is denoted by $f_D(E)$, which has the form

$$f_D(E) = 1/\{1 + \exp[(E - E_F)/kT]\} \tag{1.1}$$

where E_F is a reference energy called the Fermi energy. At $f_D(E) = 1/2$, meaning that the probability of a state being occupied by an electron for the energy level at the Fermi level is 1/2. For not too highly doped *n*-type material the Fermi level is well below the conduction band such that $(E_c - E_F) \gg kT$ and the Fermi function reduces to the simpler Maxwell–Boltzmann distribution function:

$$f_M = \exp[-(E - E_F)/kT]$$

The total density of electrons for not too heavily doped *n*-type material can then be found by the product of the density of allowed states in the conduction band, $g(E)$, and the probability that these states are filled and integrating over the conduction band:

$$\begin{aligned} n &= \int_{cb} f_M(E) g(E) dE \\ &= N_c \exp[-(E_c - E_F)/kT] \end{aligned} \tag{1.2}$$

Similarly, for moderately doped *p*-type material, the density of holes in the valence band is given by

$$p = N_v \exp[-(E_F - E_v)/kT] \tag{1.3}$$

where N_c and N_v are the effective densities of energy states at the bottom of the conduction band and at the top of the valence band, respectively. For large dopant concentrations $N_d \to N_c$ or $N_a \to N_v$ ($\sim 10^{19}/cm^3$ for silicon, these equations are no longer valid as the Fermi–Dirac distribution cannot be approximated by the Maxwell–Boltzmann distribution function and a different distribution function should be used.[45] At very high doping levels ($N_d \geq N_c$ or $N_a \geq N_v$) the semiconductor is degenerated because the Fermi level is within the conduction or the valence band. As a result, allowed states exist very near the Fermi level, just as in metal. Consequently, the electronic properties of heavily doped semiconductors become similar to those of metals.

Equations (1.2) and (1.3) essentially depict the chemical potential of the electrons, μ_e, and of the holes, μ_h, respectively:

$$\mu_e = E_F = E_c + kT \ln(n/N_c) \tag{1.4}$$

$$\mu_h = E_F = E_c - kT \ln(p/N_v) \tag{1.5}$$

At equilibrium, $\mu_e = \mu_h$, Eqs. (1.4) and (1.5) become

$$np = N_c N_v \exp[-(E_c - E_v)/(kT)] = n^2_i \tag{1.6}$$

where n_i is the intrinsic carrier density. Equation (1.6) means that at thermal equilibrium the product of the electron and hole densities for a given semiconductor and temperature is a constant. For silicon at room temperature, $n_i = 1.45 \times 10^{10}/cm^3$, which leads to $np = 2.1 \times 10^{20}/cm^3$.

For a doped silicon, depending on the dopant, one type of carrier is the majority carrier as its concentration far exceeds the other, even at low doping levels. For example, for donor concentration $N_d = 10^{15}/cm^3$, that is, $n = 10^{15}$ $p = 2.1 \times 10^5$, which is nearly 10 orders of magnitude below the majority carrier concentration.

In the neutral region of a semiconductor, the number of positive charges must be exactly balanced by the number of negative charges. This means

$$N_d + p = N_a + n \tag{1.7}$$

assuming all the dopant atoms are ionized. Thus, when there is only one dopant, either donor or acceptor, for n-type material $n \sim N_d$ ($n \gg N_a$, p), and for p-type material $p \sim N_a$.

1.2.2. Energy Levels in Electrolyte

The chemical potential of electrons for a redox couple is given by the Nernst equation

$$\varphi_{redox} = \varphi^0_{redox} + kT \ln(a_{ox}/a_{red}) \tag{1.8}$$

where ω^0_{redox} is the standard redox potential, and a_{ox} and a_{red} are the activities of the oxidized and reduced species of the redox couple, respectively.

The redox potential is generally referred to the standard hydrogen potential (SHE), which has an exactly defined energy, E_{she}, relative to the energy of the free electron in vacuum or at infinity. Thus, electrode potentials of redox couples can be expressed on the absolute energy scale according to

$$E_{redox} = E_{she} - e\varphi_{redox} \tag{1.9}$$

The negative sign of φ_{redox} in the equation is due to the different signs in the conventional and the absolute electron energy scales. E_{she} has been found to be about –4.50 eV referred to the vacuum level so that the electron energy of any redox couple is[86]

$$E_{redox} = -4.5\,eV - e\varphi_{redox} \tag{1.10}$$

1.2.3. Distribution of Energy Levels in Electrolyte

The redox potential reflects the average energy levels at equilibrium of all the individual redox species, both reduced and oxidized forms. It can be further divided into two levels: the energy level of the reduced species, E_{red}, and the energy level of the oxidized species, E_{ox}, with $E_F = 1/2(E_{ox} + E_{red})$. E_{ox} is the most probable energy level for the oxidizing species and E_{red} is the most probable energy level for the reducing species. In a liquid electrolyte, the energy levels of individual ions tend to fluctuate due to the solvation effect of the polar solvent molecules surrounding the ions. The dipoles associated with the solvent molecules constantly move to/away and rotate around the ions, causing thermal fluctuation in the polarization.

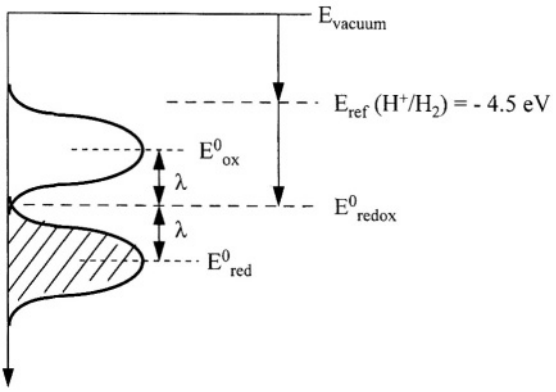

FIGURE 1.4. Electron energy levels of a redox couple with respect to the standard hydrogen electrode and the vacuum level.

The energy level, E_{ox}, and energy level, E_{red}, can be related to the redox energy level, E_{redox}, by a quantity called the reorientation energy $\lambda = 1/2(E_{ox} - E_{red})$, which is determined by the relaxation process involved in the regrouping and reorientation of the solvation shell after electron transfer between the oxidized and reduced states. The value of λ can be experimentally determined and is on the order of 0.5 to 1 eV.[44,876] The individual energy states are distributed over a certain energy range and can be described by the density of occupied states D_{red} and empty states D_{ox}. Assuming a Gaussian type of distribution and a harmonic oscillation for the solvation shell, D_{red} and D_{ox} can be described by

$$D_{red} = D^0_{red}\exp\left[-(E - E_{red})^2/(4kT\lambda)\right] = D^0_{red}\exp\left[-(E - E_{redox} - \lambda)^2/(4kT\lambda)\right] \quad (1.11)$$

$$D_{ox} = D^0_{ox}\exp\left[-(E - E_{ox})^2/(4kT\lambda)\right] = D^0_{ox}\exp\left[-(E - E_{redox} + \lambda)^2/(4kT\lambda)\right] \quad (1.12)$$

where D^0_{ox} and D^0_{red} are normalizing factors. Figure 1.4 schematically illustrates the energy levels of the reduced and oxidized species and their distribution functions.[86]

1.2.4. Energy Levels at Semiconductor/Electrolyte Interface

For a semiconductor/electrolyte interface, the equilibrium condition requires the Fermi levels of the semiconductor and solution to be equal. To achieve equilibrium, electrons cross the interface, which changes the charge distribution and the potential in the interface region until $E_F = E_{redox}$.[44]

The band structure at equilibrium for the interface region is illustrated in Fig. 1.5. The band bending V_s is the potential drop in the space charge layer. The potential drop on the solution side is measured by V_H, the Helmholtz potential. E_{cs} and E_{vs} are the conduction band edge and the valence band edge at the surface, respectively. V_m is the measured potential. Normally, the band edge positions at the surface are equal for *p*- and *n*-type materials because the same Helmholtz potential is expected for the two

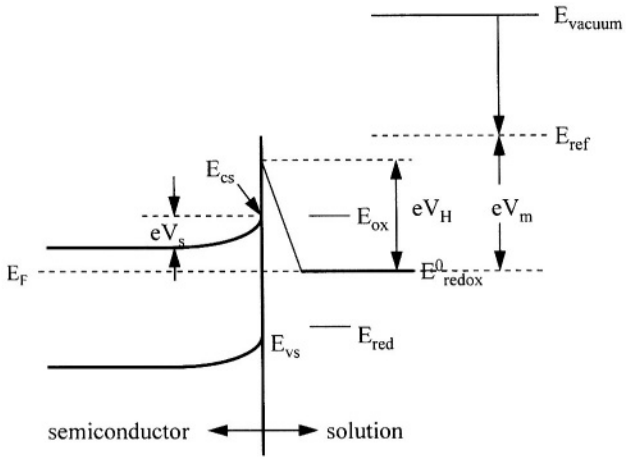

FIGURE 1.5. Illustration of the energy levels for a semiconductor/electrolyte interface. The various quantities are described in the text.

materials. The magnitude of the Helmholtz potential is determined by the adsorption/desorption processes, which in many situations is a function of pH. By adjusting the pH of the solution, V_H can be made zero and the pH at $V_H = 0$ is called the point of zero charge (pzc).

The measured potential V_m, and thus E_F and V_s, can be varied through external polarization. V_m is the applied potential when the electrode is externally polarized and is the open-circuit potential without external polarization. When the semiconductor has no excess charge, there is no space charge region and the bands are not bent. The electrode potential under this condition is called the flatband potential V_{fb}. The flatband potential is an important quantity for a semiconductor electrode because it connects the energy levels of the carriers in the semiconductor to those of the redox couple in the electrolyte and it connects the parameters that can be experimentally determined to those derived from solid-state physics and electrochemistry. It can generally be expressed as

$$V_{fb} = V_m - V_s \tag{1.13}$$

The value of the flatband potential of a semiconductor is quantitatively related to its electron affinity χ ($\chi = 4.05\,eV$ for silicon):[880,953]

$$E_{cs} = E_{ref} - \chi - eV_H = E^0_{cs} - eV_H \tag{1.14}$$

where E^0_{cs} is defined as the energy of the conduction band at the point of zero charge (pzc), that is, when the potential drop in the Helmholtz layer is zero. This means that the electron affinity in the electrolyte equals the band edge plus the energy level of the reference level on the absolute scale at the point of zero charge. Figure 1.6

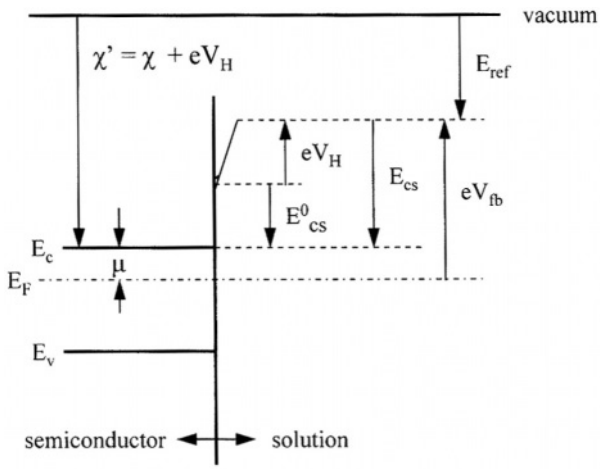

FIGURE 1.6. The energy levels and double layer potentials for the semiconductor/electrolyte interface at a flatband condition.

schematically illustrates the relation among the different potentials and energy levels. The conduction band edge is related to the flatband potential according to the following equation

$$eV_{fb} = \mu - E^0_{cs} + eV_H \tag{1.15}$$

Therefore, by measuring the flatband potential at pzc, one can determine the energy level of the semiconductor band in an electrolyte relative to the absolute scale or the vacuum scale. The pzc of a silicon electrode in aqueous electrolyte is similar to that of SiO_2, at about pH 2.2, since the silicon surface is generally covered with a thin layer of oxide.[716,903]

1.3. POTENTIAL AND CHARGE DISTRIBUTION IN SPACE CHARGE LAYER

1.3.1. Carrier Density in Space Charge Region

The charge distribution within the space charge layer can be quantitatively described by the Poisson equation:

$$d^2V/dx^2 = e/(\varepsilon\varepsilon_0)[N_d - N_a - n(x) - p(x)] \tag{1.16}$$

where x is the distance from the surface and N_d and N_a are the donor and acceptor densities, respectively. The electron and hole densities, $n(x)$ and $p(x)$, in the absence of a current, follow the Boltzmann distribution:[962]

$$n(x) = n_0 \exp[-eV/(kT)] \tag{1.17}$$

$$p(x) = p_0 \exp[eV/(kT)] \tag{1.18}$$

where $n_0 = N_d$ and $p_0 = N_a$ are bulk electron and hole densities, respectively, and $V = \varphi_{bulk} - \varphi(x)$. At the surface where $x = 0$,

$$n(x)_{x=0} = n_s = n_0 \exp[-eV_s/(kT)] \tag{1.19}$$

$$p(x)_{x=0} = p_s = p_0 \exp[eV_s/(kT)] \tag{1.20}$$

Three types of space charge layers, namely, depletion layer, accumulation layer, and inversion layer, may occur in a semiconductor depending on the bias and equilibrium conditions as shown in Fig. 1.7.

1.3.2. Depletion Layer

When the surface region is depleted of majority carriers, due to positive band bending for *n* type or negative band banding for *p* type, a depletion layer is formed as shown in Fig. 1.7(a). The depletion layer has no mobile carriers but has immobile charges associated with the ionized dopants. The Poisson equation, Eq. (1.16) for *n*-type material, can be reduced to

$$d^2V/dx^2 = -eN_d/(\varepsilon\varepsilon_0)\{\exp[-eV/(kT)] - 1\} \tag{1.21}$$

On integration with dV/dx $(V = 0) = 0$ one obtains

$$(dV/dx)^2 = 2eN_d/(\varepsilon\varepsilon_0)\{V + (kT/e)\{\exp[-eV/(kT)] - 1\}\} \tag{1.22}$$

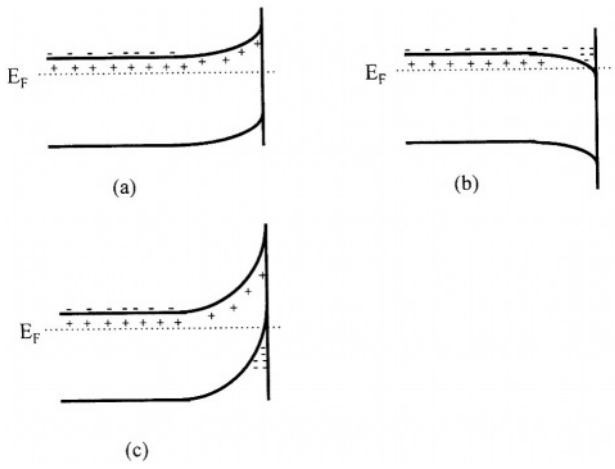

FIGURE 1.7. Types of space charge layers on an *n*-type semiconductor surface. (a) Depletion layer; (b) accumulation layer; (c) inversion layer. After Morrison.[44]

At the surface where $V = V_s$, the factor $\exp(-eV_s/kT)$ is negligible for a reasonable value of V_s. From Gauss's law we have

$$dV/dx(V = V_s) = Q_{sc}/(\varepsilon\varepsilon_0) = eN_d x_0/(\varepsilon\varepsilon_0) = \{2eN_d/(\varepsilon\varepsilon_0)[V_s - (kT/e)]\}^{1/2} \quad (1.23)$$

where Q_{sc} is the total charge in the space charge layer per unit electrode surface area and x_0 is the point in the semiconductor where the field is zero. Since the capacitance of the space charge layer $C_{sc} = dQ_{sc}/dV_s$, differentiating Eq. (1.23) with respect to V_s an expression for C_{sc} is obtained:

$$\begin{aligned} C_{sc}^{-2} &= (2/e\varepsilon\varepsilon_0 N_d)(V_s - kT/e) \\ &= (2/e\varepsilon\varepsilon_0 N_d)(V_m - V_{fb} - kT/e) \end{aligned} \quad (1.24)$$

Equation (1.24) is the much-used Mott–Schottky equation, which relates the space charge capacity to the surface barrier potential V_s. Two important parameters can be determined by plotting C_{sc}^{-2} versus V_{app}: the flatband potential V_{fb} at $C_{sc}^{-2} = 0$ (where $V_s = 0$) and the density of charge in the space charge layer, that is, the doping concentration N_d.

1.3.3. Accumulation Layer and Inversion Layer

In the case of an accumulation layer, for example, when electrons are injected into (instead of extracted from) an *n*-type sample, or holes are injected into (instead of extracted from) on a *p*-type sample, the surface charge region has an excess of the majority carriers. For *n*-type materials, according to Eq. (1.16),

$$d^2V/dx^2 = [-en_0/(\varepsilon\varepsilon_0)]\{\exp[-eV/kT] - 1\} \quad (1.25)$$

where the first term represents the contribution of electrons in the conduction band and the second represents the contribution of immobile positive ions. An accumulation layer can be formed, for example, on an *n*-type material by applying a sufficiently large negative voltage on the semiconductor relative to the solution. If the band bending is such that the Fermi energy moves into the band, a "degenerate surface" is formed, which marks the transition from semiconducting behavior to metallic behavior. The thickness of an accumulation layer is typically on the order of 100 Å. Such a layer as thin as 3 Å has been found at *n*-Si in acetonitrile.[941]

Under a depletion condition, an inversion layer is formed when near the surface the minority carriers accumulate and are in equilibrium with those in the bulk (that is, the consumption rate of the carriers in the electrochemical reactions is low). When an inversion layer occurs, the density of minority carriers near the surface may exceed that of the bulk majority carriers. Under such a condition, when $n(x) < p(x)$ within the space charge layer equation, the Poisson equation [Eq. (1.16)] becomes

$$d^2V/dx^2 = e/(\varepsilon\varepsilon_0)\{N_d + p_0 \exp[eV/(kT)]\} \quad (1.26)$$

where the first term represents the immobile ions and the second term represents the density of minority carriers, which becomes comparable to the first term at relatively

large positive potential values. The thickness of the inversion layer is on the same order of magnitude as that of the accumulation layer, namely, about 100 Å. An inversion layer does not usually occur at an electrode surface because the electrochemical reactions generally consume quickly the minority carriers and prevent their accumulation in the surface region. An inversion layer has been found to form on *n*-Si electrode in a solution of CH_3OH + 1 M $LiClO_4$ containing redox couples of high potential values.[587]

The capacitances for the accumulation layer and inversion layer are respectively given by

$$C_{sc} = [e^2 N_d \varepsilon\varepsilon_0/(2kT)]^{1/2} \exp[-eV_s/(2kT)] \tag{1.27}$$

$$C_{sc} = [e^2 p_0 \varepsilon\varepsilon_0/(2kT)]^{1/2} \exp[eV_s/(2kT)] \tag{1.28}$$

The change of capacitance of the charged layer in the surface region of the semiconductor with band bending V_s is illustrated schematically in Fig. 1.8. For negative values of V_s the surface is in an accumulation and the capacitance is very large because the thickness of the accumulation layer is thin. As V_s becomes positive, the capacity decreases as the thickness of the space charge layer increases. When an inversion layer forms at a large V_s, the surface has an excess of minority carriers. In this case the mobile minority carriers are mostly located near the surface so that the thickness is small compared with the depletion layer thickness and the capacitance increases again. In the case when minority carriers are consumed by electrode reactions and do not accumulate at

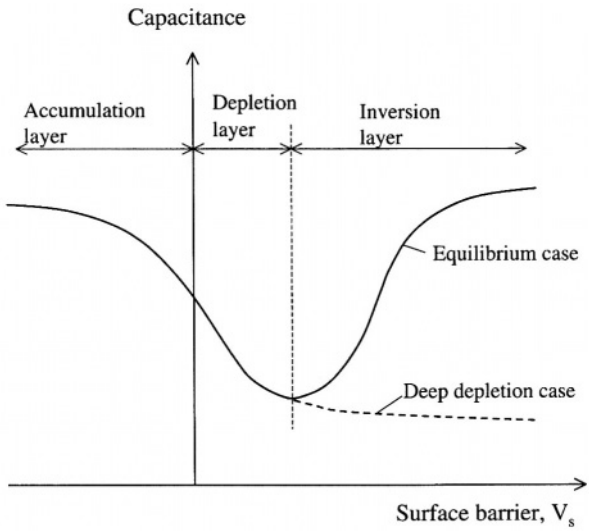

FIGURE 1.8. Variation of the space charge capacity with a band bending of V_s on an *n*-type semiconductor with an accumulation layer or an inversion layer. Mobile carriers are at the surface in the inversion so the capacity is high. If minority carriers do not accumulate at the surface at a large band bending, a "deep depletion" curve results. After Morrison.[44]

the surface, equilibrium is not established and a deep depletion layer is formed as shown by the dashed line in Fig. 1.8.

1.3.4. Helmholtz Double Layer

The potential drop in the Helmholtz layer is defined as

$$V_H = \varphi_1 - \varphi_2 = Q_H/\varepsilon\varepsilon_0 \tag{1.29}$$

where φ_1 is the potential at the solid surface and φ_2 is the potential at the ohp.

The charge on the solution side of the Helmholtz layer originates from the accumulation of ions at the ohp, whereas on the solid side it can arise in three forms: an accumulation of free charge, free charge trapped from the solid onto surface states, and adsorbed ions.[44] For nondegenerated semiconductors, V_H is primarily determined by adsorption/desorption processes between the surface and the electrolyte. The contribution from electron transfer between the surface and the bulk of the semiconductor is negligible. This is because the amount of charge captured by the surface associated with this transfer is on the order of $10^{12}/cm^2$ or less ($Q_{sc} = qN_{sc}x_0$), which is very small in comparison with the amount of charge (on the order of $10^{15}/cm^2$) associated with the adsorption/desorption processes on the surface. Thus, for non heavily doped semiconductor the applied potential variation can be considered to drop entirely in the space charge layer and the Mott–Schottky equation can be used for determination of the flat-band potential. The contribution to the Helmholtz layer by charge transfer becomes more important for degenerated semiconductors, which can accommodate more charge in the bands near the surface.

When the charge on the solid surface is determined by the specific adsorption of H^+ and OH^-, which is the case for many semiconductors, V_H is determined by the reaction

$$H_3O^+ = H_s^+ + H_2O \tag{1.30}$$

where H_s^+ is the adsorbed H^+ on the surface. At equilibrium the concentration of H_s^+ can be expressed as

$$[H_s^+]/[H_3O^+] = \exp(-\Delta G/kT) = A\exp(-eV_H/kT) \tag{1.31}$$

where A is a constant. Assuming the double layer capacitance C_H is independent of V_H, we obtain

$$e[H_s^+] = C_H V_H \tag{1.32}$$

Equations (1.31) and (1.32) indicate that $[H_s^+]$, which changes linearly with V_H, will vary slowly compared with $[H_3O^+]$, which changes exponentially with V_H. As an approximation we have

$$eV_H = B + kT\ln[H_3O^+] = B - 0.059\ \text{pH} \tag{1.33}$$

which shows that the Helmholtz potential varies by 60 mV per pH unit.

The Helmholtz capacity of a metal electrode is typically on the order of $10\,\mu F/cm^2$,[44] which is much greater than the value for a silicon electrode.[848] It has been reported that the Helmholtz layer capacitance of silicon in $0.1\,M\ K_4Fe(CN)_6 + 0.5\,M$ KC1 aqueous solution is about $3\,\mu F/cm^2$.[94] In 0.1 M tetrabutylammonium perchlorate (TBAP) in acetonitrile it is found to be about $1.5\,\mu F/cm^2$.[486] A larger C_H value, $22\,\mu F/cm^2$, has been found for deep accumulation of a silicon in acetonitrile and the value varies with the accumulated charge.[941]

1.3.5. Surface States

Surface states are the electronic energy levels that are located at the surface and are capable of transferring charges with the solid and solutions. The surface states of a clean surface, the dangling bonds resulting from the termination of the bulk structure at the surface, are called intrinsic states. For silicon the dangling bonds on the surface in solutions are generally terminated by hydrogen and other species so that there are very few intrinsic surface states.

In addition to the intrinsic states, there are also Lewis sites and adsorbed electroactive species. Lewis sites arise from the acid/base properties of the surface. A Lewis acid site is a site attractive to electron pairs from an adsorbing molecule and a Lewis basic site is able to donate electron pairs to an adsorbing molecule. For example, a Lewis acid site M or a basic site N may adsorb a OH^- ion or a H^+ from water, respectively:

$$M + OH^- = M{:}OH^- \tag{1.34}$$

$$N + H^+ = N{:}H^+ \tag{1.35}$$

Adsorption at acidic sites M causes the solution to become acidic and adsorption of H^+ on Lewis basic sites causes the solution to become basic. Lewis sites are important in two ways: they contribute to the Helmholtz double layer, and they result in chemical adsorption and passivation of the intrinsic active surface sites. The surface of silicon is dominated by basic Lewis sites as manifested by the strong hydrogen adsorption. But the associated surface states are not active because they are located energetically in the valence band.[99]

Adsorbed species other than hydrogen and hydroxyl ions that are able to give up or accept electrons are also surface states. The reaction intermediates that are able to act as donors or acceptors through charge transfer reactions can be viewed as surface states. As will be described in more detail in the section on anodic behavior, partially oxidized silicon atoms, Si^{n+} $(n < 4)$, i.e., the reaction intermediates, act as transient surface states and play an important role in a range of electrode processes.

Surface inhomogeneity such as vacancies, steps, kink sites, emergent dislocations, and foreign elements in the lattice has a significant effect on adsorption, bonding energy, and redox reactions. Such surface heterogeneity causes the energy levels of a specific type of surface state to appear as bands because the exact chemical nature of

the surface defects will vary from point to point. In some cases electrode reaction can result in the formation of bulk phases, for example, oxide films. The states and charges that exist in the oxide and/or at the semiconductor/oxide interface are another form of surface state (or interface state).

There are two kinds of surface states with respect to the energy levels of states under filled or empty conditions: one kind has different energy levels when the surface states are filled or emptied due to a reorganization effect, and the other, showing no reorganization effect, has negligible change in their energy levels when the states are filled or emptied. For example, according to Chazalviel and Rao,[83] on a silicon surface the surface states induced by deposited gold atoms belong to the second kind whereas those associated with a surface oxide formed by the reaction between silicon and water belong to the first kind.

It is generally difficult to quantitatively describe the surface states of a semiconductor electrode considering the great diversity of surface states.[486] In general, surface states are energetically distributed in the band gap of the semiconductor with a density expressed as N_{ss}/m^2eV and the associated charge density is a function of V_s. Under some idealized conditions such as when the surface states are uniformly distributed in energy or are localized at a single energy level, the charge density associated with surface states Q_{ss} can be quantitatively related to band bending V_s. For example, for a uniform distribution of acceptor surface states centering around an energy of E_0 (when the states are filled to an energy E_0 there is no net surface charge), Q_{ss} can be expressed as[270]

$$Q_{ss} \simeq eN_{ss}(E_0 - eV_s - E_F)/E_0 \tag{1.36}$$

where N_{ss} is the total number of surface states per square centimeter. Note that when $eV_s = E_0 - E_F$, $Q_{ss} = 0$.

In the case of acceptor states at a single energy level, we have

$$Q_{ss} \simeq eN_{ss}/\{1 + g_{ss}^{-1} \exp[-(E_{ss} - 2V_s - E_F)/kT]\} \tag{1.37}$$

where g_{ss} is the degeneracy of the energy level.[270]

The capacitance of surface states, corresponding to the variation of the charge stored in the surface states with V_s, is

$$C_{ss} = dQ_{ss}/dV_s \tag{1.38}$$

The surface state capacitance C_{ss} is different from the space charge layer capacitance C_{sc} and the Helmholtz layer capacitance C_H in that there is in general no distance associated with the surface state capacity.

Measurement of capacitance as a function of potential is most commonly used for evaluation of the nature of surface states. For example, when the surface states are energetically close to the conduction band they can be filled or emptied by electron transfer with the conduction band:

$$SS^0 + e(CB) \rightleftharpoons SS^- \tag{1.39}$$

where SS^0 is the empty state and SS^- the filled state. When the interaction with the solution can be neglected, the occupancy of the surface states is determined by the Fermi level and the surface state capacitance can be expressed as[808]

$$C_{ss}(\omega) = e^2/kT\left\{k_1k_2n_s/\left[\omega^2 + (k_1n_s + k_2)^2\right]\right\}N_{ss} \tag{1.40}$$

where n_s is the surface electron concentration, ω the frequency of the potential or current modulation, and k_1 and k_2 the rate constants for the forward reaction and reverse reaction described by Eq. (1.39). At low frequency where $\omega^2 \ll (k_1n_s + k_2)^2$, C_{ss} exhibits a maximum as a function of potential

$$C_{ss}(\max) = N_{ss}e^2/(4kT) \tag{1.41}$$

from which the density of surface states can be determined.

1.3.6. Fermi Level Pinning

The total charge on the solid side of the semiconductor/electrolyte interface equals $Q_{ss} + Q_{sc}$. When surface states are present and their capacitance is significantly larger than that of the space charge layer, that is, $Q_{ss} > Q_{sc}$, Fermi level pinning by the surface states occurs.[270] Figure 1.9 illustrates the effect of dopant concentration and surface state density on the magnitude of surface state charges and space charge layer charges. It can be seen that for a doping of $10^{16}/cm^3$ a surface state density on the order of $10^{13}/cm^2$, which is about 1% of the surface atomic density, can result in $Q_{ss} > Q_{sc}$. When the Fermi level is pinned, the change of potential will mainly occur in the Helmholtz layer rather than in the space charge layer as in the case without Fermi level pinning.

As a consequence of Fermi level pinning, the Schottky barrier height $\phi = e(V_{redox} - V_{cs})$ at the semiconductor/electrolyte interface becomes constant with respect to redox couples of different V_{redox} values. Fermi level pinning, which results in a constant barrier height value, has been found to occur at the *n*-Si/acetonitrile interface containing different redox couples.[486,935]

1.3.7. Equivalent Circuit and Capacitance of Semiconductor/Electrolyte Interface

The electrical nature of the semiconductor/electrolyte interface region can be described by an equivalent circuit of an array of resistors and capacitors arranged according to the physical structure of the region. Figure 1.10 illustrates a typical equivalent circuit of a semiconductor/electrolyte interface including the effect of the space charge layer, Helmholtz layer, surface states, and electrolyte resistance. On application of a voltage change of dV across the interface region, charge in the form of electrons, holes, and ions will move in the corresponding layers, which can be characterized by the capacitances of these layers.

The total potential change ΔV is divided between the space charge layer and the Helmholtz layer:

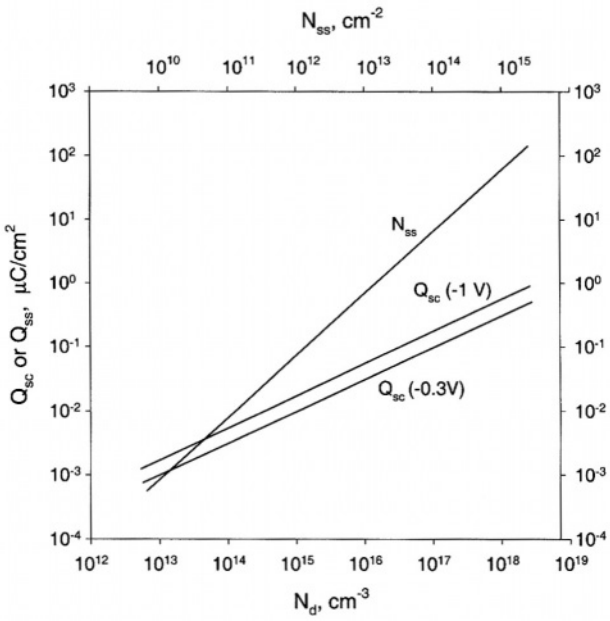

FIGURE 1.9. Surface charge in an *n*-type semiconductor: space charge, Q_{sc}, at various doping levels N_d at ΔV_s of −0.3 and −1.0 V; and surface state charge, Q_{ss}, as a function of surface state density, N_{ss}, assuming half-occupancy. Potential drop across the Helmholtz layer is $\Delta V_H = 0.085q$ (μC/cm^2) assuming $\varepsilon_H = 4$ and $d = 3$ Å. (Reprinted with permission from Bard *et al.*[270] © 1980 American Chemical Society.)

$$\Delta V = \Delta V_{sc} + \Delta V_H \tag{1.42}$$

By charge neutrality,

$$Q_{soln} = Q_{sc} + Q_{ss} \tag{1.43}$$

The overall capacity C is related to each of the capacities according to

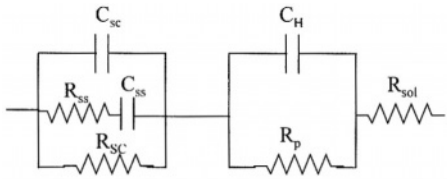

FIGURE 1.10. An equivalent circuit for the electrical components at the semiconductor/electrolyte interface in the absence of an oxide. R_{sol} represents the resistance of the electrolyte; C_H is the capacity of the Helmholtz double layer and R_p is the charge transfer resistance; C_{sc} and R_{sc} are the capacitance and resistance associated with the space charge layer in the semiconductor; C_{ss} and R_{ss} are the capacitance and resistance of the surface states.

$$1/C = \Delta V/\Delta Q = \Delta V_s/(\Delta Q_{sc} + \Delta Q_{ss}) + \Delta V_H/\Delta Q_{soln} \tag{1.44}$$

Using Eq. (1.42), we obtain

$$C^{-1} = (C_{sc} + C_{ss})^{-1} + C_H^{-1} \tag{1.45}$$

Thus, C_H acts as a capacitor in series with the parallel combination of C_{sc} and C_{ss}. In many situations because of the presence of an oxide film on the surface, particularly for silicon in non-HF electrolytes, an extra RC component is involved due to the charges and states in the oxide and at the semiconductor/oxide interface. The characteristics of these charges and states are discussed in Chapter 3 on silicon oxide.

In the absence of an interfacial phase such as an oxide, any potential drop is across the space charge layer or/and the Helmholtz layer, that is, $\Delta V = \Delta V_s + \Delta V_H$. The potential distribution across the space charge layer and in the Helmholtz layer, in the absence of surface states and interfacial layer when $Q_{sc} = Q_H$, is determined by the doping level, band bending, and the capacitance of the Helmholtz layer. The partitioning of the potential can be measured in terms of the potential in the space charge layer relative to the total potential drop across the interface region by a partitioning coefficient, $\gamma_{integral}$:[848]

$$\gamma_{integral} = V_s/(V - V_{fb}) \tag{1.46}$$

where $\gamma_{integral}$ may vary from 0 to 1. The potential partitioning can also be measured by the differential form in terms of the fraction of the applied potential change dV across the space charge layer:

$$\gamma_{differ} = dV_s/dV = C_{sc}/(C_H + C_{sc}) \tag{1.47}$$

The two coefficients are different in that $\gamma_{integral}$ quantifies the potential partitioning of the total potential drop while γ_{differ} reflects the partitioning as a result of potential change. Thus, $\gamma_{integral}$ characterizes the steady condition of the interface or the dc condition and γ_{differ} characterizes the transient condition or the ac condition. Figure 1.11, as calculated by Oskam *et al.*,[848] shows the change of these two coefficients as a function of applied potential. It can be noted that under a negative potential corresponding to an accumulation band bending, the coefficients become rather small indicating that C_{sc} becomes comparable to C_H and there is a significant drop of applied potential across the Helmholtz layer. Because of the shift in potential drop from the space charge region to the Helmholtz layer, there is a maximum band bending above which all the applied potential drops in the Helmholtz layer. For $C_H = 1\,\mu F/cm^2$ the maximum band bending in the accumulation regime is about 300 mV.

1.3.8. Flatband Potentials

Flatband potential is a very important parameter for characterization of a semiconductor/electrolyte interface as it correlates the band edges to the redox potentials in the electrolyte. It is most commonly determined by measuring the capacitance as a

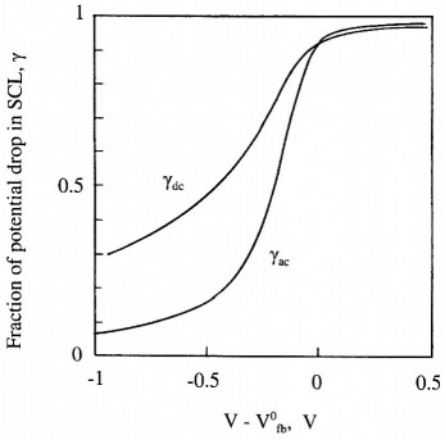

FIGURE 1.11. The fraction of the applied potential dropped over the space charge layer for dc conditions, γ_{dc}, and for ac conditions, γ_{ac}, versus band bending with $C_H = 1\,\mu F/cm^2$ and $N_d = 10^{15}/cm^3$. After Oskam *et al.*[848] (© 1998, Reprinted by permission of John Wiley & Sons, Inc.)

function of potential. Flatband potential can also be estimated by measurement of the onset potential for photocurrent.

In an idealized case when the effect of the Helmholtz layer can be neglected, i.e., when $C_H \gg C_{sc}$, there is a negligible amount of surface states, that is, $C_{ss} \ll C_{sc}$. The total capacitance of the semiconductor/electrolyte interface described by Eq. (1.45) becomes $C \approx C_{sc}$. The interface capacitance as a function of the electrode potential then follows the Mott–Schottky equation:

$$1/C_{sc}^2 = (2/e\varepsilon\varepsilon_0 N_d)(V_s - kT/e) \tag{1.24}$$

A plot of $1/C_{sc}^2$ versus potential V is linear and thus the potential where the line intersects the potential axis yields the value of V_{fb}, and the slope yields the value of doping level N_d. The resulting flatband potential can be used to determine the potential of the conduction band edge V_{cs}, at the surface

$$V_{cs} = V_{fb} - kT/e \ln(N_c/N_d) \tag{1.48}$$

where N_c is the effective density of states in the conduction band. The Schottky barrier height is $\phi_B = e(V_{redox} - V_{cs})$.

In practice, the determination of flatband potential according to the Mott–Schottky equation can be affected by a number of factors, e.g., high doping concentration (i.e., $C_H \gg C_{sc}$ is not valid), the presence of a high density of surface states (i.e., $C_{ss} \ll C_{sc}$ is not valid), and the influence of diffusion-controlled processes.[44,274,935] For highly doped semiconductors, the effect of potential drop in the Helmholtz layer, even without the influence of surface states, can be significant.[274] Figure 1.12 indicates that a significant fraction of the external potential variation can be dropped in the Helmholtz layer for moderately and highly doped semiconductors especially near the flatband potential at which the capacitance of the space charge layer is the largest. Because of the contribution from the Helmholtz layer, the Mott–Schottky plot tends to be linear

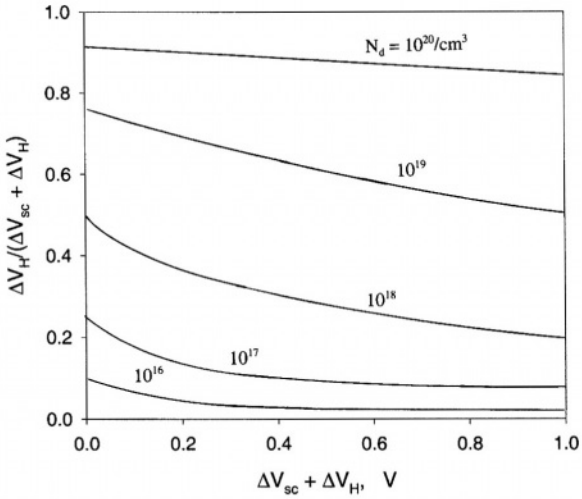

FIGURE 1.12. The ratio of the potential in the Helmholtz layer to the total potential change as a function of the total potential change for different doping levels; $\varepsilon = 173$ and $C_H = 10\,\mu F/cm^2$. After Uosaki and Kita.[274] (Reproduced by permission of The Electrochemical Society, Inc.)

at relatively large bias but curved at small bias. The potential intersection of the Mott–Schottky plot, considering the effect of the Helmholtz layer resulting from high doping concentration, is given by

$$V_{intersect} = V_{fb} + kT/e - e\varepsilon\varepsilon_0 N_d/(8\pi C_H^2) \tag{1.49}$$

where a voltage shift from V_{fb} by an amount of $e\varepsilon\varepsilon_0 N_d/(8\pi C_H^2)$ is due to the potential drop in the Helmholtz layer.[273]

When there is a high density of surface states, the Fermi level can become pinned within the potential range in which the surface states lie. For a monoenergetic surface state, the intersect of the Mott–Schottky plot is shifted from its true flatband potential value as illustrated in Fig. 1.13.[44] In this case the applied potential is dropped in the Helmholtz layer and the capacitance does not change with applied potential. When the surface states are fully occupied or fully empty, the capacitance starts to change again with applied potential according to the Mott–Schottky relation. The slope of the central region in Fig. 1.13 is related closely to the density of surface states. The higher the slope is in the central region, the lower the density of states. An infinite density of states will lead to a zero slope.[44] Assume Q_d is the positive charge when the donor surface states are fully empty and Q_a is the negative charge when the acceptor surface states are fully occupied. The effect of the donor surface states on the flatband potential can be described by $V''_{fb} = V_{fb} + Q_d/C_H$ and that of the acceptor surface states by $V'_{fb} = V_{fb} - Q_a/C_H$.

The presence of an oxide layer on the silicon surface can also cause the flatband potential to shift. The potential drop across an oxide is on the order of $\Delta V = E_s d\varepsilon/\varepsilon'$, where ε and ε' are the dielectric constants of silicon and silicon oxide, respectively, d

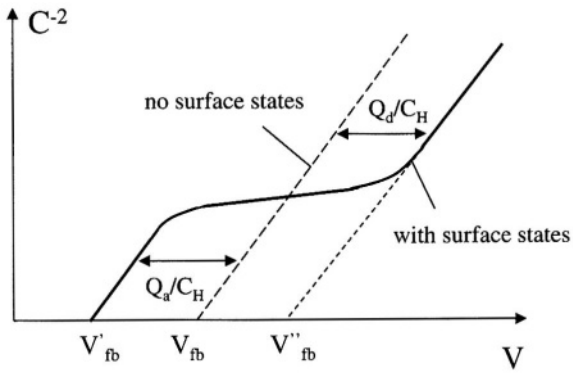

FIGURE 1.13. The influence of monoenergetic surface states on Mott–Schottky plot with V_{fb} shifted to a higher or lower electrode potential depending on the charge on the states, after Morrison.[44]

the oxide thickness, and E_s the surface field.[717] For a thin oxide film of about 20 Å, $E_s = 10^5$ V/cm, and $\varepsilon/\varepsilon' = 2$ (the dielectric constant of native oxides is much larger than that of thermal oxide due to inclusion of water molecules), $\Delta V = 40$ mV. Thus, the presence of a thin oxide film such as the native oxide has in general a weak effect on the determination of flatband potential when the oxide is not associated with a high density of surface states.

1.4. KINETICS OF CHARGE TRANSFER

1.4.1. Basic Theories

Electrochemical reactions on a semiconductor electrode involve charge transfer between the species in the solution and charge carriers in the semiconductor. The basic assumption in the theories of the kinetics of charge transfer reactions is that the electron transfer is most probable when the energy levels of the initial and final states of the system coincide.[44,79] This requires that the vibration of molecules and their surrounding solvation shell be slow compared with the actual electron transfer between the electrode and redox system in the solution. Thus, the efficiency in the redox reaction processes is primarily controlled by the energy overlap between the quantum states in the energy bands of the semiconductor and the donor or acceptor levels in the reactants in the electrolyte. Often, the overlap between the electronic states in the semiconductor and the levels in the electrolyte is unfavorable, and radical surface states that located within the band gap become the most important for the charge transfer.

In an ideal case when surface states are absent and charge transfer proceeds directly between the energy levels in the bands and in the solution, according to Gerischer,[79] an anodic current involving an electron transfer from a molecule in the electrolyte to the electrode and a cathodic current involving an electron transfer from the electrode to a molecule in the electrolyte are given by

$$i_a = F \cdot Z \cdot c \int_{-\infty}^{+\infty} \kappa(E) \cdot N_{em}(E) D_{red}(E) dE \tag{1.50}$$

$$i_c = F \cdot Z \cdot c \int_{-\infty}^{+\infty} \kappa(E) \cdot N_{oc}(E) D_{ox}(E) dE \tag{1.51}$$

where $Z \cdot c$ is the number of molecules that reach the electrode surface, $\kappa(E)$ the transition coefficient which strongly depends on the distance of the reacting molecules from the surface, $N_{em}(E)$ and $N_{oc}(E)$ the densities of empty states and occupied states in the electrode, respectively, and $D_{red}(E)$ and $D_{ox}(E)$ the densities of occupied energy states and empty states in the electrolyte defined by Eqs. (1.11) and (1.12). The anodic current, i_a, consists of an electron transfer current into the conduction band, i_a^c, and i_a^v corresponding to a transfer into the valence band. Similarly, the cathodic current, i_c, consists of the contribution from the conduction band, i_c^c, and from the valence band, i_c^v. The contributions of conduction and valence bands to the anodic and cathodic currents are illustrated in Fig. 1.14.

The magnitude of the currents depends on the overlap between the levels in the semiconductor bands and those in the solution. For a material having a large band gap ($E_g > 1.3\,eV$) the overlap generally involves only the conduction band or the valence band, whereas for a small band gap there may be overlap of a redox couple with both the conduction band and the valence band so that the contributions from both bands, i.e., i^c and i^v, are significant. In general, the electron transfer probability is mainly determined by the energy correlations between the band edges of the semiconductor, E_c and E_v, and principal energy levels of the redox couple, E_{red}^0 and E_{ox}^0. If E_{red}^0 is closer to E_c than E_{ox}^0 to E_v, electron transfer in the conduction band is the more likely process. In the opposite case, electron transfer in the valence band is more likely.

In the case of the conduction band process, the density of empty states, $N_{em} = N_c$ in the conduction band can be taken to be constant because only a few of them are occupied so that using Eq. (1.11) the conduction band anodic current, i_a^c, can be expressed as

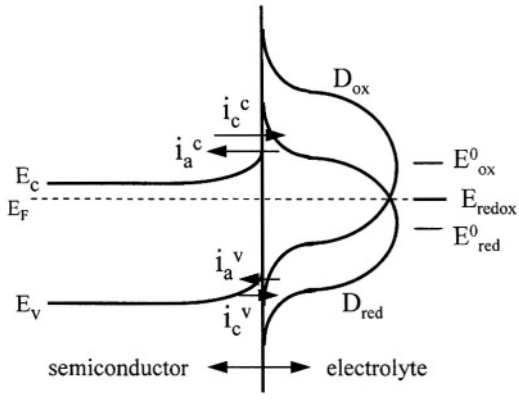

FIGURE 1.14. Illustration of the electron transfer as anodic and cathodic current via the conduction band and the valence band.

$$i_a^c = F \cdot Z \cdot c/(\pi k\lambda)^{1/2} \int_{E_c}^{+\infty} \kappa(E) \cdot N_c \exp\left[-(E - E_{redox} - \lambda)^2/(4kT\lambda)\right] dE \quad (1.52)$$

In the case of the valence band process, an electron transfer into the valence band is only possible if holes are present at the surface. This means the density of empty states equals the hole density at the surface, p_s. Thus, the valence band anodic current is

$$i_a^v = F \cdot Z \cdot c/(\pi kT\lambda)^{1/2} \int_{-\infty}^{E_v} \kappa(E) \cdot p_s \exp\left[-(E - E_{redox} - \lambda)^2/(4kT\lambda)\right] dE \quad (1.53)$$

Integrals (1.52) and (1.53) can be analytically solved only by making some assumptions. Assuming $E = E_c$ for the conduction band process and $E = E_v$ for the valence band process because electron transfer occurs mainly with 1 kT of the band edges and assuming $\kappa(E)$ is constant, integrals (1.52) and (1.53) can be approximated by the following equations for the anodic currents via the conduction and valence bands:

$$i_a^c = F \cdot Z \cdot c(kT/\pi\lambda)^{1/2} \kappa \cdot N_c \exp\left[-(E - E_{redox} - \lambda)^2/(4kT\lambda)\right] \quad (1.54)$$

$$i_a^v = F \cdot Z \cdot c(kT/\pi\lambda)^{1/2} \kappa \cdot p_s \exp\left[-(E - E_{redox} - \lambda)^2/(4kT\lambda)\right] \quad (1.55)$$

Similarly, one can obtain the approximate equations for the cathodic currents via the conduction and valence bands:

$$i_c^c = F \cdot Z \cdot c(kT/\pi\lambda)^{1/2} \kappa \cdot n_s \exp\left[-(E - E_{redox} + \lambda)^2/(4kT\lambda)\right] \quad (1.56)$$

$$i_c^v = F \cdot Z \cdot c(kT/\pi\lambda)^{1/2} \kappa \cdot N_v \exp\left[-(E - E_{redox} + \lambda)^2/(4kT\lambda)\right] \quad (1.57)$$

For non-heavily doped semiconductors, the potential variation occurs only across the space charge layer and the potential across the Helmholtz layer is constant. This means that the exponential terms in Eqs. (1.54) to (1.57) are independent of applied potential, that is, $E - E_{redox} = \text{constant}$. Thus, i_a^c and i_c^v are independent of the potential and can be taken as constants: $i_a^c = i_0^c$ and $i_c^v = i_0^v$. The only quantities that are dependent on potential are n_s and p_s, which are described by Eqs. (1.19) and (1.20). At equilibrium the anodic and cathodic currents across each energy band must be equal, i.e.,

$$i_a^c = i_c^c = i_0^c \quad \text{and} \quad i_a^v = i_c^v = i_0^v \quad (1.58)$$

Also, the surface carrier concentrations at equilibrium can be described by n_s^0 and p_s^0 which are given by Eqs. (19) and (20):

$$n_s^0 = n_0 \exp[-eV_s^0/(kT)] \quad (1.59)$$

$$p_s^0 = p_0 \exp[eV_s^0/(kT)] \quad (1.60)$$

where eV_s^0 is the band bending at equilibrium. At potentials departing from equilibrium, the surface carrier concentrations are described by

$$n_s = n_s^0 \exp[-e(V_s - V_s^0)/(kT)] \tag{1.61}$$

$$p_s = p_s^0 \exp[e(V_s - V_s^0)/(kT)] \tag{1.62}$$

The current equations (1.54) to (1.57) can now be expressed in simple forms as follows: for anodic current, $i_a = i_a^c + i_a^v$

$$i_a^c = i_0^c \qquad \text{conduction band process} \tag{1.63}$$

$$i_a^v = i_0^v \exp[e\eta_{sc}/(kT)] \qquad \text{valence band process} \tag{1.64}$$

and for cathodic current, $i_c = i_c^c + i_c^v$

$$i_c^c = i_0^c \exp[-e\eta_{sc}/(kT)] \qquad \text{conduction band process} \tag{1.65}$$

$$i_c^v = i_0^v \qquad \text{valence band process} \tag{1.66}$$

where $\eta_{sc} = V_s - V_s^0$ is the overpotential, which is a measure of the departure of the potential drop in the space charge region, V_s, from that at equilibrium, V_s^0. Figure 1.15 shows the schematic i–V curves representing Eqs. (1.63)–(1.66).[962] Under an anodic polarization which provides a positive η_{sc}, i_a^v increases exponentially with η_{sc} and i_a^c is constant. On the other hand, under a cathodic polarization, i_c^c increases exponentially with cathodic polarization but i_c^v remains constant. The exponential increase for i_a^v, which depends on the supply of holes, is limited for an n-type material by the current of holes. Similarly, the exponential increase of the electron current i_c^c for p-type material is limited by the current of electrons.

The net current is

$$i = i_a - i_c \tag{1.67}$$

$$i = i_0^c + i_0^v \exp[e(\eta_{sc})/(kT)] - i_0^v - i_0^c \exp[-e(\eta_{sc})/(kT)] \tag{1.68}$$

This equation can be further simplified by neglecting the contribution due to the minority carriers. Thus, for an n-type material Eq. (1.68) becomes

$$i = -i_0[\exp(-e\eta_{sc}/kT) - 1] \tag{1.69}$$

The current is negative when it is cathodic and positive when it is anodic. Analogously, the current on a p-type material when the contribution of minority electrons is negligible can be expressed as

$$i = i_0[1 - \exp(e\eta_{sc}/kT)] \tag{1.70}$$

This form resembles that for the Schottky barrier at a metal/semiconductor interface that is used in the literature.[964]

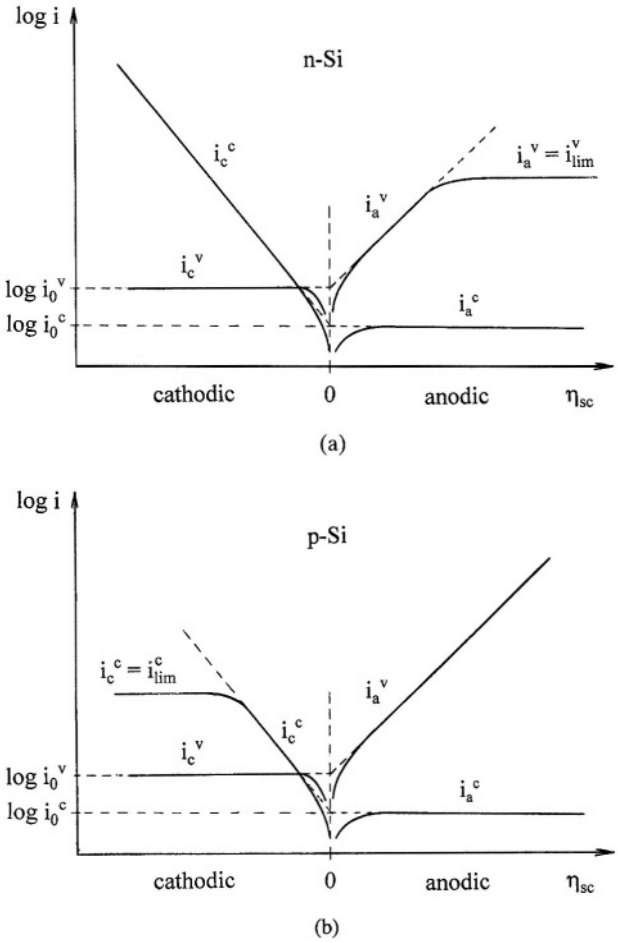

FIGURE 1.15. The dependence of the anodic and cathodic electron and hole currents as a function of overpotential across the space charge layer. (a) *n*-type; (b) *p*-type. After Pleskov and Gurevich.[962]

1.4.2. Limitations of the Basic Theories

The kinetic theory described by the above equations is derived with several basic assumptions:[962]

1. Electron transfer occurs directly between the levels in the bands and the levels in solution
2. The energies of electrons and holes in the band taking part in the charge transfer are confined in a narrow interval (on the order of kT) of the band edge at the surface.
3. The position of the band edge relative to the energy levels of the redox system is independent of the potential change in the interface region, i.e., all the applied potential drops across the space charge layer in the semiconductor.

In many circumstances these conditions are not met and the equations are not directly applicable to electrode reaction kinetics.[86,270,274] For example, when charge transfer via surface states plays a significant role in the electrode processes, the first assumption is violated. In this case as shown in Fig. 1.16a, the charge transfer process is not directly between the levels in the bands and those in the solution. In the case of a strong band bending the thickness of the space charge layer may become very small so that electron tunneling through the space charge layer occurs as shown in Fig. 1.16b. Thus, the second condition is violated because the electron tunnels from energy levels that are distant from the band edges at the surface. Violation of the third assumption may, for example, occur when the semiconductor is highly doped so that the capacitance of the space charge layer near the flatband potential is comparable to that of the Helmholtz layer and a significant fraction of the potential drops in the Helmholtz layer. This may also occur when the density of surface states is high and the associated charge is comparable to that of the Helmholtz layer.

Also, although Eqs. (1.69) and (1.70) resemble those for a Schottky barrier, there are several important differences in the physical and chemical details: (1) charge transfer between a semiconductor and a solution is a slow process, whereas that between a metal and a semiconductor is fast; (2) the diffusion of redox species in the solution toward the electrode surface is slow whereas that of charge carriers in metal is fast; (3) the reduced and oxidized species of the redox couple as donors and acceptors can change independently whereas the occupied and unoccupied states of the metal cannot be changed artificially; (4) a Helmholtz layer is present between the semiconductor electrode and the solution whereas no such layer exists at the metal/semiconductor interface.

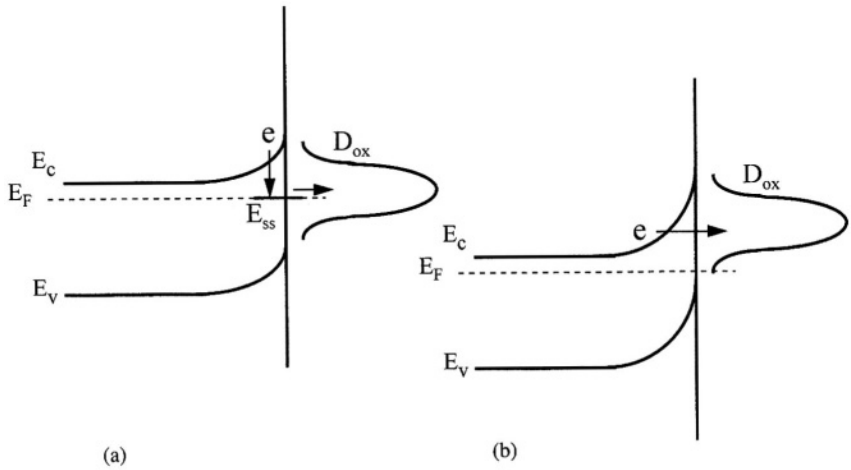

FIGURE 1.16. Circumstances in which electron transfer does not occur between the energy levels at the band edge on the surface and those in the electrolyte. (a) Electron transfer via surface states; (b) electron tunneling through the potential barrier in the space charge layer.

1.4.3. Limiting Current

The limiting current for an *n*-type semiconductor electrode under a reverse bias consists of that from majority carrier current in the conduction band and minority carriers in the valence band. The relative contribution of the two currents is a function of temperature. For silicon at room temperature the limiting current in the dark is dominated by the transport of minority carriers.[699]

When the limiting current in the dark is determined by the minority carriers, under a steady-state condition, in the absence of additional generation in the bulk for *n*-type semiconductor the hole concentration and hole diffusion current can be given by the following equations:

$$i_p = -eD_p dp/dx \tag{1.71}$$

$$D_p d^2p/dx^2 + (p - p_0)/\tau_p = 0 \tag{1.72}$$

where i_p is the diffusion current, D_p the diffusion coefficient of holes, p the hole concentration, p_0 the hole concentration at equilibrium, and τ_p the hole lifetime. Using the boundary conditions $p = p_0$ at $x = \infty$ and $p = 0$ at $x = x_d$ (boundary between the space charge layer and bulk) and solving Eqs. (1.71) and (1.72), the limiting (or saturation) hole current is obtained as

$$i_p^{lim} = eD_p p_0/L_p \tag{1.73}$$

where L_p is the diffusion length.

The limiting current described by Eq. (1.73) is the maximum hole current that can flow from the semiconductor bulk to the space charge region under a steady-state condition. It depends on the assumption that bulk thermal generation is the only source of the minority carriers. In many systems there may be other sources of minority carrier generation, for example, generation in the space charge region and through the surface states.[607,717,839] In some cases the measured limiting current can be much larger than the true limiting current due to current multiplication which generates current via injection of carriers into the band of majority carriers.

1.4.4. Breakdown

Breakdown of a semiconductor electrode occurs when the limiting current at reverse bias sharply increases with increasing potential. At breakdown the electrode loses its "insulating" character and becomes "conductive." Two types of breakdown may occur in a semiconductor at high field: Zener breakdown and avalanche breakdown.[45,964]

In Zener breakdown, the field may be so high that it exerts sufficient forces on a covalently bound electron to free it, which creates two carriers, an electron and a hole, to conduct the current. In this breakdown process, shown in Fig. 1.17a, an electron makes the transition, or tunnels, from the valence band to the conduction band without the interaction of any particles. It is essentially a band-to-band tunneling process. In

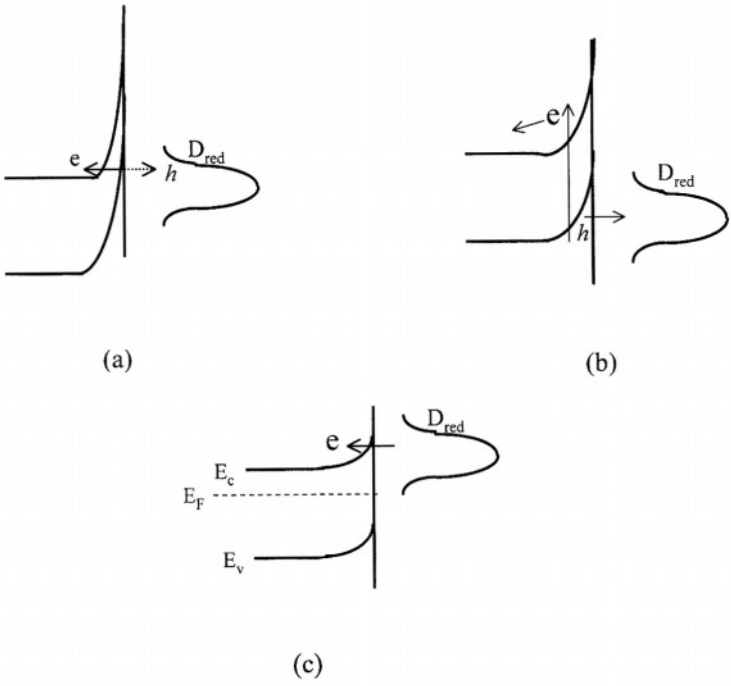

FIGURE 1.17. Illustration of the breakdown of the potential barrier at the semiconductor/electrolyte interface. (a) Zener breakdown; (b) avalanche breakdown; (c) interface tunneling.

this case the width of the space charge layer at a strong reverse bias becomes very thin so that the bound electrons in the valence band can tunnel through the band gap into the conduction band. Since the probability of the process is a strong function of the thickness of the barrier, tunneling is only significant in highly doped material in which the depletion layer is narrow.

In the case of avalanche breakdown as shown in Fig. 1.17b, free carriers are able to gain enough kinetic energy from the field in the space charge layer and break the covalent bonds in the lattice at collision. In this process, each carrier colliding with the lattice atoms creates two carriers, which can participate in further avalanching collisions, leading to a sudden multiplication of carriers in the space charge region. In the energy-band diagram of Fig. 1.17b, this process can be represented as the excitation of carriers from the valence band to the conduction band by absorption of the kinetic energy of the free carriers moving in the lattice under a high field.

The field required for breakdown to occur and the mode of breakdown depend on doping level. As the dopant concentration increases, the width of the space charge layer decreases and the probability of tunneling increases rapidly so that Zener breakdown becomes more likely than avalanche breakdown. Zener breakdown is, in general, involved in the electrode processes on p^+ and n^+ materials under a reverse bias.

Interface tunneling (shown in Fig. 1.17c), can also generate a large current at a reverse bias for a semiconductor electrode/electrolyte interface when the energetic position of a redox couple is favorable relative to the bands. Interface tunneling has been

found to be significant for silicon electrodes in HF solutions, where the dissolution intermediates are further oxidized by injecting electrons in the conduction band, resulting in current that is much larger than the minority dark limiting current.[8,38]

1.4.5. Potential Distribution

The statically charged region at the silicon/electrolyte interface is composed of a space charge layer in the silicon and double layer in the electrolyte. Any potential change across the interface must be accomondated by one of the two layers or shared by them. The partition of potential under a reverse bias when the current is very small is determined by the relative value of the capacitance at the space charge layer, the surface state capacitance, and the Helmholtz layer capacitance. On the other hand, under a forward bias the partition of potential depends not only on the relative values of the capacitances, but also on the kinetics of charge transfer across each layer. When there is an oxide present, the potential may further be partitioned among the oxide film and the two double layers.

In general, in the absence of an oxide the partition of the applied potential across the space charge layer and the Helmholtz layer depends on doping concentration and current range. There are also two different potential distributions depending on whether it is under a forward bias or a reverse bias. Under a forward bias for an anodic process on a *p*-type semiconductor electrode the current density can be described as follows[724]:

$$i = i_0 p_s / p_s^0 \exp(\alpha n F \eta_a / RT) \tag{1.74}$$

where i_0 is the exchange current density, p_s and p_s^0 are the surface concentration of holes under current flow and at equilibrium, and η_a is the overpotential for the anodic reaction. The total applied voltage, V_{app}, under anodization is the sum of the potential drop in the Helmholtz layer, η_a, in the space charge layer, V_s, and concentration overpotential in the electrolyte, η_e:

$$V_{app} = \eta_e + \eta_a + V_s \tag{1.75}$$

That is,

$$V_{app} = RT/(nF)\ln(C_B/C_0) + RT/(\alpha nF)\ln(i/i_0) + RT/(\alpha nF)\ln(p_s^0/p_s) + V_s \tag{1.76}$$

According to the calculation by Kang and Jorne,[724] the fraction of the potential drop across the space charge region depends on the doping level and exchange current density. Under the same current density, V_s decreases with increasing doping level. When the doping level is 10^{19}, the voltage drop in the space charge region is very small, on the order of millivolts, and most of the potential drop occurs in the Helmholtz layer. As the doping level decreases, a relatively larger fraction of the total overpotential occurs in the space charge region as shown in Fig. 1.18. At a very low doping level, when the concentration of holes is very small, the potential drop occurs almost entirely in the space charge layer. The plot of logarithmic current versus potential then gives a 60 mV/decade relationship.

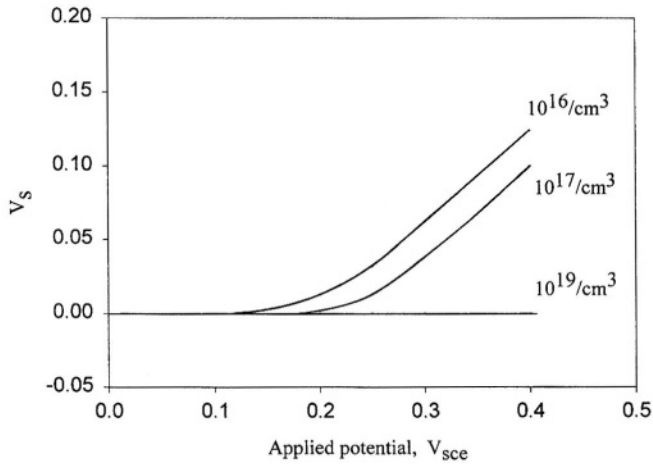

FIGURE 1.18. Potential drop across the space charge layer, V_s, as a function of the applied potential for different doping concentrations calculated according to Eq. (1.76).

At the limiting current in the dark under a reverse bias, all the change in potential occurs across the space charge layer. But at current below the dark limiting current the applied potential can be distributed over both the Helmholtz layer and the space charge layer.[717] The anodic charge transfer at a reverse bias involves two processes that are electrically in series:

1. Electrochemical charge transfer through the Helmholtz layer according to

$$\Delta V_H = (kT/\alpha e)\ln(i/i_{ex}) \tag{1.77}$$

where i_{ex} is the exchange current, ΔV_H the overpotential across the Helmholtz layer, and α the charge transfer coefficient.

2. Electron transfer from the surface to the bulk of the semiconductor through the space charge region with limiting current of i_L:

$$\Delta V_{sc} = -(kT/e)\ln(1 - i/i_L) \tag{1.78}$$

The total overpotential is

$$\eta = \Delta V_H + \Delta V_{sc} = kT/e[1/\alpha \ln(i/i_{ex}) - \ln(1 - i/i_L)] \tag{1.79}$$

This equation indicates that potential change occurs mainly in the Helmholtz layer at a current significantly less than the limiting current whereas it occurs mainly in the space charge layer at a current near or equal to the limiting current and the Helmholtz potential is almost fixed.

1.4.6. Current Multiplication

Current multiplication is a phenomenon associated with the limiting current when a reaction of several charge transfer steps occurs and only a part of these steps involves the minority carriers. For example, for an anodic oxidation of a reducing species A to its oxidized form A^{n+} on an *n*-type material, current multiplication occurs as follows:

$$A + h \rightarrow A^{+} \tag{1.80}$$

$$A^{+} + mh \rightarrow A^{n+} + (n - m - 1)e \tag{1.81}$$

where A is first oxidized by a hole to become a radical A^{+}. Because of the closer position of the intermediates to the edge of the conduction band, further oxidation to A^{n+} is accomplished by injecting (n–m–1) electrons into the conduction band. This results in a current that is $n/(m + 1)$ times larger than the limiting current by the minority carriers. It is commonly called current doubling when $n/(m + 1)$ is 2. Current multiplication with a multiplication factor of 2 to 4 has been observed during the anodic dissolution of *n*-type silicon in fluoride-containing solutions.[908,909]

1.5. PHOTOEFFECTS

When a semiconductor/electrolyte interface is irradiated with a light of energy greater than the band gap V_g, photons are absorbed, breaking the covalent bonds holding the electrons at atomic sites in the lattice, and electron–hole pairs are generated. Some of these electrons and holes, especially those formed in the bulk semiconductor beyond the space charge region, recombine with the generation of heat or emission of light. However, the field in the space charge layer causes the separation of electrons and holes. Thus, in the case of Fig. 1.19 the holes arrive at the surface at an effective potential equivalent to the valence band edge and cause the oxidation of the redox couple R/O from R to O while the electrons move into the external circuit through the semiconductor electrode lead. The flow of holes and electrons in opposite directions can be measured as photocurrent.

1.5.1. Photocurrent

The attainable photocurrent under a given illumination intensity depends on the relative depth of light penetration in the semiconductor, the diffusion length of the

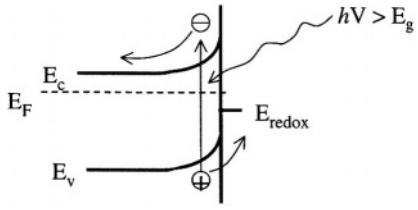

FIGURE 1.19. Creation and movement of electronic carriers at the semiconductor/electrolyte interface under illumination.

minority carriers and the width of the space charge layer. As illustrated in Fig. 1.20, the depth of light penetration is on the order of α^{-1}, where α is the light absorption coefficient defined as follows[962]:

$$I(x) = I_0 e^{-\alpha(\omega)x} \tag{1.82}$$

where I is the light intensity, I_0 the light intensity entering the electrode, ω the frequency of light, and x the distance from the surface into the bulk. The number of absorbed photons per unit time and unit volume is $\alpha I(x)$ and the rate of carrier generation for one photon to one electron–hole pair is described by

$$g(x, \omega) = \alpha(\omega) I(x) = \alpha(\omega) I_0 e^{-\alpha(\omega)x} \tag{1.83}$$

The penetration depth of light may vary in a wide range since α is a function of light frequency as shown in Fig. 1.21.[45,161] For silicon, the absorption of photons having energies greater than the band gap is almost entirely due to the generation of holes and electrons. The optical penetration depth, α^{-1}, is less than 10 nm when silicon is illuminated with high-energy ultraviolet light whereas it is 100 μm with light having a wavelength of 1 μm.

Figure 1.20 shows the two extreme cases of light absorption, $\alpha^{-1} < L_{sc}$ and $\alpha^{-1} > L_{sc} + L_p$, in relation to the diffusion length and the width of the space charge layer. In the region $x \leqslant \alpha^{-1}$, the holes generated in the depletion layer, $x < x_d$, are transported by the electric field to the surface where they are consumed in the electrode reactions. Outside the depletion layer at $x > x_d$, the photogenerated holes are transported by

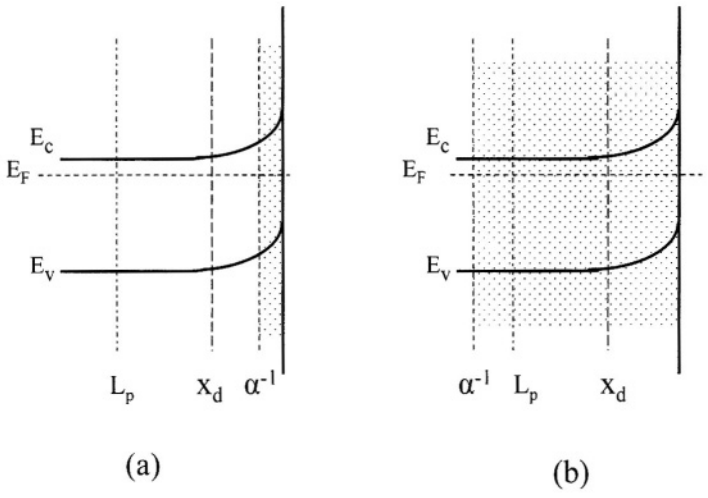

FIGURE 1.20. Correlations between the depth of light penetration in the semiconductor, α^{-1}, the thickness of the space charge layer, x_d, and the diffusion length of the photo generated carriers, L_p. (a) The light is strongly absorbed (small α^{-1}); (b) the light is weakly absorbed (large α^{-1}). After Pleskov and Gurevich.[962]

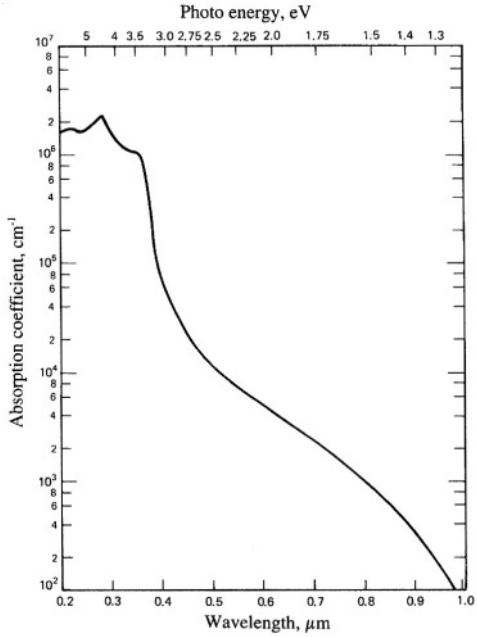

FIGURE 1.21. Absorption coefficient of light in silicon. After Muller and Kamins.[45] (© 1977, Reprinted by permission of John Wiley & Sons, Inc.)

diffusion. The distance these nonequilibrium carriers travel during their lifetime is on the order of the diffusion length. Thus, the holes generated deeper in the bulk, $x > x_d + L_p$, mainly recombine before they reach the surface.

In the case of strong light absorption so that $\alpha^{-1} < x_d$ (Fig. 1.20a), the region for photo hole generation is within the depletion layer. The photocurrent is independent of the potential and represents the maximum attainable. On the other hand, when light absorption is weak (Fig. 1.20b), the photocurrent is proportional to $x_d + L_p$ and thus depends on the potential which determines the width of the space charge layer.

Photocurrent can generally be considered to consist of two parts, that due to generation in the depletion layer, i_{dl}, and that from generation in the bulk, i_b:

$$i_{ph} = i_{dl} + i_b \tag{1.84}$$

With the assumptions that (1) there is negligible recombination in the space charge layer and at the surface and all the carriers generated in the space charge layer are driven by the field to the surface, and (2) the electrode reactions are sufficiently fast, using Eq. (1.83) the contribution due to photogeneration in the depletion layer can be described by

$$i_{dl} = -e\int_0^{x_d} g(x)dx = eI_0[\exp(-\alpha x_d) - 1] \tag{1.85}$$

The photocurrent due to generation in the bulk, $x > x_d$, can be described by

$$i_b = -eD_p dp/dx \qquad \text{at } x = x_d \tag{1.86}$$

$$D_p d^2 p/dx^2 - (p - p_0)/\tau_p + \alpha I_0 e^{-\alpha x} = 0 \tag{1.87}$$

which means that under a steady-state condition the change of hole concentration caused by diffusion, recombination, and photogeneration is zero. Using the boundary conditions $p = p_0$ at $x = \infty$ and $p = 0$ at $x = x_d$, one obtains the solution for i_b as

$$i_b = -eI_0\alpha L_p/(1 + \alpha L_p)\exp(-\alpha x_d) \tag{1.88}$$

Combining Eq. (1.84), (1.85), and (1.86), one obtains the expression for the absolute value of photocurrent:

$$i_{ph} = eI_0[1 - \exp(-\alpha x_d)/(1 + \alpha L_p)] \tag{1.89}$$

Equation (1.89) can be further simplified for the two extreme cases shown in Fig. 1.20. For $\alpha^{-1} \gg L_p$ in the case of weak absorption, Eq. (1.89) can be expanded and one obtains

$$i_{ph} \sim eI_0\alpha(L_p + x_d) \tag{1.90}$$

For strong absorption, i.e., $\alpha^{-1} \ll x_d$, Eq. (1.89) becomes

$$i_{ph} = eI_0 \tag{1.91}$$

i.e., all created carriers contribute to photocurrent and i_{ph} is independent of doping concentration and potential.

The ratio of the number of electrons transferred through the external circuit to the number of photons striking the semiconductor surface is defined as quantum yield or quantum efficiency:

$$Y = i_{ph}/eI_0 \tag{1.92}$$

The net photocurrent and the quantum yield are a function of a number of competing processes[1154] as shown in Fig. 1.22. For an *n*-type semiconductor, the externally measurable current i is the difference between the photocurrent and the forward current of electrons. The electron current is decreased to zero under certain anodic bias. While the flux of holes to the surface is exclusively controlled by the solid-state properties, all the other reaction steps depend on the surface properties of the semiconductor. The holes arriving at the surface can either (i) transfer to an electron donor in the solution, (ii) be trapped at the surface states, or (iii) recombine with electrons in the conduction band in the depletion region or at the surface. Process (iii) does not generate current in the external circuit, whereas process (ii) produces only transient current charging up the surface states. Only process (i) produces steady photocurrent. The measured photocurrent i_{ph} can therefore be different from the flux of holes to the surface due to these processes.

All these processes are strongly dependent on the band bending. In the absence of surface recombination and with a fast kinetics of electron transfer, the photocurrent

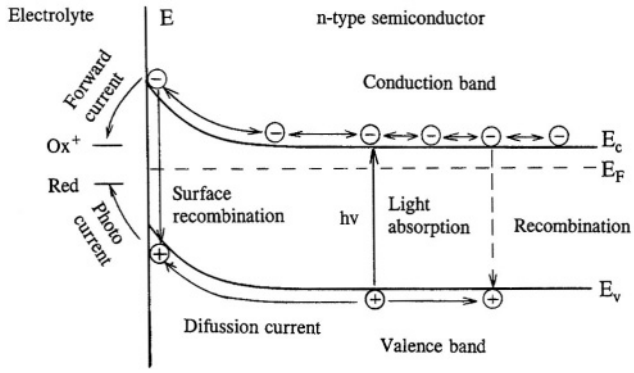

FIGURE 1.22. Kinetic processes controlling the photocurrent yield. (Reprinted from Gerischer.[1154] © 1983, with permission from Elsevier Science.)

increases steeply when the depletion layer starts to form and a saturation current is quickly reached. On the other hand, with sufficient surface recombination or in cases of slow electron transfer reactions, the apparent onset of the photocurrent can be shifted to higher bias and the saturation current is only reached at a larger band bending.

1.5.2. Photopotential

Photopotential or photovoltage is the potential change in the space charge layer resulting from charge separation of photogenerated excess carriers in the field of the space charge layer under galvanostatic conditions.[86,962] It depends on the light intensity and the original band bending in the dark. The maximum photopotential is obtained when the energy band becomes flat. Also, depending on whether it is in depletion or accumulation at the semiconductor surface, the photopotential can be negative or positive with changing sign at the flatband potential.[278] The photopotential developed in a depletion layer is much larger than that in an accumulation layer.

When an electrode is illuminated its potential becomes

$$V_{\text{light}} = V_{\text{dark}} + \Delta V \tag{1.93}$$

This change of potential by illumination, ΔV, is defined as photopotential, V_{ph}.

The current measured at V_{light} is the sum of electron and hole currents: $i = i_{\text{p}} + i_{\text{n}}$. At the open-circuit potential condition the net current is zero, that is, $i_{\text{p}} = -i_{\text{n}}$ and the photopotential is called the open-circuit photopotential, V_{oc}. When there is very little surface recombination and the electrode reaction is sufficiently fast so that the concentration of the reagents at the surface remains equal to their equilibrium values, the relation between open-circuit photopotential and light intensity for an *n*-type material can be expressed for $\alpha^{-1} \gg x_{\text{d}}$[407] by

$$V_{\text{oc}} = -kT/e \ln[(n_0 + \Delta n)/n_0] \tag{1.94}$$

where n_0 is the bulk minority carrier density and Δn is the increased carrier density due to light excitation. This equation indicates that large photovoltages are already obtained at rather low intensities of light, because the carrier density created by light excitation can easily exceed the minority carrier density. Since n_0 is a constant for a given material and Δn is proportional to the light intensity I_0, the above equation can be reduced to

$$V_{oc} = -kT/e \ln(1 + bI_0) \tag{1.95}$$

where b is a positive constant. The same expression as Eq. (1.95) can be derived for $\alpha^{-1} \ll x_d$.[962] It can be seen that V_{oc} is always negative because when an n-type semiconductor is illuminated, the band bending decreases. At relatively low intensities of illumination, i.e., $bI_0 \ll 1$, the absolute value of the photopotential increases linearly with increasing I_0, whereas at high intensities, i.e., $bI_0 \gg 1$, the change is logarithmic.

When the photoeffect is limited mainly by the bulk recombination process, i.e., the diffusion of the minority carriers, the photopotential can be quantitatively related to the minority diffusion coefficient, D_p, and the diffusion length, L_p, at a photocurrent of i_{ph}[275]:

$$V_{oc} = kT/e \ln[i_{ph} L_p N_d / (eD_p n_i^2)] \tag{1.96}$$

When the redox species in the solution do not interact with the semiconductor surface and the band edge at the surface is fixed with respect to the redox potential, the changes in the redox potential E_{redox} in the solutions will result in identical change in the photovoltage on an illuminated electrode. The presence of a redox couple with E_{redox} more negative than E_c for n-type material or more positive than E_v for p type results in an interface with no photovoltage. For E_{redox} more positive than E_v for n type or more negative than E_c for p type, the photoeffects are also expected to be minimal. Only for E_{redox} situated within the band gap can a large photovoltage be expected.

For a semiconductor that is at equilibrium with a redox couple in the solution, the band bending is determined by the redox potential. The maximum attainable photovoltage is the size of band bending, which is ideally related to the barrier height, $V_s = \varphi_b - \mu = E_{redox} - E_{cb} - \mu$. Under an equilibrium condition, E_F generally does not move into the valence band to form an inversion layer and thus the maximum band bending cannot exceed $E_g - \mu$, that is, about the band gap.[275] Thus, theoretically, the maximum attainable photovoltage is close to the band gap when the redox potential is near the valence band edge at the surface.

As a semiconductor/electrolyte interface for photoenergy conversion, the objective is to position E_{redox} close to E_v for n-type material for photoanodes, or close to E_c for p type for photocathodes to achieve the largest band bending in the dark and thus the maximum photovoltages. The maximum open-circuit photovoltage is equal to the amount of band bending or the barrier height, which can be given as[270]

$$(V_{oc})_{max} = V_{fb} - E_{redox}/q$$

The theoretical maximum value is, however, not practically achievable due to many kinetic processes at the semiconductor/electrolyte interface such as surface recombination and majority current. As a result, for a given silicon/electrolyte interface, constant photovoltage over a wide range of redox potentials can occur, that is, band bending is independent of the redox potential value. Thus, photovoltages in practical systems are often not indicative of the barrier height.

1.5.3. Efficiency of Energy Conversion

The power efficiency of a photoelectrode can be characterized by the open-circuit potential (OCP) and short-circuit current:[675,812]

$$\eta = \frac{V_{ph} i_{ph}}{\text{Optical power}} \times 100\% \tag{1.97}$$

where V_{ph} is the photovoltage at the photocurrent i_{ph}. At OCP where V_{ph} is the maximum, V_{oc}, but i_{ph} is zero so that η is zero. Large η is obtained when both V_{ph} and i_{ph} are large. In the application for photo power conversion devices, the objective is to maximize $V_{ph} i_{ph}$. The maximum theoretical solar energy conversion efficiency for a silicon electrode is found to be about 25%. Systems with efficiency up to 16% have been realized experimentally on silicon/liquid junctions.[275,917] The primary source of inefficiency is the presence of surface states at the silicon/electrolyte interface that act as recombination centers.[548,622]

1.5.4. Surface Recombination

Surface states, like the impurity levels in the bulk, may take part in the recombination of electrons and holes, which significantly affects the photoelectrochemical processes.[158,182,962] As described earlier, there are many different kinds of surface states in terms of their physical nature and energetic distribution in the band gap. Surface recombination may thus have very different rates depending on the nature of the surface states. Also, of the total number of surface states, only some of them participate in the processes of recombination.[962] For highly doped material under a large band bending (deep depletion), surface recombination by tunneling from the surface states to the bands may also be significant.[88]

For a simple case where the surface recombination involves monoenergetic surface states the basic processes are illustrated in Fig. 1.23.[962] J_{c1} represents the flux due to capture of electrons from the conduction band, J_{c2} the emission of electrons into the conduction band, J_{v1} the capture of holes from the valence band, and J_{v2} the emission of holes into the valence band. The recombination rates of electrons, $R_{n,s}$, and of holes, $R_{p,s}$ can then be expressed as

$$R_{n,s} = J_{c1} - J_{c2}, \qquad R_{p,s} = J_{v1} - J_{v2} \tag{1.98}$$

At equilibrium $J_{c1} = J_{c2}$ and $J_{v1} = J_{v2}$, the recombination rates are zero. Equation (1.98) can be further expressed as

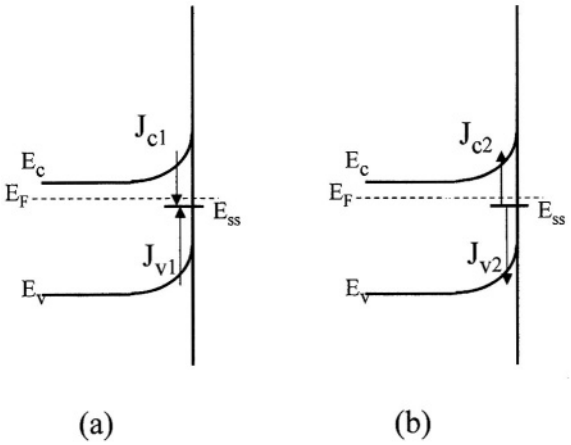

FIGURE 1.23. The elemental steps involved in surface recombination via surface states. (a) Flux of capture of electrons, J_{c1}, and holes, J_{v1}; (b) Flux of emission of electrons, J_{c2}, and holes, J_{v2}.

$$R_{n,s} = a_{n,s} N_{ss} [n_s (1 - f_{ss}) - n_1 f_{ss}] \tag{1.99}$$

$$R_{p,s} = a_{p,s} N_{ss} [p_s f_{ss} - p_1 (1 - f_{ss})] \tag{1.100}$$

where $a_{n,s}$ and $a_{p,s}$ are the capture coefficients for electrons and holes at the surface, N_{ss} is the concentration of surface states, $n_s = n_s^0 + \Delta n$ and $p_s = p_s^0 + \Delta p$ are the concentrations of electrons and holes at the surface with n_s^0 and p_s^0 the concentrations at equilibrium, n_1 and p_1 are the concentrations of captured electrons and holes in the surface states, and f_{ss} is the degree of filling of the surface states. In the steady state, $R_{n,s} = R_{p,s} = R_s$, and Eqs. (1.99) and (1.100) become

$$R_s = N_{ss} a_{n,s} a_{p,s} (p_s n_s - n_1 p_1) / [a_{n,s} (n_s + n_1) + a_{p,s} (p_s + p_1)] \tag{1.101}$$

where $n_1 p_1 = n_0 p_0 = n_i^2$. For a nondegenerated material, suppose that (1) quasineutrality is fulfilled at the boundary of the space charge layer, $x = x_d$, so that the concentrations of excess electrons and holes are equal ($\Delta n = \Delta p$), and (2) the departure from equilibrium is insignificant, that is, $\Delta n \ll p_0$, n_0, then the surface recombination velocity, which is defined as $s = R_s / \Delta n$, can be obtained from Eq. (1.101) as

$$s = N_{ss} a_{n,s} a_{p,s} (p_0 + n_0) / [a_{n,s} (n_s + n_1) + a_{p,s} (p_s + p_1)] \tag{1.102}$$

The recombination velocity, which characterizes the recombination process, may vary over a wide range, from 1 to 10^5 cm/s, at room temperature.[962] Surface recombination centers that can be described by the one discrete recombination center model have been found to exist in different silicon/electrolyte systems.[61,182,278,808] The states that can exchange charge carriers with only one of the bands are traps for electrons or holes. Surface states that contribute to the interface capacitance but do not act as the

recombination center have been found on silicon electrodes in both fluoride and non-fluoride solutions.[93,808]

1.6. OPEN-CIRCUIT POTENTIAL

OCP, or the rest potential of an electrode, is the potential of a freestanding electrode without electrical connection to any other conducting materials. Thus, at OCP there is no net current flow in or out of the electrode. OCP of an electrode is determined by the kinetic state of the electrode. It is the most easily measurable electrochemical parameter and at the same time is the most convoluted quantity as it is determined by all the kinetic factors in the system. The electrode at OCP can be at an equilibrium state or a nonequilibrium state depending on the nature of the particular electrode/electrolyte system and the reference time scale.

If no net chemical change occurs in the system during the time of measurement, the electrode at OCP can be regarded as at an equilibrium condition. This occurs, for example, as shown in Fig. 1.24a, where the Fermi level of the semiconductor has the same value as the reversible potential of a single redox couple in which the forward current i_a equals the reverse current i_c. In many situations and almost always for silicon, the electrode/electrolyte interface at OCP is at a nonequilibrium condition and a net chemical change in the system occurs when two or more redox couples are present in the electrolyte. OCP in these situations is a mixed potential. This is shown in Fig. 1.24b, where OCP is established with two redox couples, E_{redox1} and E_{redox2}, with $i_{net} = i_a - i_c = (i_{1a} + i_{2a}) - (i_{1c} + i_{2c}) = 0$ but $E_F \neq E_{redox1}, E_{redox2}$. In this case, a net chemical change is involved since $i_{1a} - i_{1c} \neq 0$ and $i_{2a} - i_{2c} \neq 0$ and a net amount of reduced species 1 and oxidized species 2 is produced for a given time peorid.

When one of the redox couples is associated with the dissolution of the electrode, $M + mh \rightarrow M^{n+} + (n - m)e$, OCP is also called the corrosion potential and the net dissolution rate at OCP is the corrosion current, $i_{corr} = i_{1a} - i_{1c}$. This is generally the case with a silicon electrode at OCP in aqueous solutions because the thermodynamic poten-

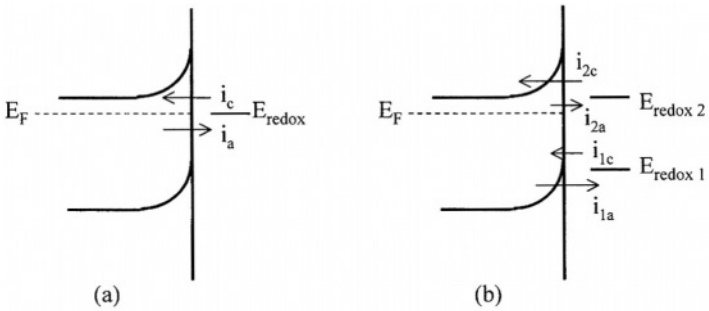

FIGURE 1.24. OCP at (a) an equilibrium condition ($E_F = E_{redox}$) and (b) nonequilibrium condition ($E_F \neq E_{redox1} \neq E_{redox2}$).

tial of silicon is much more negative than that of water. OCP of silicon in water is generally a corrosion potential. The rate of corrosion, that is, the dissolution rate at OCP, can be measured in terms of corrosion current. It can be estimated by determining the polarization resistance at OCP, which was originally formulated by Stern and Geary[1148,1149] based on the mixed potential concept for an electrode under an activation-controlled condition. In the case where the corrosion rate of the semiconductor is limited by the minority carriers, the corrosion current simply equals the limiting current as illustrated in Fig. 1.25.[962]

As can be seen in Fig. 1.25, the corrosion potential may vary not only with the value of E^0_{redox} but also with the slopes of the anodic and cathodic curves as well as the limiting current values. Since the limiting current is sensitive to the lighting condition, OCP or corrosion potential varies with the background photonflux. As stated above, the corrosion potential is determined by the anodic current and cathodic current. Any changes, such as surface preparation, solution composition and concentration, pH, temperature, time, convection, aeration, background lighting, and so on, that affect the anodic and the cathodic reactions will affect the value of the corrosion potential. Thus, the corrosion potential as well as the corrosion current can vary greatly, depending on the specific conditions.

The change of the corrosion potential in either the anodic or the cathodic direction may correspond to a decrease or increase in the corrosion current. The variation of the corrosion potential and corrosion currents under various conditions can be generalized using schematic polarization curves in Fig. 1.26.[970] The corrosion potential of an active electrode in a solution is E^0_{corr}. E^1_{corr}, E^2_{corr}, E^3_{corr}, and E^4_{corr} are the corrosion potentials under changed conditions.

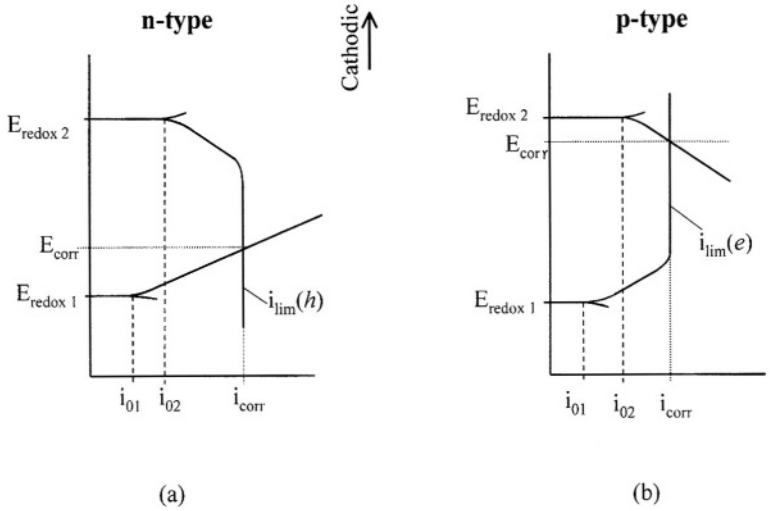

FIGURE 1.25. Illustration of corrosion potential, E_{corr}, for p and n types of semiconductors when the corrosion current is limited by the minority limiting current, $i_{lim} = i_{corr}$.

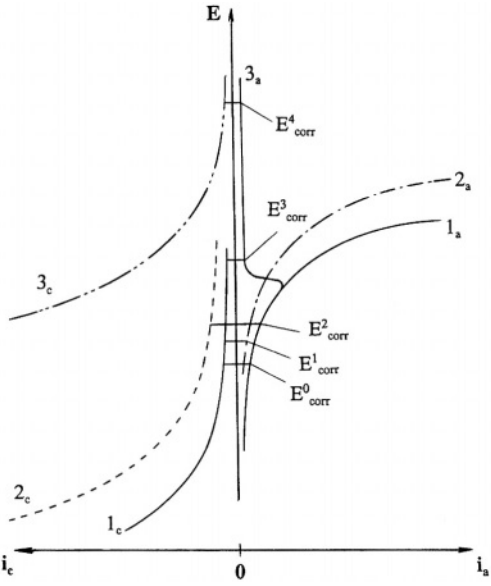

FIGURE 1.26. Schematic polarization curves illustrating E_{corr} and i_{corr} under various conditions (see text).

In the case where the anodic dissolution is inhibited, e.g., by surface adsorption of a chemical species, the anodic curve becomes 2_a. This will result in a more positive corrosion potential (from E^0_{corr} to E^1_{corr}) if the cathodic reaction remains unchanged. In such a situation the corrosion current is reduced with a more positive potential relative to the original value. On the other hand, if the anodic dissolution kinetics remains unchanged but the rate of the cathodic reactions is changed from curve 1_c to curve 2_c, the potential also becomes more positive (from E^0_{corr} to E^2_{corr}). However, in this case the corrosion current is increased with a more positive potential.

The anodic curve becomes 3_a in Fig. 1.26 when the surface is passivated. If the cathodic reaction is unchanged, the corrosion potential of the electrode becomes E^3_{corr}, which is more positive than E^0_{corr}. The corrosion current is generally much smaller than that at E^0_{corr}.

The corrosion potential values that are much more positive than E^0_{corr} are usually associated with both the passivation of the electrode surface and the presence of oxidizing agents in the solution. The cathodic and anodic polarization curves in such a solution are illustrated by 3_c and 3_a, the coupling of which yields the corrosion potential E^4_{corr}. The dissolution rate in this situation is usually very low. However, if the surface is not passivated, the dissolution rate can be very high in the presence of oxidizing agents, which is the case for etching of semiconductors in solutions containing oxidizing agents. This can be appreciated by coupling curves 1_a and 3_c in Fig. 1.26.

A decrease in potential can be caused by either faster anodic dissolution kinetics or a slower cathodic reaction. For example, a decrease in corrosion potential due to deaeration of a solution is usually observed. Deaeration removes the dissolved oxygen and thus reduces the cathodic reaction rate.

1.7 EXPERIMENTAL TECHNIQUES

Electrochemical techniques generally involve the measurement of the electrical signal of the semiconductor/electrolyte interface since the elemental step in an electrochemical reaction is charge transfer across the charged layers at the interface. In these techniques, the electrode surface is typically perturbed by a signal of potential, current, or light, and the corresponding potential, current, or light, along with the physical and chemical changes that take place on the surface, is measured. The physical and chemical nature of the interface layers and kinetics of the electrode reactions can then be analyzed. The theories and methodologies employed in electrochemical techniques are well documented.[44,932,962–964]

The properties of silicon electrodes has been investigated using a wide range of experimental techniques. Specific examples are the determination of:

- Steady-state or dynamic potential and current relationships to provide information on the energetic dependence of electrode reaction rate[2,21,34,271,939]
- Current or potential versus time to provide information concerning stability of reactions and transition or transformation of surface condition[74,77,286,291,860,874]
- Capacitance–potential relationship to reveal information on the energetic position of semiconductor bands and surface states, especially the flatband potential[61,93,475,479,716,841,942]
- Impedance–frequency relationship to yield information on the resistive and capacitive elements of the current path[9,139,486,951]
- Current on rotating electrode to give information regarding mass transport in electrolyte[14,34,939] and on rotating ring-disk electrode for reaction intermediates[21,695]
- Short-circuit current of a *p–n* junction to discriminate between a conduction and a valence band process[34,969]
- Photocurrent to provide information on quantum efficiency and types of carriers[11,73,74,873]
- Impedance under illumination to generate information on recombination processes[93,808,932]
- Photocurrent with subband light to provide information on surface states[400,935]
- Optoelectric impedance (photopotential or current response to modulated illumination) or electro-optic impedance (photoresponse to potential modulation) for information on the contribution of minority, majority, and injected carriers in recombination and multiplication[626,932]
- Microwave conductivity for instantaneous minority concentration and flatband potential[597,616]
- Optical second-harmonic generation by pulsed laser for structural information on Si/SiO_2 interface[606]
- Defletometric technique for electrolyte concentration gradien near the solid electrode surface[855,862]
- Bending beam method for stress of oxide film on the surface[1058]
- Micropatterned samples for determination of carrier distribution and lateral mobility across the electrode or near the surface[585,587]

In addition to the electrochemical techniques, many *insitu* and *exsitu* surface analytical techniques are used in studies of silicon electrodes, such as ellipsometry for determining thin surface film thickness,[98,200,240,404] infrared spectroscopy for surface adsorption,[215,227,395,409] XPS[126,260,424] for surface composition, SEM[12,247] and STM[223,234] for surface morphology, TXRF for surface concentration of metals,[135] and AFM for surface morphology.[120,135]

One particularly important aspect in electrochemical measurements is surface treatment (or surface preparation). The electrochemical behavior of silicon can be strongly affected by surface treatment procedures.[87,161,600,717] The most important goal of surface preparation is to produce a chemically clean and physically homogeneous surface that is reproducible and relatively stable so that representative and reproducible results can be generated. Since silicon is usually covered with a native oxide of various thicknesses and chemical compositions in the air or in aqueous solutions, most surface treatments are designed to remove this initial surface oxide film. The most common procedure used in surface treatment of a silicon electrode includes a dip of the electrode in a HF solution. A very common treatment of silicon electrodes for electrochemical experiments employs concentrated HF solutions such as 48% HF at room temperature with dipping time ranging from 10 to 60s.[161] Also, addition of oxidizing agents such as HNO_3 to the HF solutions is used to enhance the etching rate. The surface after a dip in HF solutions is typically terminated with hydrogen (see Chapter 2 for details). As will be seen in the rest of this book, the surface condition resulting from preparation by a specific cleaning solution may still vary to a wide extent due to the many poorly controllable material and procedure factors.

This page intentionally left blank

2

Silicon/Electrolyte Interface

2.1. BASIC PROPERTIES OF SILICON

Silicon is a semiconductor with an intrinsic conductivity of $4.3 \times 10^{-6}\,\Omega^{-1}\,cm^{-1}$ and a band gap of 1.12eV at 300K. It has a diamond crystal structure characteristic of the elements with four covalently bonded atoms. As shown in Fig. 2.1, the lattice constant, a, is 5.43 Å for the diamond lattice of silicon crystal structure. The distance between the nearest two neighbors is $\sqrt{3}a/4$, that is, 2.35 Å, and the radius of the silicon atom is 1.18 Å if a hard sphere model is used. Some physical parameters of silicon are listed in Table 2.1.

The silicon materials that are used in the electronic industry are normally doped to increase the conductivity. The common donors for silicon are P, As, and Sb and the acceptors are B, Al, and Ga. They are substitutional impurities with ionization levels located in the range of 0.04 to 0.07eV from the corresponding bands. Table 2.2 lists the resistivity, which is the reciprocal of the conductivity, of *n*- and *p*-type silicon doped with phosphorus and boron, respectively.[45]

For single-crystalline silicon the surface properties depend on the orientation. Table 2.3 lists surface properties of silicon for the three principal crystal planes. The (111) plane has the highest atomic density and the lowest surface energy, while the (100) plane has the lowest atomic density and the highest surface energy. Table 2.4 shows the density of surface bonds on various crystal planes.[235] The (100) plane has the highest surface bond density although it has the lowest atomic density. If the in-plane bonds, which are zero for the (100) and (111) planes but high on the (110) plane, are also included, the (110) plane is found to have the highest total bond density. Table 2.4 also shows the surface free energy of the different crystal planes based on the values of bond density and bond strength. The silicon surface is not perfectly flat at the atomic scale but contains defects such as steps, vacancies, kinks, etc.[1074] The step formation energy, which is the energy for creating a straight step from a flat surface at T = 0K, has been found to be 0.162eV/Å for $[\bar{1}\bar{1}2]$ step on (111) plane, and 0.22eV/Å for a kink on $[\bar{1}\bar{1}2]$ step.

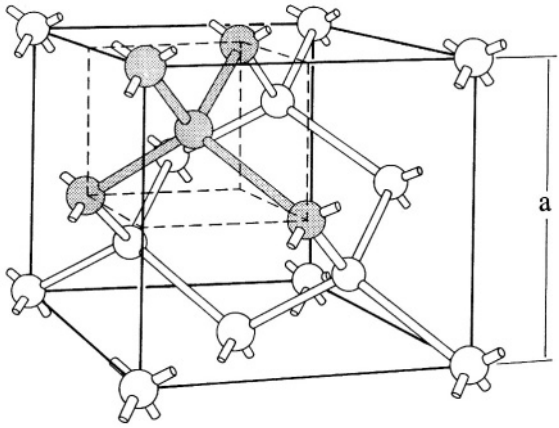

FIGURE 2.1. The diamond-crystal lattice charactrized by four covalently bonded atoms. The lattice constant, a, is 0.543 nm for silicon. Nearest neighbors are spaced ($\sqrt{3}$a/4) units apart. Of the 18 atoms shown in the figure, only 8 belong to the volume a^3. Since the 8 corner atoms are each shared by 8 cubes, they contribute 1 atom; the face atoms are each shared by 2 cubes and thus contribute 3 atoms, and there are 4 atoms inside the cube. The atomic density is therefore $8/a^3$, which corresponds to $5.00 \times 10^{22}\,cm^{-3}$. After W. Shockley.[45]

TABLE 2.1. Physical Properties of Silicon at 300 K[45,720,964]

Property		Units	Symbol
Atomic number	14		
Atomic weight	28.09	g/g-mol	M
Density	2.328 g/cm^3	g/cm^3	ρ
Atomic density	5.0×10^{22}	Atoms/cm^3	N_0
Crystal structure	Diamond		
Atoms per unit cell	8		
Lattice constant	5.43	Å	a
Distance between two neighboring atoms	2.35	Å	
Radius of silicon atom	1.18	Å	r_0
Breakdown field	~3×10^5	V/cm	E_{bd}
Dielectric constant	11.9		ε
Diffusion constant			
Electron	34.6	cm^2 s^{-1}	D_n
Hole	12.3	cm^2 s^{-1}	D_p
Effective density of states			
In conduction band	2.8×10^{19}	cm^{-3}	N_c
In valence band	1.04×10^{19}	cm^{-3}	N_v
Electron affinity	4.05	eV	χ
Energy gap at 300 K	1.12	eV	E_g
Index of refraction	3.44		
Intrinsic carrier density	1.45×10^{10}	cm^{-3}	n_i
Intrinsic Debye length	24	μm	D_L
Intrinsic resistivity	2.3×10^5	Ωcm	
Lattice constant	5.431		a_0
Melting temperature	1412	°C	T_m
Minority carrier lifetime	2.5×10^{-3}	s	
Mobility (drift)			
Electron	1500	cm^2/V-s	μ_e
Hole	450	cm^2/V-s	μ_p

TABLE 2.2. Resistivity (Ωcm) versus Dopant Concentration for Silicon at 23 °C[45]

Doping level (cm^{-3})	Phosphorus, *n*-type	Boron, *p*-type
10^{12}	3.8×10^{3}	1.3×10^{4}
10^{13}	400	1.3×10^{3}
10^{14}	43	130
10^{15}	4.5	14
10^{16}	0.52	1.5
10^{17}	0.085	0.2
10^{18}	0.023	0.045
10^{19}	5.5×10^{-3}	8.5×10^{-3}
10^{20}	7.8×10^{-4}	1.2×10^{-3}
10^{21}	1.2×10^{-4}	1.3×10^{-4}

2.2. THERMODYNAMIC STABILITY IN AQUEOUS SOLUTIONS

Silicon, with a standard potential of $-0.857\,V_{SHE}$, is a rather active element and is readily oxidized in water. The stability of silicon in water and aqueous solutions in the absence of complex formation at 25 °C is determined by the equilibrium conditions listed in Table 2.5.[304]

Figure 2.2 shows the pH–potential diagram (Pourbaix diagram) which is a graphic presentation of the equilibrium conditions listed in Table 2.5. The lines labeled *a* and *b* represent, respectively, the equilibrium conditions of the reduction of water to gaseous hydrogen and of the oxidation of water to oxygen, when the partial pressure of hydrogen or oxygen is 1 atm. According to Fig. 2.2, the stable region of silicon is far below line *a* (the stability line of water) and thus silicon is thermodynamically not stable in water and aqueous solutions. It tends to be oxidized with the evolution of hydrogen and gaseous silicon hydride (SiH_4), and the formation of silica and silicates. Silicon, as a solid substance, is, however, generally stable in most aqueous solutions because of the formation of a passive oxide film on the surface. Figure 2.2 also shows that hydride SiH_4 is unstable in the presence of water and tends to decompose into hydrogen and silica or silicates. The diagram is approximate since it does not take into account the complex nature of the solutions of silicic acid and silicates. Also, it is only valid in the absence of substances with which silicon can form compounds of insoluble salts or soluble complexes.

In the presence of fluoride ions, we find formation of soluble silicon hexafluoride, SiF_6^{2-}, which is dominant in the acidic region. Figure 2.3 illustrates the stability

TABLE 2.3. Properties of Silicon Surface[108,472,833,928]

Atomic density	(100)	(110)	(111)
Atomic density, $10^{14}/cm^2$	6.78	9.59	15.66
Spacing, Å	5.43	3.84	3.13
Surface energy, J/cm^2	2.13	1.51	1.23

TABLE 2.4. Calculated Bond Density ($\times 10^{15}/cm^2$) and Surface Free Energy (eV) of Various Silicon Crystal Planes[235]

Plane	Surface	In-plane	Total	Surface energy
(110)	0.96	0.96	1.96	1.41
(522)	1.06	0.35	1.41	1.46
(100)	1.36	0.00	1.36	1.99
(111)	0.78	0.00	0.78	1.15

regions of various silicon species, i.e., Si, SiO_2 (am), and SiF_6^{2-}, in the presence of 1M concentration of fluoride species.[100] At a fluoride concentration of 1M, silicon oxide is soluble below pH 7 (Fig. 2.3). At a lower concentration of F, SiF_6^{2-} is not stable at low pH values as shown in Fig. 2.4. For example, when $[Si] = 10^{-3}M$ and $[F] = 10^{-2}M$, the stable region for SiF_6^{2-} is confined between pH near 2 and 3.75. The reaction of silicon with fluoride in this region can be described by:[974]

TABLE 2.5. Reactions of Silicon in Aqueous Solution at Equilibrium Conditions[304]

Reaction		Standard potential or solubility	
Two dissolved substances			
1, 1′	$H_2SiO_3 = HSiO_3^- + H^+$	$\log(HSiO_3^-)/(H_2SiO_3) = -10.00 + pH$	
2, 2′	$HSiO_3^- = SiO_3^{2-} + H^+$	$\log(SiO_3^{2-})/(HSiO_3^-) = -12.00 + pH$	
Two solid substances			
3	$Si + 2H_2O = SiO_2 + 4H^+ + 4e$	$\varphi_0 = -0.857 - 0.0591\ pH$	a
		$\varphi_0 = -0.84 - 0.0591\ pH$	d
One solid substance and one dissolved substance			
4	$SiO_2 + H_2O = H_2SiO_3$	$\log(H_2SiO_3) = -5.21$	i[a]
		$= -4.11$	ii
5	$SiO_2 + H_2O = HSiO_3^- + H^+$	$\log(HSiO_3^-) = -15.21 + pH$	i
		$= -14.11 + pH$	ii
6	$SiO_2 + H_2O = SiO_3^{2-} + 2H^+$	$\log(SiO_3^{2-}) = -27.21 + 2\ pH$	i
		$= -26.11 + 2\ pH$	ii
7	$Si + 3H_2O = H_2SiO_3 + 4H^+ + 4e$	$\varphi_0 = -0.780 - 0.0591\ pH + 0.0148 \log(H_2SiO_3)$	
8	$Si + 3H_2O = HSiO_3^- + 5H^+ + 4e$	$\varphi_0 = -0.623 - 0.0591\ pH + 0.0148 \log(HSiO_3^-)$	
9	$Si + 3H_2O = SiO_3^{2-} + 6H^+ + 4e$	$\varphi_0 = -0.455 - 0.0591\ pH + 0.0148 \log(SiO_3^{2-})$	
One dissolved substance and one gaseous substance			
10	$SiH_4 + 3H_2O = H_2SiO_3 + 8H^+ + 8e$	$\varphi_0 -0.339 - 0.0591\ pH + 0.0074 \log(H_2SiO_3)/(p_{SiH_4})$	
11	$SiH_4 + 3H_2O = HSiO_3^- + 9H^+ + 8e$	$\varphi_0 -0.265 - 0.0591\ pH + 0.0074 \log(HSiO_3^-)/(p_{SiH_4})$	
12	$SiH_4 + 3H_2O = SiO_3^{2-} + 10H^+ + 8e$	$\varphi_0 -0.176 - 0.0591\ pH + 0.0074 \log(SiO_3^{2-})/(p_{SiH_4})$	
One solid substance and one gaseous substance			
13	$SiH_4 = Si + 4H^+ + 4e$	$\varphi_0 = 0.102 - 0.0591\ pH - 0.0148 \log(p_{SiH_4})$	
14	$SiH_4 + 2H_2O = SiO_2 + 8H^+ + 8e$	$\varphi_0 = -0.377 - 0.0591\ pH - 0.0074 \log(p_{SiH_4})$	i
		$\varphi_0 = -0.369 - 0.0591\ pH - 0.0074 \log(p_{SiH_4})$	ii
Stability of water			
(a)	$H_2 = 2H^+ + 2e$	$\varphi_0 = 0.000 - 0.0591\ pH$	
(b)	$2H_2O = O_2 + 4H^+ + 4e$	$\varphi_0 = 1.228 - 0.0591\ pH$	

[a] i, quartz; ii, vitreous silica.

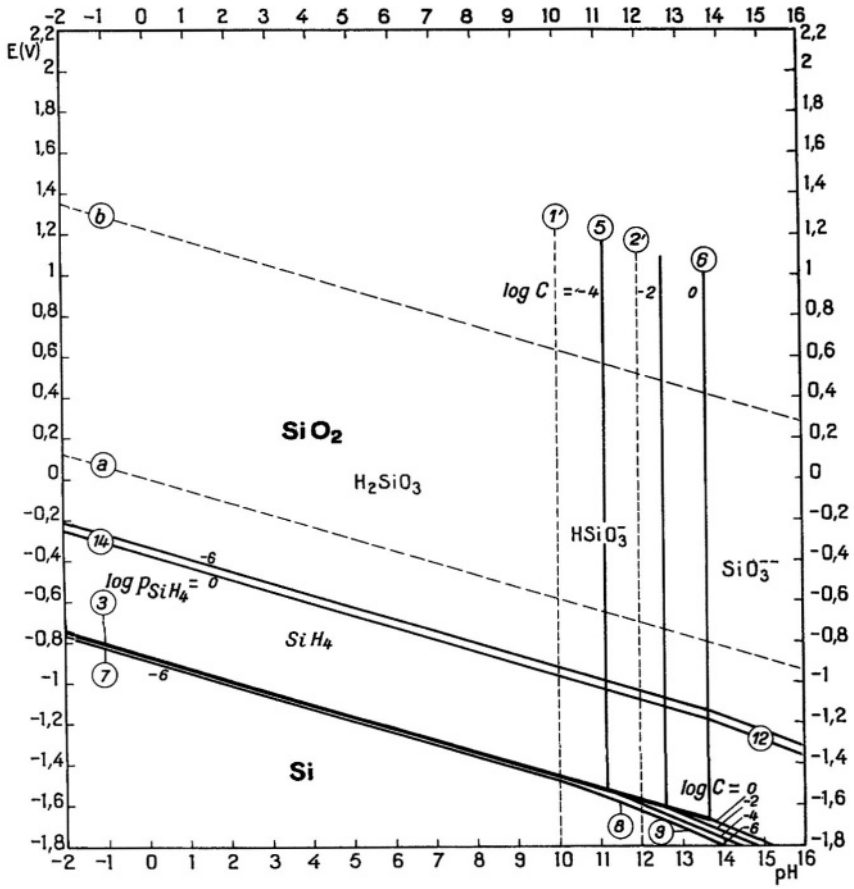

FIGURE 2.2. Pourbaix equilibrium diagram for the silicon–water system at 25 °C (considering SiO_2 in the form of quartz). After Muylader *et al.*[304] (Reprinted with permission.)

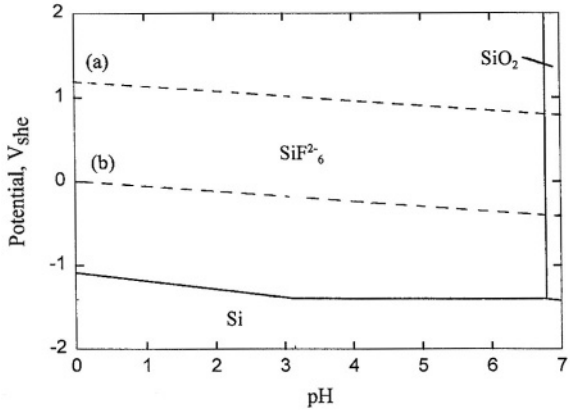

FIGURE 2.3. Pourbaix diagram for the Si–F–H_2O system at 25 °C: [Si] = 10^{-3} M, [F] = 1 M. After Asare *et al.*[100] (Reproduced by permission of The Electrochemical Society, Inc.)

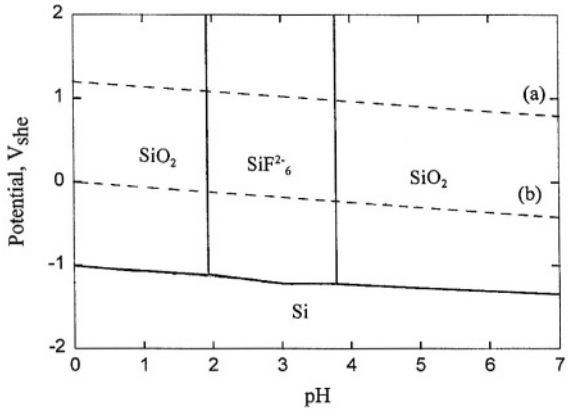

FIGURE 2.4. Pourbaix diagram for the Si–F–H_2O system at 25 °C: [Si] = 10^{-3} M, [F] = 10^{-2} M. After Asare *et al.*[100] (Reproduced by permission of The Electrochemical Society, Inc.)

$$Si + 6F^- = SiF_6^{2-} + 4e \qquad E_0 = -1.24\,V_{SHE} \tag{2.1}$$

The occurrence of two different SiF_6^{2-}/SiO_2 boundaries as shown in Fig. 2.4 is due to the change of the predominant fluoride species from the un-ionized HF molecule to the F^- ion.[100] Thus, at the low pH end, SiO_2 stability is determined by

$$SiO_2 + 6HF = SiF_6^{2-} + 2H^+ + 2H_2O \tag{2.2}$$

On the other hand, at the high pH end, the stability condition is

$$SiO_2 + 6F^- + 4H^+ \simeq SiF_6^{2-} + 2H_2O \tag{2.3}$$

In Figs. 2.3 and 2.4, SiF_6^{2-} is considered as the predominant species. These diagrams may vary somewhat when other silicon complexes, such as SiF and SiF_5^{2-}, are also considered.[709] Further, in real systems, the boundaries of the stability domains in the pH–potential diagrams depend as well on the type of SiO_2, which may have different crystallinity and structures and thus different solubilities, as shown in Fig. 2.5.[304]

Solubilities

In the absence of fluoride ions, silicon oxide has low solubility in water and acidic solutions but it has high solubility in alkaline solutions as shown in Fig. 2.5.[304] In acidic and weak alkaline solutions, the solubility of silicon is independent of pH. When the total dissolved silicon activity is relatively low ($<10^{-5}$ M), silica tends to dissolve to form the soluble species H_4SiO_4, which is a weak acid that dissociates appreciably only about 3 pH units above neutrality. On the other hand, at relatively high total silicon activity ($>10^{-4}$ M), silica SiO_2 as a solid is the stable form in nonalkaline solutions. The solubility of silica also depends on the specific type of silica as shown in Fig. 2.5.

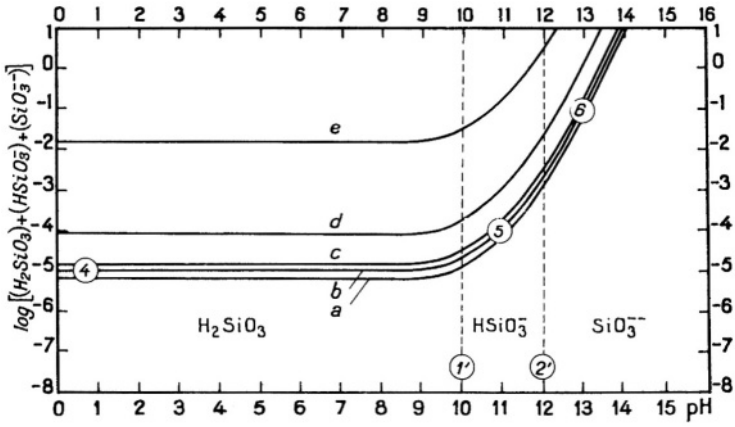

FIGURE 2.5. Influence of pH on the solubility of silica (SiO_2), at 25 °C. a, quartz; b, cristobalite; c, tridymite; d, vitreous silica; e, amorphous silica. After Muylader *et al.*[304] (Reprinted with permission.)

The solubility of silica tends to increase with increasing temperature and pressure. Increasing pressure on the solution increases the concentration of water molecules around H_4SiO_4 and thus increases the amount of time that water molecules are in the most stable configuration.[469] At silica concentrations less than 2mM, the stable form is the monomer, whereas at dissolved silica concentrations greater than about 2 mM, polymers of dissolved silica become important.[899]

The presence of other dissolved constituents can affect silica solubilities. Some solutes react with H_4SiO_4 to form complexes and others interact with water molecules to change the hydration energy of H_4SiO_4. It has been reported that the affinity of various ionic species in solutions for reaction with $H_3SiO_4^-$ decreases in the order: $H^+ > Fe^{3+} > UO_2^+ \gg Mg^{2+} > Ca^{2+} \gg Na^+$.[469] The solubility is also a function of radius of curvature of the surface described as follows:

$$\ln(C/C^\circ) = (2\times10^{-7}\sigma VB)/(3rRT) \tag{2.4}$$

where B is a geometric factor, σ the surface free energy, V the volume of the solid, C the solubility of curved surface, C^0 the bulk solubility, R the gas constant, and T the temperature. As shown in Fig. 2.6, the solubility of convex surfaces (positive radius of curvature) increases with decreasing particle size so that for radii less than ~0.1 μm the particles have an increased solubility. On the other hand, the solubility at concave surfaces (negative radius of curvature) decreases with decreasing radius of curvature, which causes silica to precipitate at the tips of cracks.

In HF solutions, SiO_2 dissolves by forming highly stable complex fluorosilicates according to

$$SiO_2 + 4HF = SiF_4 + 2H_2O \qquad K = [SiF_4]/[HF]^4 \tag{2.5}$$

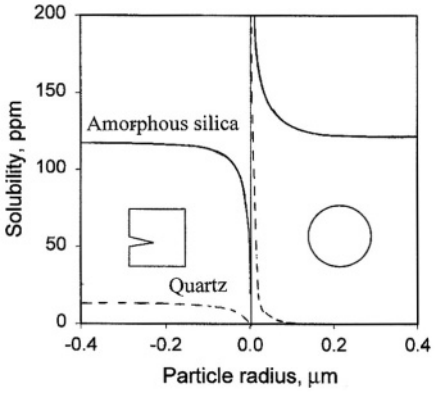

FIGURE 2.6. Dependence of silica stability on the radius of curvature of particles. After Dove and Rimstidt.[469]

As is the case in pure water, the solubility constant in HF solutions depends on the form of SiO_2. For hydrated silica formed by precipitation from an aqueous solution, K has a value of 10^8.[709]

SiF_4 may further react with fluoride ions:

$$SiF_4 + 2F^- = SiF_6^{2-} \qquad K = 1.54 \times 10^6 (20\,^\circ C) \tag{2.6}$$

$$SiF_4 + F^- = SiF_5^- \qquad K = 2.6 \times 10^5 (25^\circ C) \tag{2.7}$$

The reaction constants indicate that SiF_6^{2-} is the dominant dissolved fluorosilicate species in HF-containing solutions.

Fluorine may exist in different forms depending on the composition of the solution. As a weak acid, hydrofluoric acid ionizes only partially to fluoride F^-. The aqueous solutions HF may contain an appreciable quantity of fluorine in the form of un-ionized HF and partially ionized bifluoride HF_2^-.[824,894] The concentrations of these species in aqueous solutions are defined by the following equilibrium conditions:[75]

$$2HF = HF_2^- + H^+ \qquad \log(HF_2^-)/(HF)^2 = -2.51 + pH \tag{2.8}$$

$$HF_2^- = 2F^- + H^+ \qquad \log(F^-)^2/(HF_2^-) = -3.85 + pH \tag{2.9}$$

$$HF = F^- + H^+ \qquad \log(F^-)/(HF) = -3.18 + pH \tag{2.10}$$

Different values of the dissociation constants may be found in the literature.[57,75,123,142,238,709] In aqueous solutions of concentration up to at least 1 M fluoride, the significant fluorine species are F^-, HF, HF_2^-.[57,75] At relatively high concentrations, HF tends to polymerize.[100,238] Figure 2.7 shows the concentration of each dissolved species as a function of HF concentration.[142] The concentration of commercially available concentrated HF solution, is 49 wt%, equivalent to 24.5M.[451]

NH_4F is commonly used to prepare buffered solutions for etching of silicon and its oxides. For NH_4F-buffered HF solutions, the equilibrium is further complicated by the reaction

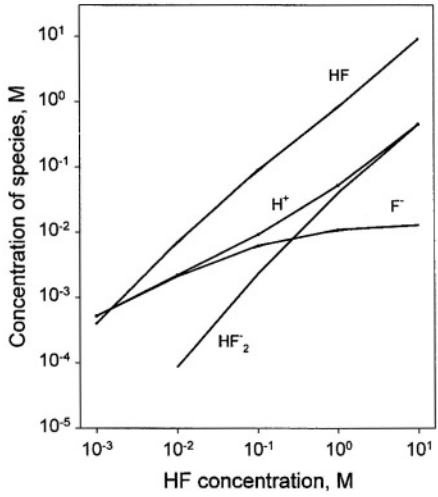

FIGURE 2.7. Ionic species concentrations in HF solutions. After Torcheux *et al.*[142] (Reproduced by permission of The Electrochemical Society, Inc.)

$$NH_4^+ = NH_3 + H^+ \qquad K_a = 6.31 \times 10^{-10} \tag{2.11}$$

Figure 2.8 shows the concentrations of each dissolved species in various mixtures of HF (40%)–NH_4F (50%) solutions.[142] NH_4F solutions with higher pH values can be made by adding NH_4OH to the system.[634] The solubility of silicon may also be affected by the presence of other species as shown in Table 2.6.

2.3. SURFACE ADSORPTION

The atoms of the very first surface layer have unsaturated bonds, the so-called dangling bonds, due to the disruption of the periodicity of the crystal structure at the surface. These atoms are highly unstable and react rapidly with the chemical species in the environment, particularly oxygen and water, to form a chemically more stable layer which passivates the surface. In air the silicon surface tends to react with oxygen forming a thin oxide film, that is, native oxide. In water and aqueous solutions the surface of silicon can be terminated by various species including hydrogen, hydroxyl, fluorine, and oxide. In addition, a silicon surface, depending on cleaning procedures,

TABLE 2.6. Solubility (mol/liter) of Various Fluoride Salts in Water at Room Temperature[936]

Cations, A	AF	A_2SiF_6
Li^+	0.1	4.7
Na^+	1	0.03
K^+	15.9	0.0054
Rb^+	13	0.0051
Cs^+	24	0.015
NH^+_4	27	1

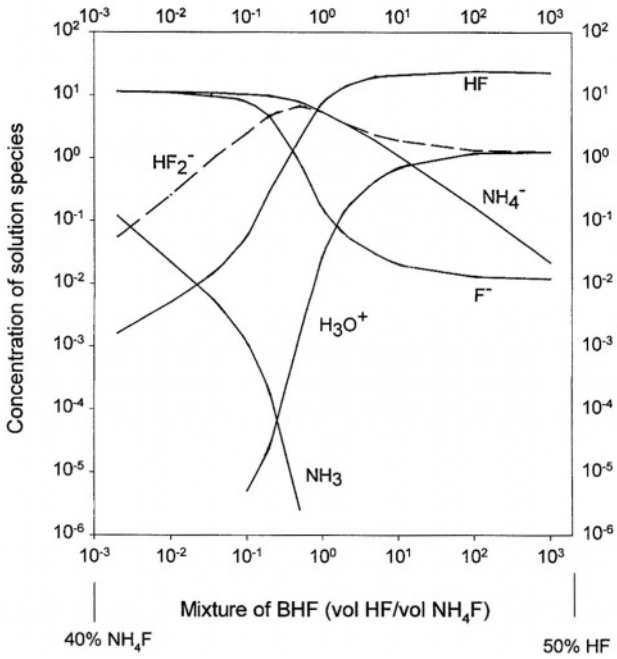

FIGURE 2.8. Ionic species concentrations in NH_4F-buffered HF solutions. After Torcheux *et al.*[142] (Reproduced by permission of The Electrochemical Society, Inc.)

can be contaminated by metallic, organic, and ceramic species. For example, an as-received silicon wafer typically has several thousand ceramic particles and metal concentrations of 10^{11}–$10^{12}/cm^2$ for Fe, Ni, Cu, and Zn.[131,488] Figure 2.9 schematically illustrates a possible surface condition of a silicon electrode.

Thus, unless in a vacuum, the surface of silicon is never "clean" because of the adsorption by foreign species. As will be seen in the following sections, the type of termination, in terms of chemical nature, thickness, and composition, is a function of how the surface is prepared and cleaned. In particular, the surface cleaned with HF solutions, which are widely used for preparation of silicon surfaces, is known to be hydrogen terminated. On the other hand, in water and non-HF solutions, silicon surfaces tend to be covered with an oxide film. Employing certain treatment processes, the surface of silicon can be terminated by different species—H and/or F and/or OH—using different cleaning solutions as shown in Table 2.7.[126]

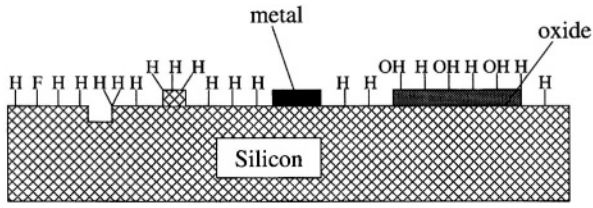

FIGURE 2.9. Schematic illustration of a surface condition of silicon in aqueous solutions.

TABLE 2.7. Termination of the Silicon Surface Treated with Different Cleaning Solutions[126]

Mixture	Water rinse	Surface oxide	Main termination
HF only	No	No	H
H_2SO_4 (97%) : H_2O_2(30%), 1:4, 2 min; or HNO_3 (70%), 80 °C, 5 min			
+10–100 ppm HF	No	Yes	F
	Yes	Yes	OH
+1000 ppm HF	No	No	F and H
	Yes	No	OH and H

2.3.1. Hydrogen Termination

In HF solutions the silicon surface is predominantly terminated by hydrogen. There may be small amounts of oxygen- and fluorine-terminated sites depending on the conditions. The phenomenon of hydrogen termination of silicon surfaces has been extensively investigated. Experimental results indicate the following general characteristics: (1) hydrogen termination is essentially complete with immersion time on the order of 1 min; (2) it is formed through chemical adsorption yielding a covalent bond having a strength close to that of the Si–Si bond; (3) each surface silicon atom can be terminated by one, two, or three hydrogen atoms depending on its geometric position in the surface lattice; (4) the surface is stabilized (or passivated) by hydrogen termination. The extent of termination and type of hydrides depend on the surface condition, solution composition, and preparation procedures. Table 2.8 shows the characteristics of hydrogen adsorption on silicon surfaces prepared by different processes.

In general, unless special procedures are taken, the silicon surfaces of both (100) and (111) orientations treated with HF solution are completely terminated by hydrogen in the form of mono-, di-, and trihydride. It is rough at the atomic scale due to the presence of terraces, steps, kinks, adatoms, and vacancies displaying a mixture of facets of (100), (111), and other orientations.[577,622] Whether the termination is dominated by mono-, di-, or trihydride depends on the orientation and roughness of the surface. The ideal (100) surface tends to be terminated by SiH_2 and (111) by SiH or SiH_3 due to the difference in the number of dangling bonds between the two surfaces.[577,820] It is more difficult to obtain a flat (100) surface with a termination completely by SiH_2 due to the more reactive nature of the (100) surface. The atoms on an ideal (100) silicon surface have two dangling bonds, which is most favorable for the formation of dihydride. The fact that appreciable amounts of mono- and trihydrides are generally also found suggests that the (100) surface after treatment in HF is atomically rough since these bonds will only be present at atomic steps where the silicon atoms may have single or triple dangling bonds.[636] Thus, the form of hydrides can be used as an indication of surface flatness at the atomic scale. The surface is characteristically rough on an atomic scale, when all three types of hydrides are present on the surface.

The (111) surface with an almost complete termination by SiH, indicating atomic scale flatness of the surface, can result from different treatment procedures including a

TABLE 2.8. Studies on Hydrogen Termination of Silicon Surface

Treatment	Adsorption and roughness	Ref.
(111) 1.5% HF, 30 s	SiH, SiH_2, SiH_3, 12% SiF, terraces and steps	635, 807
1.5% HF, 30 s + 0.5 h in H_2O, 25 °C	SiH, SiH_2, SiH_3, <1% SiF, removing steps	
1.5% HF, 30 s + 10 min in H_2O, 100 °C	SiH,<1% SiF, atomically flat	
9° (111), BHF, pH 2–8, 5 min	Complete H termination, terraces and steps	819
(111) 4.5% HF, 20 min	Complete H termination, flat	641
BHF, pH 4.5–5.3	SiH, atomically flat	
(111) 0.2 M NH_4F, 0.5 V_{sce}	Complete H termination	743
n(111), 0.2 M NaF, 0.72 V_{NHE}, pH 4–5.3	H termination associated with dark current	446
n(111), 0.2 M NaF, pH 4–5.3	No SiH at $i > i_p$, H termination under illumination at $i < i_p$ surface roughens with photocurrent	621
n(111), 0.1 M NaF, pH 4	Quantity of SiH_x increases with roughening, PSL[a] formation	775
n(111), organic solvents	H_2O adsorption, Si–O–H bonds, oxide islands	395
n(111), acetonitrile + 0.1 M TBAP	Si–H bonds decrease with aging and increasing Si–O–H bonds	929
n(111), organic solutions	Oxidation of SiH groups by residual water	619
n(110), 0.5 M NH_4F at pH 4.5, illuminated	SiH_x intensity increases with time, decays in the dark	907
(100) 5% HF	Incomplete H termination, some fluoride coverage	726
5% HF + water rinse	Complete H termination	
(100) 1% HF + UV cleaning	H/Si ≈ 1, O/Si = 0.01, C/Si = 0.018, F/Si = 0.007	563
1% HF + UV cleaning	O/Si = 0.66, C/Si = 0.23	563
p(100), *n*(111), 50% HF in ethanol	SiH_x at all potentials and current densities	215
40% HF, 1 min	SiH on (111), SiH and SiH_2 on (100), O and F < $10^{14}/cm^2$	663
40% HF, 1 min + 10 s–100 min H_2O rinse	Mainly H covered, O ~$4 \times 10^{14}/cm^2$, F < $10^{13}/cm^2$ in 3 min	
40% HF, 1 min + 50 h H_2O rinse	SiO_2 ~ two monolayers, Si–H groups in bulk side of Si	
0.5% HF, pH 9–10	SiH on (111), atomically flat Si, SiH_2, SiH_3 on (100), rough	574, 577, 622
pH < 4	SiH and SiH_2 at defects, SiH_3 at flat area on (111), rough SiH, SiH_2, and SiH_3 on (100), rough	
Poly Si, 5%HF	SiH_3 on (111), (110), SiH_2 on (100)	820
(111) in NaOH	Different stability of mono hyobride on terrace and steps	[1109]

[a]PSL, porous silicon layer.

dip in HF solutions.[574,577,622,635,663] Predominant SiH_3 termination of a flat (111) surface is also reported.[577,820] The silicon atoms on steps, which are terminated by di- and trihydrogen, are preferentially attacked, while the atoms, which are terminated by monohydrogen, are not directly attacked.[895] Surface roughening of (111) planes is generally accompanied by the formation of di- and trihydrides.[446,621]

Hydrogen termination of the silicon surface appears to occur over the whole pH range from acidic to basic whenever the surface is not covered with an oxide film. The silicon surface is found to be covered with hydrogen in alkaline solution even under

high etching rates.[227] The relative amounts of the hydrides as well as the surface flatness, however, change with pH.[446,574,621] The effect of pH can be attributed to the dependence of the concentration of HF, F^-, and HF_2^- species on pH.[437] For the (111) surface, dipping in HF solution results in termination by mono-, di-, and trihydride, whereas in basic fluoride solutions (pH 9–10) the surface is terminated exclusively by monohydride.[574,635] According to Higashi *et al.*,[574] in the basic fluoride solutions the surface steps and defects on the (111) surface which are terminated by di- and trihydride are preferentially attacked by water, resulting in Si–O bonds. These Si–O bonds are then removed preferentially in the presence of HF, resulting in the formation of ideally terminated (111) silicon surface with monohydride oriented normal to the surface. However, it has been reported that increasing pH increases the attack of the atoms on the (111) plane and thus results in large-scale roughness.[895]

Hydrogen termination is found to occur at all potentials with or without significant silicon dissolution and current flow, except for the range in which anodic oxide forms.[215,227,446,602] Rao *et al.*[215] found that the silicon surface is covered with Si–H bonds at all potentials and current densities at which porous silicon forms in HF solutions of 5% to 50% concentrations. Rappich *et al.*[227] found that the silicon surface is covered with hydrogen in alkaline solutions at the open-circuit potential at which silicon is etched at high rates. In alkaline solutions, applying a cathodic potential has no effect on the hydrogen coverage, whereas hydrogen adsorption disappears at anodic potentials where passivation occurs. In buffered HF (BHF) solutions, hydrogen coverage of the silicon surface depends on potential.[446,621,1036]

The relative amount of the hydrides depends on atomic surface flatness and water temperature.[532,895] Water rinse after dipping in HF solutions tends to flatten the surface.[262,532,641] Water tends to react with silicon di- and trihydrides and remove them from the surface, leaving hydrogen termination and a flatter surface. For example, as shown in Fig. 2.10 the (111) silicon surface after immersion in 1.5% HF is terminated by mono-, di-, and trihydrides.[635] After immersion in 100 °C water for about 500s the amount of di- and trihydrides was greatly reduced; they were replaced by monohydrogen, leaving the surface covered more homogeneously with monohydride.

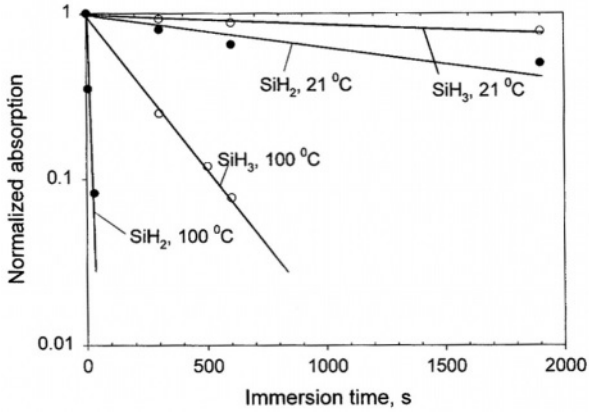

FIGURE 2.10. The dependence of hydrogen absorption on immersion time. Each value is normalized by that at 0s of immersion. After Watanabe *et al.*[635] (Reprinted with permission of The Physical Society of Japan.)

In addition to water rinse, certain other procedures also produce flatter surfaces. It has been reported that a BHF-treated surface is flatter than one treated with HE.[641] A photocurrent-assisted etching followed by a dark current transient has been found to reduce microscopic roughness.[1036] A multistep process, involving formation of an anodic oxide, dissolution in 0.2 M NH_4F at pH 4 and then at pH 4.9, produced a completely monohydride-terminated (111) surface.[743]

In organic solvents, the hydrides of HF-treated surface maintain their structure but the bond energy tends to vary with solvent type.[619] The amount of hydrides decreases with immersion time due to oxidation of the hydrogenated surface by the small amounts of water present in the organic solvents. There is a marked difference of the oxidation rates for (111) and (100) surfaces.

The silicon surface terminated by hydrogen after etching in HF is rather stable at room temperature, reacting only very slowly with oxygen or water. A change of less than 10% of the surface M concentration is found over a period of 1 month in an ultrahigh vacuum.[895] The sticking probability of oxygen on H-terminated surface is many orders magnitudes smaller than that of a clean silicon surface.[1096] In water, whereas a bare silicon surface is quickly oxidized, a hydrogen-terminated surface is replaced by a monolayer of oxide only after immersion for more than 100 min as shown in Fig. 2.11.[325,663] In particular, the ideally hydrogen-terminated Si (111) surface, that is, monohydride, is extremely stable in both highly acidic and highly basic solutions (e.g., from HC1 to NH_4OH).[574] Polyhydrides are found to be more stable than monohydride.[1096] Hydrogen termination also serves to passivate grain boundaries.[571] Terrace monohydride has different stability from step monohydride.[1109] As a result of hydrogen passivation, HF-treated silicon surface exhibits a very low density of surface states in various acids over a wide concentration range.[648]

Mechanistic Aspects. The energy of the hydrogen–silicon bond is in the range of 3–4eV, which is similar to the silicon–silicon bond.[229,914,980] On the other hand, the fluorine–silicon bond has a much higher bond energy, 6–7eV. Thus, thermodynamically, Si–F is the more stable bond. F-terminated silicon complexes are unstable in HF

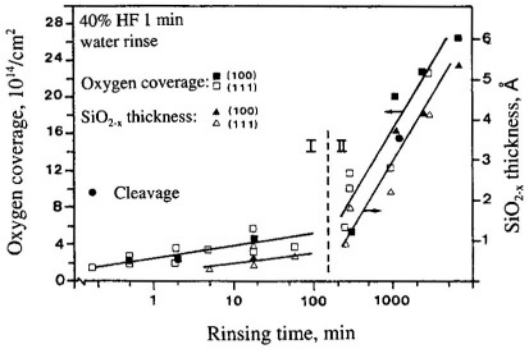

FIGURE 2.11. The oxygen coverage (left-hand scale) as a function of rinsing time shows a change in inclination of the curve after 200–300 min, which coincides with the appearance of prevalently SiO_{2-x} (right-hand scale). Both branches of the growth curve show a logarithmic dependence on time and the break indicates invasion of the lattice by oxygen. (Reprinted with permission from Graf *et al.*[663] © 1989, American Vacuum Society.)

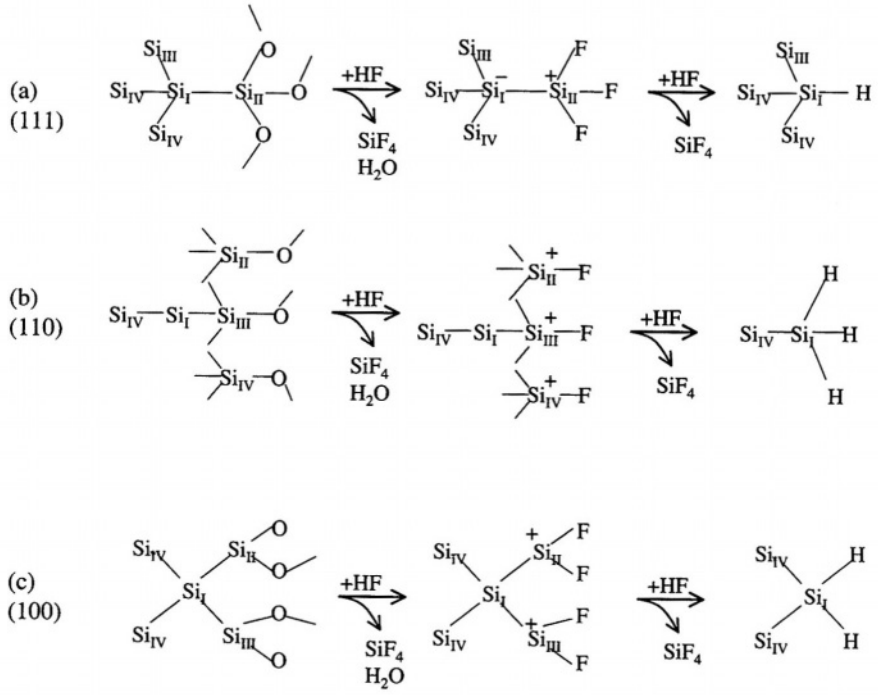

FIGURE 2.12. The possible mechanism of Si–H bond formation on Si surface by HF-etching treatments of Si/SiO_x, according to the kind of crystalline planes of Si: a, (111); b, (110); c, (100). After Ubara *et al.*[820]

solutions because of strong polarization of the Si–SiF back bonds, thus facilitating the attack by HF molecules, as originally proposed by Ubara *et al.*[820] This results in reactions such as

$$\mathrm{Si{-}SiF_3\ (surface) + HF\ (solution) \rightarrow SiH\ (surface) + SiF_4\ (solution)} \qquad (2.12)$$

which leaves a hydrogen-terminated surface. The formation of mono-, di-, and trihydrides, according to Ubara *et al.*,[820] can be described by the reactions illustrated in Fig. 2.12. The ideal (100) surface tends to be terminated by SiH_2 and the (111) surface by SiH or SiH_3 due to the difference in the number of dangling bonds between the two surfaces. The thermodymic, kinetic and structural characteristics for hydrogen interaction with silicon surface has been reviewed by Oura *et al.*[1076]

Trucks *et al.*[821] provided a kinetic explanation of hydrogen termination based on the calculation of activation energies involved in breaking up the various silicon bonds in the following reactions:

$$\equiv\mathrm{Si{-}OH + HF \rightarrow Si{-}F + H_2O} \qquad 0.55\,\mathrm{eV} \qquad (2.13a)$$

$$\equiv\mathrm{Si{-}SiF_3 + HF \rightarrow \equiv Si{-}H + SiF_4} \qquad 1\,\mathrm{eV} \qquad (2.13b)$$

$$\equiv Si\text{–}SiH_3 + HF \rightarrow \equiv SiH + SiH_3F \qquad 1.6\,eV \qquad (2.13c)$$

$$\equiv Si\text{–}H + HF \rightarrow \equiv SiF + H_2 \qquad 1.2\,eV \qquad (2.13d)$$

Reaction (2.13a) has the smallest activation energy, meaning that the Si–OH bond is highly unstable in HF solutions and if present will be quickly replaced by other bonds. Reaction (2.13b), which results in hydrogen termination, is kinetically more favorable than reactions (2.13c) and (2.13d). This means that fluoride termination tends to be replaced by hydrogen termination, which, whether in the form of mono-, di-, or trihydride, is kinetically more stable. Similar to HF, the attack by F^- and HF_2^- leading to hydrogen termination has also been proposed.[822,914]

Hydrogen termination of the dangling bonds on the surface stabilizes the silicon surface. Since the electronegativity difference is small between Si–H and Si–Si bonds, the H-terminated surface is stable due to the lack of polarization of the back Si–Si bonds.[656,896] Thus, the energy level of the hydrogen-terminated Si surface is identical to that of the top of the valence band.[99] The fast removal of di- and trihydrides in water can be explained by the difference in the extent of polarization among the different hydrides. Trihydride has three polarized Si–H bonds, whereas dihydride has two, making the back bonds of SiH_2 and SiH_3 weaker than SiH.[635]

The hydrogen atoms bonded to the silicon atoms in water, according to Niwano *et al.*,[409] are, however, not completely immobile but undergo a constant hydrogen exchange reaction with the hydrogen atom of the water molecule, generating negatively charged surface silicon atoms through the reactions $Si\text{–}H + H_2O \rightarrow H_3O^+ + Si^-$ and $Si^- + H_2O \rightarrow Si\text{–}H + OH^-$. The generation of negatively charged silicon atoms could then be a pathway for other reactions.

2.3.2. Fluoride Termination

The silicon surface after immersion in a HF solution, although terminated predominantly by hydrogen, may also be terminated by fluorine atoms to various amounts depending on solution composition. In general, fluorine content on the HF-treated silicon surface compared to that of hydrogen is very low and is not affected by the immersion time after the complete removal of the native oxide.[563,641,663,726] Higher fluorine contents on the HF-treated surface have, however, been reported. For example, the (111) surface after immersion in 1.5% HF can contain about 12% fluoride.[635] Fluorine termination of over half of the surface area is possible using HF at a concentration exceeding 50%.[563] The amount of surface fluorine tends to increase with HF concentration as indicated in Fig. 2.13.[563] It also varies with the pH of ammonium fluoride solutions as shown in Fig. 2.14; the coverage reaches a peak of about 20% at a pH of about 6.4.[260] In addition, it varies with the type of solution: The hydrogen-terminated surface has about 2.5% Si–F bonds when cleaned with 5% HF but this is reduced by two-thirds in buffered solutions with a minimum of almost zero coverage at a pH of 5.3.[634] Submonolayer of F has been reported to be present on silion surface under current doubling condition.[909]

A fluorine-terminated surface is not as stable as a hydrogen-terminated one and is readily removed by a water rinse.[126,635,663] For example, the amount of fluorine, ~1%,

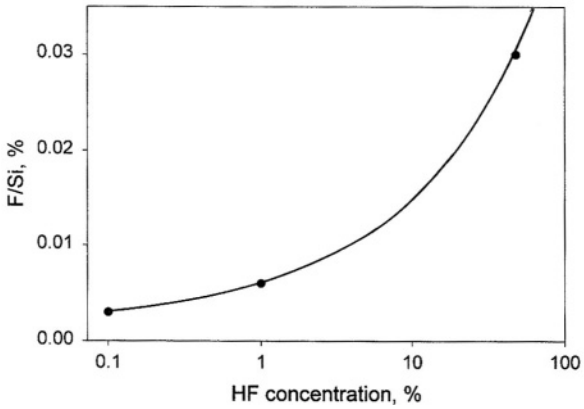

FIGURE 2.13. Fluorine concentration of the silicon surface after UV/HF cleaning versus HF concentration. After Takahagi *et al.*[563]

decreases to one-third when the surface is rinsed with pure water for about 10 s.[563] For the (111) surface after immersion in 1.5% HF, the fluoride coverage drops from 12% to 5% after immersion in deionized water for 5 s and to less than 1% after 0.5 h.[635] The fluorine sites are replaced by OH groups, producing a OH-terminated surface.[126,563] Thus, for the surface that is dominantly terminated by fluorine, dipping in concentrated HF solutions followed by a water rinse results in a hydroxyl-rich surface.

The instability of fluorine termination can readily be explained by the theory for hydrogen termination, that is, bonding with fluorine significantly weakens the back silicon–silicon bond leading to the dissolution of the atoms bonded by fluorine.

2.3.3. *Adsorption of Metal and Organic Impurities*

In addition to adsorption of hydrogen, hydroxyl, and fluorine, the silicon surface may also contain trace amounts of other species due to the impurities present in the solution. A clean silicon surface is easily contaminated by metal impurities in water or solutions. For example, the surface concentration of metals after immersion in dilute HNO_3 containing 1–3 ppb of Ba, Cu, Ni, Sr, Zn, K, Al, Ca, Cr, and Fe can be in the

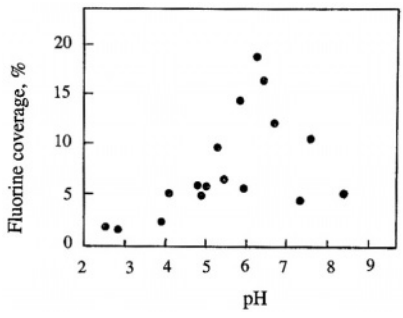

FIGURE 2.14. Dependence of fluorine coverage of silicon surfaces on the pH of 1 mol dm^{-3} ammonium fluoride solutions which were used for the surface treatment. After Fukidome *et al.*[260]

TABLE 2.9. Surface Concentrations of Deposited Metals, 10^{10}/cm^2, from Aqueous Solution at Metal Concentrations of 5×10^{-8} M and 20 °C after Immersion for 1000 s[977]

pH	Al	Ba	Ca	Cr	Cu	Fe	K	Ni	Sr	Zn
3	2.4	0.3	0.8	2.3	0.8	0.9	1.4	0.6	0.5	0.6
4.5	72.9	4.2	10.8	72.1	17	6.1	0.5	8.3	7.7	8.4
5.6	96.2	12.6	29.8	78.8	46.1	20.8	0.0	28.4	25.3	27.3

range of 10^9 to 5×10^{12} atoms/cm^2.[972] Table 2.9 shows the surface concentration of various metals after exposure for 1000 s to aqueous solutions containing 5×10^{-8} M of each metal.[977] The surface concentration appears to strongly depend on pH. Even the very active elements such as Al^{3+}, K^+, and Na^+ can be deposited on the silicon surface, reaching a surface concentration of 0.5 to 100×10^{10} atoms/cm^2 at a low concentration of 5×10^{-8} M. The amount of deposition generally increases with the concentration of Fe, Zn, and Ni in the SC-1 cleaning solution as shown in Fig. 2.15.[975]

At an impurity level of metal concentration on the order of 10^{10}/cm^2, deposition may occur by physical adsorption, chemical absorption, and displacement processes.[96,99,976] Physisorption due to van der Waals interactions takes place when the metallic impurities are in solid form such as iron in neutral or alkaline solutions. Aluminate deposition in neutral or alkaline medium is attributed to chemisorption. The deposition of noble metals such as Cu is generally via displacement reactions. The deposited metal can be bonded to silicon, attached to surface species such as OH groups, or embedded in native oxide.[915,972,975]

According to Loewenstein *et al.*,[972] the deposition of the contaminant level of metals from cleaning solution onto the silicon or silicon oxide surface occurs by replacing the hydrogen ion on the surface silanol groups:

$$\text{Si–OH} + \text{M}^{n+} \leftrightarrow \text{Si–OM}^{(n-1)+} + \text{H}^+ \tag{2.14}$$

Metals and H^+ compete for the available surface sites, the number of which depends on the manner of surface preparation. The surface concentration of the metals, σ_i, can be described by the Langmuir model for adsorption:

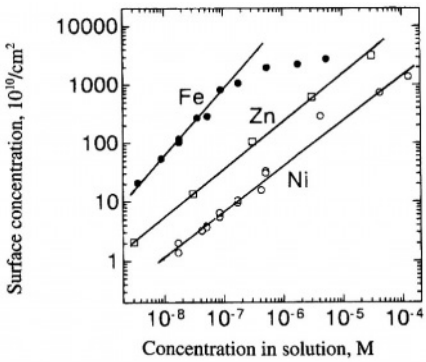

FIGURE 2.15. Adsorption isotherms of Fe(III), Ni(II), and Zn(II) on silicon wafer in SC-1 solution, after immersion for 10 min at 80 °C. After Mori *et al.*[975] (Reproduced by permission of The Electrochemical Society, Inc.)

$$\sigma_i = \sigma K_i \left[M_i^{n+} \right] \Big/ \left\{ 1 + \sum k_i \left[M_i^{n+} \right] \right\} \tag{2.15}$$

The surface concentration of a metal ion depends on (1) the adsorption site density, σ, (2) the attraction between surface sites and metal ion, K_i, (3) the concentration of the metal ion, and (4) the concentrations of other metal ions and hydrogen ion in the solution.

When silicon wafers are exposed to a clean room atmosphere, organic molecules in the air can rapidly be adsorbed onto the surface.[325,374] The amount of contamination, on the order of 10^{-11} g/cm^2 (equivalent to a surface density of 10^{11}/cm^2 assuming a molecular weight of l00g/mol), for alcohol, butyl acetate, ethylene glycol, amide, phthalate, and others, increases with exposure time. The organic species that have low boiling points tend to be adsorbed immediately and are later replaced by those with higher boiling points. Organic molecules have been found to bond covalently via Si–C bonds.[1099,1115] The amount of adsorption decreases with gradual formation of the native oxide in air.[325] The initial concentration of organic species follows the rate of adsorption, but the final concentration is determined by the desorption rate.[1146] In alcohols, freshly prepared H–Si surface may be terminated by methoxy groups.[686] UV radiation has been found to decompose the organic contaminants and its use during cleaning reduces surface carbon content to a very low level.[563]

2.4. NATIVE OXIDE

Native oxide is the oxide that grows spontaneously on a clean silicon surface exposed in an ambient environment such as air or solutions. The formation of native oxide, which is inert in most solutions, passivates the silicon surface allowing the silicon to be used as an electronic material in processing and application environments. The presence of native oxide degrades the low-temperature growth of high-quality epitaxial Si film or the precise control of the thickness and quality of very thin gate oxides.[567,579] In electrochemical experiments in particular, native oxide is part of the initial condition for a silicon surface and affects the electrode properties. It is commonly removed by dipping in a HF solution, which produces a hydrogen-terminated surface, prior to the experiment.

2.4.1. In Air

The surface of silicon in air is always covered with a very thin oxide film. Table 2.10 shows that the thickness of native oxide formed on the surface of silicon after several days in air varies from 5 to 20 Å depending on preparation conditions. Such a large variation in the thickness of native oxide indicates the great sensitivity of the surface reactivity to minute variations of environmental and material conditions.

The rate of formation of native oxide in air depends on the initial condition of the surface and the cleanness of the air. The formation of oxide on a perfectly clean silicon surface, e.g., a cleaved surface, is relatively fast, reaching 5–7 Å within a few minutes after exposure to air.[325] The formation of native oxide on the surface after being

TABLE 2.10. Native Oxide Films Formed in Air and Solutions

Surface	Ambient	Thickness (Å)	Ref.
	In air and gases		
As received	Air	7	563
	Air	~30	378
Cleavage	Air, 5–10 min	5–7	325
Cleavage	Air, 24 h	11–13	325
HF etched	Air, 5 weeks	18	325
HF etched + 10 min WR[a]	Air, 42% RH[b], <1 min	2.1	579
HF etched + 10 min WR	Air, 42% RH, 7 days	6.7	579
HF etched + 10 min WR	O_2/N_2 (1/4), 7 days	1.7	579
HF etched + 10 min WR	N_2, 7 days	1.9	579
1 min HF + 2 min WR	Air, 1 day	~1	555
1 min HF + 2 min WR	Air, 20 days	~3	555
5% HF dip	Air, 1.2% H_2O, 7 h	5.5	634
16% NH_4F + 5% HF, pH 4.5	Air, 1.2% H_2O, 7 h	3.5	634
1 N HF	Air, 17 h	5	674
	In solutions		
	Pure water, 60 min	1.0	978
	10 ppm HF, 60 min	0.4	978
HF etched + 10 min WR	Pure water, 4 days	5.6	579
Cleavage	DI H_2O, 5–10 min	3–4	325
	H_2SO_4 (97%):H_2O_2 (30%), 2 min	10	126
	H_2SO_4 (97%):H_2O_2 (30%) + 1000 ppm HF, 2 min	~0	126
	10 min in 2 M KOH after HF cleaning	~25	378
	$H_2SO_4 + H_2O_2$	5.5	554
	$NH_4OH + H_2O_2 + H_2O$	4.1	554
	0.1 M TBAP[c] in organic solvents, 7 days	6, islands	692
40% HF, 1 min	100 min water rinse	1	663
40% HF, 1 min	50 h water rinse	6	663
	HCl (31%):H_2O_2 (31%):H_2O, 1:1:4, boiling time, 10 min	30- to 70-nm islands	405, 760
	NH_4OH (29%):H_2O_2 (31%):H_2O, 1:1:4, boiling time, 10 min	30- to 70-nm islands	405, 760

[a]WR, water rinse.
[b]RH, relative humidity.
[c]TBAP, tetrabutylammonium perchlorate.

treated in HF solution is much slower. For example, in one case the HF-treated surface is covered with an oxide of 2–3 Å after exposure to air for 1 hour;[325] in another, it takes about 1 week for a monolayer to form.[555]

The slow growth of native oxide on the HF-treated surface is attributed to the hydrogen termination which passivates the surface. The formation of the first monolayer of oxide requires the breakup of the Si–H bonds. According to Graf *et al.*,[555,560] the oxide growth on HF-treated Si in air follows two distinct stages as shown in Fig. 2.16. There is an incubation period initially, during which the oxide grows very little. Afterwards, the growth shows a logarithmic dependence on time with a rate of ~5 Å/decade. Another study reported similar growth kinetics as shown in Fig. 2.17.[579]

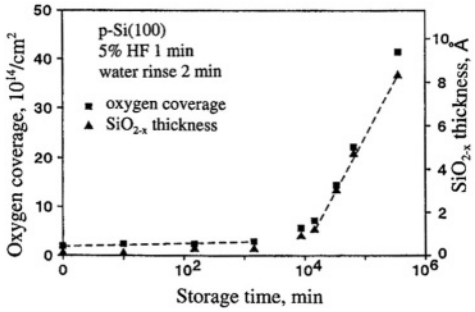

FIGURE 2.16. The oxygen coverage (left scale) as a function of storage time in air shows two branches of oxide growth with a change in inclination of the curve after about 1 week. The same dependence is measured for the SiO_{2-x} thickness (right scale; the two scales are mutually adjusted using the density of SiO_2). The second branch of the growth curve shows a logarithmic dependence on storage time. (Reprinted with permission from Graf *et al.*[555] © 1990, American Institute of Physics.)

There is very little growth up to about 200 min after which the growth rate increases significantly. The S-shaped curve in Fig. 2.17 is attributed to a layer-by-layer growth of the oxide with 5.4 to 7.6 Å corresponding to two layers of native oxide.

The growth mechanism of native oxide film, several angstroms in thickness, at room temperature differs from that of the thicker oxide formed by thermal oxidation.[554] According to Grundner and Jacob,[906] oxide growth differs for hydrophilic and hydrophobic surfaces. The oxide on hydrophilic surfaces mainly grows in the cleaning media and consists of hydrated SiO_2 through all stages of growth. On a hydrophobic surface, however, the oxidation begins with formation of a lower oxidation state, which is transformed into SiO_2 during storage in air.

The substrate condition plays an important role in the growth of native oxide on silicon. The growth rate of native oxide films is similar for lowly and moderately doped silicon substrates.[325] An increased growth rate is observed with high dopant concentration $>10^{19}$/cm^3 on both *n*- and *p*-type silicon substrates. Figure 2.17 shows that for *n* type, the oxide grows faster on heavily doped substrates.[579] In addition, it shows that

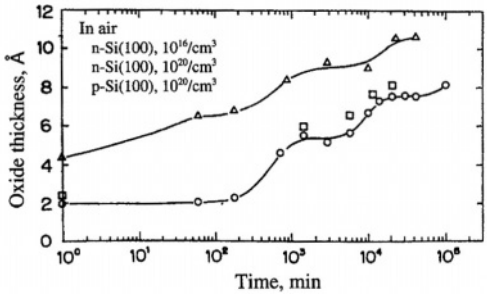

FIGURE 2.17. Oxide thickness data plotted as a function of the logarithm of the exposure time of wafers to air at room temperature. The H_2O concentration in air is 1.2% on the average (42% relative humidity). (Reprinted with permission from Morita *et al.*[579] © 1989, American Institute of Physics.)

TABLE 2.11. 7-Day Growth of Native Oxide versus H_2O Concentration[579]

Ambient	H_2O concentration	Oxide thickness, Å
Air	~1.2%, RH 42%	6.7
$O_2/N_2 = 1/4$	<0.1 ppm	1.7
N_2	<0.1 ppm	1.9

with the same doping level the growth rate is faster on *n*-Si than *p*-Si. The growth rate is greater on <111>-oriented than <100>-oriented surfaces, which is similar to thermal oxides.[325,510]

Composition of the air also has a strong effect on the initial growth of the native oxide. Water content in the air strongly affects the growth of native oxide as can be seen in Table 2.11.[579] The growth kinetics are determined by the nature of adsorption of oxygen and water molecules onto the surface.[180,701,887] Oxide does not grow much in air containing very little water.[99,579]

Factors such as solution composition, dipping time, and water rinse are important in the formation of native oxide as they affect the surface condition in terms of the type and relative amount of adsorbed species as well as surface roughness.[99,555,560,579] For example, the pH of buffered HF solutions is found to be an important factor in determining the formation of native oxide in air as shown in Fig. 2.18.[634] The growth rate is much slower in solutions having lower pH values due to the larger amount of Si–F bonds on the surface.

In particular, metallic impurities on the silicon surface, arising from contamination in the cleaning solutions, strongly enhance oxide growth. Figure 2.19 shows that the oxide growth rate in the air increases with copper content on the surface.[560] A copper coverage of 5% of a monolayer leads to a full layer of oxide within 2 min. The copper is found to be located at the Si/SiO_2 interface. Also, during the oxide growth, part of the copper shows a change in the oxidation state, forming a mixture of elemental copper

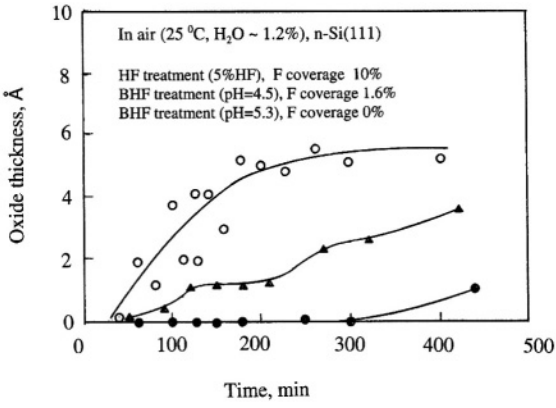

FIGURE 2.18. Native oxide growth on *n*-Si(III) after 5% HF of BHF (pH 4.5 and 5.3) cleaning in clean room air with 1.2% H_2O at 25 °C. After Yasaka *et al.*[634]

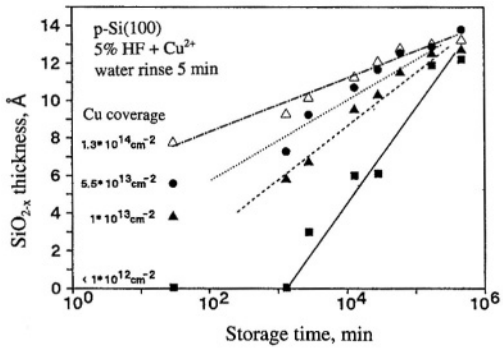

FIGURE 2.19. The oxide growth kinetics for storage of Si (100) wafers in air. After the HF treatment, wafers were water rinsed for 5 min. The copper coverages were varied up to $1.3 \times 10^{14}\,cm^{-2}$. Depending on the copper coverage, the initial oxide thicknesses vary, as correspondingly do the growth rates. SiO_{2-x} thicknesses after 1 year of storage turn out to be almost independent of the copper coverage. (Reprinted with permission from Graf *et al.*[560] © 1991, American Institute of Physics.)

and Cu^+. According to Derrien *et al.*,[499] a clean Si surface can be more easily oxidized if the Si atoms displaying their covalent sp^3 configuration are disrupted. This occurs when a few metal atoms such as Au, Cu, and Pd are evaporated onto the Si surface. These atoms interact strongly with Si and destroy the sp^3 configuration, giving rise to an intermixed surface zone where Si and metal atoms are embedded together. These silicon atoms, liberated from their sp^3 configuration, behave as metal atoms and react very easily with oxygen to form a SiO_2 film.

2.4.2. In Water and Solutions

In the presence of water for a sufficiently long time, the silicon surface is always covered with a thin oxide film independent of the initial surface condition. The thickness and the growth rate, however, depend on the initial surface condition. On a cleaved silicon surface, representing a perfectly clean condition, an oxide of 3–4 Å is found to grow on the surface after the cleavage in deionized water for 5–10min.[325] The stable thickness of native oxide films on silicon surface in water, as shown in Table 2.10, is similar to that formed in air, ranging from 5 to 10 Å. For a HF-cleaned surface, Fig. 2.20 shows that the growth of native oxide in water has two distinct stages, similar to that in the air, with a very slow growth initially followed by a faster growth.[579] The oxide remains relatively thin for about 3 h before increasing in thickness. The slow growth of native oxide on the HF-treated surface is due to the hydrogen termination, which has to be replaced by hydroxyl termination before formation of oxide. The nucleation and growth of oxide tend to follow different modes in different solutions.[405,760] Also, dissolved oxygen in the water has a significant effect on the growth of the oxide as shown in Fig. 2.20.[579] The oxide thickness increases with increasing concentration of dissolved oxygen in the water. Since the growth rate without dissolved oxygen is very slow, it has been suggested that the native film growth in water may require the presence of both water and oxygen. In ozone containing water, the amount of oxide increases with ozone concentration in the range of 0–15 mg/l.[1091] This dependence disappears at higher concentrations.

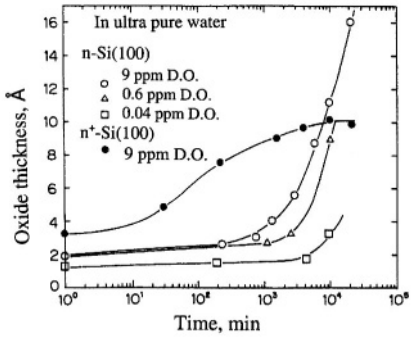

FIGURE 2.20. Oxide thickness as a function of the immersion time of wafers in ultrapure water at room temperature for different dissolved oxygen concentrations. (Reprinted with permission from Morita *et al.*[579] © 1989, American Institute of Physics.)

The presence of HF in water limits the thickness of native oxide. Oxide does not form when the concentration of HF in water is higher than l0ppm.[978] The oxide thickness is found to be near zero in sulfuric acid containing 0.1% HF.[126] Generally, in aqueous solutions the thickness at the steady state is determined by the oxide growth rate, which is a function of the oxidant concentration in the solution, and by the oxide dissolution rate, which depends on the concentration of HF in the solution. The oxide tends to be relatively thick in solutions containing a high concentration of oxidant such as H_2O_2 and a low concentration of HF. On the other hand, the oxide tends to be thin in solutions with a low oxidant content and a relatively high concentration of HF. When the concentrations of both oxidant and HF are high, the silicon is rapidly etched through oxide formation and dissolution processes. In NH_4F solutions the formation of oxide film depends on concentration.[1090] At NH_4F concentration below 10%, the formation rate increases with concentration. At concentration higher than 10%, oxide does not form because the dissolution rate is higher than the formation rate.

Dissolution of silicon in water occurs during the growth of native oxide in water as shown in Fig. 2.21.[579] The number of dissolved Si atoms is over one order of magnitude larger than the number of Si atoms in native oxide. The formation of native oxide in pure water is thus influenced by the dissolution of silicon in water. On the other hand, little dissolution of silicon in pure water was observed for the samples with native oxides formed in air or in solutions of $H_2SO_4 + H_2O_2$ or $NH_4OH + H_2O_2$. This indicates that the oxide film formed in pure water is a relatively poor barrier.

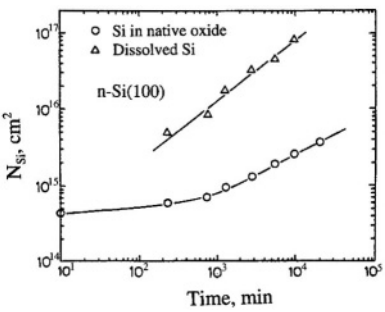

FIGURE 2.21. Time dependences of the number of Si atoms in native oxide and the number of dissolved Si atoms in ultrapure water. N_{Si} is defined as the number of Si atoms per unit area on wafer surface. (Reprinted with permission from Morita *et al.*[579] © 1989, American Institute of Physics.)

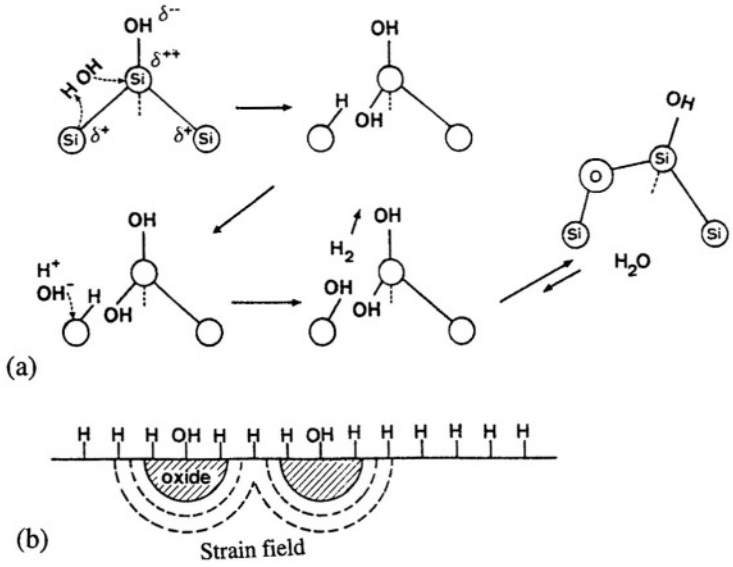

FIGURE 2.22. (a) The reaction path leading finally to condensation of Si–OH and formation of strained Si–O–Si bridges; (b) the local development of oxide nucleated by Si–OH groups on the surface. (Reprinted with permission from Graf *et al.*[663] © 1989, American Vacuum Society.)

The formation of oxide on HF-treated silicon surface in water is postulated by Graf *et al.*[663] to follow the process illustrated in Fig. 2.22. The initial appearance of Si–OH groups is due to the fast exchange reaction of SiF:

$$\text{Si–F} + \text{H}_2\text{O} \rightarrow \text{Si–OH} + \text{HF} \tag{2.16}$$

Due to the strong electronegativity of OH groups, the Si–SiOH back bond is weakened and is attacked by water:

$$\text{Si–SiOH} + \text{H}_2\text{O} \rightarrow \text{Si–H} + \text{OH–Si–OH} \tag{2.17}$$

The Si–H bond so formed is slowly replaced by water according to the reaction

$$\text{Si–H} + \text{H}_2\text{O} \rightarrow \text{Si–OH} + \text{H}_2 \tag{2.18}$$

Finally, oxide is formed through a bridging reaction of Si–OH groups:

$$\text{Si–OH} + \text{Si–OH} \rightarrow \text{Si–O–Si} + \text{H}_2\text{O} \tag{2.19}$$

In nonaqueous solutions the formation of oxide on the surface of silicon requires the presence of water.[395,692] In solvents such as acetonitrile, nitromethane, and dimethyl sulfoxide, the HF-cleaned silicon surface gradually evolves from a H-terminated passive surface to a silicon oxide-covered surface due to the residual water (~10ppm) present

in the nonaqueous electrolyte.[692] Initially, the water is molecularly adsorbed on the silicon surface, then slowly oxidizes the surface silicon atoms to form oxide. In organic solvents, adsorbed residual water can remain on the silicon surface for hours before oxidation takes place.[395] The oxidation may be uniform or in islands depending on the composition of the electrolytes.

The reported experimental results indicate that the formation of native oxide in both air and water has a strong electrochemical component because (1) the oxide growth rate depends on doping concentration; (2) the growth rate increases with the presence of oxidants such as dissolved oxygen or hydrogen peroxide in the solution; and (3) the growth rate is increased by an anodic polarization, and by the presence of a submonolayer of metal atoms. This electrochemical nature has not been considered in the existing models on the mechanism of formation of native oxide.

2.5. HYDROPHOBIC AND HYDROPHILIC SURFACES

The surface of silicon can be hydrophilic or hydrophobic depending on the surface condition. It has been reported that a hydrophilic surface is characterized by OH groups and a hydrophobic surface is covered with Si–H, $Si–CH_x$, or Si–F groups.[906] Thus, a hydrogen-terminated surface is hydrophobic whereas an oxide- or hydroxide-covered surface, which tends to be terminated by OH, is, in general, hydrophilic. A surface covered with a substantial amount of carbon bonded to oxygen is hydrophobic.

Hydrophilic and hydrophobic surfaces can be generated by treatment in certain solutions. As shown in Table 2.7, silicon surfaces with a termination of different species, giving hydrophilic or hydrophobic characters, can be obtained using different cleaning processes.[126] Hydrophilic surfaces can be generated by SC1 solution cleaning followed by DI water rinse; hydrophobic surface can be generated by dipping in dilute HF solution followed by DI water rinse.[454] Treatment with alcohols can also modify the hydrophilic and hydrophobic property.[559] The surface polarized at potentials more negative than the passivation potential is hydrophobic whereas the surface after polarized at potentials positive of the passivation potential is hydrophilic.[541] Also, a hydrophilic or hydrophobic surface tends to change during storage in air.[906] The aging effect is associated with a loss of hydroxyl groups on hydrophilic surface or the appearance of OH groups on hydrophobic surface.

Upon immersion in aqueous HF solutions a clean silicon surface becomes hydrophobic very rapidly due to the adsorption of hydrogen ions. On the other hand, a silicon oxide remains hydrophilic when exposed to such echants and a silicon substrate covered with an oxide film remains wetted by the etching solution until the oxide film is completely dissolved. This change of wetting characteristics can be used as a criterion for determining the end point in etching of an oxide film. As shown in Fig. 2.23, the surface hydrophobisation can be classified into three regimes: in regime I oxide etches at a constant rate; regime II it is hydrophilic and oxide etches with nonlinear time dependence; and regime III surface becomes hydrophobic. There is also a short time of hydrophobicity initially when the oxide becomes wet (regime w).[887]

On the other hand, lack of wettability by dilute HF solution is not necessarily an indication of a bare Si surface. A silicon oxide can also be hydrophobic when its surface

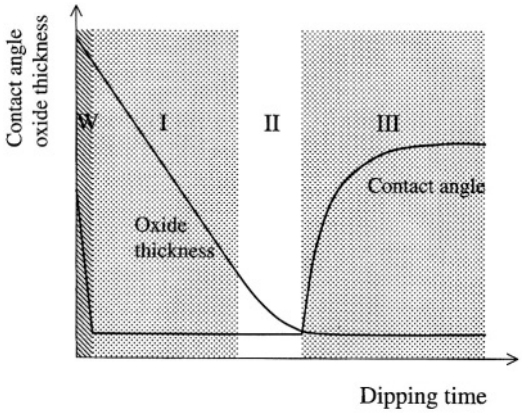

FIGURE 2.23. Schematic representations of oxide thickness change and contact angle change with HF dip time. After Kondoh *et al.*[887]

is terminated by Si–O–Si, Si–H, and $Si–CH_3$ groups.[427,906] Also, the oxide film grown in air on HF cleaned surface has a larger contact angle than that formed in pure water, indicating that the oxide formed in air is terminated by hydrogen whereas that formed in water is terminated by O or OH.[554] According to Morita *et al.*,[554] in air the oxygen species break Si–Si bonds to produce Si–O bonds. The Si–Si bonds underneath are broken after all of the Si atoms in the overlayer are oxidized, resulting in layer-by-layer growth. The Si–H bonds, which remain on the surface, are responsible for the hydrophobic behavior as shown in Fig. 2.24. The degree of hydrophobicity of a silicon surface can be modified by anodization.[1081]

2.6. SURFACE STATES

It can be expected from the nature of silicon/electrolyte interfaces described in the previous sections that the surface states on silicon electrodes may have different physical and chemical characteristics such as type, quantity, distribution, transfer kinetics, and so on, depending on the surface condition. Table 2.12 shows examples of measurements of surface states reported in the literature. Thus, while the energy levels in bulk silicon and electrolyte can be described by a general theory, those of surface states can only be dealt with by specific theories applicable to the specific situations.

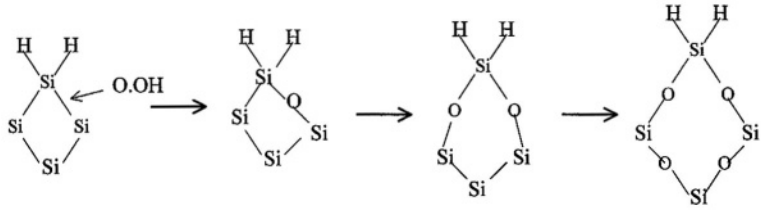

FIGURE 2.24. Reaction process for native oxide growth in air.

TABLE 2.12. Observation of Surface States at Silicon/Electrolyte Interfaces[a]

Silicon	Solution	Surface states	Ref.
n(111), 32 Ω	0.1 M $K_4Fe(CN)_6$ + 0.5 M KCl at pH 9	5×10^{11}/cm^2 D, 10^{12}/cm^2 L, 0.36 eV to E_c, oxidation intermediates	93
n, 1.8×10^{15}/cm^3	Fe(Cp) (0.01 M)/Fe(Cp)$^-$ (0.001 M) in acetonitrile + 0.1 M TBAP, lighted	10^{13}/cm^2·eV, oxidation of surface Si atoms	486, 935
n	Acetonitrile + TBAP + redox couples	Fermi level pinning, states due to oxide	935
n	1 M KCl or HCl	0.9 eV to E_c, ~10^{12}/cm^2·eV, adsorbed ions	400
p	1 M H_2SO_4	–0.05 eV to E_c	61
p	1 M H_2SO_4 + 0.01 M NH_4F	0.25 eV to E_c, possibly by adsorbed F or H	
Ion implanted	2.2 N HF + 0.5 M Na_2SO_4	Continuously distributed in the gap	174
n(100), 0.01 Ω	5% HF	4×10^{12}/cm^2·eV, 0.25 eV to E_c	39
n(111), 4×10^{13}	1 M NH_4F, pH 3–11, in the dark	2×10^{10}/cm^2 at pH 3, 10^{12}/cm^2 at pH 11	808, 841
n, 6×10^{14}/cm^3	0.5 M KCl + 0.1 M $K_4Fe(CN)_6$, pH 4	0.35 eV to E_c on n-Si, 0.75 eV to E_c on p-Si	716
n,p, Au depos.	Acetonitrile + TBAP	<10^{13}/cm^2·eV at one monolayer Au	942
Cleaned (111)	Various acids	~10^9/cm^2, defects on H-terminated surface	648
n, 4×10^{15}/cm^3	0.012 M NH_4F + 0.021 M HF + 0.99 M NH_4Cl	States associated with subsurface hydrogen	940
	2.2 M HF + 0.5 M Na_2SO_4	Uniformly distributed, by ion implantation	174
n(111) 100 Ωcm	1 M NH_4F	Potential, pH dependent intermediates	1171

[a]Abbreviations used: TBAP, tetrabutylammonium perchlorate; D, dark, L, lighted.

The surface of silicon treated in HF solutions is generally associated with a very low density of surface states because the dangling bonds are saturated by hydrogen termination.[648,940,1035] The Si–H bonding, which has an energy similar to that of Si–Si, gives rise to electronic states far into the bands and removes the dangling bond states from the band gap. A certain density of residual surface states may exist on a hydrogen-terminated surface due to defects and other inhomogeneities. It has been shown that a good H-terminated surface, when covered with a thermal oxide, is characterized by a U-shaped interstate state distribution with a low density of states less than 10^{11}/cm^2·eV at midgap.[1035] Typically, a clean silicon electrode has a density of surface states on the order of at least 10^{11}/cm^2, which is of the same order as the surface defects and contamination of metals and organic species after a normal cleaning procedure.[131,488] Large amounts of surface states occur when the silicon surface has a significant amount of adsorbed solution species, of an oxide film, or of reaction intermediates.

According to Memming and Schwandt,[61] surface states are always present on silicon electrodes in acidic aqueous solutions. The energy levels depend on whether fluoride ions are present; the surface states in acidic fluoride solutions are associated with the dissolution of the silicon. The quantity of the surface states depends on the type of silicon and the illumination intensity.[39,61] When fluoride ions are present in the solution, the n-Si surface, being oxide free and terminated by hydrogen, exhibits a low density of surface states.[940]

As an example, Fig. 2.25, reported by Madou *et al.*,[716] shows the capacitance as a function of voltage on p- and n-type silicon in a saturated KCl solution at pH 4. An

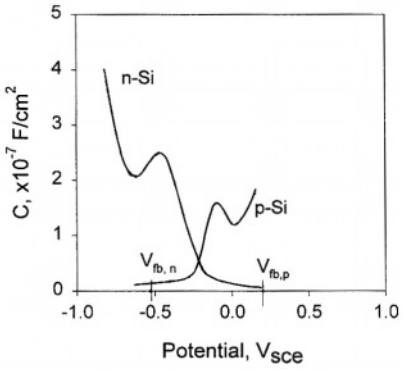

FIGURE 2.25. Capacitance–voltage plot on *n*- and *p*-type silicon in a solution of saturated KCl buffered to pH 4. Measurement frequency is 500 Hz. The flatband potentials are also indicated. After Madou *et al.*[716]

extra capacity, appearing as a peak, occurs over that expected from the space charge capacity. The peak, in height, broadness, and potential position, varies with frequency, illumination, direction of potential sweep, pH, and presence of F^- ions as shown in Table 2.13. The median energy of the band of active levels from the results of Fig. 2.25 is close to the conduction band edge for *n*-type silicon and several tenths of a volt from the valence band edge for *p*-type silicon. The frequency dependence of the capacitance indicates that the states have a certain energetic distribution since the farther the surface states are away from the band edges, the slower is the exchange of carriers in the states with the bands.

A peak similar to that shown in Fig. 2.25 is observed on a silicon surface with about 40 Å of thermally grown oxide and the peak becomes higher and broader with additional anodic thickening. The apparent density depends on light intensity and on whether the sample is biased cathodically or anodically before the measurement. This capacitance peak, however, disappears almost completely in the presence of HF, which dissolves silicon oxide. Thus, the surface states of a silicon electrode in KCl solution, according to Madou *et al.*,[716] are physically associated with the unsaturated bonds at the Si/SiO_2 interface. On the other hand, in similar solutions, Chazalviel[400] found that surface states, situated at about 0.9eV below the conduction band, are caused by the adsorbed ions but not the oxide. Thus, for an oxide-covered electrode (e.g., 12nm

TABLE 2.13. Effect of Various Factors on the Capacitance Peak[716] (relative to the standard shown in Fig. 2.25)

Conditions	Height	Broadness	Position	Hysteresis
Presence of F^-	small	similar	positive shift	similar
Prior HF rinse	lower	similar	negative shift	larger
pH from 4 to 10	similar	broader	negative shift	similar
40 Å thermal oxide	higher	broader	positive shift	no
Illumination				
After HF rinse	higher	similar	similar	increase
With native oxide	higher	narrower	similar	similar
Potential sweep				
Anodic	higher	similar	slight positive shift	
Negative	lower	similar	slight negative shift	
Increase frequency	varying	similar	varying	varying

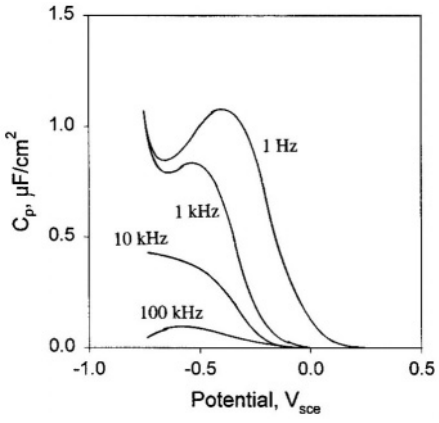

FIGURE 2.26. Parallel capacitance versus potential in the dark for various frequencies: (□) 1 Hz; (◇) 10 Hz; (○) 100 Hz; (△) 1 kHz; (▽) 10 kHz; (X) 100 kHz [measured in 0.1 M $K_4Fe(CN)_6$ + 0.5 M KCl at pH 9]. After Oskam *et al.*[93] (Reproduced by permission of The Electrochemical Society, Inc.)

thermal oxide on silicon in NaCl solutions) the surface states may also arise by surface adsorption by H^+ and OH^- ions at the oxide/electrolyte interface.[902]

In 0.1 M $K_4Fe(CN)_6$ + 0.5 M KCl at pH 9, extra capacitance over that of the space charge layer is observed at potentials between –0.7 and 0.2 V_{sce} in the dark as shown in Fig. 2.26.[93] The peak is at –0.4 V_{sce} and disappears at frequencies above 20 kHz. This peak is attributed to the reversible charge exchange between monoenergetic interface states and the conduction band. The density of the interface states is determined to be $N_{ss} = 5 \times 10^{11}\,cm^{-2}$ and its energy is located 0.36 eV from the conduction band edge. Under illumination the capacitance as a function of potential reveals two maxima at –0.3 and 0.15 V_{sce} as shown in Fig. 2.27. The two maxima are found to occur at all light intensities and their positions vary with light intensity and frequency. According to Oskam *et al.*,[93] the peak at –0.3 V_{sce} represents the same interface states as in the dark but with a higher density of $1 \times 10^{12}\,cm^{-2}$. The density of these states at 0.15 V_{sce} increases with photocurrent density and is on the order of 1×10^{12} to $3 \times 10^{12}\,cm^{-2}$. The surface states that responsible for the recombination are produced under illumination and are likely to be associated with oxidation intermediates. Surface states of similar

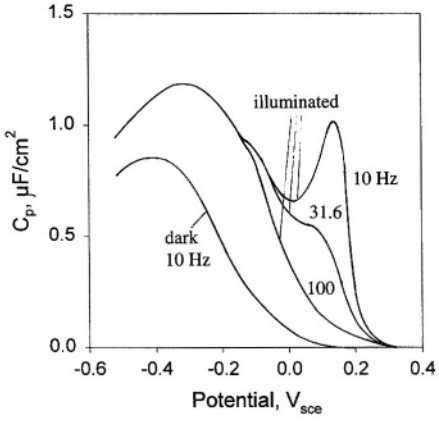

FIGURE 2.27. Capacitance versus potential as a function of frequency both in the dark and under illumination. The dark curve was measured at 10 Hz and represents the low-frequency limit. The plateau photocurrent was 5 μA cm^{-2}, and the modulation amplitude was 2 mV (rms) [measured in 0.1 M $K_4Fe(CN)_6$ + 0.5 M KCl at pH 9]. After Oskam *et al.*[93] (Reproduced by permission of The Electrochemical Society, Inc.)

energetic characteristic to that in the 0.1 M $K_4Fe(CN)_6$ + 0.5 M KCl solution are found 0.38eV below the conduction band in 1 M NH_4F.[808,841] They are independent of solution pH from pH 3 to 11, indicating that the surface states are physically the same for both hydrogen-terminated (at low pH) and oxide-passivated surfaces (at high pH), although the density is different.

In some organic solvents, the surface states are associated with the Si–O–H bonds and are independent of solvent type.[395] In acetonitrile solutions the surface states are found to increase from the initial value of $2 \times 10^{11}/cm^2$ to $5 \times 10^{11}/cm^2$ after 1 day in solution and to $20 \times 10^{11}/cm^2$ when the surface is oxidized corresponding to an increase in the amount of Si–O–H bonds.[929] The surface states are found to be absent initially when the electrode is first immersed into the electrolyte but develop gradually.[935] The rate of change depends on the type of redox couple in the electrolyte. The surface states are attributed to the slow oxidation of the surface due to the traces of water present in the organic electrolyte. They have a broad energy distribution extending through the band gap with a maximum density near the band edge.[942] In acetonitrile solution containing a redox couple of 0.01 M ferrocene/0.001 M ferricinium, the density of surface states is found to be $\sim 10^{13}/cm^2 \cdot eV$.[486] Because of the presence of surface states, the Fermi level can be pinned leading to a constant Schottky barrier height for different redox couples.[935]

The results of the large number of studies on surface states indicate that those on the surface of silicon tend to be associated with oxide when the surface is covered with an oxide or to reaction intermediates when the surface is not covered with an oxide. A high density of surface states is generally observed when the electrode is illuminated or a current is passed through. Reaction intermediates can behave like surface states.

2.7. FLATBAND POTENTIALS

The flatband potential of silicon electrodes is an important parameter that has been determined in many solutions. Table 2.14 is a collection of the flatband potentials for various silicon/electrolyte interfaces. The values of V_{fb} determined in real systems depend on a range of factors including doping concentration, type of solvent, type of electrolyte, pH, illumination, redox couple, and surface condition. Mechanistically, according to Eq. 15 in Chapter 1, the value of the flatband potential is determined by two parameters: the bulk Fermi level and the Helmholtz potential V_H. The first is subject to the variation in dopant concentration because the Fermi level with respect to the conduction band edge, μ, is equal to $kT/e \cdot \ln(N_c/N_D)$ for a nondegenerated semiconductor. The second parameter, V_H, is subject to the variation of surface condition and the nature of the electrolyte.

2.7.1. Effect of pH

It can be expected that the Helmholtz potential of a silicon electrode in an aqueous electrolyte is a strong function of pH since hydrogen adsorption is a dominant process on the surface of silicon. Table 2.15 shows the dependence of flatband potential on pH

TABLE 2.14. Flatband Potentials of Silicon Materials Determined in the Dark in Various Solutions

Silicon	Solution	E_{fb}, V_{sce}	Ref.
	Aqueous solutions		
***p* type**			
(100) 3×10^{15}	0.1% HF	0.16	475
(100) 8 Ωcm	1% HF	1.759	295
4.5×10^{16}	5% HF	1.3	241
(100) 1.5×10^{15}	35% HF	0.15	5
(111) 1.5×10^{16}	10 M HF	0.15	61
6.4×10^{20}	0.1 M Fe(II)EDTA, pH 4.6	0.18	716
(100) 8 Ωcm	1.35 M NH_4	−0.35	139
5 Ωcm	1 M H_2SO_4 + 0.1 M $S_2O_8^{2-}$	0.25	969
	1 M H_2SO_4	0.35	969
(100) 10 Ωcm	2 M KOH	0.06	21
(100) 0.8 Ωcm	2 mM methylviologen + 0.1 M KCl	−0.54	21
***n* type**			
(100) 3 Ωcm	1% HF	−0.461	295
(100) 10^{17}	1% HF	−0.57	475
(111) 2.5×10^{15}	5% HF, pH 1.4	−0.45	901
(100) 0.01 Ωcm	5% HF	−0.42	39
(111) 5×10^{15}	10 M HF	−0.35	61
(100) 8×10^{14}	35% HF	−0.495	5
(111) 4 Ωcm	1 M HCl	−0.62 V, PC	680
7 Ωcm	1 M H_2SO_4 + 0.1 M $S_2O_8^{2-}$	−0.45	969
	1 M $H_2SO_4^-$	−0.25	969
(111) 32 Ωcm	0.1 M $K_4Fe(CN)_6$ + 0.5 M KCl, pH 9	−0.4	93
(111) 0.3 Ωcm	0.1 M $K_4Fe(CN)_6$ + 0.5 M KCl, pH 6.5	−0.62	396
6.4×10^{20}	0.1 M $K_4Fe(CN)_6$ + 0.5 M KCl, pH 7.4	−0.65	716
(111) 1.8×10^{15}	1 M KCl, pH 3.3	−0.3	717
	0.1 M $K_4Fe(CN)_6$, pH 5.6	−0.81	77
(111) 100 Ωcm	1 M NH_4F, pH 4	−0.17	841
(111) 0.5 Ω	2 M NH_4F, pH 4	−0.6	904
	2 M NH_4F, pH 13	−1.0	904
(100) 5 Ωcm	1.35 M NH_4OH	−1.05	139
(100) 8 Ωcm	2 M KOH	−1.04, PC	129
(100) 5 Ωcm	2 M NaOH	−1.25	22
(111) 0.5 Ωcm	2 M NaOH	−1.03	22
(100) 10 Ωcm	2 M KOH	−1	109
(100) 2 Ωcm	20 mM Cu^{2+} in $K_4P_2O_7$, Cu = P_2O_7 (1–5)	−0.74 $V_{Ag/AgCl}$	1167
Other materials			
a-Si, *n*, 1.2×10^{17}	2 M NH_4F	−0.73, PC	199
a-Si, 4×10^{14}	0.05 M CrO_3 + 10 M HF	0.31	195
n-Si, 150 nm Au	0.1 M $K_4Fe(CN)_6$ + 0.5 M KCl	−0.52, Ag/AgCl	848
PS, 10 mA/cm^2	0.2 M Na_2SO_4 + 3.5 M C_2H_5OH	−0.17 Ag/AgCl	140
	Nonaqueous solutions		
***p* type**			
p (100) 2×10^{15}	0.1 M TBAP in MeCN	0.15	389
	0.1 M TBAP in MeCN + 30 mM $PhNO_2$ + 10 mM $PhNO_2^-$	−0.5	389
(100) 10^{15}	0.1 M TEAP in CH_3CN	0.02	402
(111) 2 Ωcm	0.1 M KBr in ammonia	0.29	373

TABLE 2.14. *Continued*

Silicon	Solution	E_{fb}, V_{sce}	Ref.
(111) 10^{15}–10^{18}	0.1 M TBAP in acetonitrile	0.2	85, 87
(111) 5×10^{15}	0.1 M $TBABF_4$ in CH_3CN	0.12	683
(100) 1.5×10^{16}	EPW	–0.58	697
13 Ωcm	2 M HF + 0.25 M TBAP in acetonitrile	0.0, PC	248
***n* type**			
(111) 5 Ωcm	0.1 M $TBABF_4$ in acetonitrile	–0.02	372
$10^{17}/cm^3$	0.1 M TBAP in acetonitrile	–0.35	935, 941
(111) 10^{15}	0.1 M $LiClO_4$ in acetonitrile	–0.32	686
	0.1 M KI in NH_3	–0.6 $V_{ag,0.1M}$	271
(100) 10^{15}	0.1 M TEAP in CH_3CN	–0.5	402
(100) 10^{15}–10^{18}	0.1 M TBAP in acetonitrile	–0.9	85, 87
(111) 4×10^{15}	0.1 M potassium hydrogen phthalate, pH 4.5	–0.5	921
10^{15}	0.1 TEAP in dimethyl sulfoxide	–0.25	546
10 Ωcm	2 M HF + 0.25 M TBAP in acetonitrile	–0.6, PC	248

[a]Abbreviations used: a-Si, hydrogenated amorphous silicon; PC, determined by photo current method; $TBABF_4$, tetrabutylammonium fluoborate; TBAP, tetrabutylammonium perchlorate.
[b]Determined by Mott–Schottky plot, unless indicated.
SCE = AgCl + 0.045 V = SHE + 0.241 V.

in different solutions. Figure 2.28 shows the flatband potential of *n*- and *p*-type silicon as a function of pH in aqueous solutions.[716] The slope of both curves is about 30 mV/pH unit, which is much lower than the 60mV/pH unit expected from Eq. 1.33.

Figure 2.29[690] shows the pH dependence of flatband potential on a silicon surface covered with a thermal oxide layer in 1 M NaCl solutions. The slope is about 40 mV/decade for pH values far from pzc and becomes smaller approaching pzc. It has been suggested that the effect of pH on flatband potential is mainly at the oxide/electrolyte interface rather than at the silicon/oxide interface.[690,902] The less than 60mV/pH unit on an oxide-covered electrode is attributed to the formation of silanol groups and adsorption of ionic species on both charged and noncharged surface sites.[853] According to Madou *et al.*,[716] the low dependence of the flatband potential on pH is probably due to a voltage across a very thin oxide that exists in non-HF solutions. The flatband potential of oxide-free silicon surface in non-HF solution could be obtained by using a

TABLE 2.15. Dependence of Flatband Potential on pH

Material	Solution	pH range	Slope, mV/pH unit	Ref.
p, $10^{15}/cm^3$	0.1 M Fe(II) EDTA	0–10	31	716
n, $6 \times 10^{14}/cm^3$	0.5 M KCl + 0.1 M $K_4Fe(CN)_6$	0–12	33	716
n, $10^{16}/cm^3$	0.5 M KCl + 0.1 M $K_4Fe(CN)_6$	0–10	27	396
		10–14	90	396
n-Si/SiO_2	NaCl	3–6	25	853
		7–10	47	853
n-Si/SiO_2 (60 nm)	1 M NaCl	4–11	40	690
n(111)	2 M NH_4F	4–13	45	904
n(100)	1 M NH_4F	<8	30	841

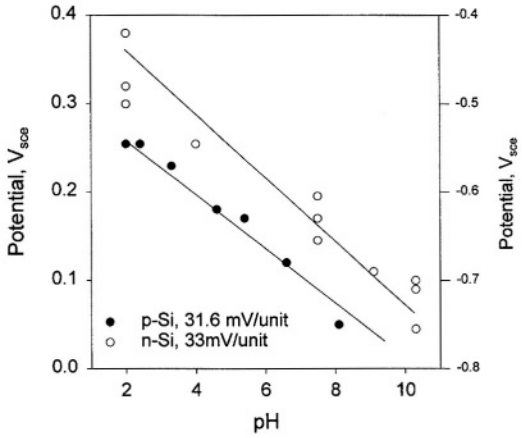

FIGURE 2.28. Flatband potential V_{fb} versus pH for *p*-type silicon in 0.5 M KCl in the presence of Fe(II) EDTA and for *n*-type silicon in 0.5 M KCl + 0.1 M $K_4Fe(CN)_6$. After Madou *et al.*[716]

solution containing a stabilizing agent such as 0.1 M $Fe(CN)^{4-}_6$ or 0.1M Fe(II) EDTA. The Fe(II) is oxidized by holes, which reduces the rate of silicon oxide formation so that the surface can remain relatively "bare" during the course of measurement.

2.7.2. *Effect of Surface Condition*

Surface states at a silicon/electrolyte interface are determined by the preparation prior to entering the electrolyte and by the changes that occur in the electrolyte. Thus, in general, an experimentally determined flatband potential is specific to the particular silicon/electrolyte interface at a given time and may significantly vary even with the same material and electrolyte.

Figure 2.30 shows that different polishing processes result in different flatband potential values in a 5% HF solution.[901] Annealing after cleaning and etching was seen

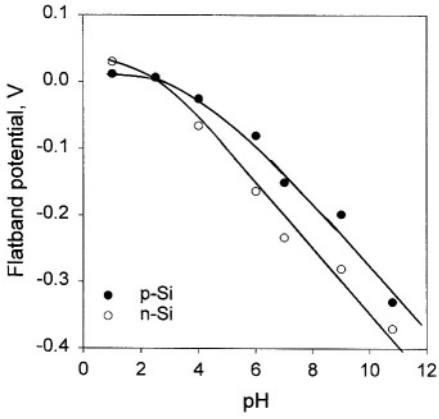

FIGURE 2.29. Plots of E_{fb} versus pH obtained by high-frequency capacitance measurements on Si/SiO_2 for *n*-Si ($N_D = 2.8 \times 10^{21}\,m^{-3}$, oxide thickness 60 nm); and for *p*-Si ($N_A = 4.8 \times 10^{21}\,m^{-3}$, oxide thickness 65 nm). In 1 M NaCl. (Reprinted from Dort *et al.*[690] © 1985, with permission from Elsevier Science.)

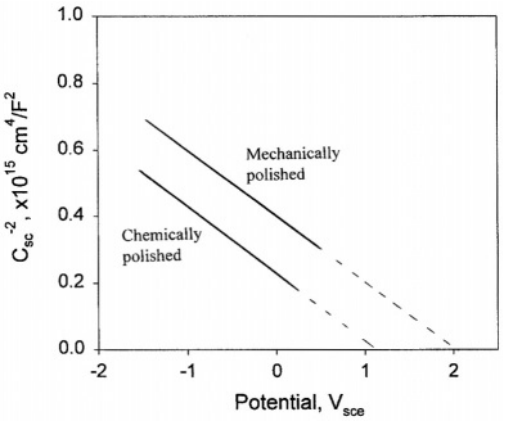

FIGURE 2.30. Mott–Schottky plots in 5% HF for mechanically polished *n*-type silicon and chemically etched sample. After De Mierry *et al.*[901]

to improve the reproducibility of the flatband potential in acetonitrile.[615] In another study, exposing a freshly HF rinsed sample in methanol vapor as a surface preparation procedure caused a shift of the flatband potential of *n*-Si in acetonitrile +0.1 M $LiClO_4$ solution from $-0.02\,V_{sce}$ to $-0.51\,V_{sce}$ and it reduced the change of flatband potential with time possibly due to the formation of $Si–O–CH_3$ groups.[686]

Similarly, time of immersion of a freshly prepared silicon sample has a significant effect on the flatband potential due to the active nature of the silicon surface. A HF-cleaned silicon surface is generally terminated by hydrogen, which, although relatively stable, tends to be replaced by a thin oxide film. The flatband potential of such a surface may change with time in the electrolyte.[83,716,1108] As an example, for an *n*-type silicon in acetonitrile +0.1 M $LiClO_4$ solution the flatband potential changes from –0.02 V_{sce} for a freshly prepared sample to $-0.16\,V_{sce}$ after 24h immersion.[686,935] The shift is due to the gradual generation of surface states as a result of the slow oxidation of the silicon surface caused by traces of water in the electrolyte.

Considering the change of surface condition with time, it is difficult to obtain reproducible flatband potentials because of the high reactivity of the silicon surface in HF solutions.[716,841] The high reactivity tends to cause roughening of the surface in general and formation of porous silicon in particular. Roughening of the silicon surface in HF solution may cause a change of capacitance by more than a factor of 5.[475,1153] As a result, the flatband potential measured in HF solutions tends to vary with many factors related to conditions and procedures. For example, the flatband potential of *n*-Si in HF solution has been found to change with the initial potential at the beginning of potential sweep.[39]

The difference between the flatband potentials of *p*-Si and *n*-Si plus the differences between the bulk Fermi level to the corresponding band edges equal the band gap, ~1.12 eV when the band edges of the two materials are the same in the solution. Such situations have been observed.[21,716] However, in many situations the measurement of flatband potentials of *p*-Si and *n*-Si does not yield the band gap. There are two possible explanations. In one the band edges of *p* -Si and *n*-Si may not have the same energy

in the solution, for example, when the Fermi level is pinned by a large density of surface states. In the other, the actual band edges of the two materials are the same but the values obtained from the flatband potentials of the two materials are different due to difficulty in obtaining definite and reproducible flatband potential values for the two materials. Usually, it is more difficult to determine a reproducible flatband potential of *p*-Si due to its more active nature.[475,901] In the presence of HF, significant dissolution occurs under an anodic polarization, resulting in a rapid structural transformation of the surface. For example, in 5% HF the flatband potential of *n*-type silicon is independent of the methods of surface preparation whereas that of *p* type strongly depends on the methods of preparation.[901] In another case, the flatband potential of *p* type in 35% HF solution is found to strongly depend on frequency; a shift of as much as 1300 mV is observed by changing the frequency from 10 to 100 kHz. On the other hand, that of *n* type is independent of frequency from 1 to 500 kHz.[5]

2.7.3. *Effect of Surface States*

A large density of surface states may be associated with certain surface conditions. When an electrode surface has a large density of states, significant amounts of potential variation may drop across the Helmholtz layer instead of the space charge layer. This results in Fermi level pinning or unpinning of the band edges. Specifically, without the influence of surface states the flatband potential is independent of the presence of the redox couple in the solution. When Fermi level pinning occurs, the flatband potential tends to change with the potential of the redox couple in the solution as shown in Fig. 2.31.[21,389,683] The more negative the redox couple is, the larger the shift of the flatband potential. However, the slope in Fig. 2.31 is less than unity, indicating that the Fermi level is not completely pinned by the surface states. It has been found that due to Fermi level pinning, the flatband potential of *p* type may show no difference from that of *n* type in an acetonitrile solution.[372]

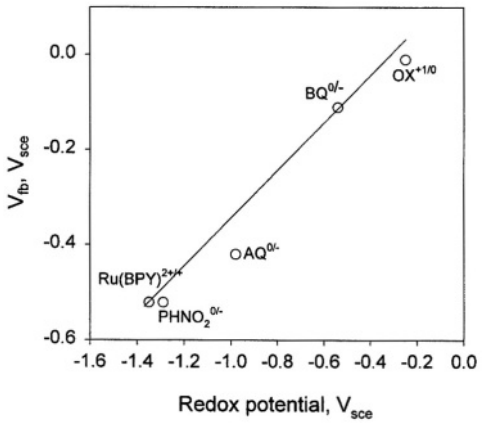

FIGURE 2.31. Flatband potential V_{fb} of *p*-Si in MeCN as a function of redox potential V_{redox} of added redox couples: oxazine (+1/0), benzoquinone (0/–1), anthraquinone (0/–1), $Ru(bpy)_3^{2+/+}$, nitrobenzene (0/–1). After Nagasubramenian *et al.*[389]

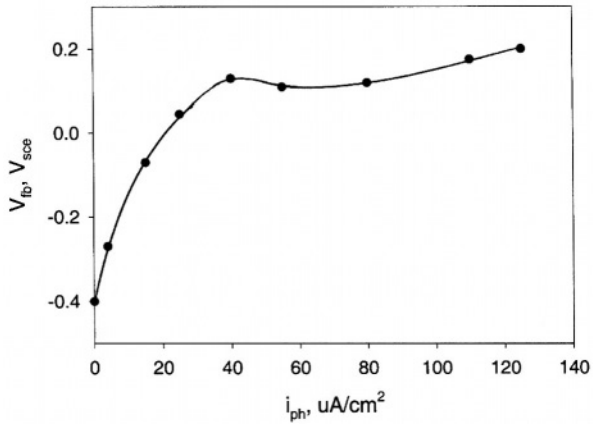

FIGURE 2.32. The flatband potential obtained from the Mott–Schottky plots for *n*-type silicon in 0.1 M $K_4Fe(CN)_6$ + 0.5 M KCl solution at pH 9 versus the plateau photocurrent density. After Oskam *et al.*[93] (Reproduced by permission of The Electrochemical Society, Inc.)

Reaction intermediates are a special group of surface states that can cause band edge shift (or Fermi level pinning). When this occurs, the flatband potential tends to change with current. Figure 2.32 shows that the flatband potential of *n*-type silicon in 0.1 M $K_4Fe(CN)_6$ + 0.5 M KCl changes with photocurrent which induces surface states.[93] The shift of 0.55V shown in Fig. 2.32 corresponds to a density of 2×10^{13} cm^{-2}. This result can be used to explain the difference between the flatband potentials determined by Mott–Schottky plot and by measurement of the onset potential for photocurrent.[94]

Flatband potential shift may also result from deposition of metallic and organic species, which act as surface states.[83,402,808,1015] Figure 2.33 shows that the flatband potential of an *n*-Si electrode in acetonitrile solution containing redox couples changes with

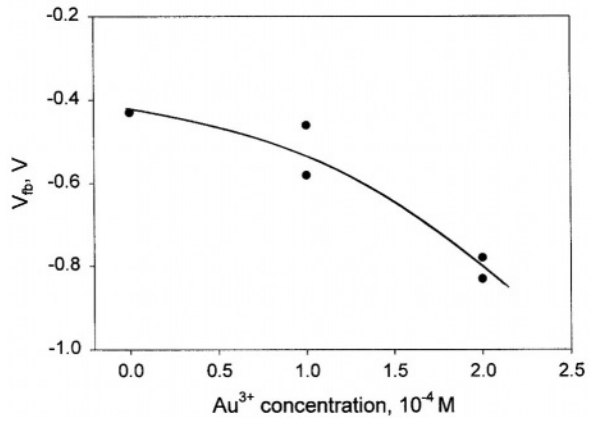

FIGURE 2.33. Initial value of the flatband potential for *n*-Si with deposited gold atoms (10^{-4} M gives about a monolayer). After Chazalviel and Stefenel.[942]

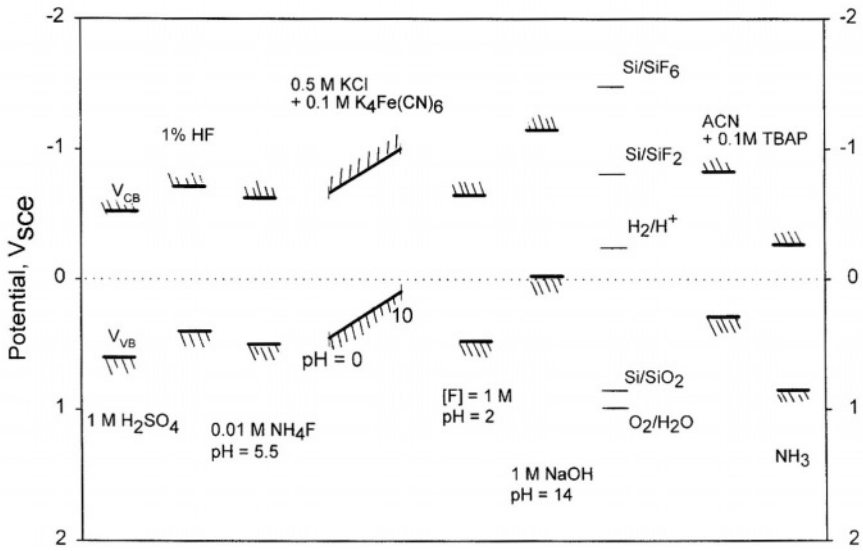

FIGURE 2.34. Examples of the energetic positions of the band edges determined for a number of silicon/electrolyte interfaces. The energy levels of the redox couples related to Si and H_2O are also plotted.

Au^{3+} concentration in the HF electrolyte used to deposit the metals.[942] The amount of shift is about 0.3 V for a coverage of about one monolayer of gold.

2.7.4. Band Diagrams

The band diagram of silicon electrode in an electrolyte can be drawn when the flatband potential of the interface is determined. Figure 2.34 shows the band diagrams for various silicon/electrolyte interfaces. As described above, the flatband potential depends on many factors specific to the silicon/electrolyte interface under a given set of experimental conditions, as does the band diagram.

2.8. OPEN-CIRCUIT POTENTIALS

As the most easily measurable electrochemical parameter, the open-circuit potential (OCP) is routinely used to indicate the condition, stability, and reproducibility of an electrode during experiments. Table 2.16 shows the OCP values of silicon electrodes in various electrolytes.

2.8.1. Effect of Various Factors

Figures 2.35 and 2.36 show the effect of silicon substrate conditions on OCP in an alkaline solution.[269] For the *p*-type materials, OCP appears to be lower at high doping levels with no clear difference between different orientations. For *n*-type materials,

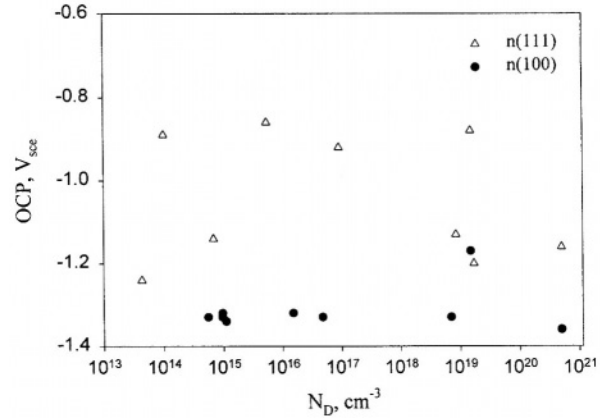

FIGURE 2.35. The open-circuit potential of $n(111)$ and $n(100)$ in 2M KOH at 21 °C as a function of doping concentration. After Palik *et al.*[269] (Reproduced by permission of The Electrochemical Society, Inc.)

there does not appear to be a correlation of OCP and doping concentration, but OCP of the (111) orientation is more positive than that of the (100) orientation. Similar results are reported in another study.[378] In TMAH solutions, *n*-Si and *p*-Si materials show similar OCP values and vary little with resistivity from 0.01 to 10 Ωcm.[1005] In 4.8% HF–64% HNO_3 solution, OCP of *p*-Si appears to increase with increasing doping concentration but that of *n*-Si does not reveal such a tendency as shown in Fig. 2.37.[111]

Examination of the data in Table 2.16 indicates that OCP of silicon electrodes is in general lower at higher pH values. Figure 2.38 shows that OCP of *p*-Si and *n*-Si decreases with increasing pH in different solutions.[111] In 1 M KCl solutions, OCP of *n*-type silicon follows approximately the Nernst law $dV_{ocp}/d(\text{pH}) \approx -2.3kT/e$ up to pH

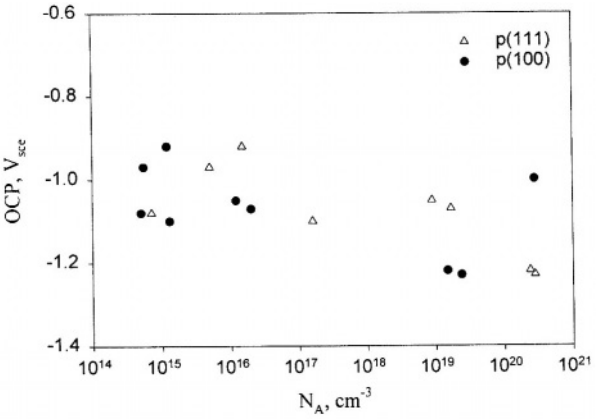

FIGURE 2.36. The open-circuit potential of $p(111)$ and $p(100)$ in 2M KOH at 21 °C as a function of doping concentration. After Palik *et al.*[269] (Reproduced by permission of The Electrochemical Society, Inc.)

TABLE 2.16. Open-Circuit Potential and Corrosion Current of Silicon in the Dark

Silicon	Electrolyte	E_{op}, V_{sce}	i_{corr}, μA/cm^2	Ref.
	Aqueous solutions			
***p* type**				
	48% HF	0.12		111
	3% $KMnO_4$ + 47% HF	0.10		111
	23% HNO_3 + 33% HF	0.23		111
	71% HNO_3	0.48		111
p, 1.5×10^{15}	35% HF	−0.350		5
p(100), B 1×10^{15}	5% HF, deaer.	−0.650		282
p(100), B 5×10^{16}	5% HF, deaer.	−0.641		282
n(100), P 2×10^{14}	5% HF, deaer.	−0.653		282
p(100), P 2×10^{16}	5% HF, deaer.	−0.708		282
(100) 10^{15}	5% HF, deaer.	−0.65		854
(100) 5×10^{16}	5% HF, deaer.	−0.64		854
p(100) 3×10^{15}	5% HF	−0.36		1153
p, 2.5 Ωcm	2% HF, deaer.	−0.633	0.0053	146
p(100), 5×10^{15}	5 M [F] + 50 mM Ni^{2+}			
	pH 1.2	−0.35		1092
	pH 8	−0.42		1092
p, 18 Ωcm	2% HF, deaer.	−0.616	0.021	146
p, 2.5 Ωcm	2% HF, oxyg.	−0.445	0.024	146
p, 18 Ωcm	2% HF, oxyg.	−0.515	0.019	146
p(100) 3×10^{15}	1% HF	−0.42		1153
p(100), 5 Ωcm	1% HF	−0.572	0.04	293
(100), 10^{15}	0.5% HF	−0.55	0.007	968
	0.5% HF + 1 M HCl	−0.48	0.003	968
	0.5% HF + 1 M NH_4F	−0.76	0.004	968
p(100), 5 Ωcm	16% NH_4F + 0.14% HF	−0.862[a]	5	293
n(100), 3 Ωcm	16% NH_4F + 0.14% HF	−0.927[a]	4	293
10^{19}	0.1 M NaCl	−1		869
	Sat. KCl	−0.52		111
	1 M KOH	−1.05		111
(100) 17 Ω	2 M KOH	−0.95		129
p(100), 19.3 Ωcm	2 M KOH	−1.19		378
p(100), 0.007 Ωcm	2 M KOH	−1.20		378
p(111), 0.007 Ωcm	2 M KOH	−1.020		378
p(111), 12.4 Ωcm	2 M KOH	−1.215		378
p(100), 17 Ωcm	2 M KOH	−1.250		129
(100) 5 Ω	40% KOH, 60 °C	−1.55		291
(111) 5 Ω	40% KOH, 60 °C	−1.28		291
(100) 4 Ω	EDP[b]	−1.37		112
(100) 15 Ω	2.5% TMAH	−1.58		516
	25% TMAH	−1.73		516
	NH_3, 50 °C	−1.1		1004
***n* type**				
	48% HF	−0.19		111
	3% $KMnO_4$ + 47% HF	−0.3		111
	23% HNO_3 + 33% HF	−0.06		111
	71% HNO_3	0.3		111
(100) 8 Ω	2 M KOH	−1.25		129
(100) 2×10^{14}	5% HF, deaer.	−0.65		854
(100) 2×10^{16}	5% HF, deaer.	−0.71		854

TABLE 2.16. *Continued*

Silicon	Electrolyte	E_{op}, V_{sce}	i_{corr}, μA/cm²	Ref.
n, 2.2 Ωcm	2% HF, deaer.	–0.672	0.044	146
n, 20 Ωcm	2% HF, deaer.	–0.695	0.2	146
n, 2.2 Ωcm	2% HF, oxyg.	–0.557	0.14	146
n, 20 Ωcm	2% HF, oxyg.	–0.568	0.2	146
n(100), 3 Ωcm	1% HF	–0.427	0.1	293
n(100) 10^{17}	1% HF	–0.43		1153
n(100) 2×10^{19}	1% HF	–0.45		1153
(100) 2×10^{14}	0.5% HF	–0.59	0.073	968
	0.5% HF + 1 M HCl	–0.54	0.026	968
	0.5% HF + 1 M HCl	–0.70	0.37	968
(111) 0.5 Ωcm	10 M NH_4F, pH 4	–0.62		904
	10 M NH_4F, pH 8	–0.8		904
n(100), 10^{16}	5 M [F] + 50 mM Ni^{2+}			
	pH 1.2	–0.4		1092
	pH 8	–0.75		1092
(111) 1.8×10^{15}	1 M KCl, pH 0.1	–0.26		717
n(100) 5 Ω	2 M NaOH	–1.38	3.7	22
	Sat. KCl	–0.62		111
	1 M KOH	–1.24		111
10 Ω	1 M KOH	–1.16		925
n(100), 15.5 Ωcm	2 M KOH	–1.330		378
n(100), 0.0043 Ωcm	2 M KOH	–1.280		378
n(111), 7.7 Ωcm	2 M KOH	–1.170		378
n(111), 0.005 Ωcm	2 M KOH	–1.180		378
n(100), 8 Ωcm	2 M KOH	–0.95		129
(111) 0.5 Ω	2 M KOH	–1.03	31	22
(100) 5 Ω	40% KOH, 60 °C	–1.54		291
(111) 5 Ω	40% KOH, 60 °C	–1.38		291
(100) 1.5 Ω	EDP	–1.46		112
(100) 8 Ω	NH_3, 70 °C	–1.1		521
	NH_3, 50 °C	–1.35		1004
(100) 13 Ω	1.9 M NH_3, 70 °C	–1.1		208
	1.9 M NH_3 + H_2O_2	–0.4		208
(100) 4 Ω	2.5% TMAH	–1.52		516
	25% TMAH	–1.72		516
1 Ω	25% TMAH, 20 °C	–1.14		996

[a] 100 ppb of copper in solution.
[b] EDP: 100 ml ethylenediamine + 16 g pyrocatechol + 32 ml water.

6.[717] At higher pH values a smaller slope is observed possibly due to the potential drop across an oxide layer of increasing thickness. No specific effect of the various anions (Cl^-, SO_4^{2-}, $C_2O_4^{2-}$) was observed. For *n*-Si in NH_4F solutions, OCP increases with pH with a slope of about 45 mV/decade from pH 4 to 13 which is similar to the pH dependence of the flatband potential.[904] This indicates that the band bending of the electrode is essentially constant at different pH values.

In HF–HNO_3 solutions, according to Turner,[111] when HF is the rate-determining reactant, OCP shifts in the negative direction with increasing HF concentration; when HNO_3 is the controlling factor, OCP becomes more positive with increasing

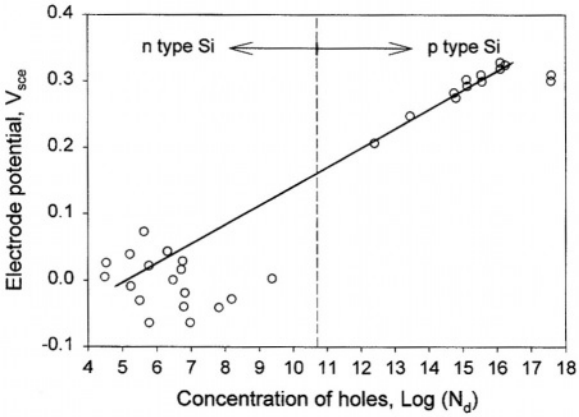

FIGURE 2.37. Electrode potentials of Si in 90% HNO_3 (71%) + 10% HF (49%) versus resistivity and equilibrium hole density. After Turner.[111] (Reproduced by permission of The Electrochemical Society, Inc.)

HNO_3 concentration. Also, when there is little etching of the materials, no significant difference exists between *p* and *n* types. On the other hand, an appreciable potential difference exists between *n* and *p* types in solutions in which the etch rate is high.

Dissolved oxygen in solutions can strongly affect OCP of silicon electrodes. Bertagna *et al.*[146,522] found that OCP of both *p*-Si and *n*-Si in 5% HF solution shifts to more positive values, by 100–150 mV, in oxygenated solution as shown in Table 2.17.[146,968] The effect of oxygen can readily be explained by the change involved in the anodic and cathodic reactions described in Fig. 1.26. An increased total cathodic reaction rate due to the oxygen reduction results in a shift of the cathodic curve from 1_c to 2_c and thus changes OCP from E^0_{corr} to E^2_{corr}.

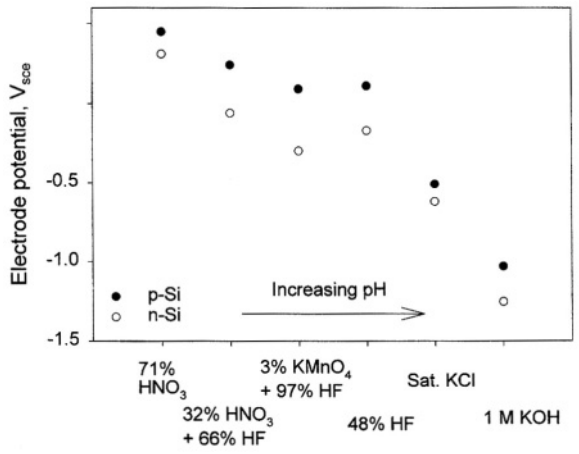

FIGURE 2.38. Electrode potentials of *n*- and *p*-type Si in various etching and nonetching solutions. Unstirred at room temperature. After Turner.[111] (Reproduced by permission of The Electrochemical Society, Inc.)

TABLE 2.17. Corrosion Potentials and Corrosion Current in Various HF Solutions[968,1047]

Solution	Condition[a]	*n*-Si, 2×10^{14}/cm^3		*p*-Si, 10^{15}/cm^3	
		E_{corr}, V_{sce}	i_{corr}, μA/cm^2	E_{corr}, V_{sce}	i_{corr}, μA/cm^2
5% HF	Deaerated				
	Dark	−0.672	0.044	−0.616	0.021
	Light	−0.71	0.245	−0.188	0.098
	Oxygenated				
	Dark	−0.557	0.14	−0.515	0.019
	Light	−0.610	1.20	−0.158	0.75
0.5% HF + 1 M HCl	Deaerated				
	Dark	−0.540	0.026	−0.480	0.003
	Light	−0.570	0.052	−0.090	0.13
0.5% HF	Deaerated				
	Dark	−0.590	0.073	−0.550	0.007
	Light	−0.603	0.32	−0.098	0.26
0.5% HF + 1 M NH_4F	Deaerated				
	Dark	−0.700	0.37	−0.760	0.004
	Light	−0.710	0.43	−0.340	0.52

[a]Deaerated: less than 0.1 ppm dissolved O_2; oxygenated: 40 ppm O_2; T = 20 °C; light intensity. 1400 lux; measurement of OCP at 2 min; corrosion current determined by linear polarization technique.

Table 2.17 also shows the effect of illumination on the change of OCP. In general, lighting results in more negative OCP for *n*-Si but more positive OCP for *p*-Si because illumination produces a flattening of the band bending. This effect is generally observed on silicon electrodes in various solutions although the magnitude of change depends on the specific experimental conditions. For example, in HF–HNO_3 solutions in which the etch rate is high, OCP does not change with normal lighting. In KOH solutions, upon illumination OCP of *p*-type silicon has been found to shift toward more positive values, whereas there is no apparent change of OCP of *n*-type silicon from that in the dark.[129]

The presence of trace amounts of metal ions with reversible potential more positive than that of silicon may significantly alter OCP.[254,854] Figure 2.39 shows OCP as a function of copper concentration in solution.[96] Figure 2.40 that reveals OCP of *p*-Si in 5% HF solution is a function of the trace amount of copper present in solution.[254] OCP rises steeply with time when copper is present and rather quickly settles at a plateau value. This plateau value increases with increasing copper concentration. The behavior is similar for *n*-Si but the time required to reach the plateau is considerably longer, nearly two orders of magnitude longer.

Other experimental conditions may also affect OCP. A 150-mV increase in OCP was observed when a limited amount of electrolyte was confined between the silicon surface and an insulating material.[854] This effect may be caused by the changing composition of the confined solution. In NH_3 the OCP does not change with flow rate of the solution.[1004]

Time is a particularly important factor that always affects the value of OCP. For an active electrode surface such as silicon, time invariably brings two basic changes to the system at OCP: (1) a change of the physical structure and chemical composition of the corroding electrode surface and (2) a change in the composition of the solution,

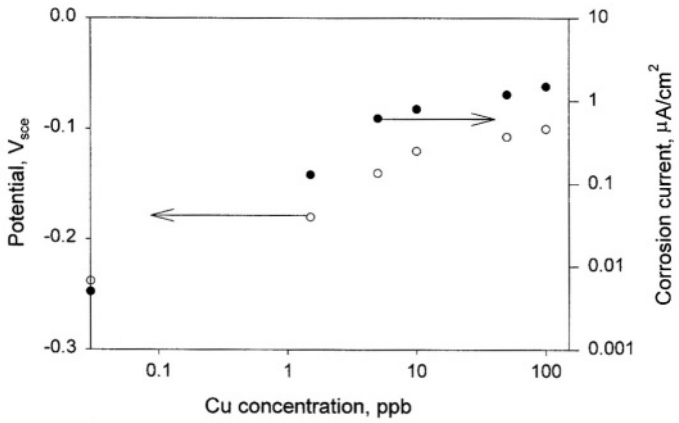

FIGURE 2.39. Corrosion potential and corrosion current density of silicon in 50:1 HF solutions. After Jeon *et al.*[96] (Reproduced by permission of The Electrochemical Society, Inc.)

particularly in the vicinity of the surface. Specific changes may occur in surface area and roughness, adsorption of species, lattice defects, formation of passive films, accumulation of dissolution products, precipitation of a solid layer loosely attached to the surface, and exhaustion of reactants. Mechanistically, these changes may lead to alteration in the equilibrium potentials of the redox couples, the type of reactions involved, the rate-controlling process, and so on. As a result, OCP may vary drastically depending on the nature and extent of these changes. The potential may not reach a constant value if the surface and solution change continuously.

Figure 2.41 illustrates that OCP of a *p*-Si varies with time in three different solutions.[968] The different values of OCP in the three solutions are interpreted by Bertagna *et al.*[968] as due to the effect of H^+ and F^- on the exchange current density of the anodic

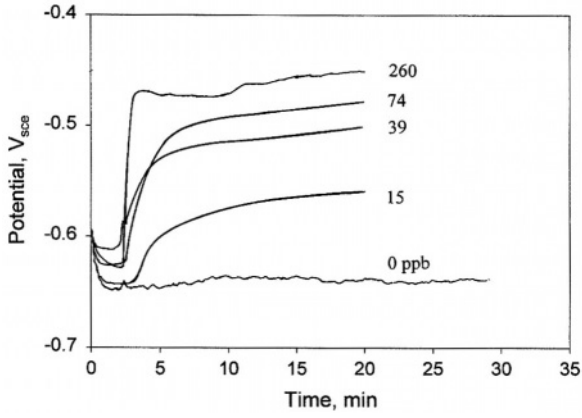

FIGURE 2.40. OCP versus time of *p*-type silicon, in the dark, in contact with deaerated 5% DHF solution, on addition of trace amounts of copper. After Bertagna *et al.*[254] (Reproduced by permission of The Electrochemical Society, Inc.)

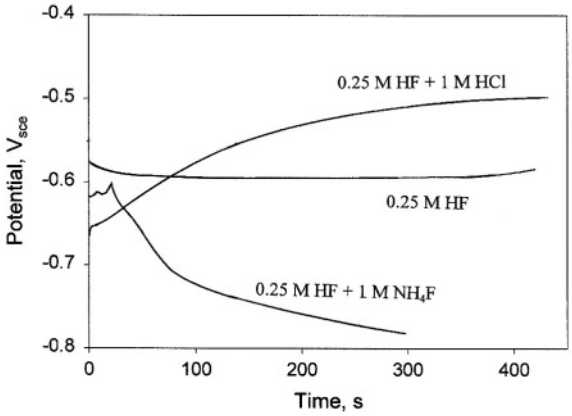

FIGURE 2.41. OCP of *p*-Si versus time in 0.25 M HF; in 0.25 M HF + 1 M HCl; and in 0.25 M HF + 1 M NH_4F. After Bertagna *et al.*[968] (Reproduced by permission of The Electrochemical Society, Inc.)

reaction and cathodic reaction at OCP. Increasing H^+ concentration leads to a higher degree of hydrogen termination of the surface, which passivates the surface and thus decreases the anodic dissolution. This effect tends to shift the potential in the positive direction. On the other hand, fluoride promotes the anodic dissolution and thus tends to shift the potential in the negative direction. The combined effect of these two species therefore determines the final OCP value.

OCP of silicon in HF solutions tends to vary with time for 0.1–0.2 V within several hours depending on the type of silicon material.[1153] The change of OCP of a *p*-Si in HF solutions is related to the change occurring on the surface; a colored film (a porous silicon layer) gradually develops on the surface. The change of OCP can be drastic when the surface is significantly altered due to the reactions at OCP as for example shown in Fig. 2.40.[254] In that case, the variation of OCP with time is due to the copper microdeposits acting as cathodic sites for hydrogen reduction. According to Bertagna *et al.*,[254] after an incubation period, which varies for *p* and *n* materials, OCP increases linearly with the density of copper nuclei which is proportional to its concentration in the solution. A plateau is reached as a saturation level of nuclei is reached and the further increase of copper coverage comes only from the growth of the nuclei which is much slower. The plateau at longer time is attributed to the weaker catalytic effect of the larger copper clusters which balances the continuing increase in the size of the clusters.

2.8.2. Corrosion Current

Corrosion current is a measure of the rate of the anodic reactions at OCP. The corrosion current may or may not be equivalent to the dissolution rate of silicon in a solution since silicon may dissolve chemically and/or electrochemically, and the corrosion current is a measure of only the electrochemical part of the dissolution. It is a useful parameter as a measure of the electrochemical reactions in processes such as

silicon etching and cleaning. In recent years a significant amount of work has been done to measure the corrosion current in various cleaning solutions due to its importance in silicon technology.[95,96,146,293,968]

Corrosion current generally increases in the presence of oxidizing species such as dissolved oxygen or dissolved metal ions, particularly those of noble elements which have low hydrogen reduction overpotentials. Increasing surface carrier concentration, both electrons and holes (e.g., due to background lighting), or rate of charge transfer across the interface (e.g., due to surface states) also tends to increase corrosion current. Since the stability of silicon strongly depends on the stability of its oxide, factors that inhibit the formation of oxide and promote the dissolution of oxide tend to increase the corrosion current. Table 2.16 lists some corrosion currents determined in various silicon/electrolyte systems.

As can be seen in Table 2.16, corrosion current is a very sensitive quantity due to its exponential dependence on potential. Unlike corrosion potential, corrosion current is not directly measurable but rather is a quantity derived from other measurable parameters such as polarization resistance.[1148,1149] The value of a current density is thus not only situation specific, but also has a poor certainty.

3

Anodic Oxide

3.1. INTRODUCTION

There are many types of silicon oxides such as thermal oxide, CVD oxide, native oxide, and anodized oxide. Only native oxide and anodic oxide are directly relevant in the context of this book. Anodic oxide film, which is involved in most of the electrochemical processes on silicon electrodes, has not been systematically understood, partly due to its lack of application in mainstream electronic device fabrication, and partly due to the great diversity of conditions under which anodic oxide can be formed. On the other hand, thermal oxide, due to its importance in silicon technology, has been investigated in extremely fine detail. This chapter will cover some aspects of thermal oxide such as growth kinetics and physical, electrical, and chemical properties. The data on anodic oxide will then be described relative to those of thermal oxide.

The materials discussed in this chapter are limited to the relatively thick oxides formed at potentials greater than several volts. It thus concerns mainly the growth and the bulk properties of anodic oxides. The data on thin oxide films are presented in other chapters. In particular, the oxide films involved in passivation at potentials within a few volts above OCP are dealt with in Chapter 5. Native oxides, which are almost always present on the surface of silicon electrodes, are discussed in Chapter 2.

3.2. TYPES OF OXIDES

Silicon oxide can exist in various crystalline forms, such as quartz, as well as noncrystalline forms, such as vitreous silica. The structure of silicon oxide in a vitreous state consists of a random three-dimensional network of SiO_2, constructed from polyhedra (tetrahedra or triangles) of oxygen ions.[444,720] The centers of these polyhedra are occupied by silicon ions. The distance between the silicon and oxygen ions is 1.62Å while that between oxygen ions is 2.27Å. SiO_2 polyhedra are joined to one another by bridging oxygen ions, each of which is common to two such polyhedra. In crystalline SiO_2, all oxygen ions play this role and all vertices of the polyhedra are tied to their nearest neighbors by these ions. In vitreous form, however, some of the vertices have nonbridging oxygen ions which belong to only one polyhedron.

This structure of vitreous silica can be modified by the presence of impurities, which can be substitutional and interstitial, as well as by water.[720] Substitutional impurities, the most common being B^{3+} and P^{3+}, replace the silicon in a silica polyhedron; they are termed network formers. Since such substitutional cations have a valence of either 3 or 5, their presence in the lattice results in charge defects. The interstitial impurities are usually large metal ions of low positive charges which enter into the network interstitially between the polyhedra. As a result, the polyhedra give up their oxygen to the interstitial, producing non-bridging oxygen ions. Impurities of this type are called network modifiers. Water is also present in the oxide structure incorporated during a wet oxidation process or as a contaminant in a dry process. On entering the oxide the water combines with bridging oxygen ions to form pairs of stable nonbridging hydroxyl groups. The various types of defects are schematically illustrated in the basic structure of vitreous silica shown in Fig. 3.1.[589,720]

Silicon oxide films can be produced by different methods, such as thermal oxidation or chemical vapor deposition, and have a diverse range of structures and properties. Characteristically, different types of oxide have distinct densities, for example, $2.66\,g/cm^3$ for quartz,[444] $2.26–2.45\,g/cm^3$ for thermal oxide,[118,310] $2.05\,g/cm^3$ for the anodic oxide formed in NH_4OH,[139] and $1.5\,g/cm^3$ in DI water.[457]

3.2.1. Thermal Oxide

Growth of thermal silicon oxide is typically carried out in a quartz tube at temperatures between 900 and 1200 °C in dry oxygen or wet oxygen that contains water vapor, or steam formed by passing dry oxygen and nitrogen through water near the boiling temperature.[45,720] The oxidation in wet oxygen or steam is much faster than in dry oxygen. The overall reactions in thermal oxidation are:

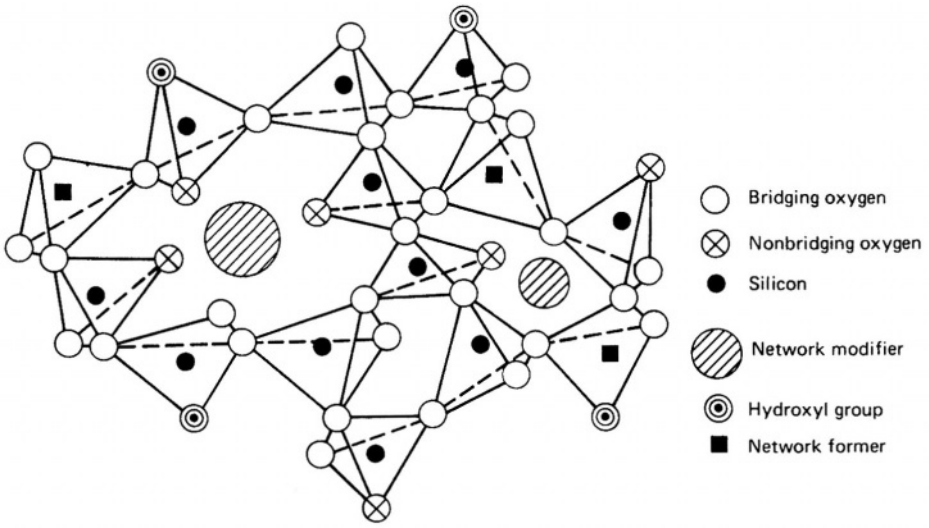

FIGURE 3.1. Structure of silica glass. After Revesz.[589] (© 1965 IEEE.)

$$Si + O_2(gas) \rightarrow SiO_2 \tag{3.1}$$

$$Si + 2H_2O(gas) \rightarrow SiO_2 + 2H_2(gas) \tag{3.2}$$

In dry oxidation the first reaction dominates whereas the second reaction dominates in wet oxidation. The growth rate is a function of temperature, oxide thickness, and substrate orientation. As an example, the average growth rate on the (100) surface in wet oxygen at 1000 °C after 1h of oxidation is about 1 Å/s. The structure of thermally grown oxide is amorphous and typically has exact stoichiometric composition. The oxide layer formed on a silicon substrate is about 2.27 times the thickness of the consumed silicon and contains about 2.2×10^{22} molecules/cm^3 of SiO_2.

3.2.2. Chemical Vapor Deposition

Silicon oxide films can be deposited by the pyrolytic oxidation of a silane or alkoxysilane in a chemical vapor deposition (CVD) system.[720] In a process using silane as the reactant, the reaction proceeds as follows:

$$SiH_4 + O_2 \rightarrow SiO_2 + 2H_2 \tag{3.3}$$

Typically, this reaction is carried out at atmospheric pressure in a cold-wall CVD system. The growth rate by the silane process is rather high, usually 8–17 Å/s.

3.2.3. Liquid-Phase Deposition

Liquid-phase deposition (LPD) of SiO_2 is a relatively new process.[258,265] The growth of the oxide is typically conducted in supersaturated hydrofluosilic acid (H_2SiF_6) solution and results from the overall reaction between H_2SiF_6 and water:

$$H_2SiF_6 + H_2O \rightarrow SiO_2 + 6HF \tag{3.4}$$

According to this reaction, SiO_2 may be formed if the concentration of H_2SiF_6 or water is increased, or the concentration of HF is reduced. Experimentally, three processes have been developed based on the above reaction to form SiO_2 deposit simply by adding either boric acid (H_3BO_3) or Al, or water to the solution. The deposition rate, 0.01–0.07 Å/s depending on solution composition, is very low relative to that of thermal oxide.

3.2.4. Native Oxide and Anodic Oxide

The thin oxide film, usually no more than 1 or 2nm in thickness, which spontaneously forms in the air and in water, is referred to as native oxide. Native oxide of a certain form and thickness exists essentially on all silicon surfaces due to the abundance of air and water and the inevitable encounters with them during the production and processing of silicon material and devices. Thicker oxides, up to 1 μm in thickness,

can be formed by passing an anodic current across the surface in an electrolyte; such oxides are called anodic oxides.

3.2.5. Use of Oxides in Device Fabrication

In the fabrication of semiconductor devices, silicon dioxide is widely used as gate insulator of metal oxide semiconductor (MOS) devices, planarization of interlayer dielectrics, isolation, passivation layers, and masking material.[258] In particular, the ability of thermally grown dioxide films to reduce the number of electrically active surface defects is most important.[479] Since the current is essentially carried along the Si/SiO_2 interface, passivation is required for the operation of MOS devices. SiO_2 films are also used to insulate conducting layers from each other or to isolate individual devices on a common silicon substrate. In addition, thin oxides are used in making capacitors in the circuit. The amount of charge stored on these capacitors is inversely proportional to the oxide thickness. Silicon dioxide films doped with phosphorus or boron are also used as doping sources for the underlying silicon. Phosphorus-doped films find many uses in protecting the underlying circuits against corrosion, ionic impurities, and mechanical damage.

Passivation coatings may be classified as primary if they are directly in contact with the single-crystal silicon from which the device is fabricated, and as secondary if they are separated from the silicon by an underlying dielectric layer.[222] The function of the primary passivation layer is to provide good dielectric properties, low surface recombination velocity, controlled immobile charge density, and device stability at the elevated temperatures under bias or operating conditions. The secondary passivation layer provides additional stability in various ambients, in both production and use, and serves as getter, impurity barrier, or mechanical shield. Anodic oxides, due to their relatively poor electrical properties, have not found much use in device technology.

3.3. FORMATION OF ANODIC OXIDES

3.3.1. General

Anodization of silicon to form a silicon oxide film can be carried out in different organic and inorganic solutions under a constant potential or a constant current density. During anodization under a constant current, the voltage typically increases with time along with an increase in oxide thickness. At a certain voltage depending on the anodization conditions, the voltage stops increasing or starts oscillating and decreasing. At this voltage, the oxide film is physically broken down often accompanying the formation of pits and nodules.

Anodization systems of various electrolyte compositions and polarization conditions have been explored as can be seen in Table 3.1. They are characterized by the yield (thickness per volt), current efficiency (CE; ionic current responsible for oxide growth), and maximum voltage, V_{max} (highest attainable anodic voltage). Several general remarks may be made based on the data in Table 3.1. (1) A high field is required for the growth of anodic film, on the order of 10^6–10^7 V/cm. (2) Ionic current efficiency

TABLE 3.1. Anodization of Silicon under Different Polarization Conditions in Various Electrolytes

Si	Solution	Condition	Yield, Å/V	CE, %	V_{max}	Ref.
	Aqueous solutions					
	DI water	14–40 μA				457
n, *p*	concd HNO_3	4 mA			160	117
n, *p*	concd H_3PO_4	4 mA			80	117
p^-(100)	1.35 M NH_4OH	0–8 V	5.4–23	20–80		449
p, *n* (100), (111)	2 M KOH	0–4 V	6.8			378
p, *n* (100), (111)	2 M KOH	6–15 V	41.7			378
n	0.2 M H_2SO_4	0.6–1.9 V_{sbe}				609
p, *n*	water + 0.04 N KNO_3	7 mA			100	228
p	1:10 $NH_4OH:H_2O$	8.4 V_{sce}	15			244
p(100)	0.1 M HCl	1–8 V	14–30			98
n	1.35 M NH_4OH	1–3 V	7			139
n	1.35 M NH_4OH	3–7 V	22			139
p	concd HNO_3	4 mA			160	117
p	concd H_3PO_4	4 mA			80	117
p	0.25 M K_2SO_4	8 mA			25	404
	Organic solvents					
	0.078 M KNO_2 in tetrahydrofurfuryl alcohol	10 mA		2.5		427
	1.5 g NO^-_2/100 ml tetrahydrofurfuryl alcohol + diethylphosphate					459
	0.04 M KNO_3 in ethylene glycol + 1–2 g $Al(NO_3)_3 \cdot 9H_2O$					106
p, p^+	*N*-methylacetamide + KNO_3	200 V	5.3	1.6–3.0		107
n, *p* (111)	*N*-methylacetamide + KNO_3	7 mA	3.8	0.8	560	117
p	0.25 N KNO_2 in tetrahydrofurfuryl	10 mA				424
	0.04 M in ethylene glycol	2.5 mA	4.5			230
p, p^+, *n*, n^+	0.04 N KNO_3 + 2 g/liter $Al(NO_3)_3 \cdot 9H_2O$ in ethylene glycol	2–8 mA	2.2			106
p	CH_3OH + NH_4Cl or NH_4SO_4	3.2 mA			7	404
p	0.04 N KNO_3 in ethylene glycol	0.5–10 mA	5.3	1–8		370
a-Si:H	0.04 N KNO_3 in ethylene glycol	0.5–10 mA	5.5	1–8		370
p(111)	0.034 M in methanol	8 mA	13.6			404
p(111)	glycol + 2% H_2O + nitrate	8 mA	4.6			404
p	0.04 N KNO_3 in ethylene glycol	17 mA			540	1039
p, *n*	0.04 N KNO_3 in ethylene glycol + 0.35% H_2O	7 mA, <150 V	5.8		495	228
p, *n*	0.04 N KNO_3 in ethylene glycol + 10% H_2O	7 mA, <150 V	16		495	228
p	*N*-methylacetamide or glycol + KNO_3 or KNO_2	1 mA	6	2		301
p, *n*	phthalate + NH_4F					603
n, *n* (Ar^+)	0.04 N KNO_3 in ethylene glycol	7 mA	5			605
p	0.04 N KNO_3 in ethylene glycol + 1.2% H_2O	1–25 mA	5.6	~2		919

is low, particularly in organic solutions where it is generally less than a few percent. (3) Except for an initial period, the growth of oxide increases linearly with time, giving a yield in the range of 2–40 Å/V. (4) For a given solution, there is a maximum voltage above which physical breakdown of the oxide film occurs. (5) Water plays a critical role in the growth and properties of the anodic oxides and thus the properties of the oxides formed in aqueous solutions and organic solutions differ greatly.

3.5.2. Effect of Solution Composition

Anodization of silicon to produce oxide film was first tried in solutions such as HNO_3 and H_3PO_4 and borate aqueous solutions.[117] In these solutions, the formation voltage was limited to less than 200 V. In a 1 M KOH solution, the forming voltage can only reach 20 V, above which the reaction is dominated by oxygen evolution.[925] Later, organic solvent-based solutions such as methylacetamide, glycols, and alcohols were used, which allowed the formation at higher voltages, and thus thicker oxide. The *V–t* curves during anodization in different electrolytes at constant current density are shown in Fig. 3.2. Since the anodic oxides obtained in organic solutions generally have better properties, most later investigations of anodic oxides were conducted in these solutions.

Among the organic solvents, ethylene glycol (CH_2OHCH_2OH) and *N*-methylacetamide (NMA; $CH_3CONHCH_3$) are the most commonly used for anodic oxidation of silicon. A small amount of salt, typically 0.04 N KNO_3, is added to increase the conductivity of the solvent. Usually a small amount of water, either as an addition or as an impurity, is also present in the solution and is important in determining the growth and properties of the anodic oxides. In terms of formation characteristics, ethylene glycol and NMA are very similar. Oxidation in both solutions at a constant current density can be continued to voltages in excess of 500 V. The growth of oxide is a linear function of potential over a wide range as seen in Fig. 3.3, which shows a yield of 5.3 Å/V for ethylene glycol and 5.6 Å/V for NMA. Also, the current efficiency for the two solutions and its dependence on water content, lowest at 1–3% water, are very similar for the two solutions as shown in Fig. 3.4.[107,919] Anodization in other types of

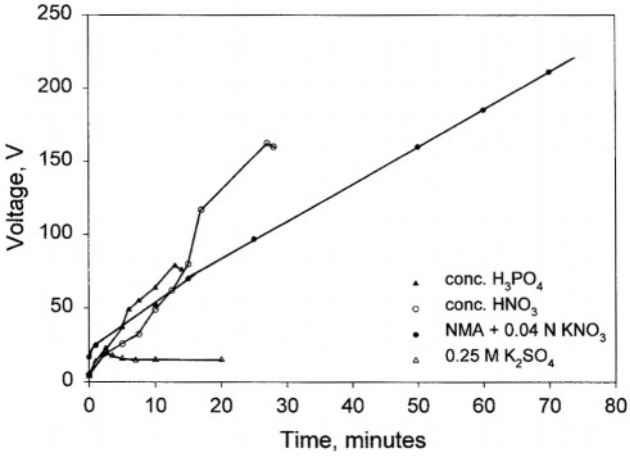

FIGURE 3.2. Variation of potential with time during anodization of Si at a constant current (6–8 mA/cm^2) in different electrolytes.[117, 404]

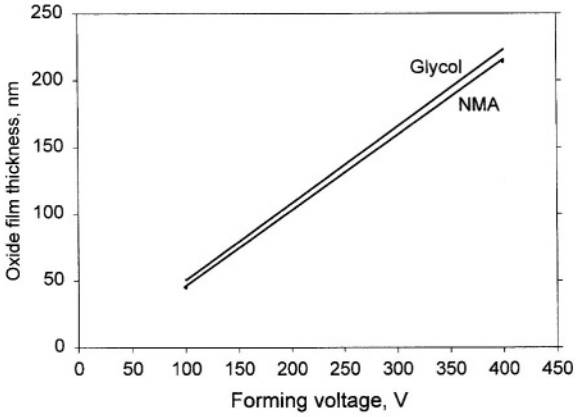

FIGURE 3.3. Thickness of anodic oxide as a function of forming voltage in NMA and glycol solutions containing 0.04 N KNO_3 at a current of 3–6 mA/cm^2. Data from Refs. 107 and 919.

organic solvents may be very different. Figure 3.5 plots the oxide thickness versus forming voltage for methanol and glycol solutions.[404] The yield of 13.6 Å/V in methanol is much higher than that in ethylene glycol.

The type of dissolved salts affects the anodization process as shown in Fig. 3.6.[404] The particular cation in the solution generally does not influence the anodization behavior.[107] On the other hand, the effects of various anions on the anodization behavior are significant.[404] In methanol, the presence of some anions such as SO_4^{2-} and ClO_4^- results in no oxide film growth but severe pits at very low voltages, whereas in glycol, anodization can be carried out up to 100 V. The presence of Cl^- (curve a) prevents the rise of voltage and thus the formation of thick anodic oxide. Similarly, it was found that silicon oxide will not form in NMA containing NaCl.[107] The effect of a specific salt is also dependent on the solvent. Oxide films of certain thicknesses can be formed in chloride-containing NMA and ethylene glycol. In chloride- or sulfate-containing methanol,

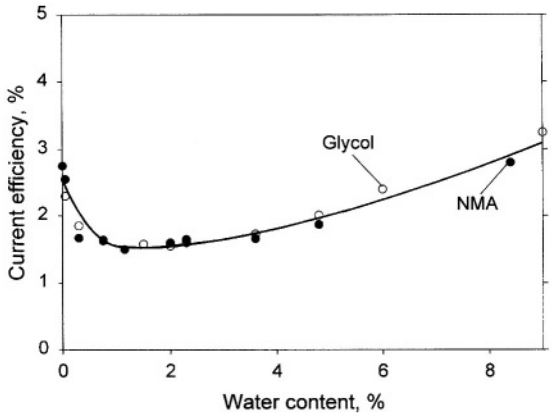

FIGURE 3.4. Current efficiency versus water content for oxide formed in NMA and ethylene glycol containing 0.04 N KNO_3. Data from Refs. 107 and 919.

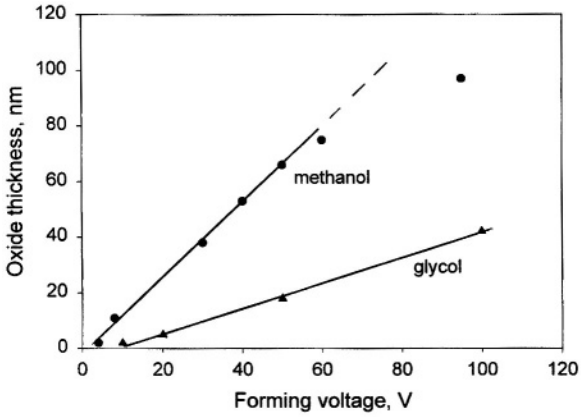

FIGURE 3.5. Thickness of anodic oxide in methanol (with 0.01% H_2O and 0.04 N KNO_3) and in ethylene glycol (with 2% H_2O and 0.04 N KNO_4). After Madou *et al.*[404] (Reproduced by permission of The Electrochemical Society, Inc.)

silicon cannot be anodized but pits form.[404] Anodization is possible in 0.1 N HCl aqueous solution at relatively low voltages, up to 8 V.[98] The effect of Cl^- on the formation of silicon is similar to that on the passivation and oxide formation on many metals. The presence of chloride ions in electrolytes causes breakdown of passive films at low potentials and thus prevents the buildup of voltage required for formation of thick oxide films. The oscillations in the curves shown in Fig. 3.6, indicating the instability or breakdown/regrowth cycles of the oxide, may be similar to those occurring during anodization of silicon in HF solutions (see Section 5.10).

The amount of water present in an organic solvent is of particular importance in the growth and properties of anodic oxides. Water as an oxidizing agent is essential in

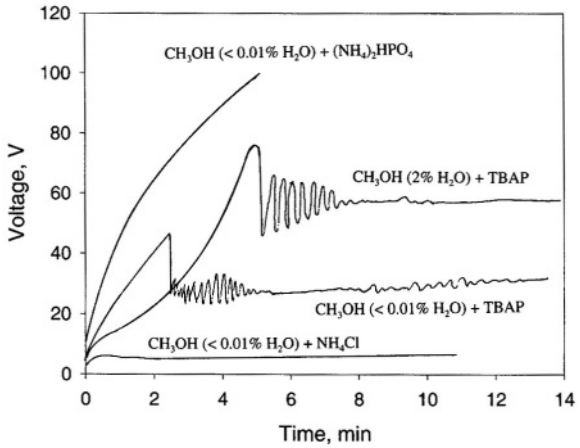

FIGURE 3.6. Voltage versus time curves for anodix oxidation of *p*-Si in methanol at a current density of 3.2 mA/cm^2 with various additives. (a) CH_3OH (<0.01% H_2O) + NH_4HOS_4; (b) CH_3OH (<0.01% H_2O) + TBAP (tetrabutylammonium perchlorate); (c) CH_3OH (2% H_2O) + TBAP; (d) CH_3OH (<0.01% H_2O) + $(NH_4)_2HPO_4$. After Madou *et al.*[404] (Reproduced by permission of The Electrochemical Society, Inc.)

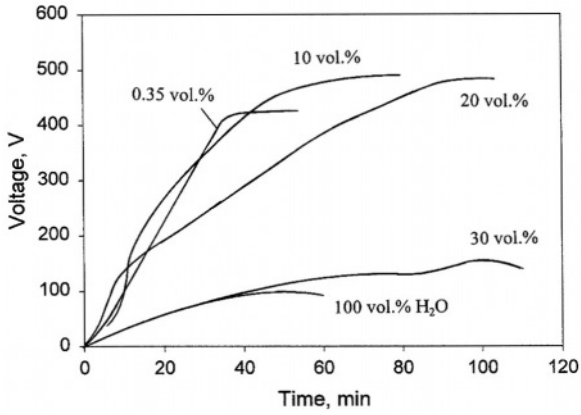

FIGURE 3.7. Cell voltage difference ΔV as a function of anodization time in ethylene glycol of different water contents. After Mende *et al.*[228] (Reproduced by permission of The Electrochemical Society, Inc.)

the formation of anodic oxide on silicon.[107] Even in "dry" solution the oxidation depends on the water initially present as an impurity, or the water resulting from oxidation of NMA. The amount of water in the solutions closely correlates to the growth rate, the critical growth thickness, and the breakdown potential of the oxides.[228] The effect of water on oxide growth in ethylene glycol is shown in Fig. 3.7. Figure 3.8 shows the maximum attainable voltage for anodization in ethylene glycol electrolyte as a function of water content. The maximum voltage is above 350 V for water content of less than 25% but is less than 150 V for water content of more than 30%. Water has a similar effect on other solvents.[404] It also has a significant effect on current efficiency. Figure 3.4 shows that current efficiency is lowest for water content of about 1–2% in both NMA and glycol solutions.[107,919] In KNO_3-containing ethylene glycol solutions,

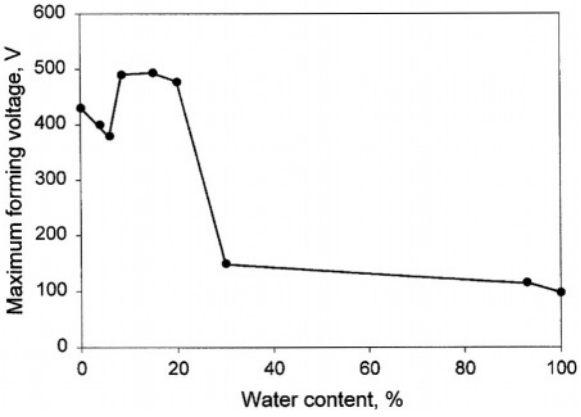

FIGURE 3.8. Maximum forming voltage as a function of water content in 0.04N KNO_3-containing ethylene glycol. After Mende *et al.*[228] (Reproduced by permission of The Electrochemical Society, Inc.)

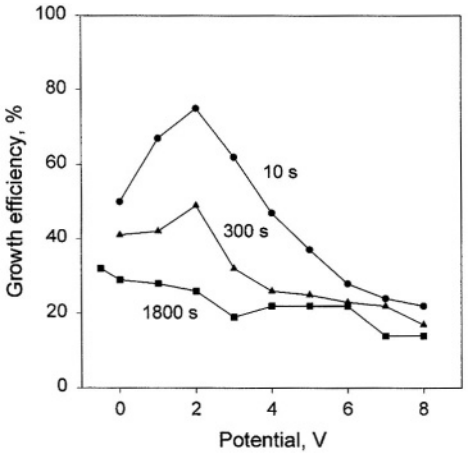

FIGURE 3.9. The growth efficiency of anodix oxide films on Si (100) formed potentiostatically for various times in aqueous 1.35 M NH_4OH solution. After Bardwell *et al.*[449] (Reproduced by permission of The Electrochemical Society, Inc.)

the current efficiency increases for water content up to 20%, but drops to much lower values for water content higher than 30%.[228]

In NMA + KNO_3 solutions, ionic current efficiency increases in the presence of chloride or fluoride ions.[117] For the anodization in ethylene glycol containing KNO_3, the efficiency increases rapidly with increasing KF concentration above 10^{-5} M which is associated with disturbances in the oxide layer and an excessive incorporation of fluorine.[835] Relatively high current efficiency can be obtained in NH_4OH solutions.[449] Figure 3.9 shows the efficiency of oxide growth in 1.35M NH_4OH as a function of potential and time. The efficiency is higher at low potentials and short anodization times, indicating that the growth efficiency decreases with oxide thickness. The low ionic current efficiency during anodization is due to the side reactions. In aqueous solutions, the side reaction is that of water oxidation leading to oxygen evolution which occurs at potentials greater than $2\,V_{sce}$.[139] In organic solvents, oxidation of the solvent molecules may also be side reactions.[301,919]

The field required for oxide growth also strongly depends on electrolyte composition. Table 3.1 shows that the field during oxide growth is in the range from 2.4×10^6 V/cm to 2.6×10^7 V/cm. The field is in general larger in organic solvents than in aqueous solutions. Higher fields are generally required with larger current densities. It has been reported that the anodization of silicon in dry electrolytes requires a field strength of about 2×10^7 V/cm; oxide growth rate falls to essentially zero if the field strength is lowered by 10% from the above value.[228] Anodization in different solvents requires different fields for growth as shown in Fig. 3.6.[404] Addition of water in organic solvent generally reduces the growth field.[228]

3.3.3. Effect of Silicon Substrate

There are few data on the effect of substrate on the formation of anodic oxide. In 2M KOH, the formation characteristics of anodic oxides on (100) and (111) surfaces in the potential range from 6 to 15V are the same.[378] Ion implantation of substrate silicon has been found to greatly affect the anodization behavior of silicon.[787,790] An increase in the anodization rate occurs after implantation of H^+, C^+, N^+, P^+, As^+, Ar^+,

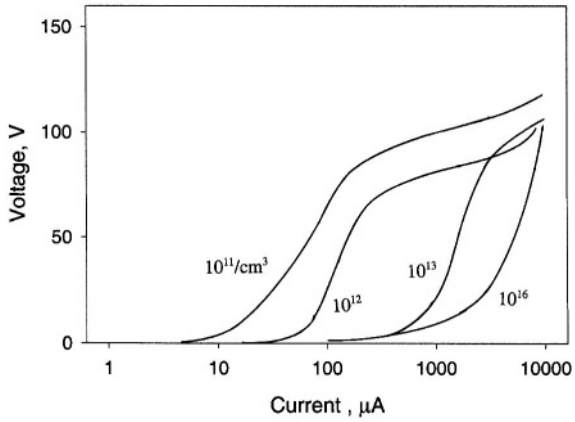

FIGURE 3.10. V_0–log I characteristics of locally Ar^+ implanted Si in comparison with unimplanted n-type silicon (V_0 is the cell voltage at the beginning of anodization at constant current I). (Reprinted from Mende *et al.*[605] © 1994, with permission from Elsevier Science.)

and Xe^+. This effect is attributed mainly to the implanted ions and not to radiation damage. On the other hand, implantation of Al^+, Ga^+, and Sb^+ ions causes a decrease in the oxidation rate, which is attributed to radiation damage. As an example, Fig. 3.10 shows that the cell voltage for high doping material at the beginning of the anodization is much lower at a given current density indicating a much lower current efficiency during the anodization with increasing Ar^+ dose. The increased current density with the implant concentration is due to the increase of generation–recombination centers, especially at concentrations higher than $10^{12}/cm^2$.[605,790] Surface roughness may affect the oxidation kinetics, especially the initial stage.[1038] It has been reported that growth rate and uniformity of anodic oxides can be better controlled by using two anodes, a disk anode in the middle and a ring anode at the perimeter.[457]

3.3.4. Effect of Polarization Conditions

Anodization can be carried out under different modes with constant potential (potentiostatic mode) or constant current (galvanostatic mode). Constant potential means that the oxide grows under different field strengths from the start to the end of anodization, whereas constant current means that the oxide grows under a constant field. Most studies on the anodization of silicon employ the galvanostatic mode.

It has been found that the mode of polarization particularly at the initial stage has a great effect on the further growth of the oxide.[98] If the oxide is grown at a higher potential, then the final oxide will be significantly thicker. Figure 3.11 shows the thickness of oxide films grown in a 0.1 M HCl solution for two different operation modes: The COSI mode is obtained by applying the potential on the sample prior to immersion into the solution, and the ramped mode is obtained by applying the potential at the open circuit value and gradually increasing it to the desired potential value.

The formation of oxide depends on the rate at which the voltage is applied as well as the area of the electrode surface under a constant potential mode. The mechanism by which the first few layers of oxide are formed is important in establishing the mechanism of growth of the entire oxide film.

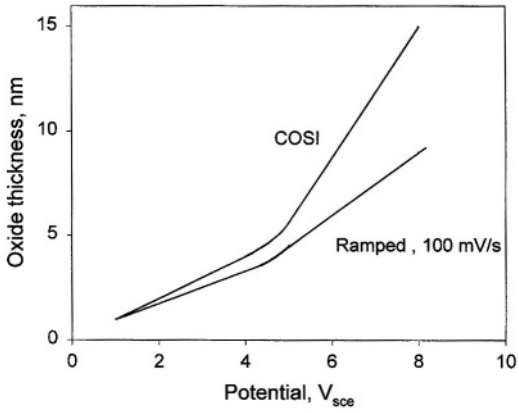

FIGURE 3.11. Oxide thicknesses as a function of applied potential for both COSI and ramped (100 mV/s) growth modes. The growth time was 30 min. The substrates were (100) *p*-type Si with a resistivity of 3 to 7 Ωcm. The electrolyte used was 0.1 M HCl. After Bardwell *et al.*[98] (Reproduced by permission of The Electrochemical Society, Inc.)

Figure 3.12 shows that the COSI mode and the stepping potential mode generate thicker oxide films than the ramp mode for large samples, >1 cm^2.[98] This phenomenon is due to the effect of electrolyte resistance, $R = \rho/(4a)$ where ρ is the resistivity of the electrolyte and a is the radius of the sample. It reduces the effective potential from 8 V_{sce} to a value lower than 5.5 V_{sce} initially and the initial oxide is grown at lower

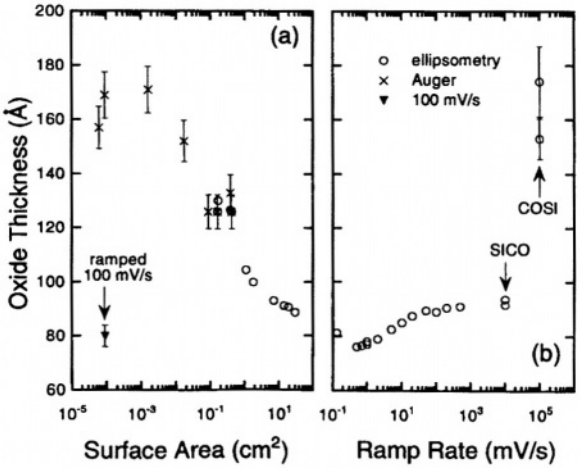

FIGURE 3.12. Anodic oxide film thickness formed on *p*-Si in 0.1 M HCl as a function of (a) the electrode surface area and (b) the ramp rate. The condition in all cases was 8 V_{sce} for 30 min. All results shown in (a) were for oxides grown by directly stepping the potential to 8 V_{sce} (SICO mode). In (b) the oxides were grown by ramping the potential from the open-circuit potential to 8 V_{sce} at various rates, and the sample size was in the range 4.5 to 7.5 cm^2. The points shown at "ramp rates" of 10^4 and 10^5 mV/s correspond to samples grown by SICO mode and COSI mode. The potentiostat was stepped to the desired potential and then the sample was gradually in which manually lowered into the electrolyte. After Bardwell *et al.*[98] (Reproduced by permission of The Electrochemical Society, Inc.)

potential than the applied value. As the surface area gets smaller, the effective potential approaches the applied value.

It has been observed that in an NMA solution, if anodization is continued after the voltage is increased to 350 V, the oxide breaks down; the voltage starts to oscillate without rising further.[117] But if the sample is held at a constant voltage of 300 V for some time, the forming voltage can be raised to 560 V at which bright sparks appear in the solution. Also, in the NMA solution, if an as-grown film is cathodically polarized at a voltage between 12 and 15 V for a certain time, the current increases in magnitude. The anodic oxide is "deformed" by the cathodic polarization because on switching the current back to the anodic direction, the voltage necessary to drive a given current is much smaller than before cathodic polarization.

3.3.5. Effect of Illumination

The effect of illumination on the *I–V* curves of both *p*-Si and *n*-Si is shown in Fig. 3.13.[370] The anodic reaction kinetics of *p*-type silicon are not affected by illumination because the reaction consumes holes which are the majority carriers and their concentration is little affected by illumination. For *n*-Si during anodization, the interface is reversely biased and in order to sustain the reaction, either holes have to be generated or electrons have to be injected from the electrolyte. Thus, in the dark, an extra voltage, V_{ex}, above that which is required for anodization of *p*-Si, is needed to drive the current.[117] For example, about 100 V is required for $7\,mA/cm^2$ initially in NMA. The extra voltage needed to anodize *n*-Si diminishes with increasing illumination intensity and at sufficient light intensity the anodic current becomes identical to that for *p*-Si. The quantum yield of illuminated anodization is low; a value as low as 1% has been found for the anodization of silicon under illumination.[605]

Figure 3.13 also shows that the sensitivity to illumination decreases with increasing oxide thickness, and at a thickness corresponding to about 380 Å further growth is no longer sensitive to light.[117,370] The sensitivity can be measured by the excess voltage

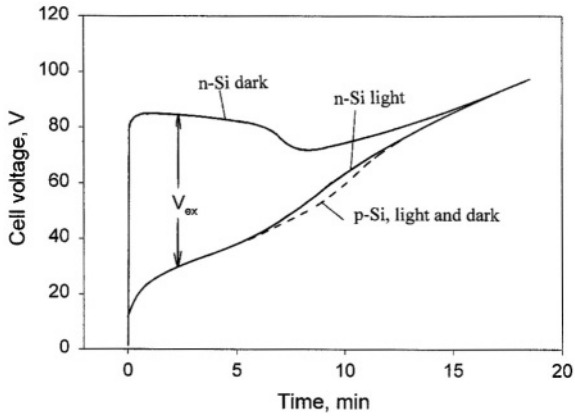

FIGURE 3.13. Comparison of constant-current anodization curves in the dark and under illumination for *p*-Si and *n*-Si. After Hasengawa *et al.*[370] (Reproduced by permission of The Electrochemical Society, Inc.)

required for the anodization of *n*-type silicon in the dark relative to that under illumination. The loss of photosensitivity at a certain oxide thickness has a twofold meaning: (1) it indicates that above 380 Å the rate-determining step changes from inside silicon to inside oxide and (2) the field at the oxide/Si interface is large enough to satisfy the supply of minority carriers for the growth of the oxide on *n*-Si. The photosensitivity also appears to be influenced by the mode of anodization. The critical thickness at which sensitivity to light disappears was found to be about 240 Å in one case[106] and 350 Å in another.[370]

3.3.6. Electroluminescence

Electroluminescence is observed to occur during anodization on both *n*- and *p*-type materials. The luminescence on *p* type is uniform on the sample surface, whereas that on *n* type is highly nonuniform.[370] It occurs only when the oxide reaches a certain thickness as shown in Fig. 3.14.[230] No light emission is observed below a thickness of 15 nm. For SiO_2 greater than 25 nm thick, the intensity of emitted light increases exponentially, the exponential factor being 10nm as shown in Fig. 3.14.

The spectrum of emitted light consists of two different regions, namely, a low-energy region (LE) and a high-energy region (HE), as shown in Fig. 3.15.[230] The LE region has a broad peak corresponding to an energy of 1.93 eV and the HE region exhibits two peaks of 3.04 and 2.76 eV. In another study, the illumination was found to be centered in two regions with LE at about 2 eV and HE at 3.44 eV.[370] The intensity of both peaks increases with oxide thickness from a few nanometers to about 100 nm. At larger thicknesses the intensity of LE still increases with increasing thickness but HE becomes relatively constant.[230] Addition of water in the ethylene glycol solution of KNO_3 reduces the intensities of both peaks whereas addition of a low concentration of KCl, 0.001 M, enhances significantly the LE peak.[1033]

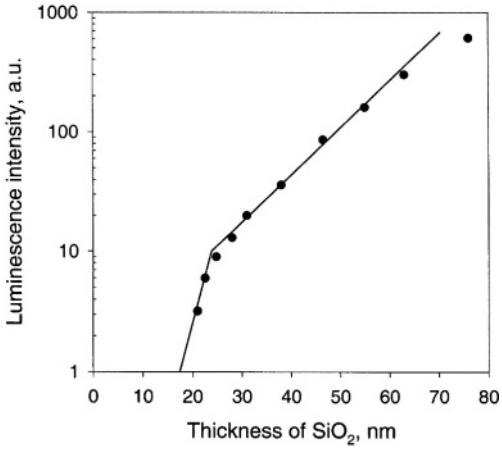

FIGURE 3.14. Integrated light intensity as a function of SiO_2 thickness in KNO_3-containing ethylene glycol. After Zhou *et al.*[230] (Reproduced by permission of The Electrochemical Society, Inc.)

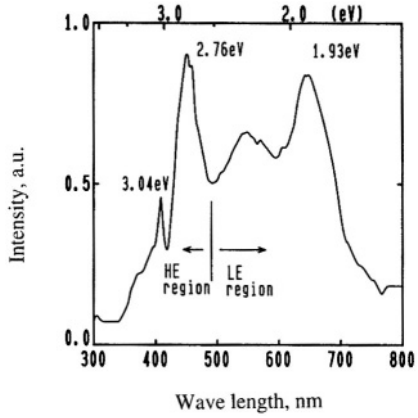

FIGURE 3.15. Emission spectrum obtained at Si oxidation in KNO_3-containing ethylene glycol. After Zhou *et al.*[230] (Reproduced by permission of The Electrochemical Society, Inc.)

3.4. GROWTH MECHANISMS

3.4.1. Reactions

The oxidation reaction of silicon is a process involving breaking Si–Si bonds and formation of Si–O bonds with conversion of the silicon atoms from a valence of 0 to a valence of 4. In anodization the four valence electrons on a silicon atom are transferred in the overall reaction

$$\mathrm{Si} + 2\mathrm{H_2O} + nh \rightarrow \mathrm{SiO_2} + 4\mathrm{H^+} + (4-n)\mathrm{e} \qquad (n \leq 4) \tag{3.5}$$

The water involved in the above reaction is the main source of oxygen in the formation of anodic oxide in various electrolytes, aqueous and nonaqueous. According to Croset *et al.*,[301] in NMA and glycol solutions, over 80% of the oxygen in the oxide comes from the water and the rest from the salts, while the solvents play little role as a direct source of oxygen. Therefore, when water is present in the electrolyte the source of oxygen does not depend on the nature of the solvents. However, when water is not present such as in dry organic solutions, the main reaction at the anode is the production of water via oxidation of the solvents, which supply the water to sustain the oxidation reaction, and this is responsible for the low oxidation efficiency in the growth of anodic oxide. The amount of water available depends on the solvent: about 0.5 mol/Faraday of water is created at the anode in NMA and 1 mol/Faraday in glycol.[301]

In dry electrolytes (initially water free) the oxygen required for oxidation can either come from the water due to the anodic decomposition of the solvent or come from the dissolved salts. According to Madou *et al.*,[404] most oxygen required for oxide growth in dry glycol stems from the water derived from the decomposition reaction of glycol. Oxygen-containing electrolytes such as KNO_3 or Li_2SO_4 are not essential for the anodization process in NMA solutions as anodization is found to be possible in a solution containing NaF and NH_4F.[107] On the other hand, in dry methanol which does not decompose into water easily, the oxygen may originate from oxyanions such as

NO_3^- and HPO_4^- as N and P are detected in the oxide formed in water-free methanol electrolyte.[424] Once water is present in methanol, the major part of the oxygen required for the oxidation comes from the water instead of the salts.

Formation of the first layers of oxide (i.e., native oxide) on the surface of silicon, according to Ozanam and Chazalviel,[692,934] appears to also require the presence of water even in nonaqueous solutions. On immersion into the solution the silicon surface is gradually evolving from a H-terminated surface (after HF cleaning) to a silicon oxide-covered surface due to the residual water present in the nonaqueous electrolyte (10 ppm).[692] Initially the water is molecularly adsorbed at the silicon surface, then slowly oxidizes the surface silicon atoms to form oxide islands. The oxide islands are about 0.6 nm thick and cover about 60% of the surface area after 1 week of immersion in various nonaqueous electrolytes.

Knowledge regarding the detailed reaction processes involved in anodic oxidation is still lacking. According to Lewerenz,[602] the oxidation process can be initiated by formation of hydroxide from water if a hole is supplied. Subsequently, two Si–OH groups form a Si–O bond splitting off a water molecule. The resulting polarization of the Si–Si back bonds then possibly leads to the insertion of O by place exchange. The consecutive steps are described as follows:

$$Si + H_2O + h \rightarrow SiOH + H^+ \tag{3.6}$$

$$2SiOH \rightarrow Si_2O + H_2O \tag{3.7}$$

$$2Si_2O \rightarrow SiO_2 + 3Si \tag{3.8}$$

The reaction steps involve Si^+ as an intermediate. It is possible that reactions with higher oxidation states such as Si^{2+} and Si^{3+}, which are considered to be present at the silicon/oxide interface, may be involved in addition to reactions (3.6) to (3.8).[702]

3.4.2. Ionic Transport within Oxide

During anodic oxidation, either the cation or the anion or both must migrate across the thickening oxide film. The mobile ions can be identified and if both move, the relative mobilities can be deduced by tagging a thin surface layer with a completely immobile marker atom and determining its position after anodizing.[346,427] They may also be identified by profiling the oxide on the concentration of labeled mobile species such as oxygen isotopes.[449] The issue of mobile species in the oxide during anodic oxidation has not been fully resolved as cation outward movement is found to dominate in some studies and anion inward movement in others.[186,346,427,449]

The results from many investigations show that inward diffusion of oxygen-containing anions is responsible for the ionic conduction in the oxide film during anodization. Mackintosh and Plattner[346] used two different noble gases Kr and Xe as markers and found that the anodic oxide growth in 0.1 M H_3BO_3 + 0.1 M $Na_2B_4O_7 \cdot 10H_2O$, 0.4 M KNO_3 in NMA, 0.3 M KNO_2 in tetrahydrofurfuryl alcohol, and 15% P_2O_5 in tetrahydrofurfuryl alcohol is governed by anion inward movement. According to Mende,[186] who determined the depth distributions of ^{30}Si implanted into

Si before and after anodization in KNO_3-containing glycol, the Si ions are the mobile ions during the anodization. Croset and Dieumegard[714] found that oxygen during the growth of the anodic films in ethylene glycol containing 0.4% KNO_2 and 0.4% H_2O, using the ^{18}O labeling technique, is the mobile species. Beckmann and Harrick[424] found that the concentration of hydroxyls in the anodic oxide formed in 0.25 M KNO_2 in tetrahydrofurfuryl alcohol increases toward the Si/SiO_2 interface as shown in Fig. 3.16. This indicates that there must be migration of the OH groups to the interface under the action of the applied field and the oxidation reaction at the interface must be the rate-limiting process to cause a higher concentration near the interface with respect to the interior of the film. Bardwell *et al.*,[449] who used the ^{18}O profiling technique, found that in the anodic oxide formed in NH_4OH solution, the ^{18}O is concentrated at the oxide/silicon interface, suggesting that inward migration of oxygen is the main ionic transport mechanism.

On the other hand, Madou *et al.*,[404] based on the identification of a small amount of P and S in the oxides formed in the glycol solutions and none in those formed in methanol solutions, suggested that Si outward movement may be involved during the oxidation in methanol. According to Schmidt and Ashner,[427,459] who used ^{32}P as marker, the growth of anodic films on Si in dry tetrahydrofurfuryl alcohol at high field strengths occurs almost exclusively by cation drift. However, they also found that at low field strengths, hydroxyl ions, if present in ample supply, are the mobile species and cause hydration of the SiO_2 film.

In a study by Schmidt and Ashner,[427] inward motion of hydroxyl ions is also found in the anodic oxidation of a steam-grown oxide, resulting in a hydrated oxide film. On contact with the electrolyte there is an induction period during which the steam-grown oxide surface is hydrated. The electrical field is able to aid the injection of hydroxyl ions after hydration takes place. According to Schmidt and Ashner, the primary step involves reaction of the oxide surface with water in the electrolyte to produce OH groups: $Si–O–Si + H_2O \rightarrow 2\ Si–(OH)$. The OH groups can then be acted on by the electrical field to migrate inward into the oxide. The diffusivity of the species

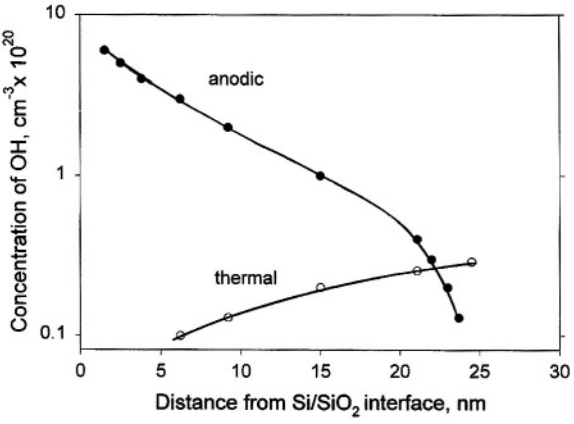

FIGURE 3.16. Concentration of OH as a function of distance from the Si/SiO_2 interface; anodic oxide formed in 0.25 N KNO_2 in dehydrated tetrahydrofurfuryl at 10 mA/cm^2. After Beckmann and Harrick.[424] (Reproduced by permission of The Electrochemical Society, Inc.)

associated with water was determined by Dreiner[836] to be 4.3×10^{-17} cm^2/s at 25 °C in water and 3.5×10^{-18} cm^2/s in KNO_3-containing ethylene glycol. According to Dreiner, water enters only into the outermost layer, then dissociates. Further diffusion is in the form of moving hydroxyl groups. The first step (water entry) is rapid whereas the diffusion is a slower process which can be increased by anodic bias.

The different results obtained from a number of studies indicate that the mobile species during anodic oxidation of silicon may depend on the anodization conditions. At relatively low field in water-containing electrolytes, anion inward movement is the dominant process, whereas at high field in water-free electrolytes, cation outward movement may be important. Based on some recent studies, the chemical nature of the mobile species may also be different under different conditions. According to Bardwell *et al.,*[449] the transport follows different mechanisms at low, <3.5 V, and high potentials, >3.5 V. At low potentials, the growth may be due to lattice diffusion of OH^- or O^{2-}, whereas at high potentials, it may be by short-circuit diffusion of O^-_2. The potential for the latter mechanism to be possible is the potential at which O_2 evolution on the electrode surface becomes important and therefore molecular oxygen is available for transport through the oxide. This change of transport mechanism is accompanied by a larger oxide growth per volt.[139] A change of the voltage growth rate from 7 Å/V in the potential range of 1–3.5 V to 22 Å/V at potentials larger than 3.5 V is observed in the anodization of silicon in NH_4OH solution.

3.4.3. Growth on n-*Si*

Anodic reaction typically involves holes which are the majority carrier in *p*-type silicon but are the minority carrier in *n*-type silicon. The anodization of *n*-type substrate thus requires generation of carriers either by extra field strength or by illumination. According to Schmidt and Michel,[117] for *n*-Si an initial high voltage, with an excess voltage, V_{ex}, above that of *p*-Si or strongly illuminated *n*-Si is needed for electrons to tunnel through the barrier at the silicon surface. The formation of the first layers of the oxide decreases the height of the barrier inside the *n*-Si and the anodization can proceed further at lower voltages. V_{ex} can be viewed as the potential drop in the space charge layer which is required for generation of charge carriers to sustain the anodization reaction.[1038]

According to Hasengawa *et al.*,[370] the excess voltage, V_{ex}, can be defined as $V_{ex}(N_D, L_0, t) = V_n(t) - V_p(t)$ and is a function of doping concentration N_D, light intensity L_0, and time t. For *n*-Si the holes required for anodization may be generated by either avalanche breakdown or illumination. In the dark, anodization of *n* type involves avalanche breakdown in the semiconductor depletion layer and V_{ex} depends on the doping level of the semiconductor as shown in Fig. 3.17. Under a sufficient illumination intensity the excess voltage is zero and the anodization curve of *n*-Si becomes essentially the same as that of *p*-Si as shown in Fig. 3.6 due to the switching of the rate-limiting process from hole supply to ionic transport. On the basis of the avalanche multiplication mechanism, the photocurrent I_{ph} through a semiconductor depletion region is given by

$$I_{ph} = I_{ph0} \Big/ \left[1 - (V/V_B)^n\right] \tag{3.9}$$

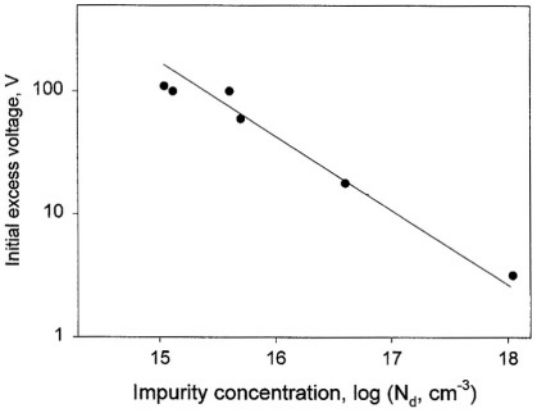

FIGURE 3.17. Initial excess voltage V_{ex} versus doping concentration for dark anodization of *n*-Si. After Hasengawa *et al.*[370] (Reproduced by permission of The Electrochemical Society, Inc.)

where V is the applied potential, V_B the breakdown potential, I_{ph0} the photocurrent at low voltage where no carrier multiplication takes place, and n a constant. The initial excess voltage during anodization is expressed as

$$V_{ex} = V_B(1 - L/L_0)^{1/n} \qquad \text{for} \qquad 0 < L < L_0 \tag{3.10}$$

$$V_{ex} = 0 \qquad \text{for} \qquad L > L_0 \tag{3.11}$$

with L the light intensity and L_0 the minimum intensity which can supply a sufficient number of holes required for anodic reaction without carrier multiplication in the depletion region.

3.4.4. Electroluminescence

According to Hasengawa *et al.*,[370] the mechanism of the luminescence can be described using the diagram shown in Fig. 3.18. The low ionic current efficiency during anodization indicates that a considerable amount of electronic current flows through the conduction band during anodization. Electrons are able to tunnel directly from the energy states in the electrolyte into the conduction band of SiO_2. Some of these electrons lose energy by emitting photons whose energy corresponds to the conduction band discontinuity, about 3.1eV, and give rise to the HE peak. Some of the electrons lose energy by falling into traps that are located about 2 eV below the conduction band of SiO_2, which is responsible for the LE peak.

A different model for the illumination mechanism is provided by Zhou *et al.*[230] In this model, dielectric breakdown is considered to occur within the oxide because the field strength in the SiO_2 layer during growth is 22 MV/cm which is around the breakdown voltage. Electron and hole pairs are generated at breakdown and the electrons are accelerated under the field to become hot electrons. The scattering of these electrons,

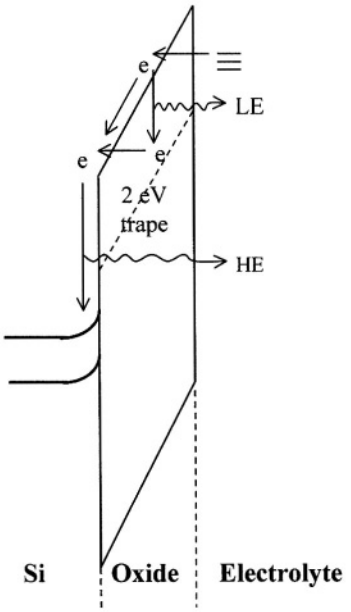

FIGURE 3.18. A model for the electroluminescence during anodization. After Hasengawa *et al.*[370] (Reproduced by permission of The Electrochemical Society, Inc.)

whose mean free path is about 10 nm, with the light emission centers in the oxide then results in the light emission corresponding to the LE peak. The HE emission is attributed to the transition due to band discontinuity at the oxide/silicon interface. The light intensity increases with the oxide thickness because the emission region increases. The emission center, located about 2 eV below the conduction band, is considered to have the same nature as that described by Hasengawa *et al.*[370]

Light emission also occurs on thermal oxide film under anodization conditions, indicating that the light emission is not associated with defects particular to anodic oxide but rather with a common phenomenon associated with the $Si–SiO_2$ system.[370] Also, that light is emitted only above a certain thickness indicates that the luminescence is not due to the chemical reaction but to the mode of charge transfer involved in the formation of SiO_2. No light emission occurs for thicknesses of less than 15 nm because up to this thickness the electron can tunnel through the oxide layer directly into Si. The fact that the energy and intensity of emission varies with thickness indicates that the process depends on the structure of the oxide. The enhancement of the low-energy peak by the addition of KCl in the solution can be explained as due to the incorporation of chloride ions in the oxide film.[1033]

3.4.5. An Overall Growth Model

The general processes involved in the anodic oxidation of silicon can be summarized by the band diagram of Si/SiO_2/electrolyte interfaces illustrated in Fig. 3.19 considering the information on the possible reactions, on the species responsible for ionic transport inside the oxide, and on the differences between *p*-Si and *n*-Si.

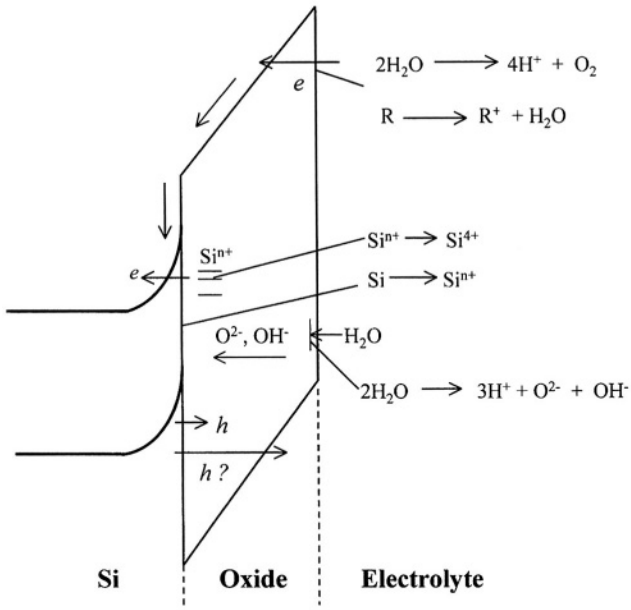

FIGURE 3.19. A model for the processes occurring during the formation and growth of an anodic oxide on Si.

Under typical anodization conditions, holes from the valence band are responsible for the oxidation reaction for *p*-Si whereas injection of electrons into the conduction band is responsible for that for *n*-Si (requiring a high voltage to narrow the surface barrier). The oxidation reaction occurs at the silicon/oxide interface through several intermediate steps forming partially oxidized species which can act as interface states. These partially oxidized silicon species, due to their different energy levels, are further oxidized by electron tunneling into the conduction band at much lower voltages. This is responsible for the oxidation of *n*-Si after it is covered with an oxide film of a certain thickness.

The oxygen required to form the oxide structure is from the water, either residual or generated during anodization, in the electrolyte. The water molecules enter into the first layers of the oxide and dissociate into ionic species, such as O^{2-} and/or OH^{-}, which then migrate toward the silicon/oxide interface under the effect of the electrical field in the oxide.

The oxide, which is capable of conducting a large current under anodizing conditions, behaves as a doped semiconductor, and is responsible for the side reactions and low ionic current efficiency. Depending on the nature of the solvent, whether aqueous or nonaqueous, the side reaction can be predominantly due to the oxidation of water in aqueous solutions, and due to the oxidation of solvent molecules, R, in nonaqueous solutions. It is not clear whether the electronic current is by hole or electron, but the band structure of the silicon/oxide interface indicates that electron conduction is more likely. In either case the charged carriers going through the energy steps at the

oxide/electrolyte interfaces, silicon/oxide interfaces, and localized states in the oxide may result in photoemission.

3.4.6. Growth Kinetics

Thermal Oxides. Before discussing anodic oxides it is beneficial to provide a brief description of the classic theory of growth kinetics of thermal oxides. The growth of thermal oxides follows different kinetics depending on the thickness of the oxide.[160] Thick SiO_2 films, from about several hundred angstroms upwards, grow according to linear-parabolic kinetics where the transport of oxidant through the oxide is the rate-limiting step. Below this oxidation regime is a thin oxide regime in which the kinetics is not described by linear-parabolic kinetics but is determined by the interface reactions. This regime can be further divided into two regimes: one from 0 to about 10 Å, representing the native oxide, and the other from 10 to several hundred angstroms.

While the kinetics of the thick oxide regime is well established, that of the native oxide and thin oxide regimes is not, due to the complexity of the reactions involved at the interface. As discussed in the section on native oxide, the thickness and growth rate of native oxides strongly depend on surface preparation and the environmental conditions regarding exposure. It is thus very difficult to prepare a native oxide of a certain quality. The thin oxide regime has been studied to a great extent not only because of its importance in affecting the nature of the thermal oxide but also because of its potential use for very thin silicon oxide/silicon systems.[160,499] In the thin oxide regime, the oxidation kinetics for wet and dry oxidants is, unlike in the thick oxide regime, very different. The kinetics in this regime is influenced by the nature of oxidants for the surface reaction such as the presence of both O and O_2, or by the strain present due to the lattice mismatch between Si and SiO_2, or by the transport through micropores, or by the presence of impurities at the interface regime to alter the oxidation reaction.[160,187] The transport of oxygen consists of two parts, one related to the interstitial transport of O_2 through the network and the other to a step-by-step motion of network oxygen atoms.[1029] A significant part of the oxygen diffusion may be of ionic nature since an electric field is found to affect the growth of oxide.[1049]

The general growth kinetics of thermal silicon oxide was originally proposed by Deal and Grove.[562] It is assumed that the transported species go through three stages: (1) from bulk of the gas to the outer surface, (2) across the oxide film toward the silicon, and (3) reaction at the silicon surface to form a new layer of SiO_2. Figure 3.20 illustrates the physical situation. It is further assumed that the fluxes of oxidant in each of the three steps in the oxidation process are identical beyond an initial transient period. The flux of the oxidant from the gas to the vicinity of the outer surface is

$$F_1 = h(C^* - C_0) \tag{3.12}$$

where h is a gas-phase transport coefficient, C_0 is the concentration of the oxidant at the outer surface, and C^* is the equilibrium concentration of the oxidant in the oxide.

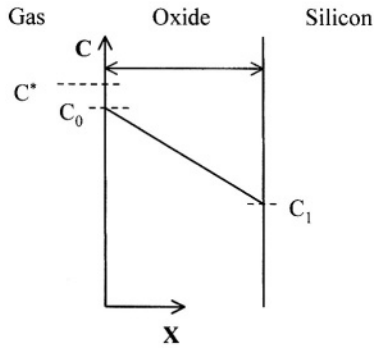

FIGURE 3.20. Model for the thermal oxidation of silicon. (Reprinted with permission from Deal and Grove.[562] © 1976, American Institute of Physics.)

C^* is assumed to be related to the partial pressure of the oxidant in the gas by Henry's law:

$$C^* = Kp \tag{3.13}$$

Henry's law holds in the absence of dissociation or association of the oxidants at the outer surface, implying the oxidant to be O_2 and H_2O in the cases of dry and wet oxygen oxidation. The flux of the oxidant across the oxide layer is assumed to follow Fick's law:

$$F_2 = -D_{\text{eft}}(dC/dx) \tag{3.14}$$

with D_{eft} the effective diffusion coefficient. Since at a steady state F_2 must be the same at any points within the film, meaning $dF_2/dx = 0$, Eq. (3.14) reduces to

$$F_2 = D_{\text{eft}}(C_0 - C_1)/x_0 \tag{3.15}$$

where C_1 is the concentration near the Si/SiO_2 interface. The reaction flux at the interface is assumed to be first order:

$$F_3 = kC_1 \tag{3.16}$$

Considering the situation under diffusion control with $C_1 \to 0$ and $C_0 \to C^*$, and combining Eqs. (3.12), (3.13), (3.15), and (3.16), we obtain

$$N_1 dx_0/dt = F_1 = F_2 = F_3 = kC^*/(1 + k/h + kx_0/D_{\text{eft}}) \tag{3.17}$$

where dx_0/dt is the rate of growth and N_1 the number of oxidant molecules incorporated into the unit volume of the oxide layer. Integration of Eq. (3.17) with an initial condition $x_0 = x_i$ at $t = 0$ yields

$$x_0^2 + Ax_0 = B(t+\tau) \tag{3.18}$$

or

$$x_0 = A/2\left\{\left[1+(t+\tau)/(A^2/4B)\right]^{1/2} - 1\right\} \tag{3.18a}$$

where

$$A = 2D_{\text{eff}}(1/k + 1/h) \tag{3.18b}$$

$$B = 2D_{\text{eff}}\, C^*/N_1 \tag{3.18c}$$

and

$$\tau = (x_i^2 + Ax_i)/B \tag{3.18d}$$

At relatively long times, i.e., $t \gg A^2/4B$ and also $t \gg \tau$, Eq. (3.18a) becomes

$$x_0^2 \approx Bt \tag{3.19}$$

which is the well-known parabolic oxidation law for relatively long times. At the other extreme, for relatively short oxidation times, i.e., $t \ll A^2/4B$, Eq. (3.18a) reduces to

$$x_0 \approx (B/A)(t+\tau) \tag{3.20}$$

which is a linear law.

The rate of thermal oxidation of silicon is orientation dependent.[105,510,911] Under typical conditions the initial oxidation rates follow the order

$$(110)>(111)>(311)>(511)>(100)$$

The order changes within the first 25 nm of the oxide to (111) > (110) with the other orientations remaining in the same order. A qualitative correlation appears to exist between the order of the initial rates and the density of the atoms of the planes.

The kinetics of thermal oxide growth depends on the type of oxidation, whether using dry oxygen, wet oxygen, or steam as the oxidation agent.[510] The growth rate in wet oxygen can be much higher, by as much as a factor of five, than that in dry oxygen. The reaction occurs at the Si/SiO_2 interface and the growth rate is dominated by the inward diffusion of the oxidizing species for oxide films more than 40 Å thick for dry oxidation and 1000 Å thick for wet oxidation.[115,316,377,562] There is a difference between wet and dry oxidation in terms of the involved oxidizing species. The wet oxidation by H_2O has faster kinetics than the dry oxidation by O_2 due to the much larger solubility of H_2O in SiO_2, about $3 \times 10^{19}/cm^3$, than that of O_2, about $5 \times 10^{16}/cm^3$, even though the diffusivity of H_2O in the temperature range for thermal oxidation is about an order of magnitude smaller than that of O_2.[562]

Anodic Oxides. Except for the first few layers of oxide, which almost always exist on the surface of silicon in an anodization electrolyte as the native oxide, the growth of the oxide film requires the diffusion and/or migration of the reactants in the form of cations or anions or both through the oxide film. In comparison with thermal oxidation, anodization operates at low temperatures at which the diffusion of either silicon species or oxidants (as can be estimated based on the information about thermal oxidation at high temperature) must be too slow to account for the oxide growth observed during anodization of silicon. Mass transport required during anodization must rely on field assisted migration. The field strength required to produce the ionic current for oxide growth on silicon is very high, in the range from 10^6 to 10^7 V/cm depending on growth rate and electrolyte composition.

Young and Zobel[961] found that the growth of anodic oxide on silicon follows the high field mechanism which describes the relationship between the ionic current and the field as: $i = i_0 \exp[-W(E)/kT]$, where $W(E) = W_0 - qaE$, q is the magnitude of the charge on the ion, a is half of the distance between successive sites occupied by the ions, and i_0 is a constant. Figure 3.21 shows the data for anodization in 0.0025 N KNO_3 in anhydrous NMA giving a line $i = 10^{-14}\exp(10^{-6}\,\text{cm/V})$ A/cm^2 with a being 0.6 to 1.5 Å.

Ghowsi and Gale[201] developed an analytical model, which agrees with the physical model illustrated in Fig. 3.19, for the growth kinetics of anodic SiO_2, taking into account both ionic current and electronic current. The total current density, including the ionic component and electronic component, i_e, is

$$i = i_i + i_e \tag{3.21}$$

The inward motion of anions is assumed to be the dominant ionic transport across the oxide. The ionic movement is field-assisted drifting and is the rate-limiting process. The diffusion of ions at room temperature is considered to be too slow to account for the oxide growth rates. The current density is written as

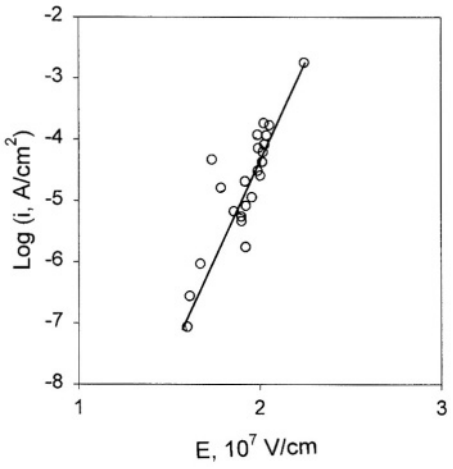

FIGURE 3.21. $\text{Log}_{10} I$ versus E for silicon during anodization. After Young and Zobel.[961] (Reproduced by permission of The Electrochemical Society, Inc.)

$$i_i(t) = -n_i q \mu_i E = n_i q \mu_i V/d(t) \tag{3.22}$$

where i_i is the ionic current, n_i the anionic concentration in the oxide, q the anionic charge, μ_i the anionic mobility, E the electric field, $d(t)$ the thickness of the oxide film, and V the voltage across the oxide.

The analytical solution gives

$$d(t) = d_0 + [2n_i q \mu_i V_0/(qN_i)]^{1/2} t^{1/2} \tag{3.23}$$

$$i_i = -0.5qN_i[n_i q \mu_i V_0/(qN_i)]^{1/2} t^{-1/2} \tag{3.24}$$

where N_i is the number of anions per unit volume of the silicon dioxide.

The electronic current is assumed to be due to electron injection by tunneling from the states in the electrolyte into the conduction band of SiO_2. It is limited by the space charge electronic current density described by

$$i_e = K\nu V^m/d^{2m} \tag{3.25}$$

where ν is the velocity of electrons due to applied voltage across the thin film of thickness $d(t)$. The solution of the electronic current density has the form

$$i_e(t) = \left[A + B(at^{1/2} + d_0)\right] \Big/ \left[(at^{1/2} + d_0)^{1.6} + C\right] \tag{3.26}$$

where A, B, and C are constants. The results calculated from Eqs. (3.21) to (3.26) were found by Ghowsi and Gale[201] to be in good agreement with experimental data.

It is interesting that Eq. (3.23), describing the growth of an anodic oxide, is in its mathematical form identical to the growth of a thermal oxide by Eq. (3.19), that is, the thickness of oxide increases parabolically with oxidation time. It is reasonable in terms of the conditions and assumptions of the two models: (1) both are under constant driving forces—the anodic anodization is under a constant potential and the thermal oxidation is under a concentration gradient—and (2) both assume a linear dependence of the inward transport of the oxidants on the driving force.

3.5. PROPERTIES

Compared to thermal oxides, there is much less systematic information on the properties of anodic oxides. Table 3.2 shows that the properties of anodic oxides vary in a wide range. Several remarks may be made on comparing the properties of anodic and thermal oxides: (1) the density of anodic oxides is lower; (2) the anodic oxide is nonstoichiometric and is silicon deficient; (3) the electrical resistance is much lower although the breakdown field strength may be similar; (4) the dielectric constant is higher; and (5) anodic oxides have higher charge and interface state densities. Figure 3.22, using the data from Table 3.2, illustrates the ratios of anodic oxides to thermal

TABLE 3.2. Properties of Anodic SiO_2[a]

Oxide[b] (Ref.)	ρ (g/cm^3)	O/Si	R (10^{16} Ωcm)	RF	BF (10^6 V/cm)	DI	$N_{cd,FB}$ (10^{10} cm^{-2})	N_{ss}, 10^{10} (eV^{-1}·cm^{-2})	$N_{IS,dis}$ (10^{10} cm^{-2})	r
Thermal, 45, 228	2.27	~2	>1	1.46	8–16	3.9	0.9	1.0	2.6	1
457	1.5			1.3	10–13					
107		2–3.9								
117				1.55						
98	2.16		$1–5 \times 10^{-5}$				6–9			
449		2.2								
370			1–5	1.49	6–7	4.0				
404 a						14.9				
404 b						5.0				
228 a					5.8		–3.0	1.8	4.2	
228 b					1.1		90	—	120	
300							20			
603				1.3–1.4				2000	170	
605 a							3.5	6		
605 b							–3	4.2		
244	2.05				10		–70	4–200		
286										11
139 a	2.05	2.27				5.2				29
139 b										14
378										5
919		1.8–3.4		1.3–1.47	0.5–2					4.5

[a]Abbreviations used: ρ, density; O/Si, atomic ratio; R, resistivity; RF, refractive index; BF, breakdown field; DI, dielectric constant; $N_{cd,FB}$, effective interface charge density at flatband potential; N_{ss}, interface surface states density; $N_{IS,dis}$, mobile ionic charge density; r, ratio of etch rate of anodic oxide to thermal oxide; a, b, two different conditions.
[b]See Table 1.

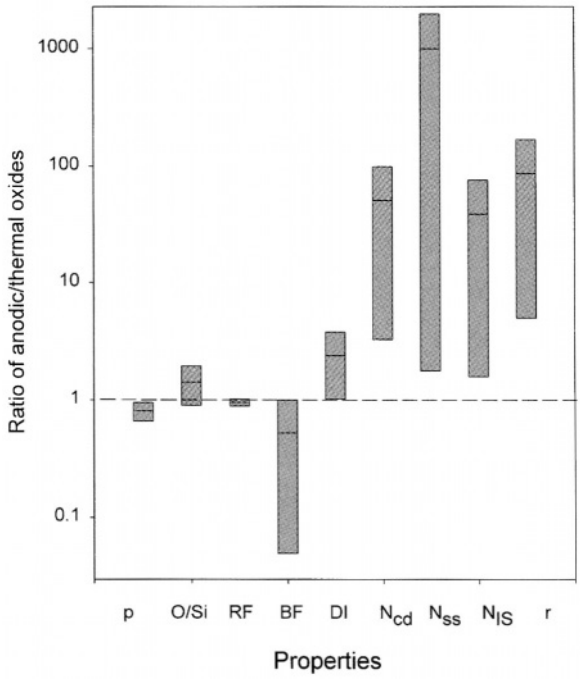

FIGURE 3.22. The physical, electrical, and chemical properties of anodic oxides relative to thermal oxides. Data from Table 3.2.

oxides for different properties. For none of the anodic oxides reported in the literature do all of the properties overlap those of thermal oxides.

3.5.1. Physical and Chemical Properties

The oxide films formed by anodization generally have a loose structure and contain a significant amount of water, hydroxyl ions, and other species, which are present in the electrolyte. Many of the physical, chemical, and electrical properties of anodic silicon oxides are determined by this loose structure and the incorporation of foreign species. This defective nature is required for the growth of an anodic oxide because a large number of charged carriers are moving within the oxide during its formation.

As-formed anodic oxides may contain Si–O bonds, SiOH and SiH groups, absorbed water, oxidation products of the solvent, and ionic impurities.[776] For example, there are $8 \times 10^{20}/cm^3$ hydroxyl and $2 \times 10^{21}/cm^3$ silicon hydride SiH groups in the anodic oxide films formed in KNO_2-containing tetrahydrofurfuryl.[424] By comparison, the thermal film produced in wet oxygen at 1050°C contains $10^{19}/cm^3$ OH groups and that produced in dry oxygen contains no OH groups. The anodic oxide grown in 0.1 M HCl contains about 4 wt % OH in the form of water and 4 wt % OH as isolated silanol.[98]

Due to the incorporation of OH and water, anodic oxides are generally nonstoichiometric with silicon-deficient structures. For example, the oxide grown in 1.35 M NH_4OH has a stoichiometry of $SiO_{2.24}$ with total (Si + O) density of 6.83×10^{22} atoms/cm^3 and contains approximately 1 atom % N.[449] The oxides formed in ethylene glycol + KNO_3 may contain 1–5% water and have O : Si ratios varying from 1.8 to 3.4 depending on current density, oxide thickness, and water content in the solution as shown in Fig. 3.23.[919] They contain a large amount of carbon compounds in the form of C—H, C═O, S—O—C, and C—C groups.[1039] The anodic oxide grown in a phthalate aqueous solution is incorporated with a substantial amount of water and/or hydroxyl groups with thinner films exhibiting a higher content.[604] In diethylene glycol contain-

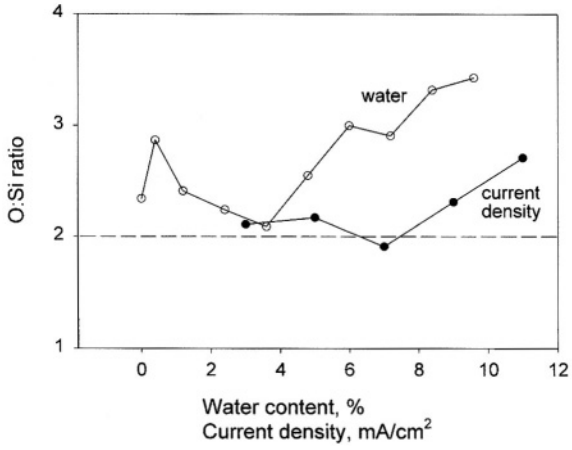

FIGURE 3.23. O:Si ratio as a function of water content (at a current density of 13 mA/cm^2) and current density (at a water content of 1.5% H_2O). After Duffek *et al.*[919]

ing KNO_3 and a trace amount of fluorine, the anodic oxide is incorporated with fluorine, and the fluorine content increases with the oxide thickness and the fluorine in the solution.[835] Fluoride content on the order of 10^{15} atoms/cm^3 is reached for a fluoride concentration of 10^{-6} M in the solution. Most of the fluorine is located in a region close to the Si/SiO_2 interface and the fluorine is linked to the silicon atoms as is oxygen in the oxide. The SiOH groups in the anodic oxides show hydrogen bonding.[1039] The hydrogen bond may form between a SiOH and the nonbridging oxygen atoms associated with defects in the oxide.[357] Large concentrations of hydroxyl ions in SiO_2 film enable penetration of protons from the electrolyte into a hydrogen-bonded network at low cathodic field strengths.[427]

The tendency for the solution-bond species to be incorporated into the structure of anodic oxide films can be used for oxide doping. For example, phosphorus-doped oxides of different concentrations can be produced by anodization in diethylphosphate (DEP)–nitrite–tetrahydrofurfuryl alcohol.[459] Figure 3.24 shows that the phosphorus concentration increases with increasing concentration of DEP in the solution. Low temperature and current density give higher doping levels, indicating that DEP adsorption decreases with increasing temperature.

According to Nannoni and Musselin,[793] the properties of anodic oxides tend to change with time after being placed in humid air or water. The action of water causes incorporation of hydrogen in the interstitial positions in the oxide. The concentration of hydrogen, on the order of 10^{19}–10^{20}/cm^3, is an increasing function of exposure time, and a decreasing function of the pH of the water and the anodic voltage applied across the oxide. The diffusivity of the species associated with water has been determined to be 4.3×10^{-17} cm^2/s at 25 °C for the oxide formed in water and 3.5×10^{-18} cm^2/s in KNO_3-containing ethylene glycol.[836] Surface roughness of anodic films grown in ethylene glycol containing 0.04 M KNO_3 is found to increase with increasing water content in the electrolyte.[228] The silicon substrate after the removal of the oxide films shows similar roughness dependence on water content.

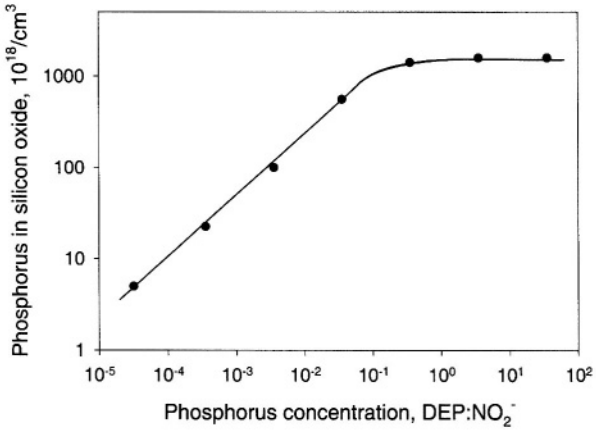

FIGURE 3.24. Relation between phosphorus incorporation and molar ratio DEP:NO_2^- in the solution. Solution temperature 25 °C; current density 6 mA/cm^2. After Schmidt *et al.*[459] (Reproduced by permission of The Electrochemical Society, Inc.)

Anodic oxides are thus less dense than thermal oxide films due to the incorporation of foreign species. The density may vary greatly with the conditions of anodization and densities as low as $1.5\,g/cm^3$ have been reported.[457] The oxide formed in ammonium borate solution is relatively dense and those formed in oxalic acid or chromate solutions are less dense.[117] The less dense nature of anodic oxides is also reflected in the etch rate, which is generally many times higher than for thermal oxides as shown in Table 3.2. The etching reaction proceeds first by adsorption of the reactants onto the active sites on the oxide surface, which are associated with the defects and discontinuities of the SiO_2 polyhedra structure. An oxide film with porous structure thus has more active sites available for the etching reaction, leading to a higher etch rate.

Anodic films can be densified by annealing in inert gases at high temperatures. A reduction of 10 to 30% in oxide thickness has been found to result from annealing.[139,457,793] The hydride SiH groups in as-formed anodic oxide films can be reduced by two orders of magnitude by heat treatment at 300 °C to a level similar to that of thermally oxidized oxides.[424] The oxide grown in 1.35 M NH_4OH contains about 1 atom % N and can be reduced to <0.5 atom % by annealing the film at 500 °C for 5 min in forming gas.[449]

The properties of anodic oxide films depend on the mode of polarization particularly at the initial stage of anodization. For example, the number of hydroxyls in as-grown oxide formed in KNO_2-containing tetrahydrofurfuryl at a constant current density of $10\,mA/cm^2$ is about $8 \times 10^{20}/cm^3$.[424] This is reduced to $2.2 \times 10^{20}/cm^3$ by switching the oxidation mode to a constant potential from the initial constant current mode.[424] The potential and how fast the potential is established determine the structure of the first few layers of oxide, and greatly affect the further growth of oxide. It is found that in 0.1 M HCl electrolyte, if the initial oxide is grown at a potential below 5.5 V_{sce}, then the final oxide will be thin and have a lower hydroxyl content.[98] Structural change is found to occur for oxide that is oxidized at a time beyond the maximum forming potential in ethylene glycol containing 0.04 M KNO_3; after anodization at 300 V for 35 h, the oxide becomes opaque.[117]

The properties of an anodic oxide are not uniform with distance but change from the Si/SiO_2 interface to the SiO_2/electrolyte interface. It has been found that the refractive index is about 1.37 at the Si/SiO_2 interface but gradually increases to about 1.42 in the bulk oxide.[603] The refractive index of the oxide films formed in ethylene glycol–KNO_3 solution generally decreases with increasing thickness.[919] The anodized silicon surface is more heavily hydrated.[427] Figure 3.16 shows that the concentration of hydroxyls increases toward the silicon/silicon oxide interface.[424] There are no data on the potential of zero charge (pzc) for anodic oxides. Data obtained on thermal oxides indicate that the pzc of silicon oxide lies between pH 2 and 3[903,943] and a linear relationship exists between the Fermi energy and pzc.[946]

Si/SiO_2 Interface. There is little information on the interface of silicon and an anodic oxide film. For thermally grown oxides, a transition region exists at the Si/SiO_2 interface where there is an excess of unoxidized Si bonds with a density on the order of the surface atom density. The interface structurally consists of two distinct regions. A few atomic layers near the interface contain Si atoms in intermediate oxidation states, i.e., Si^+ (Si_2O), Si^{2+} (SiO), and Si^{3+} (Si_2O_3). The S^{3+} atoms are located farther out than

Si^{2+} and Si^{+}. A second region extends about 30 Å into the SiO_2 film. The SiO_2 in this layer is compressed because the density of Si atoms is higher. For oxides grown in pure O_2, the density of Si atoms in the intermediate oxidation states is $1.5 \times 10^{15}/cm^2$ (about two monolayers of Si) near the interface region. The interface is not abrupt because of this high density of intermediate oxidation states. The Si/SiO_2 interface, in addition to partially oxidized silicon species, may have defects such as Si and O vacancies and interstitial elements.[165,338,479,702]

The Si intermediate complexes generated from the oxidation of a part of the excess Si bonds in this transition region are responsible for fixed charge and fast surface states.[338] They may be formed according to the reaction

$$Si - Si + (O) \rightarrow \equiv Si\cdot + (Si - O)^{+} + e \tag{3.27}$$

where the dangling bonds, $\equiv Si\cdot$, are identified with fast surface states and the $(Si—O)^{+}$ are identified with fixed positive charges.

The partially oxidized silicon species are responsible for the anodic current transient measured at the end of etching of an anodic oxide film-covered *n*-Si electrode in the dark as shown in Fig. 3.25.[74] For a clean *n*-Si surface, the anodic current is very small. This dark current during the etch-back experiment, whose peak position depends on the thickness, occurs on anodic oxide as well as on thermal oxide. The data shown in Fig. 3.25 indicate that the anodic reaction proceeds by injection of electrons from the partially oxidized silicon species at the silicon/oxide interface. The amount of charge associated with the current transient, which is similar for anodically and thermally oxidized surface, is about $4.4 \times 10^{-4}\,C/cm^2$, corresponding to two monolayers of Si^{3+} on a (100) surface. The partially oxidized species may extend to a number of atomic layers, fewer for thermal oxide than anodic oxide as shown in Fig. 3.25.

The interface property of silicon oxide can also be described in terms of dipoles which are formed due to partial charge transfer that takes place on formation of interface bonds.[76] The charge transfer occurs because of the difference in electronegativity

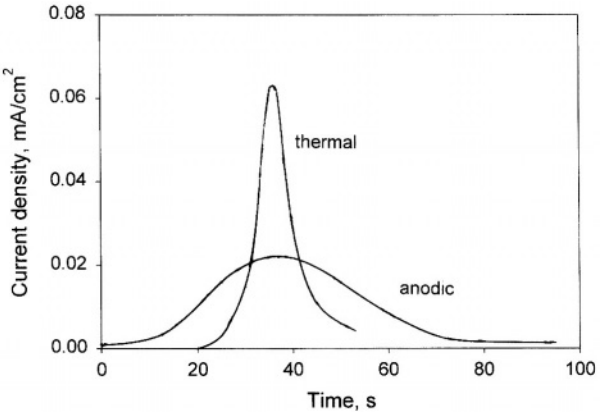

FIGURE 3.25. Anodic current transient measured on anodic oxide and thermal oxide during etch-back in a HF solution. (Reprinted from Matsumura and Morrison.[74] © 1983, with permission from Elsevier Science.)

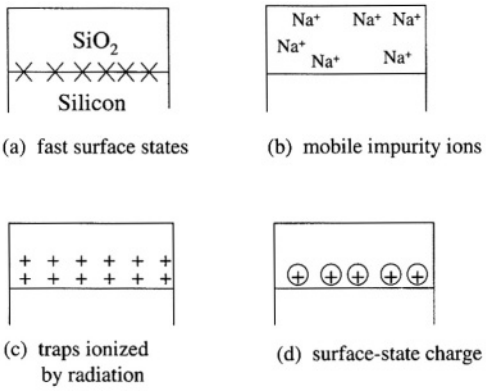

FIGURE 3.26. Charges and states associated with the Si/SiO_2 system. After Grove.[496]

between the two species across the interface. Several kinds of dipoles exist at the Si/SiO_2 interface: dipoles due to the formation of various interface bonds, dipoles due to the presence of dangling bonds, and dipoles due to impurities at the interface. According to Massoud,[76] all elements and compounds of interest have electronegativities larger than that of silicon. Also, the partial charge transfer occurring between silicon and these species generates dipoles with the positive charge on the silicon side of the interface and the negative charge on the oxide. Table 3.3 lists the charge transfer for a variety of silicon compounds. The electronic properties such as the flatband potential can be altered by the presence of the dipoles at the interface. Assuming all the silicon are bonded to SiO_2 molecules, the difference of flatband potential of (100) and (111) surfaces is calculated to be 0.476 V due to their difference in bond density and bond angle to the Si/SiO_2 interface.

3.5.2. Electrical Properties

The electrical properties of silicon oxide play a critical role in many phenomena on silicon electrodes, particularly in the growth of anodic films. Anodic oxides can

TABLE 3.3. Values of the Electronegativity and Charge Transfer in the Electron/Bond for Interface Bonds at the Si/SiO_2 Interface[76]

Compound	Electronegativity	Charge transfer, electron/bond
Si–O	3.847	0.288
Si–H	3.175	0.096
Si–N	3.571	0.209
Si–OH	3.745	0.258
$Si–SiO_2$	3.477	0.182
Si–SiO	3.305	0.133
$Si–Si_2O$	3.142	0.086
$Si–Si_2O_3$	3.407	0.162

differ greatly in structure and properties due to the diversity of electrochemical conditions under which an anodic oxide can be formed. The information on anodic oxides in this section is thus presented according to the specific conditions under which they are formed rather than being dealt with in a general fashion. A brief review of the basic electrical properties of thermal oxides is provided to serve as the baseline to which those of a specific anodic oxide can be related.

Thermal Oxides. The electrical properties of silicon to silicon oxide are associated with the various types of charges and states (or traps) in the system as shown in Fig. 3.26.[496] They include fast surface states located at the silicon/oxide interface and slow states which include charges and states within the oxide due to mobile impurity ions, such as sodium ions, or traps ionized by radiation or fixed surface state charge near the interface. The Si/SiO_2 interface contains defects which result in the interface states and charges. The defects in SiO_2 and at the interface whose charge state depends on the dc bias are called interface traps or surface states. Those independent of gate bias are classified as charges which are subdivided into fixed and mobile for as-grown oxides.

The fast surface states, or interface traps (Fig. 3.26a), arise from the disruption of the periodicity of the Si lattice at the surface. Because they are located on the surface, these states are in good electrical communication with the semiconductor bulk and can act as surface recombination centers. The density of fast surface states on a clean silicon surface, i.e., a cleaved surface, is on the order of one fast state for every surface atom, resulting in a density of about $10^{15}/cm^2$.[196] The silicon surfaces passivated by a thermal oxide film have densities of surface states that are 5 or 6 orders of magnitude less than this. Also, a silicon surface covered with an adsorption layer may have a density of fast surface states on the order of 10^{11} to $10^{12}/cm^2$ due to the stabilization of the dangling bonds on the surface. The surface states, which can be donor or acceptor, are distributed over the energy gap of silicon. The main effects of surface charges or interface traps are to decrease surface mobilities of mobile carriers across the interface, to change the surface potential at the interface under a given bias condition, and to act as recombination or generation centers for minority carriers at the surface.[479]

The impurity ionic charges (Fig. 3.26b) with a density distribution of $\rho(x)$ are mobile under an electric field, resulting in a rearrangement of the density distribution.[496] The presence of impurity ions in the oxide is the result of contamination during processing. Due to their mobile nature they affect the flatband potential by the redistribution of the ionic charge under field resulting in drift of the flatband potential and cause a shift of the *C–V* curve along the voltage axis with time.

The positive charge at the interface (Fig. 3.26c) may occur by irradiation with X rays, γ rays, or electrons. During irradiation, electron–hole pairs are created in the oxide. If no electric field is present in the oxide, the electrons and holes will recombine resulting in no net charge building up in the oxide. However, the electrons and holes tend to separate if there is a field in the oxide. If this field corresponds to the positive gate voltage, the holes are pulled toward the oxide/silicon interface gradually building up a space charge.

Finally, the surface state charge or the fixed oxide charge illustrated in Fig. 3.26d is a result of an oxide growth process that has the following characteristics:[495]

1. It cannot be charged or discharged over a wide range bending of the silicon energy band.
2. It is located within 20 nm of the Si/oxide interface and its density is on the order of 10^{10} to $10^{12}/cm^2$ depending on the oxidation conditions.
3. Its density is not significantly affected by the oxide thickness or by the type and concentration of impurities in the silicon.
4. The density is independent of doping type and concentration in the silicon in the range from 10^{14} to 10^{17}, but is a strong function of silicon crystal orientation. The ratio of the density values for silicon oriented along the (111), (110), and (100) directions is approximately 3:2:1, which follows the variation of the oxidation rate constants for these directions.
5. Its density is independent of band bending over the middle 0.7 eV of the silicon energy gap, indicating that the energy levels of the surface states are located within the forbidden gap of the oxide.
6. The density strongly depends on oxidation and annealing conditions and regardless of the previous treatments of the oxide, the final heat treatment determines the density. Its density decreases with heat treatment in inert gas and increases with increasing negative field.
7. The surface state charge is due to the excess ionic silicon present in the oxide during the oxidation, waiting to react with the oxidizing species that has diffused across the oxide/silicon interface as illustrated in Fig. 3.27.[495]

The change of potential due to the surface state charge can be calculated from

$$\Delta V = Q_{ss} x_0 / \varepsilon \tag{3.28}$$

High-quality SiO_2 films can have a resistivity exceeding $10^{16}\,\Omega cm$. The high resistivity of the film is a consequence of the large SiO_2 band gap, which preclude thermally or optically excited carriers from entering the oxide. The conduction of thin dielectric films can be due to bulk-limited processes and electrode-limited processes. In general, electronic conduction, space charge-limited conduction, ionic conduction, and impurity conduction are bulk limited whereas Fowler–Nordheim tunneling and Schottky emission are electrode limited.[309] The dominant source of dc conduction is that associated with the motion of impurity ions through the oxide.

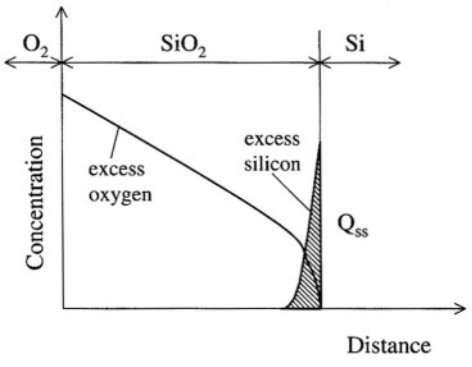

FIGURE 3.27. Schematic illustration of the proposed distribution of excess species in an oxide film during formation. After Deal *et al.*[495] (Reproduced by permission of The Electrochemical Society, Inc.)

At high field current, instability occurs and can lead to dielectric breakdown of SiO_2 films. The breakdown of thermally grown silicon dioxide films depends on the processing conditions such as oxide thickness, substrate doping concentration and orientation, cleaning procedures, oxidation temperature, and testing conditions.[307–309] The breakdown fields under a given set of conditions follow a Gaussian distribution skewed at low fields. The breakdown fields near the maximum (8–16MV/cm) represent the primary type of breakdown, which is related to the intrinsic dielectric properties of the oxide; those at fields more than 20% lower than the maximum are low field breakdowns, which are related to the defects in the oxide. Breakdown may also be differentiated in terms of electric breakdown and dielectric breakdown.[725]

The breakdown at high fields results from the destabilization of the conduction in the oxide which is associated with carriers generated by the collision ionization process.[307,309] The tunneling-through electrons drift under the influence of the field and can gain enough energy above a critical field to create additional carriers through collision, thereby forming a space charge layer. For example, with a mean free path of 34 Å and a field strength of 8 MV/cm the injected carriers are able to excite traps 2.7 eV below the conduction band. The electron–hole pairs are driven under the field to opposite electrodes. A buildup of the positive space charge in the vicinity of the cathode further lowers the barrier for tunneling. Such a positive feedback sequence eventually leads to a large current and insulator breakdown.

Anodic Oxides. The electrical properties reported in the literature on anodic oxides, such as breakdown potential, dielectric constant, and leakage current, tend to vary over a wide range due to the large differences among oxides, which are formed in the various electrolytes. Some of these parameters are listed in Table 3.2. In general, the electrical properties of anodically formed oxides are of poor quality relative to those of thermal oxides due to the high concentration of charges and states associated with the loose structure and high levels of impurities in anodic oxides.

The dielectric constant of anodic oxides is considerably higher than that of thermal oxides. This higher dielectric constant can be attributed to the presence of a significant amount of H_2O and silanols and a nonstoichiometric composition.[139] The breakdown potentials of anodic oxide films are generally lower than those of thermal oxides. It also in general decreases with increasing thickness.[919] The breakdown field strongly depends on the conditions of anodization. For example, Fig. 3.28 shows that for the oxides formed in 0.04N KNO_3 in ethylene glycol, the breakdown field decreases with increasing water content in the electrolyte.[228] Similar results were found in other studies.[776,919] The breakdown potential of the oxide formed in solutions containing trace amounts of fluorine is inversely proportional to the fluorine content in the oxide.[835] The breakdown voltage of some anodic oxides can be comparable to thermal oxides. For example, values between 5 and 10 MV/cm are found for oxides formed in NH_4OH solution.[244]

Figure 3.29 shows that the effective interface charge density and the flatband potential is a function of water content for the oxides formed in ethylene glycol containing 0.04 N KNO_3 at 7 mA/cm^2.[776] The charge density also depends on anodization mode, postanodization cleaning, and annealing treatment.

Anodic oxide films have high leakage currents.[44,307] The leakage current is a function of anodization condition. Figure 3.30 shows the *i–V* curves measured on the anodic oxide films formed in NMA + 0.04 N KNO_3, under a constant current density of 14 mA/cm^2 to 300 V and held at 300 V for different times.[117] As can be seen, the current

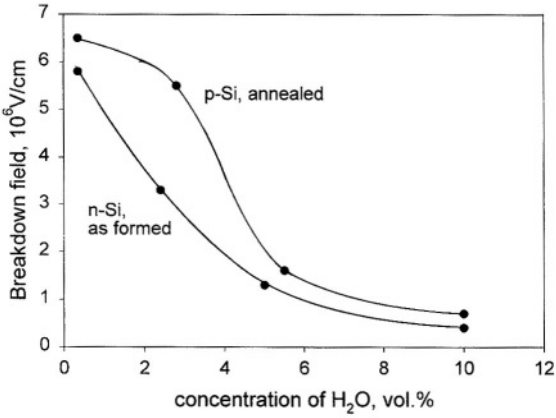

FIGURE 3.28. Breakdown field strength of anodic oxide films as a function of the water content of the electrolyte during constant anodic anodization. After Mende *et al.*[228] (Reproduced by permission of The Electrochemical Society, Inc.)

at a given voltage becomes much lower with increasing holding times, indicating that the oxide structure changes with holding time. Also, the current measured on the oxide films is higher at a cathodic potential than at an anodic potential, and it is different for *n*- and *p*-type silicon.

The *C–V* curves of the anodic oxide films formed in water and in KNO_3-containing ethylene glycol electrolyte are identical to those of thermal oxides with little shift and distortion.[228,457] The oxide films formed in aqueous NH_4OH solutions are found to give distorted *C–V* curves.[244] The distortion is attributed to the slow traps at the Si/SiO_2 interface which are charged during the cathodic sweep and discharged during the anodic sweep.[139] Annealing of the anodic oxides formed in NH_4OH generates much better *C–V* curves.

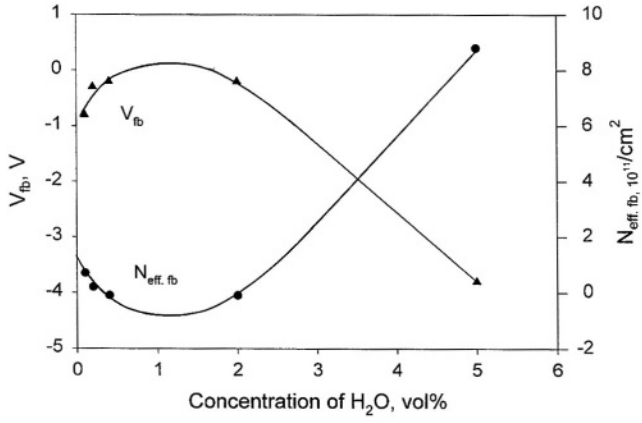

FIGURE 3.29. Interface charge density and V_{fb} as a function of water content in ethylene glycol. After Mende and Hensel.[776]

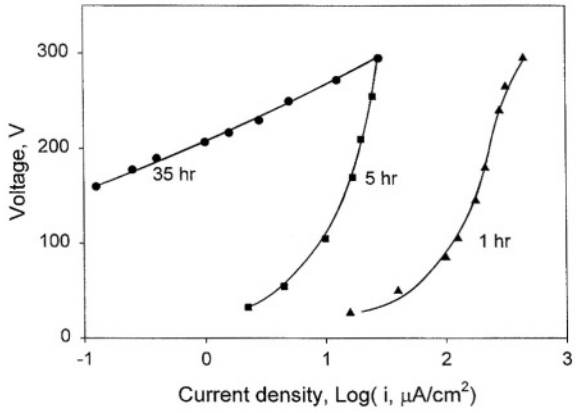

FIGURE 3.30. Electronic current through anodic oxide films formed on *p*-type Si in the anodic direction after various forming times. Forming solution was N-methylacetamide CH_3 $CONHCH_3$ + 0.04 N KNO_3 at 25 °C. All samples were formed using 14 mA/cm^2 and kept at 300 V for the periods noted. After Schmidt and Michel.[117] (Reproduced by permission of The Electrochemical Society, Inc.)

The electrical properties of anodic oxides in electrolytes, that is, electrochemical properties, tend to vary with the anodization system. Figure 3.31 shows the current–voltage curves of anodically formed oxides in the forming electrolyte.[117] The voltage necessary to drive a given current anodically differs greatly from that cathodically. For *n*-Si the voltage under the given cathodic current is almost constant whereas it increases with oxide thickness under an anodic polarization. For *p*-Si the anodic

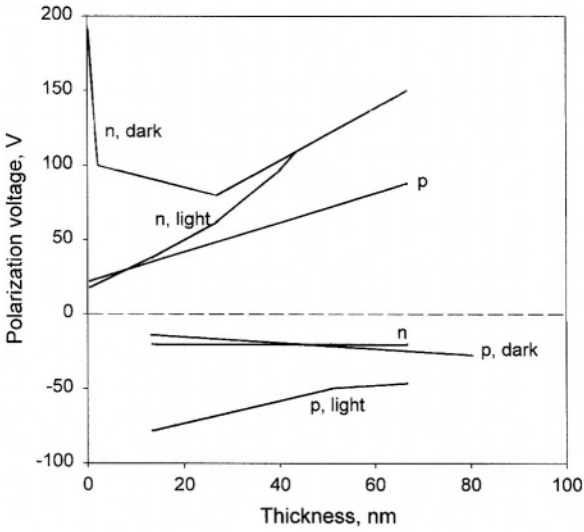

FIGURE 3.31. Polarization voltage required for an anodic or cathodic current of 10 mA/cm^2 through anodized oxides of different thickness in an NMA solution. After Schmidt and Michel.[117] (Reproduced by permission of The Electrochemical Society, Inc.)

behavior is very similar to that of *n*-Si under illumination. On the other hand, for *p*-Si under a cathodic polarization, a much larger voltage, which decreases with oxide thickness, is required in the dark than under illumination.

The difference in electrical properties in electrolyte between anodic and thermal oxides can also be revealed with impedance spectra as shown for example in Fig. 3.32.[139] In NH_4OH solution the thermal oxide, with a capacitance of $400\,nF/cm^2$ and a charge transfer resistance of $350\,M\Omega/cm^2$, shows a near-ideal capacitor behavior. On the other hand, for the anodic oxide the phase angle does not reach 90° and the charge transfer resistance is $350\,k\Omega$ which is several orders of magnitude below that of thermal oxides. The low charge transfer resistance of the anodic oxide films indicates that the transport of ions in the film is relatively large.

Transient current and transient capacitance measurements on removal of the anodic polarization, which provide information on the transient flatband potentials, indicate that both positive and negative charges are present in the anodic oxide film during its growth.[601] According to Chazalveil,[601] the positive charges are related to charged oxygen "semivacancies", O_3Si^+, and the negative charges are associated with OH^- groups and/or terminal O_3SiO^- groups. The anodic oxide is composed of an inner layer, a mostly dry, substoichiometric layer, and an outer hydrated layer. On removing the anodic polarization, the positive charge decays by backward migration and injection of holes into the electrode and the negative charges stay until the oxide layer is partly dissolved.

Kirah *et al.*[294] calculated the transient distribution of the ionic species in anodic oxide based on the experimental data of Chazalveil.[601] For the oxide formed at 5 V in a BHF solution, Fig. 3.33 shows the density of ionic species inside the oxide layer are positive and its density decreases from the electrolyte side to the Si side. It was attributed to accumulation of the positive ions transported from the Si/SiO_2 interface to the electrolyte side waiting for reaction with the oxidant species. By further assuming the total charges in the oxide to be ionic charges distributed in the bulk and trapped charges at the Si/SiO_2 interface states, the interface trapped states were found to be positive on the order of $10^{12}/cm^2$, which decreases with thinning of the oxide film.

Exposed to humid air or water after forming, the electrical properties of anodic oxides tend to decay due to the action of water incorporating significant amount of hydrogen into the oxide structure.[793] For the oxides formed in diethylene glycol containing KNO_3 after several days of immersion in water, the permittivity was found to decrease from 3.85 to 6.2 and the resistivity decreased from 10^{18} to $10^{15}\,\Omega cm$ for a field of 1 mV/cm.

Depending on the anodization system, certain conditions can result in better electrical properties of the anodized oxides. Annealing of anodized oxides generally decreases the surface state density.[139,228,244] Laser-enhanced oxidation may lead to better electrical properties than in the dark.[605] Under a constant voltage, the surface state density tends to decrease with increasing final oxidation rate.[300] In dry electrolytes, it was found that constant current anodization at a current density of less than $3\,mA/cm^2$ produces oxide films of poor quality.[117,427] This is attributed to the oxide growth at low currents occurring by the inward motion of hydroxyl ions which results in the hydrated and poor-quality films. Breakdown field, flatband voltage, fixed oxide charge density, surface state density, and mobile ionic charge density, for

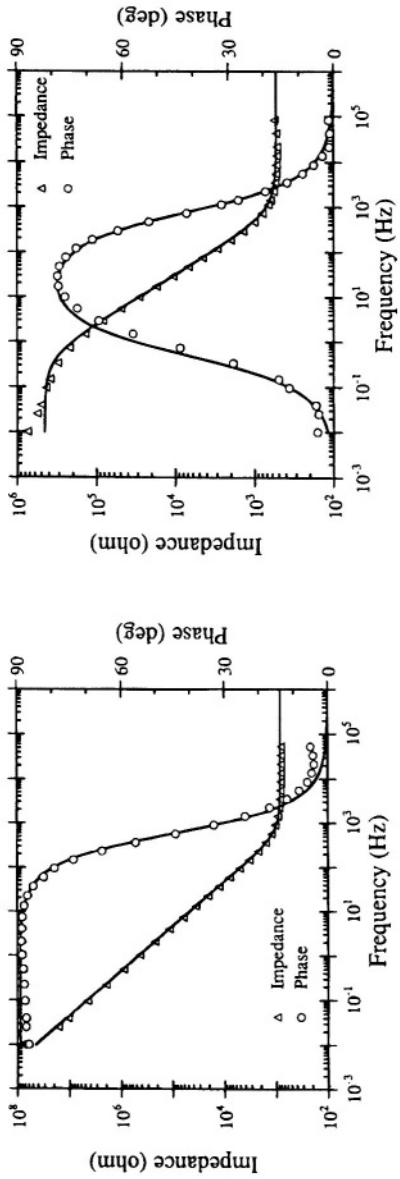

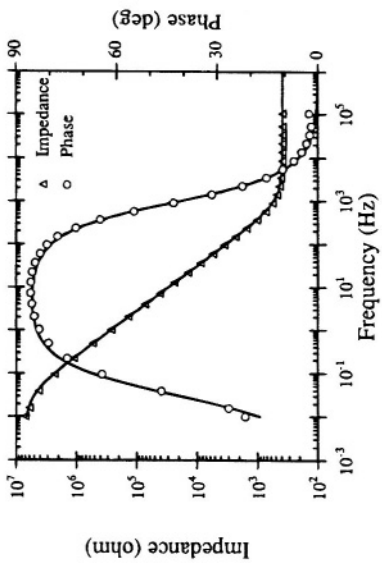

FIGURE 3.32. Impedance spectrum measured in 1 : 10 NH_4OH at 3.5 V_{sce}. (Left) Thermal oxide; (top right) anodic oxide formed by passivating for 30 min at 75 V_{sce}; (bottom right) anodic oxide after annealing for 15 min at 700 °C in N_2. After Schmuki *et al.*[139] (Reproduced by permission of The Electrochemical Society, Inc.)

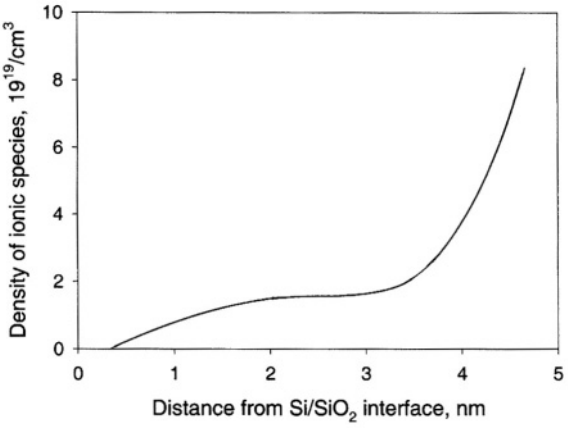

FIGURE 3.33. Density of charged species inside the oxide layer. The charge is positive and increases from the Si side to the electrolyte side. The density of ionic species is on the order of $10^{19}\,cm^{-3}$, which is a reasonable value. After Kirah *et al.*[294] (Reproduced by permission of The Electrochemical Society, Inc.)

the anodic oxides grown in ethylene glycol with a water content between 0.15 and 0.35% and proper cleaning and annealing, can be close to those for thermally grown oxides.[228]

Conductive anodic silicon oxide films can be produced by doping a submonolayer of platinum in the oxide.[609] The platinum is deposited on the silicon surface galvanostatically from 5% H_2PtCl_6 for a thickness from 0.002 to 2.5 monolayers. The silicon is then anodized in 0.2 M H_2SO_4 under illumination followed by a heat treatment. The Pt is present in the film at 0.25 (at Si/SiO_2) to 0.03 (SiO_2/solution) atom % and either as Pt or as PtO with an energy level close to the *n*-Si valence band edge.

4

Etching of Oxides

4.1. INTRODUCTION

Chemical etching is a process for removal of silicon dioxide films through dissolution in solutions. Dissolution of silicon oxides, in the context of this book, is related to the anodic behavior of silicon electrodes. However, the dissolution of anodic oxides is not well studied. In contrast, there is a wealth of information on the dissolution of other types of oxides. Much of this information must also be applicable, at least the qualitative and mechanistic nature, to that of anodic oxides. Also, because oxides of different types are commonly used in device fabrication, compiling the etch rate data of these oxides and those of silicon (presented in Chapter 7) in the same volume would be useful in practice. Additionally, because silica–water interaction, which has been extensively investigated in the geological field, is fundamental to the etching of silicon oxides, some of the results from the investigations on the dissolution of rocks and sands are also included.

4.2. GENERAL

Chemical etching of silicon oxides is a key processing step in practically all silicon-based microfabrication technologies. The premier practical application of this process is in the manufacture of integrated circuits, in wafer cleaning, and in pattern delineation. It is the very first step in chip manufacturing and in many cases it is the final cleaning after the final metal etch step. Also, etching of silicon oxide as a surface micromachining process is utilized in the fabrication of precision quartz and silicon-based micromechanical structures, where chemical etching provides a convenient method for removing undesired surface layers, and for surface micromachining of the desired microstructures.[123,451] On the other hand, etching of silicon oxide is also important in situations where the oxides are used as the masking material and etching of the oxides can be detrimental.

Dissolution of silicon oxides is geographically important since silica is one of the most abundant minerals in the Earth's crust. At least nine different SiO_2 phases are found in natural and engineered earth systems in the form of quartz, cristobalite,

tridymite, moganite, coesite, stishovite, elchatelierite, opal, and inorganic amorphous silica.[469,899] In particular, quartz, which makes up 12% of the minerals in the Earth's crust, is the pure oxide representative of the silicates which comprise 90% of the minerals in the crust. The rates of dissolution that are of interest in the chemical etching of silicon oxides in the electronic industry are usually larger than 10^{-3} Å/s, whereas those in the geological field are generally smaller than 10^{-5} Å/s. This difference thus dictates the methods for determination of silica dissolution rate in these two fields. The dissolution rates are generally determined as weight loss or change of thickness of the silica substrate in the field of materials science. In geological studies, on the other hand, they are mainly determined as change of concentration of the dissolved silicates in the solutions using silica particulate because it would take too long to cause a measurable difference in weight or thickness in the solutions that are involved in geological systems. It would take about half a day to dissolve a sand of 1 mm in diameter at a rate on the order of 100 Å/s but it would take about 10,000 years at 10^{-5} Å/s. The fields of interest regarding dissolution of silicon oxides, in terms of the range of dissolution rates, are illustrated in Fig. 4.1.

The etching of silicon oxides has been most extensively investigated in HF-based solutions. Various acids, salts, and other substances may be added to the HF solution in order to obtain better control of etch rate, sensitivity, uniformity, and stability of solution composition. The number of etching systems in terms of the possible combinations of solutions and oxides is limitless. As indicated in Table 4.1, the numerous etching solutions offer a wide range of etch rates for each specific oxide type. Also, silicon oxides produced by different processes may have vastly different etch rates in a given etch solution. For each particular solution, a given oxide has a specific etch rate and different oxides may etch very differently in different etching solutions.

Given the large number of oxide/etchant systems, it is difficult to generalize the etching characteristics of silicon oxides. However, an overall comparison can be obtained by grouping the etch rate data for the different unalloyed silicon oxides in HF solutions. Figure 4.2, which is a plot of the data listed in Table 4.1, shows the etch rates of four silicon oxides: quartz (single crystalline), thermal oxide, chemical vapor deposited (CVD) oxide, and anodic oxide. Several general remarks can be made: (1) The etch rates of all the oxides increase with HF concentration; they can be roughly described by an equation of the form: $R = kC_{HF}^{n}$, and the reaction order n is significantly

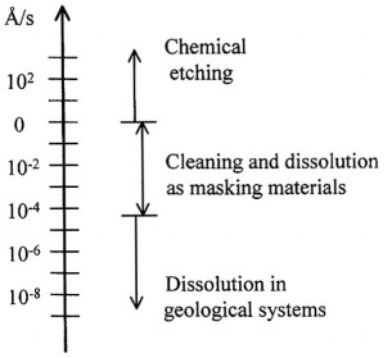

FIGURE 4.1. Range of dissolution rates of silicon oxides in different systems.

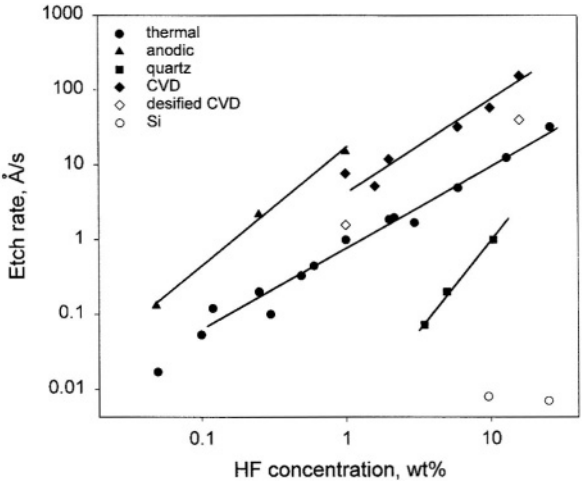

FIGURE 4.2. Etch rate of different silicon oxides as a function of HF concentration.

larger than 1 and tends to be different for different oxides. (2) The etch rates differ by several orders of magnitude for different types of oxides with quartz being the slowest and anodic oxide the fastest, reflecting the large difference in the density and structure of these oxides. (3) The etch rate of thermal oxides is much slower compared to CVD and anodic oxides. (4) The consistency of the data obtained from many different investigations indicates that the etch rate of thermal oxides is not significantly affected by formation conditions such as temperature, pressure, ambient composition, and duration. (5) Silicon, as a solid, is extremely stable in HF solutions compared to its oxide, as its dissolution rate is several orders of magnitude smaller than even that of quartz.

The activation energy for dissolution of silicon oxides varies over a wide range depending on the solution composition and the type of oxide. It appears that, based on the data in Table 4.2, the activation energy is higher in nonfluoride solutions than in fluoride solutions. In general, low activation energy in the range of 3–6cal/mol or 0.13–0.26 eV is indicative of a diffusion-limited process whereas that in the range of 10–20kal/mol or 0.44–0.87 eV is indicative of a surface reaction-limited process. According to Harrap,[153] the activation energy of thermal oxide in HF solution increases with HF concentration, C, and follows the empirical relation

$$\Delta E = \Delta E_0 + \alpha C^{1/2} \tag{4.1}$$

with $\Delta E_0 = 0.17\,\text{eV}$ and $\alpha = 0.096\,\text{eV/C}^{1/2}$. Using the above equation, for example, the activation energy is calculated as 0.18eV in 0.1% HF and 0.37 eV in 10% HF. An activation energy lower than that estimated by this equation is observed in dilute HF solutions, for example, 0.07 eV in 0.01 M HF.[239] Also, the activation energy tends to be higher at high temperatures.[153] In BHF solutions, the activation energy increases with the ratio of NH_4F to HF, suggesting that several parallel reaction paths of different acti-

TABLE 4.1. Selected Etch Rates of Different Silicon Oxides in Various Solutions[a]

Oxides	Solutions	Rate, Å/s	Ref.
Thermal	**Fluoride solutions**		
dry O_2, 700 °C	0.1% HF, room	0.053	368
dry O_2, 1000 °C	0.12%, 24 °C	0.12	628
dry O_2, 1100 °C	0.25% HF, 20 °C	0.2	286
	0.49% HF, 25 °C	0.33	97
wet O_2, 1000 °C	1% HF, 24.5 °C	0.9	153
	1% HF, 60 °C	5.6	153
dry O_2, 1100 °C	2% HF, 20 °C	1.9	286
	6% HF, room	5	139
wet O_2, 1000 °C	6% HF, 25 °C	5	468
wet O_2, 1100 °C	10 M HF, 30 °C	36.2	57
	49% HF, room	220	451
	56% HF, 25 °C	220	57
	0.1 M NH_4F, pH 4.5	0.0035	603
	1 M NH_4F, pH 5.3	0.12	602
	0.1 M KF, 24 °C	0.00008	239
	1 M KF, 24 °C	0.001	239
wet O_2, 970 °C	P etch[b], 23 °C	1.8	115
wet O_2, 1100 °C	P etch[b], 25 °C	2.4	310
wet O_2, 1050 °C	P ecth[b], 25 °C	2.1	332
wet O_2, 1000 °C	1% HF in glycerol, 25 °C	0.003	447
	0.49% HF + 40% NH_4F, 25 °C	1.1	97
	0.49% HF + 13% NH_4F, 25 °C	1.9	97
wet O_2, 970 °C	4.5% HF + 60% NH_4F, 23 °C	9.3	115
wet O_2, 1050 °C	7% HF + 55% NH_4F, 25 °C	15	332
dry O_2, 1000 °C	9/1, NH_4F/HF, 22 °C	0.98	118
dry O_2 of 500 atm, 800 °C	9/1, NH_4F/HF, 22 °C	0.82	118
wet, 1000 °C	1 ml NH_4F + 5 ml H_2O_2 + 24 ml H_2O, 80 °C	0.2	884
wet O_2, 1100 °C	5.2% HF + 34.6% NH_4F, 25 °C	16.8	310
wet O_2, 1050 °C	0.25% HF + 35% HNO_3, 25 °C	0.83	332
	1% HF + 34% HNO_3, 25 °C	2.3	332
wet O_2, 950 °C	1.5% HF + 10% H_2SO_4, room	1.3	657
wet O_2	6% HF + 30% NH_4F, 24 °C	18	491
	0.25% HF +35% HNO_3 + 15% H_2O_2, 35 °C	0.83	454
wet O_2, 950 °C	2.6 MHF, H_2O_2 : ethanol (2 : 3) 21 °C	1	512
steam, 1000 °C	7% HF + 59% NH_4F, 25 °C	15	919
	Alkaline solutions		
	10% KOH, 60 °C	0.07	206
	40% KOH, 85 °C	0.2	918
	2 M KOH, room	0.002	378
	1 : 1 hydrazine : water, 118 °C	0.03	708
	SC-1, 3.15% NH_4OH + 3.15% H_2O_2	0.02	1013
	SC-1, NH_4OH : H_2O_2 : H_2O, 1 : 1 : 5, 80 °C	0.14	982
	NH_4OH : H_2O, 1 : 5, 80 °C	0.19	982
wet, 900 °C	3.7% NH_4OH, 75 °C	0.01	711
	1.35 M NH_4OH, room	0.00012	139
steam, 1000 °C	10% TMAH, 90 °C	0.046	505
dry, 1000 °C O_2	10% TMAH, 90 °C	0.04	505
	4% TMAH, 90 °C	0.05	505
1150 °C	1140 g gallic acid + 1400 ml water+ 3830 ml ethanolamine + additives, 100 °C	0.03	506

TABLE 4.1. *Continued*

Oxides	Solutions	Rate, Å/s	Ref.
	EPW (E-705 ml:P-120 g:W-100 ml), 115 °C	0.03	918
wet, 1100 °C	E-17 ml:P-3 g:W-8 ml, 110 °C	0.06	334
Quartz			
AT-cut	1.6 M HF, 25 °C	0.072	671
	4.8 M HF, 25 °C	1	671
	4 M NH_4F·HF, 25 °C	0.97	671
	4 M HF + 1.1 M NH_4F, 25 °C	1.3	671
	3 M NH_4F·HF + 1.5 M HNO_3, 25 °C	1.9	671
	4 M HF + 2.2 M NH_4Cl, 25 °C	1.42	671
	3.6 M NH_4F·HF + 2.3 M H_2SO_4, 25 °C	3.8	671
	3 M HF + 1 M KF, 25 °C	0.83	671
natural, synthetic AT-cut	6 M NH_4F·HF, 21 °C	3.4	670
	15 M NH_4F·HF, 21 °C	9.1	670
α-quartz	5 M HF, 35 °C	2.3	709
	2.73 M NaOH, 70 °C	0.028	527
quartz particulate	0.1 M NaOH, 23 °C	1.5×10^{-5}	444
	pure water	$10^{-8.3}$	469
Deposited SiO_2			
$SiH_4 + O_2$ at 420 °C	0.17% HF	5.3	397
LPCVD	0.17% HF	2.4	397
$SiH_4 + O_2$ at ~400 °C	1% HF, 25 °C	7.8	452
densified	1% HF, 25 °C	1.6	452
450 °C	17% HF, 25 °C	155	412
densified	17% HF, 25 °C	40	412
$SiH_4 + O_2$ at 300–500 °C	2.2%HF + 18% NH_4F	60	148
densified	2.2% HF + 18% NH_4F	9.9	148
TEOS	0.49% HF, 25 °C	1–1.5	97
TEOS/ozone	1/30 BHF	2	102
$SiCl_4 + O_2 + H_2$ at 880 °C	91.5% H_3PO_4, 180 °C	0.17	328
675 °C	P etch, 25 °C	13.2	232
densified	P etch, 25 °C	2.9	232
TEOS	6% HF + 30% NH_4F, 24 °C	133	491
densified	6% HF + 30% NH_4F, 24 °C	55	49
$SiH_4 + O_2$ at 450 °C	1% HF in glycerol, 25 °C	0.13	447
densified	0.1% HF + 70% HNO_3 $+1.4 \times 10^{-5}$ $Hg(NO_3)_2$	0.2	426
Silicate glasses			
10% B	1% HF, 25 °C	8.2	452
densified	1% HF, 25 °C	3.3	452
4% P	1% HF, 25 °C	23	452
2% As	1% HF, 25 °C	7	452
2% B + 5% P	1% HF, 25 °C	33	452
densified	1% HF, 25 °C	10	452
10 % B_2O_3, 450 °C	17% HF, room	10	491
densified	17% HF, room	5	491
PSG	2.3% HF + 2.1% HNO_3, 23 °C	220–570	115
PSG	4.5% HF + 60% NH_4F, 23 °C	110–270	115
6.1% P_2O_5	10% HF + 57% NH_4F, 25 °C	98	412
densified	10% HF + 57% NH_4F, 25 °C	83	412
11.1% Al_2O_3	10% HF + 57% NH_4F, 25 °C	93	412

TABLE 4.1. *Continued*

Oxides	Solutions	Rate, Å/s	Ref.
10% B_2O_3 densified	0.1% HF + 70% HNO_3 +1.4 × 10^{-5} $Hg(NO_3)_2$	1	426
Cl-implanted SiO_2	0.16% HF	2.4	397
15% P_2O_5–SiO_2	p-etch 15 HF:10 HNO_3:300 H_2O	500	431
3.7% B_2O_3	0.5% HF + 35% HNO_3	30	332
fused silica, 3% BrO_3, 0.3% Al_2O_3	5 M KOH, 80 °C	0.52	527
Liquid phase deposited SiO_2			
as deposited	1% HF + 7% HNO_3	5	265
annealed at 350 °C	1% HF + 7% HNO_3	3.2	265
annealed at 500 °C	1% HF + 7% HNO_3	1.7	265
as deposited	2.2% HF + 2.1% HNO_3	7–10	265
annealed at 1000 °C	2.2% HF + 2.1% HNO_3	1	265
Anodic SiO_2			
10 μA/cm^2 in pure water	0.25% HF, 20 °C	2.2	286
8 V in 0.1 M HCl	0.05% HF, room	0.13	98
densified	0.05% HF, room	0.025	98
7.5 V in 1.35 M NH_4OH	1.35 M NH_4OH, room	0.0035	139
annealed	1.35 M NH_4OH, room	0.0017	139
in DI water	1% HF, room	15.2	457
in 2 M KOH	2 M KOH, room	0.01	378
phthalate solution, pH 4.5	0.1 M NH_4F, pH 4.5, room	2.1, *p*(111) 0.6, *n*(111)	603
5 V in 0.05% HF	0.05% HF, room	0.5	286
1 V in 0.3 M NH_4F, pH 3.5	0.3 M NH_4F, pH 3.5	4	122
8 V in 0.3 M NH_4F, pH 3.5	0.3 M NH_4F, pH 3.5	12	122
0.04 M KNO_3 ethylene glycol	7% HF + 59% NH_4F, room	60	919

[a]Abbreviations used. TEOS, tetraethylorthosilicate; PSG, phosphosilicate glass; BHF, buffered HF.
[b]2.3% HF + 2.1% HNO_3.

vation energies are involved in the etching process.[57] An examination of the data in Table 4.2 also suggests that for a given solution the activation energy tends to be higher for denser oxides such as quartz than for less dense ones such as CVD oxides.

4.3. THERMAL OXIDE

Figure 4.3 shows the etch rate of thermal oxide as a function of HF concentration and temperature.[153,239] A nearly seven order of magnitude variation of etching rate, from less than 10^{-5} Å/s to near 100 Å/s, can be obtained by varying the HF concentration from about 0.0001% to about 10% in the temperature range of 25–90 °C. The etching reaction has a reaction order larger than 1 in the whole concentration and temperature ranges. Etch rate could not be meaningfully determined in HF solution below 0.0001 M HF by measurement of loss in thickness or weight of etched samples.[239]

Temperature has a strong influence at high HF concentrations and relatively less effect at very low concentrations as shown in Fig. 4.3.[153,239] At very low concentrations,

TABLE 4.2. Activation Energies for Etching of Silicon Oxides

Oxide	Solution	T, °C	ΔE, eV	Ref.
silica	deionized water	25–300	0.52	899
quartz	deionized water	25–300	0.76	469
	6 M NH_4F·HF	17–87	0.44	670
	4.8 M HF	25–55	0.47	671
	5.4 M NH_4F·HF	25–55	0.44	671
	3 M HF + 1 KF	25–55	0.41	671
	2.73 M KOH	70–90	1.1	527
	NaCl, 0–0.3 M, pH 2–12	25–300	0.69–0.87	469
thermal	0.002 M HF	21–84	0.16	239
	0.01 M HF	21–84	0.07	239
	1 M HF	21–84	0.14	239
	0.1% HF	25–90	0.18	153
	10% HF	25–90	0.37	153
	10 M HF	30–60	0.30	57
	6% HF	10–30	0.36	491
	6% HF + 30% NH_4F	10–30	0.4	491
	10 M HF + 2 M NH_4F	30–60	0.36	57
	2.5 M HF + 8 M NH_4F	30–60	0.46	57
	1.05 M NH_3	40–82	0.39	706
	5% TMAH	60–90	0.5	1005
	42% KOH	40–85	0.86	206
	EDP	50–110	0.8	206
	1:5 $NH_4OH:H_2O$	50–85	0.58	982
	SC-1 $NH_4OH:H_2O_2:H_2O$	50–85	0.51	982
CVD	H_3PO_4	140–200	1.22	328
	1.05 M NH_3	40–82	0.3	706
	6% HF	10–30	0.32	491
densified CVD	6% HF	10–30	0.33	491

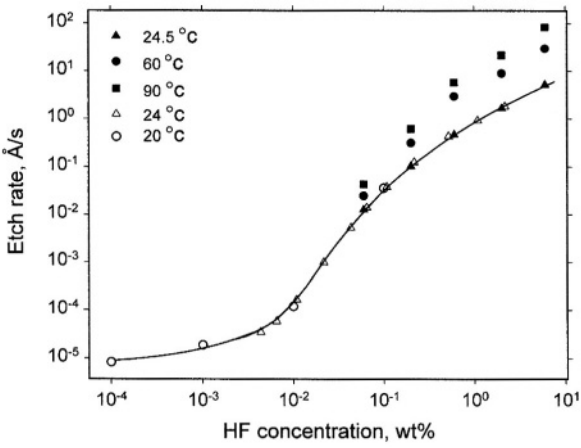

FIGURE 4.3. Etch rate of thermal oxides as a function of HF concentration. Data from Ref.[153,239]

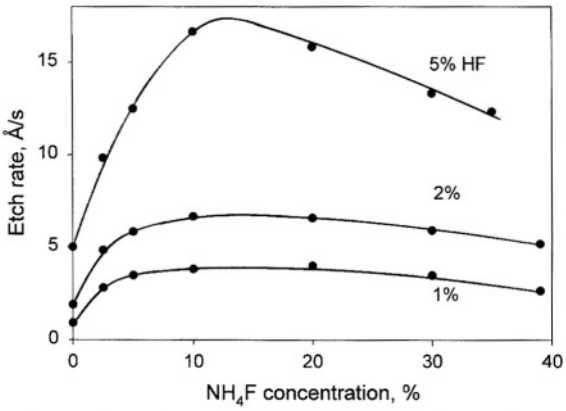

FIGURE 4.4. Etch rate of thermal oxides as a function of HF and NH_4F concentrations in buffered HF solution. After Kikuyama *et al.*[452] (Reproduced by permission of The Electrochemical Society, Inc.)

in the range between 0.005 and 0.04M, the effect of temperature is found to be minimal, in agreement with the small activation energies in these solutions.[239]

Most practical etching processes use buffered HF solutions (BHF) prepared by addition of NH_4F to avoid depletion of fluoride ions. There are many kinds of BHF with various combinations of HF and NH_4F concentrations. Figure 4.4 shows that the etch rate of thermal oxide in BHF solutions increases when the NH_4F concentration is low but is relatively independent of NH_4F concentration when the latter is higher than about 5%. Above 5% the etch rate is determined predominantly by HF concentration.[452] Figure 4.5 shows the effect of dilution of a BHF solution (40% NH_4F + 0.49% HF) with water.[97]

Addition of many chemical reagents other than NH_4F is also used to control certain aspects of the etching process. Figure 4.6 shows that addition of H_2SO_4 to a HF

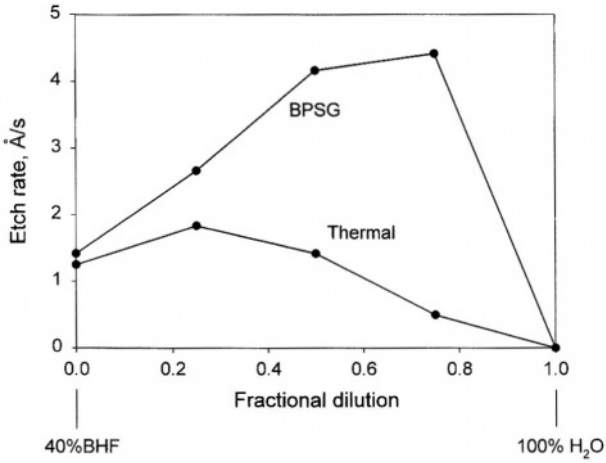

FIGURE 4.5. Etch rate of thermal oxide as a function of addition of water to 40% BHF. After Somachekhar and O'Brien.[97] (Reproduced by permission of The Electrochemical Society, Inc.)

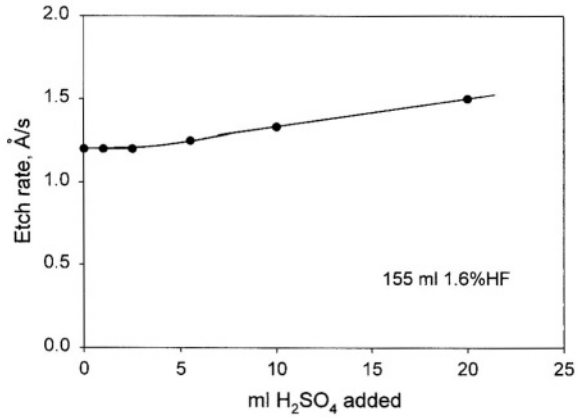

FIGURE 4.6. Etch rates of thermal oxides in 155 ml 1 : 30 HF (49%) solutions as a function of added H_2SO_4. After Schmidt *et al.*[657]

solution, which results in a decrease in pH, only slightly increases the etch rate of thermally oxidized silicon.[657] Addition of HNO_3 increases the etch rate sensitivity to the nonuniformities in oxides. It is found, for example, that 2.3% HF + 2.1% HNO_3 is extremely sensitive to differences in density, stoichiometry, bond strain, and impurities in the silicon dioxide films; it etches various types of glasses and mixed oxide layers much more rapidly than pure silicon oxides.[115,232] As another example, in 0.1% HF + 70% HNO_3 + 1.4×10^{-5} $Hg(NO_3)_2$ solution, the etch rate strongly depends on impurity concentration in the oxide, so that the etch rate profile can be used to determine the diffusion of boron into silicon from a doped glass source.[426] In pure H_2SiO_4 solution containing no HF, the etch rate of silicon oxide is very low as shown in Fig. 4.7.[800]

Surfactants may be added to etching solutions for surface roughness control. According to Myamoto *et al.*,[468] possible surfactants are hydrocarbon anionic ($CH_3CH_2CH_2CH_2OCH_3CH_2COOH$), hydrocarbon cationic ($CH_3CH_2CH_2O$

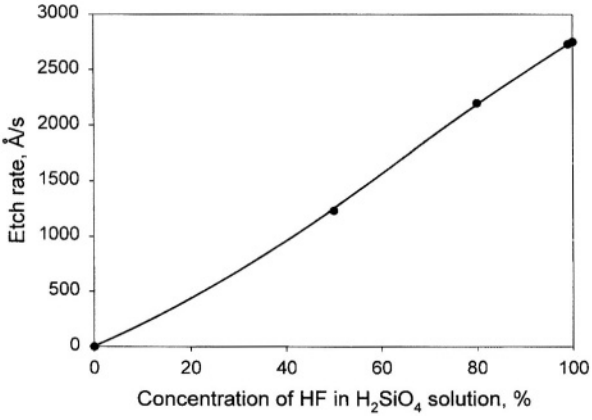

FIGURE 4.7. Etch rate of thermal oxide as a function of HF (49%) in H_2SiO_4 (20%) solution. After Monk *et al.*[800]

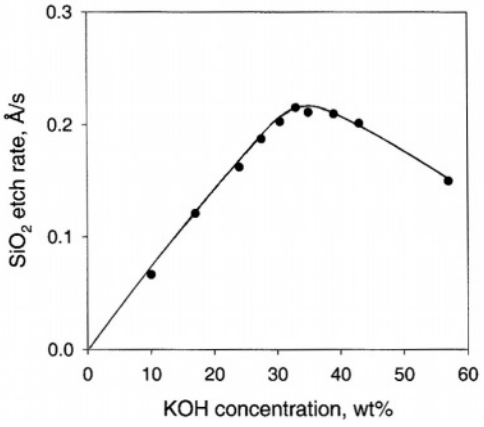

FIGURE 4.8. SiO_2 etch rate as a function of KOH concentration. After Seidel *et al.*[206] (Reproduced by permission of The Electrochemical Society, Inc.)

$CH_3CH_2NH_2$), and perfluorocarbon anionic ($CF_3CF_2CF_2CF_2CF_3CF_2COOH$). They have the effect of improving the wettability of BHF. The addition of anionic surfactants does not affect the etch rate of thermal SiO_2, PSG, and BSG films, whereas that of cationic surfactant decreases the etch rate of these films. Also, the activation energy does not change with addition of surfactants. The interruption of dissolution by surfactant adsorption is considered to be responsible for suppressing the microroughness of the etched surface.

In alkaline solutions, silicon oxides etch at very slow rates which allows them to be used as masks during silicon etching in these solutions. For example, the etch rate of thermal oxide is about 0.2 Å/s in 40% KOH at 85 °C[918] and is less than 0.02 Å/s in the standard SC-1 cleaning solution.[1013] Figure 4.8 shows that in KOH solutions the etch rate of thermal oxide increases with concentration reaching a peak value at about 35%.[206] Figure 4.9 reveals that the etch rate in TMAH solution decreases with

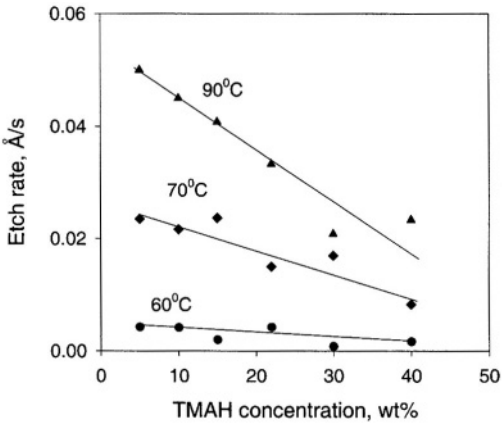

FIGURE 4.9. Dependences of SiO_2 etch rates on concentration and temperature. After Tabata *et al.*[1005]

concentration at various temperatures.[1005] Figure 4.10 plots the etch rate in SC-1 solution as a function of H_2O_2 concentration.[1013]

Residual oxide may be left in some microstructures at the end of etching and its occurrence strongly depends on geometry, surface tension, and the contact angle of the etchant.[13] It may be caused by the formation of air bubbles trapped in the structure when the wafer is being immersed in the etchant. It has been found that etching of thermal SiO_2 in a dilute aqueous solution of HF, 0.01% HF, proceeds down to ~20Å and beyond this point a thin layer that is resistant to HF remains on the Si substrate.[368] This residual film, which is several nanometers thick with the oxygen content increasing toward the surface, is hydrophobic. It has been suggested that this oxide layer near the interface is relatively dense.[628]

In etching of silicon oxide structures, the edge of a marked oxide step tends to be etched also in the horizontal direction. The etching profile is independent of the composition of $HF–NH_4F$ solutions but depends strongly on temperature as shown in Fig. 4.11.[792]

An oxide-covered wafer, after leaving the oxide etching tank, will continue to etch faster in the initial stage in the rinse tank because of the residual etchant on the surface.[97] Thus, the actual etch of SiO_2 in HF consists of etching in the HF tank and etching in the rinse tank. The amount of oxide etched during the transfer and rinse depends on the etchant. Determination of etch rates may thus be affected by the water rinse step after the etching. Also, the etching may result in the final etched pattern being U-shaped, with the center of the wafer etched more than the bottom and top.

The etch rate of thermally grown oxide may be altered by postoxidation treatments. Ion implantation at a certain level, depending on the nature of damage and distribution, has been found to increase the etch rate.[310] Also, an electric field, by applying an anodic potential onto a thermally grown oxide film, is able to inject hydroxyls into the oxide.[427] The etch rate of the hydroxyl penetrated region, depending on the hydroxyl concentration, is much faster than the unaffected thermal oxide

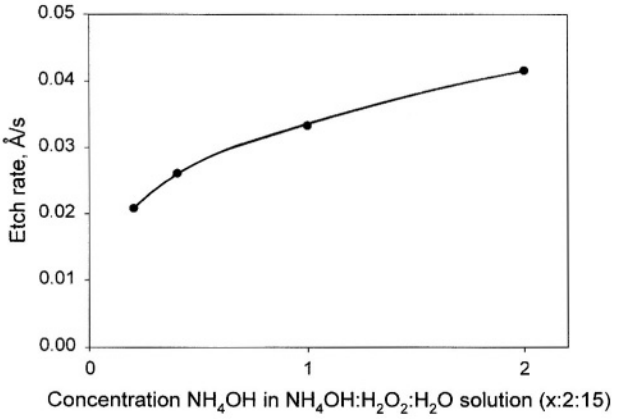

FIGURE 4.10. Etch rate as a function of concentration of NH_4OH in $NH_4OH:H_2O_2:H_2O$ solution (X:2:15). After Kaigawa *et al.*[1013]

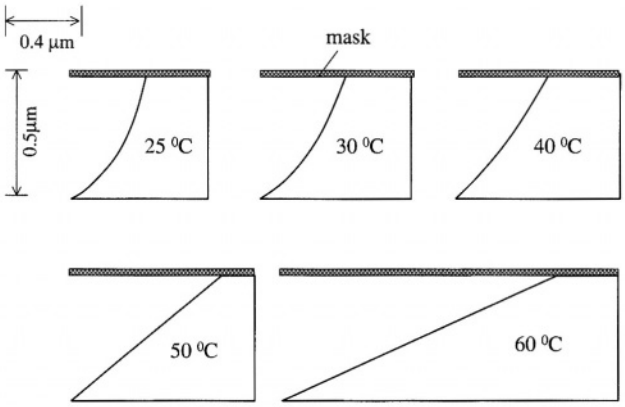

FIGURE 4.11. Underetch profiles as a function of temperature. (Reprinted from Haken *et al.*[792] © 1973, with permission from Elsevier Science.)

underneath as shown in Fig. 4.12. On the other hand, the dissolution of thermal SiO_2 in BHF solutions is found to be impeded by the application of a cathodic potential of 2–4V across the oxide film.[380]

4.4. QUARTZ AND FUSED SILICA

Quartz, being the single-crystalline form of silicon oxide, is dense and has very low etch rates in HF solutions compared to other forms of oxides as shown in Fig. 4.2. The etching of quartz in HF solutions has been extensively investigated by Vondeling,[671] who measured the etch rates in HF and $NH_4F{\cdot}HF$ with addition of various amounts of KF, NH_4F, H_2SO_4, NH_4Cl, KCl, and HNO_3. Some of the etch rate values

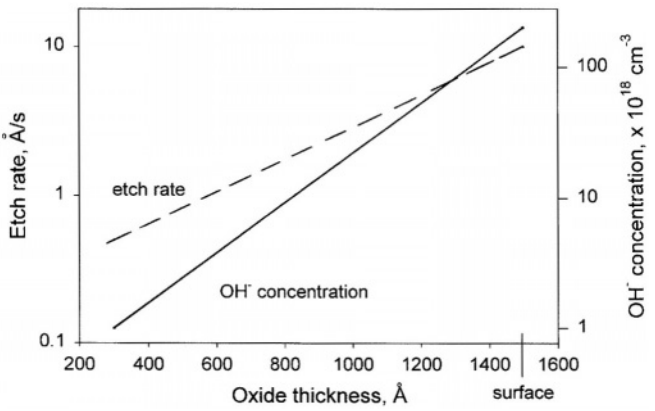

FIGURE 4.12. Etch rate of cathodically polarized thermal oxide in 0.2N HF solution and concentration of hydroxyls as a function of distance from the surface. After Schmidt and Ashner.[427] (Reproduced by permission of The Electrochemical Society, Inc.)

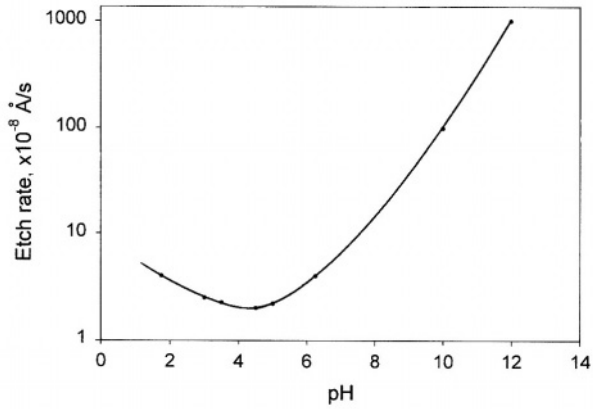

FIGURE 4.13. Etch rate of quartz as a function of pH in a sodium chloride solution. (Reprinted from Dove and Elston.[898] © 1992, with permission from Elsevier Science.)

resulting from this investigation are listed in Table 4.1. Figure 4.14 shows that in $NH_4F{\cdot}HF$ the etch rate of quartz is a linear function of $NH_4F{\cdot}HF$ concentration.[670] The etching process of quartz in HF solutions is found to be limited by the surface reactions and not affected by the resistance to diffusion. This is in agreement with the relatively high activation energy, 0.44 eV, and with the much lower etch rates relative to other oxides as illustrated in Fig. 4.2.[670,709] The dissolution can be catalyzed by salts such as NH_4Cl, NaCl, and LiCl.[916] The catalytic effect, which is a strong function of pH, is attributed to the competitive adsorption of cations at surface hydroxyls.

The etch rate of quartz depends on the crystallographic orientation of the surface. Table 4.3 shows the etch rate on the surface with different orientations.[671] The difference among the four orientations can be as large as 1000-fold. The etched surface morphology is a function of solution composition and temperature, particularly the concentration of positive ions. An etching bath with added H^+ gives terraces but no pits, a

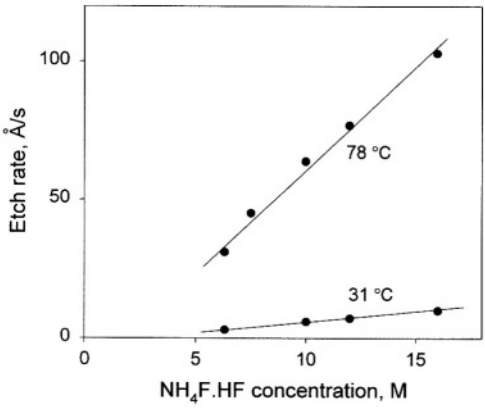

FIGURE 4.14. Plot of dissolution rate versus etchant concentration for two etching temperatures. After Tellier.[670]

TABLE 4.3. Etch Rates (Å/s) of Quartz of Different Crystallographic Orientations[671]

Solution	R_x	R_y	R_z	R_{at}	R_z/R_x
10.9 M HF	0.056	<0.014	27	4.6	240
7.2 M HF + 4 M NH_4F	0.069	0.014	6.9	3.8	102
5.4 M NH_4HF_2	0.042	0.042	3.1	1.3	73
5.4 M NH_4HF_2 + 1.8 M NH_4F	0.042	0.042	2.1	0.83	50

bath with added NH_4^+ gives terraces and pits, and a bath with added K^+ gives no terraces or pits at 25 °C.

The dissolution rate of silicon oxides in nonfluoride acidic or neutral aqueous solution is extremely low as shown in Fig. 4.13, which is responsible for the slow changes in geological systems.[898] In alkaline solutions, the etch rate of fused silica depends on the type of alkli as shown in Fig. 4.15.[527] The etch rate is not affected by solution stirring, indicating that the rate-limiting step is a surface reaction, in agreement with the high activation energy (about 0.9 eV). In NaOH and KOH solutions, there is a maximum etch rate at about 8 M. The dissolution rate tends to decrease with increasing dissolved silica in the solution at relatively low alkaline concentrations as shown in Fig. 4.16. Figure 4.17 shows the dissolution of different types of natural silicon oxides as a function of time in a diluted sodium hydroxide. In organic solutions, the dissolution requires the presence of water. The dissolution rate increases with increasing water content in a methanol solution, in which the etch rate is almost zero.

In NaCl solutions, Fig. 4.18 shows that the etch rate of silica increases sharply with increasing pH in the pH range of 5–11.[897] The concentration of NaCl also has an effect on the etch rate.

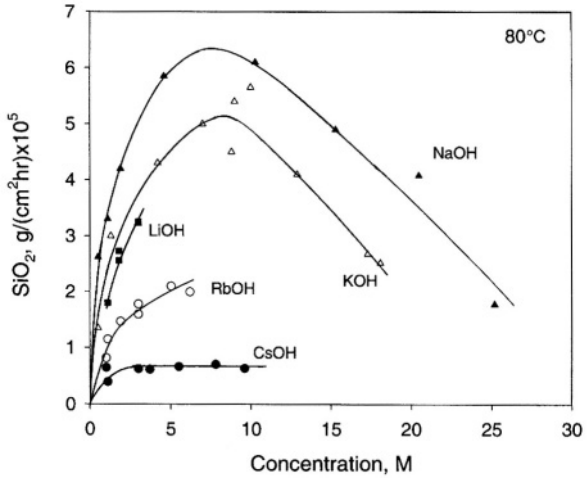

FIGURE 4.15. Rate of dissolution of Vycor 7900 at 80 °C versus concentration for various alkali hydroxides. After Hooley.[527]

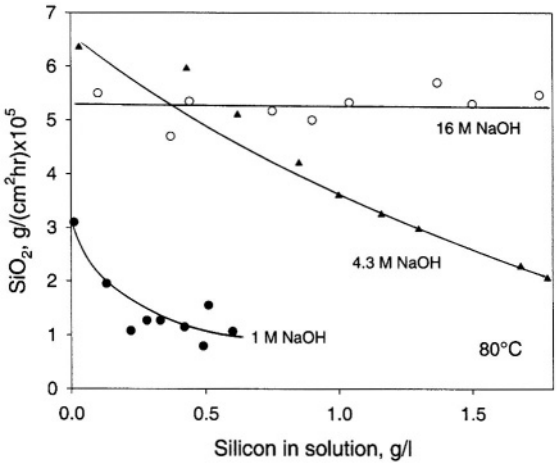

FIGURE 4.16. Rate of dissolution of Vycor 7900 at 80 °C versus total silica in solution. After Hooley.[527]

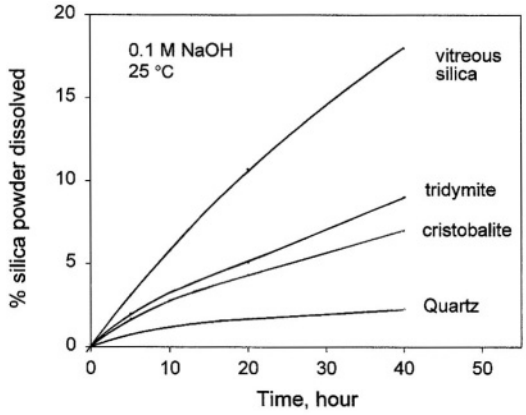

FIGURE 4.17. Dissolution of different silica powders in 0.1 N NaOH at 25 °C. After Bergman and Paterson.[959]

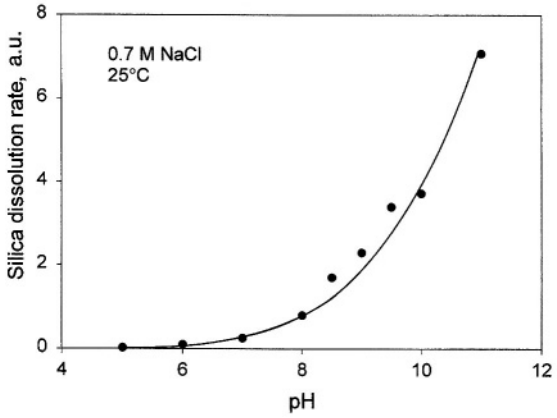

FIGURE 4.18. Log_{10} rate of silica dissolution versus pH for ionic strength of 0.70 M. After Wirth and Gieskes.[897]

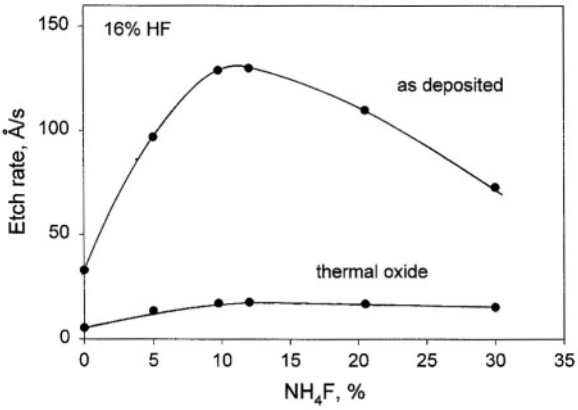

FIGURE 4.19. Etch rate of as-deposited CVD film and thermal oxide in NH_4F. After Proksche *et al.*[491] (Reproduced by permission of The Electrochemical Society, Inc.)

4.5. DEPOSITED OXIDES

The etch rate of CVD oxide is generally higher than that of thermal oxide as shown in Fig. 4.2 and Fig. 4.19.[491] It is strongly affected by the formation conditions as, for example, shown in Fig. 4.20.[784] It has been found that the etch rate of the LPCVD SiO_2 oxide in diluted HF solution is lower than conventional CVD film.[397] In addition to the formation conditions, the etch rate of CVD oxides is determined by (1) type and concentration of the dopant, (2) condition of the postdeposition treatment, and (3) composition of etching solution.[148,397,452,912]

Figures 4.21 and 4.22 show the etch rates of doped oxides, B_2O_3, P_2O_5, and As_2O_3 silicate glasses, in BHF solutions.[148] For P- and As-doped oxides the etch rate monotonically increases with increasing doping concentration whereas for B-doped

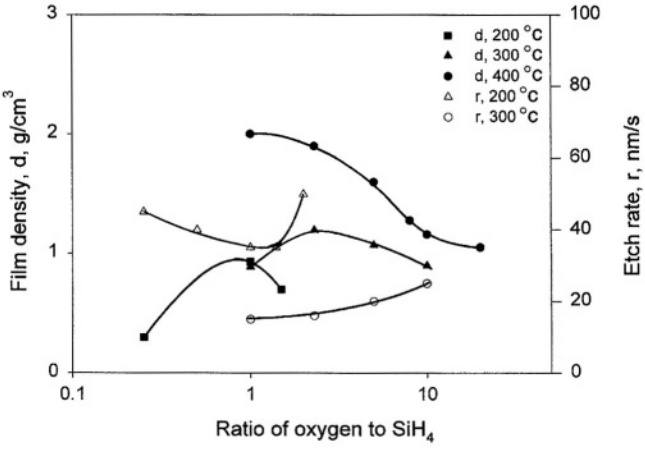

FIGURE 4.20. Effect of the ratio of oxygen to SiH_4 on the etch rate and density at various temperatures. 70% HNO_3:49% HF:H_2O (2:3:60). After Pavelescu *et al.*[784]

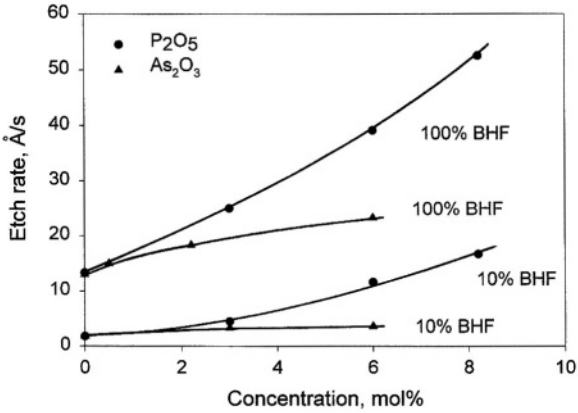

FIGURE 4.21. Etch rate of P_2O_5- and As_2O_3-doped glasses as a function of dopant concentration in BHF solutions. After Tenney and Ghezzo.[148] (Reproduced by permission of The Electrochemical Society, Inc.)

oxides the etch rate as a function of doping concentration depends on solution dilution. Similar findings were reported in other studies for the oxides doped with P,[451] As,[429] and B.[425] For BSG films the effect of B_2O_3 in the glass on etch rate also depends on etchant as shown in Fig. 4.23.[412] In SC-1 cleaning solution, the etch rate of B- and P-doped glasses slightly increases with increasing B and P concentrations.[1013]

Solution composition has a stronger effect on the etch rate of doped oxides than thermal oxides in BHF solutions as shown in Fig. 4.19[491] and in HNO_3–HF solutions.[115,369] Also, the etch rate difference between doped oxides and thermal oxides depends on solution composition; in the HF–HNO_3 solution the etch rate of a PSG film is 100 to 300 times higher than thermal silicon oxide, but in the BHF solution it is only about 10 to 30 times higher.

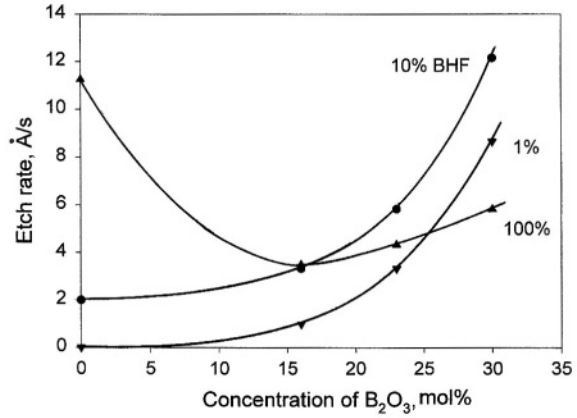

FIGURE 4.22. Etch rate of B_2O_3-doped glasses as a function of dopant concentration in BHF solutions. After Tenney and Ghezzo.[148] (Reproduced by permission of The Electrochemical Society, Inc.)

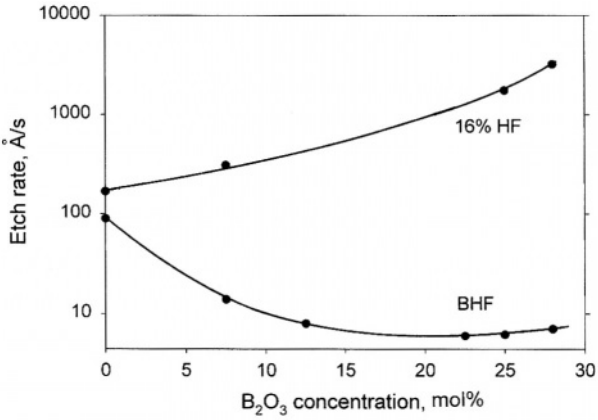

FIGURE 4.23. Etch rate of B_2O_3-doped glasses in HF and BHF solutions. After Kern and Heim.[412](Reproduced by permission of The Electrochemical Society, Inc.)

The etch rates of as-deposited oxides can be greatly reduced by annealing which results in densification of the oxides.[310,412,452,491] As shown in Table 4.1, annealing can result in two- to sixfold reduction in etch rate depending on the oxide and etching solution. For example, after annealing in steam at about 900 °C for 15min, which results in a 5% increase in the density of the oxide, the etch rate is reduced by a factor of 6.[232] The effect of annealing depends on solution composition as shown in Fig. 4.24.[452] Figure 4.25 shows the effect of annealing temperature on the etch rate of CVD SiO_2.[355] For fluorinated oxides, annealing results in the reduction of fluorine concentration as well as the etch rate.[102]

4.6. ANODIC OXIDES

There is very little systematic information on the etch rates of anodic oxides in the literature. Some of the etch rate data are listed in Table 4.1. In relative terms, the

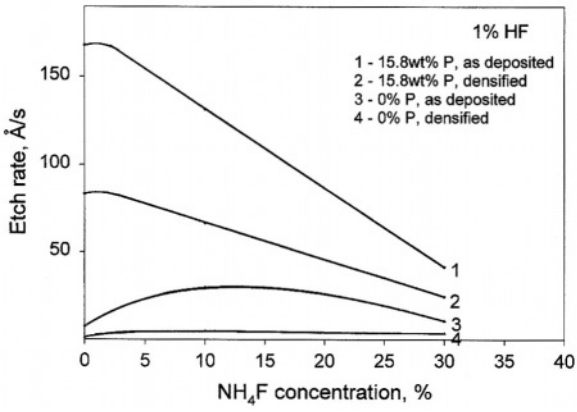

FIGURE 4.24. Etch rate of as-deposited and densified P glasses in NH_4F solutions. After Kikuyama *et al.*[452] (Reproduced by permission of The Electrochemical Society, Inc.)

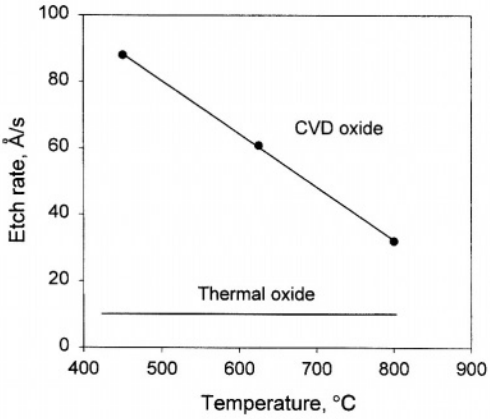

FIGURE 4.25. Etch rate versus CVD SiO_2 densification temperature. After White.[355] (Reproduced by permission of The Electrochemical Society, Inc.)

etch rates of anodic oxides, as shown in Fig. 4.2, are much higher than for other oxide types.

The etch rate of anodic oxide can be determined by methods similar to those for thermal oxide or deposited oxides. It may also be estimated from the anodic current of the oxidized electrode. The anodic i–V curve of a silicon electrode typically shows a passivation-like peak above which the dissolution occurs through a two-step process: the formation of oxide film followed by the chemical dissolution of the oxide. The steady-state anodic current measured at an anodic potential above the peak potential indicates the dissolution rate of the anodic oxide. Thus, the passivation current, i_p, listed in Table 5.5 can be used for estimation of the etch rate of the oxide film formed at the anodic potentials. (A current density of $1\,mA/cm^2$ corresponds to a silicon etch rate of 3.1Å/s or to a silicon oxide etch rate of about 7 Å/s.) For example, in 1% HF solution, i_p is $5\,mA/cm^2$, and thus the etch rate of the oxide film formed at a potential anodic of the first current peak is about 35 Å/s. In 2M KOH solution at room temperature, $i_p = 0.002\,mA/cm^2$ equivalent to an etch rate of about 0.014 Å/s. These numbers appear to be in general agreement with the data in Table 4.1.

As can be expected, the etch rate of anodic oxides depends on the formation potential. Figure 4.26 shows that the dissolution rate of the oxide films formed in 0.05% HF changes with potential, indicating that the oxides formed at different potentials are different.[286] For the oxide that is formed in the current oscillation region (see Section 5.10), the etch rate may greatly vary as a function of the distance from the silicon/oxide interface to the oxide/electrolyte interface as shown in Fig. 4.27.[950] Such drastic changes are partly due to the change of field related to the oscillation of thickness at a given potential and partly due to the change of the oxide structure during its growing process. In fluoride-containing solutions, current oscillation can occur in a certain anodic potential region, which means that the properties and the etch rate of the oxide film oscillate under that condition.[122,855] The mode of anodization, whether the final potential is imposed in one step or gradually reached, is also found to influence the etch rate.[98]

The high etch rates of anodic oxides are indicative of the loose structure of the oxides. As shown in Table 3.2, anodic oxide films have low densities and are not

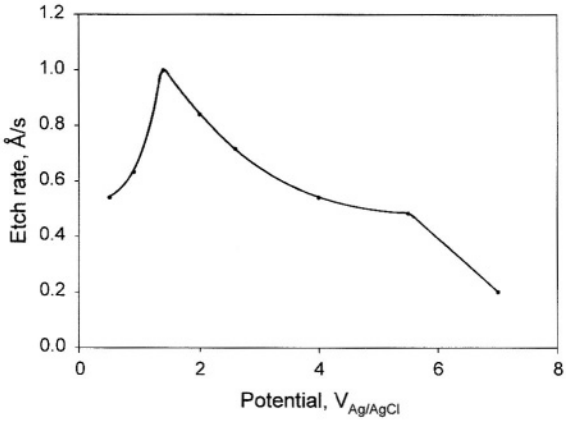

FIGURE 4.26. Calculated dissolution rate of anodic oxides as a function of formation potential V_0 (HF 0.05%). After Serre *et al.*[286] (Reproduced by permission of The Electrochemical Society, Inc.)

stoichiometric due to the incorporation of a significant amount of hydroxyl ions and water in the oxide. Silicon oxide that contains a high concentration of hydroxyl ions has a fast etch rate.[427] It has been found that a thermal oxide can be injected with hydroxyl ions under an anodic potential forming a hydrated surface layer. The hydrated layer etches much faster than the thermal oxide underneath as shown in Fig. 4.12.[427] Thus, the high etch rates of anodic oxides may be partly attributed to the loose structure and partly to the high degree of hydration. Similar to CVD films, anodic oxides can be dandified, resulting in lower etch rates. Figure 4.28 shows that the etch rate of anodic oxide films formed at 8 V_{sce} in 0.05% HF solution greatly decreases with increasing annealing temperature.[98]

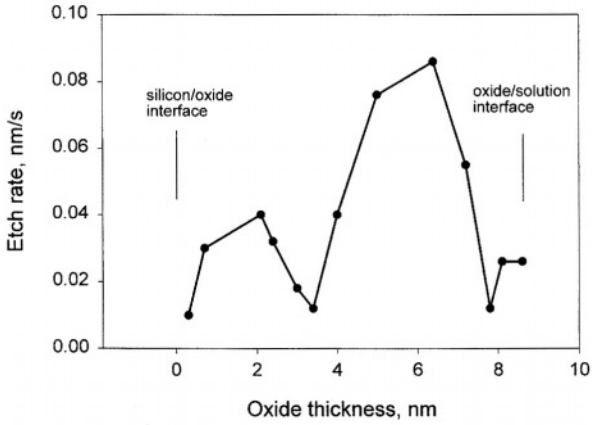

FIGURE 4.27. Dissolution rate of the anodix oxide formed at 7 V in 0.1 M [F] at pH 4.5 as a function of distance from the silicon/oxide interface. Data from Ref.[950]

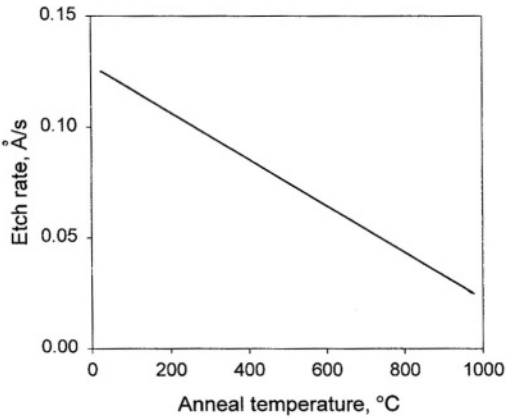

FIGURE 4.28. Etch rate of anodic oxides as a function of annealing temperature. The etching solution was 1:1000 v/v (48.8 to 49.2%) HF:H_2O. The substrates were (100) *p*-type Si with a resistivity of 3 to 7 Ωcm. The electrolyte used was 0.1 M HCl. After Bardwell *et al.*[98] (Reproduced by permission of The Electrochemical Society, Inc.)

4.7. ETCHING MECHANISMS

4.7.1. Reactions

In Nonfluoride Solutions. In water or nonfluoride aqueous solutions the dissolution of silicon oxides is determined by the reaction with water:[469]

$$SiO_2 + 2H_2O = H_4SiO_4 \tag{4.2}$$

The elemental reactions leading to the breaking of the Si–O bond involve at least three steps—adsorption, activated complex formation, and hydrolysis—as shown in Fig. 4.29.[469] The formation of the bond between the adsorbed hydrogen and the bridging oxygen weakens the Si–O bond. Among the species in water, H^+ ions perturb the bond the most; the relative effect of different ions and molecules on the bond strength of the bridging oxygen follows the sequence: $H^+ > OH^- > H_3O^+ > H_2O$.

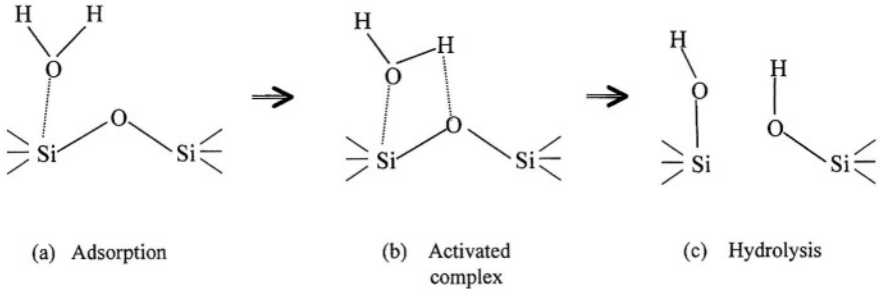

FIGURE 4.29. The elemental steps involving breaking Si–O bond. (a) Adsorption; (b) activated complex; (c) hydrolysis. (Reprinted from Dove and Rimstidt.[469] © 1994 by permission of the Mineralogical Society of America.)

The nature of the silica–water interface is determined by adsorption/desorption of the species in the water. When a silicon oxide, e.g., quartz, is fractured, the initial surface is composed of dangling silicon and oxygen bonds (Fig. 4.30a) which are not stable and hydroxylate easily with available water.[469,1150] The hydroxylated surface is dominated by SiOH groups (Fig. 4.30b). The initial adsorbed water adjacent to the surface is oriented and has properties different from the bulk water. As this adsorbed water layer increases to more than three monolayers, its properties become more like bulk water. The surface potential changes as a result of the adsorption of the ionic species in the water.[930]

The interaction of the hydroxyl groups with the protons in the water establishes an interfacial layer with a pH-dependent surface charge and potential. According to

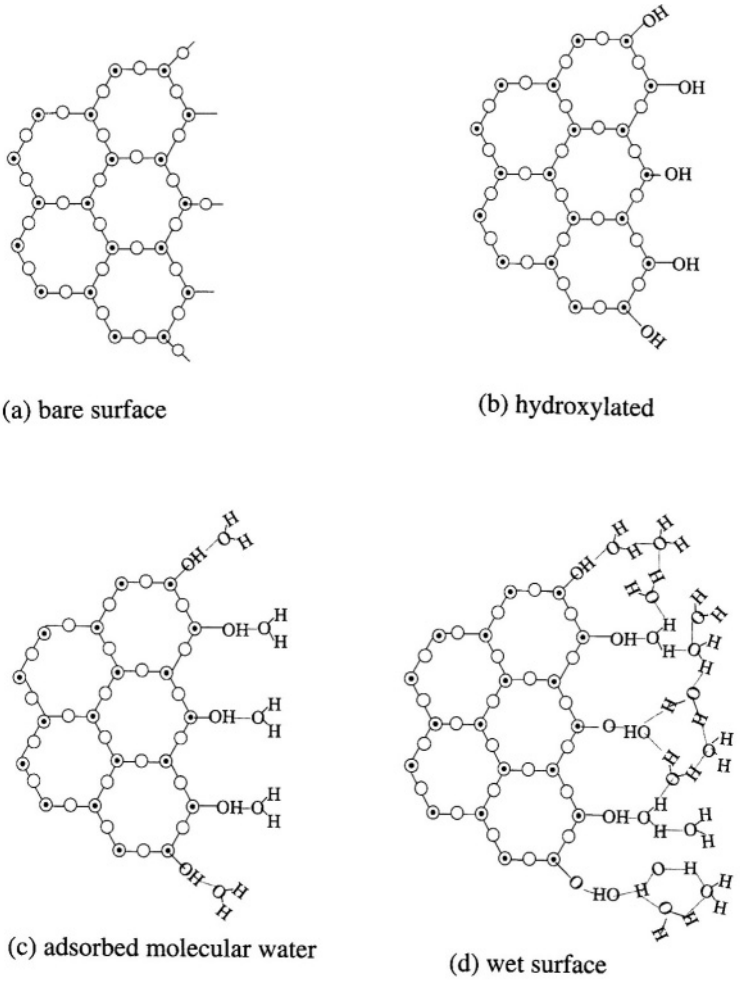

FIGURE 4.30. A schematic diagram illustrating stepwise water–surface interactions with freshly cleaved or fractured quartz. (Reprinted from Dove and Rimstidt.[469] © 1994 by permission of the Mineralogical Society of America.)

Dove and Elston,[898] this interfacial layer can be described by a triple layer surface complexation model (TLM) as shown in Fig. 4.31. The interface consists of three electrostatically charged regions, each with an associated electric potential and surface charge; these are termed the *o,* β, and *d* planes. Hydrogen ions are permitted to coordinate with the unsaturated sites of the interface at the innermost *o* layer. Sodium is positioned at the β layer or the *d* layer. The surface silicon-oxygen complex may have a different chemical character depending on the adsorbed species. In a sodium chloride solution the surface complexes can be represented as $\equiv SiOH_2Cl$, $\equiv SiOH_2^+$, $\equiv SiOH$, $\equiv SiO\text{-}Na^+$, and SiO^-. The concentration of each species depends on pH and salt concentration, and the sum of the fractions of these surface species equals 1:

$$\theta_{\equiv SiOH_2Cl} + \theta_{\equiv SiOH_2^+} + \theta_{\equiv SiOH} + \theta_{\equiv SiO\text{-}Na^+} + \theta_{SiO^-} = 1 \tag{4.3}$$

Calculation of the distribution of the species as a function of pH is shown in Fig. 4.32. The rate of dissolution of silica is then determined by the number of reactive species.

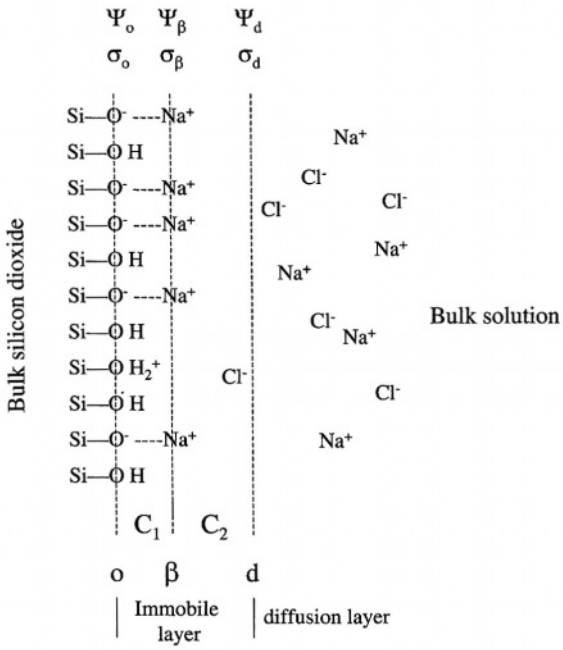

FIGURE 4.31. Schematic illustration of the triple layer model for the quartz–water–sodium chloride interface. Each of the layers is defined as having an associated interfacial potential, ψ_i (V), and charge density, σ_i ($C\,m^{-2}$), that determine the inner (C_1) and outer (C_2) layer capacitance (Faraday m^{-2}), by the relationship $C_i = \Delta\sigma_i(\Delta\psi_i)^{-1}$. The magnitude of these parameters decreases with increasing distance from the mineral surface into the region of electrostatically charged molecules comprising the solution side of the interface and finally into the bulk solution. In this model, the bulk uncharged solution is beyond the diffuse, *d*, layer. Strongly sorbed ions such as hydrogen interact closely with unsaturated oxygens in the innermost *o* layer, whereas weakly sorbed ions such as sodium are thought to interact only from distances associated with the β layer. However, the literature contains evidence that sodium influences mineral reactivity and that the nature of this interaction is cation specific. (Reprinted from Dove and Elston.[898] © 1992, with permission from Elsevier Science.)

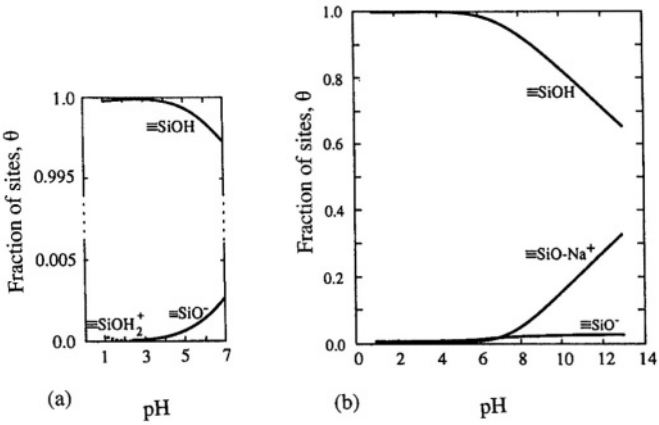

FIGURE 4.32. Results of the distribution of surface species calculations showing the fraction of each formalized site type on the mineral surface as a function of solution pH for two solution compositions. (a) A solution that does not contain cations other than hydrogen ions for pH 1–7. The pH is limited to the range 1–7 because even weakly basic solutions must contain a finite amount of alkali cations. The mineral surface is almost entirely composed of neutrally charged surface complexes. The vertical axis is discontinuous to show the very small quantities of nonneutral sites. (b) A 0.20 molal sodium chloride solution also gives a large proportion of SiOH species. At pH 12 the fraction of surface sites existing as SiOH equals 0.7. The majority of the remaining sites are associated with sodium and few of the sites remain as coordinatively undersaturated (SiO^-) species. (Reprinted from Dove and Elston,[898] © 1992, with permission from Elsevier Science.)

On the other hand, according to Wirth and Gieskes,[897] the rate-determining reaction during etching of silica is determined by the surface charge, and any ionic species, which affects the surface charge, would affect the etch rate.

In alkaline solutions, according to Hooley,[527] the dissolution of silica follows two consecutive reactions. First, an adsorption of water occurs followed by reaction with hydroxyl ions to produce soluble products:

$$SiO_2 + 2H_2O \rightarrow SiO_2 \cdot 2H_2O \tag{4.4}$$

$$SiO_2 \cdot 2H_2O + 2OH^- \rightarrow Si(OH)_6^{2-} \tag{4.5}$$

It is argued that the surface of silica consists largely of oxygen ions because the small, more highly charged silicon ions are well shielded by the highly polarized oxygen ions so that the hydroxyl ions do not react with them. The absorption of water by hydrogen bonding to the oxygen ions on the surface results in transfer of charge toward the water molecule. This decreases the screening so that silicon ions can combine with hydroxyl ions to form soluble complex. This mechanism explains the lack of dissolution of silicon oxides in NaOH containing methanol. It also explains the maximum rate with respect to NaOH concentration (Fig. 4.15). At low molarity and therefore high water content, reaction 4.5 is the rate-determining step so that the etch rate will increase with increasing molarity. On the other hand, at high molarity and thus low water concentration, reaction 4.4 becomes the rate-limiting step and thus the rate decreases with

increasing molarity. The inhibitive effect of dissolved silica in the solution also agrees with the reaction scheme. The inhibitive effect of dissolved silica is the greatest at low molarity when reaction 4.5 is the rate-limiting step and should disappear for concentrated solutions when reaction 4.4 is the rate-limiting step.

In HF-Based Solutions. The overall reaction involving the dissolution of silicon oxide in HF solution can be expressed as

$$SiO_2 + 6HF = SiF_6^{2-} + 2H_2O \tag{4.6}$$

The elemental reactions are, however, rather complicated and remain the subject of debate. For many studies on the kinetics of silicon oxide etching, identifying the fluoride species in the solution responsible for the etching reactions has been a major concern. This is because HF is a weak acid, which ionizes only partially to fluoride ions, and its aqueous solutions may contain a significant quantity of fluorine in the form of un-ionized HF and partially ionized bifluoride HF_2^-.

In an earlier study, Judge[57] found that in solutions of NH_4F and NH_4Cl close to neutral pH, essentially all fluoride is present in the unprotonated state and the solutions exhibit a near zero rate of SiO_2 dissolution. Judge thus suggested that the free fluoride ion is not one of the species responsible for the dissolution. This conclusion was further supported by Kikuyama *et al.*,[239] who found that the etch rate of SiO_2 in KF solutions, in which all the fluorine is in the form of free fluoride ions, is very small as shown in Fig. 4.33. The etch rate in 1M KF is 0.001 Å/s, which is threefold smaller than that in a HF solution of the same concentration.

According to Judge,[57] HF and HF_2^-, which are the dominant species in acidic solution of HF, HCl, NH_4F, and NH_4Cl, are responsible for the etching reactions involved. Clear correlation between etch rate and HF_2^- concentration is also observed in KHF_2 solutions in which HF_2^- is a major species as shown in Fig. 4.34.[239] HF_2^- is also found to be the rate determining species in $HF–H_2O–CH_3CH_2OH$ solutions.[512] According to Kikuyama *et al.*,[239] because the dependence of etch rate on HF_2^- is different in HF and

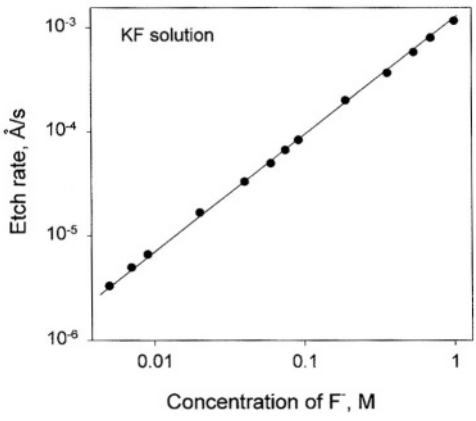

FIGURE 4.33. Relationship between etch rate and F ion concentration of KF solution. Etch rate and F ion concentration can be expressed as $R \approx 0.067 \times [F]^{1.11}$. After Kikuyama *et al.*[239] (Reproduced by permission of The Electrochemical Society, Inc.)

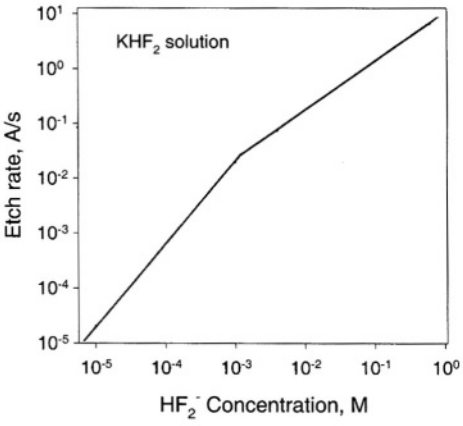

FIGURE 4.34. Relationship between etch rate (at 24 °C) and HF_2^- concentration of KHF_2. After Kikuyama *et al.*[239] (Reproduced by permission of The Electrochemical Society, Inc.)

KHF_2 solutions, H^+ and K^+ may also have a significant effect on the etching process. Verhaverbeke *et al.*[238] further suggested that in addition to HF_2^-, HF dimer, $(HF)_2$, which is a dominant species in solutions with a concentration higher than 1M, is also an important etching species. Thus, depending on relative dominance of the species, the following parallel reactions may be involved:

$$SiO_2 + HF \rightarrow \text{intermediate} \tag{4.7}$$

$$SiO_2 + HF_2^- \rightarrow \text{intermediate} \tag{4.8}$$

$$SiO_2 + (HF)_2 \rightarrow \text{intermediate} \tag{4.9}$$

HF, HF_2^-, and $(HF)_2$ may further participate in the reaction with the intermediates to complete in the dissolution process.

H^+ may also be an important species involved in the dissolution process. According to Monk *et al.*,[451] the etching of SiO_2 film is probably a two-step process. In the first step, H^+ interacts with the surface which opens the SiO_2 network so that, in the second step, more of the fluorinated species is able to attack the silicon in the films. Thus, adding H^+ to HF solutions results in higher etch rates. The importance of H^+, as postulated by Osseo-Asare,[123] is in the regulation of the surface potential. According to Osseo-Asare, the formation of the Si–F bond is the rate-determining step. H^+ is particularly important as its adsorption on the surface determines the surface concentration of Si–OH which is the site for fluoride adsorption. Adsorption of positive ions, such as H^+, which changes the electronic configuration of the surface, is considered to also be important in the etching reactions of quartz.[671] On the other hand, White[786] found that DF exhibits a weak isotope effect of 1.4 (R_{H_2O}/R_{D_2O}) and found no isotope effect for DF_2^-, so that protons may not play a major role in the rate-determining step in the etching reaction.

A number of pathways may be possible in the formation of surface species leading to breaking of the Si–O bonds as has been suggested by Monk *et al.*[800] Figure 4.35I

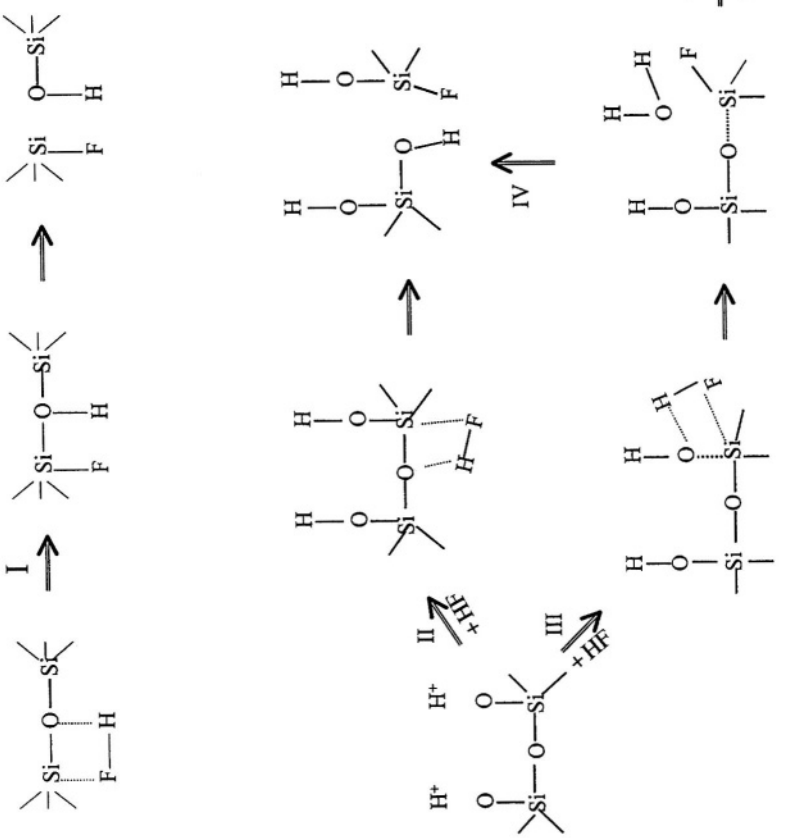

FIGURE 4.35. Possible reaction pathways resulting in the dissolution of a silicon atom in HF. After Monk *et al.*[800]

shows the case when HF reacts directly with the surface leading to breaking of Si–O bonds. On the other hand, if the adsorption of hydrogen on the oxygen to form hydroxyl groups is the first step, the following step to break the Si–O bond may have two possible paths. In the first path, as shown in Fig. 4.35II, formation of the hydroxyl group causes polarization and weakening of the underlying Si–O bond, thus facilitating the attack by a fluoride species.[452] In the second path, as shown in Fig. 4.35III, the hydroxyl group is replaced by the fluoride ion, which results in weakening and breaking of the underlying Si–O bond.

Osseo-Asare[123] proposed an etching model based on the effect of surface charge on the absorption of solution species. It was postulated that the SiO_2/water interface contains neutral hydroxylated surface groups (Si–OH) which can protonate to give positively charged sites ($Si–OH_2^+$) or deprotonate to give negatively charged sites ($Si–O^-$), depending on the pH. The adsorption of the fluoride ion, as a surface ligand exchange reaction ($Si–OH + HF = Si–F + H_2O$), results in the polarization of the underlying Si–O bonds. The subsequent detachment of the surface Si–F complex constitutes the dissolution event.

The basic idea in Osseo-Asare's model is that when protons, hydroxyl ions, ligands, or water molecules bind to the surface sites, they cause a polarization of the underlying silicon–oxygen bonds. With a sufficient number of bound species, the Si–O–Si bonds become sufficiently weakened to permit detachment of the surface silicon ion. In the absence of ligands, the dissolution rate is determined by the surface concentration of protonated species (MOH^+_2) at pH < pzc, of water at pH ~ pzc, and of deprotonated species (MO^-) at pH > pzc. The surface charge is modulated by the protons in the solution immediately adjacent to the solid surface according to the reactions

$$SiOH_2^+ + OH^-(s) \leftrightarrow SiOH + H_2O \tag{4.10}$$

$$SiOH \leftrightarrow SiO^- + H^+(s) \tag{4.11}$$

The specific adsorption of an anion at the oxide/electrolyte surface, which changes the surface charge, may be viewed as a surface complexation reaction. Thus, fluoride ions that are adsorbed at the silicon oxide surface centers form Si–F complex:

$$Si-O-Si(OH)_3 + HF = Si-O-Si(OH)_2F + H_2O \qquad K_{sF} \tag{4.12}$$

where K_{sF} is the surface complexation constant. The Si–F bond polarizes the underlying Si–O bonds and this leads to the detachment of the surface silicon center:

$$Si-O-Si(OH)_2F + H_2O \rightarrow SiOH + Si(OH)_3F \qquad k \tag{4.13}$$

$$Si(OH)_3F + 5HF = SiF_6^{2-} + 2H^+ + 3H_2O \text{ (fast)} \tag{4.14}$$

4.7.2. Rate Equations

The dissolution in neutral water is proportional to the interfacial area between silica and water. Since silica has low solubility in neutral water, the dissolution can be

considered to occur at a near-saturation condition. According to Rimstidt and Barnes,[899] the rate of reaction of silica in water can be expressed as $r = k(1 - S)$, where k is the product of the rate constant and activities of the reacting species, and S is a quantity measuring the degree of saturation. The term $(1 - S)$ is a measure of departure from equilibrium and when $S = 1$ the system is at equilibrium and the net rate of reaction is zero. Table 4.4 lists the factors that may influence the rate of silica–water interaction as summarized by Rimstidt and Barnes.[899]

The dissolution rate equation for silica in nonfluoride solutions may also be expressed according to the surface complexation model described by Eq. (4.3) and Fig. 4.32 considering the contributions of different surface complexes: $\equiv SiOH_2^+$, $\equiv SiOH$, $\equiv SiO\text{-}Na^+$, and $\equiv SiO^-$.[898] The rate equation for the dissolution of silica in NaCl solutions at pH 2–13 at 25 °C can be described as[898]

$$\text{rate} = 10^{-13}(\theta_{\equiv SiOH})^n + 10^{-10.8}(\theta_{\equiv SiO-Na^+} + \theta_{\equiv SiO^-}) + 10^{-9.2}\left(\theta_{\equiv SiO-Na^+} + \theta_{\equiv SiO^-}\right)^2 \quad (4.15)$$

According to Fig. 4.32, $\equiv SiOH$ is the predominant species and its concentration determines the dissolution rate at low pH. The low dissolution rates of silica in acidic solutions (Fig. 4.32) indicate that this species is most resistant to hydrolysis. The more reactive species $\equiv SiO\text{-}Na^+$ and SiO^- become important at higher pH at which the dissolution rate is faster as shown in Fig. 4.13.

In acidic fluoride solutions, many etch rate equations, empirically or mechanistically derived, have been proposed.[57,153,239,451,491] The most quoted rate equation is that of Judge,[57] who found that the etch rate of thermal oxide in HF and NH_4F solutions can be expressed as a function of HF and HF_2^- concentrations:

$$R = A[HF] + B[HF_2^-] + C \quad (4.16)$$

Curve fitting indicated that the rate of attack by HF_2^- is about four to five times that of HF as shown in Fig. 4.36. A more general equation, including the effect of temperature, is

$$R(\text{Å/s}) = 5 \times 10^7[HF_2^-]e^{\Delta E_a/RT} + 2.2 \times 10^6[HF]e^{\Delta E_b/RT} + 0.025(T - 292) \quad (4.17)$$

where $\Delta E_a = -38.1\,\text{kJ/mol}$ and $\Delta E_b = -33.9\,\text{kJ/mol}$.

TABLE 4.4. Factors that Influence the Rate of Silica–Water Reactions[899]

Variable	Effect on reaction rate[a]
Temperature	Experimental dependence (Arrhenius equation)
Pressure	Very little effect
Extent of system	Rate directly proportional to A^b and inversely proportional to M^c
Activity of H_4SiO_4	Rate proportional to $(1 - Q/K)$
Mechanism	Rate controlled by breaking of strong Si–O bonds
Silica phase present	Determines K and therefore S
pH	No indication of any effect on reaction mechanism near neutrality
Salts	Reduces the activity of water and thus silica solubility
Particle size	Very small particles have higher solubilities than macroscopic grains

[a]Symbols used: [b]A: interfacial area; [c]M: mass of water in the system; Q, activity product; K, equilibrium constant; $S = Q/K$, degree of saturation.

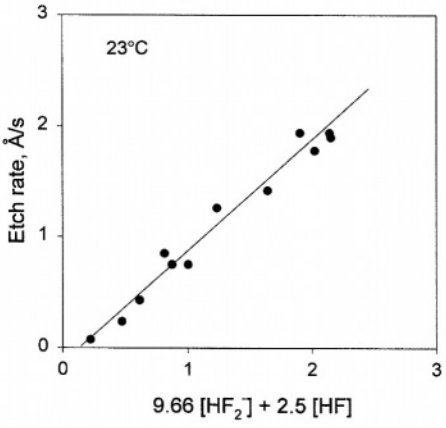

FIGURE 4.36. Linear dependence of the dissolution rate of SiO_2 at 23 °C on the plotted function of $[HF_2^-]$ and [HF]. After Judge.[57] (Reproduced by permission of The Electrochemical Society, Inc.)

A similar rate equation has been proposed by Proksche *et al.*[491] in NH_4F solutions. They plotted the ratio of etch rate to the maximum rate as a function of NH_4F concentration in Fig. 4.37, revealing that the etch rates of various oxides as a function of NH_4F concentration can be divided into two regions. For low concentrations (<12%) the etch rates increase to a maximum, with the slope of the normalized etch rate the same for all oxide types. For high concentrations (>12%) the etch rate strongly depends on the oxide type. The activation energy is also different in the two regions for different oxides, indicating that different mechanisms are involved in the two regions. In the low-concentration region the etching is mainly due to the reaction with HF_2^-, whereas in the high-concentration region reaction with HF becomes more important.

In strong acidic solutions, with addition of HCl, the dissolution of silica is first order with respect to HF concentration.[910]

Verhaverbeke *et al.*[238] considered the effect of HF dimer, $(HF)_2$, in addition to HF_2^-, on the etching of SiO_2 in HF and HF/HCl solutions. It was reasoned that although

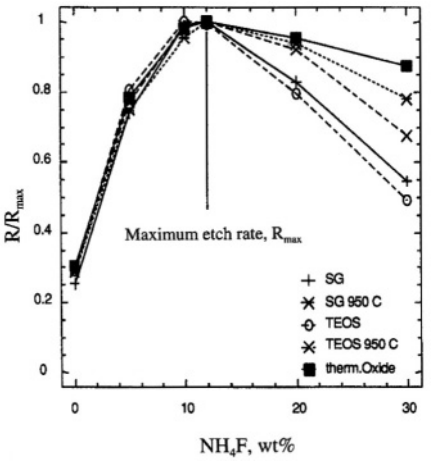

FIGURE 4.37. Standardized (V_E/V_{EMAX}) etch rates versus ammonium fluoride concentration (wt %) for various silicon dioxide layers in 30 wt % NH_4F and 6 wt % HF at 24 °C. After Proksche *et al.*[491] (Reproduced by permission of The Electrochemical Society, Inc.)

HF constitutes a large fraction of the dissolved species, it does not participate in the reaction since a solution consisting of only HF molecules is not able to attack the SiO_2 structure at an appreciable rate. They found that the etch rates fit the equation

$$R = a[(HF)_2] + b[(HF)_2]^2 + c[HF_2^-] + d[HF_2^-]\log([H^+]/[HF_2^-]) \qquad (4.18)$$

The relative contribution of $(HF)_2$ and HF_2^- in the etching process changes with total HF concentration as shown in Fig. 4.38. At very low HF concentration, etching is primarily due to HF_2^-. At high HF concentration, the etching by $(HF)_2$ dominates. The relative contribution in the etching by $(HF)_2$ or HF_2^- can be controlled by adding NH_4OH, HCl, or NH_4F.

Vondeling[671] found that the etch rate of quartz in $HF + NH_4F{\cdot}HF$ solutions can be described by

$$R = 0.185([H^+]{\cdot}[HF])^{1.2} + 0.095([HF^+{}_4]{\cdot}[HF])^{1.3} \qquad (4.19)$$

Based on this empirical equation, the author suggested that positive ions and HF are the important species in the etching reactions on quartz and that, unlike in the etching of thermal oxides, the concentration of $HF^-{}_2$ does not appear to significantly affect the etch rate of quartz. It was also suggested that the etching mechanism involves the adsorption of positive ions, e.g., H^+, onto the quartz surface, which changes the electronic configuration of the surface and facilitates the etching reactions.

Osseo-Asare[123] proposed a model described Eqs. (4.10) to (4.14). According to this model, the effect of pH on the concentration of surface fluoride species is related to the effect of pH on (1) the concentration of the SiOH sites, (2) the concentration of fluoride-containing species, and (3) the competitive adsorption of fluoride-containing species and hydroxyl ions. The surface site balance can be written as

$$[SiOH]_T = [SiOH] + [SiOH_2^+] + [SiO^-] + [SiF] \qquad (4.20)$$

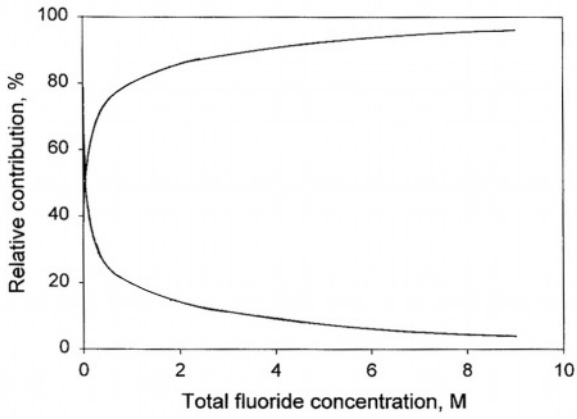

FIGURE 4.38. Etch rate contributions of $(HF)_2$ and HF_2^- normalized to 100% in a dilute HF solution as a function of the total fluoride concentration. After Verhaverbeke *et al.*[238] (Reproduced by permission of The Electrochemical Society, Inc.)

where $[SiOH]_T$ is the sum of all surface species. The ionization of the silica/aqueous interface through protonation and deprotonation reactions means that the silica surface acquires a surface charge (σ) and this, in turn, generates a surface potential (ψ). As a result, the proton concentration immediately adjacent to the solid surface differs from the bulk according to Boltzmann's distribution law:

$$[H^+]_s = (H^+)\exp[-F\psi/RT] \tag{4.21}$$

The concentration of SiOH, using Eqs. (4.10)–(4.12), (4.20), and (4.21), can then be expressed as

$$[SiOH] = [SiOH]_T / \{1 + ([H^+]/K_{s1}\exp[F\psi/RT]) + (K_{s2}\exp[F\psi/RT]/[H^+])\} \tag{4.22}$$

The dissolution rate is determined by reaction (4.13), which is the rate-determining step, and can be expressed as

$$R = k[SiF] = A[SiOH] \tag{4.23}$$

where [SiF] and [SiOH] are the surface concentrations of adsorbed fluoride and hydroxyl sites; $A = kK_{sF}[HF]$ according to Eq. (4.12).

It is seen from Eq. (4.22) that at low pH, [SiOH] increases with increasing pH, whereas at high pH, it decreases with increasing pH. Since [SiF] is proportional to [SiOH], this means that there is a maximum [SiF] as a function of pH, which explains the observed etch rate maximum shown in Fig. 4.39. By considering the equilibria in NH_4F–HF solutions, Osseo-Asare also explained the occurrence of the etch rate maximum as a function of NH_4F in these solutions. For a fixed concentration of HF, increasing the concentration of dissolved NH_4F has two major effects: (1) It increases the total concentration of dissolved fluoride which in turn increases the surface

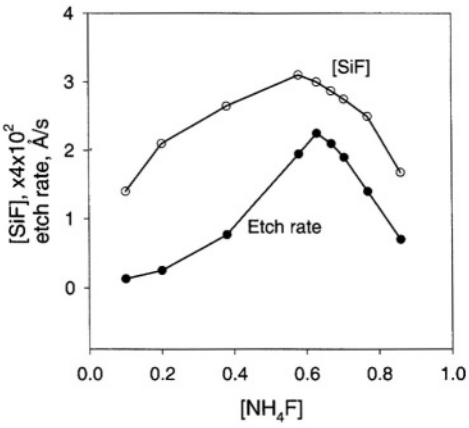

FIGURE 4.39. Comparison of the dependence of the surface fluoride cocnentration ([SiF], M) and the etch rate on the NH_4F concentration (M) in the SiO_2–H_2O–HCl–NH_4F–NH_4Cl system; etch rate data from Judge.[57] After Osseo-Asare.[123] (Reproduced by permission of The Electrochemical Society, Inc.)

concentration of adsorbed fluoride and (2) it increases the pH and this decreases [SiF]. At low $[NH_4F]$, the fluoride concentration effect predominates and etch rate increases with $[NH_4F]$, whereas at relatively high $[NH_4F]$ the pH effect dominates and a decline in etch rate is observed.

According to Monk *et al.*,[451,800] it is difficult to use the rate equations that are based on the concentrations of the ionic or complex species in the solutions because of the uncertainties in the equilibrium data for high concentrations of HF. It is more convenient to describe the etch rate equations only as a function of HF in the mathematical forms using simply the concentration of HF. Depending on the specific etching systems, etch rate equations can be expressed as follows:

$$\text{Non-first-order kinetics} \qquad R = kC^n_{\text{HF}} \tag{4.24}$$

$$\text{Freundlich adsorption isotherm kinetics} \qquad R = k_1(1 + k_2 C^a_{\text{HF}})C^b_{\text{HF}} \tag{4.25}$$

$$\text{Langmuir–Hinshelwoodkinetics} \qquad R = k_1 C_{\text{HF}}/(1 + k_2 C_{\text{HF}}) \tag{4.26}$$

Data fitting to Eq. (4.24) $R = aC^n$ gives n = 1.37–1.5 for etching of thermal oxides at high HF concentrations and n = 0.75–1.07 at low concentrations as well as in BHF solutions. For low-temperature CVD films, it is in the range of 1.6–2.0 in HF solutions and 0.5–1.0 in buffered solutions. The dependence of etch rate on HF concentration, according to Monk *et al.*,[451] is due to the two-step etch reaction. In the first step, hydrogen ions break up the siloxane bonds to form silanol species on the surface, and in the second step the fluorinated species attack the silicon in the silanol species. At low concentrations, because of the limited supply of the reactants the silicon bonds are broken in series resulting in a first-order reaction. However, at higher HF concentrations, more reactant species will be available so the rate-limiting reaction may take place with two reactants simultaneously resulting in a second-order reaction.

4.7.3. Effect of Oxide Structure

The many etch rate equations described above are empirical in nature even though mechanistic arguments are made in each specific case. One important omission in these quantitative formulations on the etching kinetics is the lack of consideration of the effect of the structure of silicon oxides. As shown in Fig. 4.40, etch rate can vary over more than three orders of magnitude for different types of oxides. It increases with increasing disorder of the oxide structure with the most ordered oxide, that is, quartz, having the lowest etch rate. The structural disorder of the silicon oxide can be due to impurities, partial oxidation of the silicon atoms, and degree of crystallinity.

Qualitatively, the effect of oxide composition has been considered in many investigations, particularly those related to the etching of doped glasses. Tenny and Ghezzo[148] suggest that the etch rate of doped glasses is limited primarily by the dissolution of the SiO_2 in the glasses since the etch rate increases with increasing dopant concentration for phosphosilicate and arsenosilicate glasses in BHF and for borosilicate glasses in dilute BHF. According to Brown and Kennicott,[425] the fact that B_2O_3–SiO_2 glasses

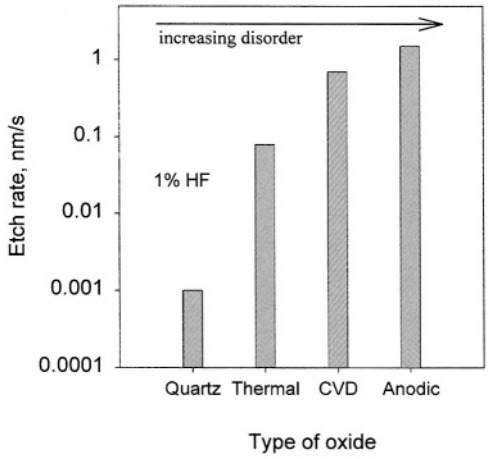

FIGURE 4.40. Etch rate of different oxides in 1% HF. The disorder in composition and structure increases from quartz to anodic oxide.

dissolve faster in HF solution than in BHF solution is because B_2O_3 is hygroscopic and more soluble in water than is SiO_2.[425] The etching process of doped glasses may thus be seen as a combined result of the dissolution of the SiO_2 by fluoride species and that of the dopant oxide by water. This hypothesis is supported by the observations that (1) there is an initial increase in the etching rate of heavily doped glasses with increasing water content and (2) in BHF the etch rate maximum shifts to more dilute solutions with increasing dopant concentration. The relative contribution of the dissolution of B_2O_3 by water and the dissolution of SiO_2 by HF determines the overall etching rate of B_2O_3–SiO_2 glasses. The difference in the etch rates of the glasses with different dopants is then related to the relative solubilities of the dopant oxides.

Monk *et al.*[451] attributed the role of doping elements in the oxide to the electronic characteristics of the elements. Whether the doped atom is electrophilic or nucleophilic toward the Si atom governs how easily HF_2^- is coordinated with the Si atom. If the oxide film has an electrophilic dopant, the etch rate increases, and if it is nucleophilic, the etch rate decreases. In a PSG film the doped P atom, which has a valence of 5, has one valence electron more than Si. This means that a doped oxide can provide the electron to oxygen more easily than can a nondoped one. Therefore, the silicon–oxygen bond in P-doped oxide can be broken more easily.

The presence of hydroxyl in silicon oxide causes a high etch rate since hydroxyl groups are nonbridging oxygen in the oxide network and a high concentration of hydroxyl groups means looser structure. If a thermal oxide is hydrolyzed, the etch rate becomes much higher (Fig. 4.12).[427] Also, the relatively high etch rates of anodic oxides (Fig. 4.2) can be attributed to their loose structure due to the high concentration of water and hydroxyl groups in the oxides.

Nielsen and Hackleman[380] found that the dissolution of thermal SiO_2 in BHF solutions is impeded by the application of a cathodic potential of 2–4V across the oxide film and postulated that a layer of partially reduced oxide is formed on the surface and

FIGURE 4.41. Disruption of silicon oxide structure due to the presence of an impurity element. (a) Structure without impurity; (b) structure with impurity.

this layer is not soluble in the HF solution. This layer is, however, soluble in HF/HNO_3 solutions, which have strong oxidizing power. Thus, for an oxide that contains nonsaturated silicon bonds due to incomplete oxidation, the etch rate is relatively low but can be increased with addition of oxidation agents such as HNO_3; to remove the partially oxidized silicon atoms requires that they first be fully oxidized. This mechanism explains well why $HF + HNO_3$ is a sensitive etching solution for differences in density, stoichiometry, bond strain, and impurities in silicon oxides; it etches various types of glasses and mixed oxide layers much more rapidly than silicon oxide.[115,232] It may also explain why a layer about 1 nm thick, which has a much lower etch rate than the bulk oxide, is left on the surface of the silicon substrate at the end of etching in some circumstances.[368] A large fraction of the silicon atoms within a region of a few monolayers at the silicon/oxide interface is known to be only partially oxidized for both thermal and anodic oxides.[74,338]

The structure of silicon oxide, consisting of a three-dimensional network of SiO_2 constructed from polyhedra of oxygen and silicon ions, may exhibit various crystalline and vitreous forms depending on the composition and degree of crystallinity. The crystalline forms, such as quartz, due to their highly compact structure and uniform Si–O bond strength, are more resistant to chemical dissolution than the vitreous forms. Different forming conditions and alloy elements affect the etch rate by affecting either the compactness of the structure or the distribution of the valence electrons which determines the strength of the bonds and the openness of the structure. For example, a substitutional impurity with a valence of 3 may create irregularity in the structure and nonbridging bonds as shown in Fig. 4.41 and change the bond strength of the neighboring Si–O bonds. Also, the presence of an alloying element may enhance or inhibit the dissolution of the silicon oxide depending on the bond strength of A–O and solubility of the alloying element A in the solution.

This page intentionally left blank

5

Anodic Behavior

5.1. INTRODUCTION

The anodic behavior of silicon electrodes has been extensively studied due to its importance in a number of applications involving passivation, oxide film, etching, cleaning, photoelectrochemical cells, and porous silicon. A wide range of phenomena have been characterized, such as current multiplication and the change of dissolution valence, the occurrence of passivation and current oscillation, and the drastic variation in the distribution of reactions on the silicon surface from extremely uniform, which results in electropolishing, to extremely nonuniform, which results in the formation of porous silicon. These phenomena can be categorized according to two principal aspects: (1) the chemical nature of reactions on the atomic scale and the experimentally observed kinetic quantities (such as current density), which are the average of the atomistic events, and (2) the physical nature of the silicon surface (such as orientation, geometry, and homogeneity), and its evolution during the anodic reactions. The materials described in this chapter are limited to the first aspect. The physical nature of the surface in terms of morphology, geometry, and transformation is dealt with in Chapter 7 on Etching of Silicon and Chapter 8 on Porous Silicon. The anodic oxide films formed under large potentials are discussed separately in Chapter 4. Those formed at relatively low potentials of less than a few volts, are discussed in the chapter.

5.2. CURRENT–POTENTIAL RELATIONSHIP

Anodic behavior of silicon can best be characterized by i–V curves. Neglecting the details associated with a silicon substrate such as doping, the current–potential relationship of silicon in aqueous solutions can be considered to be principally determined by the pH and HF concentration as illustrated in Fig. 5.1. In nonalkaline and nonfluoride aqueous solutions, silicon as an electrode is essentially inert, showing a very small current at anodic potential due to the presence of a thin oxide film. In alkaline solutions, silicon is also passivated by an oxide film at anodic potentials but is active below the passivation potential, V_p. In fluoride solutions, the silicon electrode is active in the whole anodic region as shown by the large anodic current.

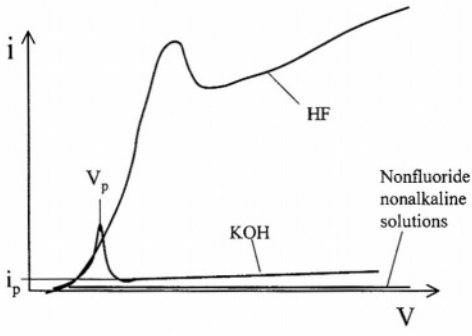

FIGURE 5.1. Typical *i–V* curve in HF and nonfluoride, nonalkaline solutions.

5.2.1. Fluoride Solutions

The *i–V* curves, as shown in Fig. 5.2, are different for *p*-Si and *n*-Si in the dark due to the difference in the concentrations of holes, which are required for the anodic reactions, in the two types of materials.[73] Large currents can be obtained on *p*-Si by anodic polarization which gives a forward bias to increase the concentration of holes at the surface. On the other hand, for nondegenerated *n*-Si the anodic current is limited by the availability of holes. The *i–V* curve for n-Si becomes identical to that for *p*-Si when *n*-Si is illuminated at a sufficiently high light intensity.

The anodic polarization curves of *p*-Si or strongly illuminated *n*-Si in fluoride solutions are typically characterized by two peak currents, J_1 and J_2, and two plateau currents, J_3 and J_4 as shown in Fig. 5.2. At anodic potentials up to that at J_1, the electrode behavior is characterized by an exponential dependence of current on potential and by the uneven dissolution of silicon surface leading to the formation of porous

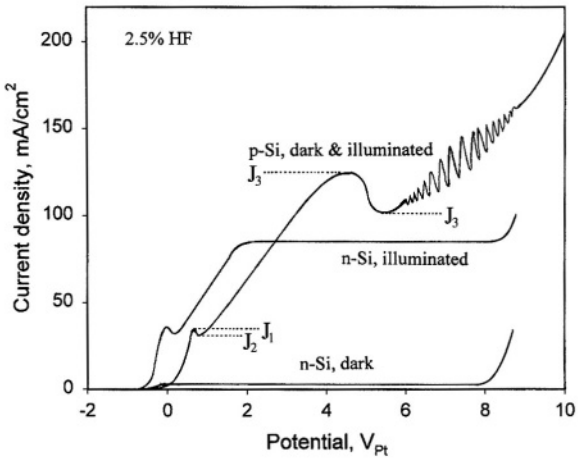

FIGURE 5.2. Current–potential curves for dark and illuminated *p*- and *n*-Si electrodes in a 2.5 wt % HF electrolyte. After Lehmann and Foll.[73] (Reproduced by permission of The Electrochemical Society, Inc.)

silicon (PS).[2] At potentials more positive than that of J_1, it is characterized by the formation and dissolution of a surface oxide film resulting in a smooth surface, referred to as electropolishing.[33] The current in this region indicates the growth and dissolution rates of the oxide film. Also, the current at potentials more positive than that of J_1 is not constant, indicating that the oxide formed at different potentials has different properties. The values of the characteristic currents, J_1 to J_4, which may occur at different potentials for *p*-Si and *n*-Si, are a function of electrolyte composition but are largely independent of doping, since they are determined by the properties of the anodic oxide. At potentials more positive than the second plateau current, J_4, current oscillation may occur. Also, oxidation of water becomes an important reaction at these positive potentials in addition to the oxidation reaction of the silicon electrode. The surface resulting from dissolution at potentials higher than the second peak is brightly smooth, while that produced between the first and second peak is relatively less smooth.[38]

The anodic behavior is the same for *p*- and *n*-type materials when the rate of carrier transfer between the surface and the semiconductor bulk is sufficiently fast.[2,69,700,763] The *i–V* curves of the two materials, when the current is not limited by the supply from holes in the semiconductor, are largely identical except for a shift along the potential axis for materials of different doping levels. For *n*-Si, large currents can be achieved by either sufficient illumination intensity or degenerate doping. Thus, the reaction processes, which are the same for all types of silicon, are determined by the chemical nature of silicon material and the electrolyte independent of the electronic nature of silicon. Different doping conditions affect the rate of charge transfer between the surface and the semiconductor but not the chemical nature of the reactions.

Figure 5.3, as a detailed *i–V* curve around the first peak, shows that the current increases exponentially with increasing potential from OCP.[2] It breaks off from the exponential dependence on potential at large overpotentials, exhibits a peak, J_1, and then attains a relatively constant value at J_2. Examination of the surface of the samples,

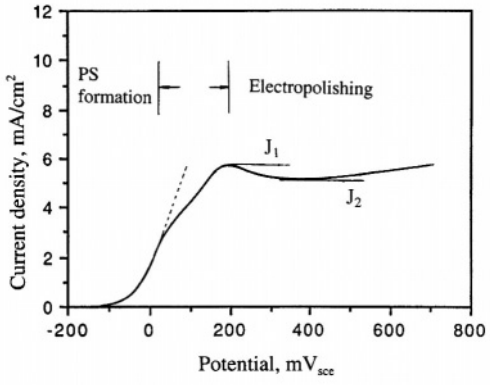

FIGURE 5.3. Current–potential curve of p^+ silicon sample in 1% HF solution with potential sweep rate of 2 mV/s. After Zhang *et al.*[2] (Reproduced by permission of The Electrochemical Society, Inc.)

which are anodized at different potentials in this region, indicates that porous silicon forms in the exponential region but not at potentials more positive than the peak potential. The potential corresponding to the maximum slope of the i–V curve is about the upper limit for formation of a uniform porous silicon layer.[2] At potentials between the maximum slope and the current peak, the porous layer may still form but its surface coverage is not uniform. The anodic behavior, in terms of the morphology of the surfaces, is characterized by the transition from porous silicon formation to electropolishing with increasing potential from OCP to more positive than that of the current peak.[2,33]

The potentials of the two current peaks, J_1 and J_2, extend to more positive values for lowly doped p-Si. A difference of as much as 1 V for the first current peak and about 1.5 V for the second is found between lowly and highly doped p-type materials as shown in Fig. 5.4.[700] This is attributed to a larger potential drop in the space charge layer of the lowly doped sample.

For n-Si, the onset potential at which current rises sharply in the dark marks the breakdown of the barrier layer and initiation of interface tunneling on the silicon surface.[8] The breakdown potential depends on the doping level of the material: the lower the doping, the higher the breakdown potential as shown in Fig. 5.5.[12,38,42,858] For n-Si at potentials negative of the breakdown potential, the anodic reactions require illumination to supply holes. When the current is lower than J_1 independent of the potential, the dissolution results in the formation of porous silicon. At a current higher than J_1, the reactions associated with electropolishing become dominant. Also, the peak current J_1 for n-Si tends to increase with decreasing scanning rate due to the increased surface area as a result of surface roughening related to PS formation.[8]

Effect of Solution Composition. Figure 5.6 shows that the i–V curves greatly vary with solution composition, particularly the fluoride concentration and pH value.[939] The characteristic current values, J_1 to J_4, as a function of pH and fluoride

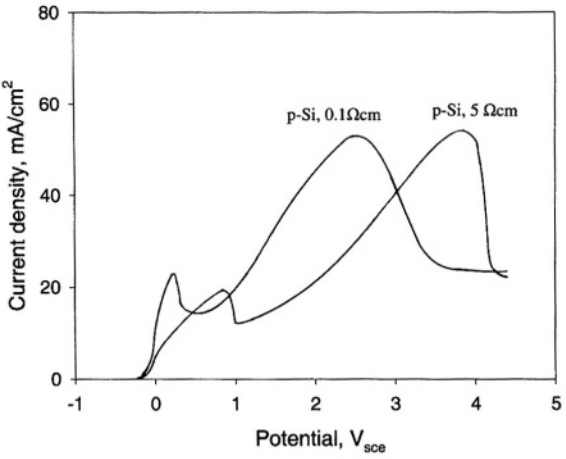

FIGURE 5.4. Current–potential curve obtained for (a) p-type silicon (0.075–0.125 Ωcm) and (b) p-type silicon (4–6 Ωcm) in oxide etchant at a dilution of 0.05 in 6.5% HF + 35% NH_4F. (Reprinted from Eddowes.[700] © 1980, with permission from Elsevier Science.)

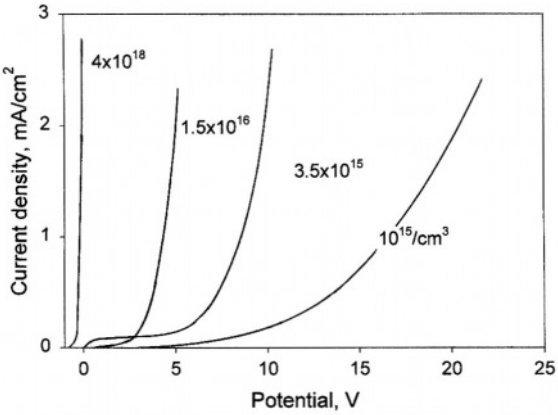

FIGURE 5.5. Current density versus electrode potential for various donor concentrations in 5% HF. After Theunissen.[42] (Reproduced by permission of The Electrochemical Society, Inc.)

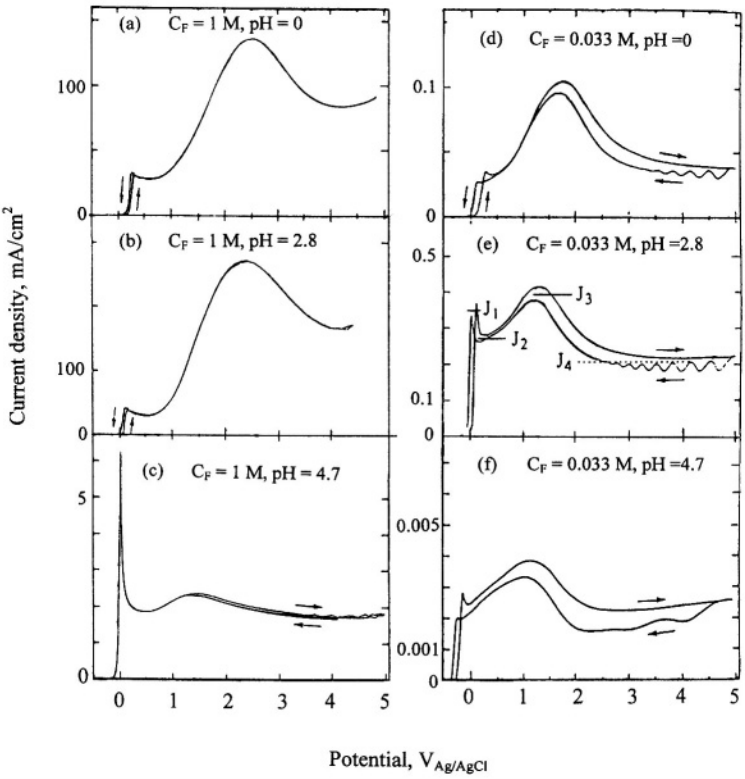

FIGURE 5.6. Voltammograms obtained for a (100)-oriented *p*-Si electrode in various electrolytes. Rotation rate 3000rpm. C_F = 1M (a–c) and 0.033M (d–f). pH = 0 (a, d), 2.8 (b, e), and 4.7 (c, f). Sweep rates 100mV/s (a, b), 10mV/s (c), 1mV/s (d), 5mV/s (e), and 0.05mV/s (f). (Reprinted from Chazalviel *et al.*[939] © 1991, with permission from Elsevier Science.)

concentration are shown in Fig. 5.7. All the currents increase with increasing fluoride concentration but exhibit a maximum. The plateau currents, i.e., J_2 and J_4, which are determined by the chemical dissolution rate of the oxide film, have been empirically fitted to pH and fluoride concentration:

$$J_2 \sim \left\{(0.1[HF_2^-] + 0.01[HF])^{-1} + (10[HF_2^-])^{-1}\right\}^{-1} \tag{5.1}$$

$$J_4 \sim 10[HF_2^-][H^+]^{0.5} \tag{5.2}$$

The general features of the i–V curves at potentials positive to those of J_1 in fluoride solutions are relatively insensitive to the presence of anions such as Cl^- or SO_4^{2-}.[939] The effect of cations is, however, significant as shown in Fig. 5.8 for different types of cations.[861,936] Thus, the dissolution rate of the oxide is different in solutions containing different cations, which is attributed to the change of the aggressiveness of the electrolyte since the property of the oxide is little affected by the electrolyte in which it is formed. According to Hassan *et al.*,[861] the effect of cations on the dissolution kinetics is via adsorption on the oxide surface resulting in an increased polarization of the Si–O bonds. The largest increase in current is obtained with the cations that are most easily adsorbed. The change in reaction rates in the presence of the cations can also be partially attributed to the difference in the solubilities of the corresponding fluorides and silicates.[936] Thus, the large hysteresis on the i–V curves of Rb^+ and K^+ may be due to the formation of an insulating salt layer of Rb_2SiF_6 and K_2SiF_6, respectively, whereas the decreased current on addition of Ca^{2+}, Ba^{2+}, or Al^{3+} may be related to their tendency to form low-solubility fluoride compounds or complexes.

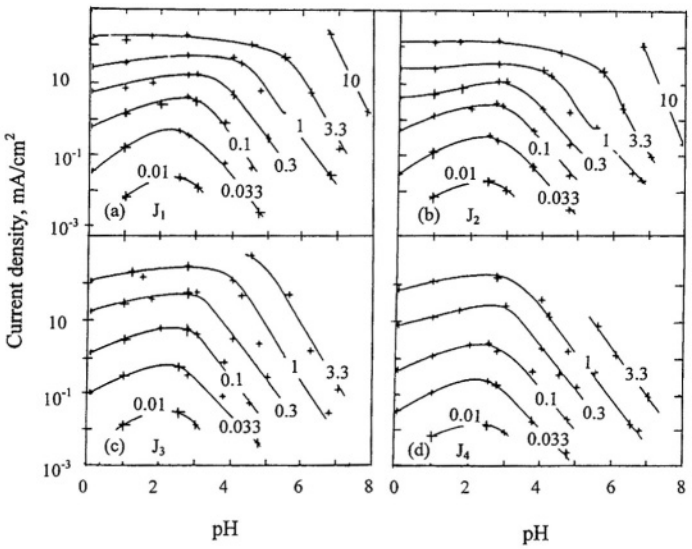

FIGURE 5.7. Plots of the characteristic current densities J_1 (a), J_2 (b), J_3 (c), and J_4 (d) as a function of pH. For various values of C_F (labeled on the curves in units of mol/liter). (Reprinted from Chazalviel *et al.*[939] © 1991, with permission from Elsevier Science.)

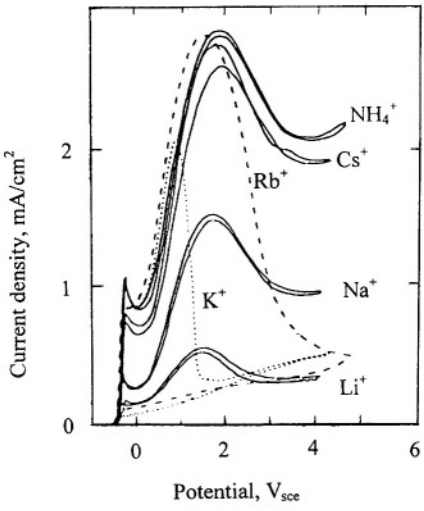

FIGURE 5.8. Voltammograms of a rotating *p*-Si electrode in fluoride solutions containing 1 M alkali metal chlorides (scan rate 50 mV s^{-1}). C_F = 0.33 M, pH 2.9, N = 324 rpm. (Reprinted from Hassan *et al.*[936] © 1995, with permission from Elsevier Science.)

In nonfluoride acids such as H_2SO_4 solutions, the anodic current is due to the formation and thickening of the oxide film.[353] Addition of fluoride species to these solutions results in *i–V* behavior similar to that in HF solution.[2,253]

5.2.2. *Alkaline Solutions*

The anodic behavior of silicon electrodes in alkaline solutions is characterized by the formation of an oxide film and passivation of the surface. Typical *i–V* curves of *n*- and *p*-type silicon in KOH solution are shown in Fig. 5.9.[129] Silicon surface is passivated at an overpotential marked by a small current peak. The potential at the current peak is called the passivation potential, V_p, and in the systems shown in Fig. 5.9 it is –0.92 and –0.71 V_{sce} for *n*- and *p*-type silicon, respectively. The small current at

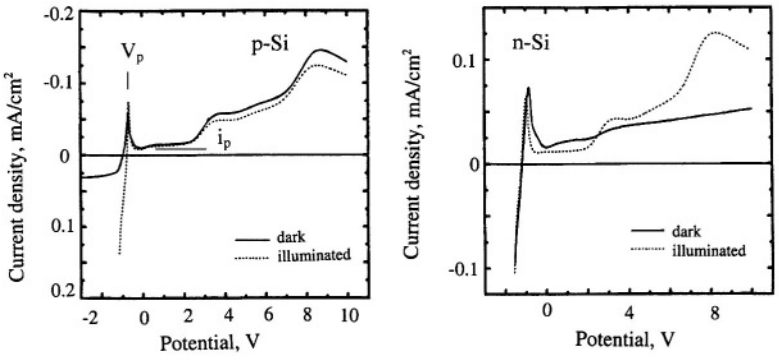

FIGURE 5.9. *i–V* curves of *p*-Si and *n*-Si in 2 M KOH in the dark and illumination. After Chen *et al.*[129] (Reproduced by permission of The Electrochemical Society, Inc.)

potentials more positive than V_p is called the passivation current, i_p, which, at a steady state, reflects the dissolution rate of silicon in the passive region.

For *p*-Si, the *i–V* curves are generally independent of illumination and there are two relatively steep increases in current at 3.7 and 8.7 V_{sce}. For *n*-Si, the current in the passive region increases steadily from 0 to 10 V in the dark but it is similar to that for *p*-Si under illumination. Also, the *i–V* curves are essentially identical for samples with different doping levels.[925] The data show, similar to the fluoride solutions, that the basic features of the anodic behavior in alkaline solutions are determined by the chemical nature of the silicon material but not by the electronic properties. The *i–V* curves in other alkaline solutions are in general similar to those shown in Fig. 5.9 (see Chapter 7).

5.3. PHOTOEFFECT

Illumination with light having a wavelength larger than the band gap of silicon generates a photocurrent under an anodic potential on an *n*-Si electrode but has essentially no effect on *p*-Si, as would be expected from the basic theories of semiconductor electrochemistry.[69,962] However, the photocurrent may not be sustained because of the formation of an oxide film, which passivates the silicon surface to various degrees depending on the electrolyte composition. In solutions without fluoride species, the photocurrent is only a transient phenomenon before the formation of the oxide film. In fluoride solutions, in which oxide film is dissolved, a sustained photocurrent can be obtained.

The anodic photocurrent of *n*-Si in aqueous solutions in the absence of fluoride decays very rapidly due to the formation of an oxide film.[77] It decays less rapidly in the presence of a reducing agent which can compete efficiently for the holes from the valence band and slow down the rate of oxidation. Ferrate ions and iodine ions have been found to compete favorably with the oxidation of the silicon surface.[77,600] On the other hand, in solutions containing a small amount of fluoride ions insufficient to completely remove the oxide film, the photocurrent exhibits a fast decay. According to Matsumura and Morrison,[77] the rapid decay of the photocurrent in solutions with a small amount of fluoride is due to the catalytic effect of fluoride ions at the Si/SiO_x interface.

The photocurrent in nonfluoride solutions is affected by the amount of preanodic current passed through the sample as shown in Fig. 5.10.[873] It is also seen that the photocurrent onset potential is shifted to more anodic values with formation of an oxide film and the amount of shift is related to the thickness of the film. This shift is due to the potential drop across a growing oxide layer and is one of the reasons for the difference between the photocurrent onset potential and the flatband potential.[77,695]

When the concentration of fluoride is sufficiently high to prevent the formation of an oxide film, sustained photocurrent can be obtained. The photocurrent value increases with increasing light intensity until it reaches a value which is double that in the absence of fluoride in the solution as shown in Fig. 5.10 due to electron injection into the conduction band resulting in current multiplication.[873] At certain higher light intensities, depending on fluoride concentration, photocurrent will again

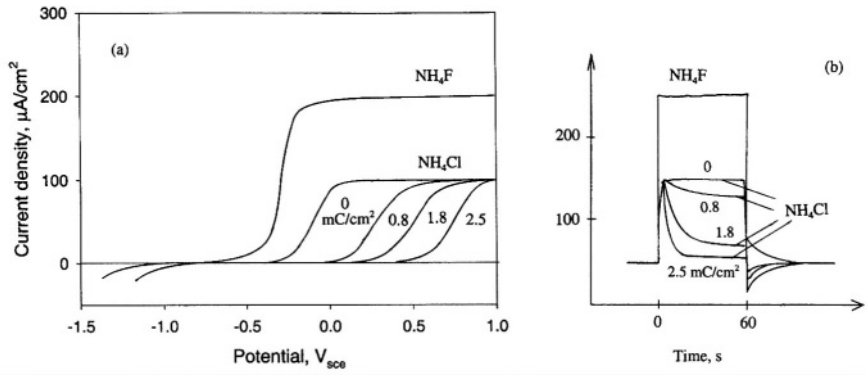

FIGURE 5.10. (a) Photocurrent voltage curves in 1 M NH_4Cl and 1 M NH_4F at pH 4.5; (b) photocurrent transients at +0.5 V. Data in NH_4Cl also show the effect of oxide layer formation as a function of the amount of coulombs having passed before the experiment. (Reprinted with permission from Gerischer and Lubke.[873] © 1987 Wiley-VCH.)

decay because the rate of formation of oxide film becomes faster than the rate of its dissolution.

The current multiplication due to the presence of fluoride depends on the pH of the solution, as shown in Fig. 5.11.[873] It decreases with increasing pH and almost disappears above pH 7. At high pH, formation of oxide prevents direct reaction of silicon with fluoride species, and the pH value at which this occurs decreases with increasing light intensity.

5.3.1 Quantum Yield and Surface Recombination

The photocurrent quantum efficiency, Y, of n-Si electrode in fluoride solutions depends on current as shown in Fig. 5.12.[73] It is high at low current densities and decreases with increasing current densities to a plateau value of about 2; Fig. 5.12 shows

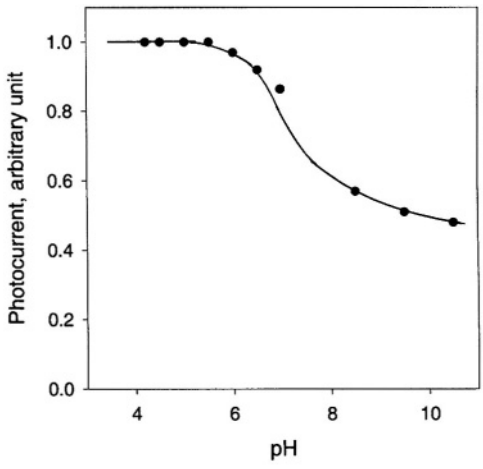

FIGURE 5.11. Photocurrents at +0.2 V as a function of the pH in 1 M NH_4F solution. (Reprinted with permission from Gerischer and Lubke.[873] © 1987 Wiley-VCH.)

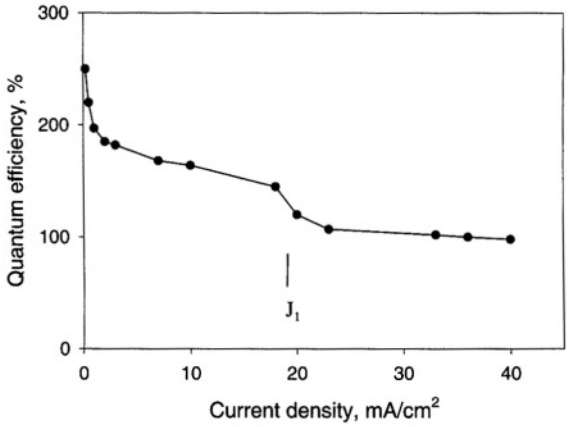

FIGURE 5.12. The ratio n of collected charge carriers per incident photon as a function of the current density for 2.5% HF in aqueous solution. After Lehmann and Foll.[73] (Reproduced by permission of The Electrochemical Society, Inc.)

that the plateau region is between 1 mA/cm^2 and J_1 in 2.5% HF. It drops to 1 at currents higher than J_1. At very low light intensities the quantum efficiency approaches 4, that is, current quadrupling occurs, as shown in Fig. 5.13.[599] This change of quantum efficiency with light intensity does not occur in nonfluoride solutions as shown in Fig. 5.14.[74]

Figure 5.15 shows the spectral response of n-Si in a solution of CH_3OH-1.0 M $LiClO_4$-$LiClO_4$-5 mM dimethylferrocene$^{+/0}$ solution. The semiconductor/electrolyte

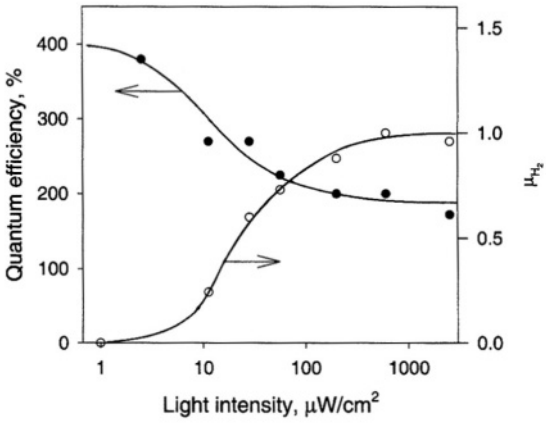

FIGURE 5.13. Intensity dependence of the quantum efficiency Q for n-Si (111) and the corresponding hydrogen production efficiency η_H measured in the ring-disk arrangement. Electrolyte: 1.0 mol dm^{-3} NH_4F, pH 4.7. λ: 632.8 nm. Rotation rate: 20 Hz. (Reprinted from Blackwood *et al.*[599] © 1992, with permission from Elsevier Science.)

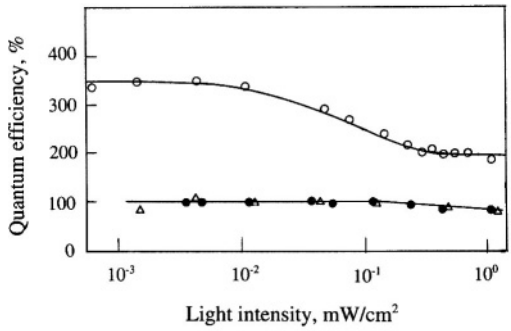

FIGURE 5.14. Quantum efficiency of the photocurrent for an illuminated *n*-Si electrode measured in various solutions at 1.0 V versus SCE and 22 °C: (○) 1 M NH_4F (pH 4.9); (●) 1 M NH_4F (pH 9.6); (△) phthalate buffer (pH 4.50). (Reprinted from Matsumura and Morrison,[74] © 1992, with permission from Elsevier Science.)

interface has a very low surface recombination velocity and gives a photo response similar to that at a silicon/metal interface. The long wavelength spectral response is dominated by the collection properties of the photo generated minority carriers. The response at short wavelength (200–600 nm), at which the penetration depth is smaller, is affected by both the collection properties of the majority and minority carriers. Also, at short wavelength the photo generated carriers are influenced by both the field and concentration gradient. This leads to a wavelength dependent majority carrier photocurrent, which opposes the minority carrier photocurrent, resulting in a lowered quantum yield at short wavelengths as shown in Fig. 5.15.

Photocurrent on *n*-Si can also be caused by surface generation processes with sub-band-gap light illumination.[400] Figure 5.16 shows that the quantum yield from sub-

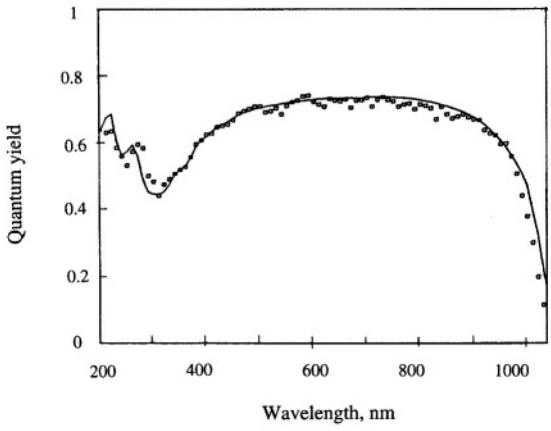

FIGURE 5.15. Photo spectral response of the *n*-Si in CH_3OH-1.0 M $LiClO_4$-5 mM dimethylferrocene$^{+/0}$. (Reprinted with permission from Kumar and Lewis.[584] © 1990 American Chemical Society.)

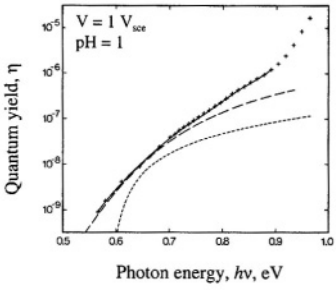

FIGURE 5.16. Quantum yield as a function of photon energy. The points are experimental and the full curve is based on calculation. The fast increase of η near $h\nu = 0.95$ eV is due to the onset of band gap transitions. After Chazalviel.[400] (Reproduced by permission of The Electrochemical Society, Inc.)

band-gap light illumination on *n*-Si in 1 M HCl or KCl solutions is very low, below 0.9 eV. At photoenergy above 0.9 eV, a relatively large increase in the current occurs due to the onset of band gap transition. It is increased by a factor of 5 by changing the pH from 1 to 4.7. However, the subband photocurrent is still several orders of magnitude smaller than the dark current.

A similar effect is observed in acetonitrile solutions.[935,942] Subband photocurrent slowly increases with time due to the development of surface states by the slow oxidation of the surface. It is greatly enhanced by monolayer quantity of metal deposits. Also, it is affected by the redox couples present in the solution. According to Chazalviel,[400,942] the subband photocurrent is caused by the presence of surface states associated with adsorbed ions which lie 0.7–0.9 eV below the conduction band. The surface generation by subband photon excitation can arise via two processes: either by electron excitation from the valence band into the empty surface states or by electron excitation from the occupied surface states into the conduction band. The relative contribution of these two processes is different for *p*-Si and *n*-Si and different quantum yields for the two materials are found.

In the absence of surface recombination and with a fast rate of electron transfer, the photocurrent increases with increasing potential when the depletion layer starts to form and a saturation current is quickly reached. On the other hand, with a fast surface recombination or in the case of slow electron transfer reactions, the apparent onset of the photocurrent is shifted to higher bias and the saturation current is only reached at larger band bending.[808,1154] Among other factors, surface treatment strongly affects the photocurrent onset potential due to its effect on surface states which determine the recombination process.[600,717,1154]

Surface recombination for a well prepared silicon surface in HF solutions is very low. The surface recombination velocity of silicon/HF electrolyte, which can be as low as 0.25 cm/s, is lower than those of oxide-covered surface, in air and in solutions.[73,648] For example, surface recombination velocity of an *n*-Si in CH_3OH + 1 M $LiClO_4$ solution is about 100 cm/s.[585] Such low values found in HF solutions are due to surface termination by the covalent Si–H bonds, which leaves virtually no surface dangling bonds to act as recombination centers. The hydrogen-terminated surface is rather stable as it shows low recombination velocities in different acids. Figure 5.17 shows that the recombination velocity increases with acid concentration and is largely similar for the different acids, indicating molarity rather than pH is responsible for the change in veloc-

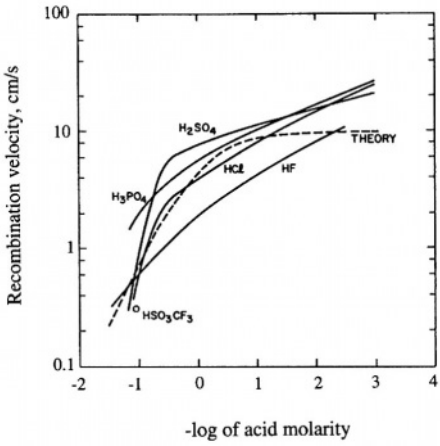

FIGURE 5.17. Surface-recombination velocity for properly prepared surface when immersed in various acids. The dashed theory line is an acid–base equilibrium model. After Yablonovitch.[648] (Reprinted with permission.)

ity.[648] On the (100) surface the recombination is 50% faster than on the (111) surface. Also, the change in velocity with concentration is reversible on the time scale of 15 min, which is explained by Yablonovitch *et al.*[648] as due to the acid–base equilibrium associated with the interaction of the acids with a small density of defects still present on the surface.

The surface recombination of silicon electrode in 0.1 M Na_2SO_4 involves one discrete recombination center as shown in Fig. 5.18 which can be described by Eq. (1–40).[182] In H_2SO_4 and HF + NH_4F solutions, the surface recombination curve is similar to that in Fig. 5.18.[61] The recombination is attributed to the surface states

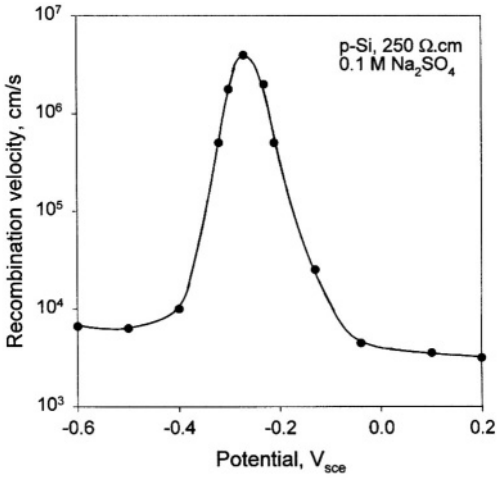

FIGURE 5.18. Experimental curve of the surface recombination velocity versus electrode potential of *p*-Si in 0.1 M Na_2SO_4. After Memming.[182]

involved in the reactions with fluoride species in the solution. Presence of mettalic contaminants can strongly affect rate of recombination.[1016] An increase of 100 folds in the rate of recombination is found with the presence of 100 ppb Cu in the solution.

The occurrence of the recombination peak shown in Fig. 5.18 can be qualitatively explained by the relative concentrations of the majority and minority carriers.[158] Recombination requires availability of both majority and minority carriers. With small band bending the number of minority carriers at the surface is small, resulting in low surface recombination. On the other hand, with large band bending the minority carriers created by light or injection cannot recombine at the surface because the majority density is low. At a certain bending condition, when the density of both types of carriers is large, the recombination reaches a maximum. The width of the recombination peak depends on the relative distribution of the potential drop in the space charge layer to that in the rest of the interface region.[278] The recombination peak for silicon electrodes in various electrolytes can be widened with increasing dopant concentration or increasing oxide film thickness, which causes an increase in the relative amount of the applied potential dropped across the Helmholtz layer and the oxide film.

Figure 5.19 shows that for *n*-Si in 0.1 M $K_4Fe(CN)_6$ + 0.5 M KCl at pH 9, the density of surface recombination centers increases with increasing light intensity.[94,808] These recombination centers are suggested to be physically associated with the oxidation intermediates in the oxide formed under illumination.

5.4. EFFECTIVE DISSOLUTION VALENCE

The effective dissolution valence is defined as the average number of electrons flowing through the external circuit per dissolved silicon atom. It reflects the nature of the reactions during the dissolution processes, e.g., the extent of electrochemical reactions relative to the chemical reactions. For silicon, the effective dissolution valence of

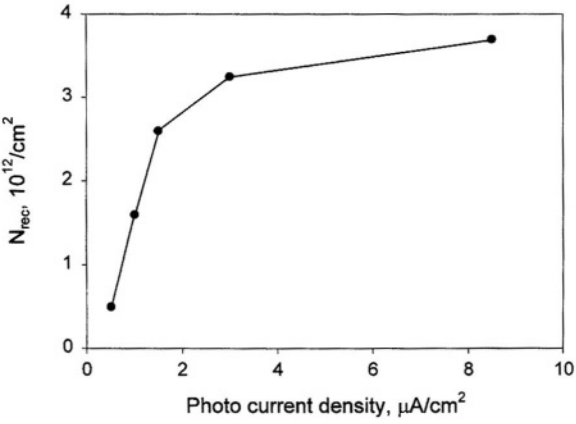

FIGURE 5.19. The density of recombination centers N_{rec} versus the plateau photocurrent density. 0.5 M KCl + 1 M NH_4F + $K_4Fe(CN)_6$. After Oskam *et al.*[808]

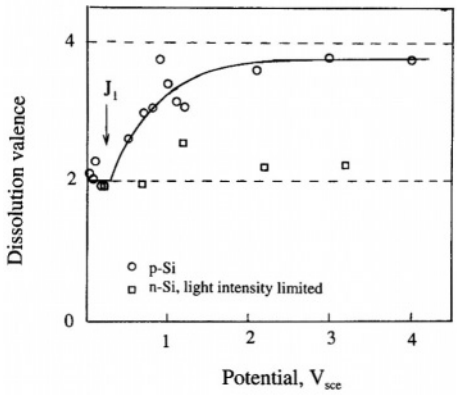

FIGURE 5.20. Dissolution valence for controlled potential oxidation of (○) *p*-type silicon (0.075–0.125 Ωcm) and (□) *n*-type silicon (0.375–0.625 Ωcm) under illumination intensity limitation, versus applied potential. (Reprinted from Eddowes.[700] © 1991, with permission from Elsevier Science.)

4 indicates that the dissolution process is completely electrochemical, whereas effective valence less than 4 indicates the involvement of chemical reactions. The effective dissolution valence of silicon has been found to vary with silicon material, solution composition, anodic polarization, and illumination conditions.

In fluoride-containing solutions the dissolution valence varies from 2 in the exponential region to near 4 in the electropolishing region as shown for *p*-Si in Fig. 5.20.[700] For *n*-Si the dependence of dissolution valence on potential varies with illumination intensity. At high illumination intensity, when the process is not light intensity limited, the variation of n with potential is observed to be similar to that of *p*-Si. For a given solution the dissolution valence increases with current for all types of materials as shown in Fig. 5.21.[12] There is a sharp increase in n at the current density corresponding to the first peak current density J_1. The current range of sharp change shifts to higher

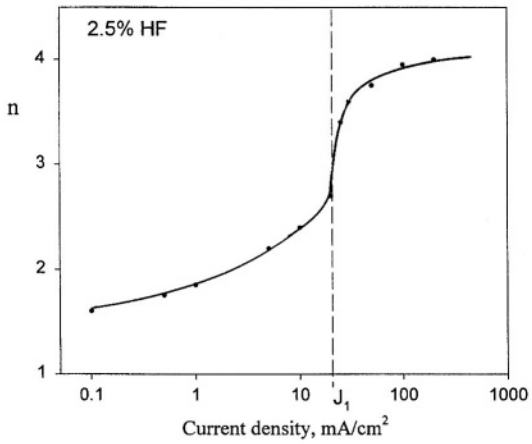

FIGURE 5.21. Effective dissolution valence of *p*-Si and *n*-Si as a function of anodic current density in 2.5% HF. (Reprinted from Lehmann.[12] © 1993, with permission from Elsevier Science.)

values with increasing HF concentration because J_1 increases with HF concentration.[2,40,939] Figure 5.21 also shows that the dissolution valence is less than 2 at relatively low current densities for a given solution. This is due to the chemical dissolution of the porous silicon formed on the surface (see Chapter 8).

The value of dissolution valence in the electropolishing region is somewhat lower than 4 as shown in Figs. 5.20 and 5.21. This indicates that hydrogen reaction, which is a chemical reaction, still occurs at such high anodic potentials, where the reactions are characterized by the formation and dissolution of an anodic oxide film.

In alkaline solutions, the effective dissolution valence at OCP, as shown in Table 5.1, is zero and changes only very slightly with anodic polarization before the passivation peak; it is less than 0.4 at V_p. The dissolution reaction below the passivation potential is almost completely chemical.[22,108,109] The dissolution valence in the passive region in alkaline solutions, which is not found in the literature, is likely close to 4 since the growth of anodic oxide films should be identical to that in HF solutions (see Chapter 3).

The data in Table 5.1 show that for *p*-Si at cathodic potentials there is no participation of carriers and the reaction is almost 100% chemical such that the etching of silicon is characterized by the dissolution of one silicon atom and the evolution of two hydrogen molecules. For *n*-Si at cathodic potentials only a part of the evolved hydrogen is the result of directly reacting silicon and the rest is due to capturing the electrons from the semiconductor, which leads to a much reduced etch rate compared to that at OCP. Palik *et al.*[108] noted that the charges are not balanced for *n*-Si at cathodic potentials, meaning that some of the hydrogen gas is not collected during the experiment. One possibility is that some hydrogen may enter the silicon substrate, as has been reported to occur in HF solutions at cathodic potentials.[241] At

TABLE 5.1. Etch Rates and Ratios of Dissolved Si, H_2, and Carrier Involved in the Etching at Various Potentials Near OCP in 2M KOH at 22 °C[108]

Silicon (100)	Potential	Ratio, Si/H_2/carrier	Etch rate, Å/s
	OCP		
n, 6.3 Ωcm		1/2.12/0	0.88
	OCP-0.4 V		
p, 4.1 Ωcm		1/2.07/0.033	1.35
n, 0.17 Ωcm		1/2.61/4.11	0.06
n, 1.5 Ωcm		1/1.56/1.01	0.09
	$(OCP + V_p)/2$		
p, 6 Ωcm		1/2.17/0.53	0.67
n, 7.2 Ωcm		1/1.46/0.2	1.07
	$V_p - 0.1$ V		
p, 1–10 Ωcm		1/2.22/0.21	2.92
n, 1–10 Ωcm		1/0.74/0.45	2.23
	V_p		
p, 3 Ωcm		1/1.13/0.21	3.23
n, 4.6 Ωcm		1/1.22/0.48	2.15

anodic potentials between OCP and V_p, the data in Table 5.1 indicate that silicon etching with evolution of hydrogen is still the dominant reaction process. For *p*-Si, the ratio of Si/H_2/carrier changes little but the etch rate significantly increases with potential between OCP and V_p.

5.5. HYDROGEN EVOLUTION

Visible hydrogen evolution occurs in HF solutions at anodic potentials in the exponential region anodic of OCP.[2,34] The rate of hydrogen evolution substantially decreases as potential approaches the current peak. Hydrogen evolution (visually) ceases above the above current peak. Since hydrogen evolution is a reduction reaction and consumes electrons, it is responsible for an apparent dissolution valence smaller than 4 below the current peak. Thus, the effective dissolution valence can be used as a measure for the hydrogen efficiency. A silicon dissolution valence of 2 means 100% efficiency for hydrogen evolution, i.e., for every dissolved silicon atom one hydrogen molecule is generated.

Results from rotating a ring-disk electrode indicate that the efficiency of hydrogen evolution is near 100% in the exponential region but drops to about 50% at the first peak potential as shown in Fig. 5.22.[599,767] In addition, a considerable number of hydrogen molecules, corresponding to 10% to 13% efficiency, are generated throughout the electropolishing region. An equivalent of about 10% of the silicon atoms dissolve into the solution effectively divalent at potentials up to 10 V.[38,700] In the electropolishing region, silicon dissolution proceeds with oxide formation and dissolution of the oxide. An apparent dissolution valence less than 4 means that some silicon atoms are only partially oxidized in the oxide forming stage but the oxidation is completed during the dissolution stage.

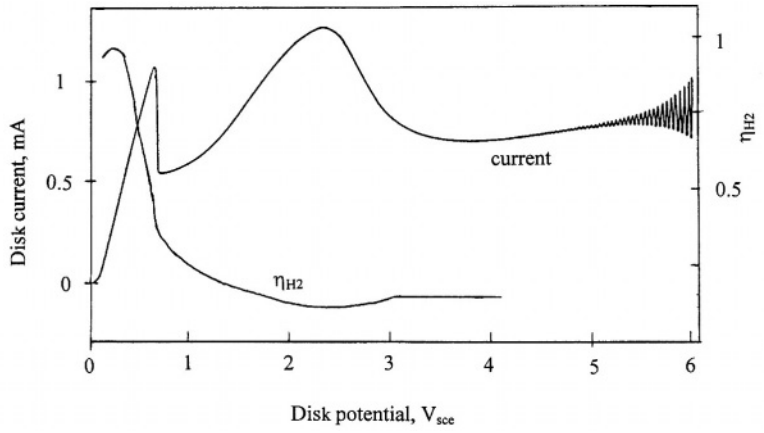

FIGURE 5.22. The *i–V* curve and efficiency for hydrogen evolution η_H during positive sweep of a *p*-Si (100) disk in 0.3 mol dm^{-3} NH_4F at pH 3.5. Rotation rate 40 Hz. Scan rate 10 mV/s. (Reprinted from Blackwood *et al.*[599] © 1992, with permission from Elsevier Science.)

For *n*-Si the efficiency of hydrogen evolution depends on illumination intensity as shown in Fig. 5.13.[599,695] The efficiency of hydrogen evolution is close to zero at low light intensity but increases with increasing light intensity to 100% at high light intensities. The increased efficiency of hydrogen evolution corresponds to a decrease of the quantum efficiency of the photocurrent from near 4 at low light intensities to about 2 at high light intensities.

The efficiency of hydrogen evolution and effective dissolution valence are directly correlated, and their relation varies with potential, illumination, and doping of the silicon. The overall relation among these two parameters and the factors are summarized in Fig. 5.23.

5.6. LIMITING CURRENT

The intrinsic limiting current for *n*-Si depends on the diffusion of the minority carrier as follows:

$$i_p^{lim} = qD_p p_0 / L_p \tag{5.3}$$

For an *n*-Si with doping of $10^{16}/cm^3$, L_p of 5–300 μm,[275,569] and D_p of $12.3\,cm^2/s$,[25] i_p^{lim} is on the order of 10^{-9}–$10^{-11}\,A/cm^2$. The dark limiting currents measured on silicon electrodes in electrolytes are usually several orders of magnitude larger than these values, as shown in Table 5.2. The large dark limiting current may be due to several causes such as surface states, electron injection from silicon oxidation intermediates, and interface tunneling by the redox species in the solution.

Due to the role of surface states, the dark limiting current of silicon electrode is extremely sensitive to surface defects and thus surface preparation. Any scratch even barely visible on the mirror like surface can result in a significant increase of the anodic limiting current. According to Chazalviel,[717] defects associated with surface treatment are primarily responsible for the large limiting current values reported in the literature. The effect caused by surface states may, however, be reduced by the formation of a

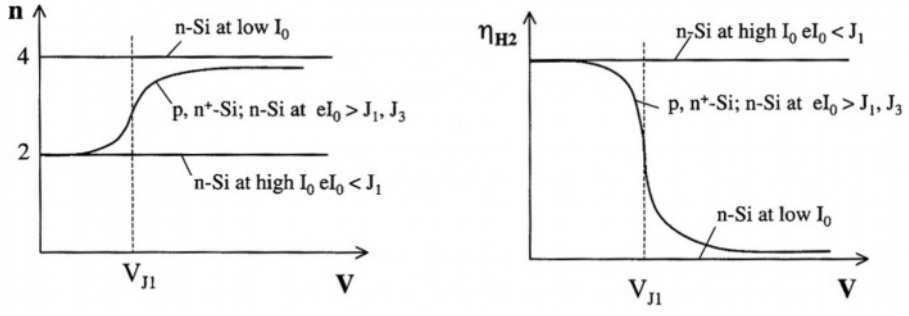

FIGURE 5.23. Summary of effective dissolution valence and hydrogen evolution efficiency as a function of potential for different materials and illumination conditions. I_0 is illumination intensity.

TABLE 5.2. Limiting Current Observed in Various Silicon/Electrolyte Systems

Material	Solution	Potential	i_L, μA/cm²	Ref.
***p* type**				
(100), 10Ω	10M HF + 0.5M HBr + 10mM Br_2	<–0.2V	<5	14
	5% HF	–0.5 to –8V	0.1–3	839
(111) 4.5×10^{16}	5% HF	–3V	<3	241
3Ω	0.5M K_2SO_4, pH 9.5	–1.5V	2–3	875
(111) 0.1Ω	50% HF	–1.5V	20	1153
***n* type**				
(111) 32Ωcm	0.1M $K_4Fe(CN)_6$ + 0.5M KCl, pH 9	>–0.2V_{sce}	<1	93
	5% HF	>1V	6	839
(111) 1Ω	5% HF	>0.2–4V_{sce}	8–10	38
(111) 3Ω	1M NH_4F, pH 4.8	>–0.2V_{sce}	8	95
(100) 4Ω	1M NH_4F, pH 4.8	>–0.2V_{sce}	13	95
(100) 4Ω	1M KF, pH 4.8	>–0.2V_{sce}	18	95
(111) 4×10^{15}	2M NH_4Cl, pH 4.5	>0.0V	0.2	873
(111) 4×10^{15}	2M NH_4Cl + 2M NH_4F, pH 4.5	>0.0V	0.5	873
(111) 2×10^{15}	1M KCl, pH 3.3	0–5V	3–4	717
(111)	0.2M NaF, pH 5.3	1V	17	446
(111)	0.2M NaF, pH 3	1V	3	446

native oxide film in nonfluoride solutions or surface termination by hydrogen in HF solutions.

In nonfluoride solutions such as KCl, HCl, and H_2SO_4, the dark limiting current on well-prepared samples (relatively few defects) is on the order of several microamperes per square centimeter, which is much higher than the bulk diffusion current.[717] The origin of the large current is related to the surface states arising from adsorption or reaction intermediates, which is strongly affect by the presence of oxide on the silicon surface. Figure 5.24 shows that the surface covered with an oxide has a limiting current several orders of magnitude smaller than that on an oxide-free surface. It also shows that an initially oxide-free surface, when in contact with the aqueous electrolyte, is quickly covered by an oxide resulting in a decrease of the dark limiting current. According to Chazalviel,[717] the transient current shown in Fig. 5.24 may be described by

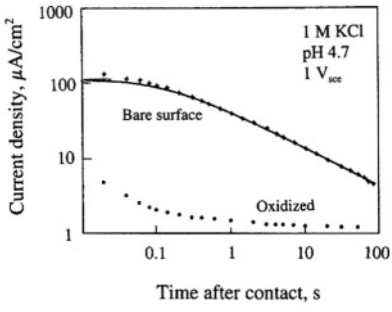

FIGURE 5.24. The decay of the current density obtained with the transient technique in 1 M KCl at pH 4.7. The measured initial current density is $J_0 = 120\,\mu A/cm^2$. Quite different results are obtained by starting from an oxidized surface. (Reprinted from Chazalviel.[717] © 1979, with permission from Elsevier Science.)

$$i = i_0(1 + t/\tau)^{-\alpha} \tag{5.4}$$

where i_0 is the initial current, that is, the limiting current of an oxide-free surface, α and τ are two constants which vary with pH. The relatively large i_0 and its variation with pH and doping concentration are attributed to the change in Schottky barrier height. It can be described by

$$i_0 = i_{00} \exp(eE_s d/kT) \tag{5.5}$$

$$E_s = [2(V - V_{fb} - kT/e)eN_d/\varepsilon\varepsilon_0]^{1/2} \tag{5.6}$$

where E_s is the field strength at the surface and i_{00} is exchange current when the field is zero. Thus, increasing doping concentration would result in a reduction of the barrier height and thus an increase of the initial limiting current. Increasing solution pH is also found to reduce the barrier height and increase the limiting current.

When HF is present in the solution, the current does not decay to near zero as shown in Fig. 5.24 but reaches a steady-state value.[717] The time required to reach the steady-state value decreases with increasing concentration from 100 s at 1 M HF to 10 s at 10 M HF. The decay of current in HF solutions is due to hydrogen termination of the silicon dangling bonds, unlike in non-HF solution where formation of an oxide film is responsible for the current decay. The initial limiting current in fluoride solutions depends on pH as shown in Fig. 5.25.[446] At pH below 5.3, the dark currents reach a current peak followed by a plateau; however, at pH 5.3 the current increases slowly to a plateau value without a current peak prior to the plateau current. Surface analysis indicates that hydrogen termination is associated with the surface at pH below 5.3. The hydrogen adsorption process begins after the current maximum and is completed when the current levels out. No hydrogen can be detected at pH values above

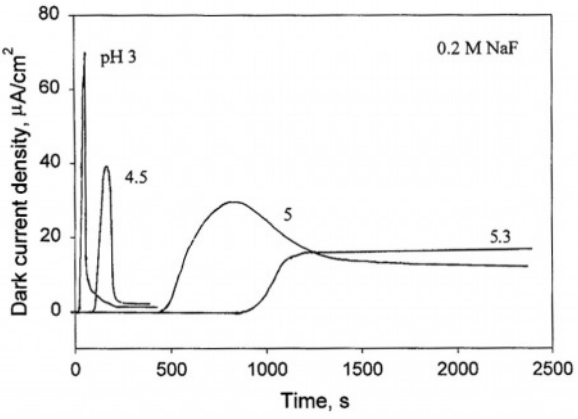

FIGURE 5.25. Dark current density during the etching process of the oxide-covered *n*-type Si (111) surface in 0.2 M NaF at pH values of 3.0, 4.5, 5, and 5.3 as a function of time. The anodic polarization was kept at +0.72 V_{NHE}. After Rappich and Lewerenz.[446] (Reproduced by permission of The Electrochemical Society, Inc.)

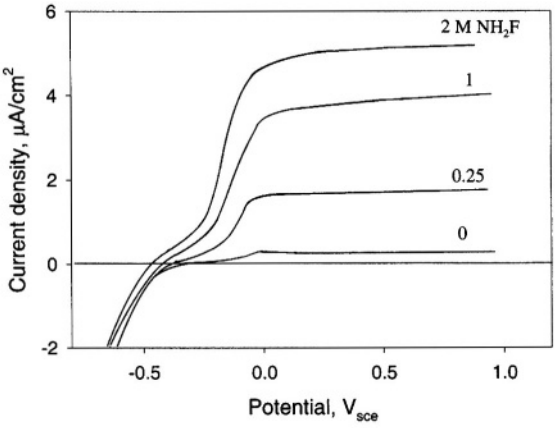

FIGURE 5.26. Current–voltage curves of an *n*-Si (111) electrode ($N_D = 4 \times 10^{15} cm^{-3}$) as a function of the fluoride concentration in mixtures of NH_4F and NH_4Cl (2M) at pH 4.5. (Reprinted with permission from Gerischer and Lubke.[873] © 1987 Wiley-VCH.)

5.3 due to the formation of oxide. These results indicate that hydrogen termination has a much lower steady-state dark limiting current compared to the surface covered by an oxide.

Interface tunneling from reaction intermediates is another cause for a large dark limiting current on the silicon electrode. For example, Fig. 5.26 shows that the limiting current increases with increasing F concentration.[873] The effect of fluoride concentration on the limiting current varies with pH as shown in Fig. 5.27.[904] At pH > 4 the limiting current increases with fluoride concentration from 0.2M and up with a log–log slope of 0.3. Although the surface of silicon tends to be terminated by

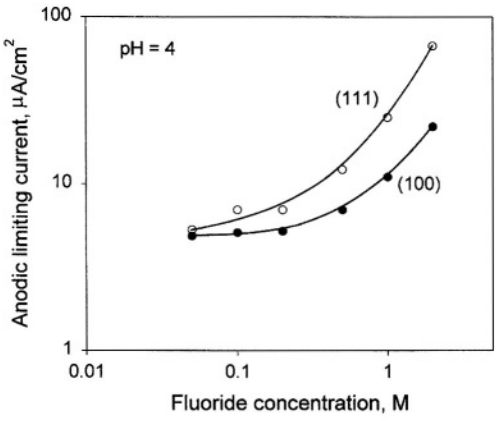

FIGURE 5.27. Variations of anodic limiting current as a function of [F⁻] for solutions of pH 2 for Si (111) and (100). (Reprinted from Allongue *et al.*[904] © 1995, with permission from Elsevier Science.)

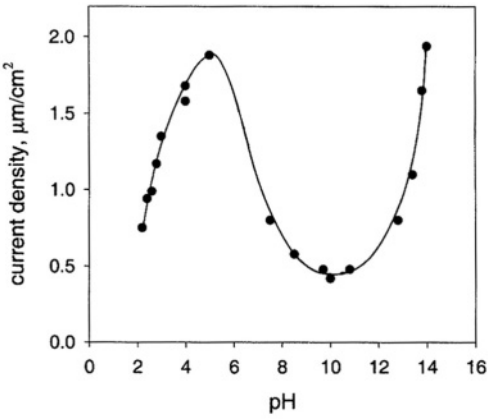

FIGURE 5.28. pH dependence of the anodic current at 0.2 V_{sce} in 1 M NH_4F solution. (Reprinted with permission from Gerischer and Lubke.[873] © 1987 Wiley-VCH.)

hydrogen, increasing the fluoride concentration increases the number of Si–F bonds and the dissolution intermediates capable of transferring charge into the conduction band. Figure 5.28 shows the effect of pH on the dark current in fluoride solutions. The current is the lowest at pH 10 when silicon oxide is the most stable in the HF solution. The dependence of dark current on pH is similar for (111) and (100) surfaces as shown in Fig. 5.29, but that on the (100) surface is about 1.5 times higher than the (111) surface.[95,904]

Large dark current may also be generated by interface tunneling due to the presence of oxidizing species. For example, Fig. 5.30 shows that the dark current on the silicon electrode in NH_4F increases with Br_2 concentration.[11] According to Gerischer

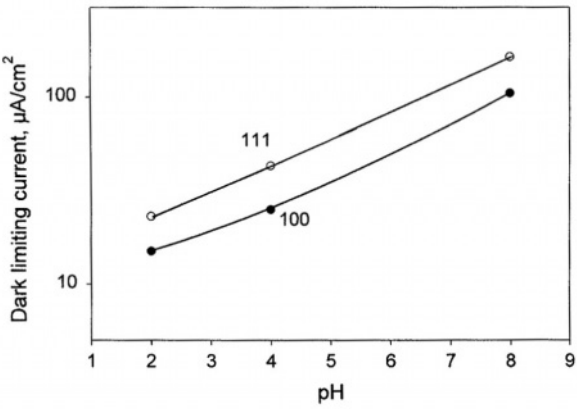

FIGURE 5.29. Dark limiting current of *n*-Si as a function of pH in a NH_2F solution; note that the current is higher on (111) than (100) surface. (Reprinted from Allongue *et al.*[904] © 1995, with permission from Elsevier Sicence.)

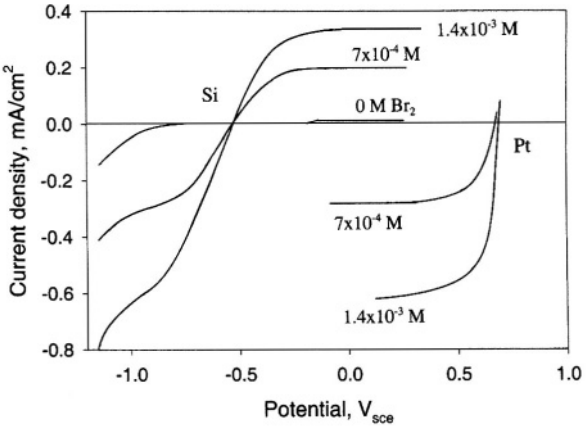

FIGURE 5.30. Current–voltage curves for *n*-Si and Pt electrodes in 0.5 M KBr + 0.2 M NH_4F (pH 4) with addition of Br_2, ν = 1500/min. After Gerischer and Lubke.[11] (Reproduced by permission of The Electrochemical Society, Inc.)

and Lubke,[11] reduction of Br_2 generates holes equivalent to the photogenerated holes. The holes so generated are consumed by the oxidation of silicon forming intermediates which are further oxidized by injecting electrons into the conduction band as shown in Fig. 5.31. In this case the limiting current depends on the rate of Br_2 reduction controlled by the mass transport of Br_2. A similar effect is observed by adding to the solutions other oxidants such as Cu^{2+}, $Ir(Cl_6)^{2-}$, $Fe(CN)^{3-}{}_6$, or MNO_4^-.[256,541,969]

5.7. IMPEDANCE OF INTERFACE LAYERS

The impedance of an electrode/electrolyte interface is one of the characteristic quantities that reveals the electrical nature of the interface. The electrical structure of the interface layers and the resistance to charge storage and movement can be analyzed by determining the impedance as a function of frequency. The characteristics of the electrochemical impedance of the silicon/electrolyte interface are different for *n*-Si and *p*-Si and depend on among other factors, electrolyte composition and particularly the concentration of fluoride.

Figure 5.32 shows the impedance plots for on a lowly doped *p*(100) silicon sample in 1% HF solution at potential values corresponding to those marked on the *i–V* curve in Fig. 5.33.[9,475] The impedance exhibits three characteristic capacitive loops. At low potentials, close to OCP, a single loop is observed as shown in Fig. 5.32a at $-0.4\,V_{sce}$. This loop, loop I, may be seen at more positive potentials at high frequencies as shown in Fig. 5.32b. The capacitance associated with this loop is estimated to be about $20\,nF/cm^2$. According to Searson and Zhang,[9] since a near-perfect Mott–Schottky relation is also observed in this potential region, the single capacitive loop occurring at $-0.4\,V_{sce}$ ariseses from the space charge layer in the silicon.

A second capacitive loop, loop II, starts to be seen at potential values about $-0.3\,V_{sce}$ which is about 0.1 V more positive than that shown in Fig. 5.32a, and gains

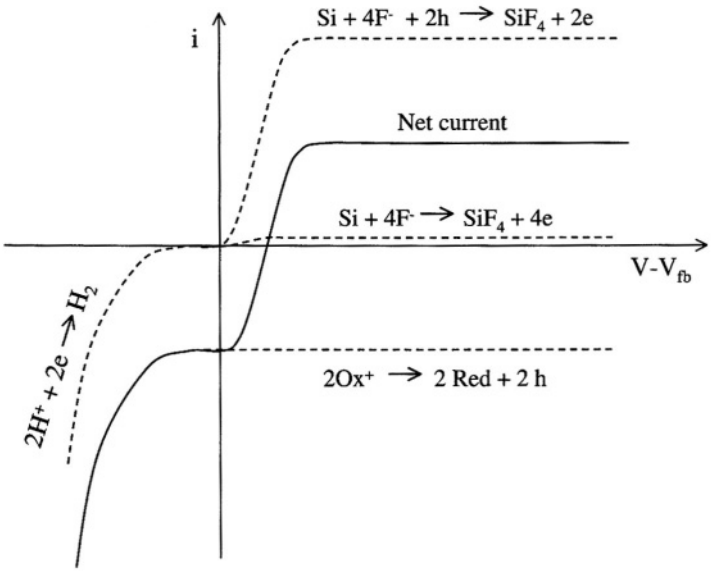

FIGURE 5.31. Ideal current–voltage curve for an *n*-Si electrode in fluoride solution in contact with a hole injecting oxidant, constructed from the partial current–voltage curves with current doubling by electron injection for the anodic process. The ground curve without the oxidant has a small anodic current due to the thermal generation of holes on the surface at anodic bias. After Gerischer and Lubke.[11] (Reproduced by permission of The Electrochemical Society, Inc.)

prominence at potentials more positive than $-0.2\,V_{sce}$ as shown in Fig. 5.32b, The capacitance associated with this loop is potential dependent and increases from about $0.1\,\mu F/cm^2$ at low potentials to about $1\,\mu F/cm^2$ above $0.2\,V_{sce}$, This impedance is clearly separated from that of the space charge layer dominating at more negative potentials. Since it is the only capacitive loop seen in the potential region (Fig. 5.32c) where the Tafel relation between current density and potential is observed, it is associated with the Helmholtz double layer.

A third capacitive loop, loop III, is seen at more positive potentials (Fig. 5.32d). It starts to appear in the transition region between PS formation and electropolishing and dominates in the electropolishing region at low frequencies. The capacitance associated with this loop is estimated to be about $2\,mF/cm^2$ and is essentially independent of potential within the experimental range (between 0.2 and $1\,V_{sce}$). Loop III is clearly separated from loops I and II, and thus is associated with neither the space charge layer nor the double layer. It is attributed to the oxide film formed in the electropolishing region. This agrees with the fact that the impedance response in the electropolishing region, characterized by loop III, is virtually independent of doping type and concentration as shown in Fig. 5.34. Due to the presence of oxide film in the electropolishing region, the difference in the substrate materials is masked.

At potential corresponding to the Tafel region and in the transition region, an inductive impedance also occurs as shown in Fig. 5.32c,d. This may be indicative of the relaxation of coverage by intermediate species to the dissolution of silicon.

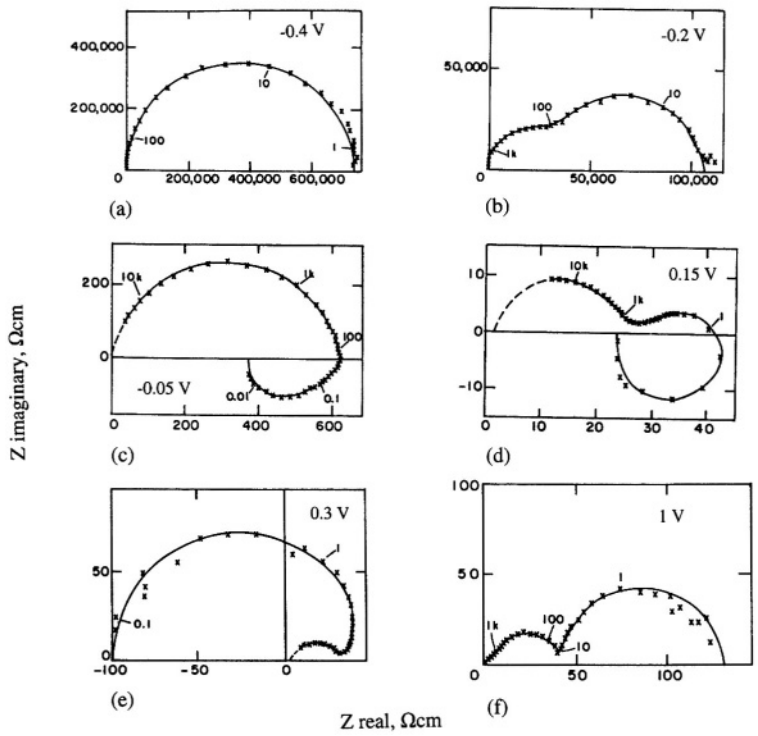

FIGURE 5.32. Complex plane impedance plots for p-Si (3×10^{15}/cm^3) in 1% HF solution. The corresponding i–V curve is shown in Fig. 5.33. After Searson and Zhang.[9] (Reproduced by permission of The Electrochemical Society, Inc.)

The impedance and its evolution with increasing potential observed on p^+ and n^+ silicon samples are similar to those on p^- except for the high-frequency loop, loop I, associated with the space charge layer. For heavily doped n^+ and p^+, the impedance associated with the space charge layer is not revealed, indicating that the impedance of the space charge layer compared to that of the Helmholtz layer is negligible. On the other hand, for lowly or moderately doped n-Si, the impedance in the entire anodic

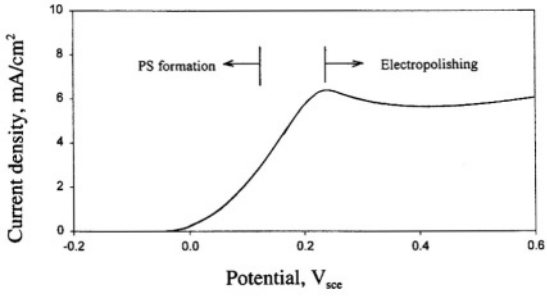

FIGURE 5.33. i–V curve of $p(100)$, 3×10^{15}/cm^3 in 1% HF. After Searson and Zhang.[9] (Reproduced by permission of The Electrochemical Society, Inc.)

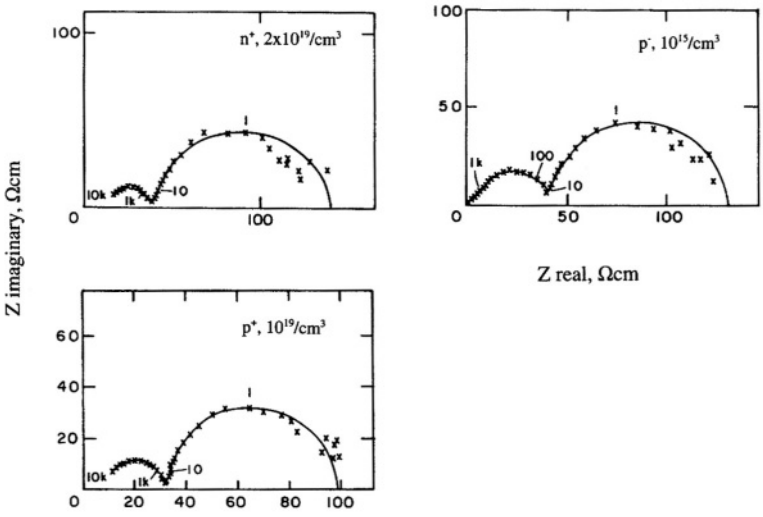

FIGURE 5.34. Complex plane impedance plots for n^+, p^+, and p^- silicon at 1 V_{sce} in 1% HF solution under conditions of electropolishing. After Searson and Zhang.[9] (Reproduced by permission of The Electrochemical Society, Inc.)

potential region exhibits a capacitive loop characteristic of the space charge layer. For *n*-Si, the applied potential, up to tens of volts depending on doping level and HF concentration, drops entirely across the space charge layer. Illumination greatly reduces the semicircles of loop I due to a larger capacitance associated with a thinner space charge layer resulted from photo abosorption.[295]

At potentials more positive than the second current plateau, J_2 (see Fig. 5.2), where current oscillation occurs the impedance diagram is dominated by a set of loops characteristic of resonant behavior as shown in Fig. 5.35.[951]

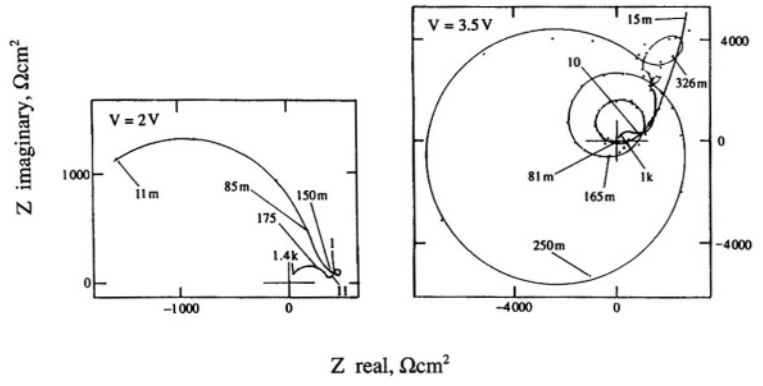

FIGURE 5.35. Impedance diagrams in the current oscillation regime at 2 and 3.5 V on *p*-Si (111) in an electrolyte of $C_F = 0.05$ M and pH 3. The measurement frequencies (in Hz) are indicated for some points on the diagrams. Notice the successive loops, corresponding to the fundamental resonance (the one closest to the origin) and to the successive overtones. After Ozanam *et al.*[951] (Reproduced by permission of The Electrochemical Society, Inc.)

5.8. TAFEL SLOPE AND DISTRIBUTION OF POTENTIAL

5.8.1. Tafel Slope

The slope of the plot of logarithm of current density versus potential, which characteristically is linear for an activation-controlled reaction, is defined as the Tafel slope. The Tafel slope determined in the exponential region of an i–V curve in HF solutions is about 60 mV/decade for p types and heavily doped n types of silicon samples as shown in Table 5.3. For lowly doped n-Si, since illumination is required

TABLE 5.3. Tafel Slope of i–V Curves in the Exponential Region

Silicon	Solution	Current range, mA/cm^2	B, mV/decade	Ref.
p				
(100)				
10^{19}	1%	0.01–1	67	2
	2%	0.01–1	63	1153
	5%	0.01–1	50	1153
	10%	0.01–1	47	1153
	20%	0.01–1	45	1153
	30%	0.01–1	44	1153
	30%	0.01–1	65	1153
10^{15}	1%	0.01–1	78	2
	2%	0.01–1	67	1153
	5%	0.01–1	48	1153
	10%	0.01–1	42	1153
	30%	0.01–1	57	1153
	50%	0.01–2	77	1153
2.5×10^{15}	35:30	2–60	59	194
1.3×10^{17}	35:30	2–60	59	194
10^{19}	35:30	2–60	59	194
2.5×10^{19}	35:30	2–150	72	5
5 Ωcm	25%	0.05–50	60	724
0.2 Ωcm	25%	0.05–50	58	724
0.01 Ωcm	25%	0.05–50	58	724
0.1 Ωcm	6.5:35	0.05–0.5	108	700
(111)				
1	10 N + 0.5 N NH_4F	0.005–1	60	34
2×10^{18}	1%	0.01–1	67	1153
	20%	0.01–1	50	1153
(110)				
3×10^{18}	1%	0.01–1	83	1153
	5%	0.01–1	56	1153
n				
(100)				
16 Ωcm	6.5:35	0.002–0.2, illu.	78	700
2×10^{19}	1%	0.01–1	57	2
	20%	0.01–1	66	1153
(111)				
2×10^{19}	20%	0.01–1	48	1153

to generate electrode reactions, the exponential region occurs only at sufficiently high illumination intensities such that the availability of holes is no longer the rate-limiting step. Under such a condition, the Tafel slope of *n*-Si is similar to that of other silicon materials.

Phenomenologically, the occurrence of the 60 mV/decade Tafel slope can be attributed either to a rate-limiting process involving charge transfer in the Helmholtz layer or to one involving carrier supply in the space charge layer. If it is in the Helmholtz layer, the Tafel slope $= kT/2.3\alpha nq$ is 60 mV/decade, assuming the charge transfer coefficient is 0.5 and the number of charges per dissolved silicon atom is 2. If it is in the space charge layer, it also gives 60 mV/decade since $V/\log i$ for the current involving carrier supply in the space charge layer is $kT/2.3q$. The slope will not be 60 mV/decade if the rate determining process involves both layers.

Deviation of 60 mV/decade can be seen in Table 5.3 under different conditions. In addition to the potential distribution in the two double layers, there are two other possible causes for the deviations. The first is possible potential drops in other parts of the electrical circuit, e.g., in the electrolyte and semiconductor. The second possibility is the change of effective surface area due to the formation of a porous silicon layer during the course of *i–V* curve measurement.[2] In addition, if the reaction is controlled by a process involving the Helmholtz layer, the apparent Tafel slope may be smaller than the 60 mV/decade as would be expected from the formula, $B = kT/2.3\alpha nq$, because the effective dissolution valence n is not a constant with respect to potential but varies from 2 to 3 in the exponential region.

5.8.2. *Potential Distribution*

The impedance data on *p*-Si and *n*-Si at different doping concentrations suggest that the distribution of the applied potential depends on silicon material as well as potential range. Table 5.4 is a summary of the potential distribution of different materials in the three potential regions, from OCP to the potential of onset current, the exponential region, and the region above the passivation potential. While the distribution of the potential below V_p depends on doping type and concentration, the applied potential is principally dropped in the oxide film at potentials higher than V_p for all materials. There is a transition zone between the regions, where the potential drop changes from predominantly in one layer to predominantly in another.

TABLE 5.4. Distribution of the Applied Potential in the Electric Layers at the Silicon/Electrolyte Interface in HF Solutions

Material	OCP to V(i–0)[a]	Exponential region	$V > V_p$
p^+, n^+	Helmholtz layer	Helmholtz layer	Oxide film
n	Space charge layer	Space charge layer	Oxide film
p	Space charge layer	Helmholtz layer and space charge layer	Oxide film

[a] V(i~0) is the potential before the rising of current.

For *n*-Si the *i–V* behavior, impedance response, and near-perfect Mott–Schottky show that the applied potential is predominantly dropped across the space charge layer in the semiconductor. It is not so obvious for *p*-type and heavily doped *n*-type silicon samples. All of these samples display, besides a shift along the potential axis, similar *i–V* curves which show a Tafel region at lower potentials and a current plateau at higher potentials. The origin of the 60 mV/decade Tafel slope of the silicon electrode in HF solutions has been attributed to either a rate-limiting process involving charge transfer in the Helmholtz layer or one involving carrier supply in the space charge layer.[2,5,194,724]

For heavily doped materials, either *n* or *p* type, the surface is degenerated and the material behaves like a metal electrode, meaning that the charge transfer reaction in the Helmholtz double layer is the rate-determining step. This is supported by the lack of an impedance loop associated with the space charge for the heavily doped materials. Also, for heavily doped *n*-Si large current in the dark is due to electron injection, which is not characterized by a slope of 60 mV/decade. For *p*-Si, electron injection into the conduction band may also occur during the anodic dissolution.

For non-heavily doped *p*-Si the potential is mostly dropped within the space charge layer before the onset of current. At potentials higher than that at which current becomes measurable, the potential is likely to drop also in the Helmholtz layer in addition to the space charge layer. This would mean a Tafel slope larger than 60 mV/decade. Also, for very lowly doped material, potential drop in the bulk semiconductor can be significant.[700]

Thus, as a summary, Tafel slopes of the *i–V* curves observed on differently doped materials, although they have similar values, are determined by different factors. The experimentally observed values of about 60 mV/decade in the exponential region are due to several factors which have different effects on the current–potential relationship: (1) relative potential drops in the space charge layer and the Helmholtz layer; (2) increase in surface area during the course of an *i–V* curve measurement due to formation of PS which tends to reduce the slope; (3) change of the dissolution valence with potential which has an effect of reducing the slope if a significant part of the potential is dropped in the Helmholtz layer; (4) electron injection into the conduction band which reduces the slope; and (5) potential drops in the bulk semiconductor and electrolyte, which increases the slope.

5.9. PASSIVATION

5.9.1. Occurrence

Passivation is a process in which the electrode surface changes from an active state to a relatively inactive state owing to the formation of a surface barrier layer. The processes involved in passivation play a critical role in many anodic electrode phenomena on silicon such as electropolishing, cleaning, etching, porous silicon formation, and current oscillation. In nonfluoride and nonalkaline solutions the surface silicon electrode is, in general, passivated due to the formation of a thin layer of oxide film. Very small current can pass through the passivated silicon surface of either *n*- or *p*-type

materials in the dark or under illumination. In fluoride-containing or alkaline solutions, in which SiO_2 has a high solubility, passivation requires the application of an anodic potential.

The phenomenon of passivation can be simply characterized by an i–V curve as shown in Fig. 5.1. In the active state, the electrode dissolves and the dissolution current increases sharply with increasing potential. At the passivation potential the current starts to decrease rapidly to much lower values and marks the onset of passivity. The current on the passivated surface, called the passivation current, i_p, can be several orders of magnitude smaller than that on an active surface at the same potential. The passivation current indicates the dissolution rate in the passive state, that is, the dissolution rate of anodic oxide. The passivation potential tends to change with potential scanning rate.[969] A certain amount of oxidation, measured by the total charge under the current peak, is required for passivation, so that the faster the scanning rate the more positive is the passivation potential. Table 5.5 lists the passivation potentials and passivation currents observed in various silicon/electrolyte systems. The passivation current can vary in a wide range from a few microamperes per square centimeter in 1 M KOH solution to the order of $10^4\,\mu A/cm^2$ in 1 M HF solution. In non-aqueous solution containing HF, passivation does not occur at anodic current as high as 1 A/cm^2 due to the lack of water in the solution.[136,1015]

The silicon surface in nonfluoride and nonalkaline solutions is spontaneously passivated due to the formation of a thin native oxide film at a rate depending on many factors as discussed in Chapter 2. For n-Si samples in aqueous solutions under illumination the occurrence of passivation causes a decrease of the photocurrent as shown in Fig. 5.11.[74,873] In the absence of HF, photocurrent rapidly reduces to near zero due to the formation of an oxide film. The stationary photocurrent increases with increasing HF concentration. For a given light intensity, there is a HF concentration above which the photocurrent does not decrease from the initial value. The surface is free of oxide film at this HF concentration.

The reactions on passivated silicon surface are characterized by two essential processes, oxide formation and dissolution. In practice, the low current measured on silicon electrode at anodic potentials in alkaline solutions is generally attributed to passivation. On the other hand, the occurrence of current peak and the subsequent current plateau in HF solutions are generally not regarded as due to passivation. However, in essence, the processes that produce current at potentials higher than V_p in both HF and KOH solutions are largely identical in chemical nature, that is, oxidation of silicon atoms at the silicon/oxide interface and ionic transport in the oxide. Kinetically, the passivation in HF solutions, in which the silicon oxide dissolves rapidly yielding a large passivation current, i_p, is different from that occurring in the alkaline solutions where the passivation current is very small.

5.9.2. Passivation in Alkaline Solutions

The passivation of silicon surface in KOH at anodic potentials has been extensively investigated in relation to anisotropic etching. Figures 5.36 and 5.37 show the typical i–V curves of n- and p-type silicon in KOH.[109,378] Substrate conditions, particularly orientation and type of doping, have significant effects on the characteristics of

TABLE 5.5. Passivation Potential and Passivation Current of Various Systems

Silicon	Solution	V_p, V_{sce}	V_p-OCP, V[c]	SiO_x, Å	i_p, μA	Ref.
***p* type**						
(100) 10^{19}	2% HF	0.24	0.5		13000	2
	1% HF	0.2	0.62		5000	2
(100) 10^{15}	0.3% HF	0.12	0.55		1200	2
(111) 1Ω	0.1M HF + 0.9M NH_4F	0.2			650	34
(100) 4Ω	1M KCl + 0.005M HF					
	+ 0.005M KF	−0.14		70, 3.7V	15	948
(100) 4×10^{15}	1M [F], pH 4.7	0			2000	939
	0.033M [F], pH 4.7	−0.24			2.3	939
	0.033M [F], pH 2.8	−0.14			280	939
	0.033M [F], pH 0	0			30	939
(111) 10^{15}	0.1M NH_4F, pH 4	−0.14		40, 5V	350	866
5Ω	0.3M NH_4F, pH = 3.5	1		10	3500	122
(100) 4×10^{15}	[F] = 0.05M, pH 3	0			550	938
(100) 7Ω	1M KCl	0.75		14, V_p		969
(100) 5Ω	40% KOH, 60°C	−1.04			35	291
(111) 5Ω	40% KOH, 60°C	−0.959			28	291
(100) 8Ω	1.35M NH_4F	−0.7			4	139
0.5Ω	1M KOH	−0.8	0.4		6	925
(100) 17Ω	2M KOH	−0.71	0.24		2	129
(100) 19.3Ω	2M KOH	−0.69	0.50	20[b]		378
(100) 0.007Ω	2M KOH	−0.92	0.28	20		378
(111) 0.007Ω	2M KOH	−0.90	0.24	20		378
(111) 12.4Ω	2M KOH	−0.78	0.45	20		378
(100) 44.9Ω	EDP, 110°C	−0.74				369, 112
(100) 15Ω	2.5% TMAH	−0.79	0.79			516
	25% TMAH	−1.04	0.69			516
	12% NH_3, 70°C	−0.60			1	521
2.5Ω	25% TMAH, 20°C	−0.59				996
***n* type**						
(100) 2×10^{19}	1% HF	0.12	0.66		6000	1153
	0.1% HF	0.03	0.5		200	1153
(100) 5Ω	1M KCl	0.9				969
0.6–45Ω	1M KOH	−0.8			6	925
(100) 5Ω	40% KOH, 60°C	−1.08			30	291
(111) 5Ω	40% KOH, 60°C	−0.955			33	291
(100) 8Ω	2M KOH	−0.92	0.33		2	129
(100) 15.5Ω	2M KOH	−0.68	0.65	20[b]		378
(100) 0.0043Ω	2M KOH	−0.97	0.31	20		378
(111) 7.7Ω	2M KOH	−0.66	0.51	20		378
(111) 0.005Ω	2M KOH	−0.80	0.37	20		378
(100) 23Ω	EDP[a], 110°C	−0.90				112, 369
	2.5% TMAH, 80°C	−1.06	0.36			516
	25% TMAH, 80°C	−1.17	0.55			516
	12% NH_3, 70°C	−0.85	0.35		1	521
1Ω	25% TMAH, 20°C	−0.87				996

[a]100 ml ethylenediamine + 16 g pyrocatechol + 32 ml water.
[b]At OCP.
[c]V_p-OCP, passivation overpotential.

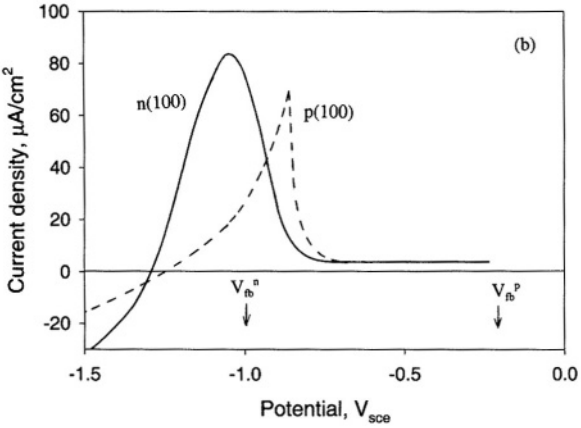

FIGURE 5.36. The room-temperature i–V curves for n-type (solid line) and p-type (dashed line) samples of (100) orientation. V_{fb} is the flatband potential. After Glembocki *et al.*[109] (Reproduced by permission of The Electrochemical Society, Inc.)

i–V curves. The peak is sharper and almost one order of magnitude higher for the p type than for the n type. The passivation of silicon electrode in other types of alkaline solutions such as NH_4OH, NaOH, EDP, and hydrazine is in general similar to that in KOH and specific information in these solutions is discussed in Chapter 7. The essential steps involving passivation have been postulated to be the formation and condensation of surface Si–OH bonds.[22,108] In KOH solutions the Si–H bonds which terminate

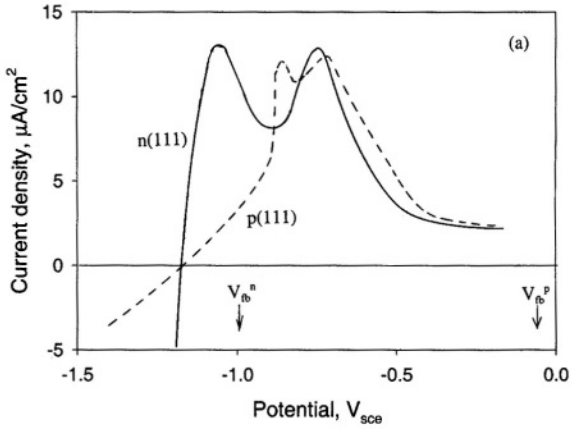

FIGURE 5.37. The room-temperature i–V curves for n-type (solid line) and p-type (dashed line) samples of (111) orientation. The more negative peaks in both curves are spurious and caused by the passivation of exposed edges, which may have (110) or (100) orientations. After Glembocki *et al.*[109] (Reproduced by permission of The Electrochemical Society, Inc.)

the surface may be hydrolyzed. With increasing anodic potential the rate of hydrolyzation of Si–H bonds increases and at a certain potential the H termination of the silicon surface is no longer preserved. Passivation corresponds to the condensation of neighboring surface Si–OH bonds forming Si–O–Si bridges.

The characteristics of passivation have been found to strongly depend on substrate orientation. The current peak on the *i–V* curves, shown in Figs. 5.36 and 5.37,[109] is about six times smaller on the {111} samples than on the {100} samples. Also, the *i–V* curve repeated after the first curve is similar to the first curve on the (111) surface, but not on the (100) where the current of the second curve is much smaller than the first curve.[22] The shape of the current peak also depends on the silicon substrate; {100} samples have a single peak whereas {111} samples have two peaks as shown in Figs. 5.36 and 5.37.[109] The double peaks for (111) samples are not found in 40% KOH solution at 60 °C.[192]

The behavior of (111) and (100) samples also differs according to current transients.[22,183,291] A smaller amount of charge is required to reach a steady-state condition for the (111) than the (100) surface when the potential is stepped from OCP to an anodic potential.[22] This suggests that the passivation of a (111) surface requires less material to be oxidized than a (100) surface. In addition, current transients at various potentials positive of OCP on the (111) samples exhibit a current decrease within the initial few seconds followed by a current peak while the current transient on (100) samples shows only a monotonic decrease.[291] For the (111) material the transients consist of only one maximum at potentials between OCP and V_p. On the other hand, they have two maxima at potentials positive of the passivation potential. According to Smith *et al.*[291] the first current maximum is due to the dissolution of a film preexistent at OCP while the second is associated with the formation of an anodic oxide film on the (111) surface. The amount of charge associated with this transient increases with applied potential and is higher on *p*-Si than on *n*-Si. Smith *et al.*[192] also found that the passivation potential in KOH is independent of the potential sweeping rate for (100) samples whereas it changes with sweeping rate for (111) samples as shown in Fig. 5.38. The behavior of (111) silicon is attributed to the presence of a prepassive layer with a charge density of 2.4 mC/cm^2 which is converted to oxide at a potential positive of the passivation potential.

For non-heavily doped materials, the *i–V* characteristics near the passivation potential are essentially independent of carrier density.[109,378] However, for heavily doped materials, the current peak, marking the occurrence of passivation, is much lower as shown in Fig. 5.39; the ratio of the peak current on lowly doped sample to that on heavily doped sample is about 6.[269] For lowly doped materials, long-duration immersion in the solution causes very little change of the *i–V* characteristics, whereas it causes the current peak to disappear for highly doped materials. Also, the dependence of passivation potential and passivation overpotential, V_P-OCP, on temperature appears to be opposite for lowly and highly doped materials as shown in Fig. 5.40.[269]

Figure 5.41 shows that the passivation potential decreases with doping concentration and is largely independent of orientation. The change in the values of passivation potential is more than 1 V from low to high. The distribution of this extra potential associated passivation in the Helmholtz layer, in the space charge layer, in a preexistent oxide, or in the substrate has not been determined. The passivation overpotential,

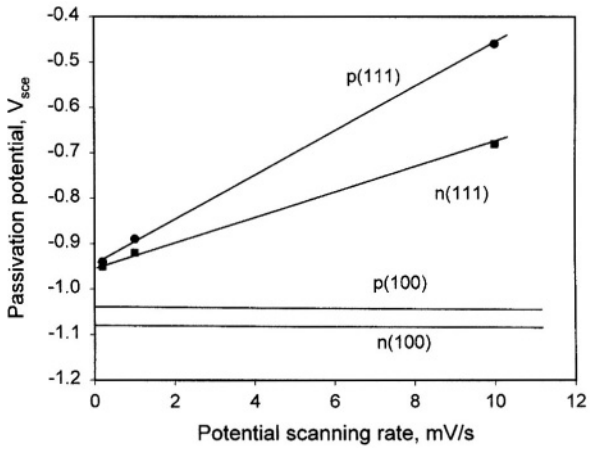

FIGURE 5.38. Passivation potential of the materials with different types and orientations as a function of potential scanning rate in a KOH solution. After Smith *et al.*[192]

V_p-OCP, appears to have a similar dependence on doping concentration as does the passivation potential as shown in Fig. 5.42. It requires a relatively small overpotential to produce passivation for highly doped silicon samples, which may be associated with the relatively low etch rates of highly doped materials.[207,269,594] This aspect will be further discussed in Chapter 7.

The dissolution rate of silicon in alkaline solutions at anodic potentials is relatively high in the active region and is low in the passive region as shown in

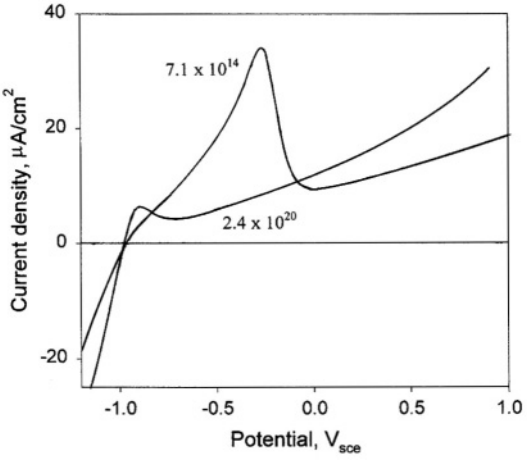

FIGURE 5.39. *i–V* curves for $p\{111\}$ Si sample with $n_p = 7.1 \times 10^{14}\,cm^{-3}$ and $2.4 \times 10^{20}\,cm^{-3}$. Scanning rate 17 mV/s. After Palik *et al.*[269] (Reproduced by permission of The Electrochemical Society, Inc.)

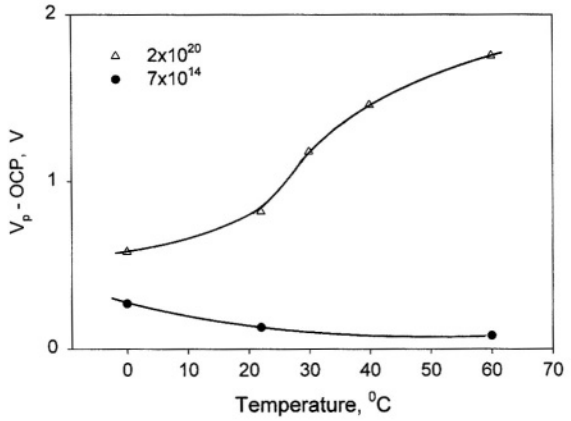

FIGURE 5.40. Passivation potential (a) and passivation overpotential (b) as a function of temperature for lowly doped and highly doped materials. Data from Ref.[269]

Fig. 5.43.[109,925] In the passive region, the amount of dissolution is more than the current can account for, indicating that the dissolution in the passive region is partially chemical in nature due to the small amount of hydrogen evolution in the passive region.

5.9.3. Passive Films

Passive films formed on a silicon surface in aqueous solutions are in general oxide films. There is rather limited systematic information on the structure and properties of thin silicon anodic oxide films, particularly those formed in solutions of high silicon solubilities. On the other hand, the thicker oxide films formed at large potentials have been better characterized (see Chapter 3) and the information associated can be used for understanding the thin oxide films formed at relatively low potentials.

The studies on anodic oxide films reveal the following characteristics: (1) anodic oxides of silicon are amorphous and nonstoichiometric; containing varying contents of water, hydroxyl ions, and other foreign species depending on formation conditions; (2) the properties of anodic oxides formed on *n*- and *p*-type materials are similar; (3) the structures and properties of anodic films are not stable and tend to change with time; (4) when the oxide is a continuous phase of one to a few monolayers, it acts as a barrier to the interaction between the silicon surface and the electrolyte, resulting in a drastic reduction of the electrode reactions; (5) the formation rate of anodic oxide films is a function of potential, electrolyte composition, substrate condition, and oxide film thickness; (6) the dissolution rate of passive film depends sensitively on formation conditions; (7) the solubility of silicon oxides is high in both HF and alkaline solutions, but the dissolution rate is high in HF solutions and low in alkaline solutions; (8) the composition and structure of passive film varies in thickness from the silicon/oxide interface to the oxide/electrolyte interface; (9) some silicon atoms which enter into the oxide phase are only partially oxidized and tend to locate near the silicon/oxide interface

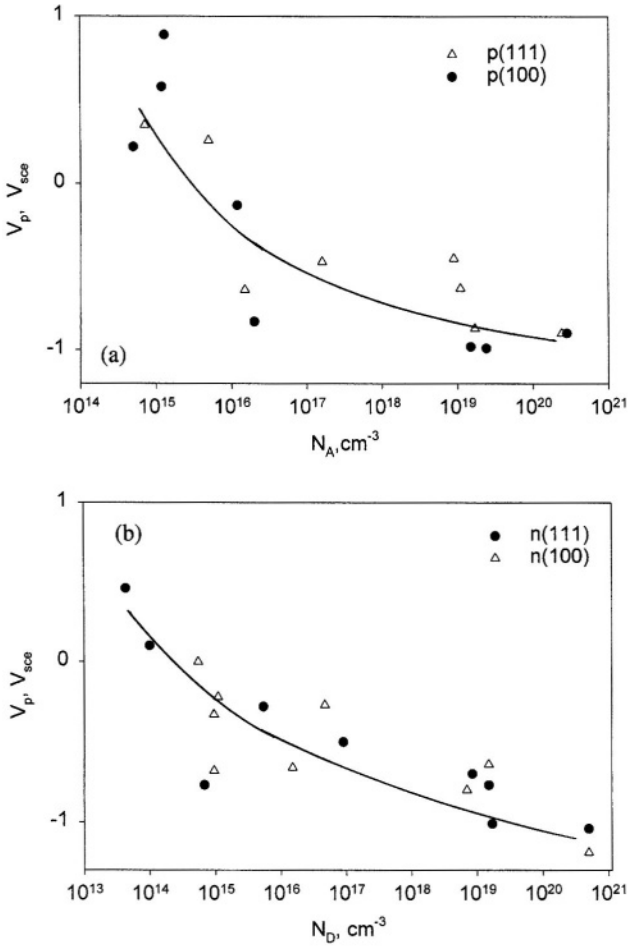

FIGURE 5.41. Passivation potential as a function of doping concentration for (a) $p(111)$ and $p(100)$ and (b) $n(111)$ and $n(100)$. Data from Ref.[269]

region; (10) the partially oxidized silicon atoms are responsible for the large interface charge and their further reduction by hydrogen ions is responsible for the nonelectrochemical part of silicon dissolution. These characteristics of anodic passive films play important roles in a diverse range of electrode phenomena observed on silicon electrodes such as electropolishing, porous silicon formation, current oscillation, etch stop, and so on.

Figure 5.44 shows that in KOH solutions the oxide film thickness as a function of applied potential has three regions: (1) an oxide ~20 Å thick is formed at the potential just above V_p; (2) from V_p to 5 V the growth rate is relatively slow, about 6.8 Å/V; and (3) at higher potentials it is higher, about 42 Å/V.[378] A similar growth pattern is observed in NH_4OH solutions.[139] The thickness of anodic oxide in acidic fluoride

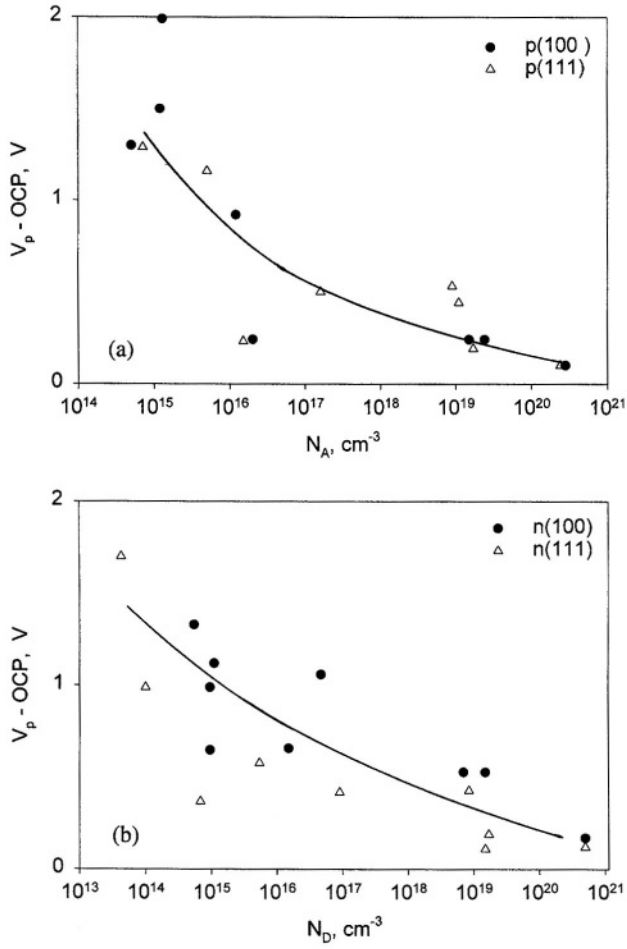

FIGURE 5.42. Passivation overpotential as a function of doping concentration for (a) $n(111)$ and $n(100)$ and (b) $p(111)$ and $p(100)$. Data from Ref.[269]

solutions is limited due to dissolution of the oxide. Figure 5.45 shows that the thickness of an anodic oxide also varies with potential in acidic fluoride solutions.[122]

Since the reaction rate at potentials above V_p is limited by the dissolution of oxide and the dissolution rate depends on the nature of the oxides (see Chapter 4), the change of current with potential indicates that oxide composition/structure varies with the formation. The nonstoichiometric composition of an anodically formed oxide film can be expressed as SiO_n with a higher value of n close to the oxide/electrolyte interface and a lower value of n close to the Si/oxide interface.[874] A thicker oxide film has a bulk composition closer to the stoichiometric SiO_2. The dissolution rate of anodic oxide depends on the composition of the electrolyte as shown in Fig. 5.46.[874] (also Fig. 5.7[939]). It depends little on the type of material and doping levels.[2,73,700]

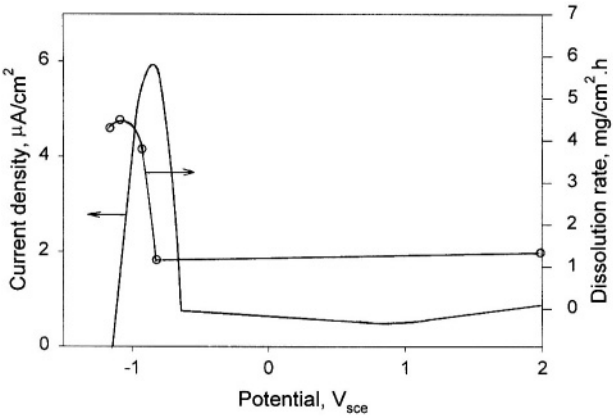

FIGURE 5.43. Correlation of silicon dissolution rate with *i–V* curve in 1 M KOH. (Reprinted from Hurd and Hackerman,[925] © 1964, with permission from Elsevier Science.)

One reason for the variation of properties from the Si/oxide to oxide/electrolyte interfaces is that some silicon atoms in the anodic oxides are not fully oxidized. Figure 5.47 shows that a current peak occurs during the etching of the anodic oxides which are formed on illuminated *n*-Si.[74] The partially oxidized silicon atoms have relatively high energy levels and are capable of injecting electrons into the conduction band and generating a current at the end of the oxide dissolution. The position of the current peak increases with decreasing HF concentration and with increasing anodic potential indicating that the partially oxidized silicon atoms are concentrated near the silicon/oxide interface. The occurrence of this anodic current during etch-back in HF solutions is general for essentially all anodic oxide films formed in HF solutions as well as in alkaline solutions on both types of materials.[74,286,602] The amount of charge associated with the partially oxidized silicon atoms, up to an equivalent of several monolayers of Si^{3+},

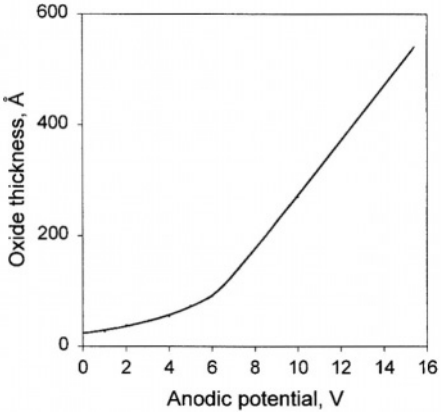

FIGURE 5.44. Thickness of anodized oxide film determined ellipsometrically as a function of voltage above passivation potential. After Faust and Palik.[378] (Reproduced by permission of The Electrochemical Society, Inc.)

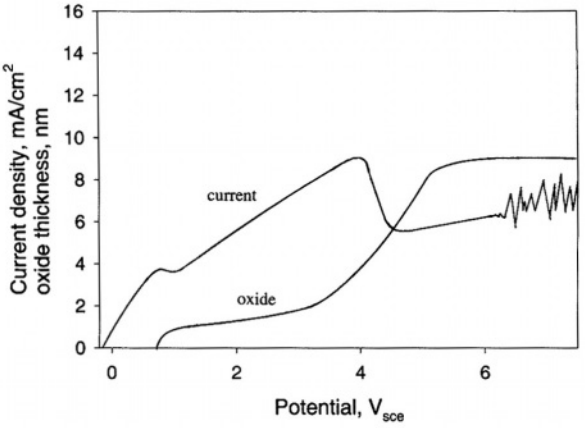

FIGURE 5.45. The current density versus voltage curve of a *p*-type Si electrode in NH_4F (0.3 M, pH 3.5) recorded with 50 mV/s. Current oscillations are observed in the potentiostatic regime for potentials positive of the one corresponding to the second current minimum. After Lehmann.[122] (Reproduced by permission of The Electrochemical Society, Inc.)

increases with increasing oxide thickness up to a certain thickness as shown in Fig. 5.48.[74]

On the other hand, according to Serre *et al.*,[286] the current transient at the end of etching of anodic oxide films in HF solutions is related to hydrogen termination. It is argued that because an anodic charge, equivalent to a nonstoichiometric oxide of ~50 Å, is also passed at the end of etching of a thermal oxide, the presence of a

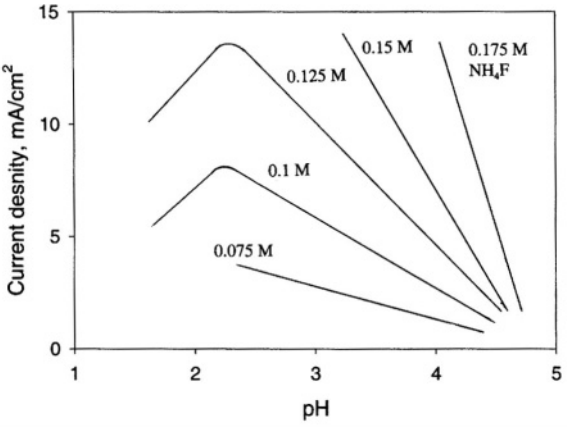

FIGURE 5.46. Influence of pH on the stationary currents of illuminated *n*-Si at 2 V for different fluoride concentrations. After Gerischer and Lubke.[874] (© 1987, Reprinted by permission of John Wiley & Sons, Inc.)

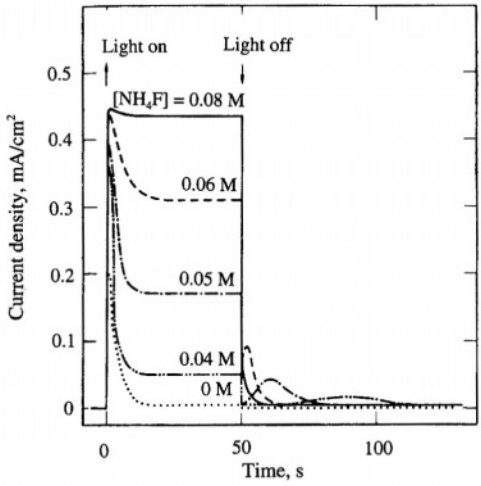

FIGURE 5.47. Current changes under illumination and dark conditions for an *n*-Si electrode at 1.0 V_{sce} in 0.1 M potassium phthalate solution containing various concentrations of NH_4F. (Reprinted from Matsumura and Morrison.[74] © 1990, with permission from Elsevier Science.)

nonstoichiometric layer the Si/oxide interface, which is not likely to exist in the thermal oxide film, must not fully responsible for the anodic current at the end of oxide film etching. To generalize, it can thus be said that the current transient at the end of etching of an anodic oxide film is due to the electrochemical processes involved in the transition from the silicon/oxide interface to the silicon/electrolyte interface. The amount of charge involved in the etch-back may consist of (1) the oxidation of partially oxidized

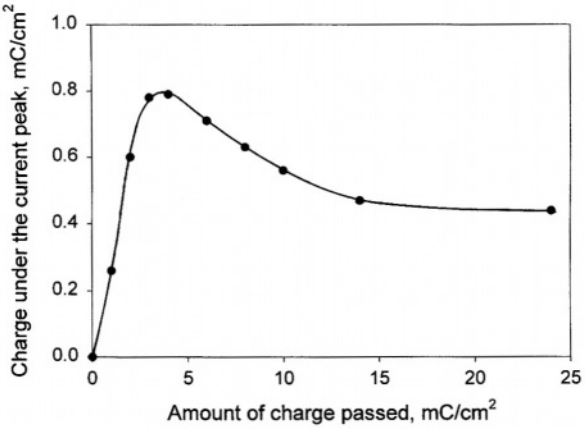

FIGURE 5.48. The relationship between the amount of charge passed (Q_{ox}) during the photoanodic oxidation of the *n*-Si electrode in 0.5 M H_2SO_4 solution, and the integral of the anodic dark current (Q_a) observed when the oxidized electrode was immersed in 1 M NH_4F solution (pH 4.3) at 1.0 V_{sce}. (Reprinted from Matsumura and Morrison.[74] © 1990, with permission from Elsevier Science.)

species at the silicon/oxide interface, (2) surface reconstruction (e.g., hydrogen termination, or OH^- termination) which may or may not stabilize the surface, and (3) dissolution of silicon substrate during the reconstruction process.

5.10. CURRENT OSCILLATION

Current oscillation is a phenomenon that has been observed to occur during the anodic polarization of silicon in fluoride-containing solutions in the potential region of 1.5 to 8 V_{sce}.[602,860,939] Depending on the specific system, oscillation may occur spontaneously or by a perturbation of the potential.[693]

The occurrence of current oscillation is independent of doping type; it is identical for *p*-type and strongly illuminated *n*-type materials. It, however, depends strongly on solution composition. The data from the literature indicate that in HF solutions, sustained oscillation is observed only above 1.8% HF and below 5% HF. Below 1.8% HF, the oscillation is damped, whereas above 5%, the oscillation becomes chaotic.[122] At pH below 2.5, the oscillation disappears after a certain time and the stationary current remains relatively high. At pH above 5, the oscillation also disappears after a certain time.[544] Oscillation is also observed in non-aqueous solutions such as MeCN-xF, where x represents non H ligand.[1071] In addition, the occurrence of oscillation depends on operating procedures such as scanning speed, series resistance in the circuit, or perturbation during the anodic polarization.

5.10.1. Amplitude and Frequency

The characteristics of the oscillation in terms of amplitude, frequency, and their variation with time depend on solution composition as shown in Fig. 5.49.[860]

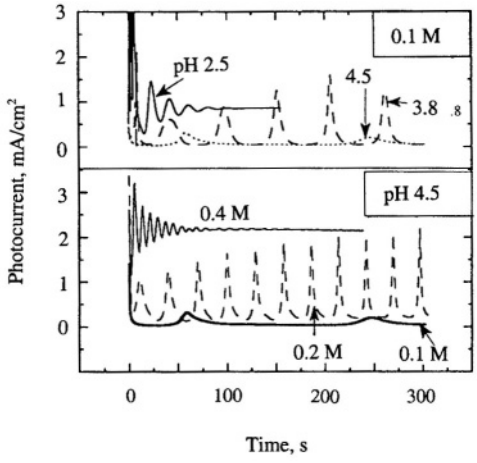

FIGURE 5.49. Photocurrent oscillations on illuminated *n*-Si: (a) in 0.1 M NH_4F for different pH; (b) in 0.1, 0.2, and 0.4 M NH_4F at pH 4.5; light intensity 70 mW cm^{-2}, electrode potential 6 V_{sce}. (Reprinted from Aggour *et al.*[860] © 1992, with permission from Elsevier Science.)

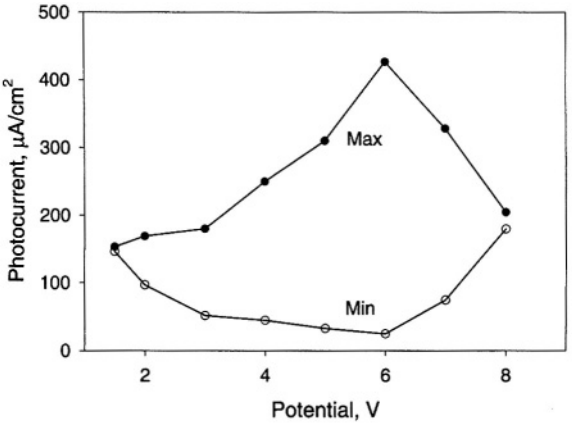

FIGURE 5.50. The amplitude of the photocurrent oscillations on illuminated *n*-Si as a function of the applied potential in 0.1 M NH_4F at pH 4.0, light intensity 70 mW cm^{-2}. (Reprinted from Aggour *et al.*[860] © 1990, with permission from Elsevier Science.)

The amplitude as a function of potential in 0.1 M NH_4F at pH 4 is shown in Fig. 5.50. In this solution below 1.5 V and above 8 V_{sce} oscillation is not observed and between 1.5 V and 8 V the amplitude increases with potential reaching a maximum and then diminishing. The potential range in which oscillation occurs varies with solution composition.

In HF solutions the frequency of oscillation increases with HF concentration.[122,951,1136] In buffered fluoride solutions, Fig. 5.51 shows that the frequency depends on pH and NH_4F concentration.[544] The frequency increases with increasing fluoride concentration at a given pH and has a U-shaped dependence on pH for a given fluoride

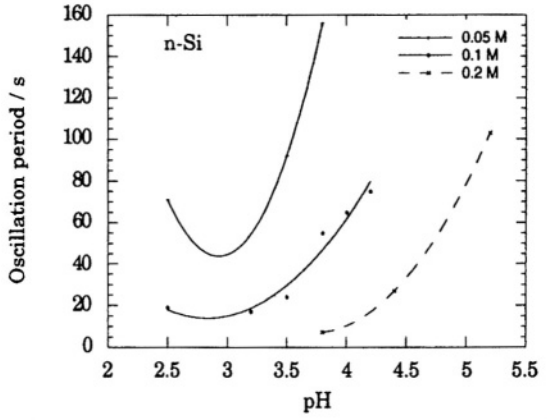

FIGURE 5.51. Dependence of the period of oscillation on the calculated etch rate as a function of pH in different NH_4F solutions. (Reprinted from Lewerenz and Aggour,[544] © 1993, with permission from Elsevier Science.)

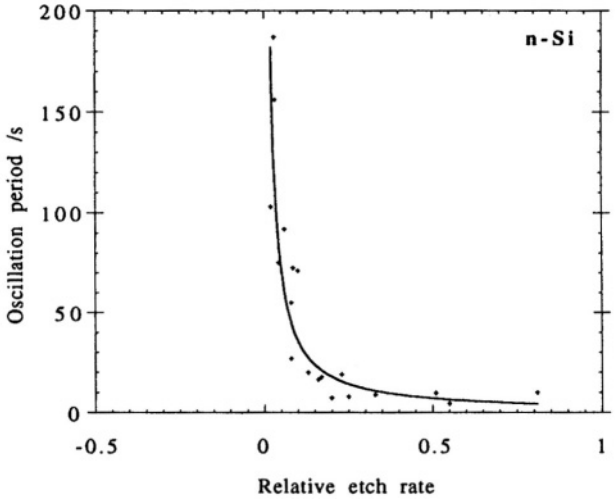

FIGURE 5.52. Dependence of the oscillation period on the relative etch rate for *n*-Si at different NH_4F concentrations and pH values. (Reprinted from Lewerenz and Aggour,[544] © 1993, with permission from Elsevier Science.)

concentration. It has generally been found that the frequency of oscillation increases with increasing etch rate as shown in Fig. 5.52, or equivalently, with increasing current such that $f \approx \lambda J_4$ where λ is on the order of $0.1\,\mathrm{Hz\,mA^{-1}\,cm^2}$ and depends on potential.[544,937] The fact that oscillation is not observed in concentrated fluoride solutions, in which J_4 is large, may be because at the large oxide dissolution rates the frequency is too high for oscillation to be observed. The dependence of frequency on potential is related to the frequency.[1136] For low-frequency oscillation the frequency tends to decrease with potential,[860,951,1136] and for high-frequency oscillation the opposite can be seen.[1136]

Although the period of oscillation depends on solution composition, it is found that the product of the period and the current is only a function of potential; it is essentially constant over a large set of the solution compositions corresponding to an oscillation current span of about two orders of magnitude as shown in Fig. 5.53.[951] This result indicates that, at a given potential, a constant amount of silicon is dissolved during one period of oscillation independent of electrolyte composition.

Damped or sustained oscillation amplitude can be regulated by adding a series resistance into the current flowing path as shown in Fig. 5.54.[693] The series resistance may be associated with the electrolyte, the electrode, or the back contact. It is particularly significant in concentrated fluoride solution in which the anodic current is high and the critical resistance for such a crossover to occur is small. Thus, depending on the electrochemical system the true intrinsic interface behavior appears when such series resistance is zero. This finding also implies that some of the differences among spontaneous, perturbed, or damped oscillation reported in different studies may be due to the effect of the series resistance existing in the system.

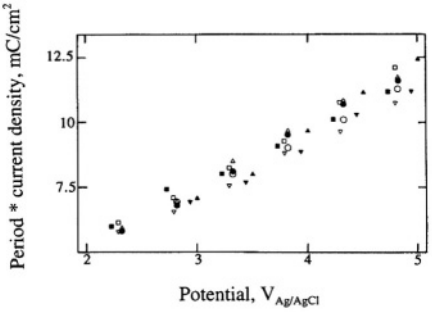

FIGURE 5.53. Plot of the characteristic charge involved in one oscillation period as a function of the potential, for various electrolyte compositions. This characteristic charge is the product of the oscillation period and the steady-state current. It amounts to the charge needed for creating the oxide dissolved during one oscillation period. For this plot, a Nernstian correction to the potential has been applied, depending on the pH of the electrolyte; the actual scale is that for pH 0. Electrolyte composition: (■) c_F = 0.33 M, pH 4.75; (▽) c_F = 0.1 M, pH 3.75; (□) c_F = 0.05 M, pH 3.75; (○) c_F = 0.1 M, pH 3; (●) c_F = 0.05 M, pH 3; (△) c_F = 0.033 M, pH 3; (▼) c_F = 0.1 M, pH 1; (▲) c_F = 0.05 M, pH 0. After Ozanam *et al.*[951] (Reproduced by permission of The Electrochemical Society, Inc.)

5.10.2. Oscillation of Anodic Oxide Thickness and Properties

Various surface analytical techniques have been used to investigate the changes in the physical and chemical properties of the oxide film during oscillation.[122,408,860,950] During the oscillation the thickness of the oxide film on the silicon surface varies periodically, the frequency of which coincides with the associated current oscillation. Figure 5.55, for example, shows the variation of oxide thickness, about 2 nm in amplitude (or about 25% of the average thickness), during the photocurrent oscillation of *n*-type silicon at 7 V_{sce} in a solution of 0.1 M [F] and pH 4.4.[950] The anodic current is

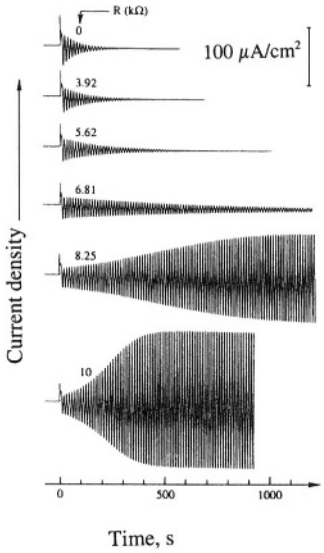

FIGURE 5.54. Current transients observed in response to a +100 mV step-potential excitation, for an electrode with an externally added series resistor. The value of the added series resistance (kΩ) is indicated on the different curves. *p*-Si [$N_A = 2 \times 10^{15}$ cm^{-3}, (100) orientation, surface area 0.12 cm^2]/0.025 M HF + 0.025 M NH_4F + 0.95 M NH_4Cl, rotating disk electrode 300 rpm. Initial electrode potential is set at +3 V (corrected for the ohmic drop in the added series resistance). Note the decreased damping rate, as the series resistance is increased, and the change to a sustained oscillation between 6.81 and 8.25 kΩ. (Reprinted from Chazalviel *et al.*[693] © 1996, with permission from Elsevier Science.)

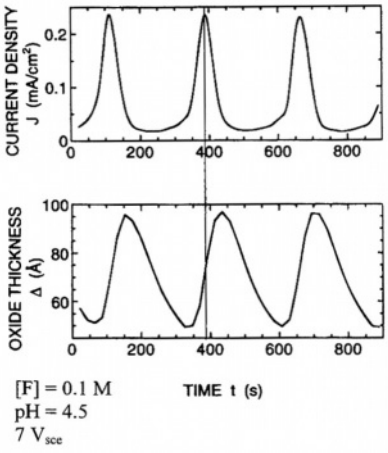

FIGURE 5.55. Oscillation of oxide thickness along with current oscillation in 0.86 M NH_4Cl + 0.1 M NH_4F + 0.04 M NH_4Ac + 0.06 M HAc at pH 4.5 at 7 V_{sce}. After Chazalviel *et al.*[950] (Reproduced by permission of The Electrochemical Society, Inc.)

found to follow the rate of change in thickness of the oxide film and it reaches a maximum when the rate of change in thickness is the largest.[855,862,950] Figure 5.56 shows that the rate of thickness change of the oxide film has a maximum coinciding with the generation current peak and a minimum coinciding with the maximum of the dissolution rate during a period of current.[950] The amplitude of oxide thickness oscillation depends on solution composition and potential.[948,950] Figure 5.57 shows the minimum and maximum oxide thicknesses as a function of potential; both increase with increasing potential but the maximum thickness increases more than the minimum thickness.

Other properties of the anodic oxide also oscillate. It is found that the current peak, corresponding to the maximum oxide growth rate, is accompanied by a decrease in the density of the oxide film indicating the oxide film at the current peak is of lower quality than that at the current valley.[408,950] The variation of the density of the oxide formed at different times during a period of oscillation in turn results in the variation of the etching rate of the oxide as shown in Fig. 5.56.[950] Such a change of oxide property is also shown in the etch rate variation in the direction normal to the oxide film as shown in Fig. 4.27. Compressive stress is found to develop in the oxide during oscillation with the maximum stress associated with the potential maximum.[122] The effective dissolution valence, about 4, is also found to oscillate along

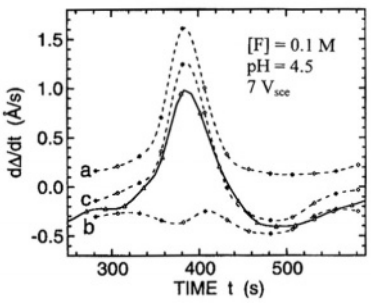

FIGURE 5.56. Rate of oxide thickness variation during current oscillation in 0.86 M NH_4Cl + 0.1 M NH_4F + 0.04 M NH_4Ac + 0.06 M HAc at pH 4.5 at 7 V_{sce}. Solid line: measured variation of oxide film. Curve a: oxide generation rate. Curve b: oxide dissolution rate. Curve c: sum of contributions a and b. After Chazalviel *et al.*[950] (Reproduced by permission of The Electrochemical Society, Inc.)

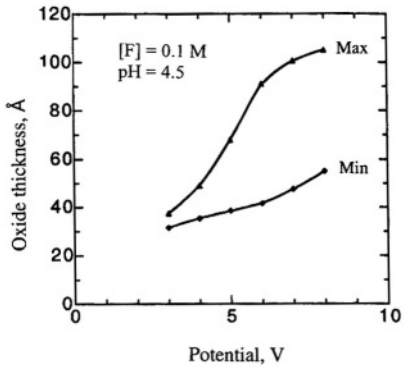

FIGURE 5.57. Minimum and maximum values of oxide thickness during potentiostatic oscillation, as a function of potential. After Chazalviel *et al.*[950] (Reproduced by permission of The Electrochemical Society, Inc.)

with current.[676,950] The infrared absorption, microwave reflectivity, electrode admittance, hydrogen evolution, photocurrent, surface roughness, and electron injection during the current oscillation are found to also oscillate in the same frequency as the current oscillation.[408,602,855,862,1100,1116]

5.10.3. Mechanisms

A number of models have been proposed for the mechanism of current oscillation on silicon electrode. A brief description of the major models is given below.

Lewerenz and Aggour[544,860,1100,1116] attributed the oscillation to the opening and closing of the pores or point defects existing in the oxide film. The point defects are formed at the oxide/silicon interface and develop into pores by selective etching of the defects by HF. The opening of the pores then results in an increase in current which forms oxide film at the bottom of the pores. The current decreases when the oxide film grows in thickness until new sites of pores open up resulting in a sudden current increase.

Cattarin *et al.*[855,862] measured the concentration gradient in the diffusion layers of the electrolyte near the surface. They postulated that the rapid transition of electrode potential from high to low is associated with a structural modification of the compact oxide layer resulting in an increased etching rate of the oxide film. The fact that the minimum thickness occurs at the maximum potential and maximum thickness at the minimum potential suggests the formation of two types of oxide films: one type requires a higher field to grow and is more compact than the other type, and the phase transition between them occurs at a certain film thickness.

Ozanam *et al.*[949,951] considered current oscillation to originate in the lateral variation in the surface oxide film at the microscopic level. They proposed a microdomain model in which the electrode surface is viewed as a collection of adjacent, self-oscillating areas. In a steady-state condition the contributions of the various domains to the total current are completely uncorrelated. But on a potential excitation these contributions are synchronized giving rise to the oscillation phenomenon. The physical origin of the microscopic oscillation is considered to involve the defects in the

oxide film which may affect the transport inside the oxide as well as the etch rate of the oxide.

Lehmann[122] proposed a model ascribing the anodic oscillation to the stress-induced phase transformation of the surface oxide film from a dense state to a less dense state which results in changes in the etch rate of the oxide film. As shown in Fig. 5.58, in HF solutions the growth of oxide is accompanied by its dissolution. If the dissolution rate of the dense film is below its formation rate, the thickness of the oxide film will increase. At a certain thickness (about 11 nm) the transition in the oxide morphology to a state highly permeable to chemical species occurs. This leads to a sudden drop in potential. As the etch rate of this less dense film is larger than the growth rate of the dense film at the silicon oxide interface, the total film thickness decreases until the dense slow etching film is exposed to the electrolyte. At a certain thickness the phase transition occurs. Lehmann also postulated that the oscillation in fluoride-free solution follows the same mechanism as in HF solutions except that there is little dissolution of the oxide film and thus the total film increases all the time with periodic transformation of the dense film at the oxide/silicon interface. However, because of the monotonic increase in the total oxide thickness the oscillation is damped after a few periods. Similar to the phase transition mechanism Parkhutik *et al.*[508] proposed that the oscillation is due to formation of a thin oxide film and it subsequent lift-off.

Chazalviel *et al.*[950] proposed a model that differs from Lehmann's only in the cause of the phase transformation. Their model is based on a defective nature of the oxide and the change of oxide property is considered to be due to a sudden loss in the ion and electron blocking properties of the oxide. Breakdown of oxide occurs at the high field condition resulting in a large electronic current or ionic current.

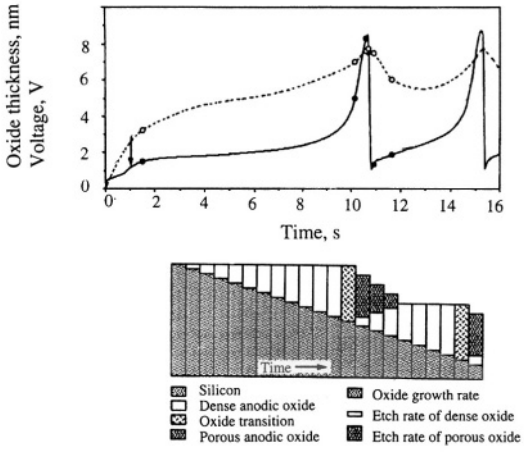

FIGURE 5.58. Voltage versus time curve (solid line) for an n^+-type silicon electrode anodized with a constant current density in NH_4F. The thickness of the anodic oxide was measured by ellipsometry (open circles, dashed line fitted as a guide to the eye). The OCP dissolution time of the anodic oxide in the electrolyte was measured (values above arrows) at different points of the oscillation. The bar graph visualizes the proposed oscillation mechanism. After Lehmann.[122] (Reproduced by permission of The Electrochemical Society, Inc.)

According to Chazalviel *et al.,* the oxide is always being formed with high quality, but can become low quality under a high field. The essential sequence at a constant potential is as follows: (i) fast chemical dissolution of the top low-quality oxide until the high-quality oxide is exposed; (ii) slower dissolution of the high-quality oxide leading to oxide thinning and increasing the field inside the oxide; (iii) breakdown of the oxide under the high field which turns the oxide into the low-quality form accompanying a large current flow; and (iv) fast dissolution of the low-quality oxide occurs along with the growth of the high-quality oxide underneath the low-quality oxide which results in a decrease of current and brings the system back to step (i).

Carstensen *et al.*[1127,1136,1142] proposed a detailed model based on measurements of current transients at different time of a current oscillation period. The macroscopic oscillation is postulated to result from the synchronization of the microscopic oscillators associated with the growth and dissolution of the oxide. Thus, this model is similar to that proposed by Ozanam *et al.*[949,951] in its physical nature, that is, the anodic oxide film on the silicon surface is not uniform laterally but consists of small domains with different thicknesses. At any given time, some of these domains with a thin oxide act as the active channel to conduct current resulting in increase of the oxide thickness to reach a maximum thickness, growth then stopping; some other domains with a thick oxide do not conduct current until the oxide is thinned by the dissolution to a minimum value when a breakthrough current occurs. These local domains act as microscopic oscillators. Macroscopic oscillation occurs when the events associated with these microscopic domains on a macroscopic scale are synchronized. On the other hand, no oscillation occurs when they are not synchronized. In order for this model to agree with the experimental data, a number of assumptions were made: (1) The size of the domains is on the same order as the thickness of the oxide. (2) There are two types of oxides on a macroscopic scale, one being relatively homogeneous and existing at the minimum of the current oscillation and the other being an oscillating oxide. The dissolution rates of the two oxides are constant in the thickness direction with the rate of the oscillation oxide being about 1.7 times that of the homogeneous oxide. (3) The growth of oxide at the local domain is a noncontinuous event regulated by the field; oxide will start to grow when the maximum field, $E_{max} = V/d_{min}$, is obtained, where V is the applied potential and d_{min} is the minimum thickness; the growth will stop when the minimum field, $E_{min} = V/d_{max}$, is reached.

In all of the models described above, the processes involved in the growth and dissolution of the anodic oxide film are recognized to be responsible for the oscillation. The physical and chemical properties of anodic oxides change with time during oscillation, thus resulting in the variation in the oxide growth rate and the chemical etch rate. The models differ from each other only as to the cause of the periodic change of the oxide properties. These models can be grouped according to the assumptions made on the physical origin of the oscillation: those attributing it to the microdomains associated with the lateral inhomogeneity in the oxide film, and those attributing it to a sudden change in the properties of the oxide film during its growth. For the microdomain models, the physical basis for the occurrence of these domains is not clear. A related problem with the microdomain model is its implied micro surface roughness. However, the silicon surface after the dissolution in the potential range, in which oscillation occurs, is most smooth.[38] As far as the models based on a sudden change of

properties are concerned, there is also a difficulty of finding the physical basis. It is known that the oxide films formed under anodic polarization are amorphous in nature and vary in stoichiometry and density. It is unlikely that an amorphous structure would have sudden phase transformations like a crystalline structure. Amorphous structure, being random in its atomic arrangement, should change gradually rather than suddenly. Lacking the physical basis for the models, none of them can rationally explain the conditions for current oscillation to occur.

A New Model. The results of the studies on anodic oxide films (see section 5.9 and chapter 3 on passive film and anodic oxides) show that anodic oxide properties (oxidation state, degree of hydration, O/Si ratio, degree of crystallinity, electronic and ionic conductivities, and etch rate) are a function of the formation field (the applied potential). Also, they vary from the surface to the oxide/silicon interface, which means that they change with time as the layer of oxide near the oxide/silicon interface moves to the surface during the formation and dissolution process. The oxide near the silicon/oxide interface is more disordered in composition and structure than that in the bulk of the oxide film. Also, the degree of disorder depends on the formation field which is a function of thickness and potential. The range of disorder in the oxide structure is thus responsible for the variation in the etch rate of the oxide formed at different times during a period of the oscillation. The etch rate of silicon oxides is very sensitive to the structure and composition (see Chapter 4).

As illustrated in Fig. 5.59, the oxides at points A and B in the same film have different properties at a given time. The properties of the oxide at A, when it moves to the surface, gradually change to become identical to those of the oxide at B within

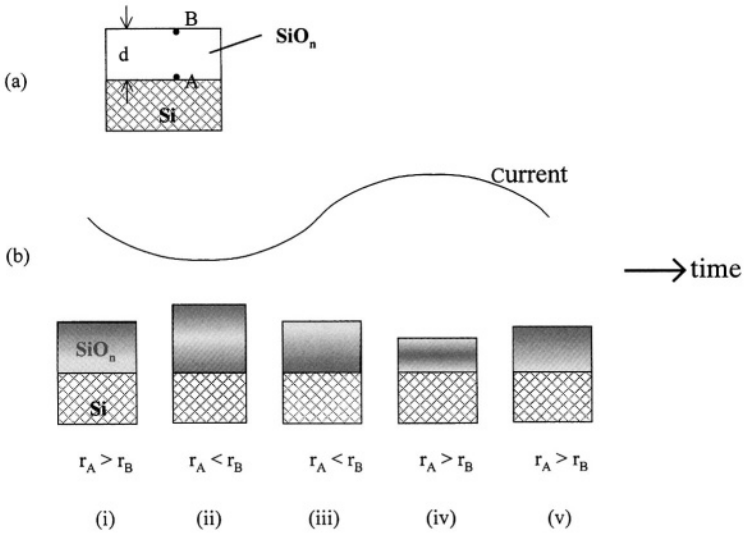

FIGURE 5.59. Schematic illustration of oxide properties and thickness during current oscillation. (a) Oxides at point A of the interface and point B at the surface have different properties. (b) Change of oxide density (shade) and thickness along with the change of current during current oscillation.

a time which is determined by the thickness and the dissolution rate of the oxide, $t = d/r_B$. Such a gradual change of the properties of the anodic oxide from the time of its formation to the time of its dissolution can explain the phenomenon of current oscillation. The difference of this model from the previous ones is that it does not assume micro domain effects nor sudden change of oxide structure. Oscillation is viewed as a result of inconsistency between fromation and dissolution rates of oxide in response to current or potential perturbations on the aging process of the oxide as it moves from A to B.

When the conditions are such that the oxide formed at the Si/oxide interface, A, as it is moved to the surface, changes to the oxide at point B and has the etch rate of oxide B, the system is stable and no oscillation occurs. On the other hand, when the property of the oxide formed at A is not the same as that of the oxide by the time it reaches point B, the etch rate of the oxide film will vary and current oscillation may occur. When current oscillation occurs, as illustrated in Fig. 5.59b, the thickness and variation of properties in the thickness direction change with time. The structure and etch rate of the oxide formed at A with a thin film are different from that with a thick film because of the difference in aging time.

In a given solution, the rate of oxide growth is a function of the field, that is, $r_A = f(V/d)$. The dissolution rate of oxide is a function of solution composition, formation field, and the time lapse between formation and dissolution of the oxide, $t_{A\text{-}B}$, that is, $r_B = f([F], pH, V/d, t_{A\text{-}B})$. At a steady state, the rate of oxide growth equals the rate of its dissolution, $r_A = r_B$, and the thickness of the oxide film is constant. When $d/r_B \neq t_{A\text{-}B}$, that is, the oxide formed at A has different properties and a different etch rate from that at point B when oxide A reaches the surface, $r_A \neq r_B$, oscillation can occur when the following condition exists.

$$|dr_B/dd| > |dr_A/dd| \tag{5.7}$$

That is, oscillation occurs when the rate of change of the dissolution rate is larger than that of the formation rate. When the change of the oxide formation rate cannot keep up with that of the dissolution rate to make up the corresponding change in the oxide thickness, the thickness will change more, which destabilizes the system. Figure 5.59b illustrates the relative rates of oxide growth and dissolution and the change of oxide thickness and density during an oscillation period.

On the other hand, when $|dr_B/dd| < |dr_A/dd|$, the oxide formation rate is capable of keeping up with the change of the oxide film thickness due to the change of the dissolution rate. Current oscillation will not occur by a perturbation in the system. The variation in the occurrence of oscillation, oscillation amplitude, and frequency with respect to conditions can be further detailed by analyzing the two functions $r_A = f(\Delta V/d)$ and $r_B = f([F], pH, \Delta V/d, t_{A\text{-}B})$.

5.11. PARTICIPATION OF BANDS AND RATE-LIMITING PROCESS

The conduction of the charge carriers in the space charge layer during anodization of silicon can occur either by electron injection into the conduction band or by hole capturing from the valence band. For *p*-type silicon, the anodic reactions in HF

and KOH solutions proceed predominantly over the valence band.[34,73,108,109,207] For *n*-Si, anodic reactions in the dark at current densities higher than the limiting current are a conduction band process but can involve both the conduction band and the valence band under illumination. The relative participation of conduction band versus valence band is a function of light intensity; the conduction band dominates at low light intensity and the valence band at high light intensity.[74,695,873] Table 5.6 summarizes the participation of the two carrier bands under different conditions.

The charge transfer mechanism across the interface barrier layer is different for lowly doped and heavily doped *p*-type silicon. For lowly doped *p*-type silicon the process is by thermal emission of holes to go over the barrier layer whereas it is by Zener tunneling for heavily doped materials.[34,964] For *n*-Si the conduction band processes depend on doping density and on illumination intensity. For heavily doped *n*-Si it is by Zener tunneling and the *i–V* curve is identical to that for *p*-Si. For moderately or lowly doped *n*-Si in the dark the reaction is limited by the minority holes, which are required to initiate the dissolution process. Significant dissolution of *n*-Si can proceed when a large number of holes are generated by illumination.

Large current can also be generated on *n*-Si in HF solutions in the dark at a relatively high anodic potential due to an interface tunneling process.[8,38] When a large anodic polarization is applied to the interface, a large band bending occurs at certain potential values. The space charge layer becomes very thin so that electrons can tunnel through directly from the silicon atoms on the surface into the conduction band in the semiconductor.[1151] Interface tunneling is in essence the same process as current multiplication under illumination in that both proceed by electron injection from the surface into the conduction band. The difference is in the energy levels of the surface species from which the electron injection occurs. The electron injection in current multiplication occurs from the reaction intermediates, the energy levels of which are located near

TABLE 5.6. Participation of Conduction Band and Valence Band in Carrier Conduction

	Conduction band			Valence band		
		n-Si			*n*-Si	
Solution	*p*-Si	Dark	Lighted	*p*-Si	Dark	Lighted
HF						
$V = \text{OCP}$	0	0	partial	0	0	partial
$\text{OCP} < V < V_p$	~0	~100%	partial	~100%	~0	partial
$V > V_p$	~0	~100%	~0	~100%	~0	~100%
KOH						
$V = \text{OCP}$	~0	~0	~0	~0	~0	~0
$\text{OCP} < V < V_p$	?	100%	?	?	~0	?
$V > V_p$	?	100%	?	?	~0	?

Only the electrochemical part of the reactions is considered. The chemical part, which is responsible for almost 100% of the dissolution reaction at OCP in KOH solutions and about half at $\text{OCP} < V < V_p$ *in HF solutions, is not considered. Contribution from minority carriers in the dark is neglected. This table is constructed based on the results presented in Section 3-5 in this chapter and Refs. 8, 22, 34, 73, 74, 108, 207, 269, 695, 700, and 873.*

or above the conduction band edge and can inject electrons into the conduction band without significant band banding. On the other hand, the electron injection in the dark is from the surface silicon atoms which are not oxidized and are located energetically much lower than the conduction band edge and can only inject electrons into the conduction band at large band bending. The energy levels and density of the surface species are related to the fluoride concentration in the solution since the potential needed for a large current decreases with increasing HF concentration.[9]

The results discussed in the preceding sections indicate that the rate-limiting process in the anodic electrode reactions can be involved in the bulk of silicon, in the space charge layer, in the oxide, or in the electrolyte depending on the potential range, silicon type, illumination condition, and solution composition. As schematically illustrated in Fig. 5.60, each of the possible processes in the multilayer silicon/electrolyte interface region can be the rate-limiting process under certain conditions. For example, the anodic reaction processes on *n*-Si in the dark are limited by the minority hole transport in the bulk of silicon, that is, r_2. For *p*-Si and illuminated *n*-Si in fluoride solutions at potentials negative of positive of the first current peak, J_1, the reaction rate is determined by the charge transfer process across the electrode/electrolyte interface, that is, r_4 and r_5. At potentials positive of J_1, i.e., the electropolishing region, the rate-determining step in the anodic reaction is the dissolution of the anodic oxide film, that is, r_{10}. The dissolution of the oxide film formed in the electropolishing region at low fluoride concentrations is mainly kinetically controlled, that is, r_{10}, whereas for high fluoride concentrations the process is mainly diffusion controlled, r_{11}.

In KOH solutions the rate-limiting process at OCP is of chemical nature, i.e., only r_6 is involved. Electrochemical processes, that is, r_4 and r_5, are increasingly involved

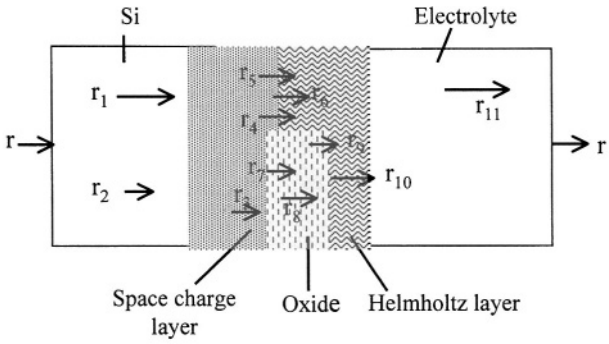

r_1 & r_2 - majority & minority carrier transport, r_3 - transport of holes to the surface
r_4 - charge transfer across the Helmhotz layer, r_5 - electron injection
r_6 - chemical dissolution, r_7 - oxide formation, r_8 - ionic transport in oxide,
r_9 - injection of oxidants, r_{10} - dissolution of oxide,
r_{11} - mass transport in electrolyte

FIGURE 5.60. Schematic illustration of the processes involved in the transport of charge and species in the different phases in the interface region.

as potential is increased from OCP to V_p. At potentials larger than V_p the anodic reaction is limited by the dissolution rate of the oxide, r_{10}, which, unlike in fluoride solutions, is completely kinetically controlled in KOH solutions. Table 5.7 summarizes the rate-determining processes identified for the anodic reactions on silicon under different conditions.

5.12. REACTION MECHANISMS

The rich phenomena observed on silicon electrodes suggest that the detailed mechanisms of anodic reactions on silicon are extremely complicated. Any successful model for the mechanisms must account for the essential aspects: (1) variation of effective dissolution valence of silicon atoms, (2) hydrogen surface termination and evolution, (3) participation of minority and majority bands, (4) formation and dissolution of SiO_2, and (5) the effect of doping, potential, solution composition, and illumination. Numerous models have been proposed focusing on various aspects of anodic reaction mechanisms since the early works of Turner[33] in the late 1950s and Memming and Schwandt in the mid-1960s. In this section, a review of the models on the reaction mechanisms will be given to provide a historical connection among the different models. Based on these models, an overall reaction scheme is then proposed to account for the reactions in both HF and KOH solutions and the specific kinetic characteristics.

5.12.1. Turner–Memming Model

The reactions involved in the anodization of silicon in aqueous solution, depending on whether or not fluoride ions are present, as originally proposed by Turner[33] and Memming and Schwandt,[34] have two different paths determined by the two essential reactants, H_2O and HF.

TABLE 5.7. Rate-Limiting Steps Involved in the Anodic Oxidation of Silicon[a]

	HF				KOH			
	r[b]	p	n	p^+, n^+	r[b]	p	n	p^+, n^+
Dark								
OCP	~0	r_3	r_3	r_3	large	r_6	r_6	r_6
$OCP < V < V_p$	large	r_4	r_2 or r_5[c]	r_4	large	r_6	r_6	r_6
$V \geq V_p$	large	r_{10}, r_{11}	r_{10}, r_{11}	r_{10}, r_{11}	small	r_{10}	r_{10}	r_{10}
Illuminated								
OCP	large	r_4	r_3	r_4	large	r_6	r_6	r_6
$OCP < V < V_p$	large	r_4	r_3 or r_5[d]	r_4	large	r_6	r_6	r_6
$V \geq V_p$	large	r_{10}, r_{11}	r_{10}, r_{11}	r_{10}, r_{11}	small	r_{10}	r_{10}	r_{10}

[a]In aqueous solutions containing no redox couples other than the ones associated with HF, KOH, and H_2O; the effect of redox couples on dissolution is dealt with in Chapter 6.
[b]Qualitative comparison to the dark limiting current density.
[c]It is r_2 below the breakdown potential but it is r_5 above the breakdown potential.
[d]It is r_3 when the current equals the saturation photocurrent, r_5 when the current is larger than the saturation photocurrent, or less.

In solutions of low HF concentrations the surface was considered to be terminated by hydroxyl groups and the anodic reaction proceeds with the formation of $Si(OH)_4$:

$$Si + 4OH^-_{ad} + \lambda h \rightarrow Si(OH)_4 + (4 - \lambda)e \qquad (\lambda - 4) \tag{5.8}$$

where λ is the number of holes involved in the reaction depending on the type of silicon. Figure 5.61 illustrates the steps involved in reaction (5.8). In this reaction, step (b) is rate limiting because it requires a certain thermal activation for a $Si(OH)_2$ group to swing away from the corresponding Si atom. At potentials positive of the passivation potential, the reaction further proceeds to form silicon oxide:

$$Si(OH)_4 \rightarrow SiO_2 + H_2O \tag{5.9}$$

SiO_2 is not soluble in water so that its formation in the absence of HF in the solution leads to the passivation of the surface. In the presence of HF the oxide dissolves to form fluoride complex:

$$SiO_2 + 6HF \rightarrow H_2SiF_6 + 2H_2O \tag{5.10}$$

The overall reaction valence from reactions (5.8) to (5.10) is 4, which accounts for the reactions occurring in the electropolishing region in HF solutions. To account for the effective dissolution valence of 2 at potentials below the passivation potential (potential of the peak current, J_1), it was proposed that silicon reacts directly with HF.

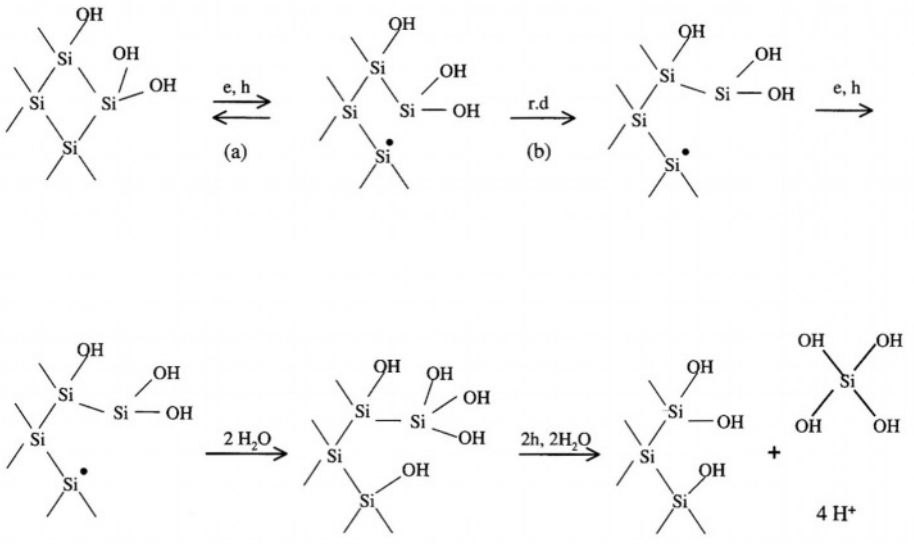

FIGURE 5.61. Mechanism of the anodic dissolution of silicon in low HF concentrations at higher anodic potentials (tetravalent dissolution). After Memming and Schwandt.[34]

$$Si + 2F_{ad}^{-} + \lambda h \rightarrow SiF_2 + (2 - \lambda)e \qquad (\lambda - 2) \tag{5.11}$$

The individual steps involved in this electrode reaction are illustrated in Fig. 5.62. In this reaction scheme the surface is considered to be terminated by fluoride. The first reaction begins at the fluoride-terminated surface. When a field is applied across the interface, holes move toward the surface. One hole is trapped at the surface and a Si–Si bond is weakened (step a). A certain thermal activation is required so that the SiF_2 group swings away from the corresponding Si atom at which the hole is trapped (step b). This process is the rate-determining step and can work only if holes are present and the hole is trapped sufficiently long. The product of reaction (5.11), silicon difluoride, is not stable and tends to change into the stable tetravalent form by further reacting with HF:

$$SiF_2 + 4HF \rightarrow H_2SiF_6 + H_2 \tag{5.12}$$

Reaction (5.12) results in H_2 evolution which is of chemical nature and is responsible for the effective dissolution valence of 2. The Turner–Memming model explains the overall characteristics of the anodic reactions, that is, two different reaction paths in HF and in non-HF solutions; passivation by an oxide film at high anodic potentials; evolution of hydrogen to account for the effective dissolution valence being less than 4. However, it lacks the details to account for phenomena such as surface termination by hydrogen, current multiplication, and variation of effective dissolution valence.

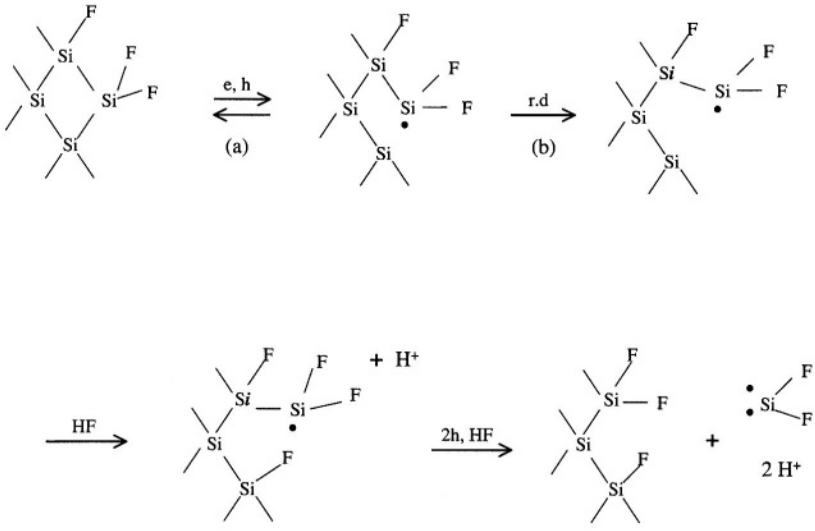

FIGURE 5.62. Mechanism of the anodic dissolution of silicon in concentrated hydrofluoric acid solutions (divalent dissolution). After Memming and Schwandt.[34]

5.12.2. *Later Modifications*

Model to Account for Electron Injection into the Conduction Band. Later studies showed that the quantum efficiency of illuminated *n*-Si in HF solutions varies from 400% (current quadrupling) at low light intensities to 200% (current doubling) at high light intensities as shown in Fig. 5.15.[74,177] The efficiencies of 200% and 400% suggest that the λ value in the following reaction varies from 1 to 2 corresponding to current quadrupling and current doubling:

$$Si + 6HF + \lambda h \rightarrow H_2SiF_6 + 4H^+ + (4 - \lambda)e$$

For current quadrupling this means, according to Matsumara and Morrison,[74] that during the oxidation of Si to Si^{4+} all steps except perhaps the first occur via electron injection into the conduction band. Whether current doubling or quadrupling occurs is determined by the competing processes depending on the availability of holes as illustrated in Fig. 5.63. At low illumination, reaction step III is more favorable and current quadrupling occurs. At high illumination intensities, which generate a large quantity of holes, reaction via steps IV and V is more favorable than step III, resulting in current doubling. This model still assumed a fluoride-terminated initial surface. Also, it did not consider the effect of hydrogen evolution on quantum efficiency.

Modification for Hydrogen Termination. In the late 1980s and early 1990s an extensive amount of research established that the surface of silicon in HF solution is terminated by hydrogen. The models proposed afterwards generally take into account this aspect.[71,700,904,921] Figure 5.64, for example, shows a model, proposed by Lehmann and Gosele,[71] for dissolution at anodic potentials negative of the potential for the first current peak (J_1 in Fig. 5.3). In this potential region, the adsorbed hydrogen atoms are first replaced by fluoride atoms. The fluoride-terminated silicon atoms then react with HF molecules to break the silicon atoms in the lattice and dissolve into the solution.

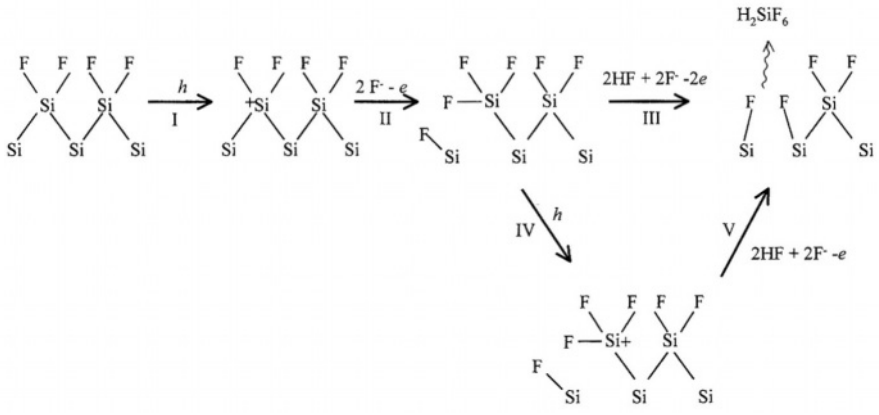

FIGURE 5.63. Reaction pathways during anodic dissolution in HF solution accounting for different quantum efficiencies. (Reprinted from Matsumura and Morrison.[74] © 1983, with permission from Elsevier Science.)

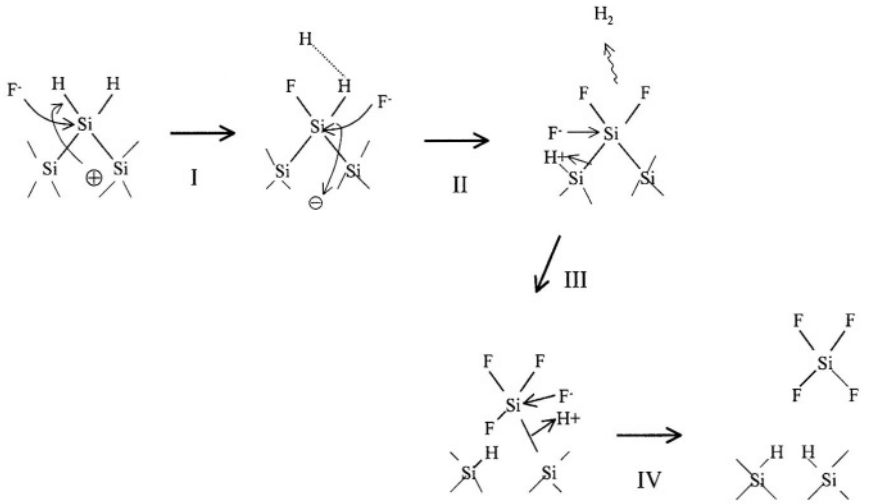

FIGURE 5.64. A model illustrating the breaking of Si–Si back bond due to the polarization resulting from fluoride adsorption. After Lehmann and Foll.[73] (Reproduced by permission of The Electrochemical Society, Inc.)

An important feature of the scheme is that after the dissolution of each layer of silicon atoms the new surface is terminated with hydrogen.

Consideration of Chemical versus Electrochemical Reaction. Based on a study of the effect of pH on the relative contribution of the chemical versus electrochemical reactions in $HF–NH_4F$ solutions, Allongue *et al.*[904] proposed a reaction scheme which consists of a chemical path in competition with an electrochemical path. In the chemical path the first step is $Si–H + H_2O \rightarrow Si–OH + H_2$. The Si–OH bond is then replaced by Si–F followed by attacking of the Si–Si back bond by water, leading to the detachment of the silicon atom. In the electrochemical path the first step is $Si–H + H_2O \rightarrow Si–OH + 2H^+ + 2e$ in which the oxidation of the hydrogen in the surface Si–H bond is considered to require catalytic involvement of F^-. The proceeding steps are the same as those in the chemical path. As pH increases, the chemical reaction, which is relatively low at low pH, becomes dominant. The model, however, lacks the detail to account for the participation of holes and electrons and the different reactions under various conditions.

Individual Steps in the Transfer of Valence Electrons. A number of studies, for example, by Lewerenz *et al.*[626,908] and Stumper and Peter,[599,695,921] have shown that the current multiplication factor varies with light intensity from about 4 at low intensities to about 2 at high intensities while the efficiency of hydrogen evolution changes from 0 to near 1 as shown in Fig. 5.14. They proposed a reaction scheme that involves hole capturing as the first step followed by electron injection as the second step. The oxidized silicon intermediate, having a valence of 2, is then further oxidized by injection of two electrons or reaction with the hydrogen ions depending on light intensity:

$$Si + h \rightarrow Si^{+} \tag{5.13}$$

$$Si^{+} \rightarrow Si^{2+} + e \tag{5.14}$$

$$Si^{2+} + 2H^{+} \rightarrow Si^{4+} + H_2 \tag{5.15}$$

Reaction (15) competes with

$$Si^{2+} \rightarrow Si^{4+} + 2e \tag{5.16}$$

At high light intensities, reaction (5.15) dominates, resulting in hydrogen evolution and the effective dissolution valence of 2. On the other hand, at low light intensities, reaction (5.16) is the dominant reaction and there is little hydrogen evolution, resulting in the effective dissolution valence of 4. However, this reaction scheme does not explain why transition occurs from (5.15) to (5.16) when the light intensity changes from high to low.

An explanation for the transition of the dissolution reaction from valence 4 to valence 2 with increasing light intensity was given in a model proposed by Kooij and Vanmaekelbergh.[261] They assume the presence of an intermediate Si(I), which is an electron-deficient surface silicon atom and has a catalytic effect on the hydrogen reduction reaction. The essential steps in the reaction scheme are described by the following equations:

$$\begin{array}{c} Si(0) + h_{vb} \rightarrow Si(I) - e_{cb} \rightarrow Si(II)_{lattice} - e_{cb} \rightarrow Si(III) - e_{cb} \rightarrow Si(IV) \\ \downarrow + Si(I) \\ Si(II)_{solution} \rightarrow Si(IV) \end{array} \tag{5.17, 5.18}$$

The chemical detail of reaction (5.18) is

$$HSiF_3 + HF + 2F^{-} \rightarrow SiF_6^{2-} + H_2 \tag{5.19}$$

Reaction (5.17) involves one hole from the valence band and the injection of three electrons into the conduction band with no hydrogen evolution. Reaction (5.18) requires the participation of radical Si(I) which is mobile within the layer of surface back bonds and depends on the availability of holes from the valence band, $Si(II)_{solution}$, in the form of $HSiF_3$, is not stable and will further react to form SiF_6^{2-} and H_2 as described by reaction (5.19). The formation rate of Si(I) is proportional to the product of the surface hole concentration p_s and hole capturing rate constant k_p whereas electron injection is a thermally activated process, depending only on the electron injection rate constant k_n. At low light intensities, the reaction via electron injection dominates as the product $k_p p_s$ is smaller than k_n, but as the number of photogenerated holes increases at high light intensities, $k_p p_s$ and thus the concentration of Si(I) increase, which facilitates reaction (5.18), so that hydrogen evolution becomes the predominant process.

This model assumes a rather complicated process, with the involvement of two intermediates, $Si(II)_{lattice}$ and Si(I), as well as one F^- to complete the step of forming $Si(II)_{solution}$. It is not convincing that such a multibody reaction step can significantly compete with the much simpler step to form Si(III) in reaction (5.17) which involves only $Si(II)_{lattice}$.

5.12.3. Models for the Reaction Mechanism in Alkaline Solutions

The mechanisms of the electrochemical reactions of silicon electrodes in alkaline solutions at OCP have been investigated in many studies due to their importance in the etching processes in micromachining. An important issue involving the reaction mechanisms has been whether the etching process at OCP is of chemical or electrochemical nature, that is, whether charge transfer processes associated with silicon dissolution and hydrogen evolution involve the carriers in the electrode.

The experimental results in support of the chemical mechanism are (1) there is little difference between the etch rates of *n*-Si and *p*-Si at OCP[109] and (2) the etch rate is essentially independent of the carrier concentration up to about $10^{19}/cm^3$ [207,259,403] On the other hand, the experimental results supporting the electrochemical mechanism are (1) the etch rate varies with electrode potential with the maximum near OCP, and the etch rates of *n* and *p* types are only similar near OCP, differing significantly at anodic and cathodic potentials as shown in Fig. 7.15; and (2) the *i–V* curves for *n*-Si and *p*-Si, although identical in terms of the chemical nature, are different in terms of carrier involvement, and the values of the characteristic potentials such as OCP and V_p are different for *n*-Si and *p*-Si and for different doping levels.

According to Seidel *et al.*,[206] the dissolution at OCP is an electrochemical process with concurrent anodic dissolution of silicon and reduction of hydrogen ions. The oxidation of silicon gives out electrons which are consumed for the reduction of hydrogen. Both OH^- and H_2O are the active species in that OH^- is involved in silicon dissolution and H_2O in hydrogen evolution:

$$Si + 4OH^- \rightarrow Si(OH)_2O_2^{2-} + 2H^+ + 2e \tag{5.20}$$

$$2H_2O + 2e \rightarrow 2OH^- + H_2 \tag{5.21}$$

The reaction scheme is supported by the fourth power dependence of the etch rate on OH^- and H_2O concentrations observed experimentally (see Chapter 7 on etching of silicon).

On the other hand, Palik *et al.*[114,379,984] suggested that silicon etching in KOH solutions at OCP is of chemical nature and the etching reactions involve H_2O attack on Si–Si bonds to form Si–H and Si–OH bonds followed by OH^- attack to form $Si–O^-$ and H_2. Since the etching product is found to be silicate $SiO_2(OH)_2^-$ the overall reaction was suggested to follow

$$Si + 2H_2O + 2OH^- \rightarrow Si(OH)_2O_2^{2-} + 2H_2 \tag{5.22}$$

which has a ratio of $Si/H_2/carrier$ of 1/2/0. The individual steps were proposed by Palik *et al.* to follow the scheme illustrated in Fig. 5.65.

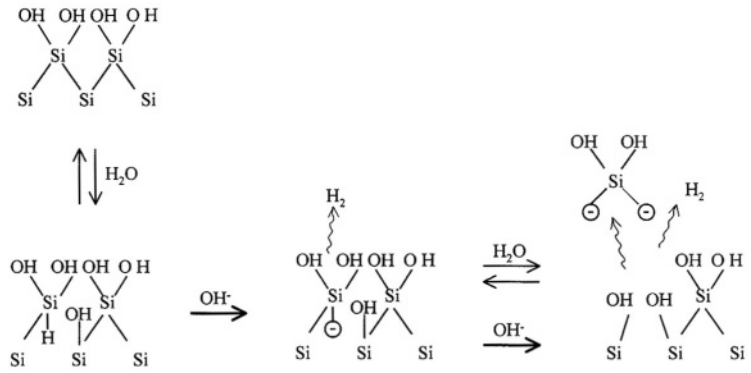

FIGURE 5.65. Reaction steps involved in the dissolution of silicon in alkaline solutions. After Palik *et al.*[114] (Reproduced by permission of The Electrochemical Society, Inc.)

Variation of the ratio of $Si/H_2/carrier$ (see Table 5.1) with potential and type of silicon indicates that other reaction routes also exist according to Palik *et al.*[108] The following reactions are suggested to be responsible for the ratio data observed under different polarization conditions:

$$2H_2O \rightarrow H_2 + 2OH^- + 2h \qquad 0/1/2 \qquad (5.23)$$

$$-\underset{|}{Si}(OH)_2 + 2H_2O \rightarrow Si(OH)_4 + 2e + H_2 \qquad 1/1/2 \qquad (5.24)$$

According to Palik *et al.* for p-Si at potentials negative of V_p the reaction is dominated by reaction (5.22). For *n*-Si at cathodic potential it is a mix of reaction (5.22) and (5.23) while reaction (5.24) is increasingly involved with decreasing potential. However, the reaction scheme described by equation (5.22) to (5.23) results in a OH^- terminated surface which is not in agreement with the later experimental findings that silicon surface is also terminated, dynamically, by hydrogen in KOH solutions similar to that in HF solutions.

The ratio of electrochemical to chemical dissolution rate was measured by Allongue *et al.*[22] to be 0.005 for *n*(100) and 0.075 on *n*(111) at OCP in NaOH solution. The electrochemical portion increases with increasing potential up to the passivation potential above which it is almost completely an electrochemical reaction. It is postulated that since the silicon surface in KOH solutions is also terminated with hydrogen, the first step must then involve a dissociation of the Si–H bond by hydrolysis to form a Si–OH bond.[22,227] Because of the polarization by the Si–OH bond the Si–Si back bonds are weakened and attacked by water, detaching the partially oxidized silicon atom from the surface. The detached silicon atom is a radical and will further react with water to generate another hydrogen molecule. The following are the reaction steps proposed by Allongue *et al.*[22]

$$Si\text{–}H(surface) + H_2O \rightarrow Si\text{–}OH(surface) + H_2 \qquad (5.25)$$

$$Si\text{–}OH(surface) + 2H_2O \rightarrow HSi(OH)_3(solution) + H^+(surface) \qquad (5.26)$$

$$HSi(OH)_3 + H_2O \rightarrow Si(OH)_4 + H_2 \qquad (5.27)$$

The process involved in the second step may generate intermediates to inject electrons into the conduction band, thus accounting for the electrochemical component of the reaction. Depending on whether it is anodically polarized or there are oxidizing species in the solution, the contribution from the intermediates in the chemical and electrochemical paths varies.[541] Figure 5.66 shows the possible reaction processes, proposed by Allongue *et al.*,[22] for the dissolution of silicon at OCP. In the first path, one H_2 molecule is generated in the first step (I) by hydrolysis of one Si–H bond. The second H_2 is produced by the decomposition of the primary product $HSi(OH)_3$ in solution (step IV). Alternatively, both SiH bonds may first be hydrolyzed before the Si–Si bonds are broken. In this case, the two H_2 molecules are generated in the heterogeneous reaction on the surface. In the second path, the Si–Si back bonds are attacked first by H_2O leading to the detachment of the silicon atom (step V) which then further reacts with water to form $Si(OH)_4$ and two hydrogen molecules.

The electrochemical component of the reaction process was considered by Allongue *et al.*[22] to be due to the electron injection associated with the hydrogen replacement step by OH^-:

$$Si\text{–}H + H_2O \rightarrow S\text{–}OH + 2H^+ + 2e \tag{5.28}$$

Figure 5.67 illustrates the reaction steps of the electrochemical path.

According to Campbell *et al.*,[679] the difference between the chemical and electrochemical mechanisms is the way in which the reaction sequence is initiated. In the

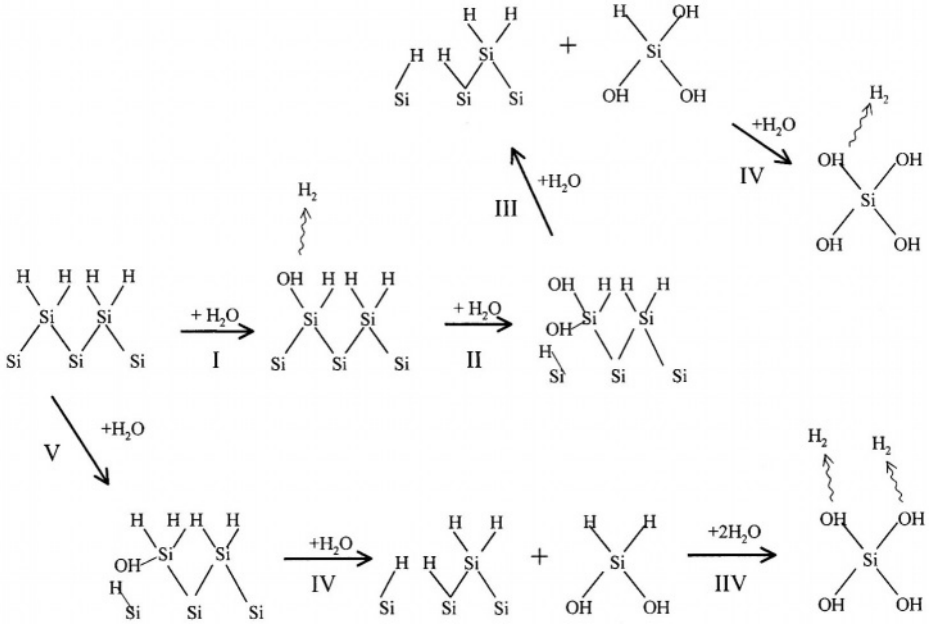

FIGURE 5.66. Possible reaction paths for the chemical dissolution in KOH. After Allongue *et al.*[22] (Reproduced by permission of The Electrochemical Society, Inc.)

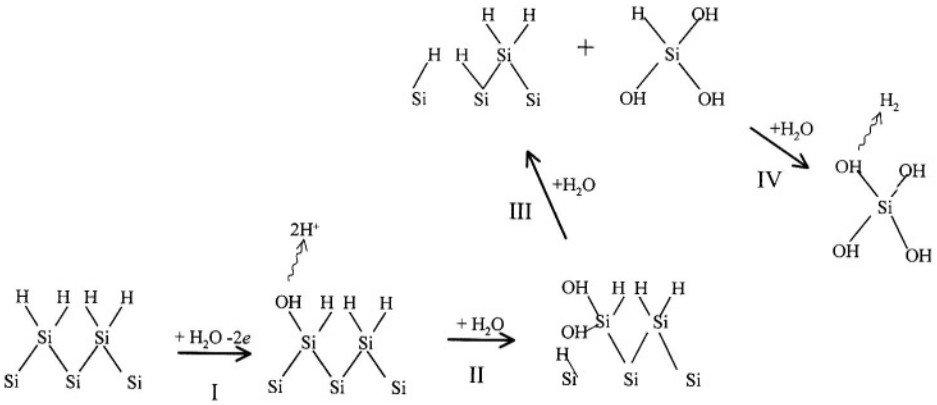

FIGURE 5.67. Reaction path for the electrochemical reaction in KOH. After Allongue *et al.*[22] (Reproduced by permission of The Electrochemical Society, Inc.)

chemical pathway, attack of a Si–Si bond is initiated by water, whereas in the electrochemical pathway, the oxidation reaction is initiated by hole and ligand attachment onto a Si–Si bond.

5.12.4. An Overall Reaction Scheme

The results presented in the previous sections show that the anodic reactions on a silicon electrode may proceed via different paths depending on the conditions and that those in HF solutions and those in KOH solutions are rather different. They also show that the mechanistic models proposed for the reactions in HF and KOH solutions from the many studies in the literature are largely separated. However, in both HF and KOH solutions, the silicon/electrolyte interface is fundamentally similar differing only in the concentrations of hydroxyl and fluoride ions. Thus, a reaction scheme must be coherent with respect to the experimental observations in both HF and KOH solutions. For comparison, Table 5.8 summarizes the characteristic features of the reactions occurring on silicon in HF and KOH, in terms of nature of the reaction, rate, effective dissolution valence, photoeffect, and uniformity of the surface.

Despite the many differences in HF and KOH solutions as shown in Table 5.8, the overall reactions are similar in two important aspects: the silicon surface is dynamically terminated by hydrogen and breaking of the silicon–silicon back bond is facilitated by the adsorption of electronegative ligands such as F^- or OH^-. More specifically this means: (1) the initial surface is hydrogen terminated; (2) the Si–Si back bond requires that the hydrogen termination is first replaced by F^- or OH^-; and (3) the silicon atoms on the newly exposed layer are terminated by hydrogen so that the surface after the dissolution of one silicon layer is identical to that before the dissolution.

A key aspect of the reaction scheme is the valence state of the silicon and hydrogen atoms at different stages of the various reaction paths. The nonpolarized nature of the Si–H bond indicates that the hydrogen atom bonded to the silicon atoms on the

surface is at a reduced state with a valence of 0. The lattice silicon atoms bonded to hydrogen atoms also have a valence of 0 (or four valence electrons). The silicon atoms on the surface which are bonded to one hydroxyl ion or one fluoride ion, on the other hand, have a valence of +1.

Elemental Steps. The dissolution of a surface silicon atom involves first the replacement of the surface hydrogen atom by a OH^- in KOH solutions and by F^- in HF solutions. The difference between the hydrogen replacement by OH^- and F^- is whether holes are involved. As shown in Fig. 5.68, in KOH, on the hydrogen replacement by OH^-, the silicon atom becomes a radical, which in the following reaction steps is neutralized by the reduction of hydrogen ions. In HF, the replacement of hydrogen by F^- requires a hole which results in a neutralized Si–F bonding. The valence state of the

TABLE 5.8. Characteristics of Silicon Electrode in HF and KOH Solutions at Different Potentials[a] and Illumination Conditions

	HF	KOH
Dissociation of solutes	$K = 10^{-3}$–10^{-4} ($HF = F^- + H^+$)	complete ($KOH = K^+ + OH^-$)
Concentration of OH^-	extremely low	high
Activity of H_2O	high	low at high [KOH]
Solubility of SiO_2	high	high
Rate of SiO_2 dissolution	high	low
Hydrogen termination at OCP	yes	yes
Dissolution rate of Si at OCP	none	high
At OCP $\leq V < V_p$	increase with V	decrease with V
	lowest at OCP	highest near OCP
At $V > V_p$, r_p	high, $r_p >> r_{ocp}$	low, $r_p << r_{ocp}$
Effective dissolution valence		
At OCP	no dissolution	~0
At OCP $< V \leq V_p$	2–4	<1
Low light intensity, *n*-Si	~4	<1
High light intensity, *n*-Si	~2	<1
At $V > V_p$	~3.6	~4
Chemical reaction	H_2 evolution	H_2 evolution
At OCP	low	high, ~100%
At OCP $< V \leq V_p$	high, <50%	high, >50%
At $V > V_p$	~0.4	~0
Photocurrent quantum efficiency, *n*-Si		
OCP $\leq V \leq V_p$		
Low light intensity	~4	~0
High light intensity	~2	~0
$V > V_p$	1	1
Band bending at OCP	*p*-Si downward, *n*-Si upward	*p*-Si and *n*-Si downward
Dependence on orientation		
At $V < V_p$	yes	yes
At $V > V_p$	no	no
Dissolution uniformity		
At $V < V_p$	porous silicon formation	anisotropic
At $V > V_p$	uniform	uniform

[a] r_p, dissolution rate in passive region; r_{ocp}, dissolution rate at OCP.

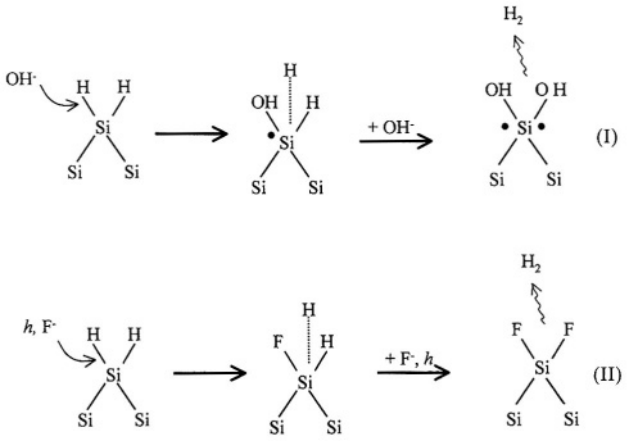

FIGURE 5.68. Elemental steps in the replacement of H by OH^- or F^-.

bonded hydrogen before and after the replacement is not changed in both solutions. The important difference is that after being terminated by a OH^- ion, the silicon atom is a radical with two extra electrons, whereas in Si–F termination the bonds associated with the silicon atom are neutralized.

The hydrogen adsorption onto a silicon atom is a reduction process since the valence of the hydrogen atom is changed from +1 to 0. It occurs when the back bond of Si–SiF or Si–SiOH is broken by reacting with H_2O or HF. Transfer of one electron from the Si–OH bond to the hydrogen of the Si–H bond must then occur as illustrated in Fig. 5.69. An important feature of this process is that no carriers from the solid are involved, and thus this reaction is chemical in nature. This is the key reaction step responsible for the chemical character of the dissolution process in that a hydrogen ion

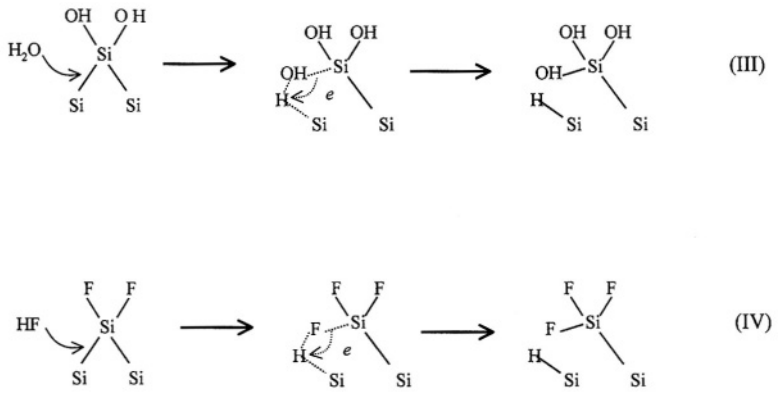

FIGURE 5.69. Elemental steps involved in breaking of Si–Si back bond and termination by hydrogen.

is reduced by an electron from the Si–Si bond. The breaking of the Si–Si back bond by any groups other than HF and H_2O does not preserve the local charge neutrality (the two specific atoms involved in the bonding) and has to involve carriers from the bulk. This would explain why hydrogen adsorption onto silicon does not occur easily by the dissociated hydrogen ions in the solution but rather by H_2O or HF molecules through the attacking of the Si–Si back bonds.

It is experimentally established that even though the surface is predominantly terminated by hydrogen, there is still a small portion of the surface silicon atoms terminated by fluoride. These fluoride atoms may be adsorbed at the surface defects such as kink sites. It can be assumed that the surface fluoride atoms are at equilibrium with the fluoride and hydrogen ions in the solution at OCP:

$$\text{Si–H}_{\text{defects}} + \text{F}^- + \alpha h \rightleftharpoons \text{Si–F} + \text{H}^+ + (2-\alpha)\text{e} \qquad 0 \le \alpha \le 2 \tag{5.29}$$

Note that this reaction results in the oxidation of the adsorbed hydrogen from valence of 0 to +1 and requires the participation of carriers. Thus, reaction (5.29), which results in the replacement of hydrogen by fluoride, is different from reaction (II) in Fig. 5.68, which does not oxidize the replaced hydrogen atom.

Therefore, OH^- and H_2O are the reactants involved in KOH solutions, and F^-, HF, and H_2O are those involved in HF solutions. OH^- and F^- are responsible for initiating the attack by replacing the adsorbed hydrogen atoms, and H_2O and HF are responsible for attacking the Si–Si back bonds. The elemental steps involving these reactions shown in Figs. 5.68 and 5.69 account for the essential features, that is, dynamic hydrogen termination of the silicon surface and weakening and breaking of the silicon back bond due to adsorption of fluoride or hydroxyl ions. The relative contributions of these processes in the reactions can then account for the variations in the effective dissolution valence and in the quantum efficiency under different conditions. An important aspect is that electronic carriers in the silicon semiconductor do not affect the chemical nature of the reactions so that the reactions shown above are the same on *p*- and *n*-type materials. The electronic carriers, however, affect the rate of the reactions and the path of the reactions as will be illustrated in the following.

Reactions Paths. Figures 5.70–5.73 show the reaction schemes for the various situations occurring on silicon electrodes in HF and KOH solutions. The elemental reaction steps (I) to (IV), and reaction (5.29) described above involve different combinations in these reaction paths depending on the solution, potential range, and illumination condition. These different paths can account for the many details experimentally observed in the dissolution or passivation of silicon in HF and KOH. Table 5.9 summarizes the reaction paths involved in different potential ranges in HF and KOH solutions. Variations of the reaction paths from those shown in Figs. 5.70–5.73 are also possible based on the elemental steps outlined in the previous section.

Reaction paths (I) and (II) in Fig. 5.70 account for the anodic reactions on *p*-Si and illuminated *n*-Si in HF solutions at high light intensities. Path (I) is involved in the exponential region at an anodic potential much lower than V_p responsible for direct dissolution of silicon and dissolution valence of 2, while path (II) is involved at a potential above V_p responsible for the indirect dissolution of silicon through formation and dissolution of oxide and for the dissolution valence of 4. At a potential that is lower

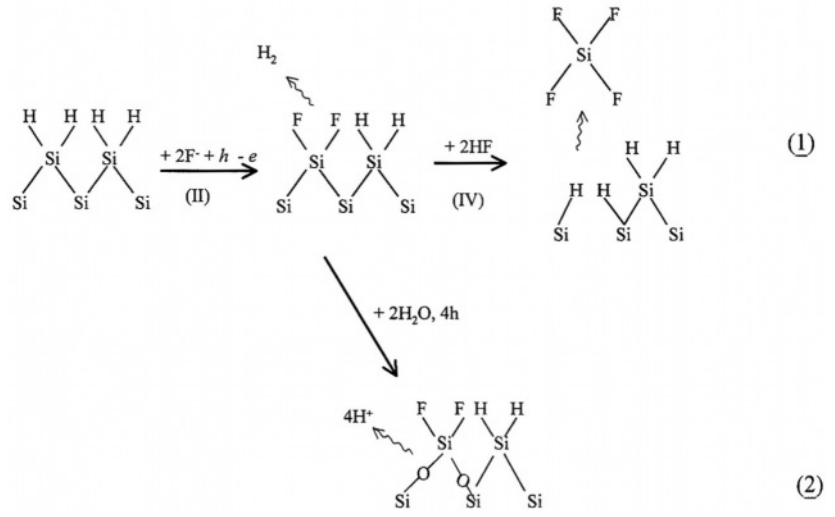

FIGURE 5.70. Possible reaction paths in HF solutions at anodic potentials.

than but close to V_p both paths (1) and (2) are involved resulting in a dissolution valence between 2 and 4.

Reaction path (3) shown in Fig. 5.71 is responsible for the dissolution valence and quantum efficiency of 4 observed on *n*-Si in HF solutions at low light intensities. It results in a dissolution valence and quantum efficiency of 4. This reaction path, which is a combination of reaction step (IV) in Fig. 5.69 and Eq. (5.29), is slow and is revealed only at a low light intensity when the reaction (1) is small. At high light intensities this reaction path is still active but the dissolution valence and quantum efficiency is less than 4 as reaction (1) becomes dominant.

Figure 5.72 shows the reaction paths in KOH solutions. Path (4), which involves no holes and electrons, is responsible for the chemical dissolution in KOH solutions at OCP. A possible alternative of (4) is (4a) as shown in Fig. 5.73. Path (5) involves two carriers and is responsible for the electrochemical part of the dissolution reaction at

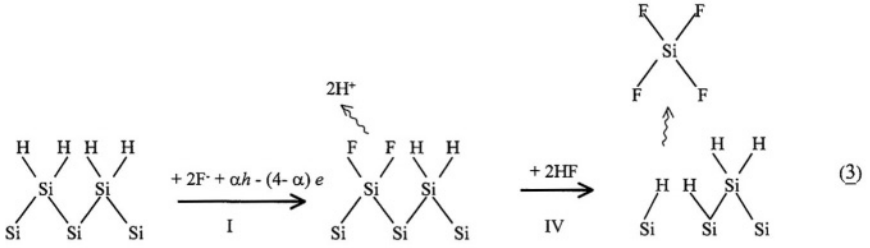

FIGURE 5.71. Reaction path for *n*-Si in HF at low light intensities.

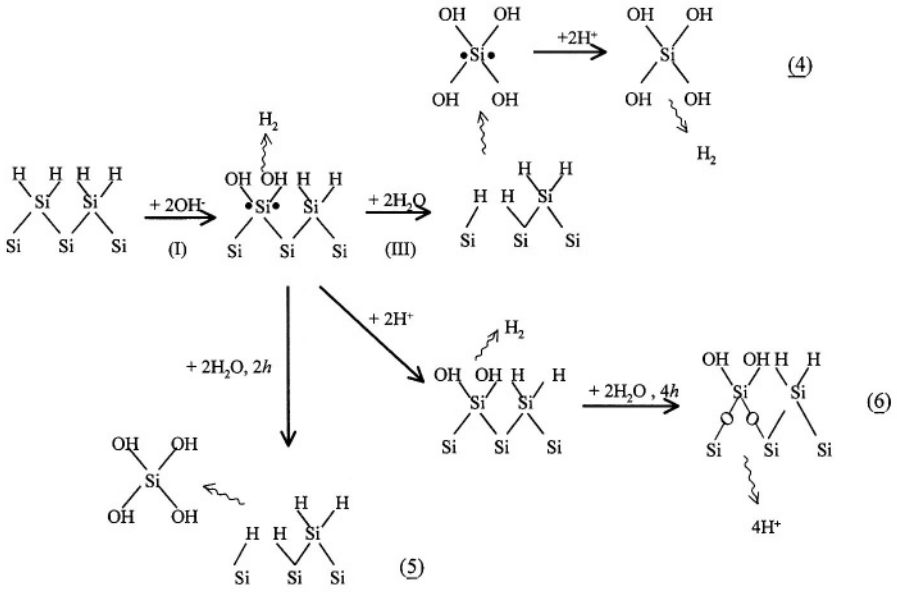

FIGURE 5.72. Possible reaction paths in KOH solutions.

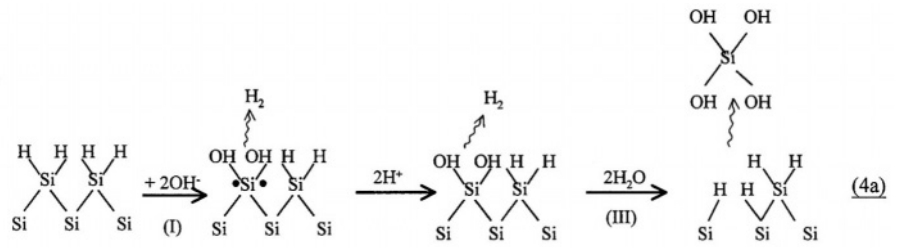

FIGURE 5.73. An alternative of reaction path (*4*) in KOH.

TABLE 5.9. Effective Dissolution Valence and Conditions for Different Reaction Paths Shown in Figs. 5.70–5.73

Path	n	Conditions
		HF
(1)	2	OCP < V << V_p
(1) and (2)	2 < n < 4	OCP << V < V_p
(2)	4	$V \geq V_p$
(3)	4	n-Si, low light intensity, current quadrupling
		KOH
(4)	0	OCP
(4),(5),(6),(7)	<1	OCP < V < V_p
(7)	4	$V > V_p$

anodic potentials below V_P. Path (6) results in formation of the Si–O–Si bond and is responsible for the oxide formation and passivation at potentials above V_p.

Except for reaction path (4) which is purely chemical in nature, all the other reaction paths are electrochemical in nature, at least partially. These electrochemical reactions depend on the carrier transfer between the states at the interface and those in the semiconductor and thus their rates increase with increasing potential or illumination. While reaction paths (1), (3)–(5) result in the direct dissolution of silicon, reaction paths (2) and (6) result in the formation of Si–O–Si bonds. The rate of reaction paths (2) and (6) also increases with potential. As the coverage of the surface by Si–O–Si bonds increases with increasing potential, the surface becomes increasingly less active and becomes passivated when these bonds fully cover the surface as shown in Fig. 5.74. Further reaction has to proceed via the dissolution of the Si–O–Si bonds which is fast in HF solutions but is very slow in KOH solutions. The surface of the oxidized silicon layer is terminated by OH in KOH and may be terminated by both OH and F in HF. In HF on the surface covered by an anodic oxide layer the adsorption of OH is required for the growth of the oxide whereas the adsorption of F may be required for the dissolution of the oxide. The Si–O–Si bonds are rather stable in KOH such that the dissolution rate in the passive region is very low. On the other hand, the Si–O–Si bonds are not stable in HF due to the attack by the fluoride species and the dissolution rate is high in the passive region (at potential higher than that of first current peak, J_1).

For the anodic dissolution of silicon in HF solutions, the first step involving replacement of hydrogen by fluoride and evolution of hydrogen, the rate is proportional to the product of $[H_{Si}]\cdot[F^-_{solution}]\cdot[hole_{surface}]$ according to reaction (1). The following step involving breaking the Si–Si back bond is proportional to [Si–F]·[HF]. On the other hand, for the chemical dissolution of silicon in KOH solutions, the rate of hydrogen replacement is proportional to $[H_{Si}]\cdot[OH^-_{solution}]$ and is proportional to $[Si–OH]\cdot[H_2O]$ in breaking the Si–Si back bond according to reaction (4). A major difference between the reactions in the two solutions is that the hydrogen replacing step in HF requires holes whereas in KOH it does not. Thus, it can be seen that in HF solutions the reaction rate is low at OCP but rapidly increases with potential. On the other hand, in KOH

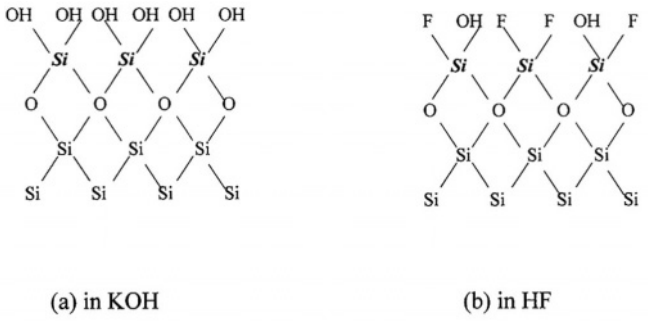

(a) in KOH (b) in HF

FIGURE 5.74. Schematic illustration for the formation of Si–O bonds in KOH and HF solutions at potentials more positive than the passivation potential.

solutions the rate of the dissolution reaction is high and does not increase with potential because carriers are not involved. Due to the high concentration of OH^-, the rate of reaction (4) is high in KOH solutions, but the rate is very low in HF solutions because of the extremely low OH^- concentration.

According to reactions (1) and (4), the concentration of hydrogen ions in both solutions does not play a direct role in the reaction processes. This is because the concentration of adsorbed hydrogen $[H_{Si}]$, which is generated when the silicon back bond is broken, depends on [HF] in HF solutions or $[H_2O]$ in KOH solutions independent of the hydrogen ion concentration in the solution $[H^+]$. This explains why high dissolution rates are observed in KOH solutions, in which the concentration of hydrogen ions is extremely low. It needs to note that in non-aqueous fluoride containing solutions with salts such as BF^-_4, the silicon surface is not terminated by H.[1015,1011] The dissolution process is completely electrochemical and does not involve the formation of oxide due to the lack of HF and H_2O in the solutions.

This page intentionally left blank

6

Cathodic Behavior and Redox Couples

6.1. INTRODUCTION

This chapter concerns the reactions that occur at cathodic potentials and those related to redox couples. The cathodic reactions of many silicon/electrolyte systems have been the subject of numerous studies, but they generally have not been investigated to the level of details comparable to the anodic reactions in fluoride and alkaline solutions. As a result, cathodic processes such as hydrogen evolution and metal deposition are not as well characterized and are much less understood than those at anodic potentials. This had been largely due to the lack of mainstream applications of the cathodic reactions in the silicon technologies. However, the research activities on cathodic reactions, most notably on metal deposition on silicon, have, significantly increased in recent years because of the demand for higher quality wafer surface and the industry's drive to use copper instead of aluminum as the conducting material for microdevices. It can be expected that in the future, research progress in this area will be fast as many details of the cathodic reactions on silicon are characterized and deeper systematic understanding of the various phenomena is obtained.

6.2. HYDROGEN EVOLUTION

Hydrogen evolution is a particularly important electrode reaction on silicon in that it is involved in almost all reactions at both anodic and cathodic potentials. Hydrogen reaction is a principal process that determines the surface condition of silicon. The surface of a silicon electrode can be passivated by hydrogen termination of the surface silicon dangling bonds, which is a technologically very important feature. Hydrogen evolution is a part of the etching process of silicon in alkaline solutions and occurs during anodic dissolution in fluoride-containing solutions. Thus, hydrogen reaction affects all electrode processes on silicon in aqueous electrolytes, such as cleaning, metal deposition, redox reactions, formation of anodic oxides, and quantum efficiency of photocurrent.

The data presented in the following section concern only the hydrogen reaction at cathodic potentials. Those on hydrogen termination are presented in Chapter 2 and on silicon dissolution in Chapter 5. It is to be noted that as a reduction reaction, hydrogen evolution has not been well investigated at cathodic potentials although it has been the subject of numerous studies on the phenomena at anodic or open-circuit potentials.

6.2.1. Kinetics

Hydrogen evolution is the dominant cathodic reaction on silicon electrodes in aqueous solution lacking other redox couples. In HF solutions, H_2 evolution is the only cathodic reaction and the charge transfer process proceeds almost entirely over the conduction band.[34,73] Figure 6.1 shows the i–V curves measured on *n*-Si in 1% HF.[1153] The current increases exponentially with decreasing potential with the apparent Tafel slope being 140–160mV/decade. The exponential *i–V* relationship is also seen on illuminated *p*-Si at currents that are significantly lower than the saturation value as shown in Fig. 6.2.[812] The Tafel slope for the hydrogen reaction for all types of silicon materials in the dark or under illumination appears to be between 140–200mV/decade.[869] This is much higher than the 60mV/decade required for the processes that are limited by the supply of electrons from the semiconductor, which suggests that the charge transfer reaction involved in the hydrogen evolution at cathodic potentials is mainly controlled by the processes in the Helmholtz layer.

A relatively large overpotential is required for hydrogen evolution to occur at appreciable rates. Figure 6.2 shows that the potential required for the onset of hydrogen evolution on silicon is about 300mV more than that on platinized Si.[812] An overpotential as high as 1.1V was required for a reduction current of hydrogen at a current of about $100\,\mu A/cm^2$ on an *n*-Si in a H_2O–CH_3CN–NaI solution.[272] The evolution of hydrogen on silicon electrodes, both for *n*-Si in the dark and for illuminated *p*-Si, is

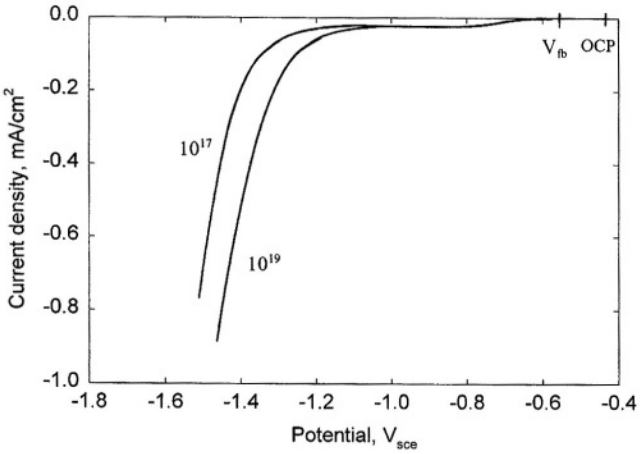

FIGURE 6.1. Cathodic *i–V* curves measured on *n*-Si in 1% HF. After Zhang.[1153]

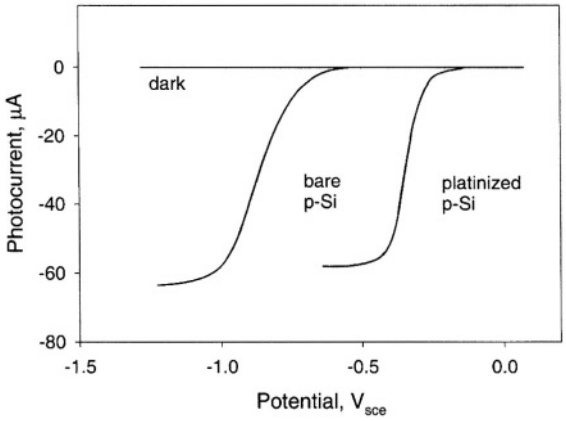

FIGURE 6.2. Steady-state photocurrent–voltage curves for naked *p*-type Si and for platinized *p*-Si. Aqueous solution buffered to pH 6.6. Illumination is at 632.8 nm, 2.5 mW/cm^2. The platinized *p*-type Si was prepared by photoelectrochemical redution from 1×10^{-3} M K_2PtCl_6 in 0.1 M $NaClO_4/H_2O$ at -0.3 V_{sce} until 1.1×10^{-2} C/cm^2 had passed. After Dominey *et al.*[812]

thus a slow process, in agreement with the fact that very few materials yield a high exchange current density for the H_2O/H_2 redox couple.[1155]

The exchange current density for hydrogen reduction is in the range of 10^{-6}–10^{-11} A/cm^2 depending on the specific conditions of the silicon/electrolyte system. For example, it is on the order of 5×10^{-9} A/cm^2 on *n*-Si in 5% HF solution.[254] In 2% HF, it varies from 2.8×10^{-11} to 1.8×10^{-10} A/cm^2 depending on doping levels.[146] The exchange current of illuminated *p*-Si appears to be much higher than that of *n*-Si in the dark. It is about 1.6×10^{-6} A/cm^2 on illuminated *p*-Si in 0.1M NaCl solution and changes very little with light intensity.[869] Similar values are found on illuminated *p*-Si in 2% HF.[146] For comparison, the exchange current of hydrogen evolution in acidic solutions on Pt is on the order of 10^{-3} A/cm^2, representing a fast reaction, and it is on the order of 10^{-13} A/cm^2 on Pb, representing a very slow reaction.[1155]

The rate of hydrogen evolution varies with solution composition and in particular with pH. It is higher at neutral pH values than at acidic pH, which is not consistent with that observed on Pt.[812] The kinetics may also greatly change due to the adsorption of solution species or presence of solid phases on the surface. For example, hydrogen evolution in H_2SO_4 on illuminated *p*-Si is inhibited by addition of formic acid in the solution due to the chemisorption of HCOOH on the electrode surface.[688]

The reaction kinetics is particularly sensitive to trace amounts of noble metal impurities in the solution such as Cu and Au, which tend to deposit on the silicon surface. For example, an increase of the exchange current density from 5×10^{-9} A/cm^2 to 2×10^{-7} A/cm^2 is measured with 15 ppb copper ions as contaminant in the solution.[254] On the other hand, deposition of metals such as Pb and Cd, which have lower exchange currents than silicon, inhibits the hydrogen evolution.[688]

Hydrogen evolution can be catalyzed through deposition of a layer of metal or polymer on the silicon surface or by addition of a redox couple in the solution.[553,848,875]

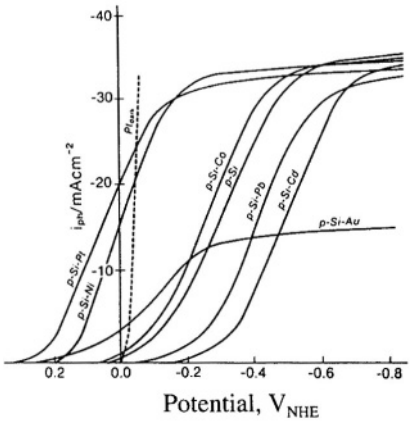

FIGURE 6.3. Cathodic *i–V* curves on *p*-Si-Me electrodes (50 mW/cm^2 Xe light, 0.5 M H_2SO_4). (Reprinted with permission from Szjkarczky and Bockris.[829] © 1984 American Chemical Society.)

Figure 6.3 shows the effect of different metal deposits (as islands equivalent to a few monolayers with about 90% surface coverage) on the photocurrent of *p*-Si.[829] The shift of the *i–V* curve from that of bare material is due to the catalytic effect of the metal on hydrogen evolution. For a metal deposit the photocurrent is parallel to the exchange current density for the dark evolution of H_2; Pt, as a catalyst, has the highest exchange current whereas Pb, as an inhibitor, has a very low exchange current.

Hydrogen evolution on *p*-Si can also be catalyzed by adding a redox species to the solution as shown in Fig. 6.4.[826] The reactions involved are postulated by Bookbinder *et al.*[826] as

$$PQ^{2+} + \text{light} \rightarrow PQ^{+}\cdot \tag{6.1}$$

$$2PQ^{+}\cdot + 2H_2O \rightarrow 2PQ^{2+} + H_2 + 2OH^{-} \tag{6.2}$$

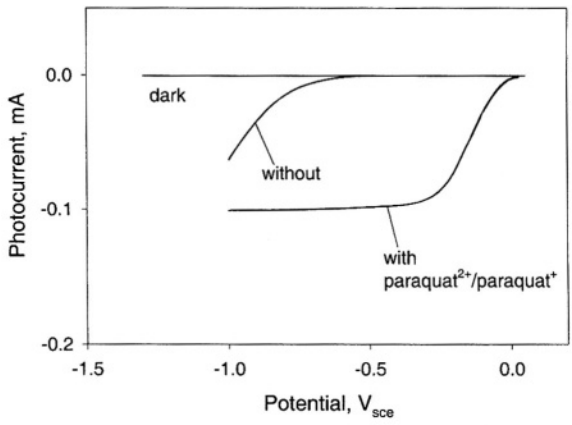

FIGURE 6.4. Effect of a redox couple on the *i–V* curves on *p*-Si in the dark and under illumination in a mixture of H_2O and CH_3CN with 0.1 M NaI. After Bookbinder *et al.*[826]

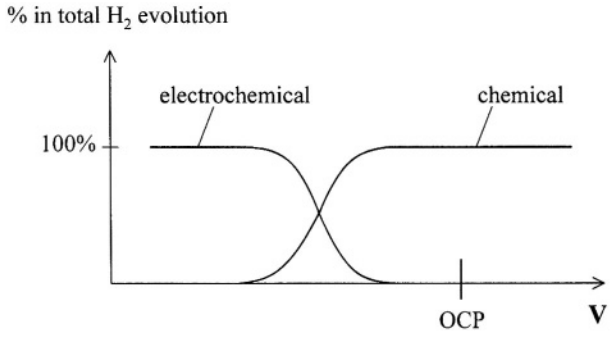

FIGURE 6.5. Schematic illustration of the relative contributions of chemical path versus electrochemical path in H_2 evolution.

Hydrogen evolution on silicon may proceed chemically or electrochemically depending on the conditions. As discussed in Chapter 5 on anodic behavior, hydrogen evolution near the OCP and at anodic potentials can proceed completely chemically, i.e., without involving the carriers from the electrode. A change from a chemical process to an electrochemical process occurs as the potential varies from anodic values to cathodic values as schematically illustrated in Fig. 6.5. At anodic potentials, hydrogen evolution is a result of the chemical reaction involved in the dissolution of silicon. At cathodic potentials, silicon does not dissolve and the concentration of electrons on the surface of *n*-Si or illuminated *p*-Si is high. Thus, hydrogen evolution at cathodic potentials is predominantly electrochemical due to the lack of silicon dissolution and abundance of electrons on the surface.

6.2.2. Surface Transformation

In non-fluoride-containing solutions, silicon is stable due to the presence of an oxide film and the electrode behavior can remain constant under a continuous cathodic polarization.[396] The surface of a silicon electrode in fluoride-containing aqueous solution at the open circuit potential is also stable due to hydrogen adsorption. However, surface transformation can occur at cathodic potentials due to formation of hydrides. Thermodynamically, silicon hydride can be a stable phase at certain cathodic potentials as shown in Fig. 2.2.

Formation of a hydrogen-rich layer on the silicon surface in HF at cathodic potentials has been observed.[241] Figure 6.6 shows that the limiting current for hydrogen evolution on illuminated *p*-Si in 5% HF is less than $3\,\mu A/cm^2$ up to $-3\,V_{sce}$ but increases with the duration at cathodic polarization. The hydrogen-rich surface layer can be removed by maintaining the sample at the OCP or at an anodic potential for some time during which the surface is etched. According to de Mierry *et al.*,[241] during the hydrogen evolution, hydrogen atoms enter the surface region to a depth of about $0.1\,\mu m$ causing amorphization and strain-induced defects which can act as generation centers responsible for the increase in dark current. The surface, which has been polarized at $-3\,V_{sce}$ under illumination, shows circular patterns due to H_2 bubbles adhering to the

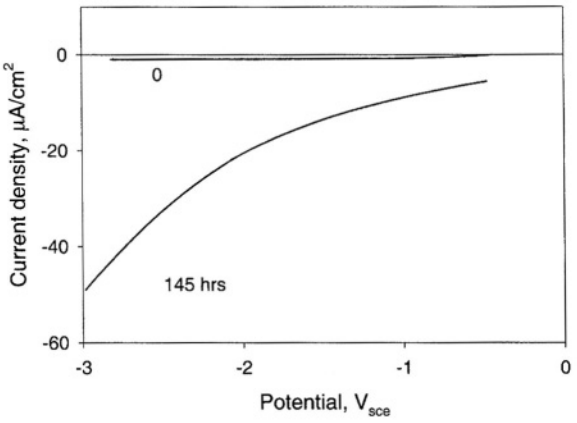

FIGURE 6.6. Evolution of the reverse current on *p*-Si in dark and during a prolonged photocathodic polarization at $3\,V_{sce}$. After de Mierry *et al.*[241] (Reproduced by permission of The Electrochemical Society, Inc.)

surface. The area not covered by the bubbles is etched by about 50–100 nm after polarization for about 50 h. The dissolution at this negative potential implies that the absorption of hydrogen results in an increased reactivity of the silicon.

Formation of an amorphous silicon hydride surface layer can also occur during anodic photoetching of *n*-Si. For example, surface Si–H bonds corresponding to about 40 monolayers of hydrogen on an *n*-Si have been observed to form at a photocurrent of $i_{ph} = 0.5\,mA/cm^2$ in 0.5mM NH_4F.[704]

Thus, the silicon surface is fully covered by an oxide film at anodic potentials higher than V_p, whereas it is fully covered by hydrogen at potentials more negative than the OCP. From the OCP to V_p, the surface coverage of hydrogen gradually decreases as the coverage of hydroxyl increases. Also, whereas at potentials near the OCP and below V_p the hydrogen or oxide layer is on the order of a monolayer, the hydride layer at cathodic potentials and the oxide layer at $V > V_p$ is thicker than one monolayer. Figure 6.7

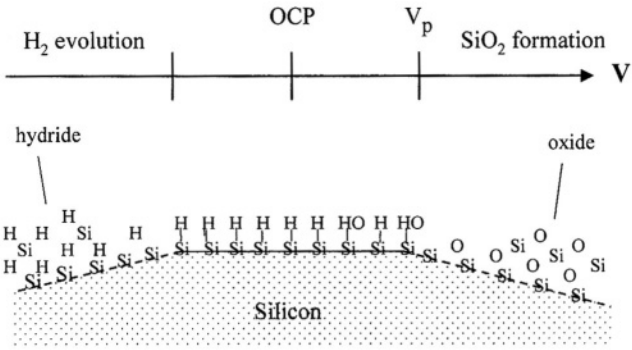

FIGURE 6.7. Schematic illustration of the surface condition of Si as a function of potential.

schematically illustrates the surface condition of silicon electrodes in terms of hydride and oxide coverage and thickness in the different potential ranges.

6.3. METAL DEPOSITION

Metal deposition can occur either electrolessly at the OCP or under a cathodic bias. Both processes are electrochemical in nature in that the deposition of metal atoms is a reduction reaction involving charge transfer with the substrate. Although deposition under bias provides the best quantitative control of the deposition process, it is the electroless deposition that has received more attention for metal deposition on silicon surface, mainly due to the simplicity of the process. In most cases, as shown in Table 6.1, the deposition is limited to noble metals such as copper, gold, and platinum mainly due to their excellent conductivity and chemical stability, which are important in the application of microdevices. Also, the electroless deposits from trace amount of metals on silicon during wet processing steps are very important in silicon technology since they cause serious problems in further processing and eventual performance of devices. However, metal deposition on silicon, as pointed out in a recent review by Oskam *et al.*,[848] despite its potential importance in metal/semiconductor contact technology, has not been well investigated. The recent interest in replacing aluminum metallization by copper has resulted a renewal of research activities in electrochemical deposition of metals onto silicon.

6.3.1. Kinetics

The driving force for metal deposition on a semiconductor electrode is determined by the difference between the Fermi level of the electrode and the reversible potential of the metal species in the solution. For the noble metals this difference at the OCP is generally negative indicating that the deposition process is spontaneous, which is the basis for electroless deposition. As shown in Fig. 6.8, the redox potentials of the

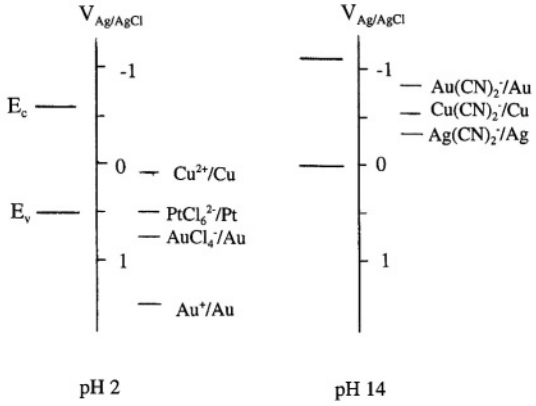

FIGURE 6.8. The effective equilibrium potentials for various metal/metal ion complexes with respect to the position of the band edges for silicon surfaces in aqueous solution at pH 2 and 14. After Oskam *et al.*[848] (© 1998, Reprinted by permission of John Wiley & Sons, Inc.)

TABLE 6.1. Examples of Studies on Metal Deposition on Silicon Electrodes

Metal	Solution	Method	Focus	Refs.
Au	$KAu(CN)_2 + KCN$	*i–V*, *i–t*	growth kinetics	848, 1145
	$KAu(CN)_2$	*i–V*, *i–t*	deposition on *p-i-n* amorphous Si	315
Cu	5% HF + 5 ppm Cu^{2+}	AFM	deposit morphology	120
	1% HF + 0.1 ppm Cu^{2+}	ac impedance	deposition kinetics	295
	BOE[a] + up to 0.5 ppm Cu^{2+}	TXRF	surface concentration	135
	$CuCO_3 + H_3BO_3 + HBF_4$	*i–V*, *i–t*	growth kinetics	848
	1% + 0.1 ppm Cu^{2+}	TXRF, *i–V*	kinetics	96
	50 mM $Cu^{2+} + H_3BO_3 + HBF_4$	*i–V*, *i–t*, SEM	nucleation on Si/TiN	990
	$H_2SO_4 + CuSO_4 + HF$	AFM	deposit morphology	798
	20 mM Cu^{2+} + 0.1 M $K_4P_2O_7$, pH 8.5	*i–V*, *C–V*, *i–t*	nucleation kinetics	1167
Co	$CoSO_4 + H_3BO_3 + HF$	X-ray, SEM	crystalline structure	143
Ni	$NiSO_4 \cdot H_2O$ + additives	AES, SEM	production of metal dots	1043
	$Ni^{2+} + H_2PO_2^- + NH_4^+ + Cl^-$		deposit for electrical contact	840
	$NiSO_4 + NiCl_2 + H_3SO_3$	*i–V*, SEM	morphology	305
	50 mM Ni^{2+} + 5 M NH_4F, pH 1.2, 8	*C–V*, *i–V*, SEM	kinetics, morphology	1092
Pb	$Pb(ClO_4)_2 + HClO_4$	AFM, *i–V*	nucleation kinetics	831
	$Pb(ClO_4)_2 + HClO_4$	STM, *i–t*	growth microclusters	967
Pt	$(NH_4)_2PtCl_6 + HNa_2PO_4 + HF$	*i–V*, *i–t*	growth kinetics	848
	0.1 mM Pt + $Na^+ + Cl^-$	SEM	deposit morphology	253
	HF	AFM, TEM, XPS	morphology	264
Al, Au, Cu, Sn, Pd	0.5 M H_2SO_4 + HF	AFM	morphology	660, 694

[a]BOE, buffered oxide etchant.

TABLE 6.2. Critical Copper Concentration (in ppb) at Which the Driving Force Is Zero[407]

Light	*n*-Si	*p*-Si
Off	4×10^{-6}	2×10^{-1}
On	2×10^{-9}	2×10^{-7}

noble metals are all below the conduction band edge of silicon indicating that these metals can be deposited electrolessly as well as cathodically.[848] The driving force can be altered by changing electrode potential, metal concentration, and complexing agents in the solution. Also, illumination increases the driving force for both *n* and *p* types of materials due to the negative shift of the quasi Fermi level on illumination.[259]

Electroless deposition of noble metals, even at trace levels, on silicon is practically always possible due to the large driving force. For example, Table 6.2 shows that the critical concentration of copper in solution at which the driving force is zero is extremely low.[407] The critical concentrations are even lower for Au, Ag, and Pt because they have move positive standard potentials than copper.

Figure 6.9 shows the *i–V* curve of copper deposition in a $CuCO_3 \cdot Cu(OH)_2$ solution.[848] The onset of reduction of Cu^{2+} occurs at $-0.3\,V_{Ag/AgCl}$ with a diffusion-limited peak at $-0.38\,V_{Ag/AgCl}$. The current increases again at a more negative potential, about –0.8V, due to hydrogen evolution at the copper deposits which catalyzes the hydrogen evolution reaction. On the reverse scan in Fig. 6.9 a current of about $0.8\,mA/cm^2$ is due to the continuous growth of the copper clusters. The reverse scan does not show an anodic peak indicating that the rate of anodic dissolution of the copper deposits is low due to the large barrier height, about 0.6 eV, existing at the Si/Cu interface. Although copper deposition dominates the cathodic reaction, hydrogen

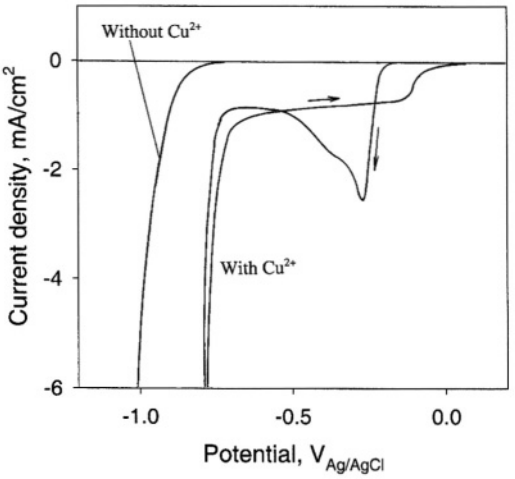

FIGURE 6.9. The current–potential curve for *n*-Si(100), $N_D = 10^{15}\,cm^{-3}$, in 7.5 mM $CuCO_3 \cdot Cu(OH)_2$ with 20 g/liter H_3BO_3 and 9.6 g/liter HBF_4 (pH 14) at a scanning rate of 10 mV/s. After Oskam *et al.*[848] (© 1998, Reprinted by permission of John Wiley & Sons, Inc.)

evolution may significantly compete with copper deposition particularly at very low copper concentrations.[293] The characteristics of the i–V curve for gold deposition onto n-Si in a $KAu(CN)_2$ solution are similar to those for copper.[848,1145]

Deposition of metals on a silicon surface can be either a conduction band process or a valence band process depending on the redox potential of the metal and solution composition. Deposition of Au on p-Si in alkaline solution occurs only under illumination indicating that it is a conduction band process due to the unfavorable position of the redox couple for hole injection.[848] On the other hand, deposition of platinum on p-Si can occur in the dark by hole injection into the valence band. For Cu, although the deposition proceeds via the conduction band as shown in Fig. 6.9, it can also proceed via the valence band because a large anodic current of n-Si occurs in the dark in copper-containing HF solution as shown in Fig. 6.10.[256] The reduction of copper under this condition is via hole injection. The holes are consumed by silicon dissolution and the silicon reaction intermediates then inject electrons into the conduction band, resulting in the anodic current on n-Si in the dark.

The electroless deposition of metals on a silicon surface in solutions is a corrosion process with a simultaneous metal deposition and oxidation/dissolution of silicon. The rate of deposition is determined by the reduction kinetics of the metals and by the anodic dissolution kinetics of silicon. The deposition process is complicated not only by the coupled anodic and cathodic reactions but also by the fact that as deposition proceeds, the effective surface areas for the anodic and cathodic reactions change. This is due to the gradual coverage of the metal deposits on the surface and may also be due to the formation of a silicon oxide film which passivates the surface. In addition, the metal deposits can act as either a catalyst or an inhibitor for hydrogen evolution. Furthermore, the dissolution of silicon may significantly change the surface morphology.

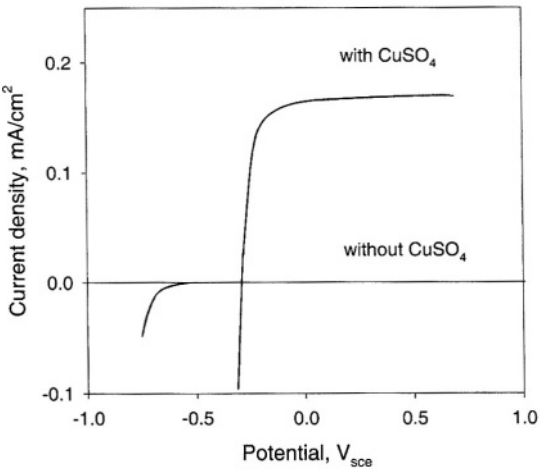

FIGURE 6.10. Current versus potential curves (20 mV/s) obtained on n-Si in the dark with an electrolyte containing 163 mM HF with and without 26 mM $CuSO_4$. After Maritins *et al.*[256] (Reproduced by permission of The Electrochemical Society, Inc.)

Thus, whether a metal can be deposited by electroless deposition onto a silicon surface depends on the redox potential and its relative position to the band edges and on whether the silicon can be dissolved under those conditions. On the other hand, whether the deposition can be sustained to cover the entire surface area depends, on nucleation and growth kinetics of the deposits, the catalytic effect of the deposits on silicon dissolution and hydrogen evolution and the evolution of the morphology of the surface. The formation of a continuous and uniform metal film by electroless deposition is intrinsically difficult because a certain amount of bare silicon surface area is required for silicon dissolution in order to sustain the deposition.

The electroless deposition of Ni in fluoride solutions depends on pH; it does not occur at pH 1.2 but does occur on both *p*-Si and *n*-Si.[1092] This is attributed to the less favorable position of the Ni^{2+}/Ni couple relative to the band edges at low pH than at high pH. Also, the deposition is much faster (~10 times) on *n*-Si than on *p*-Si because the deposition on *n*-Si proceeds in the conduction band with the majority carriers whereas it is through hole injection on *p*-Si. The rate of deposition is limited by the dissolution of silicon on *n*-Si and is limited by Ni reduction on *p*-Si. Figure 6.11 shows the *i–V* curve for Ni deposition on *n*-Si.

Electroless deposition of Au in $KAu(CN)_2 + HF$ can be controlled by both the kinetic process and the diffusion process.[971] The deposition is a two-step process, with initial diffusion-limited deposition of the intermediate species, followed by surface-limited reduction of this species. For electroless deposition of Pt, it has been reported that the rate-determining step is the deposition on *n*-Si, whereas it is the dissolution of silicon on *p*-Si.[253] Electroless copper deposition does not occur on SiO_2-covered silicon surface due to the lack of anodic dissolution of silicon.[237] In a non-HF solution, the deposition of copper on a bare silicon surface results in the formation of oxide around the metal particles. In HF solutions, the deposition of copper proceeds very slowly in the dark on both *p*-Si and *n*-Si samples due to the lack of carriers.[295] The

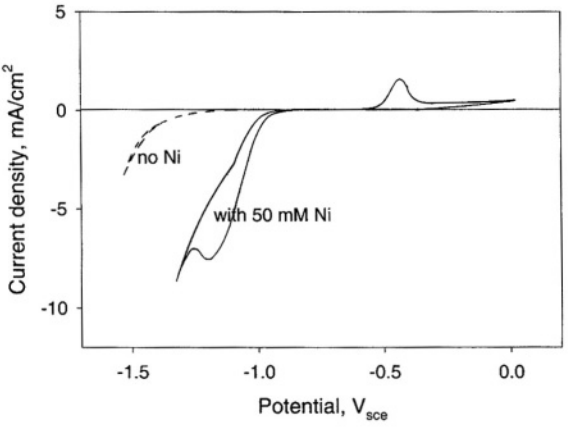

FIGURE 6.11. Cyclic voltammogram of an *n*-Si electrode immersed in the dark. (a) 5 M NH_4F, pH 8.0, no nickel added; (b) with addition of 50 mM Ni. After Agius *et al.*[1029]

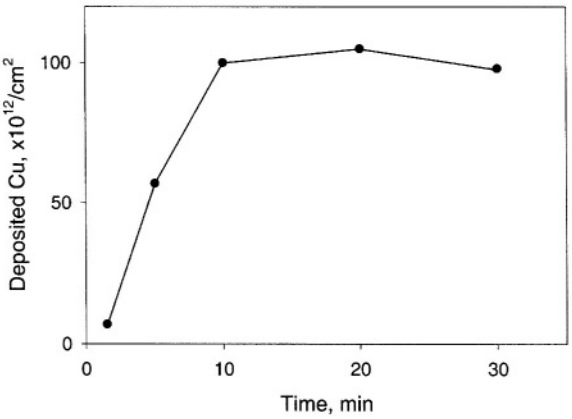

FIGURE 6.12. Copper deposition kinetics on *p*-type silicon from buffered hydrofluoric acid solution containing 100ppb Cu^{2+} under illumination. After Li *et al.*[293] (Reproduced by permission of The Electrochemical Society, Inc.)

deposition kinetics is greatly increased by illumination but decreases with increasing HF concentration.[295,694] The deposition rate changes with time. For example, Fig. 6.12 shows that copper deposition is initially rapid but virtually ceases after 10min, which is attributed to the decreased area for anodic reaction.[293]

Electroless metal deposition at trace levels in the solution is an important factor affecting silicon wafer cleaning. The deposition rate of most metals at trace levels depends mainly on the metal concentration and some may also depend on the interaction with other species as well.[483] For copper the deposition rate at trace levels in HF solutions is different for *n* and *p* types. It depends on illumination for *p*-Si but not for *n*-Si.[293] It is also different in HF and BHF solutions. In a HF solution the deposition process is controlled by both the supply of minority carriers and the kinetics of cathodic reactions.[120] Thus, a high deposition rate occurs on *p*-Si only when both Cu^{2+} and illumination are present. In the BHF solution, the corrosion process is limited by the supply of electrons for *p*-Si whereas for *n*-Si it is limited by the dissolution of silicon because the reaction rate is independent of Cu^{2+} concentration and illumination. The amount of copper deposition does not correlate with the corrosion current density, which may be attributed to the chemical reactions associated with hydrogen reduction. More information on trace metal deposition can be found in Chapters 2 and 7.

Preferential deposition of a metal onto selected areas of an electrode surface can occur when a difference in doping type or in the amount of oxide exists on different areas of the surface. Preferential plating of Au on the *n* region of a *p–n* junction can be generated under illumination.[837] In this case, the *p* region acts as the anode consuming the holes diffused from the *n* region. The greater the potential difference across the junction, the larger is the deposition rate on the *n* region. Such selective deposition has been used as a method for delineation of *p–n* junctions[381] and for producing micro metal structures.[659,756]

6.3.2. *Morphology*

The morphology of metal deposits is determined by the kinetics of the formation process, which in general occurs in two stages: nucleation of deposits and growths of the deposit islands to form a continuous film followed by thickening of the film. On a semiconductor, once a continuous film is formed the semiconductor is isolated from the solution and subsequent growth depends on the properties of the metal deposit.[848] Thus, the effect of the substrate on the morphology occurs predominantly in the nucleation and growth of islands before the formation of continuous film. According to Oskam *et al.*,[848] the deposition of continuous metal films onto a semiconductor surface can be difficult. The interaction energy between metal adatoms and the semiconductor surface is generally small and deposition usually follows the 3D island growth mechanism. In order to obtain a continuous deposit layer the density of nuclei must be sufficiently high for the islands to merge during the deposition. Once the nuclei are formed, further growth into a continuous film requires a non-diffusion-controlled condition to enhance the ratio of lateral growth to vertical growth. Thus, to deposit a continuous film requires an initial large current to produce a high density of nuclei followed by growth at relatively low current.

Metal deposition on the silicon surface may follow an instantaneous or a progressive nucleation process followed by a diffusion-limited growth of the nuclei. The growth of nuclei can be either kinetically limited, diffusion limited, or under a mixed control. The current transients measured by Oskam *et al.*[848,1167] at various potentials of cathodic deposition of copper, platinum, and gold indicate that the deposition of these metals at relatively low metal concentrations proceeds via a nucleation followed by diffusion-limited growth. At high concentrations and large cathodic overpotentials the deposition may proceed through instantaneous nucleation. The nucleation sites become saturated after a short time, a fraction of a second, depending on the potential. Gold

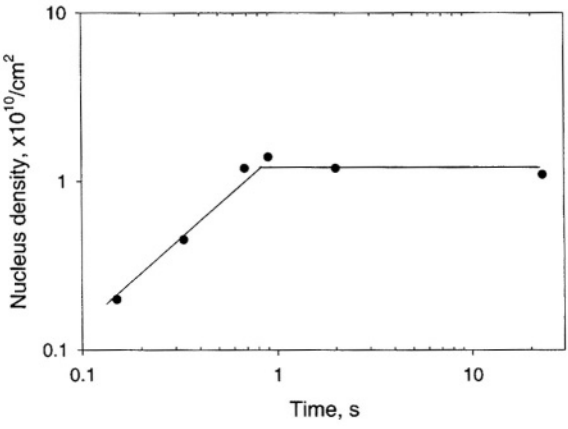

FIGURE 6.13. The nucleus density as a function of the pulse length for deposition at −1.30 V from 2 mM $KAu(CN)_2$ +0.2 M KCN (pH 14), determined using SEM. The nuclei were grown at −1.10 V after the nucleation pulse so that the deposition charge was −3.0 mC/cm^2. After Oskam and Searson.[1145] (Reproduced by permission of The Electrochemical Society, Inc.)

deposition onto *n*-Si in a $KAu(CN)_2$ solution and copper deposition in a $CuCO_3 \cdot Cu(OH)_2$ solution at relative small overpotentials are found to follow the progressive nucleation model whereas copper deposition at large overpotentials follows instantaneous nucleation. The density of the nuclei, depending on many factors, increases rapidly with increasing deposition overpotential. It is about $3 \times 10^7/cm^2$ for copper deposited at –0.8V in a 7.5 mM $CuCO_3 \cdot Cu(OH)_2$ solution. Figure 6.13 shows that the nucleus density is determined by the deposition at $-1.3\ V_{Ag/AgCl}$ whereas it is little affected by subsequent deposition at –1.1 V.[1145] At time less than 0.9 s the deposition is dominated by nucleation whereas it is by growth at a longer time. The rate of nucleation increases linearly on a logarithmic scale with increasing cathodic overpotential.

During electroless deposition of copper in HF solution, the nucleation process dominates initially for about 60 s to produce nanometer-sized nucleus deposits; then growth of the copper grains takes over.[120] As soon as nuclei of metal deposits are formed, the kinetics of deposition is changed as the metal nuclei act as catalytic sites for further metal deposition. The rate of deposition increases with increasing HF concentration.[789] The silicon surface roughens as the deposition continues due to the corrosion reactions.

Deposition of Pb in 5mM $Pb(ClO_4)_2$ and 10mM $HClO_4$ solution at large overpotentials occurs via a 3D island growth.[831,967] It follows a progressive nucleation process at low overpotentials and is mainly initiated at the surface inhomogeneities. The number of atoms in the critical nucleus is estimated to be very small, about 11. The small Pb clusters are stable within a certain anodic potential range.

The morphology of nuclei can be characterized in terms of deposit size and density. Figure 6.14 shows copper precipitate size distribution of *n*- and *p*-Si materials in 0.5% HF solution.[407] The density is higher on *n*- than on *p*-type silicon whereas the size is larger on *p*-Si than on *n*-Si indicating that the rate of nucleation is higher on

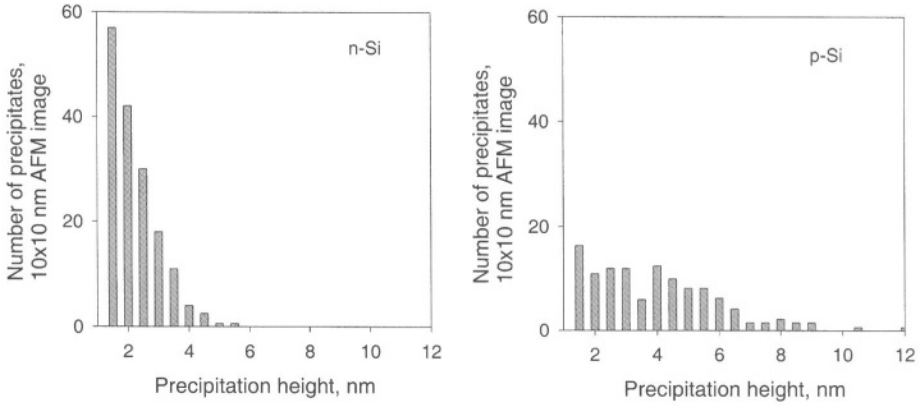

FIGURE 6.14. Precipitate size distribution of the wafers immersed for 5 min, in 1:100 HF containing 400 ppb Cu^{2+} (light on). After Norga *et al.*[407] (Reproduced by permission of The Electrochemical Society, Inc.)

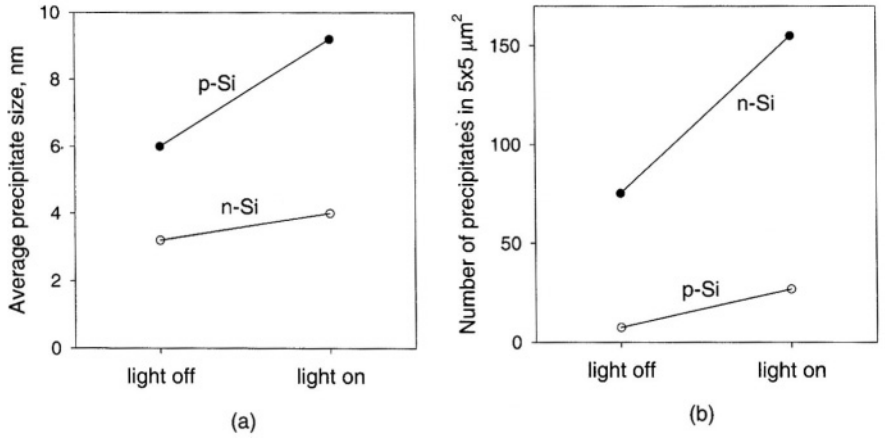

FIGURE 6.15. The effect of illumination on precipitate size (a) and density (b) for *n*- and *p*-type wafers immersed for 2 min in 1 : 100 HF containing 200 ppb Cu^{2+}. Density and average precipitate size were obtained from 5×5 μm AFM images. After Norga *et al.*[407] (Reproduced by permission of The Electrochemical Society, Inc.)

n-Si whereas the growth rate is higher on *p*-Si This is attributed to the higher surface electron concentration on *n*-Si which is required for Cu^{2+} reduction and to the higher hole concentration on *p*-Si surface required for silicon dissolution. Figure 6.15 shows the effect of illumination on the size and density of precipitates. Illumination results in a large increase in density of precipitates. For *p*-Si illumination increases surface electron concentration and for *n*-Si it increases the driving force measured by the difference in the Fermi level of the electrons and the redox potential of the copper in the solution.[253,407] Also, during electroless deposition, dissolution of silicon substrate leads to the formation of pits.[237,293] For *n*-type samples, metal deposition and silicon dissolution occur locally with nuclei growing in the bottom of etched pits toward the surface. In contrast, for *p* samples the deposition occurs on the surface. Deposition of nickel microdots is found to be more uniform on the SiO_2 patterned surface due to the hydrophilic nature of the oxide. It has been reported that deposition of Pt in 0.5 M Na_2SO_4 at pH 2.9 at certain potentials results in the formation of nanoholes 20–80 nm wide and 0.6–0.7 nm deep.[1044]

6.4. DEPOSITION OF SILICON

Silicon can be deposited at large cathodic potentials in solutions of $SiHCl_3$, $SiCl_4$, $SiBr_4$, K_2SiF_6, and other silicon-containing compounds in organic solutions.[363,419] The *i–V* curves show a passivationlike current peak and a much smaller current in the reverse scan. Smooth films up to 0.25 μm thick can be deposited but a thicker film tend to develop cracks. Also, the film contains F, C, O, and N as impurities and can be doped

with boron or phosphorus by adding small amount of their salts into the solutions. Amorphous films up to 0.5 μm thick can be deposited from acetic acid containing $Si(OC_2H_5)_4$.[414,417] As-deposited amorphous silicon contains hydrogen bonds as SiH and SiH_2. The growth rate, morphology, and composition of amorphous films can be modified by changing bath composition and temperature.

6.5. REDOX COUPLES

The reactions of many redox couples on silicon electrodes have been investigated as shown in Table 6.3. These redox couples can be divided into two major groups, organic and inorganic. In general, the organic redox couples are investigated in search of suitable reagents for silicon-based photoelectrochemical cells and the inorganic ones

TABLE 6.3. Studies on the Kinetics of Redox Couples in Various Solvents

Si	Electrolyte	Redox couple, V_{sce}	Feature studied	Refs.
Water, H_2O, $\varepsilon = 78.54$				
n, p	10 M HF + 0.5 M HBr	$Br^{0/-}$	etching	14
n, p	0.1 M KCl	$MV^{2+/+}$, –0.69 $MV^{+/0}$, –1.1	stability, EL	21, 969
p	KCl	AQ/AQH_2, –0.075	photoreduction	678
n	NH_4OH	H_2O_2	etching	208
p	1 M H_2SO_4	Ce^{4+}, $IrCl_6^{2-}$, MnO_4^-, H_2O_2, Fe^{3+}	reduction kinetics	629
p, n	Na_3PO_4	H_2O_2	etching	595
p, n	HF	Cr^{6+}/Cr^{3+}	etching	195, 196
p	0.5 M H_2SO_4	$SiW_{12}O_{40}^{4-}$	photoreduction	691
n	0.1 M $Na[CF_3CO_2]$	$[Ru(NH_3)_6]^{3+/2+}$, –0.26	photoanode	825
	0.1 M $NaClO_4$	$[Fe(CN)_6]^{3-/4-}$, 0.45; $I^{0/-}$, 0.32		
p		$PQ^{2+/+}$, –0.7	H_2 generation	826
n, p	1 M H_2SO_4	$S_2O_8^{2-}/SO_4^{2-}$, 1.72	hole injection	969
n	KCl	Cr-ferrocene	photocell	485
n	KCl	$Fe(CN)_6^{4-}$, Fe^{2+}(EDTA)	stabilizing Si anode	955, 960
n	HF	HNO_3	etching	981
n	1 M NH_4 + 0.2 M NH_4F	$IrCl_6^{2-}$, MnO_4^-, Br_2	oxidation of Si	11
n	$NaClO_4$	$I^{0/-}$	rate constant	877
p	0.5 M H_2SO_4	HCOOH	H_2 evolution	688
n	2 M KOH	$Fe(CN)_6^{3-/4-}$	etching of Si	541
n, p	0.1–1 M KCl	$PQ^{2+/+}$, –0.66; $MV^{2+/+}$, –0.69	H_2 evolution	812
n, p	1 M H_2SO_4	$Fe(CN)_6^{3-/4-}$, 0.26, $Cl^{0/-}$, 1.03	heterojunction	814
n	1 M HCl + 8.5 M LiCl	$Fe^{3+/2+}$, 0.36, $I^{0/-1}$, 0.19	surface modification	679
n	0.1 M $HClO_4$	CF, 0.46	surface modification	682
n		$Fe(C_2O_4)_3^{4-}/Fe(C_2O_4)_3^{3-}$, I^-/I_3^-, Fe^{2+}/Fe^{3+}, Br^-/Br_2, $Fe(CN)_6^{4-/3-}$	surface modification	791
n, p	HF, KOH	Miscellaneous	galvanic etching	1181
Methanol, CH_3OH, $\rho = 0.791$, $T_{mp} = -97.8\,°C$, $T_{bp} = 64.7\,°C$, $\varepsilon = 32.63$				
n	1 M $LiClO_4$	$I^{-/0}$, 0.185	V_{oc}, η, photoanode	622
n	1 M $LiClO_4$	$(CH_3)_2Fc^{+/0}$, 0.16; $Fc^{+/0}$, 0.27	solvent mix	675
n	1 M $LiClO_4$	$Me_2Fc^{+/0}$	quasi Fermi levels	585
n	1 M $LiClO_4$	$Me_2Fc^{+/0}$, $Fc^{+/0}$, $Me_{10}Fc^{+/0}$	transductance	587

TABLE 6.3. *Continued*

Si	Electrolyte	Redox couple, V_{sce}	Feature studied	Refs.
Acetonitrile, CH_3CN, $\rho = 0.787$, $T_{mp} = -45\,°C$, $T_{bp} = 81.6\,°C$, $\varepsilon = 38.8$				
p		$Co(Cp)_2^{+/0}$, −0.95	V_{oc}, η, photocathode	623
p	0.1 M $[n\text{-}Bu_4N]ClO_4$	MeNi1, −1.22; MeNi2, −1.29; MeCo1, −1.32; MeCo2, −1.70	Ni(II), Co(II) complexes	687
p		$[Fe(\eta^5\text{-}C_5H_5)_2]^{+/0}$, 0.45	reduction kinetics	809
p	$[n\text{-}Bu_4N]ClO_4$	$PQ^{2+/+}$, −0.45; $PQ^{+/0}$, −0.85; $Ru^{2+/+}$, −1.3; $Ru^{+/0}$, −1.49; $Ru^{0/-}$, −1.73	photovoltage	270
n, *p*	0.1 M $[n\text{-}Bu_4N]ClO_4$	$PQ^{2+/+}$, −0.45; $MV^{2+/+}$, −0.45	redox reaction	812
p	0.1 M $[n\text{-}Bu_4N]ClO_4$	$PQ^{2+/+}$, −0.30	H_2 evolution	826
n, *p*	0.1 M $TBABF_4$	$MV^{2+/+}$, −0.46; alizarine$^{0/-}$, −0.80 $AQ^{0/-}$, −0.94; 2-amino-$AQ^{0/-}$, −1.10	band bending charge transfer process	683, 684
n	0.1 M TBAP	$Cr(Cp)_2^{+/0}$, $Co(Cp)_2^{+/0}$, $Ni(Cp)_2^{+/0}$	Fermi level pinning	551
p	0.1 M TBAP	$YbCl_3$, −0.65; $Eu(ClO_4)_3$, 0.16	photocathode	372
n, *p*	0.1 M TBAP	$TMPD^{+/0}$, 0.05; $BQ^{+/0}$, −0.55; $AQ^{+/0}$, −1.0; $Ru^{2+/+}$, −1.4; $DPA^{0/-}$, −2.0; BZN, −2.3	relative energy levels	87
p	0.1 M TBAP	CO_2/CO	surface modification	689
Ethanol, CH_3CH_2OH, $\rho = 0.789$, $T_{mp} = -130\,°C$, $T_{bp} = 78.5\,°C$, $\varepsilon = 24.3$				
n	0.1 M $[n\text{-}Bu_4N]ClO_4$	$Fe(Cp)_2^{+/0}$, 0.4; $TMPD^{+/0}$, 0.7 $BF^{+/0}$, 0.31; $BF^{2+/+}$, 0.64 $BFD^{+/0}$, 0.13; $BFD^{2+/+}$, 0.72	voltammetry, V_{oc}, η	553, 583 625, 956
n	0.1 M $[n\text{-}Bu_4N]ClO_4$	$Fe(Cp)_2^{+/0}$, 0.45	rate constants	877, 827
n	1 M $LiClO_4$	$Me_2Fe^{+/0}$	theoretical modeling	699
Acetone, CH_3COCH_3, $\rho = 0.788$, $T_{mp} = -94\,°C$, $T_{bp} = 56.5\,°C$, $\varepsilon = 20.7$				
n	1 M LiClO	$(CH_3)_2Fc^{+/0}$, 0.18; $Fc^{+/0}$, 0.29; $(CH_3CO)Fc^{+/0}$, 0.56	solvent mix	675
Ammonia, NH_4, $\rho = 0.638$ (at −32 °C), $T_{mp} = -77.6\,°C$, $T_{bp} = °C$, $\varepsilon = 16.9$				
n, *p*	0.1 M KI	$NP^{0/-}$; $BP^{0/2-}$; $PhNO_2$	reaction kinetics	271
p	0.1 M KBr	NH_4^+/NH_3	flatband potential	373
Mixture of solvents				
n	CH_3CH_2OH/CH_3OH (3:1) + 0.1 M $[n\text{-}Bu_4N]ClO_4$	$[Ni(S_2C_2Ph_2)_2]^{2-/1-}$, −0.8 $[Fe(\eta^5\text{-}C_5H_5)(CO)]_4^{1-/0}$, −1.3	photooxidation	681
n	H_2O/CH_3OH (7:3) + 0.1 M NaI	PQ^{2+}/PQ^{+}, −0.61	photocathode	272
p	H_2O/CH_3CN (7:3) + 0.1 M NaI	$MV^{2+/+}$, −0.46	surface modification	886
p	H_2O/CH_3CN (7:3) + 0.1 M NaI	$PQ^{2+/+}$, −0.32	H_2 generation	826

AQ/AQH_2, 9,10-anthraquinone-2,6-disulfonate/9,10-anthrahydroquinone-2,6-disulfonate; TMPD, *N,N,N′,N′*-tetramethylphenylenediamine; BF, biferrocene; BFD, bis(fulvene) diiron; TBAP, tetrabutylammonium; PQ^{2+}, *N,N′*-dimethyl-4,4′-bipyridinium; BQ, *p*-benzoquinone; AQ, 9,10-anthraquinone; BZN, benzonitrile; DPA, 9,10-diphenylanthracene; MV^{2+}, divalent methylviologen cation; EL, electroluminescence; NP, naphthalene; BP, benzophenone; $PhNO_2$, nitrobenzene; $TBABF_4$, tetrabutylammonium tetrafluoroborate; MeNi1, $[(Me_6(14)dieneN_4)Ni(II)]^{2+}$; MeNi2, $[(Me_6(14)aneN_4)Ni(II)]^{2+}$; MeCo1, $[(Me_6(14)dieneN_4)Co(II)]^{2+}$; MeCo2, $[(Me_6(14)aneN_4)Co(II)]^{2+}$; CF, Cr-ferrocene complex; Me_2Fc, dimethylferrocene; Note: the number following the redox couple is the redox potential.

for applications in the etching of silicon. For the organic redox couples, the potentials are commonly determined by measuring the average of the cathodic and anodic current peaks of the reaction on a Pt electrode against a reference electrode.[552] This practice assumes that the electrode reactions for the redox couples at the Pt electrode are reversible.

6.5.1. *Individual Redox Couples*

Cr^{6+}/Cr^{3+}. Cr^{6+} is an agent widely used for crystal defect etching. The kinetics of its reduction reaction in relation to etching silicon in HF solution has been systematically investigated by Meerakker and Vegchel.[195,196] Figure 6.16 shows the *i–V* curves measured in a high HF/CrO_3 ratio solution for *n*-Si and *p*-Si. A cathodic plateau current on *p*-Si indicates the injection of holes into the valence band by the reduction of Cr^{6+}. This current is proportional to the concentration of Cr^{6+} and is essentially independent of HF concentration. Rotation of the electrode has a very slight effect on the reaction rate indicating that the reaction is almost fully kinetically controlled. There is a shoulder on the cathodic *i–V* curve on *n*-Si, the magnitude of which is similar to that of the current plateau on the *p*-Si due to the reduction of Cr^{6+}. The reaction in the current plateau region is hydrogen evolution and the plateau current on *p*-Si increases with illumination with a quantum efficiency of 1.

At low HF/CrO_3 ratios a reduction peak followed by a lower current plateau at more negative potentials occurs on *n*-Si and *p*-Si as shown in Fig. 6.17[196] indicating the inhibition of the reaction as a result of the reduction reaction. Both the peak and plateau currents are independent of the CrO_3 concentration but dependent on the HF

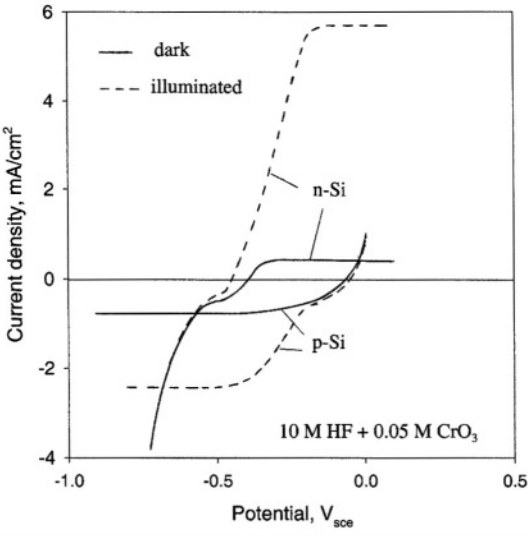

FIGURE 6.16. Current–potential curves for *p*-Si and *n*-Si in a solution of 10 M HF + 0.05 M CrO_3. After Meerakker and Vegchel.[195] (Reproduced by permission of The Electrochemical Society, Inc.)

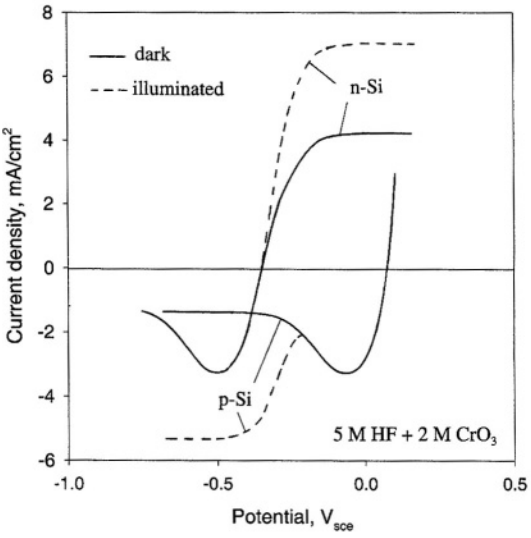

FIGURE 6.17. Current–potential curves for *p*-Si and *n*-Si in a solution of 5M HF + 2M CrO_3. After Meerakker and Vegchel.[195] (Reproduced by permission of The Electrochemical Society, Inc.)

concentration. On the *n*-Si electrode at more negative potentials than the plateau region, current sharply increases due to hydrogen evolution. Under illumination, the quantum efficiency of the *p*-Si is about 2 due to the injection of holes from the Cr^{6+}, which is different from that at high HF/CrO_3 ratios.

An anodic plateau current is measured on *n*-Si in the dark thus indicating electron injection into the conduction band. This plateau current is only slightly affected by HF concentration but is proportional to Cr^{6+} concentration. Illumination of the *n*-Si causes an increase of the anodic plateau current with a quantum efficiency of about 2.8 due to electron injection into the conduction band by the silicon dissolution intermediates. The quantum efficiency for the anodic photocurrent depends on the HF/CrO_3 ratio, about 2.8 at a high HF/CrO_3 ratio (>20) and about 1 at very low ratios.

According to Meerakker and Vegchel,[195,196] the reduction kinetics of Cr^{6+} in HF solution on silicon electrodes depends on the ratio of HF/CrO_3 from 0.5 to 1000. At high HF/CrO_3 ratios (>20) the reduction proceeds on the bare silicon surface whereas at low ratios (<10) the reduction is inhibited by the formation of a chromium complex containing trivalent and hexavalent entities $[Cr^{3+} \sim Cr^{6+} \sim Cr^{3+}]$.

$$Cr^{6+} \rightarrow Cr^{3+} + 3h \quad \text{high ratio} \tag{6.3}$$

$$3Cr^{6+} \rightarrow [Cr^{3+} \sim Cr^{6+} \sim Cr^{3+}] + 6h \qquad \text{low ratio} \tag{6.4}$$

$[Cr^{3+} \sim Cr^{6+} \sim Cr^{3+}]$ can decompose under the effect of HF, resulting in hole injection which is responsible for the high quantum efficiency of the cathodic photocurrent on *p*-Si.

$$[Cr^{3+} \sim Cr^{6+} \sim Cr^{3+}] + e \rightarrow 3Cr^{3+} + 2h \tag{6.5}$$

The anodic dissolution of silicon in these solutions occurs by the following reactions

$$Si + h \rightarrow Si^{+} \tag{6.6}$$

$$Si^{+} \rightarrow Si^{4+} + 3e \tag{6.7}$$

$$Si^{+} + 3H^{+} \rightarrow Si^{4+} + 3/2\,H_2 \tag{6.8}$$

Reaction (6.6) represents creation of an intermediate by a hole, which in the case of *n*-Si is provided by the reduction of Cr^{6+}. Reactions (6.7) and (6.8) represent two possible reaction routes for the intermediate Si^{+}, one by electron injection into the conduction band and the other by a chemical reaction with hydrogen ions. The injection of electrons into the conduction band accounts for the anodic current on *n*-Si in the dark. The reaction with hydrogen ions accounts for the hydrogen evolution during the anodic dissolution of *n*-Si.

The chromium complex may also react with the silicon dissolution intermediate

$$[Cr^{3+} \sim Cr^{6+} \sim Cr^{3+}] + Si^{+} \rightarrow 3Cr^{3+} + Si^{4+} \tag{6.9}$$

This reaction competes with reactions (6.7) and (6.8) and is responsible for the decrease of photo quantum efficiency to about 1 on *n*-Si at very low HF/CrO_3 ratios.

For etching at the OCP where the amount of anodic dissolution equals that of cathodic reduction, reactions (6.3), (6.6), (6.8), and (6.9) operate at high HF/CrO_3 ratios whereas reactions (6.4) to (6.9) are involved at low HF/CrO_3 ratios.

NO_3^-/NO_2^-. HNO_3 is a commonly used oxidant in HF solutions for isotropic etching of silicon. Figure 6.18, reported by Kooij *et al.*,[969,981] shows the etch rate and current as a function of potential for *n*- and *p*-type silicon in the dark. The cathodic current plateau measured on *p*-Si is not due to a diffusion-controlled process but to the reduction of HNO_3 involving hole injection in the valence band. This limiting current also appears as a shoulder on the *i–V* curve of *n*-Si indicating that the reduction of HNO_3 on *n*-Si is similar to *p*-Si. The large current on the *n*-Si at more negative potentials is due to hydrogen evolution. The cathodic plateau current on *p*-Si decreases with electrode rotation rate indicating that surface-bond reaction intermediates, rather than the HNO_3 from the bulk, are responsible for the hole injection into the valence band. Also, during silicon etching, gas evolves and the composition of the gas is found to be about 80% H_2 with the rest being nitrogen oxides in the form of N_2O. The etch rate decreases with the rotation speed of the electrode indicating the removal of active reaction species from the surface (HNO_2 or NO_2).

The current at anodic potentials on the *p*-Si is similar to that in HF solution without HNO_3. The anodic current plateau on *n*-Si indicates that electrons are injected into the conduction band from the dissolution intermediates. The etch rate decreases with cathodic polarization for both *n*-Si and *p*-Si due to the more effective removal of the injected holes as shown in Fig. 6.18. A comparison of the anodic current plateau

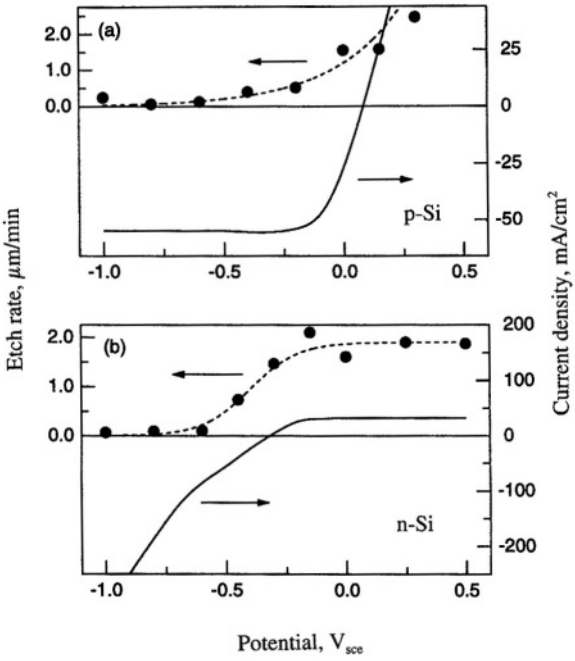

FIGURE 6.18. Current–potential and etch rate–potential curves of stationary (a) *p*-type and (b) *n*-type crystalline silicon electrode in a 6 M HNO_3, 6 M HF solution. After Kooij.[969] (Reprinted with permission.)

and the cathodic current plateau indicates that for every two holes injected into the valence band, one electron is injected into the conduction band.

Quantitative analysis of the data shows that a H_2 molecule is generated for two dissolved Si atoms, indicating that the effective dissolution valence of silicon is 3. According to Kooij *et al.*,[981] the etching reactions on *p*-Si and *n*-Si are different in terms of the involvement of the charge carriers. For the *p*-Si the reaction is

$$Si + 3h + H^+ \rightarrow Si^{4+} + 1/2\,H_2 \tag{6.10}$$

and on *n*-Si the reaction is

$$Si + 2h + H^+ \rightarrow Si^{4+} + e + 1/2\,H_2 \tag{6.11}$$

The hydrogen ion reacts chemically with an intermediate Si^n (Si^+, Si^{2+}, or Si^{3+})

$$Si^n + H^+ \rightarrow Si^{n+1} + 1/2\,H_2 \tag{6.12}$$

The reduction of HNO_3, which provides holes for the oxidation of silicon, is considered to be a complex process involving multiple reaction steps.

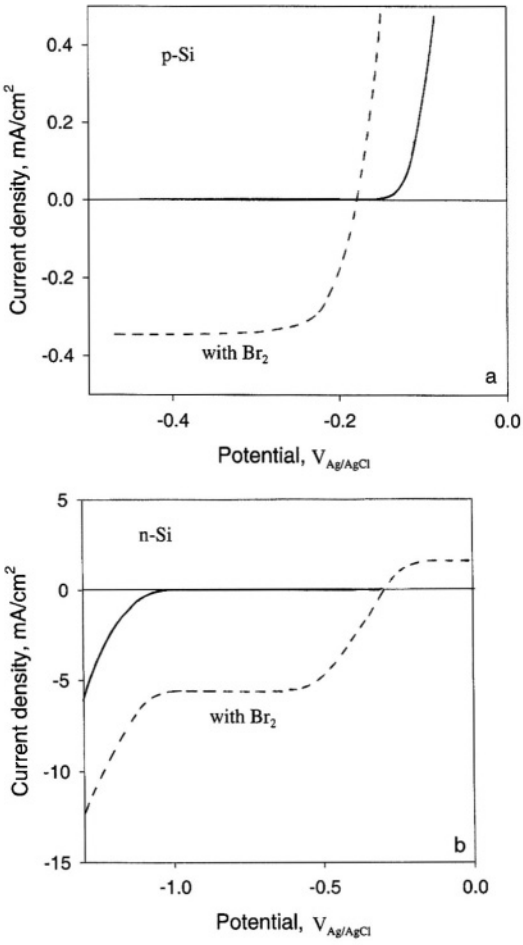

FIGURE 6.19. Dark current–potential curves of a *p*-type Si(100) RDE (a) and an *n*-type Si(100) RDE (b) in a 10 M HF + 0.5 M HBr solution with and without Br_2 (10 mM). The scan rate was 50 mV/s and the rotation rate was 400 rev/min. (Reprinted from Bressers *et al.*[14] © 1996, with permission from Elsevier Science.)

$$HNO_3 \rightarrow HNO_2 \rightarrow NO \rightarrow HNO \rightarrow H_2N_2O_2 \rightarrow N_2O \qquad (6.13)$$

Br/Br^-. Figure 6.19 shows the dark *i–V* curves *of p*-Si and *n*-Si for the reactions involving the reduction of Br_2 in 10M HF + 0.5M HBr + 10mM Br_2 solution.[14] The cathodic current on *p*-Si in the dark is due to hole injection into the valence band. On the other hand, the cathodic plateau current on *n*-Si is much larger than on *p*-Si indicating that the reduction process is mainly a conduction band process. When conduction band electrons are not available, the reduction of Br_2 may proceed via the valence band as is the case with *p*-Si in the dark. The current plateau at cathodic potentials on both *p*-Si and *n*-Si is limited by the diffusion of Br_2. The small plateau current on *p*-Si indicates that only a small fraction of Br_2 is reduced electrochemically and most of the

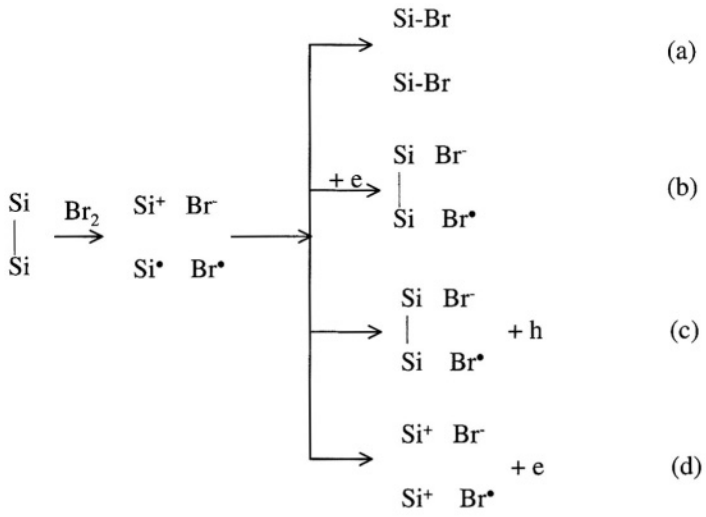

FIGURE 6.20. Reaction scheme of the two-step mechanism for the interaction of bromine with a Si–Si surface bond, including chemical and electrochemical reaction via a common etch intermediate. (Reprinted from Bressers *et al.*[14] © 1996, with permission from Elsevier Science.)

Br_2 reacts chemically with silicon resulting in the etching of silicon (etch rate of *p*-Si is large and is independent of the cathodic potential). On the other hand, on *n*-Si at cathodic potentials the reduction of Br_2 can proceed more favorably by capturing the electrons from the conduction band than by injecting holes into the valence band. Thus, the etch rate of *n*-Si at cathodic potentials is almost zero due to the lack of holes to initiate the dissolution process. The anodic current on *n*-Si in the presence of Br_2 in the dark is due to electron injection from the silicon reaction intermediates.

According to Bressers *et al.*,[14] because the ratio of bromine to silicon is 1:1.6 for the etching reaction at the OCP, one bromine atom is involved in the dissolution of more than one silicon atom and the attack is probably at the Si–Si back bonds to form two Si–Br bonds. They proposed the reaction scheme shown in Fig. 6.20 for the dissolution of silicon in the presence of Br_2 in HF. The first step involves a chemical attack of the silicon back bond producing silicon and bromine reaction intermediates which are surface states with energy levels in the midband gap. There are four possible paths for the reaction of intermediates to proceed depending on the type of silicon and potential range. The first is by further chemical reaction causing the formation of two Si–Br bonds (path a, which involves no carriers).

The other three paths are electrochemical reactions involving carriers in the bonds. At sufficiently negative potentials on *n*-Si or on illuminated *p*-Si, electrons from the conduction band can be captured by the surface states causing the repair of the Si–Si bond (path b) which constitutes the first step of the bromine reduction. In the dark on *p*-Si when conduction band electrons are not available, this reduction process can also proceed by hole injection (path c). The dark anodic current on *n*-Si is due to electron injection into the conduction band causing oxidation of a silicon atom (path d).

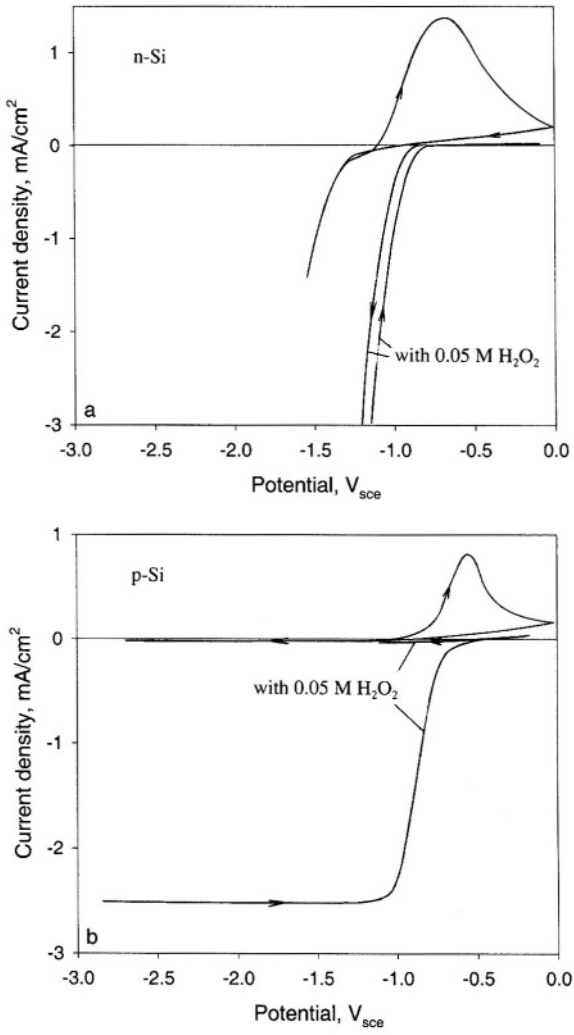

FIGURE 6.21. (a) Voltammograms of *n*-Si in a solution of pH 12.0 with 0.05 M H_2O_2 at 70 °C in the dark. (b) Voltammograms of *p*-Si in a solution of phosphate buffer of pH 12.0 at 70 °C in the dark. The scan rate was 100 mV/s. The arrows indicate the scan direction. (Reprinted from Meerakker.[595] © 1990, with permission from Elsevier Science.)

H_2O_2/H_2O. The reduction of H_2O_2 on silicon is rather complex.[208,595] Figure 6.21 shows the *i–V* curves of *p*-Si and *n*-Si under different conditions. In the absence of H_2O_2 the cathodic current on *n*-Si is due to hydrogen evolution and there is no cathodic current on *p*-Si. The anodic current peak is due to passivation which is characteristic of silicon in alkaline solutions without H_2O_2. When H_2O_2 is present at a concentration higher than the critical concentration (about 3×10^{-3} M) at which the silicon surface is spontaneously passivated at the OCP, the anodic current peak is not measured in an *i–V* curve.

On *n*-Si the cathodic current shows similar dependence on potential with positive (initially active surface) and negative (initially passive surface) potential scan directions. However, on *p*-Si cathodic current is only observed on an active surface in the dark (with a positive scan rate). Also, the cathodic current on illuminated *p*-Si on a passivated surface is much smaller than that on an active surface. Furthermore, the cathodic photocurrent on *p*-Si at low light intensity is double that without H_2O_2. At high light intensities the photocurrent becomes the same on active and passive surfaces and the current multiplication factor is less than 2.

According to Meerakker,[595] on a passivated surface the reduction of H_2O_2 is by a conduction band electron forming a reaction intermediate which then injects a hole into the valence band:

$$H_2O_2 + e \rightarrow OH^- + \cdot OH \tag{6.14}$$

$$\cdot OH \rightarrow OH^- + h \tag{6.15}$$

The reduction current on *p*-Si is small in the dark because it is limited by reaction (6.14), which requires electrons. On the active surface the reaction scheme is more complex due to the interaction between silicon radical and hydrogen peroxide generating a ·OH radical:

$$Si\cdot + H_2O_2 \rightarrow Si\text{-}OH + \cdot OH \tag{6.16}$$

The ·OH then injects a hole into the valence band, which is responsible for the reduction current observed on an active surface of *p*-Si in the dark. At anodic potentials, reaction (6.16) competes favorably with the electron injection into the conduction band from the silicon radical because when H_2O_2 is present the anodic current peak on *n*-Si (due to the electron injection) disappears.

When an active *p*-Si surface is illuminated, both reactions (6.14) and (6.15) take place resulting in a current which is larger than that on the passivated surface. At high light intensities, reduction of ·OH, instead of via a valence band by reaction (6.15), may also proceed via the conduction band:

$$\cdot OH + e \rightarrow OH^- \tag{6.17}$$

Reaction (6.17) accounts for the reduced multiplication factor at high light intensities.

Other Redox Species. Reduction of ferricyanide in KOH solution takes place via hole injection into the valence band.[541] The reaction path depends on whether an oxide film is present on the surface. On an oxide-free *p*-Si the reduction proceeds by hole injection as shown in Fig. 6.22. On an oxide-covered electrode, which is anodized at 0 V prior to the transient, the drop of current at about 3.5 min is due to the complete dissolution of the oxide film, resulting in the same current as that on the oxide-free surface. The lower current on the oxide-free surface is attributed by Bressers *et al.*[541] to the reaction of silicon, which consumes a part of the injected holes by the reduction of ferricyanide. On the oxide-covered surface, silicon dissolution does not occur and all of the injected holes flow into the semiconductor. Figure 6.23 shows the dependence

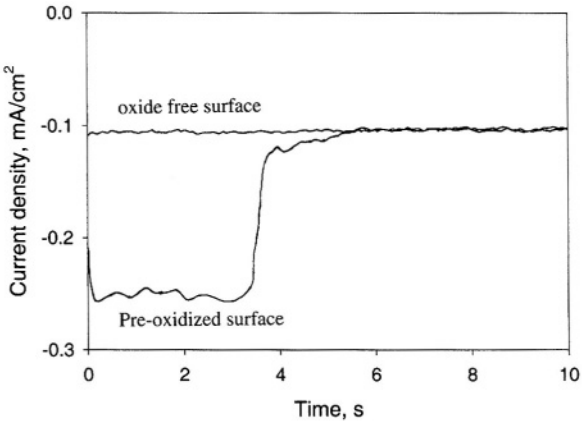

FIGURE 6.22. Current–time transients at –2.0 V on *p*-Si(100) in 2M KOH at 45 °C: measured for an oxide-free chemically etching electrode when 3 mM ferricyanide was added to the solution at $t = 0$; measured after anodic oxidation at 0.0 V when, at $t = 0$, the potential was stepped back to –2.0 V in a solution containing 3 mM ferricyanide. (Reprinted from Bressers *et al.*[541] © 1995, with permission from Elsevier Science.)

of the reduction current on potential. The current dip after the passivation peak is due to the reduction of ferricyanide through the thin oxide film, the rate of which decreases to zero as the film thickness increases at more positive potentials.

The reduction of $Fe(CN)_6^{3-}$ in NH_4F solutions, in contrast to that in KOH solutions, does not proceed on *p*-Si in the dark indicating that the reduction can only proceed with conduction band electrons.[986] However, the presence of defects such as disloca-

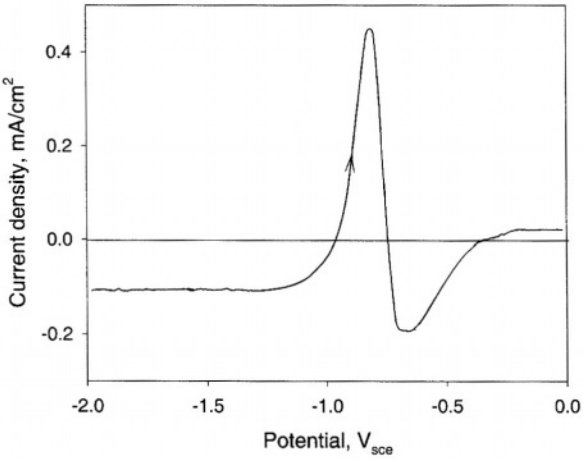

FIGURE 6.23. Current–potential curve of *p*-Si(100) in 2M KOH + 3 mM $Fe(CN)_6^{3-}$ at 45 °C. The scan was from –2.0 to 0.0 V at a rate of 2 mV/s. The arrows indicate the scan direction. (Reprinted from Bressers *et al.*[541] © 1995, with permission from Elsevier Science.)

tions generated by mechanical polishing can increase the reaction rate by the hole injection mechanism. According to Morrison *et al.*,[986] dislocations can behave like microelectrodes (~2nm) for hole injection and the holes are conducted along the dislocation lines, where tunneling to the valence band becomes possible.

Figure 6.24 shows the *i–V* curves of *p*- and *n*-type silicon in 0.1 M KCl solution containing 2mM methylviogen (1,1′-dimethy1-4,4′-bipyridinium) (MV^{2+}).[969] The cathodic *i–V* curve has two reduction maxima indicating a metalliclike behavior. The first peak is ascribed to the reduction of MV^{2+} to MV^{+} and the second to the reduction of MV^{+} to MV^{0}. The peak value depends on the potential scanning rate and rotation of the electrode indicating that the reactions are diffusion limited. The two-step reduction proceeds via the conduction band. Figure 6.24 also shows that the reduction on *n*-Si is under an accumulation condition whereas on *p*-Si it is under a depletion condition.

Kooij *et al.*[629,969] investigated the cathodic reaction of a number of one-electron oxidizing agents such as Ce^{4+}, $IrCl_6^{2-}$, MnO_4^-, Fe^{3+}, H_2O_2, and $S_2O_8^{2-}$, on *p*-Si in 1M H_2SO_4. The agents with redox potentials considerably more positive than the flatband potential of the electrode ($V_{vb} \sim 0.4$–$0.5\ V_{sce}$) tend to inject holes into the valence band as shown in Table 6.4.[629] The rate of injection is high for those agents with redox potentials much more positive than the valence band edge, such as Ce^{4+} and $IrCl_6^{2-}$. The rate of injection is weak for the redox couples with potentials close or negative of the valence band edge. For Fe^{3+}, which has a redox potential similar to $IrCl_6^{2-/3-}$, hole injection does not occur due to the adsorption of Fe^{3+} to form surface states which interact only with conduction band electrons. The hole injection is strong for MnO_4^- but very weak for HNO_3.

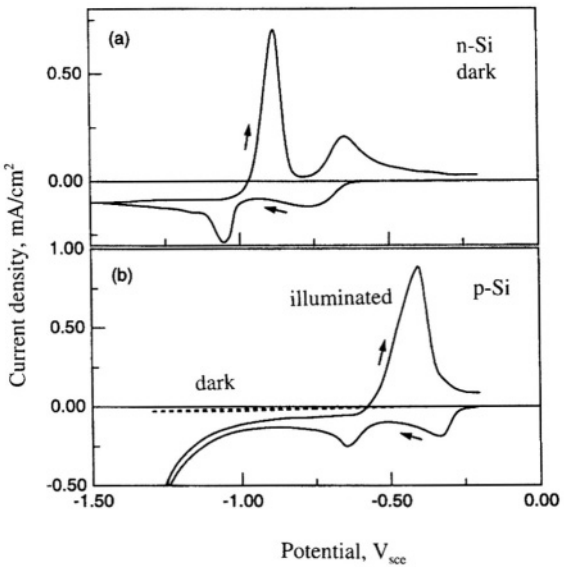

FIGURE 6.24. Current–potential curves of stationary *n*-type (a) and *p*-type (b) crystalline silicon electrodes in 2mM $MVCl_2$, 0.1M KCl aqueous solution. Measurements with the *n*-type electrode were made in the dark, whereas the *p*-type electrode was in the dark (dashed line) and under illumination (solid line). After Kooij.[969] (Reprinted with permission.)

TABLE 6.4. Hole Injection Intensity for *p*-Si in Solution Containing 0.1 M Oxidizing Agents in 1 M H_2SO_4[629]

Oxidizing agent	E^0_{redox}, V_{she}	Hole injection
none		no
Ce^{4+}	Ce^{4+}/Ce^{3+}, 1.44	strong
$S_2O^{2-}_8$	$S_2O^{2-}_8/HSO^-_4$, 2.12	weak
Fe^{3+}	Fe^{3+}/Fe^{2+}, 0.77	weak
HNO_3	NO^-_3/HNO_2, 0.934	very weak
MnO^-_4	MnO^-_4/MnO^{2-}_4, 0.558	strong
H_2O_2	H_2O_2/H_2O, 1.78	very weak
$IrCl^{2-}_6$	$IrCl^{2-}_6/IrCl^{3-}_6$, 0.867	strong

Hole injection from the oxidizing species in the solution into the valence band is postulated to be responsible for the chemiluminescence observed on porous silicon in these solutions at the OCP.

However, for H_2O_2, Br_2, and $S_2O_8^{2-}$, despite their very positive redox potentials, the reduction proceeds primarily via the conduction band with minimal hole injection into the valence band.[14,629] The weak hole injection with strong oxidizing agents H_2O_2 and $S_2O_8^{2-}$ is attributed to the two-electron reduction process in which the first step requires a conduction band electron to create reaction intermediates, $\cdot OH$ and $SO_4^{-}\cdot$, which can then inject a hole into the valence band. The reduction reaction can be more complicated when more than one redox couple is present. It has been found that hole injection by H_2O_2 is increased when Fe^{3-} is also present in the solution. The Fe^{3+} ions react with H_2O_2 to generate hydroxyl radicals in the solution. This implies that hole injection during the reduction of H_2O_2 occurs from the intermediate which is in the solution rather than on the surface as surface states. Hole injection from the redox species in the solution into the valence band can also be affected by other factors. As shown in Fig. 6.22, hole injection is affected by the formation of surface oxide. For $S_2O_8^{2-}$, hole injection involves the hydrogen reaction that also occurs in this region.

The redox couples, which inject holes into the conduction band, induce anodic current on *n*-Si in the dark. According to Gerischer and Lubke,[11] anodic current is due to electron injection by silicon dissolution intermediates for redox couples with one electron transfer per molecule. Depending on the number of electrons involved in the reduction process of the redox couple, the photocurrent may have a quantum yield varying from 1 to 2. The quantum yield is 2 without redox couples. It remains the same when a redox couple with only one oxidation step per molecule such as $(IrCl_6)^{2-}$ is present. However, for the oxidizing agents Br_2 and MnO_4^{2-}, the reduction of which involves two electrons, the quantum yield is smaller than 2 as shown in Fig. 6.25. This is attributed to the adsorption of the reduction intermediates on the surface, which inhibits the electron injection from silicon dissolution intermediates responsible for the quantum yield of 2.

In general, it is difficult to oxidize a redox species on silicon in aqueous electrolytes because of the highly reactive nature of silicon; oxidation of silicon results in a passive oxide film in nonfluoride solutions, whereas dissolution of silicon is the

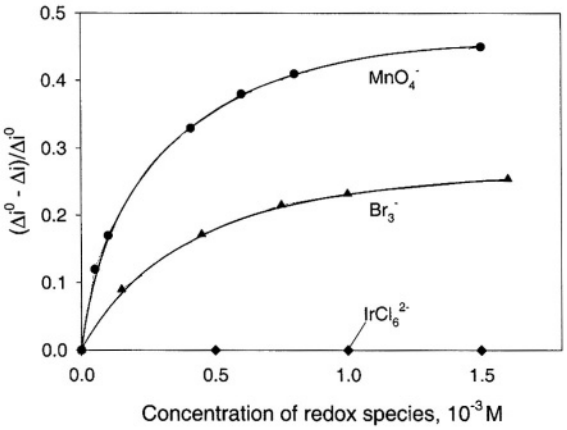

FIGURE 6.25. Relative decrease of the photocurrent Δi_{pH} of an *n*-Si electrode in 1 M NH_4F (pH 4) as a function of the concentration of the added oxidants ($\Delta i^0_{pH} = 0.25\,mA/cm^2$), ν = 1500/min. (Reprinted from Gerischer and Lubke.[11] © 1988, with permission from Elsevier Science.)

dominant anodic reaction in fluoride-containing solutions in which the oxide dissolves quickly. The reduction of some redox species is, however, found to compete favorably with the oxidation of silicon, which can be used to stabilize silicon anodes against photooxidation. For example, $[Bu_4N][Ni(S_2C_2Ph_2)_2]$ and $[Fe(\eta^5\text{-}C_5H_5)(CO)]_4$, which can be efficiently photooxidized on *n*-Si electrode, are found to stabilize the silicon electrode.[681] Ferricenium/ferrocene, $Fe(Cp)_2^+/Fe(Cp)_2$, is capable of stabilizing *n*-Si against photoanodic oxidation in EtOH solvent by efficiently capturing the holes.[78] $Fe(CN)_6^{4-}$ and $Fe^{2+}(EDTA)$ are also found to be effective in competing for photogenerated holes on *n*-Si and thus stabilizing the electrode.[955,960] According to Loo *et al.*,[960] in non-HF aqueous solution anodic photocurrent results in the formation of a thin oxide film. Without a reducing species, the oxide film will grow in thickness and passivate the surface. In the presence of a reducing species such as $Fe(CN)_6^{4-}$ the field buildup in the oxide film results in a shift of the valence band relative to the redox potential and the reduction of the redox species becomes more favorable than the oxidation of silicon as described in Fig. 6.26. As a result, the silicon electrode is stabilized.

Participation of surface states may be important in the reactions of redox couples.[272,553] It can result in the redox reaction to show an *i–V* curve with two one-electron waves. Such *i–V* curves are characteristic of metallic behavior rather than one two-electron wave as is expected at a semiconductor surface free of surface states. Metalliclike behavior may also be due to the interaction of redox species with silicon electrode, which may result in changes in the barrier height or cause chemical changes to form an ohmic-like interface.

In summary, the reaction processes of redox couples are complex. Each redox couple may have several different reaction paths, in addition to all of the possible reaction schemes on the silicon electrodes without the redox couple. The kinetic behavior of a redox couple has several general characteristics. (1) The condition of the electrode surface is an important factor in the reaction kinetics; it differs for oxide-covered and

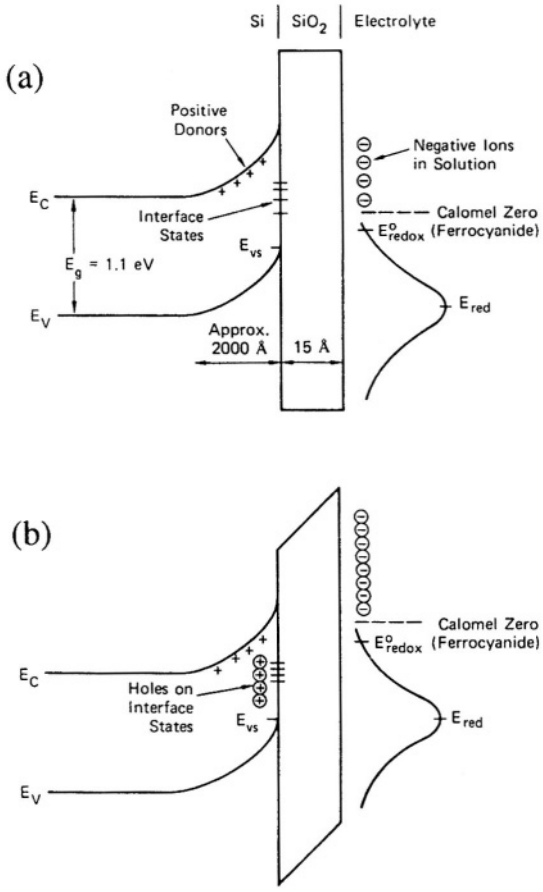

FIGURE 6.26. Band model of Si/SiO_2/electrolyte to show field in oxide when interface states becomes charged (a) in the dark or (b) under illumination. (Reprinted from Loo *et al.*[960] © 1981, with permission from Elsevier Science.)

oxide-free surfaces. (2) The value of the redox potential relative to the band edge determines the extent of conduction band process versus valence band process. (3) For the redox species with more than one oxidation step per molecule, the reaction intermediates may have very different behavior from that indicated by the value of the redox potential. (4) The interaction between the redox species and its intermediates with silicon atoms on the electrode strongly affects the contribution from the valence band relative to the conduction band and the ratio of electrochemical reaction to chemical reaction. (5) The interaction between two or more redox couples may also occur, which further complicates the reaction mechanism of each individual redox couple.

6.5.2. Electroluminescence Associated with Redox Reactions

Electroluminescence is a process in which light of a certain wavelength is emitted from a semiconductor electrode as a result of electrochemical reactions. The results

of Kooij[969] on porous silicon show: (1) Chemiluminescence, with wavelength varying between 650 and 720 nm, occurs on *p*-Si at the OCP in 1 M H_2SO_4 containing strong oxidizing agents with potentials considerably more positive than the flatband potential. Species such as Ce^{4+} and $IrCl_6^{2-}$ can inject holes into the valence band during reduction reaction. On the other hand, H_2O_2 and $S_2O_8^{2-}$, which have very positive potentials, do not inject holes into the valence band but the reduction proceeds via the conduction band. (2) The luminescence intensity on *p*-Si increases with the concentration of the oxidants and is independent of the cathodic potential. (3) In contrast to *p*-Si the emission intensity on *n*-Si depends on potential; it decreases from a relatively high value at the OCP to a lower value in the cathodic potential region. (4) The luminescence on *n*-Si is quenched at more negative potentials at which hydrogen is evolved. The luminescence on *p*-Si is not affected by cathodic potential because hydrogen does not evolve on *p*-Si due to the lack of conduction band electrons. (5) In contrast, for $S_2O_8^{2-}$, which does not inject holes during reduction, luminescence occurs at large cathodic currents where hydrogen evolution occurs. (6) Luminescence does not occur on samples that are not covered with a porous silicon layer.

According to Kooij *et al.*,[629,969] luminescence is due to hole injection from the reducing species in the solution into the valence band. The holes are captured in Si–Si surface bonds which leads to the formation of an oxidation intermediate. Subsequent electron injection from the intermediate into the conduction band and the radiative recombination of the electrons with holes in the valence band results in the emission of photons. Such a reaction mechanism is postulated to be responsible for the chemiluminescence of porous silicon in these solutions at the OCP.

Kooij *et al.* described the individual steps involved as follows:

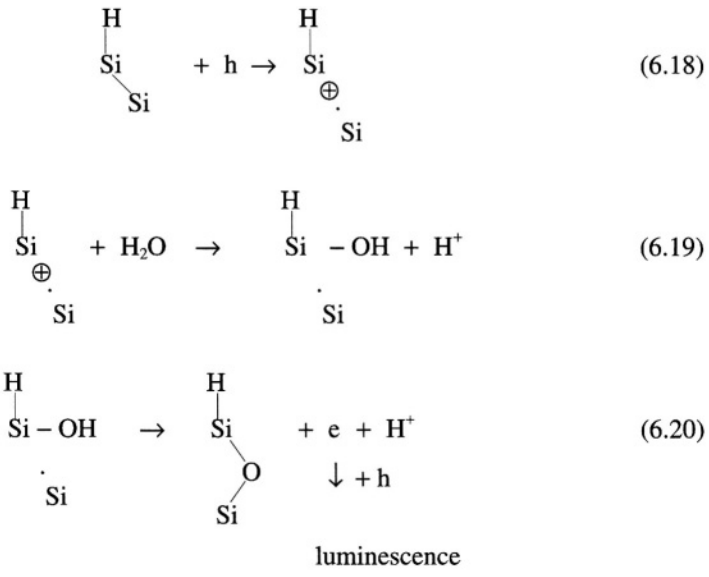

According to them, strong oxidizing agents like H_2O_2 or $S_2O_8^{2-}$ give very limited luminescence at OCP[969] because the reduction of these two-electron redox couples requires

a conduction band electron in the first step, which is not possible without an electron-injecting species in the solution. The quenching effect of hydrogen evolution on luminescence is ascribed to the surface adsorption of hydrogen atoms leading to the formation of Si–H bonds which prevent the injection of an electron into the conduction band. On the other hand, for *n*-Si in H_2SO_4 containing $S_2O_8^{2-}$, photoemission only occurs at the cathodic potentials at which hydrogen is evolved, which may be attributed to the interaction of the reduction intermediates of $S_2O_8^{2-}$ with the hydrogen evolution reaction.

In certain situations, photoemission occurs only when both cathodic potential and light are present.[87,646] For example, blue emission is observed by illuminating *p*-Si in acetonitrile containing $DPACl_2$(9,10-dichloro-9,10-dihydro-9,10-diphenylanthracene) at cathodic potentials where $DPACl_2$ is reduced. The emission does not occur with illumination or cathodic potential alone because neither the energy of the light, less than 1.7eV, nor the electrical energy reaches the threshold energy for the production of the emitted photons of 3.0 eV.[87]

6.6. OPEN-CIRCUIT PHOTOVOLTAGE

The open-circuit photovoltage of silicon depends on the minority carrier diffusion length, majority carrier dopant density, photocurrent density, and oxide growth.[161] It has been calculated that for an *n*-Si (7.7×10^{15}) material without any recombination processes other than bulk recombination, V_{oc}, i.e., the maximum photovoltage at $i_{ph} = 17\,mA/cm^2$, is about 0.6 V.[275] In order to obtain the largest photovoltage it is necessary to choose the redox couple with a potential located in the most favorable position relative to the energies of the band edges. For example, for an *n*-type semiconductor it is desirable to have a redox couple located as close to E_{vs} as possible in order to maximize the output voltage.[553] Photovoltages close to the maximum value have been obtained in nonaqueous CH_3CN solutions.[276,569,583] A crucial factor for achieving open-circuit voltage is the initial photoelectrochemical oxide formation which passivates surface recombination sites.

The open-circuit photovoltage of silicon electrodes may or may not change with redox potentials depending on the system. When V_{oc} follows the variation with redox potential, the band bending is related to the redox potential: $V_s = E_{redox} - E_{cb} - \mu$ for *n*-Si and $V_s = E_{vs} - E_{redox} - \mu$ for *p*-Si. Figure 6.27 shows V_{oc} on *n*-Si and *p*-Si as a function of redox potentials in a methanol solution.[275] However, the V_{oc} for redox couples with very negative potentials on *p*-Si or very positive potentials on *n*-Si vary very little with redox potential. The lack of variation in V_{oc} with redox potentials may be due to the effect of carrier inversion or Fermi level pinning.

Silicon electrodes in nonaqueous solutions with appropriate redox couples are more stable than in aqueous solutions. The V_{oc} in solvents such as acetonitrile is generally not very large (max $V_{oc} < 0.4$ V).[686] In methanol it is found to be considerably larger (up to 0.67 V), which is attributed to the formation of $Si–O–CH_3$ bonds which result in an improved stability and low density of surface states. Figure 6.28 shows the dependence of V_{oc} on temperature; it decreases as temperature increases.[699] The effect of temperature on V_{oc} is mainly by changing the magnitude of the minority dark saturation current.

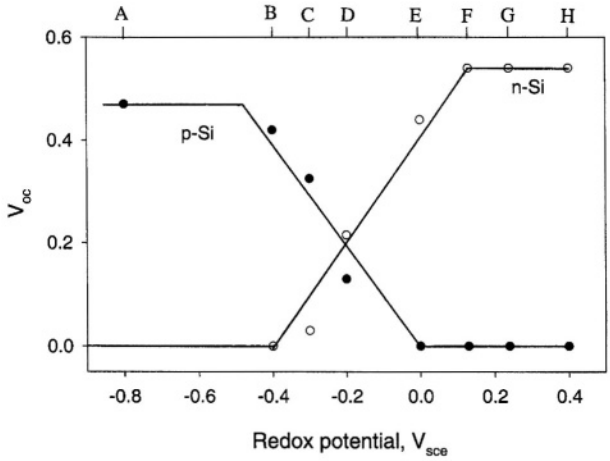

FIGURE 6.27. Open-circuit photovoltage versus solution redox potential for *n*-Si and *p*-Si photoelectrodes in 1.0 M KCl/CH_3OH solution. The redox couples used were: (A) cobaltocene$^{+/o}$; (B) *N,N'*-dimenthyl-4,4'-bipyridinium dichloride$^{2+/+}$; (C) *N,N'*-dibenzyl-4,4'-bipyridinium dibromide$^{2+/+}$; (D) decamethylferrocene$^{+/0}$; (E) *N,N,N',N'*-tetramethylphenylenediamine$^{+/0}$; (F) dimethylferrocene$^{+/0}$; (G) ferrocene$^{+/0}$; (H) octylferrocene$^{+/0}$, A tungsten–halogen bulb was used to provide light intensities which yielded short-circuit photocurrent densities of 25–30 mA/cm^2. After Lewis.[275] (Reproduced by permission of The Electrochemical Society, Inc.)

In many circumstances, photovoltages are found to be almost constant for redox couples whose formal potentials span a range exceeding the band gap of silicon as shown for example in Table 6.5.[270] A similar effect has been observed in pure acetonitrile and acetonitrile–acid mixtures in which a large number of redox couples with a large span of formal potentials exhibit a similar photovoltage.[272,683] The departure from the ideal situation described by Eq. (1.96) is often attributed to Fermi level pinning

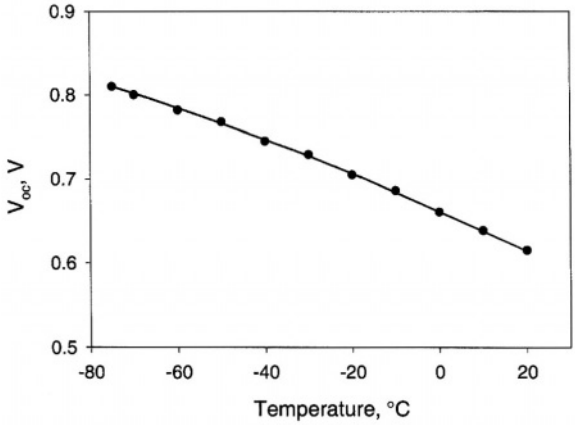

FIGURE 6.28. Temperature dependence of V_{oc} for *n*-Si in 0.1 M Li ClO_4 methanol. Light intensity 100 mW/cm^2 (5×10^{15} cm^{-3}). (Reprinted from Kobayashi *et al.*[699] © 1990, with permission from Elsevier Science.)

TABLE 6.5. Open-Circuit Photovoltage on *p*-Si in CH_3CN/$(n\text{-}Bu_4N)ClO_4$ in the Presence of Different Redox Couples[270]

Redox couple	E^0, V_{sce}	Photovoltage, V
PQ^{2+}/PQ^{+a}	−0.45	0.39
PQ^{+}/PQ^{0}	−0.85	0.42
$Ru(2,2'\text{-bipyridine})_3^{2+/+}$	−1.3	0.42
$Ru(2,2'\text{-bipyridine})_3^{+/0}$	−1.49	0.42
$Ru(2,2'\text{-bipyridine})_3^{0/-}$	−1.73	0.38

[a] PQ^{2+}: *N*,*N*′-dimethyl-4,4′-bipyridinium.

caused by the large density of surface states, which results in the potential drop in the Helmholtz layer instead of in the space charge layer.

In aqueous solutions, where the dissolution of silicon and formation of oxide film is significant, the photopotential cannot be predicted according to the energetic positions of the bands and the redox couples in the solution. For example, in solution without HF, photovoltage has been found to be relatively large on *n*-Si but very small on *p*-Si.[392] In HF solutions the photovoltage on *p*-Si is manyfold larger. In another study, open-circuit voltage of *p*-Si of about 0.4V is measured in 0.5% HF solution but only about 0.02V on *n*-Si.[968] The complex photoresponses in these solutions can be attributed to the presence of surface states associated with surface defects, dissolution intermediates, adsorbed species, and oxide film. Also, surface states may affect the reduction and oxidation of a redox couple differently; they can facilitate the reduction of a redox couple A^+/A from A^+ to A but not the oxidation from A to A^+ without light to detrap the electrons in the surface states.[553]

Numerous studies have been conducted to optimize the product of $V_{oc}i_{ph}$ to make silicon an efficient photocathodic material.[161,275,573,812] Depending on the system, the energy conversion efficiencies of silicon/electrolyte electrodes have been found to greatly vary, from a fraction of 1% to more than 10%. Efficiency can vary from 0.2 to 2% by simply changing the pH of the solution.[812] An efficiency exceeding 10% for *n*-Si in CH_3OH, and for *p*-Si in CH_3CN has been realized.[622,623,847] A surface textured sample shows a higher efficiency than a polished surface due to lower reflectivity and increased surface area.[552]

6.7. SURFACE MODIFICATION

Silicon is highly unstable in aqueous electrolytes due to the formation of an insulating oxide film which prevents the use of *n*-Si as photoanode. On the other hand, the silicon electrode has poor kinetics for hydrogen evolution which is not desirable for its use as a photocathode. Many methods have been explored to stabilize Si electrodes in aqueous solutions for possible applications as photochemical cells. They include coating the surface with noble metals, metal oxides, metal silicides, or organic materials as shown in Table 6.6. Also, some redox species, the reduction of which can favorably compete with the oxidation of silicon, can be used to stabilize silicon anodes

TABLE 6.6. Studies on Surface Treatments

Material	Coatings	Solvent	Redox couple	Refs.
n,p	PAQ[a]			546
n	DCFL			553
n	I	CH_3CN	[*n*-Bu_4N]ClO_4	828
n	I	H_2O	I_3^-/I^-, $[Ru(NH_3)_6]^{3+/2+}$ $[Fe(CN)_6]^{3-/4-}$	825, 827
n	polypyrrole	H_2O	Fe^{3+}/Fe^{2+}	810
n	polypyrrole	solid electrolyte	KI/I_2	481
p	PQ^{2+}	CH_3CN	$[Fe(\eta^5\text{-}C_5H_5)_2]^+$	809
n,p	In-Sn oxide	H_2O	$[Fe(CN)_6]^{3-/4-}$	814
n,p	PMDC	methanol	$Mo^{+/0}$	816
p	FCP	H_2O	$H^{+/0}$	815
n	silicides, RuO_2	H_2O	Br/Br^-, Cl/Cl^-, O/O^{2-}	817
n	PPR	H_2O	I/I^+, Fe^{3+}/Fe^{2+}	818
p	Cd, Pb, Pt	H_2O	HCOOH, $H^{+/0}$	688
n	Ar-NO_2 monolayer	NaOH		931
n	Pt	H_2O	Br^-/Br_3^-, Fe^{2+}/Fe^{3+}	598, 791
n	I	EtOH	e.g., I/I^-	712
n	Pt silicide	HCl, Na_2SO_4	Fe^{3+}/Fe^{2+}	483, 484
p^+n	TiO_2, Fe_2O_3, WO_3	H_2O	I/I^-	710
n	Pt-Fe_2O_3	KOH	CH_3OH/CH_2OH	482
n	Tl_2O_3	NaOH	$[Fe(CN)_6]^{3-/4-}$	480
p	Pt, Au	H_2O	$H^{+/0}$	666, 680
p	composite layer	H_2O	$H^{+/0}$, $PQ^{2+/+}$	878, 886
n	H_2Pc, CuPc	H_2O	I/I^-	879
n	textured	ethanol	*n*-$Bu_4N^{+/0}$	552
n	Fe_2O_3	H_2O		610
p	In_2O_3, polymers			677
n	PPR	H_2O	$Fe^{3+/2+}$	679
p	[Re(CO)$_3$(v-bpy)Cl]	CH_3CN	CO_2/CO	689
n	Cr-ferrocene complex	H_2O		682
n	Pt, Pb	H_2O	HCOOH	613
n	PPR	H_2O	$Fe^{3+/2+}$	418
n,p	PPR	CH_2CN		402
n,p	Au, PPR	H_2O	$Fe^{3+/2+}$	415
p–n	W, Mo	H_2O	$I^{0/-}$	416

[a]PAQ, anthraquinone groups; DCFL, dichlorodiferrocenylsilane (III); I, (1,1′-ferrocenediyl)dichlorosilane; PQ^{2+}, *N,N′*-dimethyl-4,4′-bipyridinium; PMDC, polymer-bound molybdenum dinitrogen complexes; FCP, polymer bound [1,1] ferrocennophanes; PPR, polymerized pyrrole; H_2Pc, metal-free phthalocyanine; CuPc, copper phthalocyanine.

against photooxidation.[955,960] Another approach is to use nonaqueous solutions which do not react with silicon in a wide potential range.[87,675]

The silicon surface can be stabilized using surface modification techniques which are divided into three categories[161]: (1) attachment of redox mediator which consumes the holes on the surface; (2) attachment of electronically conducting polymer; and (3) coating with thin metal or semiconducting films to create a buried semiconductor interface. Combinations of these approaches can also be used to stabilize the silicon surface.[415]

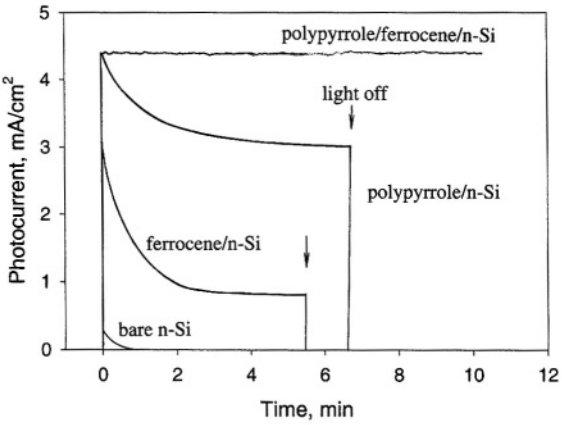

FIGURE 6.29. Photocurrent–time behavior of bare *n*-Si; ferrocene/*n*-Si; polypyrrole/*n*-Si; and polypyrrole/ferrocene/*n*-Si electrodes. (Reprinted from Malpas and Rushby.[679] © 1983, with permission from Elsevier Science.)

Figure 6.29 shows, as an example, the effect of surface modification on the stability of silicon electrode in an aqueous solution.[679] The bare silicon surface is quickly passivated in aqueous solution under illumination. Coating the electrode with a layer of either ferrocene or polypyrrole gives an improvement in the stability. The stability is further improved by a two-layer coating of ferrocene/polypyrrole as shown in Fig. 6.29.

6.7.1. Metal Deposits

Deposition of a small amount of noble metals such as Cu, Pt, and Au increases the kinetics of redox reactions on silicon electrodes as shown in Fig. 6.3.[829] Deposition of equivalent of 1 to 10 monolayers of Pt on silicon surface results in a shift of about 0.2V of the onset potential for hydrogen evolution to the positive direction.[875] Because the flatband potential does not change with the Pt deposition, the enhanced hydrogen reaction kinetics is due to the catalytic effect of the deposited metal. The energy levels of the deposited metal grains are considered to lie in the middle of the band gap and communicate favorably to the surface states both energetically and spatially. The photovoltage of *n*-Si coated with sparsely scattered Pt islands has been found to increase proportionally to the increase in the potential of the redox couple.[178] Noble metal islands effectively collect photoelectrons and thus prevent the oxidation of the silicon surface by the photoelectrons.

The surface coverage by a deposited metal is critical for the catalytic effect on photoactivity. The photoelectrochemical behavior of *p*-Si coated with a very thin layer of Pt or Au can greatly change depending on the structure of the metal layer.[413,680] It has been found that with a uniform coating of Au or Pt, the electrode loses its photoactivity and behaves just like a simple metal electrode. Only when the electrode is coated with very minute metal islands (5nm wide and separated by 20 nm) does it cause hydrogen photoevolution at potentials much more positive than those for the

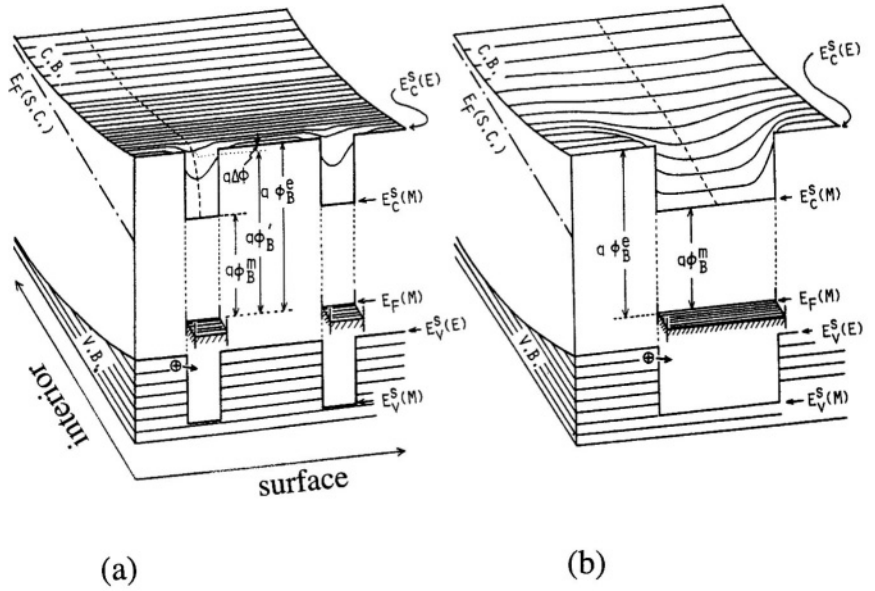

FIGURE 6.30. Schematic potential barrier diagrams for electrodes modified with ultrafine (a) and relatively large (b) metal islands. A case where E_C^S (M) is lower than E_C^S (E). (Reprinted from Nakato and Tsubomura.[598] © 1992, with permission from Elsevier Science.)

corresponding metal electrode or the naked *p*-Si electrode. Conversion from solar energy to chemical energy with a relatively large exchange current can be constructed using Pt-deposited silicon electrode.[847]

A silicon electrode with a small amount of deposited noble metals such as Pt does not behave as a buried junction and the photoelectrode properties are still determined by contact of the electrolyte, not the metal.[812] The photovoltaic response of the Pt-deposited silicon electrode is due to the incomplete coverage of the surface by Pt so that the interface energetics remains dominated by the contact of the semiconductor surface with the electrolyte. The mechanism of the hydrogen reduction processes involves first photoexcitation of electron–hole pairs followed by charging of the small Pt islands with excited electrons. The charged Pt islands react with H_2O at a high rate.

According to Nakato *et al.*,[598,666,791,811] the effect of metal islands on the photoelectrochemical properties of silicon electrode is a function of the relative dimension of the metal islands, W_m, to the width of the space charge layer, x_d. As shown in Fig. 6.30b when the metal islands are as large as the space charge layer, the effective barrier height at the metal/electrolyte interface, which determines the magnitude of photopotential, is ϕ_B^m. On the other hand, when $W_m \ll x_d$, the modulation of the field in the semiconductor results in an effective barrier height at the metal/electrolyte interface, which is almost equal to that at the semiconductor/electrolyte interface as shown in Fig. 6.30a. In this case, a large barrier height and large photo potential can thus be obtained. The high effective barrier at the metal/semiconductor interface also means that the dark saturation current is mainly determined by the minority carriers, similar to that without metal deposition.

A continuous metal deposit layer may behave as an ohmic contact or a Schottky barrier. For a relatively thick metal film the silicon can still behave like a semiconductor before the onset of current. For example, for *n*-Si deposited electrochemically with 150nm Au, the electrode behavior is similar to that of bare silicon electrode: At positive potentials the anodic current is small whereas at cathodic potentials current from hydrogen evolution increases with increasing polarization.[848] In the potential region before the onset potential for the cathodic current a linear Mott–Schottky plot is obtained giving a flatband potential similar to that of bare silicon sample. In the potential region where hydrogen evolution occurs, it behaves like a metal with potential drops mostly in the Helmholtz layer.

Silicon electrodes can also be stabilized by depositing a layer of compounds of oxides and silicides such as RuO_2,[817] molybdenum dinitrogen complexes,[882] manganese oxide,[191] indium–tin oxide,[814] aluminum oxide and aluminosilicate.[596] In contrast to the noble metals, deposition of islands of Pb and Cd tends to inhibit hydrogen evolution in H_2SO_4 solution.[688]

6.7.2. Polymer Coatings

Coating the surface of silicon electrodes with a polymer coating can also be an effective method of stabilizing the electrodes and improving the photovoltage and kinetics of electrode reactions[78,546] The polymer film effectively insulates the semiconductor from the superoxide ion and prevents chemical reaction and deterioration. At the same time, the polymer behaves like a surface-bond redox couple to mediate the charge transfer between the semiconductor and the redox species in the solution. Various types of polymers can be used to coat silicon electrodes as shown in Table 6.6.

For *n*-Si the surface-confined material can serve two functions: (1) photogenerated holes are transferred to the attached redox reagent to preclude silicon oxidation and (2) the photooxidized polymer oxidizes the solution species.[553] Because whether the species in solution can be oxidized depends on the nature of the surface-confined polymer, the electrode can be designed to oxidize certain species selectively.

An example is shown in Fig. 6.31 for a polymer with a redox couple M^+/M that is attached to the silicon surface through chemical bonding.[78] On illumination M^+ is converted to M. The resulting oxidized surface is then capable of oxidizing a second species B to B^+. The redox species B is not efficient in capturing holes directly from silicon due to its distance from the valence band. When the Si surface is covered with a polymer, the location of electron transfer is within the polymeric film rather than at the solid interface.[546,815] The photocurrent response of derivatized electrode is similar to that of bare silicon surface but the stability is significantly improved.[827]

The presence of a derivatized surface layer can affect the energetics as well as the kinetics of electrode reactions.[712] It has been found that the flatband potentials of *n*-Si and *p*-Si electrodes coated with conducting polypyrrole films are shifted by 300 and 500 mV in CH_3CN solution.[402] The reaction kinetics on polymer derivatized surface can further be enhanced by impregnation of noble metals such as Pt particles into the

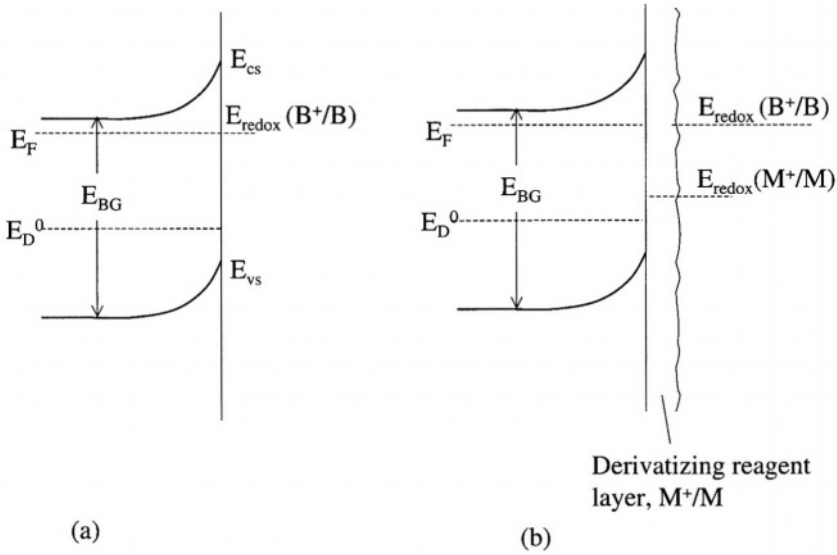

FIGURE 6.31. Contrast of situations for photooxidation of B to B^+ at a naked semiconductor and a derivatized electrode. The mediation system M^+/M is the $Fe(Cp)_2^+/Fe(Cp)_2$ couple attached via hydrolytic reaction of Si-Cl bonds with surface OH groups. At the naked semiconductor, B must capture the photogenerated h^+ which comes to E_{VB}, while at the derivatized electrode M^+ oxidizes B and the photogenerated h^+ need only be transferred to M to generate the M^+. Ideally, the M^+/M system would be more negative than E_D^o in order to suppress decomposition of the semiconductor E_D^o is the decomposition potential of semiconductor. (Reprinted with permission from Wrighton *et al.*[78] © 1978, American Vacuum Society.)

polymer film.[812,878,886] Improvement of stability can also be obtained by coating with two layers of surface-bond redox couples.[679]

Deposition of polymers on a silicon surface can be obtained electrochemically.[78,553,931] Deposition of uniform and well-ordered polymers is emerging as an active research area for their technology potentials.[1115] Deposition of organic molecules is more difficult than metals in that the bonds between organic molecules and silicon substrate are directional and covalent. The maximum coverage depends not only on the size of molecules relative to that of the surface unit cell but also on the matching between the orientation of surface bonds. It has been found that electrochemical deposition of organic compounds such as phenyl groups can be made by reduction of $^+N_2$–Ar–X cations where the substituent X may be Br, NO_2, COOH, CN, C_nH_{2n+1} (n = 1,4,12).[931,1112,1115,1174] The electrochemical process occurs on H-terminated Si(111) surface and is self-stopped after completion of the first monoplayer. The nature of bonding between the polymer and silicon is Si–C.[1099] The reaction involved has been postulated to generally follow

$$\text{Si–H} + \text{R}\cdot \rightarrow \text{Si}\cdot + \text{RH} \tag{6.21}$$

$$\text{Si}\cdot + \text{R}\cdot \rightarrow \text{Si–R} \tag{6.22}$$

where Si· and R· represent radicals.[1099]

Direct Si–C bonding to the H-terminated silicon surface is expected to lead to a modified surface that has a much better stability against oxidation than that of the H-terminated surface. It has been reported that the (111) Si surface can be completely methylated by anodization in a Grignard reagent.[1110]

6.7.3. Nonaqueous Solutions

The use of organic solvents, such as acetonitrile and liquid ammonia, offers several advantages over aqueous solutions.[172,271] First they have an extended potential range where solvent oxidation or reduction does not occur so that photoprocesses of added redox couples can be investigated with little interference from the background effects. This allows the investigation of redox processes, which is not possible in aqueous solutions, and is thus useful in determining the potentials of redox couples of wide range in relation to the band structure. Also, the smaller interaction of the solvent with the electrode material results in higher stability under polarized or illuminated conditions. Anodic decomposition in organic solvents occurs at a more positive potential compared with aqueous solutions. Also, there are a large number of organic soluble reversible redox couples that are not soluble in water.[956] A major disadvantage is that the conductivity of nonaqueous solutions is generally smaller than that of aqueous solutions. Other difficulties with nonaqueous solutions are: limited stability of both forms of the redox couple, excessive absorption of light by the solution, and the presence of trace amounts of corrosive water.[573] Table 6.3 shows the properties of organic solvents and the redox couples investigated in these solutions.

For example, in acetonitrile solution the cathodic polarization can be extended to about –3V without noticeable reactions for both *n*- and *p*-type materials. Figure 6.32 shows the *i–V* curves of *p*- and *n*-Si in acetonitrile solution with 0.1 M TBAP as electrolyte.[87] Figure 6.33 shows a cyclic voltammogram of a *p*-Si in liquid ammonia with

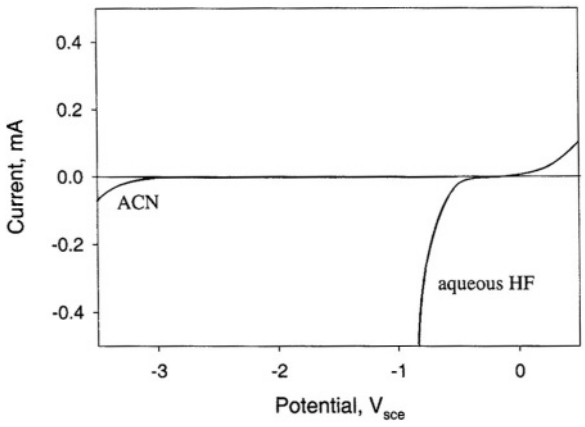

FIGURE 6.32. Cathodic current on *n*-Si in 0.1 M TBAP, ACN and in 20% HF aqueous solution. After Kaser and Bard.[87]

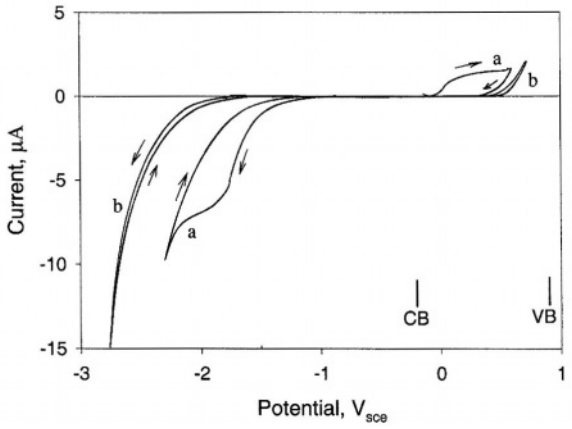

FIGURE 6.33. Cyclic voltammogram on a *p*-Si electrode in liquid ammonia (water $C < 10^{-3}$ M). a: $V = 80$ mV/s, etched crystal; and b: on *p*-Si, nonetched, with added water ($C = 10^{-1}$ M). After Amerongen *et al.*[373] (Reproduced by permission of The Electrochemical Society, Inc.)

0.1M KBr as electrolyte.[373] The anodic current observed above 0.6V is due to the solvent oxidation through hole capture from the valence band:

$$4NH_3 + 3h \rightarrow 1/2\,H_2 + 4NH_4^+ \tag{6.23}$$

It has been found that for various organic solvents—acetone methanol, 2-methoxyethanol, 2-ethoxyethanol, 1-propanol, 2-propanol, 2-methyl-1-propanol, propylene carbonate, ethylmethylketone, *N*-methylformamide, and tetrahydrofuran—appreciable photocurrents are only observed in acetone and methanol.[675] Higher photocurrent is observed in acetone than in methanol. But the open-circuit voltage is independent of the redox couples in methanol and is higher than in acetone, in which the open-circuit potential depends on the redox couple. In the case of methanol solution a rise in barrier height occurs due to the chemisorption of methanol. In general, the open-circuit photopotentials of silicon electrodes in solvents such as acetonitrile are not very high ($\max V_{oc} < 0.4$ V).[686] However, V_{oc} up to 0.67 V, which is close to the theoretical value, have been found in methanol.[276,569] According to Lewis *et al.*,[276,569] the crucial factor in achieving high open-circuit voltage is the initial photoelectrochemical oxide formation which passivates the surface recombination sites. On the other hand, according to Chazaviel *et al.*,[686] it is the formation of $Si–O–CH_3$ bonds that is responsible for the improved stability and low density of surface states in organic solvents.

The electrode behavior of silicon in nonaqueous solvents strongly depends on the presence of water. The presence of a very small amount of water will cause the formation of silicon oxide at anodic potentials and cause reduction of water at large cathodic potentials.[372,373] The presence of a thin oxide layer due either to native oxide or to water presence affects the electrode behavior by acting as a physical barrier and source of interface states. It has been found that with 10 ppm water in organic electrolytes the silicon surface is oxidized slowly via formation of oxide islands which grow to 0.6 nm thick and cover about 60% of the surface after 1 week of immersion.[934]

In ethylenediamine–pyrocatechol (EPW) solution, water is necessary for the electrochemical reaction as no anodic current is measured when water is not present in the solution.[697] Water is required for the formation of the complex structure between pyrocatechol and Si(IV). Figure 6.33 shows the significant change of *i*–*V* behavior in liquid ammonia due to the presence of a small amount of water.[373]

7

Etching of Silicon

7.1. INTRODUCTION

Etching, in the context of this book, refers to the dissolution processes that uniformly or preferentially remove material from silicon crystals immersed in a solution. Etching of silicon has been extensively explored due to its useful applications in the fabrication of electronic devices. Since the 1950s, when etching started to be used in device fabrication processes, numerous investigations have been carried out to develop and characterize the etching systems for micromachining, delineation of defects, surface polishing, and so on. The amount of information generated from these investigations is enormous considering the diversity of circumstances under which etching is performed, and the infinite possible combinations of solutions, materials, processing procedures, and structure/geometry factors that may be involved in a given circumstance.

The information considered in this chapter is limited to the etching aspects that are directly relevant to the electrochemical properties of the silicon material, whereas those related to etching procedures and structure/geometry are not dealt with in detail. Emphasis is put on the planar etch rate, which is the most important quantitative parameter in an etching solution. The spatially preferential, or nonplanar, etch rates are discussed in relation to the planar etch rates. The preferential etchings caused by the effect of doping and crystal orientation, which are widely utilized in device fabrications, are dealt with in detail particularly the mechanisms in relation to the large amount of electrochemical information presented in the other chapters. Also, the surface roughness resulting from etching, which essentially affects all aspects of silicon technology, is discussed in a separate section. Finally, etching as a process used in the various applications involving the fabrication of devices is briefly reviewed.

7.2. GENERAL

The two principal etching solution systems for silicon are HF solutions and alkaline solutions. This is because silicon is inert in aqueous solutions due to the formation of an insoluble surface oxide except for HF solutions or alkaline solutions in which the oxide is soluble. Various chemical agents can be added to these two solutions so as to

control the etch rate, etch selectivity, solution stability, and quality of the etched surface. A major difference between these two systems is that the etch rate of silicon HF solutions is similar among the various crystalline orientations, i.e., is isotropic, whereas in alkaline solutions it strongly depends on the crystalline orientation, i.e., is anisotropic. Another difference is that silicon oxide, which may be present on the silicon surface prior to or during an etching process, etches fast in HF solutions whereas it etches very slowly in alkaline solutions relative to the etch rate of silicon.

Examples of the specific etch rates in various solutions reported in the literature are given in Table 7.1. Several points may be made regarding the data in Table 7.1. (1) Silicon can be etched at a wide range of rates, as much as nine orders of magnitude; (2) the highest etch rates are observed in HF solutions; (3) the etch rates of the three major crystal planes vary only marginally in HF solutions but vary greatly in alkaline solutions; (4) the etch rate is specific to a given set of etching conditions. In addition to material and solution conditions, the etch rate of silicon in a given system depends on many operational parameters such as size and geometry of the sample, volume of the solution, stirring condition, ambient (light and air) control, and etching time. Thus, for a given silicon material and solution composition, the etch rate may vary significantly when it is measured under different operating conditions. This is responsible for the sometimes large difference in etch rates that can be found in identical systems studied by different investigators.

There are three major etching solution systems with respect to the uniformity of the etched surface, that is, relative etching rates on silicon surfaces of different crystallographic characters: (1) isotropic etching system represented by $HF–HNO_3$, (2) anisotropic etching system represented by alkaline solutions, and (3) defect etching system represented by $HF–CrO_3$ solutions (Fig. 7.1).

Table 7.2 shows the activation energies determined for the various etching systems. In general, the apparent activation energy, as determined from the dependence of etch rate on temperature, is 3–6 kcal/mol or 0.13–0.26eV for diffusion-limited reactions, whereas it is 10–20 kcal/mol or 0.44–0.87 eV for surface-controlled reactions.[289] Using these criteria to evaluate the values of activation energy in Table 7.2, it appears

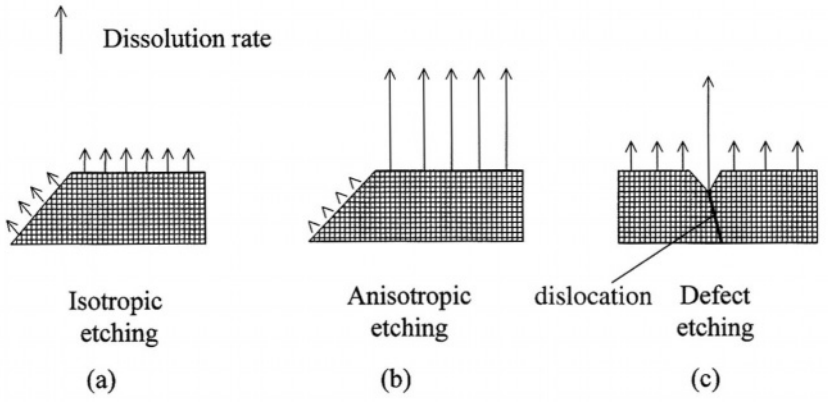

FIGURE 7.1. Schematic illustration of the three major etching systems.

TABLE 7.1. Etch Rates, Å/s, of Single Silicon Crystals in Various Solutions

Si[a]	Solution	T	(100)	(111)	(110)	Ref.
	HF solutions					
n, 2Ω	9.6% HF, 15h	rt		8×10^{-3}		985
n, 2Ω	9.6% HF, 15h	rt		5×10^{-3}		985
p, 1Ω	25% HF, 5 days	rt	10^{-3}	7×10^{-4}		715
p, 1Ω	48% HF, 5 days	rt	4×10^{-4}	3×10^{-4}		715
am Si, Si^+ imp	48% HF	rt	0.012			384
am Si, As^+ imp	48% HF	rt	>0.028			384
n, 3Ω	1M NH_4F, pH 4.2	rt		0.03–2		95
	1M NH_4F, pH 4.25	rt		0.03		95
	1M NH_4F, pH 8.25	rt		10^{-3}		95
	HF + oxidants					
poly Si	0.2% HF + 50% HNO_3	25	0.83			454
poly Si, 10^{-10}	2% HF + 50% HNO_3	rt	115			667
n^+ poly Si	2% HF + 50% HNO_3	rt	90			667
	2% HF + 50% HNO_3	rt	60			667
p	1.3% NH_4F + 5% H_2O_2	78		0.3		884
p	0.1% HF + 10% H_2O_2	rt	0.05			99
n, 3Ω	33.5% HF + 23.1% HNO_3	rt		280000		149
n, 3Ω	10% HF + 56% HNO_3	rt	14000	13300	12700	103
n, 0.002, 3Ω	1% HF + 3.8×10^{-4}M $KMnO_4$	rt	70			337
p, 0.01, 4Ω	1% HF + 3.8×10^{-4}M $KMnO_4$	rt	55			337
	49% HF + 0.22M $KMnO_4$	rt	730			337
9–23Ω	2M CrO_3 + 1M HF	rt	4.2			196
9–23Ω	0.05M CrO_3 + 2M HF	rt	5.0			19
9–23Ω	0.01M CrO_3 + 2M HF	rt	2.2			195
p,n	10M HF + 0.5M HBr + 10mM Br_2	rt	7.2			14
n, 10–100Ω	3M NH_4F + 1M $Cu(NO_3)_2$	22	31	2	20	1024
poly Si	0.25% HF + 35% HNO_3 + 15% H_2O_2	35	0.3			454
	8% HF + 75% HNO_3 + 17% CH_3COOH	rt	~830	~830	830	54
	1.3% HF + 49% HNO_3 + 49.7% CH_3COOH	rt	70	65	5	524
	1% HF + 40% HNO_3 + 15% CH_3COOH	rt	~33	~25		544
p, 3Ω	5% HF + 24% HNO_3 + 50% CH_3COOH	rt		200		91
p, 3Ω	3% HF + 15% HNO_3 + 70% CH_3COOH	rt	18	9.7		915
n, $>8 \times 10^{18}/cm^3$	0.42% HF + 17.5% HNO_3 + 67% CH_3COOH	rt	480[b]			1025
n, $<10^{18}/cm^3$	0.42% HF + 17.5% HNO_3 + 67% CH_3COOH	rt	27[b]			1025
p, $>7 \times 10^{18}/cm^3$	0.42% HF + 17.5% HNO_3 + 67% CH_3COOH	rt	330[b]			1025
p, $<10^{18}/cm^3$	0.42% HF + 17.5% HNO_3 + 67% CH_3COOH	rt	33[b]			1025
p,n	Secco etch	rt	250			319
0.6–15Ω	Schimmel etch	rt	292			340
1–3Ω	Sirtl etch	rt	385			433

TABLE 7.1. *Continued*

Si[a]	Solution	T	(100)	(111)	(110)	Ref.
1–3 Ω	Wright etch	rt	100			433
	Yang etch	rt	250			387
	MEMC etch	rt	833			204
n,*p* 0.1–16 Ω	Sopori etch	rt	3500			933
	HF + light or potential and others					
p,p^+,n^+	5% HF, 0.5 V_{sce}	rt	155			2
p,p^+,n^+	1% HF, 0.5 V_{sce}	rt	16	15	15	2
p,p^+,n^+	0.3% HF, 0.5 V_{sce}	rt	3			2
n, 0.3 Ω	39% HF, laser illum. at 1000 W/cm^2	rt	100			758
	91.5% H_3PO_4	180	0.05[b]			328
	Inorganic alkaline solutions					
	20% KOH (~4.2 M)	30	6	0.06	9	206
	20% KOH	100	560	19	930	206
	34% KOH	70	100	1.5	216	1002
n, 1 Ω	23.4% KOH + 13.3% IPA	80	130	8	55	1026
poly Si	23.4% KOH + 13.3% IPA	80	38			1026
n,*p*	0.5 M KOH	23	0.5			984
n,*p*	0.5 M KOH, stirred	23	6			984
n,*p*	0.1 M KOH, stirred	23	3.5			984
n	2 M KOH	rt	3.5	0.6		269
p	2 M KOH	rt	3.5	2		269
n,*p*	2 M KOH (~10 wt %)	23	1			984
n,*p*	2 M KOH, stirred[6]	23	3			984
n,*p*	2 M KOH	70	50			984
p, 0–30 Ω	35% KOH, stirred	80	390		740	672
	44% KOH	80	1750	5.8	3500	478
	2 M LiOH	25	2		7.5	984
	2 M LiOH	60			70	984
	2 M NaOH	25			3	984
	2 M NaOH	70			14	984
	25% RbOH	50	21		33	249
	50% RbOH	50	22		17	249
	25% RbOH	70	89		33	249
n,13 Ω	1.9 M NH_3	70	22			208
p	10% NH_4OH	70	10.7			266
p,5 Ω	3.7 wt % NH_4OH, stirred	75	67	2.8	22	711
n,13 Ω	3×10^{-3} M H_2O_2 + 1.9 M NH_3	70	73			208
p, 10	0.5 M NH_4OH + 0.09 M H_2O_2	80	0.28			1011
p, 10	5 M NH_4OH + 5 M H_2O_2	80	0.12			1011
p, 20 Ω	2.65 M NH_3 + ~0.01 M H_2O_2	80	194			706
n, 0.05 Ω	2.65 M NH_3 + ~0.01 M H_2O_2	80	333			706
deposited Si	NH_4OH + H_2O (1:5), pH 12.4	70	0.23[b]			982
deposited Si	SC1	70	0.14[b]			982
p,*n*,0.2–20 Ω	1:1 water:hydrazine	110	360	57	216	708
	48% hydrazine + 20% IPA + 32% H_2O	boiling	50			542

TABLE 7.1. *Continued*

Si[a]	Solution	T	(100)	(111)	(110)	Ref.
	Organic alkaline solutions					
0.001–100 Ω	EDP, 8 ml H_2O + 17 ml $NH_2(CH_2)_2NH_2$ + 3 g $C_6H_4(OH)_2$	110	139	8.3	83	334
	B etch	115	69	5.2		342
	F etch	115	225			342
	S etch	115	125			342
	S etch	115	170	4.2	190	206
(100) 10^{19}	S etch	110	120			207
(100) 10^{20}	S etch	110	1.1			207
p,13 Ω	etch 1	118	305			221
p, 10–75 Ω	etch 2	117	100	53	111	519
	25% TMAH	50	6.7			659
p, 7 Ω	5% TMAH	80	117			581
n, 40 Ω	22% TMAH	90	170	7.7	230	1005
n, 40 Ω	5% TMAH	90	225	5.4	308	1005
	25% TMAH	70	42	2.2		15
	25% TMAH,	70	45.3	1.5	89.9	1001
n,p, 15 Ωcm	29% TMAH + 8.5% IPA	80	61	3.9		1012

[a] cm^{-3} or *cm*-Ω.
[b] Orientation not specified.
[c] HF solutions are generally in volume concentration while OH solutions are in weight concentration; because the concentration of solvent water is not specified.
am: amorphous; imp: implanted.
etch 1: 100 g gallic acid + 305 ml ethanolamine + 140 ml water + 1.3 g pyrazine + 0.26 ml *FC129* (3 *M*) surfactant.
etch 2: 100 g gallic acid + 317 ml ethanolamine + 144 ml water + 0.3 ml of 10% FC129 (3 M) surfactant.
EDP or EPW: $NH_2(CH_2)_2NH_2 + C_6H_4(OH)_2 + H_2O$.
IPA: iso-2-propyl alcohol.
SC1: $NH_4OH : H_2O : H_2O_2$ mixtures.
TMAH: tetramethyl ammonium hydroxide.
B etch: 7.5 ml $NH_2(CH_2)_2NH_2$ + 1.2 g $C_6H_4(OH)_2$ + 2.4 ml H_2O.[342]
F etch: 7.5 ml $NH_2(CH_2)_2NH_2$ + 2.4 g $C_6H_4(OH)_2$ + 2.4 ml H_2O.[342]
MEMC etch: 35 : 25 : 18 : 21 (49% HF : 70% HNO_3 : HAc : H_2O) + 1 g $(NO_3)_2 \cdot 3H_2O$ per 100 ml of mixed solution.[204]
S etch: 7.5 ml $NH_2(CH_2)_2NH_2$ + 1.2 g $C_6H_4(OH)_2$ + 1 ml H_2O + 0.045 g pyrazine.[342]
Schimmel etch: 0.33 M Cr^{6+} + 33% HF without ultrasonic agitation.
Secco etch: 2(49% HF) : 1(0.15 M $K_2Cr_2O_7$) at room temperature with ultrasonic agitation.[119]
Sirtl etch: 1 : 1 [48% HF: 5 M CrO_3].[992,340]
Sopori etch: 36 : 20 : 2 [HF (49%):CH_3COOH (glacial) : HNO_3(70%)].
Wright etch: 60 ml 49% HF, 30 ml HNO_3 (69%), 30 ml 5 M CrO_3, 2 g $Cu(NO_3)_2 \cdot 3H_2O$, 60 ml acetic acid (glacial), and 60 ml H_2O.[433]
Yang etch: 0.75 M CrO_3 + 25% HF.

that the etching process in each of the three etching systems may be under either diffusion control or surface reaction control depending on the specific solution composition and the operating conditions.

The etch rate of silicon relative to other materials is also important in device fabrications. The data on relative etch rate, which is specific to a specific set of conditions, are widely spread in the literature. For example, the relative etch rate of silicon has been reported for: $Si_{1-x}Ge_x$ in NH_4OH,[219,266] boron monophosphide epitaxial layer in HF–HNO_3,[321] SiO_2 in HF solutions,[664] SiO_2 in KOH,[478] SiO_2 and nitride in TMAH,[15,505,1012] SiO_2 in NH_4OH,[982] different oxides and metallic films,[706] various glasses and silicides and metals in ethanolamine etchants,[506] silicon oxide and metals in EDP,[334]

TABLE 7.2. Apparent Activation Energy[a] in Various Etching Solutions

Si	Solution[b]	E_a, eV	Ref.
	Acidic solutions		
p(111), 3 Ω	5% HF + 24% HNO_3 + 50% CH_3COOH	0.42	91
n(111), 0.002 Ω	0.42% HF + 17.5% HNO_3 + 67% CH_3COOH	0.23	1025
n(111), 5 Ω	0.42%HF + 17.5% HNO_3 + 67% CH_3COOH	0.54	1025
p,n	5% HF + 63% HNO_3	0.17	103
n(100)	7 M NH_4F + 1 M $Cu(NO_3)_2$	0.52	1024
n(111) 30 Ω	69.5 ml HNO_3 + 8 ml HF + 22 ml H_2O + 80 ml glacial acetic acid	0.21	329
p(111) 10 Ω	[CrO_3]/[HF] of 0.03–0.72 with 50 g CrO_3 in 100 ml H_2O and 48% HF	0.34–0.41	1009
	91.5% H_3PO_4	1.15	328
	Inorganic alkaline solutions		
n(100) 5–50 Ω	25–45% KOH	0.56	245
(100)	42% KOH	0.59	206
(110)	42% KOH	0.60	206
(211)	6 M KOH, 50–90 °C	0.641	1010
n(100) 1 Ω	23.4% KOH + 13.3% IPA	0.77	1026
n(110) 1 Ω	23.4% KOH + 13.3% IPA	0.76	1026
n(111) 1 Ω	23.4% KOH + 13.3% IPA	0.59	1026
(100)	25% RbOH, 50–80 °C	0.47	249
(110)	25% RbOH, 50–80 °C	0.54	249
(100)	NaOH, 30 °C-BT	0.70	549
(100)	3.7 wt % NH_4OH	0.22	711
(110)	3.7 wt % NH_4OH	0.19	711
(111)	3.7 wt % NH_4OH	0.19	711
deposited Si	HN_4OH + H_2O_2 (1:5), pH 12.4	0.46	982
deposited Si	SC1	0.57	982
(100)	1:1 water:hydrazine	0.28	708
(110)	1:1 water:hydrazine	0.41	708
(111)	1:1 water:hydrazine	0.25	708
(100)	1:1 water:hydrazine, 20–50 °C	0.43	542
(100)	1:1 water:hydrazine, 50–120 °C	0.27	542
	Organic alkaline solutions		
n(111) 1 Ω	EDP, 8 ml H_2O + 17 ml $NH_2(CH_2)_2NH_2$ + 3 g $C_6H_4(OH)_2$	0.48	334
(100)	B etch	0.47	342
(100)	B etch + pyrazine	0.36	342
(100)	EDP	0.40	206
(110)	EDP	0.33	206
(111)	EDP	0.52	206
(100),10^{15}/cm^3	25% TMAH	0.52	594
(100),2×10^{19}/cm^3	25% TMAH	0.64	594
(110)	22% TMAH, 60–90	0.39	1005
(100)	22% TMAH, 60–90	0.61	1005
(111)	22% TMAH, 60–90	0.40	1005

[a]Activation energy: 1 cal/mol = 4.19 J/mol = 0.044 eV.
[b]See Table 7.1 for solution compositions.

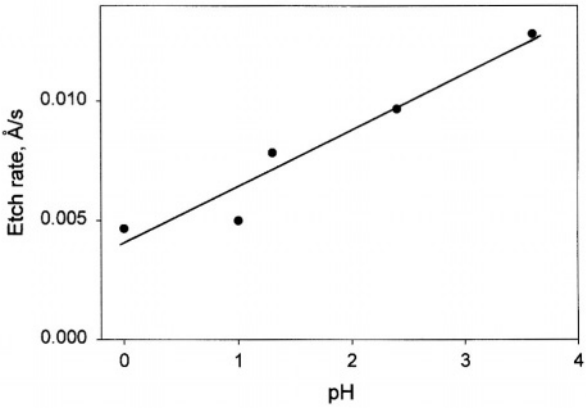

FIGURE 7.2. Etch rate of Si in 48% HF at 25 °C as a function of pH. After Hu and Kerr.[985] (Reproduced by permission of The Electrochemical Society, Inc.)

Al and SiO_2 in TMAH,[518,1005] nitride and oxide in H_3PO_4,[328] SiO_2 in SCl solutions,[884] and SiO_2 in $HF + HNO_3 + H_2O_2$.[454]

7.3. FLUORIDE SOLUTIONS

7.3.1. Absence of Oxidants

The etch rate of silicon in HF solutions at room temperature at the OCP is very low, on the order of 10^{-3} Å/s in concentrated solutions (>25% HF).[715] Dilution of concentrated HF results in an increased etch rate, which is attributed to the increased OH^- concentration as shown in Fig. 7.2.[985] Figure 7.3 shows the effect of pH; the etch rate increases from a pH of about 4, peaks at 6.5, and then decreases drastically to near zero at about 8.5.[95] The etch peak is attributed to the involvement of HF_2^- as the etching

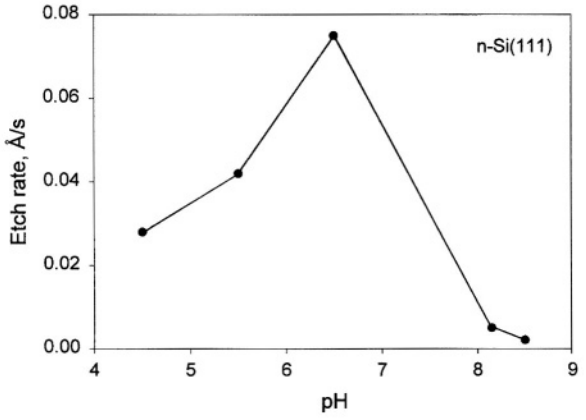

FIGURE 7.3. pH dependence of the etch rate of *n*-Si(III) in 1 M NH_4F. After Matsumura and Fukidome.[95] (Reproduced by permission of The Electrochemical Society, Inc.)

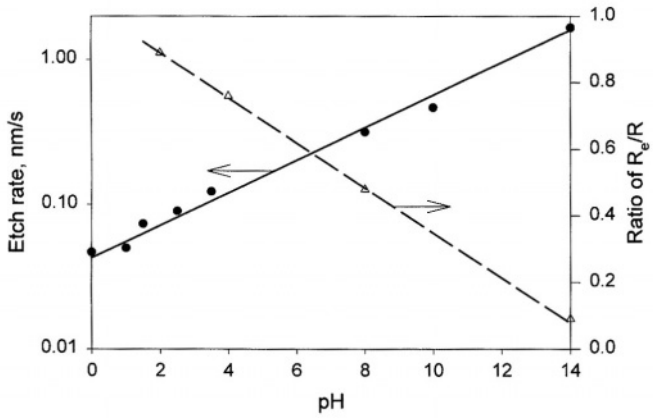

FIGURE 7.4. pH dependence of etch rate and ratio of the contribution of electrochemical reaction to that of chemical reaction, R_e/R, on *n*-Si. At pH 14 the solution is 2M NaOH. (Reprinted from Allonque *et al.*[904] © 1995, with permission from Elsevier Science.)

species, which shows a concentration peak at a pH of about 6. According to Fukidome *et al.*,[260] the etch rate in HF is determined by the competing reactions of Si with HF, HF_2^-, and OH^-, the concentration of which depends on pH. The concentration of surface Si–F bonds has a peak at a pH of about 6.4. The low etch rate in the low-pH region is due to the large coverage of SiH bonds resulting from reaction with HF, which has a high concentration at low pH. On the other hand, the low etch rate in the high-pH region is attributed to the decrease of HF_2^-. In $HF–NH_4F$ solutions, the etch rate decreases with increasing HF at a constant NH_4F concentration and it increases with increasing NH_4F at a constant HF concentration.[468] Figure 7.4 shows the etch rate of *n*-Si(111) in 10M NH_4F solution as a function of pH.[904]

Etch rate depends on the time of immersion. Figure 7.5 shows that the etch rate of *p*-Si in concentrated HF decreases with immersion time from about 0.5 Å/s at 1 min to about 2×10^{-4} Å/s at 10 days.[715] The relatively higher rate at the beginning is attributed to the etching of native oxide and the lower etch rate at longer times is due to the

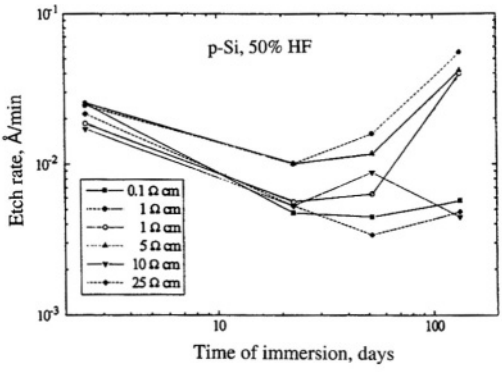

FIGURE 7.5. Etch rate in concentrated HF as a function of time. After Willeke and Kellermann.[715]

slow attack of OH^- ions on the relatively stable Si–H bonds. The Si–H bond is practically unpolarized and thus has a high degree of chemical stability. In contrast, an Si–O bond is 46% ionic and a Si–F bond is 67% ionic which results in a strong polarization and weakening of the back bonds of the silicon atoms. These surface silicon atoms are not stable and are prone to chemical attack by solution species such as OH^- and HF. Thus, in the etching process in HF solutions, the replacement of the adsorbed hydrogen by fluoride or hydroxyl ions is the rate limiting step followed by a fast process of breaking of the back bonds and removal of the silicon atoms. Such a reaction scheme is more likely to occur at surface defects resulting in their removal. According to Willeke and Kellermann,[715] a prolonged immersion in HF solution results in a more atomically smooth surface, and a large decrease of etch rate with time is due to the decrease of defect density on the surface.

The etch rate of silicon in HF does not seem to have a clear dependence on dopant concentration as shown in Fig. 7.5. Oxygen in silicon is found to have little effect on the etch rate in HF, indicating that oxygen is not efficiently reduced at the OCP.[985] However, the reactivity of silicon in HF solution may be significantly increased when active elements such as sodium are present in the silicon. A sodium-containing silicon powder is found to dissolve in an acidic NaF solution with spontaneous hydrogen evolution.[352] The elemental sodium in the silicon reacts with water to remove a protective silica layer and leaves a reactive silicon surface. The etch rate of silicon has been found to increase with ion implantation which produces an amorphous structure with a high density of dangling bonds.[384]

According to the reaction mechanisms discussed in Chapter 5, silicon dissolves chemically in KOH solutions by reacting with OH^- ions but electrochemically in HF solutions which requires the participation of electronic carriers. In HF solutions at the OCP, the chemical dissolution rate is low because the concentration of OH^- is low. The electrochemical reaction is also low because there are few carriers at the OCP. Thus, the increased etch rate in HF with dilution can be attributed to the increased OH^- concentration. The lack of direct proportionality between etch rate and OH^- concentration suggests that the rate depends on the surface concentration of OH^-, the adsorption of which is very fast.[985] The relative contribution of chemical and electrochemical reactions depends on pH. Figure 7.4 shows that in HF solutions, the dissolution reaction of silicon is mainly electrochemical but the chemical reaction path becomes more important at higher pH values.[904]

In general, the dissolution of silicon involves two essential steps, namely, oxidation followed by dissolution:

$$\mathrm{Si} + (n-m)\mathrm{h} \rightarrow \mathrm{Si}_{\mathrm{surface}}^{n+} + m\mathrm{e} \qquad n \leq 4 \qquad \text{Oxidation} \tag{7.1}$$

$$\mathrm{Si}_{\mathrm{surface}}^{n+} \rightarrow \mathrm{Si}_{\mathrm{solution}}^{4+} + (4-n)\mathrm{e} \qquad \text{Dissolution} \tag{7.2}$$

A high etch rate is only obtained when both rates of oxidation and dissolution are high. The etch rate can be increased either by addition of effective oxidizing agents into the solution or by anodic polarization which increases the surface concentration of carriers. As shown by the *i–V* curve (Fig. 5.1) the anodic dissolution of silicon in HF solutions consists of three regions. At potentials below the current peak, nonuniform anodic

dissolution occurs, which is accompanied by significant hydrogen gassing, leading to the formation of a porous silicon layer (see Chapter 8 for details). At potentials above the current peak, uniform dissolution occurs without hydrohen evolution, leading to electropolishing. The effective dissolution valence in the electropolishing region is close to 4 corresponding to an almost 100% current efficiency. Thus, the etch rate can be calculated from Faraday's law:

$$R = (mi/\rho nF) \times 10^5 \tag{7.3}$$

where i is the current density (mA/cm^2), m the molar mass (28 g/mol for silicon), ρ the density ($2.33\,g/cm^3$ for silicon), n the effective dissolution valence which is 4 in the electropolishing region, and F the Faraday constant (96,500 C/mol). According to Eq. (7.3) a current density of $1\,mA/cm^2$ corresponds to 3.1 Å/s.

The etch rate in the electropolishing region, where the silicon surface dissolves uniformly, is essentially the same for different doping conditions and orientations as shown in Fig. 8.3. The etch rate in the electropolishing region varies only with HF concentration and temperature. At a given temperature, the etch rate of silicon in the electropolishing region as a function of HF solution is shown in Fig. 8.5. The presence of H_2SiF_6 has no effect on the etching rate in the electroplishing region.[33] Large etch rates can be obtained in HF containing anhydrous organic solutions at high anodic potentials due to the lack of oxide formation.[891] The effect of various factors on the rate of dissolution under anodic potentials is described in Chapter 5.

7.3.2. *Effect of* CrO_3

The HF–CrO_3 etching system is widely used for defect sensitive etching and delineation of junctions between silicon layers of different doping concentrations.[246,387] The etch rate of silicon in pure HF solution is very low due to the lack of holes at the OCP. Addition of CrO_3 increases the etch rate due to the increase of surface hole concentration resulting from the reduction of Cr^{6+}. CrO_3 dissolves in water to form $HCrO_4^-$, CrO_4^{2-}, and $Cr_2O_7^{2-}$. At a concentration of 0.5 M or higher, $Cr_2O_7^{2-}$ is the predominant species.[1021] The presence of chromic acid suppresses the ionization of hydrofluoric acid so that the concentrations of F^- and HF_2^- are small, less than 1 % of the HF present in the solution.

Heimann[1009] suggested that etching in CrO_3–HF–H_2O solutions follows a two-step reaction mechanism. In the first step, silicon is oxidized to form a silicon suboxide SiO_x ($0.67 < x < 1$). The second step consists of the dissolution of the silicon oxide by HF. According to Chu and Gavaler,[1021] the dissolution rate of silicon in HF–CrO_3 solutions is second order with respect to the concentration of HF as shown in Fig. 7.6. It is first order with respect to $Cr_2O_3^{2-}$ ions. Figure 7.6 shows that the n-Si and highly resistive p-Si exhibit about the same etching rate whereas the other types of silicon materials have higher rates. Because the etching process is controlled by the carrier transfer across the space charge layer, different materials have different hole concentrations and thus dissolve at different rates. For p-Si, the hole concentration is high at the surface, and for heavily doped n-Si, electrons can tunnel through the space charge layer.

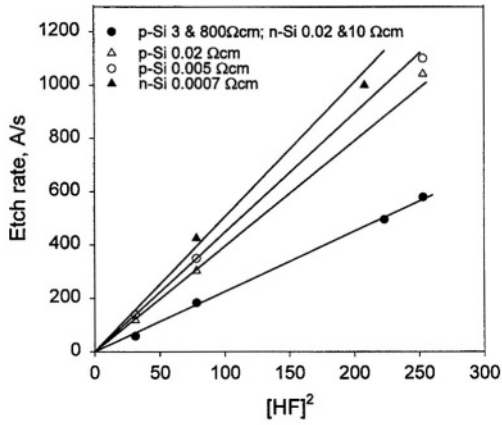

FIGURE 7.6. Dissolution rates of silicon samples of different resistivities as a function of HF concentration in solutions containing 2*M* CrO_3. (Reprinted from Chu and Gavaler.[1021] © 1965, with permission from Elsevier Science.)

According to Meerakker and Vegchel,[195,196] the etching process has different kinetics at high and low HF/CrO_3 ratios as shown in Fig. 7.7. A rate equation for etching in CrO_3–HF solutions with high HF/CrO_3 ratios (>20) can be expressed as

$$r = 1.91[CrO_3]\left(1+0.23[HF]^{1.5}\right)\Big/\left(4+0.23[HF]^{1.5}\right) \tag{7.4}$$

where r is in micrometers per minute and concentrations are molar. At low HF/CrO_3 ratios (<10) the rate equation is

$$r = [CrO_3][HF]^{1.5}\Big/\left(38[CrO_3]+1.8[HF]^{1.5}\right) \tag{7.5}$$

The details of the reactions on silicon electrodes in HF–CrO_3 solutions are presented in Chapter 6. The information on defect etching in some specific etching solutions is presented in Section 7.8.1.

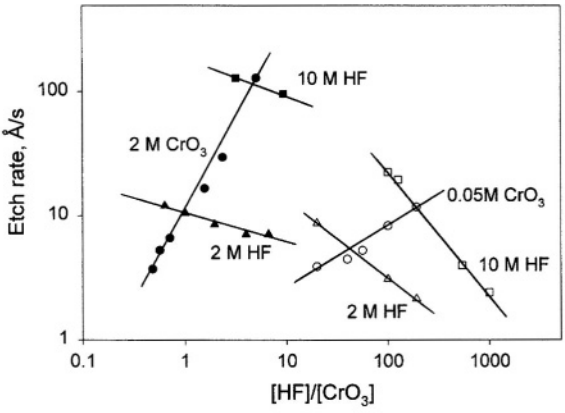

FIGURE 7.7. Etch rate as a function of the ratio of HF and CrO_3 concentrations ([HF]/[CrO_3]). After Gaspard *et al.*[194] and Meerakker and Vegchel.[195]

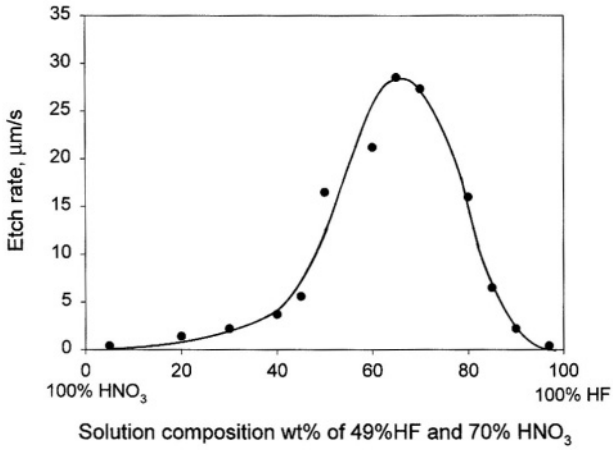

FIGURE 7.8. Solution composition in wt % of 49% HF and 70% HNO_3. After Turner[111] and Robbins and Schwartz.[149] (Reproduced by permission of The Electrochemical Society, Inc.)

7.3.3. Effect of HNO_3

The $HF–HNO_3$ etching system is perhaps the mostly widely used isotropic etchant for silicon.[720,981] Figure 7.8 shows the etch rates in different mixtures of concentrated HF and HNO_3 acids without dilution.[149] The etch rate shows a maximum at 33% HF and 23% HNO_3 (about 1:4.5 molar ratio) with a value of about 28 μm/s (equivalent to a current density of 90 A/cm^2 assuming dissolution valence of 4 and 100% current efficiency). The mixtures of these two concentrated acids can be diluted with water or other dilutent to give a wide range of etch rates as represented by the triaxial plot shown in Fig. 7.9.[150] The etch rate with respect to composition of the etchant shows two extreme modes of behavior. In the region of high nitric acid composition, etch rates are only a function of HF concentration, whereas in the region of high HF concentrations, the nitric acid concentration determines the etch rate. The etch rates decrease with addition of a diluent but are little affected in the two extreme regions. As a diluent, acetic acid acts qualitatively the same as water.[150] However, acetic acid is preferred because it results in less dissociation of the nitric acid, which preserves the oxidizing power of the HNO_3 for a wider range of dilution than water.[720] The etch rate of both types of materials are sensitive to the change of potential (see Chapter 6).

The $HF–HNO_3$ etching system has been systematically investigated by Schwartz and Robbins.[103,149,150] The results on the effect of temperature indicate that in the region of low HF concentration region, the etching process has a single low value of activation energy, 4kcal/mol, in the temperature range of 0–50 °C. This is characteristic of a diffusion-controlled process, which is in agreement with the fact that the etch rates of different silicon materials in this concentration region are essentially the same. In the region of high HF, two different values of activation energy are observed, one in the range of 10–14kcal/mol at higher temperatures and the other in the range of 20kcal/mol at lower temperatures; both are characteristic of a surface-controlled process.

Consequently, dopant concentration, crystal orientation, and defects play an imporant role in the etching process. Addition of a diluent results in an activation energy that is between these two ranges.

The etching in $HF–HNO_3$ solutions is isotropic with the etch rate of the (100) surface very close to that of the (111) surface.[54,103,524] In 0.42% HF + 17.5% HNO_3 + 67% CH_3COOH, the etch rate depends on doping concentration with the etch rate of lightly doped materials being more than 10 times lower than that of highly doped materials (it is the opposite in alkaline solutions).[1025] The activation energy of lowly doped material is 12.3kcal/mol indicating a surface-controlled process whereas that of highly doped material is 5.15 kcal/mol indicating a diffusion-controlled process.

According to Schwartz and Robbins,[103,149] the etching of silicon in the $HF–HNO_3$ system follows a chemical process with two basic reaction steps. In the first step, silicon is oxidized by HNO_3 which is followed by dissolution of the oxidized Si by HF. The overall reaction is

$$3Si + 12HF + 4HNO_3 = 3SiF_4 + 4NO + 8H_2O \tag{7.6}$$

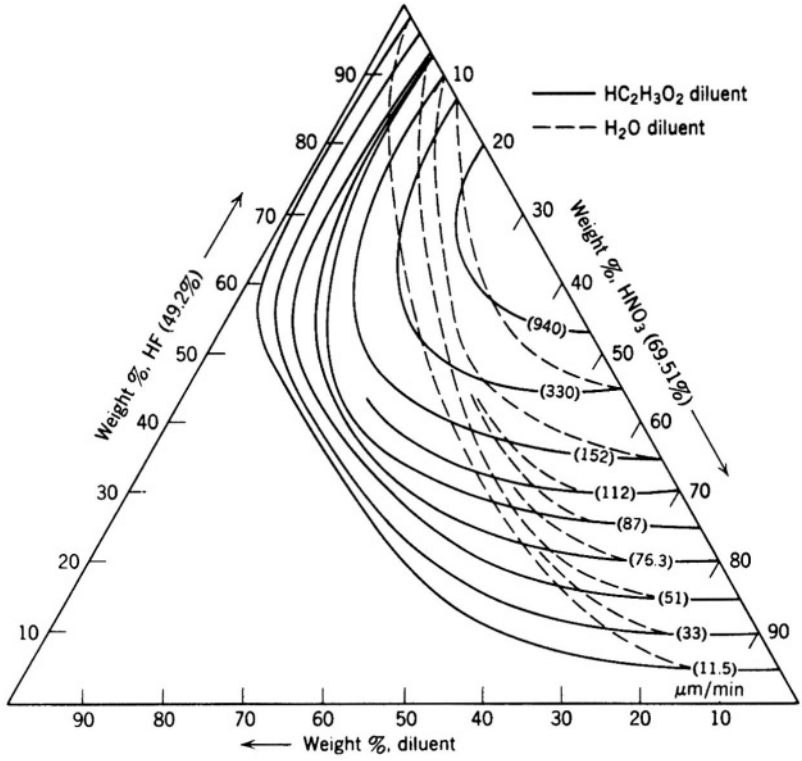

FIGURE 7.9. Iso-etch curves for silicon ($HF:HNO_3$ diluent system). After Robbins and Schwartz.[150] (Reproduced by permission of The Electrochemical Society, Inc.)

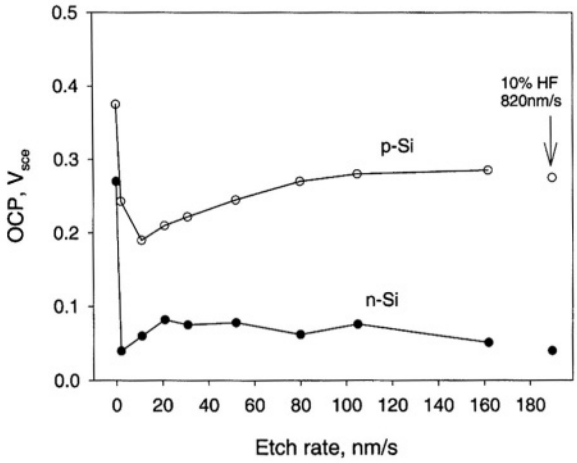

FIGURE 7.10. Effect of etch rate on the electrode potentials of *n*- and *p*-type Si in HF–HNO_3 mixtures. Rate of etching increased by adding HF to HNO_3. After Turner.[111] (Reproduced by permission of The Electrochemical Society, Inc.)

This reaction is considered to involve several intermediate steps. HNO_2 is produced and acts as an active oxidizing agent because addition of trace amounts of $NaNO_2$ increases the etch rate in the solutions. It is an autocatalytic process because for many compositions the etching, which started on a work-damaged surface, fails to continue after the specimen is taken out and reintroduced in the solution, indicating that the catalytic agent is a surface bond intermediate. A steady-state condition can be achieved only after a concentration of HNO_2 in excess of a threshold value is built up in the vicinity of the surface either through the reduction of HNO_2 at a sufficiently high etch rate or by addition of small amounts of $NaNO_2$ in the solution.

Turner[111] found that the OCP varies with type of doping and concentration as shown in Fig. 2.37. The OCP as a function of the etch rate in the solutions is shown in Fig. 7.10. Because the OCP varies with doping concentration and etch rate, Turner concluded that the etching process of silicon in HF–HNO_3 solutions is an electrochemical process in which the dissolution of silicon takes place at local anodic sites while the oxidizing agent is reduced at local cathodic sites. The etching process may also depend on the surface carrier concentration determined by doping because lowly doped materials etch slower than highly doped materials.[1024] This indicates that the reduction of HNO_3, in addition to injecting holes into the semiconductor, has an effect of changing the OCP, which in turn changes the surface concentration of the carriers. The variation of the OCP due to the oxidation and reduction reactions through the coupling effect is illustrated in Fig. 1.26. The electrochemical nature of the etching in HF–HNO_3 has been further studied recently by Kooij *et al.*[969,981] The etching, with a rate about the same for both *n*-Si and *p*-Si, proceeds mainly through capturing the holes, which are injected into the valence band due to the reduction of HNO_3. The details of the reaction processes involving the reduction of HNO_3 are described in Chapter 6.

7.3.4. Effect of Other Oxidants

Figure 7.11 shows the etch rates of *n*-Si and *p*-Si in a Br_2-containing HF solution.[14] According to Bressers *et al.*[14] the etching process, unlike that in the HNO_3 solutions, is mainly of chemical nature. At the OCP Si reacts directly with Br_2 without involving charge carriers in the bands. The reduction of Br_2 at cathodic potentials is facilitated by the electrons from the conduction band. The etch rate, which is independent of doping type and surface orientation, is limited by the mass transport of the Br_2 in the solution. Thus, as shown in Fig. 7.11 for *p*-Si, the etch rate is almost constant at cathodic potentials at which no electron is present on the surface. On the other hand, the etch rate of *n*-Si decreases to zero at cathodic potentials because Br_2 is efficiently reduced with the conduction band electrons. The reactions involved in the etching of silicon and reduction of Br_2 are discussed in Chapter 6.

Figure 7.12 shows the effect of H_2O_2 on the etching in NH_4F of different concentrations.[884] The etch rate is 0.1–0.3 Å/s in the concentration range of 10^{-3} to 1.3wt % NH_3F with 5wt % H_2O_2. It increases rapidly with further increasing fluoride concentration. The reduction of H_2O_2 on silicon in HF solutions is similar to Br_2, being primarily a conduction band process with very little hole injection into the valence band.[629]

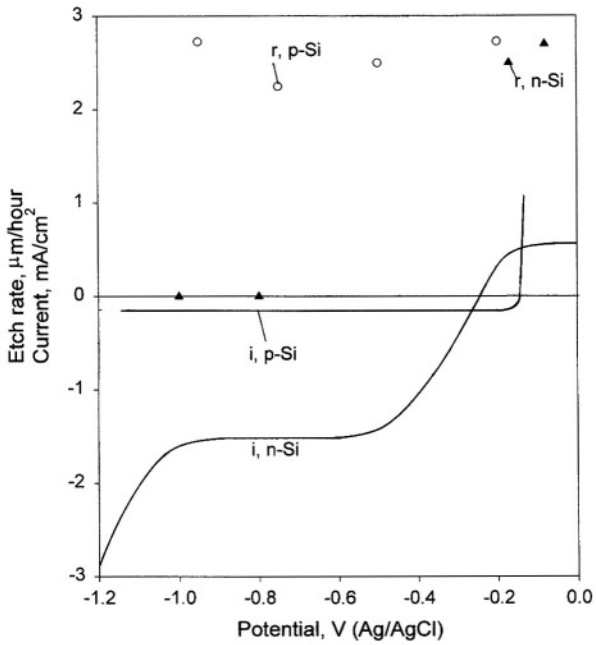

FIGURE 7.11. Current, *i*, and etch rate, *r*, of *n*-Si and *p*-Si of stationary electrodes in 10M HF + 0.5M HBr + 10mM Br_2. Etch rate was determined after 30min. (Reprinted from Bressers *et al.*[14] © 1996, with permission from Elsevier Science.)

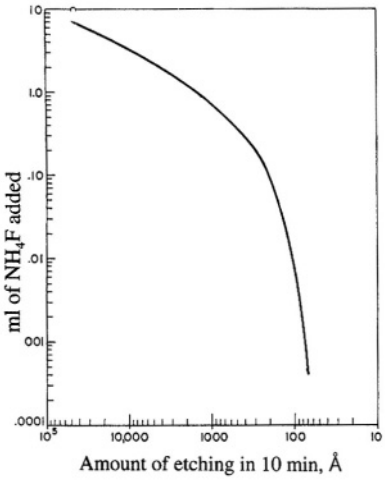

FIGURE 7.12. Etch rate of (111)-oriented silicon in ammonium fluoride solutions (solution composition: 5 ml 30% H_2O_2, aliquot 40 wt % NH_4F solution, diluted with H_2O to total volume of 30 ml). After Kern and Puotinen.[884]

7.4. ALKALINE SOLUTIONS

Alkaline solutions are another major group of etchants widely used for etching of silicon materials. The most commonly used alkaline solutions have been KOH and EDP (or EPW) which is a mixture of ethylenediamine (ED or E), pyrocatechol (P), and water (W).[206,708] Other solutions such as NH_4OH, hydrazine, ethanolamine, and tetramethyl ammonium hydroxide (TMAH) are also used. The development and application of these etching solutions are dictated by a number of factors such as etch rate, anisotropic selectivity, corrosiveness to masking materials, surface quality, processing controllability, safety, and more recently environmental impact.

The advantages of KOH solutions are its high (100)/(111) etch rate ratio and nontoxic nature.[478] The disadvantages are the significant etch rate of SiO_2, undesirable etching of metallic film, and potential potassium contamination.[918,594] KOH solutions also lack the controlled uniformity and boron specificity as do the EDP solutions.[221] On the other hand, EDP has three properties that make it very useful for micromachining: It is anisotropic, it is highly selective and can be masked by a variety of materials such as SiO_2, Si_3N_4, Cr, and Au, and it exhibits near-zero etch rates on heavily boron doped silicon.[918] However, EDP solutions have much lower anisotropic etch rate ratios than do KOH. Also, like KOH, EDP etches aluminum rapidly and EDP solutions have to be controlled at a specific temperature range to avoid precipitation. In addition, EDP is carcinogenic.[221] Because of the disadvantages of these two etching solutions, other systems of varying etching characteristics have been developed.[249,462,506,708]

Silicon etching in KOH solutions has been extensively investigated, resulting in a body of information that shapes the current understanding of the etching behavior of silicon in alkaline solutions. It appears that the major characteristics and the principal reaction processes involved in all alkaline solutions are similar to those in the KOH system although details vary from system to system. Most notably, all alkaline solutions show the sensitivity of etch rate to crystal orientation, which is the basis for anisotropic etching. Also, all of these etchants show an etch rate reduction for highly

boron doped materials. Also, although the alkaline etchants can be made of organic and inorganic solutions, all of them appear to require the presence of water to etch silicon at significant rates. In this section, the KOH etching system is taken as a model, to which other solution systems are compared.

7.4.1. KOH Solutions

The etch rate of silicon in KOH may vary from as low as 1 Å/s in dilute KOH (e.g., 0.5 M) at room temperature to as high as 2000 Å/s in a concentrated solution (e.g., 40% KOH) at high temperatures. Figure 7.13 shows that the etch rate of (100) silicon in KOH solution at room temperature increases with concentration, peaks at about 5 M, and then decreases with further increasing concentration.[984] Agitation of the solution can significantly increase the etch rate, indicating that mass transport is involved in the rate-determining processes. Also, the etch rate tends to decrease with etching time; a decrease of a factor of 3 is observed over a period of 24 h.[557]

A similar etch rate dependence on concentration is found for the three major surfaces in KOH-IPA solutions as shown in Fig. 7.14, but unlike at lower temperatures, solution stirring has little effect on the etch rate.[206,1026] The activation energy of the etching process is 0.56–62 eV for KOH of different concentrations indicating that the etching is controlled by a surface process.[206] KOH solutions are often buffered with isopropyl alcohol (IPA), which results in a decrease of etch rates.[378,1026]

The most characteristic feature of etching in KOH solution is its anisotropic nature, i.e., the etch rate varies with the crystal orientation of the silicon wafer. The etch rate for the major crystal planes follows {110} > {100} > {111}.[478] The exact difference between the etch rates of these planes depends on concentration, temperature, and measurement procedure. For example, in 20% KOH at 100 °C the etch rates for (110): (100) : (111) are 930:560: 19 Å/s corresponding to a ratio of 50:30:1. The difference between the etch rates of (110) and the (100) planes and that of the (111) plane is larger at room temperature, giving a ratio of 160:100:1 in 20% KOH. Addition of

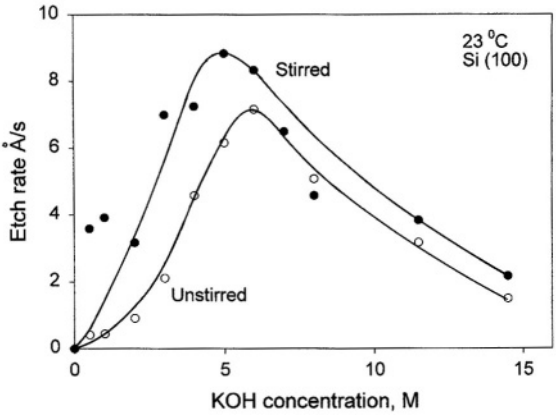

FIGURE 7.13. Etch rate versus molarity for 23 °C on the (100) surface. Data for *n*- and *p*-type Si samples were virtually the same. After Glembocki *et al.*[984] (Reproduced by permission of The Electrochemical Society, Inc.)

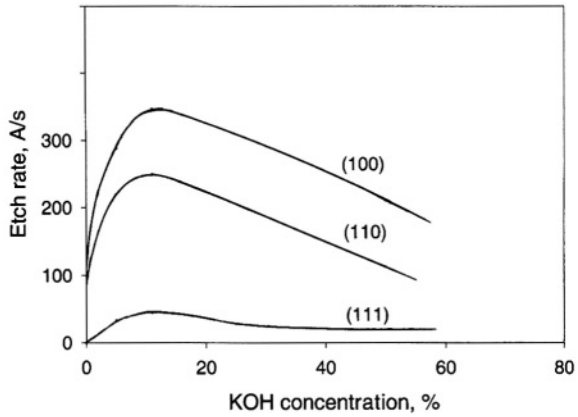

FIGURE 7.14. Etch rate of the three main crystal orientations in KOH with IPA at 80 °C. After Price.[1026]

IPA to KOH results in different decreases of etch rates for the three major orientations.[1026] As a result, at certain alcohol concentrations, the order of the etch rates is changed for (100) and (110) as in the case shown in Fig. 7.14. The effect of various factors on anisotropic etching is discussed in more detail in Section 7.6.

For a given type and orientation the etch rate is essentially independent of doping concentration up to a concentration of about $10^{19}/cm^3$, above which the etch rate drastically decreases with further increasing doping concentration, particularly for boron-doped materials.[207,269] The reduction in the etch rate for heavily doped materials is commonly referred to as etch stop and will be discussed later.

The etch rate of all silicon materials depends, to a varying extent, on potential.[109,192,541] Figure 7.15[109] shows the effect of potential on the etching rate in a 2 M KOH solution at room temperature. The etch rate is the highest at the OCP and for the (100) surface the etch rate is similar for *p*-Si and *n*-Si but on the (111) surface it is much higher for *p*-Si than *n*-Si. At potentials positive of the passivation potential the etching stops due to the formation of oxide film. At cathodic potentials the effect is different for *n*-Si and *p*-Si. For *n*-Si the etch rate decreases with increasing cathodic bias and etching stops at certain potentials. For *p*-Si the etching maintains relatively high rates comparable to those at the OCP. Formation of a sluggish layer, which was observed on *n*-Si at cathodic potentials but much less on *p*-Si, was suggested by Palik *et al.*[114] to be responsible for the etching stop of the *n*-Si. The surface of the samples etched at potentials more negative than the passivation potential is hydrophobic, indicating a high degree of hydrogen termination, whereas the surface after polarization at potentials positive of the passivation potential is hydrophilic.[541]

The morphology of the etched surface depends on the composition of the solution. In general, due to the anisotropic nature of the etching of the crystal confined in a given area, perfectly smooth lateral (111) sidewalls form on both (100) and (110) wafers.[54,531] During etching of silicon in KOH, formation of a white residual may occur, the tendency of which increases with increasing concentration below 15%.[206] According to Seidel *et al.*,[206] the high etch rate at these concentrations results in an accumulation of $Si(OH)_4$ at the surface leading to the formation of SiO_2. Also, at low KOH

concentrations, below 30%, there is a tendency to form pyramidal islands on the (100) surface.[206] The density of hillocks varies with temperature, potential, and the presence of chemical agents in the solution.[114,541] The aspect of surface roughness will be dealt with in more detail in Section 7.7.

Etching Mechanism. The etching of silicon in KOH is a process of dissolution and hydrogen evolution. Two hydrogen molecules are evolved for each silicon atom dissolved during the etching.[114] The main etching product is determined to be $SiO_2(OH)_2^{2-}$ which can further be polymerized.[379,1144] Raman spectra also indicate that OH^- is an active etching species, the OH^- intensity decreasing during etching. Water is also an active species because silicon does not etch in water-free alcohol that contains KOH.[114] K^+ as a cation present in the solution is not directly involved in the etching

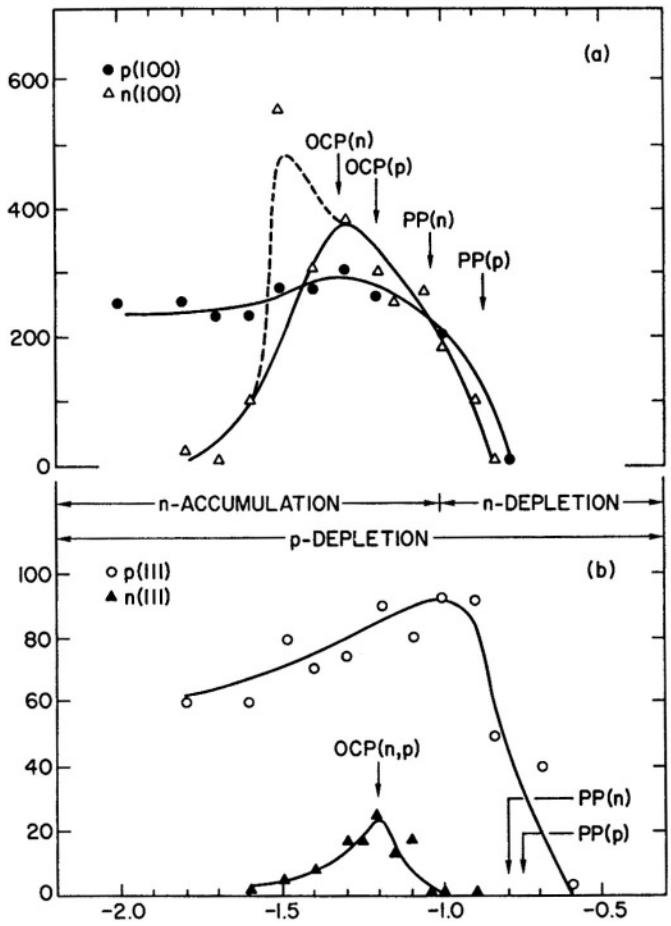

FIGURE 7.15. The bias dependence of the etch rates for (a) $p(100)$ and $n(100)$, and (b) $p(111)$ and $n(111)$ low-doped Si. The data have an experimental spread of approximately ± 20%. The open-circuit (OCP) and passivation (PP) potentials are marked. Note that the OCP is the same for the $n(111)$ and $p(111)$ samples. After Glembocki *et al.*[109] (Reproduced by permission of The Electrochemical Society, Inc.)

reaction because the etching behavior of silicon is essentially similar in different alkali solutions.[207,984] In IPA-buffered solutions, the IPA does not alter the composition of the solutions or participate in the etching reactions.[379,1144]

With the identification of H_2O and OH^- as the reactants and H_2 and $Si(OH)_2(O^-)_2$ as the reaction products, the overall reaction during etching in KOH solutions has been established:[114,206,984]

$$Si + 2H_2O + 2OH^- \rightarrow 2H_2 + SiO_2(OH)_2^{2-} \tag{7.7}$$

The details of this reaction are discussed in more detail in Chapter 5. As far as the etching kinetics is concerned, according to Seidel *et al.*[206] the dependence of etch rate on KOH concentration in the concentration range of 10 to 60% can be best fitted by the equation

$$R = k[H_2O]^4[OH^-]^{1/4} \tag{7.8}$$

Glembocki *et al.*[984] proposed a model based on the activities of H_2O and OH^-. According to them, water exists in two forms, hydrated and free, and it is the free water and free hydroxyl ions that are responsible for etching reactions. The corresponding rate equation is

$$R = C[H_2O_{free}]^r[OH^-_{free}]^s \tag{7.9}$$

which has a form similar to Eq. (7.8). According to Glembocki *et al.* at low hydroxide concentrations, $[OH^-_{free}]$ is low resulting in a low etch rate, while at very high concentrations $[H_2O_{free}]$ is low resulting in also low etch rates. In moderately concentrated solutions, both $[H_2O_{free}]$ and $[OH^-_{free}]$ are high and etch rate exhibits a maximum as shown in Fig. 7.13. The etch rate dependence on concentration in different alkaline solutions is due to the different hydration numbers of the solutions. The model is, however, not applicable for low concentrations from 0.1 to 2 M at which the etch rate is relatively constant as a function of concentration. According to Glembocki *et al.* it is perhaps due to a rate-limiting reaction associated only with free water, the concentration of which is almost constant at low KOH concentrations.

The difference between *n*-Si and *p*-Si at the cathodic potentials indicates the effect of carriers on the etching process. The hydrogen evolution may either obtain the electron directly from the dissolving surface silicon atom or from the semiconductor. For *n*-Si, cathodic bias provides a high concentration of surface electrons for the hydrogen reaction resulting in a decrease of the dissolution rate. However, for *p*-Si electrons are the minority carriers, which are not available at a cathodic bias, and the etch rate remains more or less constant at cathodic potentials.

7.4.2. Other Inorganic Solutions

The etching processes in all alkali hydroxides are similar to those in a KOH solution, namely, free H_2O and OH^- are the active agents. It has been suggested that the difference among solutions such as NaOH, LiOH, NH_4OH, RbOH and CsOH is mainly

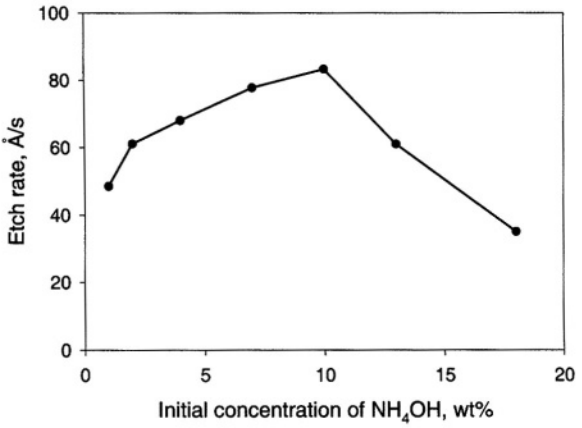

FIGURE 7.16. (100) silicon etch rate with respect to the initial NH_4OH concentration in water. After Schnakenberg *et al.*[711]

due to the difference in hydration number of the solutions.[206,249,549,984] Some etch rate data for these etchants are listed in Table 7.1.

NH_4OH Solutions. Among the inorganic alkaline solutions NH_4OH is special in two respects. First, when mixed with H_2O_2, it is widely used as a solution (known as SCl solution) for cleaning organic and metallic contaminants on silicon surface. Second, it contains ligands that is characteristic of both inorganic alkaline etchants such as KOH and organic echants such as EDP. It has a low etch rate for thermal SiO_2 giving an Si/SiO_2 etch rate ratio of 1:8000.[706] Another advantage of NH_4OH is the much lower heavy metal concentrations available in reagent grades of this chemical compared with other hydroxides.[1008] However, NH_4OH tends to decompose at elevated temperatures, especially with more concentrated solutions. Also, in NH_4OH–H_2O_2 mixtures, H_2O_2 decomposes with a half-life of 16min at 70 °C.[208]

Figure 7.16 shows the etch rate in NH_4OH solutions as a function of concentration.[711] The etch rate as a function of pH is shown in Fig. 7.17, and is considerably higher than that in NaOH solutions at the same pH values, indicating that NH_4^+ plays a significant role in the etching processes.[208] The etch rate is dependent on potential with the peak etch rate of both *p*-Si and *n*-Si occurring near the OCP.[521] The etch rate of *p*-Si decreases but maintains a definite value at cathodic potentials whereas that of *n*-Si decreases to zero at large cathodic potentials.

Figure 7.18 shows the etch rate in NH_4OH as a function of H_2O_2 concentration.[208] A sharp drop of etch rate to nearly zero is observed for concentrations above 3.2×10^{-3}M, which is due to the passivation by formation of silicon oxide on the surface. In solutions containing more than 3.2×10^{-3}M H_2O_2, the H_2O_2 as an oxidant polarizes the silicon surface to a potential value ($-0.4\,V_{sce}$) above the passivation potential. The etching of silicon in the solutions with a H_2O_2 concentration below the critical value has a chemical component and an electrochemical component due to the reduction of H_2O_2. The relative contribution of the two components changes with the concentration of H_2O_2.[488]

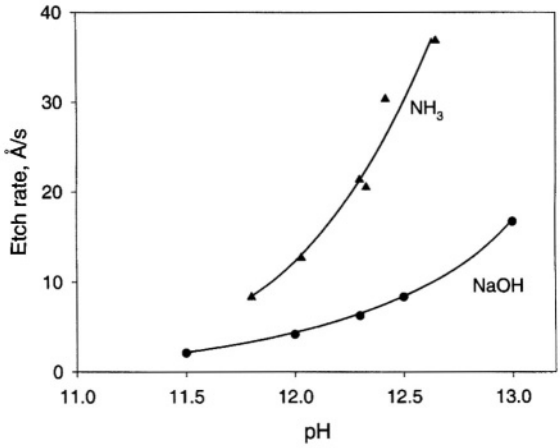

FIGURE 7.17. Etch rate of a silicon wafer as a function of the pH of an aqueous solution of NH_3 and NaOH at 70°C. After van den Meerakker and van den Straaten.[208] (Reproduced by permission of The Electrochemical Society, Inc.)

Figure 7.19 shows the effect of NH_4OH concentration in NH_4OH–H_2O_2 solutions on the etch rate of silicon.[1011] The etch rate increases with increasing NH_4OH concentration and reaches saturation at a certain concentration. The saturation etch rate decreases with increasing H_2O_2 concentration. Figure 7.20 shows that the saturation etch rate is inversely proportional to H_2O_2 concentration, reaching a limiting value of about 0.12 Å/s at high concentrations. According to Fig. 7.18 the silicon surface in the solutions in Figs. 7.19 and 7.20 is passivated, implying that the etch rates shown in Figs. 7.19 and 7.20 are in essence the etch rates of the passive silicon oxide film.

Formation of pyramidal hillocks bounded by (111) crystal planes on the (100) wafer is a problem in NH_4OH solutions for all concentrations, temperatures, stirring

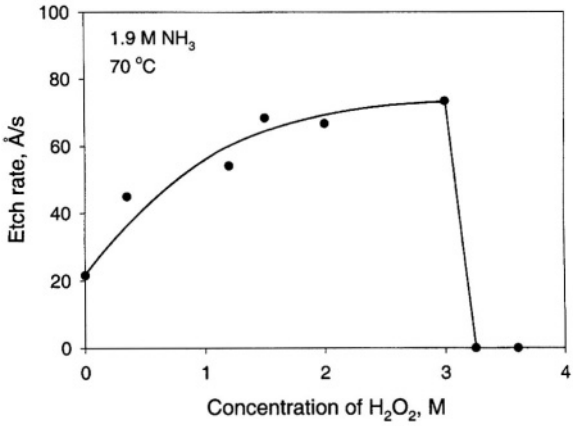

FIGURE 7.18. Etch rate as a function of the H_2O_2 concentration in a solution of 1.9 M NH_3 at 70 °C. After van den Meerakker and van den Straaten.[208] (Reproduced by permission of The Electrochemical Society, Inc.)

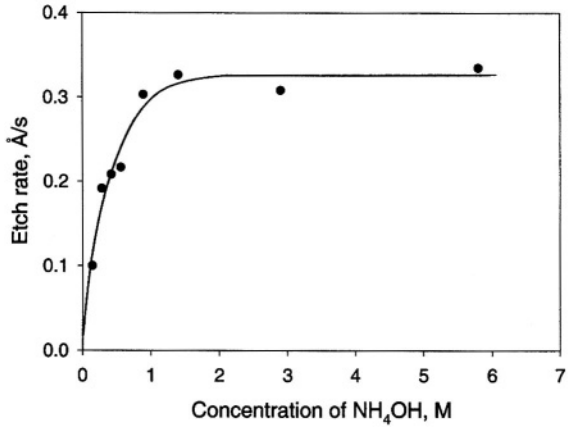

FIGURE 7.19. Relationship between etch rate and NH_4OH concentration. After Kobayashi *et al.*[1011]

conditions, and sample preparations. The formation of hillocks significantly reduces the etch rate in the (100) direction.[706] Addition of H_2O_2 to NH_4OH solution acts to suppress the formation of hillocks.

Hydrazine. As a close relative of NH_4OH, aqueous hydrazine solutions have also been investigated to a significant extent. Hydrazine, N_2H_4, may be thought of as derived from NH_3 by replacing a H atom by the NH_2 group. A hydrazine-water (1:1) solution shows some desirable characteristics.[708] The etch rate of oxide, nitride, and most metals in hydrazine solutions is very low. No precipitation occurs during etching and the etching produces good surface quality and sharply defined corners. This etchant, however, has a low anisotropic selectivity and is also toxic.

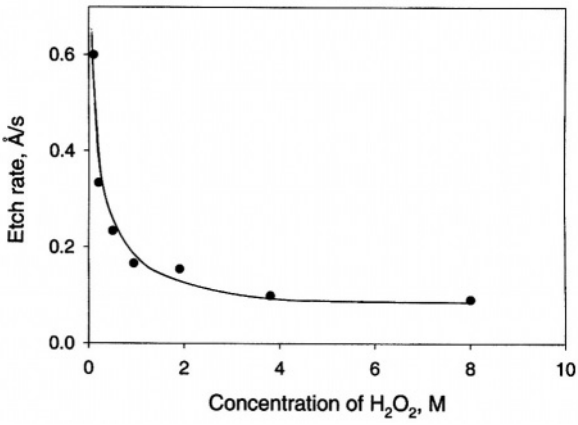

FIGURE 7.20. Relationship between saturation etch rate and H_2O_2 concentration for $NH_4OH > 1$ M. After Kobayashi *et al.*[1011]

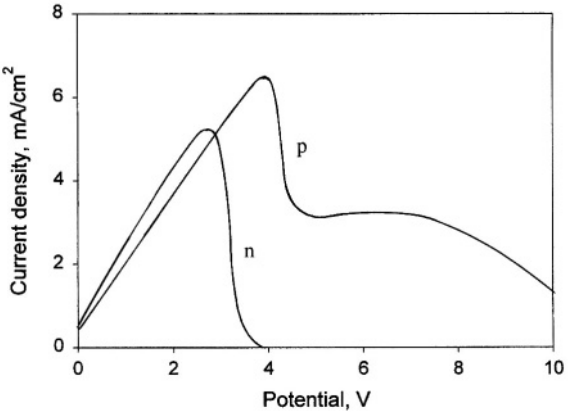

FIGURE 7.21. *i–V* curves of *p*-Si and *n*-Si in aqueous hydrazine. After Xu and Huang.[205] (Reproduced by permission of The Electrochemical Society, Inc.)

A 1:1 hydrazine solution at 110°C gives an etch rate of 360 Å/s and a (100)/(111) ratio of about 6.[708] Anodic polarization of silicon electrode in hydrazine reveals that *i–V* curves are similar to those in other alkaline solutions as shown in Fig. 7.21.[205] The different behaviors on *p*-Si and *n*-Si are attributed to the effect of surface states on the surface potential that is different for *p*-Si and *n*-Si. Figure 7.22 shows the ternary etching system of hydrazine, IPA, and water.[323,542] The etch rate is the highest when the mixture contains no IPA, indicating that IPA acts only as a diluent and not as a complexing agent. Some mixtures may result in stains on the surface, whereas other may result in the formation of an oxide film which stops the etching. The slowest etching planes are the (111) planes and the fastest planes are the (211) planes. The etched surfaces vary from being highly faceted to very flat. The faceted surfaces are made up of square pyramidal hillocks, and the flat surfaces are marked by a cellular structure. The quality of etched surfaces in terms of formation of hillocks and corner undercut strongly varies with water content and temperature.

7.4.3. Organic Solutions

EDP Solutions. EDP or EPW is a mixture of ethylenediamine (ED or E), pyrocatechol (P), and water (W). This solution is usually employed at 110–120°C (about boiling point).[342] The typical compositions and etch rates can be found in Table 7.1. Figure 7.23 shows the etch rate as a function of the water content.[334] No silicon etching occurs in solutions lacking water and the maximum etch rate is observed with a water molar fraction of about 0.6. Figure 7.24 shows the effect of pyrocatechol on the etch rate. The etch rate increases with increasing pyrocatechol content to about 5mol % above which the etch rate becomes constant. There is a definite etch rate without addition of pyrocatechol, indicating that it is not an essential component of the etching system but rather is acting as an catalyst. Addition of other agents such as pyrozine and *p*-benzoquinone has a similar effect.[342]

EPW etch solutions can be affected by many operational factors such as bath design, contamination levels, silicon content in the solution, and oxygen pressure.[342]

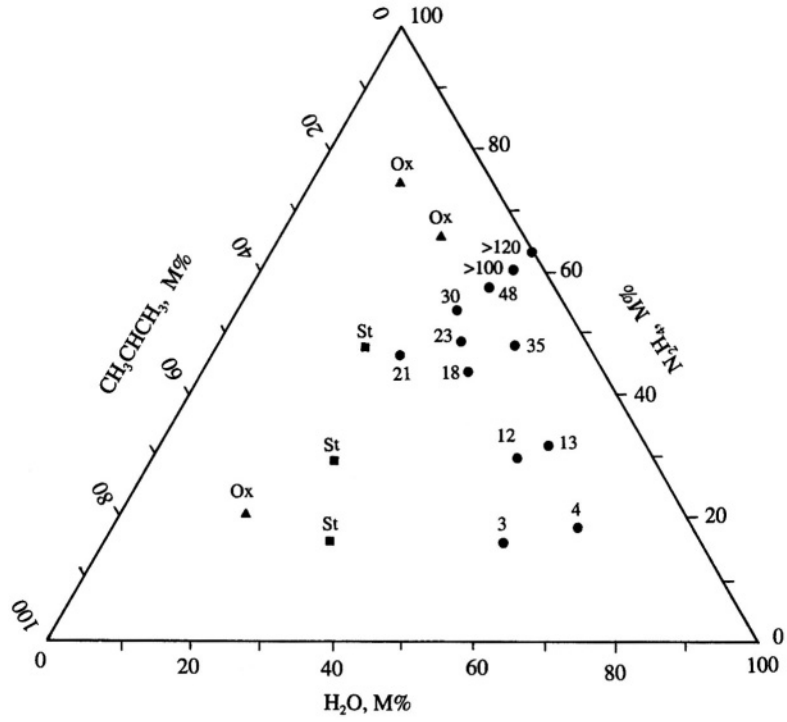

FIGURE 7.22. Etch rate (μ/h^2) of (100) silicon in ternary mixtures of hydrazine, water, and iso-2-propyl alcohol at their boiling point at atmospheric pressure. ox, silicon surface oxidized by the mixture and not etched; st, silicon surface stained by the mixture and not etched. (Reprinted with permission from Lee.[542] © 1969, American Institute of Physics.)

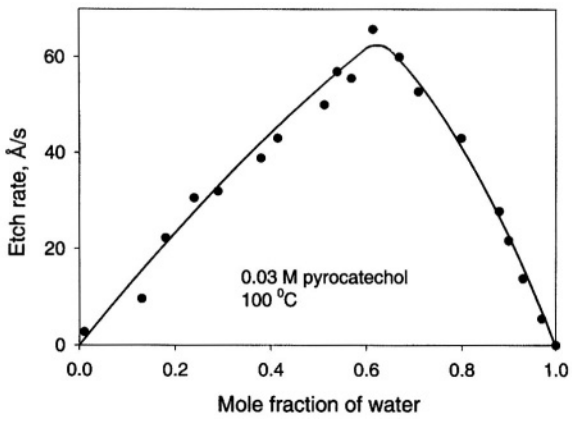

FIGURE 7.23. Etch rate of silicon as a function of the water content of the etch with pyrocatechol content held constant (0.03 M). After Finne and Klein.[334] (Reproduced by permission of The Electrochemical Society, Inc.)

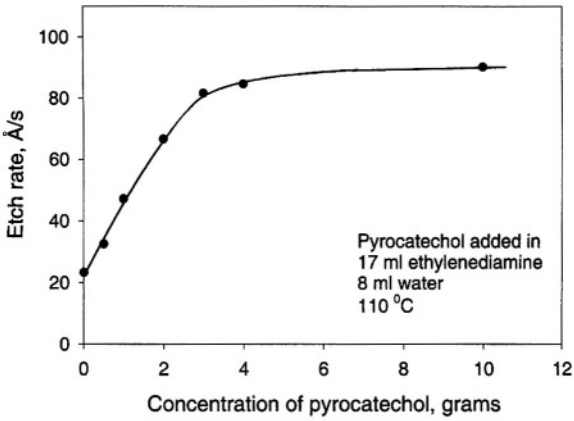

FIGURE 7.24. Etch rate of silicon as a function of the pyrocatechol content of a constant EDP composition. After Finne and Klein.[334] (Reproduced by permission of The Electrochemical Society, Inc.)

Diffusion plays an important role in the etching of silicon in EDP.[206] A trace amount of chemical agents such as diazine, pyrazine, and quinone changes the etch rate and the difference in the etch rates between the crystal planes.[386] The etch rate changes significantly when exposed to air due to the effect of dissolved oxygen. Also, insoluble residues and rough raindrop-like patterns tend to form at low temperatures and with aged solutions.[342,350] Residue formation occurs with certain compositions even at high temperatures. Etch rate in EPD is independent of illumination.[386] *p–n* junctions have no effect on the etch rate.[398]

The effect of potential is shown in Fig. 7.25; the etch stops at the passivation potential and decreases with cathodic polarization for both *n*-Si and *p*-Si.[112,697] The etch rate dependence on potential is rather different from that in KOH, where the *p*-Si etch rate varies only slightly with cathodic polarization (Fig. 7.15). Also, the etch rates at

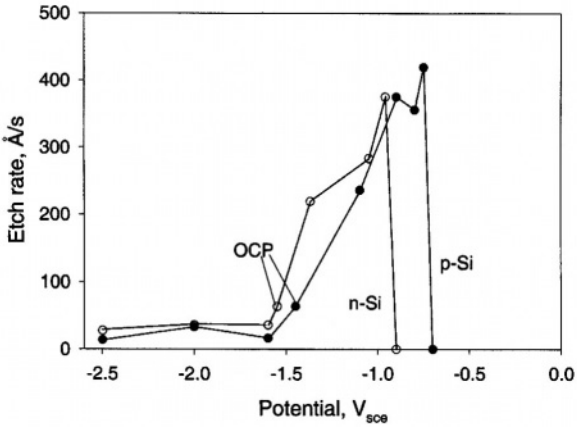

FIGURE 7.25. The effect of potential on etch rate of silicon in EDP etchant. After Gealer *et al.*[112] (Reproduced by permission of The Electrochemical Society, Inc.)

the OCP shown in Fig. 7.25 are much smaller than the peak values indicating that electrochemical processes play a more important role than in KOH.

Etching Mechanism. Water is essential for anodic current and etching to occur in EDP.[342,697] Water is the active etching species, as no etching occurs for either anhydrous amine or anhydrous amine–pyrocatechol mixtures.[334] Etching does not occur without water even in the presence of fluoride ions. Measurement of etch rates indicates that etching of silicon in EDP is mainly a chemical process with about 20% electrochemical contribution, which is considerably higher than that in KOH solutions.[22] The stoichiometry of the evolved hydrogen and dissolved silicon is close to 2. This indicates that evolution of hydrogen is the only reduction reaction accompanying the oxidation of silicon. The dissolution product is identified to be $SiC_{22}N_4H_{30}O_6$.[342]

The etching activation energy is about 0.48 eV in a solution with an E: P: W ratio of 28%: 3%: 69% suggesting that the etching process is probably not controlled by diffusion.[334] Etching occurs via oxidation of the silicon by water and hydroxyl ions resulting in evolution of hydrogen and hydrous silica at the silicon surface. According to Finne and Klein,[334] the hydrous silica is removed through the formation of the amine-soluble silicon(IV). The overall reaction process was suggested to occur as follows:

$$NH_2(CH_2)_2NH_2 + H_2O \rightarrow NH_2(CH_2)_2NH_3^+ + OH^- \qquad \text{Ionization} \qquad (7.10)$$

$$Si + 2OH^- + 4H_2O \rightarrow Si(OH)_6^{2-} + 2H_2 \qquad \text{Oxidation} \qquad (7.11)$$

$$Si(OH)_6^{2-} + 3C_6H_4(OH)_2 \rightarrow [Si(-O>C_6H_4)_3]^{2-} + 6H_2O \qquad \text{Chelation} \qquad (7.12)$$

According to Finne and Klein,[334] an amine environment is required for the pyrocatechol to dissolve (chelate) the hydrous silica. Different amines have different effect on the etching due to their protophilic activity. For small-chain-length amines such as diamine where the amine separation is small, the positive charge on the monocation withdraws electrons from the second amine group, reducing its protophilic activity. In ethylenediamine the charge separation is greater and the second amine retains its protophilic activity. The alkalinity of EDP medium is weak in comparison to KOH solutions. The low alkalinity of EDP medium does not allow the formation of a soluble silicate and the solvation of silicon is provided by chelating with pyrocatecholate which exists as a partially dissociated monoanion but further dissociates on complexation with Si(IV).[697]

According to Campbell *et al.*,[697] the reaction process in EDP is the same as that in KOH because of the essential role of water which acts not only as the oxidant but also as a solvation agent. Etching does not occur in anhydrous ethylenediamine containing strong organic oxidants, suggesting that water is not only the oxidant but is also involved in the solvation steps of the oxidized silicon species. The only difference is that the final step in the dissolution of Si(IV) corresponds to the formation of an organic complex in EDP rather than a silicate in KOH.

Ethanolamine. Ethanolamine ($NH_2CH_2CH_2OH$)-based anisotropic etchants have been developed so as to replace the toxic EDP etchant.[221,520] Linde and Austin[221] reported a functional formula of 100 g gallic acid + 305 ml ethanolamine + 140ml water

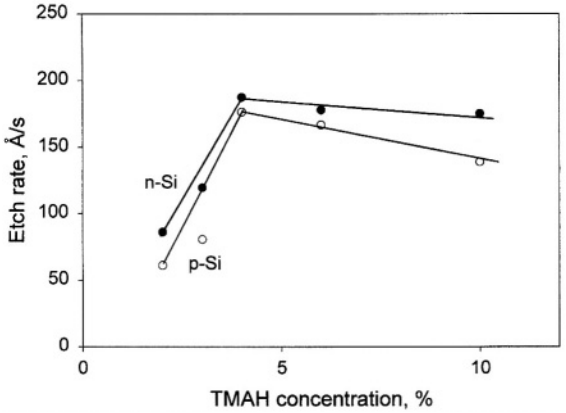

FIGURE 7.26. Silicon etch rate as a function of TMAH concentration. After Thong *et al.*[505]

+ 1.3 g pyrazine + 0.26ml FC129 (3M) surfactant. The typical etch rate of (100) silicon in this etchant at 118 °C is about 300 Å/s. It has high boron selectivity and good uniformity.[221] Also, the etch rate ratios for silicon to other materials such as carbide, nitride, oxides, and most metals in ethanolamine etchants are very large.[506]

Gallic acid functions as an effective silicon complexing agent in aqueous ethanolamine solutions. In its absence the etch rate is zero. Etch rate increases with water content. The additions of pyrazines, pyridazines, and triazoles show various catalytic effects on the etching process.[520] The catalysts that lead to faster oxidation result in faster etch rates, and the difference among the catalysts is due to a steric effect. Oxidative catalysts tend to influence the etching selectivity of the major crystal orientations.[519]

Tetramethyl Ammonium Hydroxide (TMAH). TMAH, $(CH_3)_4NOH$, etchant has been developed more recently for anisotropic etching of silicon.[505,518,996] It is relatively safe to use and presents no special disposal issues. It has a very low oxide etch rate and does not attack aluminum if the solution contains a certain amount of silicates. However, hillocks tends to develop in this solution.[518,1005]

Figure 7.26 shows the etch rate as a function of TMAH.[505] At a concentration above about 4% TMAH the etch rate is basically independent of the concentration. Figure 7.27 shows that the etch rates of (100) and (110) planes decrease as a function of TMAH concentration at higher concentreations.[1005] The etch rate tends to increase with increasing amount of dissolved silicon in the solution as shown in Fig. 7.28.[518] The selectivity in etching rate between (111) and other planes is poor compared with that in KOH solutions.[1001] The etch rate ratio of (100)/(111) planes varies with TMAH concentration and temperature with a minimum at about 25% TMAH.[1005] The slowest etching plane is found to be (111), 1.5 Å/s, and the fastest one (210), 99.5 Å/s.[1001] The etch rate of *n*-Si is slightly higher than that of *p*-Si.[505] Addition of IPA to TMAH solution slows down the etch rate linearly with increasing IPA concentration but changes very little with the etch rate ratio of (100)/(111).[1012] Addition of 1–4g/liter pyrazine to 25% TMAH solution increases slightly the etch rate and improves the surface smoothness.[594]

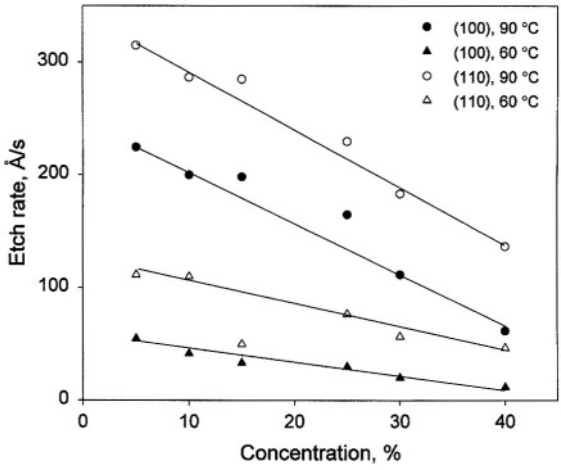

FIGURE 7.27. Etch rate of Si(110) in TMAH as a function of concentration and temperature. After Tabata *et al.*[1005]

Illumination during etching has no effect on the etch rate.[505] The etch rate decreases sharply at anodic potentials corresponding to the occurrence of passivation as shown in Fig. 7.29.[516] The etch rates at the OCP are close to the peak values which is similar to the situation in KOH, indicating very little contribution from electrochemical etching at the OCP. At cathodic potentials *n*-Si and *p*-Si are different; whereas the etch rate on *p*-Si remains relatively unchanged, that of *n*-Si decreases with increasing cathodic polarization which is also similar to that in KOH. Also, the qualitative etching characteristics and potential-dependent etch rate are not affected by the addition of IPA. The dissolution products in 2 and 20% TMAH solutions are mainly

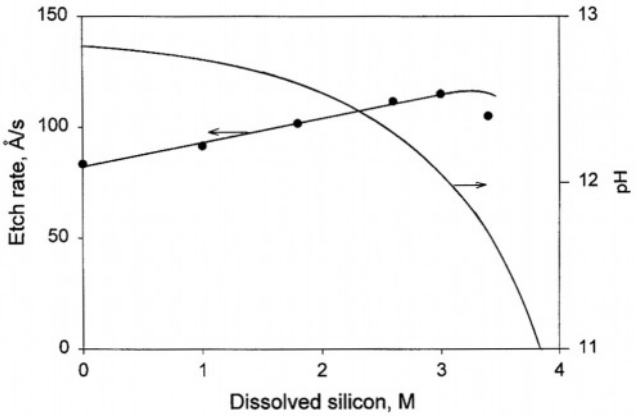

FIGURE 7.28. Dependence of Si(100) crystal plane etching rate on the concentration of dissolved silicon in 22% TMAH at 80 °C. After Tabata.[518]

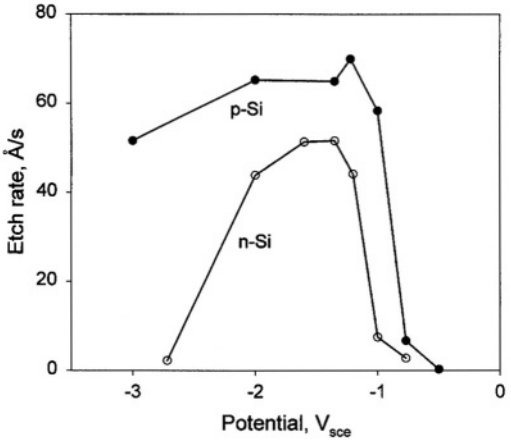

FIGURE 7.29. Etch rate versus voltage of *n*- and *p*-type silicon in 25 wt % TMAH solution. After Acero *et al.*[516]

$SiO_2(OH)_2^{2-}$ and its polymers.[888] The etching mechanism is suggested to be similar to that in KOH.

7.5. ETCH RATE REDUCTION OF HEAVILY DOPED MATERIALS

For a given type and orientation the etch rate of silicon in alkaline solutions is largely independent of doping concentration up to about $10^{19}/cm^3$.[207,269] At a doping level of about $2 \times 10^{19}/cm^3$ the etch rate of boron-doped silicon drastically decreases with increasing dopant concentration.[207,341,711] Reduction by as much as three orders of magnitude can be obtained by varying the boron concentration from about $10^{19}/cm^3$ to above $10^{20}/cm^3$, where etching virtually stops. This feature has been widely used as an etch stop technique for the fabrication of silicon microstructures.

Doping with other elements such as Ge and P (*n*-type dopant) also results in etch rate reduction but at higher concentrations than B as shown in Fig. 7.30.[207] It has been reported that ion implantation of species such as As to a level of $10^{17}/cm^3$ reduces the etch rate.[385] On the other hand, doping with As, P, and Sb was found to change little from 10^{14} to $10^{20}/cm^3$ in 23.4% KOH + 13.3% IPA.[1026] Carbon implantation to concentrations greater than $10^{20}/cm^3$ causes drastic etch rate reduction as shown in Fig. 7.30.[214] The effect is more pronounced in EDP than in KOH.

The occurrence of etch rate reduction on highly boron doped materials appears to be independent of doping methods, whether by solid-source diffusion, epitaxial growth, or ion implantation.[251] However, the boron concentration at which significant reduction occurs is different for different methods of doping. The critical boron concentration for etch rate reduction to occur is affected by the defect density in different doped materials. It is found that for similar boron concentrations the amount of etch rate reduction in KOH solutions decreases with increasing defect density.[251] In

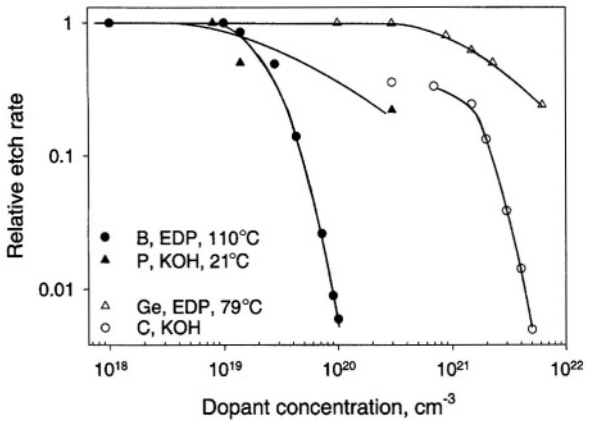

FIGURE 7.30. Normalized <100> silicon etch rates as a function of dopant concentration for boron, phosphorus, germanium, and carbon in KOH and EDP solutions. After Seidel *et al.*[207] and Lehmann *et al.*[214] (Reproduced by permission of The Electrochemical Society, Inc.)

particular, etch rate reduction on highly boron doped polycrystalline material which contains the highest level of defects is found to be significantly less than that on single-crystalline substrate.[251,506]

Etch rate reduction is not observed for highly doped silicon in HF-based solutions.[2,918] It is observed on highly boron doped silicon for (100), (110), and (111) orientations in all major alkaline etching solutions.[207,269] Figure 7.31 shows the dependence of etch rate on boron concentration in different alkaline solutions.[207,594] For KOH solutions, the decrease becomes less steep with increasing KOH concentration. In NH_4OH the etch rate reduction is stronger than in KOH. A much larger etch rate reduction, as high as 8000-fold, is observed.[711]

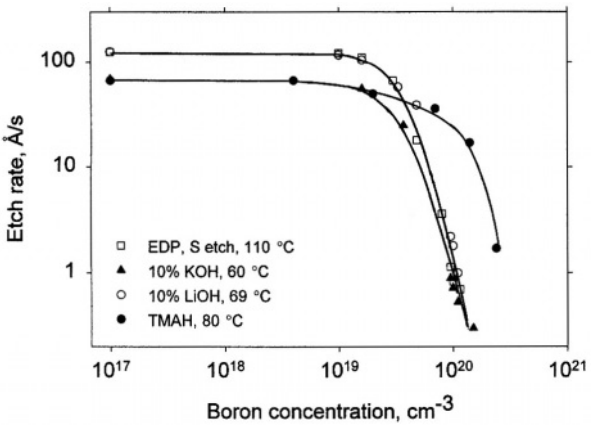

FIGURE 7.31. Effect of heavy doping on the etch rate of Si in different alkaline solutions. After Seidel *et al.*[207] and Steinsland *et al.*[594] (Reproduced by permission of The Electrochemical Society, Inc.)

Mechanism

The mechanism of boron-induced etch rate reduction has been extensively investigated since its first observation in the late 1960s.[207] Several models have been proposed attributing the phenomenon to increased lattice distortion and defect density, or surface passivation, or electron deficiency. As described below, although each of these models provides an explanation of some aspects of the phenomenon, a coherent account for the underlying mechanism is still lacking.

In an earlier investigation, it was suggested that etch rate reduction is caused by the increased lattice distortion from high doping. Later studies indicated that the reduced etch rate of high-boron-doped material is not likely to result from lattice distortion or stress. According to Seidel *et al.*[207] who measured the etch rate on stress-compensated boron/germanium co-doped samples, neither lattice strain nor crystal defects induced by the high boron concentration play a significant role in the etch stop phenomenon. In one study, the etch rate of highly doped samples actually increased with increasing lattice defect density.[251] This is the opposite of what one would expect were etch rate reduction the result of increased lattice distortion. In another study, the etch rate of highly doped silicon significantly increased with sputtering damage whereas that of lightly doped silicon changed very little, indicating that lattice damage does not cause etch rate reduction.[386]

The shortened electron life model is mainly based on the observation that the decrease of etch rate with boron concentration exhibits an inverse fourth power dependence on the boron concentration.[207,251,386] Raley *et al.*[386] postulated that etching in KOH is a corrosion process and that the etch rate reduction at high boron doping levels is due to the decreased electron concentration required for the reduction of hydrogen in the etching process described by the following reactions:

$$\mathrm{Si} + 2\mathrm{OH}^- \rightarrow \mathrm{Si(OH)}_2^{2+} + 4\mathrm{e} \qquad \text{Oxidation} \tag{7.13}$$

$$\mathrm{Si(OH)}_2^{2+} + 4\mathrm{H_2O} + 4\mathrm{e} \rightarrow \mathrm{Si(OH)}_6^{2-} + 2\mathrm{H_2} \qquad \text{Reduction} \tag{7.14}$$

The rate of reduction reaction is a fourth-order reaction with respect to electron concentration:

$$R \propto n^4 \tag{7.15}$$

The surface concentration of electrons, n, which are generated by the oxidation reaction is determined by Auger recombination and is related to the hole concentration by

$$n \propto 1 \Big/ \left[1 + (h/A)^2\right] \tag{7.16}$$

where h is the hole concentration and A a constant. Thus,

$$R = B \Big/ \left[1 + (h/A)^2\right]^4 \tag{7.17}$$

Seidel *et al.*[207] proposed a similar model, ascribing the reduced etch rate of highly doped material to the reduced electron concentration which is caused by degeneracy

induced by the heavy doping.[207] According to this model, the etch rate decreases at a concentration corresponding to a doping level of 2.2×10^{19} at which the material is degenerated and the Fermi level moves into the valence band making silicon behave like a metal. As a result of degeneracy the space charge layer on the silicon surface shrinks to a value on the order of one atomic layer. The electrons injected into the conduction band by the oxidation steps are no longer confined to the silicon surface but rather penetrate into the bulk where they have a high probability of recombining with holes. As a result, these holes are no longer available for the reduction of water as part of the etch reactions. The fourth-power decrease of etch rate is then explained by the fact that for the dissolution of one silicon atom, four charges are required.

The electron deficiency model implies that etch stop should not occur on *n*-Si where there are abundant electrons in the conduction band. Unable to explain the etch rate reduction on phosphorus- or germanium-doped *n*-Si, Seidel *et al.*[207] suggested that the etch rate reduction observed on phosphorus-doped *n*-Si is caused by a different mechanism. Also, the electron deficiency model assumes that electrochemical reactions are responsible for the etching process in alkaline solutions. However, experimental results indicate that the etching process is mainly of chemical nature as described in detail in Chapter 5.

The passivation model, proposed by Palik *et al.*,[151,269] attributed the etch rate reduction to the easier formation of an oxide film on highly doped silicon which passivates the surface. This model is supported by a number of experimental observations. First, the difference between passivation potential and OCP decreases with increasing doping concentration (Fig. 5.42) implying easier passivation for highly doped materials. Second, ellipsometric measurements of the samples during etching in KOH solutions indicate the existence of a surface phase on highly doped materials but not on lightly doped materials. This coincides with the *i–V* curves of highly doped material, which shows no current peak, implying that an oxide film already exists near the OCP. Due to the relatively slow etch rate of oxides in alkaline solutions, boron oxide and hydroxides, once formed, tend to stay on the surface and would thus passivate the surface and prevent further dissolution of the silicon. The fact that EDP exhibits more effective etch stop than KOH at high boron doping is another indication of the possible passivation mechanism, because EDP etches oxides at a much slower rate than does KOH. The passivation model can also explain the lack of etch rate reduction in the $HF–HNO_3$ system because silicon oxide etches at high rates in HF-based solutions.

Palik *et al.*[151,269] suggested that the tendency to grow an oxide layer on highly doped materials is due to the strain in the silicon surface which enhances the Si–B bond such that a borate glass is formed. The atomic concentration of boron-doped silicon at etch stop levels corresponds to an average separation between boron atoms of 20–25 Å and is near the solid solubility limit (5×10^{19}) for boron substitutionally introduced into the silicon lattice. Silicon doped with boron is under tension as the smaller boron atom enters the lattice substitutionally, thereby creating a local tensile stress field. At high boron concentrations the tensile force becomes so large that it is more energetically favorable for the excess boron to enter interstitial sites. It is proposed that the strong B–Si bond tends to bind the lattice more rigidly, therefore increasing the energy required to remove a silicon atom high enough to stop etching. Formation of Si–X

bonds, with X being a doping element that is more resistant to chemical attack than the Si–Si bond in alkaline solutions, is a rather plausible explanation for the reduced etch rate of highly doped materials. The increased number of such bonds can then account for the gradual reduction of etch rate with increasing doping concentration.

7.6. ANISOTROPIC ETCHING

7.6.1. Sensitivity of Etch Rates to Crystal Orientation

Anisotropic etching, i.e., different dissolution rates on different crystal planes, is a characteristic feature of silicon etching in alkaline solutions. Strictly speaking, the etch rate of silicon always depends, to a variable extent, on crystal orientation in all etching solutions, acidic or alkaline. However, the etch rate difference for different planes is very small in acidic HF solutions relative to those in alkaline solutions. Figure 7.32 shows the etch rate ratios of (100)/(111) and (110)/(111) planes in various solutions. In HF-based solutions the ratios are close to 1, varying only slightly with different solution compositions. Exceptions, however, exist. For example, in NH_4F solution with addition of copper ions, the etch rate ratio of (100)/(111) is found to be as high as 15.[1024] Addition of silver or gold ions does not have such an effect. Because etching in solution with metal ion oxidants is accompanied by deposition of the metal on the

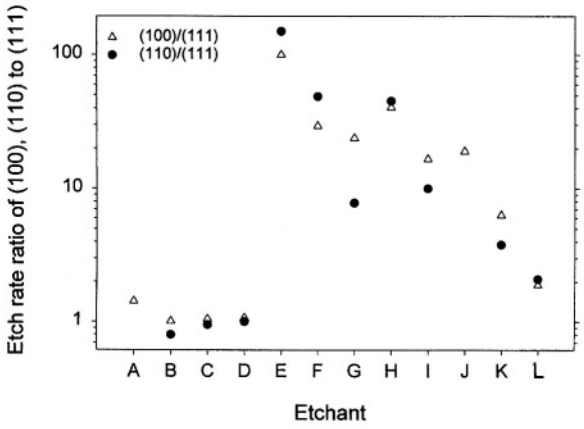

A 25% HF
B 1.3%HF + 49% HNO_3 + 17% CH_3COOH
C 10% HF + 56% HNO_3
D 1% HF at 0.5V_{sce}
E 20% KOH at 30 ^{0}C
F 20% KOH at 100 ^{0}C
G 3.7wt% NH_4OH
H S etch
I 8ml H_2O + 17ml $NH_2(CH_2)_2NH_2$ + 3g $C_6H_4(OH)_2$
J TMAH
K 1:1 water:hydrazine
L etch 2

FIGURE 7.32. Etch rate ratio of (100)/(111) and (110)/(111) in different etching solutions. Data from Table 7.1.

surface, the special effect of certain metals such as copper ions on anisotropy may indicate that the copper deposition process may be anisotropic instead of silicon dissolution in the NH_4F solution. The etch rate ratio in alkaline solutions, in contrast to HF solutions, tends to be large and greatly change with solution composition and etching conditions. Thus, in real practice the HF solutions, due to the near-unity etch rate ratios, are considered as isotropic etchants whereas those of alkaline echants are referred to as anisotropic etchants. All anisotropic etchants practically used for etching silicon are aqueous alkaline solutions.[206]

Anisotropic etching can be measured by a number of methods: (1) measuring the in-depth etch rate of samples of different surface orientations,[54,342,542] (2) using silicon samples masked by a fan-shaped pattern consisting of radially divergent segments and measuring the lateral underetch of the segments of different orientations,[206] (3) measuring the depth of etching groove bounded by (111) planes relative to the lateral etching under the defining mask,[487] (4) using spherical, hemispherical, or cylindrical samples and identifying the orientation of the resulting vertices and faces,[235,1001,1019] (5) analyzing the shape of etched surface profiles of silicon surfaces of different orientations.[672,673] The orientations most used for anisotropic etching are (100) and (110) wafers; (111) wafer is rarely used.[995]

KOH-based etching solutions are the most widely used anisotropic etchants.[206,478,851] These etchants show the highest etch rate ratio of (100)/(111) and (110)/(111) planes. Ratios as high as 300–400 for (100)/(111) and 600 for (110)/(111) can be obtained.[487,918] The etch rate ratio is even higher at room temperature; a ratio as high as 2500 is achievable for (110)/(111) planes in KOH solution.[487] Of the organic alkaline systems, solutions consisting of ethylenediamine, water, and pyrocatechol (EDP) are among the most widely used. The etch rate ratio in EDP, although lower than that of KOH, is rather high compared with other organic etchants as shown in Fig. 7.32. The (100)/(111) etch rate ratio varies from 12.5 to 50 in the concentration range of 5–40% and temperature range of 60–90 °C.[1005]

Etch rate ratios are almost constant with respect to doping concentration up to the heavily doped levels where etch rate reduction occurs.[206,269,334] The degree of anisotropicity in terms of etch rate ratio of (100)/(111) depends strongly on etching conditions. For example, in a 20% KOH solution the ratio can change from about 100 near room temperature to about 30 at 100 °C and in EDP solution the etch rate changes with addition of hydrazine to the solution as shown in Fig. 7.33.[342] Figure 7.34 shows that the etch rate of silicon in EDP is independent of the type of doping and dopant concentration but strongly depends on orientation giving an etch rate ratio of 139:83:8.3Å/s for (100):(110):(111) planes.[334]

The (111) surface is the slowest etching plane in alkaline etchants in all reported investigations.[206,542,1001] The fastest etching plane in alkaline solutions, on the other hand, depends on solution composition. For example, for silicon surfaces of different orientations ranging from 0° to 45° from the (010), the plane of fastest etch rate is (210) in 35% KOH at 80 °C.[672] In the binary and ternary etching systems of hydrazine and water, and hydrazine, IPA, and water, the fastest plane is (211).[54,542] In KOH, (411) was found to be the fast etching plane in one study[592] and (320) in another,[235] (331) in KOH–propanol–water system,[54] and (110) in CsOH.[235] Table 7.3 shows that (210) and (310) are the fastest etching planes in TMAH solution whereas (110) and (320) are

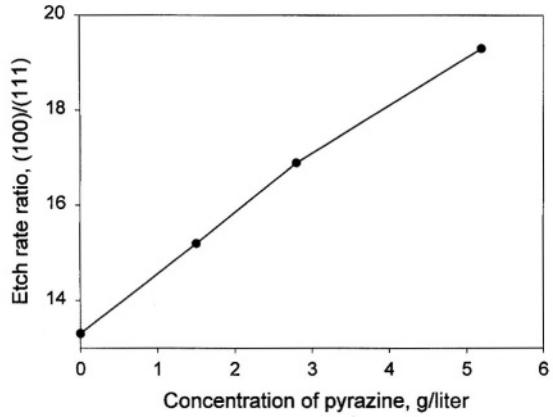

FIGURE 7.33. Effect of pyrazine concentration on etch rate ratio of (100)/(111) in EDP. After Reisman *et al.*[342] (Reproduced by permission of The Electrochemical Society, Inc.)

the fastest in KOH solution.[1001] For (110) and (100) planes, which one etches faster depends on the formulation of the etchant as shown in Fig. 7.32. Crystal surfaces other than {100}, {110}, or {111} can be considered to be composed microscopically of the main crystal planes.[206] Figure 7.35[478,1019] shows the etch rates of silicon material of different crystal planes in 10 M KOH solution at 62 °C. It is interesting to note that the etch rate of the (111) plane may not be the lowest in HF solutions as shown in Table 7.1.

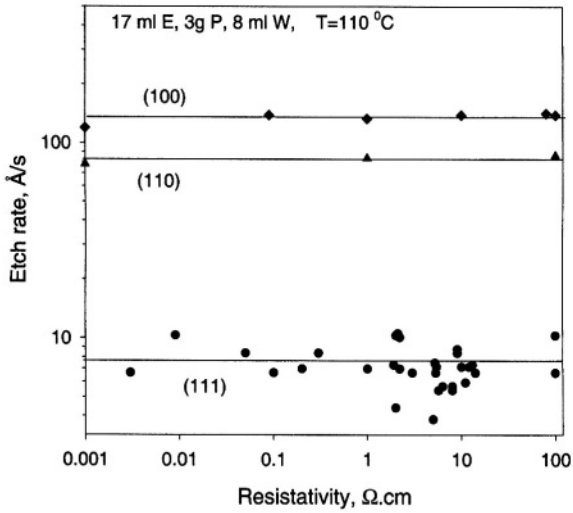

FIGURE 7.34. Etch rate of silicon as a function of resistivity in EDP (17 ml E, 3 g P, and 8 ml W) at 100 °C. After Finne and Klein.[334] (Reproduced by permission of The Electrochemical Society, Inc.)

TABLE 7.3. Etch Rates of Different Crystallographic Planes in 25% TMAH and 34% KOH at 70 °C, in Å/s[1001,1002]

	TMAH		KOH	
Orientation	Etch rate	Ratio of X/(111)	Etch rate	Ratio of X/(111)
(100)	45.3	30.2	100	67
(110)	88.7	59.1	216	144
(210)	99.5	66.3	212	141
(211)	87.8	58.5	151	101
(221)	79.5	53	94	63
(310)	98.2	65.5	181	121
(311)	96.0	64	179	119
(320)	95.7	63.8	220	147
(111)	1.5	1.0	1.5	1.0

The etch rate in the vicinity of {111} crystal planes is extremely sensitive to small angular misalignments as shown in Fig. 7.36.[206,334,1001] Deviation by 1 °C from the (111) plane leads to an increase of etch rate by a factor of 5 in EDP and TMAH and by a factor of about 2 in KOH. Due to the sensitivity of etch rate to small deviation from the (111) planes, etch rate ratios may be much reduced for slightly misoriented (111) samples relative to those of perfectly oriented (111) material. The etch rate ratio of different planes, by measuring the etch depth of a groove bounded by (111) planes relative to the lateral etching, is very sensitive to misalignment of the mask. According to Kendall,[184,478] mask misalignment is responsible for the large variations sometimes reported in the literature on etch rate ratios under identical conditions. It is shown that due to the increased etch rate on misoriented (111) surface for a misorientation of half a degree in the alignment of the mask the etch rate ratio of {110}: {111} in 44% KOH at 85 °C changes from above 400 to 70. To explain this effect, Kendall[184] suggested that the major etching that occurs on a slightly misoriented (111) plane is due to etching of the ledges on the misoriented surface.

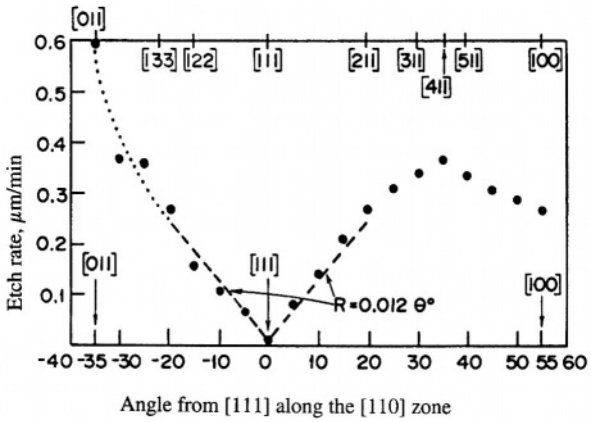

FIGURE 7.35. Etch rate of the crystal planes as a function of the deviation from the (111) plane in 40% KOH at 62 °C. (Reprinted with permission from Weirauch.[1019] © 1975, American Institute of Physics.)

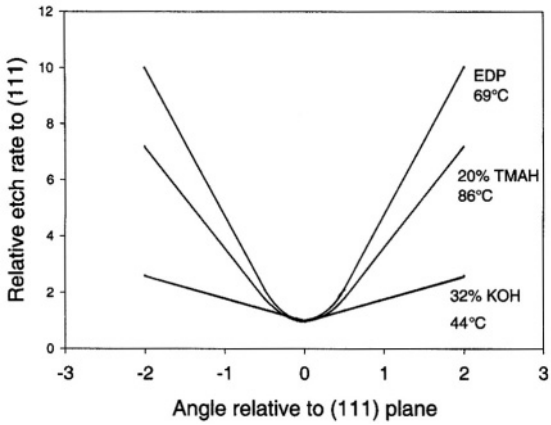

FIGURE 7.36. Etch rate as a function of the angle of deviation from the (111) plane in three different alkaline solutions. Data from Refs. 206 and 1001.

A highly defective surface, such as a saw-damaged surface, may not exhibit anisotropic etching rates as shown in Fig. 7.37 for as-cut (100) and (111) wafers.[490] The difference in the etch rates between the two orientations becomes clear after the damaged material is removed.

7.6.2. Mechanisms

Many models have been proposed for the silicon anisotropic etching in alkaline solutions. They can be classified into two large groups: those that attribute the relatively slower etch rate of (111) planes to the presence of a passive oxide film on the surface, and those that consider the etch rate difference among different orientations being governed by the reaction kinetics.

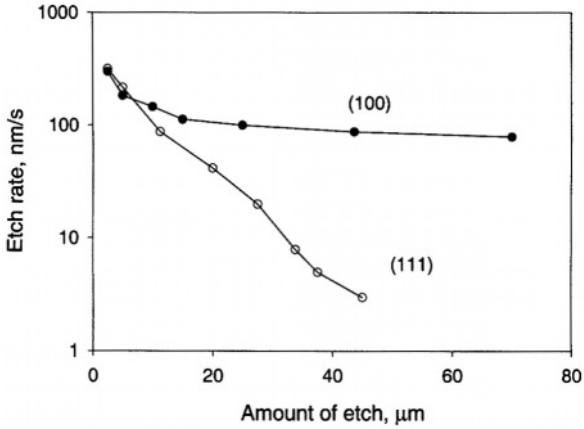

FIGURE 7.37. Average and layer etch rates versus removal, 53% KOH, 110 °C. After Dyer *et al.*[490] (Reproduced by permission of The Electrochemical Society, Inc.)

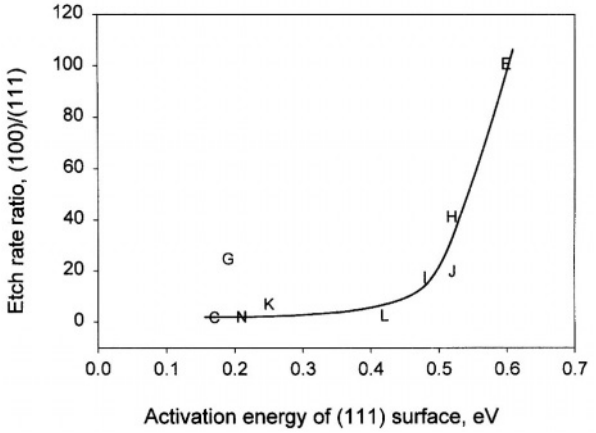

FIGURE 7.38. Etch rate ratio of (100)/(111) versus activation energy in different solutions. See Fig. 7.32 legend for definition of letters. Data from Table 7.2.

Rate-Limiting Process. Etching anisotropicity arising from differences in the atomic arrangement on the surface of different orientations necessarily indicates that the process is controlled by surface reactions that depend on lattice structure. Because anisotropic etching essentially results from surface-controlled reactions, any shift from surface-controlled processes to nonsurface processes, either within the silicon semiconductor or in the electrolyte, will result in a decrease of anisotropicity. This is in general agreement with the experimental data. Although mass transport may be rate limiting for the etching of the fast etching planes in some solutions, surface-controlled processes are the rate-limiting steps in the etching of the (111) plane in all anisotropic etchants.

The rate-controlling process can also be evaluated by the apparent activation energy as shown in Table 7.2 and Fig. 7.38. The activation energy for the various anisotropic etchants seems to indicate an increase of etch rate ratio with increasing activation energy, the highest ratio and activation energy being in KOH. In general, the apparent activation energy, as determined from the dependence of rate on the reciprocal of temperature, is generally 0.13–0.26 eV for diffusion-limited reactions whereas it is 0.44–0.87 eV for electrochemical reactions.[289] For given etching conditions the activation energy corresponds closely to etch rate, and is larger for crystal planes with slower etch rate.[206] The larger the etch rate is, the larger the diffusion effect. It is noted that high activation energies, indicating surface-controlled reaction process, are found in $HF–HNO_3$ solutions with high HF concentrations which are isotropic etchants. However, the rate-controlling surface process involved in $HF–HNO_3$ solutions is principally associated with the surface carrier concentration and not with the lattice structure. An important difference between isotropic etching and anisotropic etching, when both are controlled by surface processes, is that the former is not lattice structure sensitive whereas the latter is.

Passivation Models. The models based on surface passivation suggest that a passive layer, similar to the silicon oxide formed under an anodic potential, exists on

(111) silicon at the OCP but not on other planes. Faust and Palik[378] found that the passivation peak current of the (111) surface is only a small fraction of that on the (100) surface and postulated that a prepassive layer existing on the (111) surface at potentials cathodic of the passivation potential is responsible for the slow etch rate of the (111) surface. Smith *et al.*[291] also suggested that an oxide film may be present at the OCP which passivates the surface.

In a slightly different angle, Kendall[478] reasoned that because the {111} surface is oxidized thermally more rapidly than other low-index surfaces, the silicon surface can be covered with a silicon oxide (or a hydrated silicon oxide) during etching in aqueous solution, much faster than other planes. The formation of the oxide film passivates the {111} plane and blocks the dissolution reactions. This model implies that the etch rate of a {111} surface should be similar to that of silicon oxide in KOH solution. Alternatively, Kendall *et al.*[984,1008] proposed that the (111) surface is blocked by inactive hydration complexes of K^+ and OH^-. According to this hypothesis, in concentrated KOH solutions the (111) surface is almost completely passivated by $OH:3H_2O$ hydration complexes attaching to the individual surface atoms. The fact that the relative etch rates of the different planes vary with the type of solution is attributed to the orientation-dependent adsorption of solvation complexes on the surface.

The passivation models are not in agreement with a number of experimental observations. First, it has been found that the (111) surface in KOH at the OCP is free of oxide but terminated by hydrogen and formation of an oxide film occurs only at more anodic potentials.[227,234] Also, the passivation potential for the (100) surface in KOH solutions is more negative than that of the (111) surface indicating that it is easier to passivate the (100) surface than the (111) surface.[192,697] Furthermore, the etching of silicon at the OCP in alkaline solution is mainly a chemical reaction; etch rate changes very little with potential in the vicinity of the OCP.[22,109,697] The difference in passivation currents between (100) and (111) surfaces may be due not to a preexisting suboxide layer on the (111) surface but rather to the reaction kinetics. The effect of passivation at an anodic potential, which reflects only the electrochemical portion of the reactions, may not be related to the etching reactions occurring at the OCP. Because the passivation potential is several hundred millivolts from the OCP, the contribution of the electrochemical reaction in the electrode behavior at the passivation potential must be very different from that at the OCP.

The etch rate of the (111) surface, although much smaller than those of the (100) and (110) planes, shows definite values, in the range of 2–10 Å/s in KOH solutions. It is still much larger than the dissolution current density on a passivated surface in KOH (a dissolution rate of 2–10 Å/s is equivalent to a current density of several milliamperes per square centimeter). In alkaline solutions, the dissolution rate of silicon oxide is less than 0.01 Å/s (see Chapter 4), which is several orders of magnitude smaller than the etch rates of a (111) surface. Thus, it is unlikely that the silicon surface of any orientation is covered by SiO_2 during etching.

Surface Reaction Kinetics-Based Models. The basic consideration in reaction kinetics models is that the reaction rate is determined by the lattice structure on the surface. The difference in the lattice structures of various crystal planes gives rise to differences in surface bond density, electron density, surface free energy, and so on, which then determine the dissolution rate of the surface silicon atoms. All etching

FIGURE 7.39. Schematic illustration of the bonding condition of (100) and (111) Si surface.

mechanisms involve an attack on a subsurface Si–Si bond. The rate of this reaction is determined by the bonding condition of the surface silicon atoms.[237,697] The {111} plane has only one Si–OH surface bond whereas the {100} surface has two. The surface lattice configuration for (111) and (100) surfaces can be simplistically represented by the scheme in Fig. 7.39.[109,237] The atoms on the (100) surface have weaker back bonds to the underneath silicon atoms compared with those on the (111) surface due to the large electronegativity of OH^-. As a result, the silicon atoms on the (100) surface are etched at a faster rate than those on the (111) surface. This model appears to offer a reasonable explanation for the anisotropic etching in alkaline solutions although it is unable to explain why such effect does not occur in HF solutions.

The difference in etch rate between (111) and (100) surfaces was related to the bond densities on the two surfaces in the early surface kinetics models.[109] According to Hesketh *et al.*,[235] the etch rate difference between (100) and (111) planes is due to the difference in the surface free energy of the crystal planes which is proportional to the number of bonds on the surface. The (111) plane, which has the lowest surface free energy measured in vacuum, has the lowest bond density and thus has the lowest etch rate. They postulated that the etch rate of crystal planes is a function of the total number of bonds at the surface, that is, the sum of the in-plane, lateral bonds between atoms in the plane of the surface, and surface bonds, dangling bonds. It was recognized however, that this effect alone will not cause etch rate differences of more than a factor of two.[109]

Jakob and Chabal[895] reasoned that the silicon atoms, such as those at the steps and kink sites, that are most physically accessible are preferentially attacked. The reactants and the dissolved complex have certain physical dimension and orientation so that certain pathways may be forbidden due to steric constraints. While this argument is intuitively sound, its verification requires information on the solvation structure of the involved species and their interaction with the surface atomic structures.

Seidel *et al.*[206] proposed that the rate of silicon atom dissolution depends on the density of energetically favorable surface states based on the assumption that the etching of silicon in alkaline solutions is of electrochemical nature. They attributed the anisotropic etching to the different energy levels of surface states on (111) and (100) surfaces arising from binding surface atoms to OH^-. According to Seidel *et al.*, the difference in the activation energy of various crystal planes corresponds to the difference in the energy states of the back bonds of differently oriented surfaces. A difference of 0.12eV between the activation energies of two different planes was considered to be sufficient to cause an etch rate ratio of 100:1 for (100) and (111) planes.

In a similar approach, Campbell *et al.*[697] postulated that because the work functions of (111) and (100) planes differ by about0.25eV, the flatband potentials may differ by a similar extent. This difference in the flatband potential is then responsible for the different etching rates of the two surfaces. They recognized, however, that the electrochemical dissolution contributes only a very small fraction of the total amount of etching and suggested that the etching of silicon in alkaline solutions is not solely due to the supply of carriers. Some chemical reactions must also play an important role and the origin of anisotropic etching is related to the differences in the rates of the chemical reactions as well as in the surface potentials of the different silicon surfaces.

Allongue *et al.*[22,234] found with STM imaging, the silicon surface during etching in NaOH consists of hydrogen-terminated (111) terraces and dissolution principally occurs at the terrace edges. The dissolution rate of the terrace surface is negligible compared with that at the terrace edge. Based on this observation and the knowledge that the etching at the OCP is mainly of a chemical nature, they proposed that the anisotropic etching is due to the chemical substitution of Si–H bonds by Si–OH bonds preferentially at the kink-site atoms at the edges of terraces.

A similar atomic step-dependent etching mechanism has also been proposed by Elwenspoek[17] who postulated that anisotropy of etch rate is related to anisotropy of step-free energy which is the free energy required to generate steps on a flat surface. The kinetics of crystal dissolution in solutions is governed by the kinetics of step formation and removal. If the crystal surface is flat, the rate-determining step in the dissolution process is the step generation and not the removal of atoms from the steps. Thus, the etch mechanism of a smooth face is characterized by a nucleation barrier associated with the step-free energy. The difference between the etch rates of the major crystal planes (111), (110), and (100) is due to the difference in step-free energy, which is the largest for the (111) surface. For a rough face with many steps, e.g., a misoriented crystal plane, there is no nucleation barrier as the step-free energy is near zero. Atoms may be removed from the surface without changing the number of steps.

Mechanism of Anisotropic Etching. The rich details as to anisotropic etch rates, nature of reactions, and surface topography indicate that a complex mechanism is involved in silicon etching in alkaline solutions. A coherent mechanistic model has to address three basic aspects: (1) the physical cause of the difference in the removal rates of atoms from the surface of different crystal orientations, (2) the kinetic processes that actualize such physical cause, and (3) the surface condition that determines the global removal rate of the surface atoms.

The physical cause in the first aspect is, most convincingly, associated with the back-bond strength theory. That is, atoms on the (111) surface have three bonds connected to the substrate lattice while those on the (100) surface have only two as shown in Fig. 7.39. Bonding of the surface silicon atoms to solution species such as OH^- reduces the strength of the back bonds. The number of back bonds and the strength of surface bonds to the adsorbed species are then responsible for the different reactivity of different crystal surfaces. This can be regarded as the fundamental physical cause of anisotropic etching.

Regarding the second aspect, generally, as shown in Fig. 7.40, three species may be involved in the etching reaction: species in the form of charge carrier, i.e., electrons

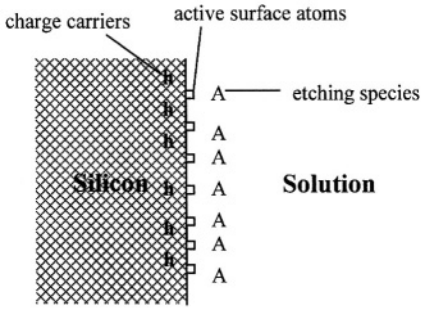

FIGURE 7.40. Schematic illustration of the elemental species involved in the dissolution reaction of silicon. h, carriers inside the semiconductor; □, active silicon atoms on surface; A, etching species in the solution.

and holes, at the semiconductor surface; chemical species such as OH^-, NO_3^-, and H_2O near the surface in the solution; and active surface silicon atoms which are favorable for reaction and removal. Unlike the other two species, charge carriers may or may not be involved depending on whether the reaction is of electrochemical nature. The concentrations of each of these species are determined by different processes such as diffusion, migration, adsorption, and solvation. In particular, the concentration of surface active silicon atoms depends on crystal orientation, which is the third aspect to be discussed below.

The anisotropic etching in alkaline solutions occurs on a bare surface of silicon free of oxide. Formation of an oxide film will mask the crystallographic differences among the surfaces of different orientations and thus result in isotropic etching. Also, experimental results indicate that although isotropic etching may occur under either diffusion control or activation control, anisotropic etching can only occur by processes that are surface controlled at least for the slow etching surfaces. Anisotropic etching does not occur when the etch rates of all of the surfaces, including those with the slowest etching rates, are controlled by supply of the solution species. Whether charge carriers are involved in etching reactions is also important. Charge carriers are involved in the isotropic etching in HF solutions but not in the anisotropic etching in KOH solutions.

The third aspect in the etching mechanism concerns the nature and concentration of the active surface silicon atoms. Because the surface atom stability depends on the number of back bonds, it can be proposed that the probability of atom removal from a perfect (111) surface lattice is very small and etching on the (111) surface proceeds only at lattice inhomogeneities such as steps, kinks, and vacancies. Thus, a perfect (111) surface will have an extremely low etch rate and the etch rate of real (111) surfaces is determined by the etch rate at the steps (including other surface lattice defects) and the density of steps.

This is in agreement with experimental findings. The etch rate of the (111) surface is extremely sensitive to a minute misorientation of the specimen (Fig. 7.36); a deviation of less than 1° can cause a several-fold increase in etch rate.[206,478] A consequence of misalignment from the (111) surface is the appearance of terraces and steps. According to STM imaging on a slightly misoriented (111) surface (0.7°), the higher etch rate is principally due to the preferential dissolution at the terrace edges in alkaline solutions.[22,237,967]

It can now be summarized regarding surface condition that (1) the etch rate of perfect (111) surfaces is negligibly small; (2) the etching of (111) surfaces is due to the etching along the edges of (111) steps; (3) the amount of (111) steps depends on the degree of misorientation from the perfect (111) plane; (4) all crystallographic planes can be considered to be composed of (111) terraces and steps at a microscopic level. Thus, the etch rate of a surface with an angle from the (111) surface can then be correlated with that at (111) steps as shown in Fig. 7.41. The vertical etch rate, V_v, which is the nominal planar etch rate measured in experiments, is

$$V_v = V_s a/b \tag{7.18}$$

where a is the step height, b the terrace width, and V_s the step etch rate. For a small angle θ, it becomes

$$V_v \approx V_s\theta \tag{7.19}$$

Thus, the etch rate of a surface is proportional to the angle of deviation from the (111) surface, which agrees with experimental observation (Fig. 7.36). For a given surface with a dimension of l, the above equation can also be expressed as

$$V_v = V_s an/l \tag{7.20}$$

where n is the number of steps over the length l. Thus, the larger is the misaligment from the (111) surface, the more the terraces and steps and thus the larger the etch rate. This means that the surfaces with large angles to the (111) surface have higher etch rates relative to the (111) surface. Essentially, this implies that etch does not proceed perpendicular to any surface at the atomic scale but only at (111) steps in a direction parallel to the (111) terrace.

In the case of a perfectly oriented (111) surface, such as the sidewalls of an etched cavity on a (100) wafer, there may still be a definite etch rate due to the fact that steps may be generated from surface defects such as vacancies and dislocations. The etch rate of the perfectly oriented (111) surface can be viewed as being limited by the rate of step generation, i.e., a nucleation process.

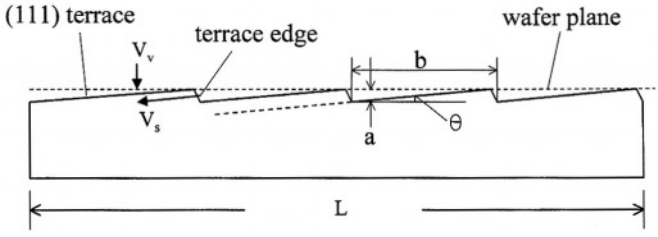

FIGURE 7.41. Relationship between vertical etch rate, V_v, step etch rate, V_s, and the angle from the (111) plane, θ.

As shown in Fig. 7.40, in general, the dissolution of a silicon surface involves three essential species: A, etching species such as OH^- in the electrolyte; □, active silicon atoms on the surface; and h, charge carriers from the semiconductor. The etch rate of the surface can then be expressed as

$$V = k[\mathrm{A}]^a[\square]^b[\mathrm{h}]^c \tag{7.21}$$

where *k,* a, b, c, are constants. In KOH, the dissolution is of chemical nature, meaning the etching is independent of [h]. Equation (7.21) is reduced to

$$V = k[\mathrm{A}]^a[\square]^b \tag{7.22}$$

On the other hand, in HF solutions the dissolution reaction strongly depends on carrier concentration and the etch rate is described by Eq. (7.21). The reason that the planar etching rate in HF is isotropic can be attributed to the fact that the etched surface in HF is rough at an atomic scale. Therefore, the density of active silicon atoms on such a rough surface is similar for different orientations. In the electropolishing region, where the dissolution proceeds through oxide formation and dissolution, the etching is isotropic due to the fact that amorphous anodic oxide is identical on surfaces of different orientations. The etching in this region is intrinsically isotropic.

Thus, the mechanistic model described above is consistent with the characteristics of the anisotropic etching of silicon in alkaline solutions as well as the isotropic planar etching in HF solutions. It is also a useful simple model for explanation of the etched features and surface roughness as will described in the following sections.

7.6.3. Basic Features of Anisotropically Etched Surfaces

Anisotropic dissolution of crystal surface results in the formation of surface contour whose geometric features depend on the crystal orientation.[672] During steady-state etching the etched surface profile exhibits a characteristic shape—either convex or concave.[289] A convex surface will be bounded by fast etching planes whereas a concave surface will be bounded by slow etching planes. As shown in Fig. 7.42(a), two planes intersecting in a concave configuration constitute a stable configuration if there is no other plane with lower etching rate lying between them. In such a case, the etch rate as a function of orientation must exhibit a maximum at the intersection of these planes. On the other hand, the intersection of two planes in a convex configuration is stable if there is no other plane with higher etching rate lying between them as shown in Fig. 7.42(b).

Etching of a sphere, which is a convex surface, will result in a polyhedron bounded by faces that exhibit high etch rates, and vertices corresponding to minima in etch rates.[289] Because the fast etching planes vary with solution composition, the faces and vertices of etched polyhedron also vary. For example, in KOH solutions the polyhedron has six 4-sided <100> vertices and eight 6-sided <111> ones, defining 24 {320} fast etching planes.[253] In CsOH solution the polyhedron has eight 3-sided <111> vertices and six 4-sided <100> giving 12 {110} fast etching planes. A sphere etched in

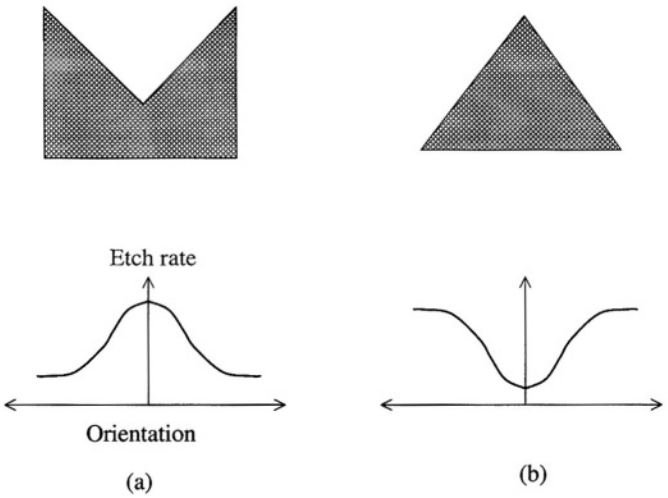

FIGURE 7.42. Stable configurations of intersecting crystal planes during etching. (a) Concave configuration; (b) convex configuration. After Gatos and Lavine.[289]

hydrazine–water mixture gives 8 curved faces with the center of the faces as (100) planes and the corners point in the <111> directions.[542] In RbOH solution the polyhedron has 14 vertices and 24 curved faces.[249]

Using masks of different shapes and orientations and controlling the planes to disappear and develop during etching, various etched features such as cavity or pyramid can be obtained from anisotropic etching.[513] Cavities and mesas etched on silicon in alkaline etchants are bounded by sidewalls which represent the slowest etching (111) planes of the crystal. The exact geometry of cavities etched through a mask opening is a function of the orientation of the wafer, the geometry of the opening, its alignment relative to the wafer's crystal axes, and the duration of etching.[531] Figure 7.43 illustrates the shape of three cavities anisotropically etched on (100) surfaces through openings of different geometry defined by the masks. After sufficient etching time, the intersection of the cavity to the surface is a rectangle bounded by four (111) planes which enclose the opening defined by the mask.

The final rectangular cavity bounded by four (111) planes independent of the initial opening shape can be explained with the (111) step etching model illustrated in Fig. 7.41. All of the (111) steps that intercept the etching (100) surface and are exposed within the opening defined by the mask are etched in a direction parallel to the (111) planes. The etching along these planes will continue until perfect (111) planes, which define the walls of the etched cavity, are reached and all of the exposed (111) steps vanish.

The etched cavities on (100) wafer bounded by the convergent {111} planes have an angle of 54.74° with respect to the surface plane. The dimensions of the resulting square pyramidal cavity, as shown in Fig. 7.44, are given by

$$W_o = W_{Si} - \sqrt{2}t_{Si} \tag{7.23}$$

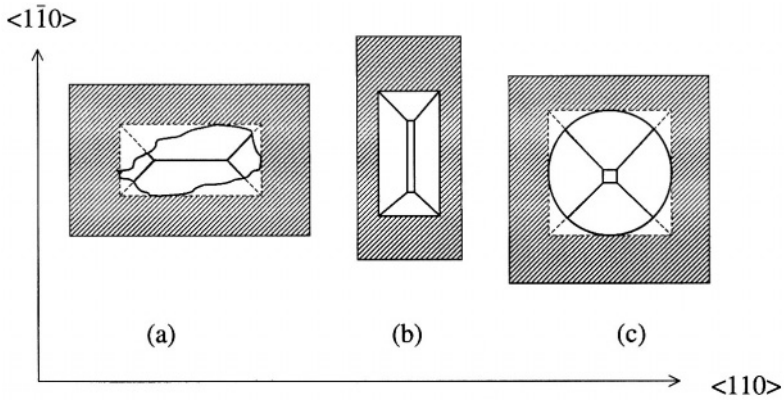

FIGURE 7.43. Anisotropically etched holes through small openings of different geometry in a surface film on a (100)-oriented silicon wafer. Four convergent self-limiting {111} etch planes define the sidewalls of each cavity. The geometry of the opening is (a) arbitrary, (b) circular, and (c) rectangular. The four sets of {111} planes in a (100) crystal are equivalent and intersect each other at the surface along the [100] directions. After Bassous.[531] (© 1978 IEEE.)

where W_o is the side of the square apex or orifice, W_{Si} the side of the etched square cavity in the wafer surface, and t_{Si} the etched depth or wafer thickness. The undercutting due to the etching of the (111) planes $U = R_{(111)}t/\sin\theta$ represents the difference between the mask opening and the intersect of the etched cavity wall with the mask. Similar to fabrication of a cavity, a convex feature like pyramids can be fabricated by etching a masked (100) silicon surface as shown in Fig. 7.45.[503,524,529]

For a (110) wafer the geometries of the etched holes are different because the four sets of {111} planes which form the sidewalls of the cavities are not equivalent. Vertical grooves with a high aspect ratio can be obtained by etching a masked (110) wafer because two sets of {111} planes are vertical to the (110) surface.[478]

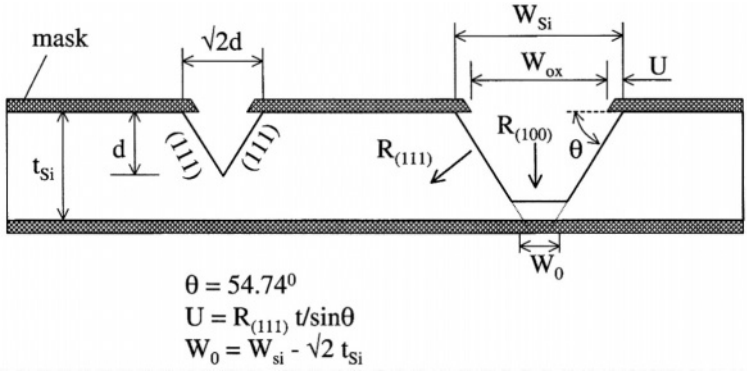

FIGURE 7.44. Cross section through anisotropically etched pattern in Si(100). The orifice dimension $W_o = W_{Si} - \sqrt{2}t_{Si}$, and the underetching U are a function of the etch rate $R_{(111)}$ of the {111} planes and etching time t for an accurately aligned pattern and a defect-free Si–SiO_2 interface. After Bassous.[531] (© 1978 IEEE.)

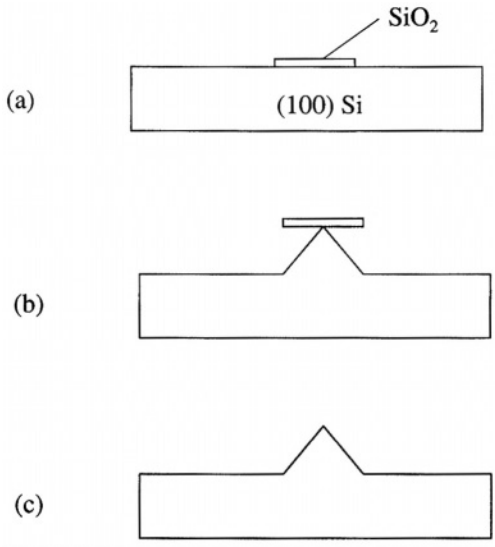

FIGURE 7.45. Processing steps to form a silicon pyramid. (a) One SiO_2 island after HF etching; (b) one pyramid after anisotropic etching of the silicon; (c) after dissolution of SiO_2. After Busta *et al.*[530] (© 1989 IEEE.)

For a convex square or rectangular structure, etch undercutting occurs at corners which can be a problem in etching of deep structures.[54,245] The amount of corner undercutting is proportional to the depth of the etching feature as shown in Fig. 7.46.[54] Such clear proportionality is due to the definite etch rate of the particular fast etch planes in the etchant. Because the fast etchant planes are etchant-specific, surfaces that define the etched corner may be different depending on the etchant. The planes are found to be {331} in KOH–propanol–H_2O etchant.[54,981] They are {411} planes in pure KOH solu-

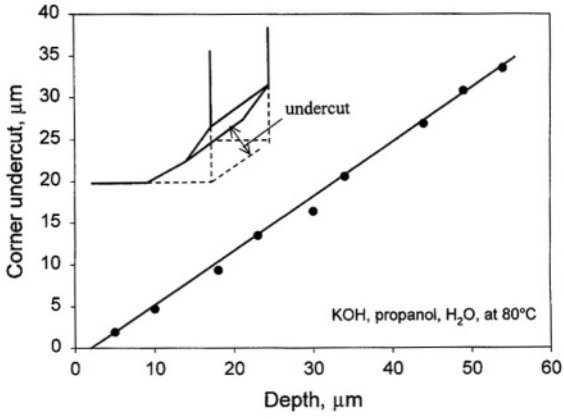

FIGURE 7.46. Amount of undercut as a function of etching depth in KOH + propanol + H_2O at 80 °C. After Bean.[54] (© 1978 IEEE.)

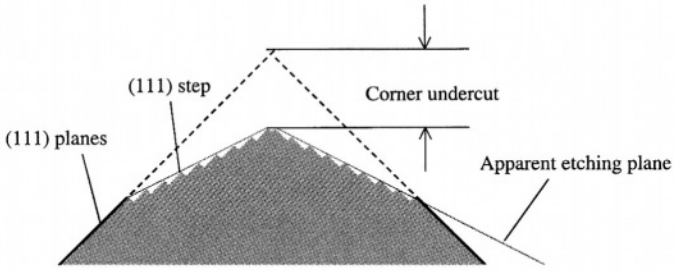

FIGURE 7.47. Schematic illustration of corner undercut based on the (111) step etching model.

tions[592,989] and can vary with KOH concentration.[254] In KOH–propanol–water solutions the etched corner is bounded by {331} planes.[54] In hydrazine–water solutions, {211} planes are found to define the etched corner.[323,542] The problem of corner undercutting can be circumvented using compensation masks.[592,707,989,1003]

Etching of a corner defined by (111) planes can also be explained by the (111) step etching model illustrated in Fig. 7.41. The etching of perfectly oriented (111) planes is determined by the generation of steps. The corner, being the terminating line of the two (111) planes, can serve as the site to generate (111) steps. Once a (111) step is generated it will be etched at a rate determined by the etching conditions. The apparent orientations of the two etched surfaces are determined by the rates of step generation and step etching as illustrated in Fig. 7.47. For example, a fast step etch and a slow step generation will result in a surface with a small angle to the (111) plane.

7.7. SURFACE ROUGHNESS

Surface roughness, which appears as a series of peaks and valleys on a microscopic scale, is a measure of the degree of unevenness of a solid surface. At an atomic scale, it describes the uneven termination of the lattice at the surface relative to a perfectly flat reference plane. Roughness is commonly described on two levels: microroughness and macroroughness. Microroughness is used to describe the surface unevenness due to adatoms, vacancies, kinks, and steps associated with the few layers of atoms on the surface, and macroroughness describes the surface topological variations beyond the first few atomic layers. Macroroughness usually exceeds the microscopic roughness by several orders of magnitude.[1000] Figure 7.48 illustrates the two levels of roughness. Table 7.4 shows that surface roughness, for silicon surface treated in different solutions, may vary by many orders of magnitude.

The roughness of etched silicon surface can be measured by a number of different methods: profilometer,[458,557,1002] reflection electron microscopy,[631,1046] optical microscopy,[302,303] interference microscopy,[302,303] STM,[488,494] AFM,[968,1000] SEM.[127,490] Two methods are commonly used for quantifying surface roughness: area averaged surface roughness which is defined as the root mean square (rms) of the height distribution on a defined area of the surface, and valley-to-peak roughness which measures the largest height difference between valleys and peaks on the surface of a given area.[458] Table 7.4

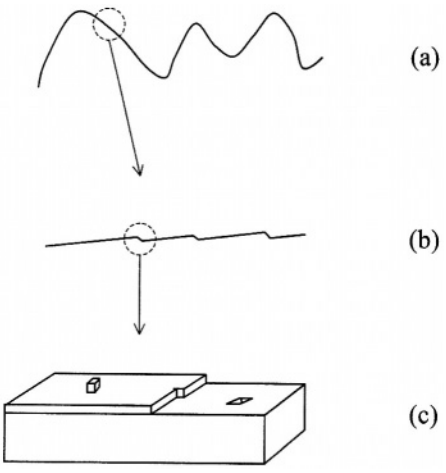

FIGURE 7.48. Schematic illustration of macroscale roughness (a), microscale roughness (b), and atomic scale roughness (c).

shows the roughness measured on the silicon surfaces cleaned or etched in various solutions.

The root mean square roughness is generally much smaller than that of the valley-to-peak roughness, as one is a measure of the average and the other is the maximum. For example, the surface roughness is 0.2nm by the area average method but is 1–2 nm by the valley-to-peak method for the same sample.[631] The size of the sampling area is also important in roughness measurement. For example, for a KOH etched silicon surface the valley-to-peak roughness measured over a distance of 1000 μm is 0.5 μm whereas it is only 25 nm over a distance of 5 μm.[458] Thus, a surface that is macroscopically (over a large area) rough may be miscroscopically (over a small area) smooth.

Surface roughness is an important factor in the performance and reliability of devices having microscopic dimensions.[488] It can essentially affect all aspects of silicon technology.[382,458] In order to guarantee the performance of electronic devices the microstructures fabricated from silicon are required to be smooth, with roughness much smaller than the dimensions of the structure components.[557] For example, in order to obtain high-quality extremely thin oxide film on the order of 10nm thick or less, it is essential to realize atomic-order surface roughness.[99,488] As the device dimension gets smaller, the device will be composed of thinner oxides and shallower junctions and the effect of surface roughness will become critical.

As an important parameter for surface quality, roughness is discussed in almost every article on cleaning and etching. However, in most cases it is treated as a quality control issue. As a result, the data on surface roughness reported in the literature for silicon surfaces are obtained under diverse conditions and are generally not comparable due to the fact that data are often reported without clear definition of the methods of determination and the area of sampling.

7.7.1 Microroughness

Microroughness, or surface unevenness, at the atomic scale is always present on a real surface whether it is smooth or rough at the macroscopic scale. For a macro-

TABLE 7.4. Roughness of Etched Silicon Surface in Various Solutions

Material	Solution	T, °C	t, min	R, nm	Ref.
	Cleaning solutions				
p,n(100)	as received			0.2[c]	488
p,n(100)	after RCA cleaning			0.4[c]	488
p(100) 10Ω	RCA cleaning			0.2[c]	631
p(100) 10Ω	RCA cleaning			1–2	631
n(100) 10Ω	0.5% HF	rt	10	0.35[c]	537
p(100) 20Ω	0.5% HF + 1 M HCl	rt	30	0.27[c]	968
p(100) 20Ω	0.5% HF	rt	30	0.29[c]	968
p(100) 20Ω	0.5% HF + 1 M NH_4F	rt	30	1.65[c]	968
p,n[b]	1% NH_4HF_2 + 30% glycerine + 70% H_2O	rt	30	2.5	303
p(100), 5Ω	97% H_2SO_4:30% H_2O_2 (1:4) + 100 ppm HF	120	2	0.035[c]	126
n(111)[b]	0.1 M NH_4F pH 4	rt	40	0.7[c]	494
	42% HNO_3 + 0.05% HF	25	5	1.1[c]	454
	0.25% HF	25	2	0.1[c]	454
	30% HNO_3 + 0.25% HF + 15% H_2O_2	35	3	0.047[c]	454
p(100), 10Ωcm	1–7 M NH_4OH + 0.94 M H_2O_2	80	10	0.13[c]	1011
	Etching solutions				
(100)	34% KOH	70	85	11	1002
(110)	34% KOH	70	85	113	1002
(111)	34% KOH	70	85	116	1002
(100)	25% TMAH	70–90	100	60	1012
(100)	13% KOH	90	>100	3000	458
(100)	30% KOH	90	>100	200	458
(111)	13% KOH	90	>100	1200	458
(111)	30% KOH	90	>100	180	458
p(100)[a]	4 M KOH, under N_2 pressure at 1000 bars	60	180	>2000	696
p(100)[a]	4 M KOH, under O_2 pressure at 100 bars	60	90	<200	696
p(100)	35% KOH, stirred	80	45	2500	672
p(110)	35% KOH, stirred	80	45	690	672
n(111)	1 M NaOH, *in situ* under STM	rt		0.4	234
(111)[a] Si sphere	50% CsOH	50	840	>2000	235
p(100), *pn* junction	2.5% TMAH	80	30	9000	516
p(100), *pn* junction	25% TMAH	80	~30	50	516
(100) wafer, top	5.9 M KOH	95	~30	77[c]	124
(100) wafer, bottom	5.9 M KOH	95	~30	8.7[c]	124
	45% KOH	80–120	2	1300	490
p(111), back side	25% KOH	70	100	100[c]	1000
p(111), front side	25% KOH	70	100	20[c]	1000
p(111)	5% HF, 0.1 V_{sce} + illumination, 4 C/cm^2	rt		~200	600
	1 HF (49%) + 3 HNO_3 (70%) + 2 acetic	20–40	0.5?	5800	490
p(100), 4×10^{18}/cm^3	50% HF	rt	288,000	~2000	1007
p	0.5% HF + 0.4 ppm Cu^+	rt	5	9	407
n	0.5% HF + 0.4 ppm Cu^+	rt	5	5	407

[a]*Estimated from photograph.*
[b]Applying an anodic potential in the electropolishing region.
[c]Average surface roughness defined as root mean square of the height distribution of an area.

scopically smooth surface the microroughness is mainly determined by the wafer polishing and cleaning processes that are used to prepare the surface for further processes. As-received wafers generally have very small microroughness, typically 0.15–0.4 nm (rms).[126,488,631] Any cleaning process may alter the microroughness.

Cleaning with the RCA process is found to increase the microroughness of as-received wafers from 0.2nm (rms) to about 0.4nm.[488] The SC1 cleaning step is found to be mainly responsible for the increase in microroughness after the RCA cleaning. The acid cleaning and water rinse steps have relatively much less effect. The roughness tends to increase with increasing the relative concentration of NH_4OH in the SC1 solution and is related to the etch rate of the solution.[1011] Modifications to each of the steps used in the RCA cleaning can also affect the microroughness.[126,468,488,631,895,968,1011] However, the effects of surface cleaning factors on microroughness reported in different studies are not consistent, probably due to the minute differences in the cleaning conditions and measurement procedure.

The microroughness of the silicon surface in various cleaning solutions generally increases with time, that is, with material removal.[468,488,631,968] Thus, the small roughness observed on the surface treated in cleaning solutions is mainly due to the small amount of material etched during the cleaning process. Much larger surface roughness is observed on the etched surface, where generally a large quantity of material is removed.

Etching in HF-containing solutions is particularly important as they are involved in almost all cleaning processes for silicon surfaces. It is often the last cleaning step in surface preparation for further processing. The silicon surface that is treated with HF solution is terminated by hydrogen (see Chapter 2). The atomic level flatness is related to the concentrations of monohydride, dihydride, and trihydride.[574,635,641] On a (111) surface monohydrides tend to form on the perfect lattice while dihydrides and trihydrides tend to form at steps and defects. An atomically flat (111) surface is dominated by monohydrides and straight step is dominated by dihydrides.

It has been reported that silicon surfaces, both (111) and (100) orientations, after being treated in HF solutions are rough at an atomic scale and have surface features such as steps, kinks, and defects.[641,662,895] The microroughness of silicon surfaces treated in HF solutions varies with pH. Results from slightly misoriented (111) surface show that at pH < 3 the (111) terraces are rough. At pH 6.6 the surface is characterized by flat (111) terraces and straight steps, indicating that the atomic-scale defects on the terraces and the corner and kink atoms on the steps are preferentially removed. At pH > 7.8 the surface becomes rougher due to the formation of multiple steps. The formation of multiple steps with increasing pH is attributed to the faster etching rate which causes larger fluctuations of terrace length. Such variation of surface atomic-scale features with pH shows the importance of solution composition in determining the surface microroughness.[126,488,631] pH may have different effects in a different solution composition. For example, in a $HF–H_2SO_4$ solution for cleaning oxide, the smoothest surface is obtained at pH 0.5.[657] In NH_4F solutions the slightly misoriented (111) surface lacks well-defined terraces at pH 4 but has well-defined terraces at pH 8.[904] In another study it is found that the Si(111) surface treated in BHF is atomically flat and is less flat in HF.[641] Also, water rinse significantly flattens the HF-treated (111) surface but is less effective for the (100) surface.

7.7.2. *Macroroughness*

Macroroughness is a measure of the surface topographic variations at a scale much larger than the atomic scale. The macroroughness of a silicon surface treated in a solution can be determined by numerous factors associated with the initial surface condition (cleanness and roughness), the crystal orientation, solution composition, treatment procedure, and time.

In HF solutions, in which silicon etches only very slowly, a silicon surface tends to become rough due to the formation of etch pits over a period of days to months.[1007] These pits, formed by processes similar to formation of porous silicon, tend to vary in size with doping concentration. Similarly, roughness tends to develop in $HF–NH_4F$ BHF solutions due to surface pitting.[468] In $HF–HNO_3$ solutions, in which the etch rate is high, the roughness of etched surfaces depends on the composition of the solution. For a given HF concentration, there is a concentration range of HNO_3 within which a smooth surface is obtained.[204,331] In $HF–CrO_3$ solutions the surface roughness is found to decrease with decreasing HF/CrO_3 ratio.[195,196]

The roughness of the etched silicon surface in KOH solutions has been investigated by Palik *et al.*[557] The roughness varies with KOH concentration with a peak at about 5 M as shown in Fig. 7.49 and it is lower in stirred solutions than in nonstirred solutions at room temperature. In nonstirred solutions the roughness is parallel to the etch rate which also shows a peak at about 5–6 M, but in the stirred solutions it remains at a relatively small value over the whole concentration range. Kwa *et al.*[458] found that the roughness of (100) etched surface decreases with KOH concentration at different temperatures as shown in Fig. 7.50. Results similar to those in Fig. 7.50 are also reported by Sato *et al.*[1002] Roughness in KOH tends to decrease with increasing temperature. Cleaning with different water and HF rinses has little effect on the roughness of the etched surfaces in KOH solution, implying that native oxide on the surface is not important in determining the roughness.[124,557,1000]

In TMAH solutions a smooth etched surface is obtained at concentrations above 22% TMAH.[1005] Addition of l–4g/liter pyrazine to 25% TMAH solution increases slightly the etch rate and improves the surface smoothness.[594] Dissolved silicon in the etchant results in higher roughness as shown in Fig. 7.51.[518] In the ternary etching system of hydrazine, IPA, and water,[542] the etched surfaces vary from being highly faceted to very flat. The faceted surfaces are made up of square pyramidal hillocks whereas flat surfaces are marked by a cellular structure. In ethanolamine-based etchants, the roughness of etched surface appears to be associated with the formation of precipitates.[520]

Surface roughness is generally a strong function of potential.[2,18,33,541,957,1004] For example, it has been found that the etched $p(100)$ surface in KOH at potentials negative of the OCP is rough, covered with pyramidal hillocks, whereas that etched at anodic of the OCP is mirrorlike.[541] In HF solutions the silicon surfaces etched at anodic potentials below the current peak are extremely rough due to the formation of porous silicon, whereas those etched at potentials above the current peak are mirrorlike (see Chapter 8). It has been reported that the surface roughness of (111) silicon in 0.1 NH_4F at pH 4 decreases from 4 nm to 0.7 nm after being treated in the current oscillation region.[494]

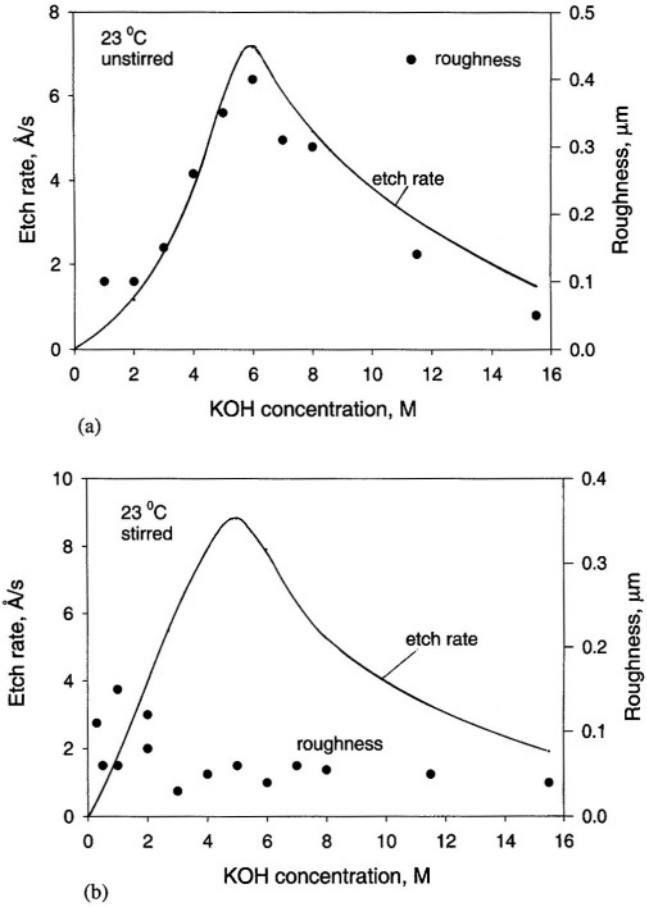

FIGURE 7.49. (a) Etch rate and roughness versus molarity for 23 °C, unstirred, HF + H_2O rinse (several minutes). (b) Etch rate and roughness versus molarity for 23 °C, stirred, HF rinse + H_2O wash (several minutes). (Reprinted with permission from Palik *et al.*[557] © 1991, American Institute of Physics.)

Roughness also changes with many operating conditions. For example, addition of ppm levels of surfactants can significantly change the etch rate and surface roughness in KOH solutions[1000] and in fluoride-based solutions.[537] Ionic surfactants produce much smaller roughness than do nonionic surfactants. Roughness that developed in a BHF solution of 6% HF + 30% NH_4F can be inhibited by addition of surfactants.[468] Increasing the flow rate of the etchant is found to decrease roughness.[1004] A wafer growth process which gives different levels of oxygen content has an effect on the roughness of the etched surface in KOH.[458] Silicon wafer has varied roughness from one side to the other depending on the position and orientation of the wafer in the etching tank.[124] Si(111) surface is smoothed on the atomic scale by anodic oxidation in NaOH followed by oxide stripping in 5% HF, and final stabilization in 40% NH_4F.[831]

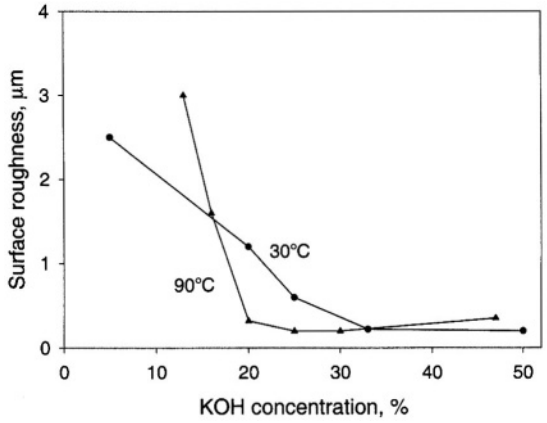

FIGURE 7.50. Membrane surface roughness as a function of the solution concentration at temperatures of 30, and 90 °C. After Kwa *et al.*[458] (Reproduced by permission of The Electrochemical Society, Inc.)

Surface roughness varies with etching time and thus the mount of material removed. Roughness increases with etching time for initially micro smooth surfaces but may decrease for initially rough surfaces.[434,458,557,1002] Figures 7.52 and 7.53 show that roughness increases with time on the polished front side (initial roughness 2.5 nm) but decreases with time on the back side (initial roughness 300nm).[1000] Figure 7.54 shows the roughness of the three principal surfaces as a function of etching time.[1002] The roughness of the (110) plane increases with time whereas that of the (111) and (100) planes remains relatively constant. Similar results are found for the (100) surface.[557] Etching of the saw-damaged zone of silicon wafers in $HF–HNO_3$ solutions results in a reduction of roughness from about $30\,\mu m$ to about $6\,\mu m$.[490] In KOH solutions as soon as the duration of etching exceeds a critical time, about 15min, characteristic pits or hillocks develop on the etching surface.[672,673]

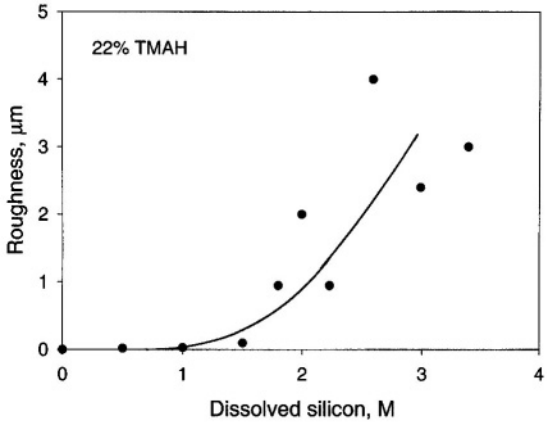

FIGURE 7.51. Dependence of etched surface roughness on amount of dissolved silicon. After Tabata.[518]

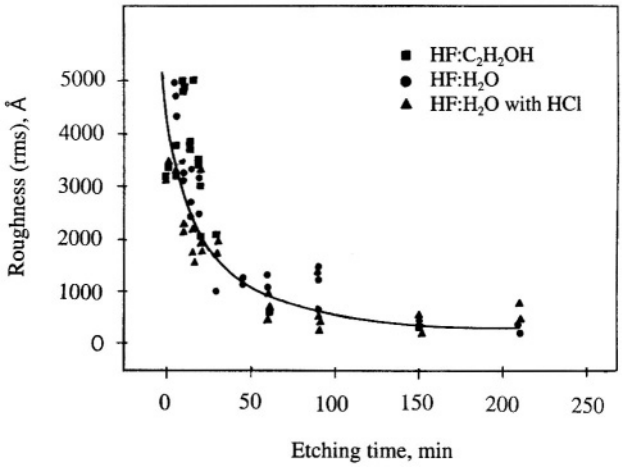

FIGURE 7.52. The evolution of the roughness (rms) on the unpolished back side of the wafer Si(111). After Divan *et al.*[1000]

For a given etching system, there is a steady-state roughness. If the initial roughness is smaller than this roughness, the roughness of the etching surface tends to increase, and if the initial roughness is larger than the steady-state roughness, it tends to decrease. Generally, as-received silicon wafers have a very small surface roughness, and in most etchants the roughness tends to increase as etching proceeds. In the etching in 25% KOH at 70°C, a steady-state roughness is reached at about 4h for the (111) surface and much longer for the (100) surface.[1000]

Crystallographic Characters and Formation of Hillocks. The surface roughness of silicon single crystals has clear crystallographic characteristics as illustrated in

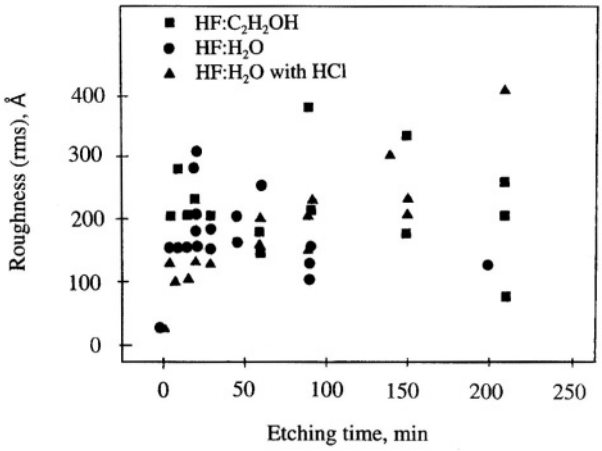

FIGURE 7.53. The evolution of the roughness (rms) on the polished front side of the wafer Si(111). After Divan *et al.*[1000]

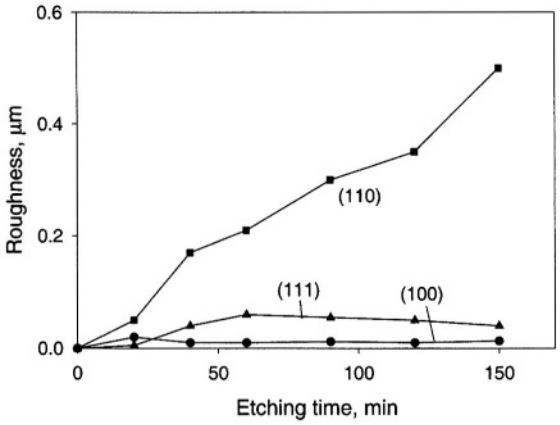

FIGURE 7.54. Roughness change as a function of etching time, 34 wt % KOH, 70 °C. After Sato *et al.*[1002]

Fig. 7.55.[1002] At a microscopic scale, roughness is associated with lattice steps, vacancies, and so only which are determined by the lattice structure of the surface. At a macroscopic level, crystallographic character may be revealed in the topographic features, for example, hillocks formed on the (100) surface. It has been found that the etched surface in 25% KOH has well-defined terraces and step features, whereas it has a nodule type of appearance in 50% KOH solution.[245] Table 7.5 provides a summary of the characteristics of the surface etched features in KOH with respect to the crystal orientation of the surfaces.

In particular, the macroroughness of the etched silicon surface in alkaline solutions is a function of surface orientation.[206,672,673,1002] Sato *et al.*[1002] found that the

TABLE 7.5. Geometrical Features of Final Etching Patterns ($t = 45$ min) as Revealed by SEM Examination[672]

Ω from (100)	Geometric features
0°	Flat pits fitted into each other
5°	Terraced pits with flat bottom
10°	Features similar to those related to $\varphi = 5°$, but in addition dissolution overlap
14°	Steady hillocks aligned along the x-axis fitted onto each other and presenting striations arranged along the [001] axis
18°	Bumpy surface composed of numerous folds aligned along the [001] axis
23°	Features close to those related to $\varphi = 18°$
26°	Features similar to those related to $\varphi = 23°$; however, the rather elongated hillocks seem to be bounded by two small facets
30°	Bumpy hillocks whose sides are composed of limiting facets. Striations along the [001] axis are still present
34°	Features similar to those related to $\varphi = 30°$ with a predominance of facets
37°	Elongated "bumps" bounded by facets. The direction of alignment corresponds to the x-axis
42°	Linearly textured surface with elongated "pits" aligned along the x-axis
45°	Linearly textured surface composed of grooves arranged along the x-axis

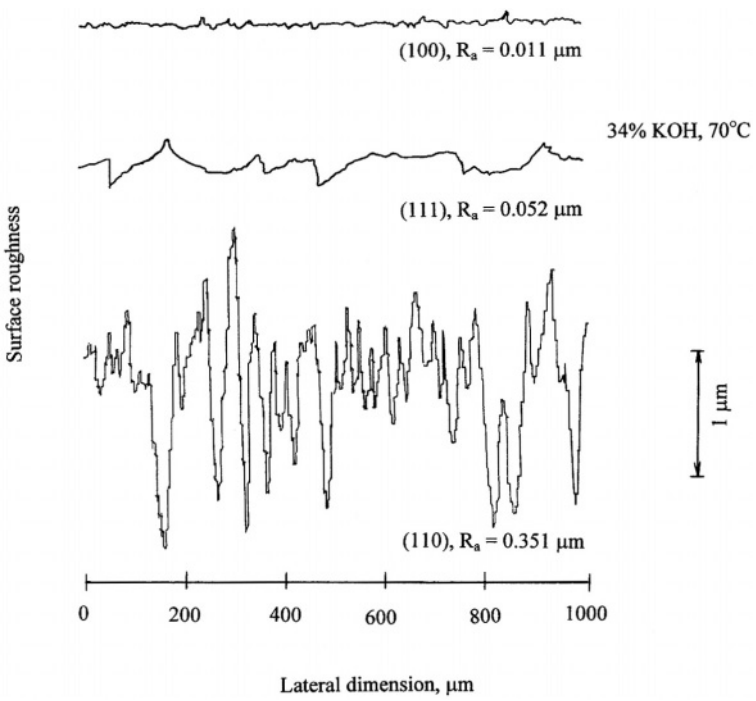

FIGURE 7.55. Surface roughness R_a of three principal Si crystal orientations after etching for 10 min in 34% KOH, 70 °C. After Sato *et al.*[1002]

smoothest surface appeared at the (100) plane whereas the (320) and (210) planes which also have higher etch rates than other planes are very rough as shown in Fig. 7.56. The relative roughness among the different planes can be quite different as reported by different investigators.

The (100) surface tends to roughen quicker than the (111) surface and the roughness tends to be permanent on the (100) surface whereas it is transient on the (111) surface.[114] Such crystal orientation-dependent roughness can also be explained by the anisotropic etching mechanism illustrated in Fig. 7.41. The preferential etching at the (111) steps of the (111) terraces results in the removal of the terraces and reduction of the (111) steps and a reduction of microroughness.

In particular, the hillocks formed on the (100) surface are crystallographic structures bounded by four (111) planes resulting from the anisotropic etching and their formation directly contributes to the roughness of the surfaces.[557] Hillocks may, under certain conditions, form in HF-based solutions,[349] but most commonly in alkaline etchants.[518,557,706] Because the (111) surface etches very slowly, the formation of hillocks leads to a decreased etch rate.[557,706]

The extent of hillock formation in alkaline solutions depends strongly on solution composition and operating conditions. Formation of hillocks in KOH solutions occurs in certain concentration ranges.[206,557] Solution stirring and higher solution temperature reduce the hillock-associated surface roughness. The density of hillocks is

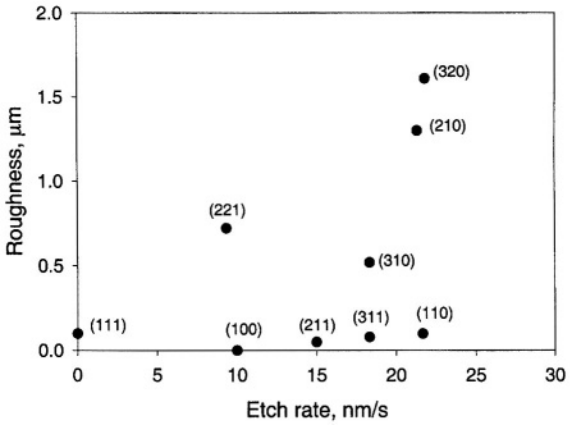

FIGURE 7.56. Relationship between the roughness and the etching rates in 34% KOH at 70 °C. After Sato *et al.*[1002]

found to decrease with addition of a reducing agent, such as ferricyanide, to the solution.[541] In NH_4OH solutions it occurs for all concentrations, temperatures, stirring conditions, and sample preparations.[706,711] It can be suppressed by the addition of H_2O_2. In TMAH solutions at concentrations lower than 25%, small hillocks start to develop and the size and number increase with decreasing concentration.[1002,1005] Addition of IPA in TMAH increases the size of hillocks but does not change hillock density. Electrode potential can also affect hillock formation. It is found that the $p(100)$ surface etched in KOH at potentials negative of the OCP is rough covered with pyramidal hillocks whereas that etched at potentials anodic of the OCP remains mirrorlike.[541] Increasing the pressure above the etchant bath is found to enhance the formation of hillocks in KOH solution.[696]

Hillocks tend to readily form on poorly cleaned surfaces and in etchants containing excessive amounts of dissolved silicon.[349,434,518,577] Hillocks may result from local masking by contaminants or deposits of reaction products. The pyramidal hillocks have been found to be associated with a microsubstance, a few nanometers in size, at the apex of the pyramidal hillocks.[349] The development of hillocks is similar to the formation of a pyramid on a masked surface as shown in Fig. 7.45. The anisotropic dissolution of the material around the masked area results in the formation of pyramids. Initially the pyramids at the surface are tiny but as etching continues new pyramids are formed while the existing ones grow. Once the surface is fully covered with hillocks, the etch rate in the (100) direction will drop as the surface is covered by planes of slower etch rate. The masking substances causing the initiation of hillocks can be surface contaminants, precipitates in silicon material, surface deposits, and formation of gas bubbles. Formation of hydrogen bubbles, which is a basic reaction in the etching of silicon at the OCP in aqueous solutions, and precipitation of silicates have been considered to be most important for hillock formation and associated surface roughness.[518,557] The four (111) planes of hillocks are flat, as the {111} planes resulting from cavity etching of both (100) and (110) wafers are smooth at the macroroughness level in all of the anisotropic etchants.[54,206,458]

Formation of hillocks can be reduced by controlling solution composition, temperature and agitation, electrode potential, surfactants, pressurizing, and so on.[557,706,1005] In general, increasing silicon solubility and reducing gas formation results in the reduction of hillock formation. It has been found that addition of an oxidizing agent such as hydrogen peroxide, which effectively inhibits the formation of hydrogen bubbles, inhibits the formation of hillocks.[706,1005] Pressurizing with oxygen is also found to reduce the formation of hillocks.[696] It was suggested that the reaction of oxygen with the hydrogen atoms on the surface occurs before the formation of bubbles. Other practices such as increasing solution temperature, solution stirring, and decreasing the concentration of dissolved silicon in the solution, are effective in reducing the possibility of formation of solid silicates on the surface and thus the formation of hillocks.

7.7.3. Origins of Roughness

Roughness developed in a cleaning or etching solution is a result of uneven dissolution across the crystal surface. Many factors in an etching process may cause the uneven distribution of the dissolution rate at both micro and macro scales. One particular example is the roughness associated with the formation of hillocks. In general, any process that causes temporary or permanent surface inhomogeneity will result in preferential dissolution of some areas relative to other areas.

The surface roughness that develops on the etched surface in KOH is attributed to the masking by hydrogen bubbles resulting from the etching reactions.[124,557] The surface area that is masked by a hydrogen bubble is not etched until the bubble grows to a certain size and leaves the surface. The roughness, depending on the amount of preferential etching of the masked and unmasked areas, increases with the size of hydrogen bubbles. Increasing convection and temperature increases the rate of reaction but decreases the hydrogen bubble dwell time, leading to the formation of more and smaller bubbles.

The precipitate of etching products on the surface is a common cause of surface roughness. Residues tend to form on the etched surface in KOH of low concentrations.[206] Varied roughness in ethanolamine-based etchants is associated with the formation of precipitates.[520] Staining may occur during etching in HNO_3–HF, EDP, hydrazine solutions, resulting in the formation of various kinds of surface features.[337,342,542] Stain is also found to form in etching HF solutions with Cr^{6+}, Fe^{3+}, Cu^{2+}, and I^0 as oxidants. Highly boron doped material is found to be more susceptible to stain formation.[337] The composition of stain has been identified to be SiH_x, SiO_y, or SiH_xO_y with $1 < x < 2$ and $1 < y < 2$.[387]

Roughness of etched surfaces can be attributed to several causes: (1) native oxide, (2) residuals left from the cleaning process, (3) defects in the crystalline structure, (4) hydrogen bubbles, (5) metal deposits (6) anisotropic etching and (7) formation of pores. They may be grouped into two categories, process-dependent and material-dependent, as shown in Fig. 7.57. The process-dependent causes are the deposition of metal or nonmetal particles (Fig. 7.57a,b) or bubbles (Fig. 7.57c) which provide masking to the deposited areas. The difference in the masking effect between a metal and a nonmetal particle is that metal can actively participate in the dissolution reaction by a galvanic action. The material-dependent causes, such as preferential dissolution at lattice defects

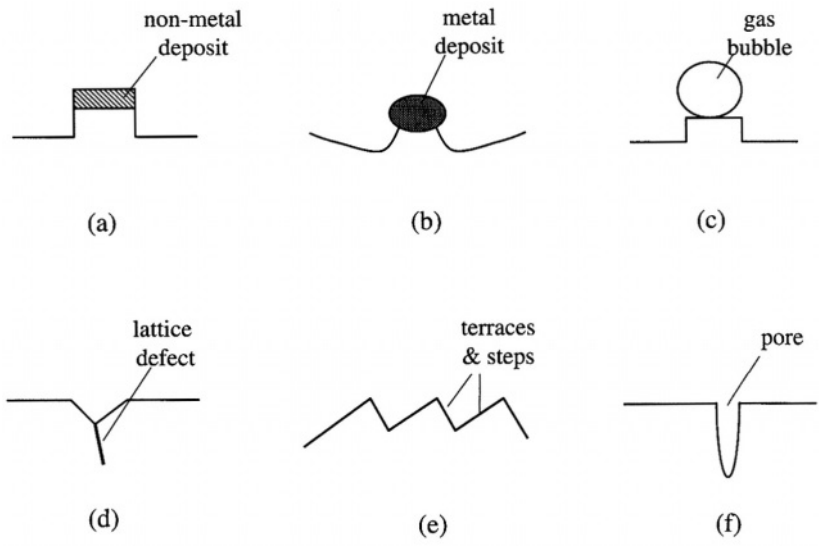

FIGURE 7.57. Schematic illustrations of the possible origins of surface roughness.

(Fig. 7.57d), anisotropic dissolution (Fig. 7.57e), and formation of pores (Fig. 7.57f), are associated with the structure and properties of the silicon crystal.

The surface of the silicon crystal, no matter how it is finished, will have a certain number of lattice defects, which tend to dissolve preferentially resulting in formation of etch pits and other features. Terraces and steps of various sizes are inevitable consequences of anisotropic dissolution of the surfaces misoriented from the (111) surface. Also, a silicon surface, whether initially smooth or not, in HF solutions, has an intrinsic tendency to roughen and form micropores governed by sensitivity of the electrochemical reactions on a semiconductor electrode to surface curvature.[8] Furthermore, the two groups of factors shown in Fig. 7.57 may affect each other. For example, the initial lattice inhomogeneities may provide the sites for deposition whereas localized deposition may enhance the development of etch features such as pits or hillocks.

7.8. APPLICATIONS

The applications of etching can be broadly classified into three categories: (1) surface preparation, (2) structural characterization, and (3) device fabrication.[289] In category 1, etching is used to prepare suitable surfaces for subsequent physical and chemical measurements or processing. Here etching is used as a tool for cleaning or polishing, for removing the damaged or defective surface layer, or for surface stabilization. In category 2, etching is used for the identification of defects such as dislocations, for microstructrural studies, and for orientation examination, or for impurity distribution. In category 3, etching is used for removing materials and for machining structures in device fabrication.

7.8.1. Cleaning

A clean surface is essential for device reliability and performance.[220] It becomes critical as the dimensions of devices become smaller and smaller as a result of ever-increasing integration and complexity. It has been estimated that over 50% of yield losses in integrated circuit fabrication are due to microcontamination.[203] Currently, tremendous efforts are devoted to contamination control and better cleaning procedures, thus resulting in a very active research field and generating a large volume of technical literature. This section is not an attempt to summarize the results of these ongoing research activities but to present cleaning as an application of etching and its importance to the electrochemical properties discussed in the rest of this book.

Today, a typical process flow for advanced ICs consists of 300 to 500 steps, 30% of which are wafer cleaning steps.[407] Many process steps during IC fabrication may introduce contamination, which must be cleaned before the next process step. For example, in processes such as steam oxidation, resist etching, and ion implantation, metallic contamination typically introduces a surface concentration of 10^{12} to $10^{13}/cm^2$.[461] The need for wafer cleaning can be separated into three areas: (1) preparation of the wafer surfaces for oxidation, diffusion, deposition, and metallization; (2) preparation for the application of photoresist; and (3) removal of photoresist after the etching process.[464,669]

Cleaning prior to thermal process steps such as gate oxidation, dopant diffusion, and epilayer deposition is especially critical in ensuring yield and reliability of the finished devices.[407,466] Trace amounts of impurities such as sodium ions, metals, and particles are especially detrimental when present on silicon surfaces during high-temperature processing (thermal oxidation, diffusion, epitaxial growth) because they spread and diffuse into the semiconductor interior. Also, metallic contaminants on submicrometer devices are detrimental. When present, heavy metals often form midband gap states which act as generation–recombination centers, increasing the leakage current. They also tend to precipitate and decorate extended defects leading to junction shorting and degradation of gate oxide integrity.[407]

Contaminants on silicon surfaces can be classified as molecular, ionic, and atomic or as hydrocarbons, metals, and particles.[242,472,884] Typical molecular contaminants are waxes, resins, oils, and organic compounds which are commonly generated in the processes after sawing or from human skin and plastic containers. They are usually attached to the surface by weak electrostatic forces. Ionic contaminants such as Na^+, Cl^-, F^-, and I^- are present after etching in HF or alkaline etchants. They may be precipitated on the surface by physical adsorption or chemical adsorption. The atomic contaminants of concern are metals such as gold, iron, copper, and nickel originating from acid etchants. The metallic impurities can only be effectively removed by wet cleaning processes.[99,488] The particles such as SiC, Si_3N_4, Al_2O_3, SiO_2, and C originate to a large extent from wet processes and cleaning baths. These particles are attracted by the electrical field generated by the wafers, which are negatively charged in water.[242] The contaminants may be physically located in different phases at the silicon/electrolyte interface depending on whether the surface is covered with an oxide film and whether the contaminants are adsorbed onto the surface before, during, or after the formation of the oxide film as illustrated in Fig. 7.58.

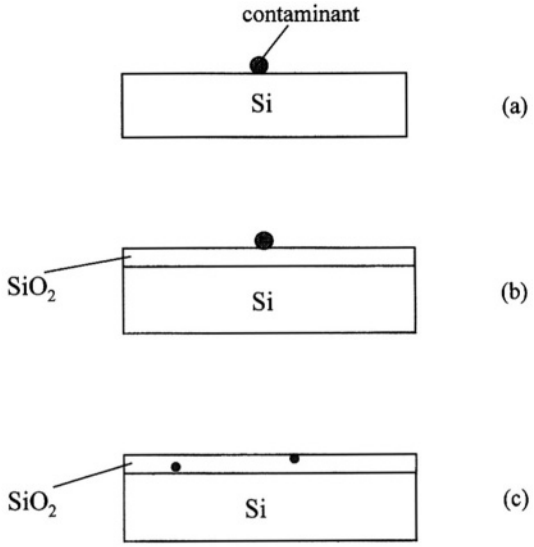

FIGURE 7.58. Schematic illustrations of the physical location of contaminant on the surface of Si (a) on bare surface, (b) on surface covered with an oxide, and (c) within the surface oxide.

A cleaned silicon wafer is characterized as (1) particle free, (2) without organic contaminants, (3) minimal metallic contamination, (4) free of native oxide, and (5) minimal surface roughness.[99,254] It has a surface concentration of contaminants such as Fe, Cu, and Ni of less than $10^{10}/cm^2$ and a microroughness of about 0.2nm.[488] As-received wafer typically has several thousand particles, a roughness of about 0.2 nm, and metal concentrations of about 5×10^{10}–$10^{12}/cm^2$ for Fe, Cu, and Zn as shown in Fig. 7.59.[131,488,493] The degree of cleanness is constantly improved as cleaning technology continues to progress. As a result, the surface metal concentration has been reduced

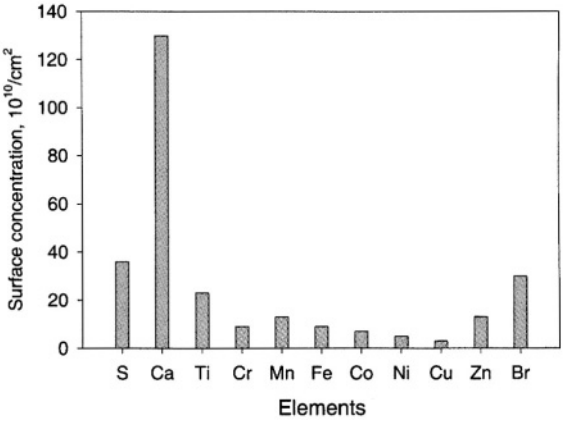

FIGURE 7.59. Upper limits of metallic contamination content of as-received wafers. After Filho *et al.*[131] (Reproduced by permission of The Electrochemical Society, Inc.)

by about one order of magnitude per decade, from more than $10^{13}/cm^2$ to less than $2 \times 10^{12}/cm^2$ in the 1970s, and to less than $10^{10}/cm^2$ in the 1990s.[488,630]

According to Ohmi,[99] the removal of metallic and organic contaminants from the Si surface to a very low level requires the use of a solution containing high redox potential. The metallic particles are ionized and dissolved in the solution while the organic impurities are decomposed to CO_2, H_2O, and so on. Two requirements must be satisfied in order to remove particles from the surface: (1) the zeta potential of the substrate surface and particles should be in the same polarity in the solution so as to cause repulsive electric force between the surface and the particles, and (2) the substrate surface or the particle surface should be slightly etched in order to lift particles off the substrate surface. Also, the formation and cleaning of the oxide film in the cleaning solution and in air have a special significance in obtaining a clean silicon surface. Ohmi pointed out that when a hydrogen-terminated silicon surface is exposed to the air in a clean room, moisture of several tens of molecular layers is adsorbed within seconds. If the ambience is composed only of moisture or oxygen, the Si surface will not be oxidized at room temperature.

RCA Cleaning. The RCA process, which was originally developed by Kern and Puotinen in 1970,[884] is still the basis of the current wet cleaning process for bare or oxide-covered silicon surfaces. Table 7.6 details a current RCA cleaning process.[220,461] The original RCA cleaning, which tends to etch 30–40 Å silicon substrate during the process,[454] is based on two hydrogen peroxide solutions: an alkaline mixture with ammonium hydroxide followed by an acidic mixture with HC1.[203] In the first treatment, a hot solution of NH_4OH (27%), H_2O_2 (30%) and H_2O, with a proportion of 1:1:5 to 1:2:7 by volume of the chemical agents, known as SC1 cleaning solution, is used.[203] SC1 solution is designed to remove organic contaminants by both solvating action of the ammonium hydroxide and the oxidizing action of the peroxide. The oxidizing action by H_2O_2 also results in the formation of surface silicon oxide which dissolves slowly in the solution. It is thus very effective in particle removal as continuous oxidation and etching of the oxide take place under the particles.[126] The metal surface contaminants

TABLE 7.6. RCA Procedure for Si Wafer Cleaning[461]

Step	Process	Duration	Step	Process	Duration
1	H_2SO_4–H_2O_2 (4:1)	5	13	NH_4OH–H_2O_2–H_2O	10
2	UPW rinse	5		(0.05:1:5), 90 °C	
3	H_2SO_4–H_2O_2 (4:1)	5	14	UPW rinse	5
4	UPW rinse	5	15	Hot UPW dip, 90 °C	10
5	H_2SO_4–H_2O_2 (4:1)	5	16	UPW rinse	10
6	UPW rinse	10	17	HF–H_2O_2–H_2O	1
7	HF–H_2O_2–H_2O (0.03:1:2)	1	18	UPW rinse	10
8	UPW rinse	10	19	HCl–H_2O_2–H_2O	10
9	H_2SO_4–H_2O_2 (4:1)	5		(1:1:6), 90 °C	
10	UPW rinse	10	20	Hot UPW dip, 90 °C	10
11	HF–H_2O_2–H_2O	1	21	UPW rinse	10
12	UPW rinse	10	22	HF–H_2O_2–H_2O	1
			23	UPW rinse	10
			24	Drying	

such as gold, silver, copper, nickel, cadmium, zinc, cobalt, and chromium are also oxidized by H_2O_2 and dissolved by the complexing effectiveness of the ammonium hydroxide; copper, for example, forms the $Cu(NH_3)_4^{2+}$ amino-complex.[203,488,630]

The second treatment step exposes the rinsed wafer to a solution known as SC2, which is a hot mixture of H_2O_2 (30%), HC1 (37%), and H_2O in the proportions of 1:1:6 to 2:1:8 by volume. This cleaning solution is designed to remove alkali ions and cations such as Al^{3+}, Fe^{3+}, and Mg^{2+} that form NH_4OH-insoluble hydroxides in the alkaline solution. It also cleans metallic contaminants that are not entirely removed in SC1 solution such as gold and prevents displacement replacing from solution by forming soluble complexes with the resulting ions.[884] A preliminary cleaning step with hot H_2SO_4–H_2O_2 mixture (2:1) can be used for grossly contaminated wafers having visible residues. A short dipping in dilute HF solution may also be used after SC1 cleaning to remove the hydrous oxide film formed in SC1 solution.[203] More recently, this cleaning solution has often been used with a concentration only one-tenth of the original solution in order to avoid surface roughness and to reduce production cost and the effect on the environment.[1013]

Strict control of the purity of water and materials used for preparation of the cleaning solutions is essential in obtaining good results, as recontamination may also occur in the cleaning solutions. Figure 7.60 shows, as an example, that the surface concentration of Fe, Ni, Cu, and Zn increases linearly with the impurity concentration in SC1 solution.[1017] The deposition process is found to follow the Langmuir adsorption/desorption theory. Cu, Ag, Au, and Mo at 100–1000 ppb in HF and BHF solutions can all cause deposition at levels higher than $10^{10}/cm^2$.[438] Deposition of metal impurities at ppm levels in HF solutions is severe for Cu, Au, and Cr and is much lower for Fe and even less for Zn.[883]

The precipitation of metals onto a silicon surface is essentially a corrosion process, in which the ionic metal species in the solution are reduced and deposited on the surface simultaneously with oxidation of the silicon atoms. The rate of metal depo-

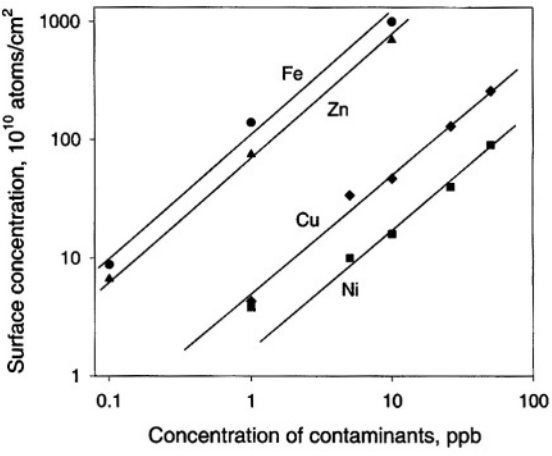

FIGURE 7.60. Effect of the impurity concentration in intentionally contaminated SC1 solution on the surface concentration. After Ryuta *et al.*[1017]

sition tends to depend on the type and doping level of silicon, because deposition involving charge exchange with the surface depends on the electronic properties of the substrate.[461] In addition to electrochemical deposition, metals may also precipitate onto the silicon surface in the form of an oxide. According to Ohmi *et al.*[220] metals such as Al, Cr, and Fe, which have a larger enthalpy of oxide formation than Si, tend to be oxidized more easily than Si and tend to be included as particles in the silicon oxide.

Cleaning of metallic impurities on a silicon surface requires the oxidation and dissolution of the metal atoms. Most metals have a standard potential that is much higher than that of silicon. To oxidize the metal atoms the electrode potential, at least in the local area of the deposits, has to be raised to the level of the reversible potential of the metal in the solution. For example, in SC1 solution the potential of silicon is $0.4\,V_{sce}$ at which the silicon surface is passivated (it is $-1.10\,V_{sce}$ without H_2O_2).[208] This means that in SC1 solution the species with reversible potential less than $0.4\,V_{sce}$ tend to be oxidized on the surface. Passivation is also responsible for the slow etch rate in SC1 solution, for only about 30–40 Å material is removed during the RCA cleaning.[454] The fact that the silicon surface is passivated serves three purposes: (1) It allows the surface to be anodically polarized which is required for oxidizing of metal impurities, (2) it prevents much etching of the substrate during the cleaning process, and (3) it helps to physically dislodge the metal atoms from the surface by forming an oxide layer between the metal atoms and the silicon surface.

The surface condition—whether a native oxide is present or not—has a significant effect on bonding of iron and copper deposited on the surface and thus the cleaning efficiency.[453] Each metal has its own characteristic chemical state.[454] Metal impurity such as Fe tends to be present on the silicon surface oxide layer in the form of oxidized Fe(III), whereas Cu tends to bond directly to Si atoms in the elemental state. The former can be cleaned by etching away the oxide whereas the latter can only be removed by a redox reaction.

Experimental results have shown that after RCA cleaning, the number of particles and zinc concentration on a silicon wafer are drastically reduced, while copper and iron concentrations remain similar to the as-received condition.[131,493,665] With SC1 solution it is not easy to reduce surface heavy metals such as Fe below $10^{11}/cm^2$.[631] Modified SC1 solutions are used to remove the Fe, Cu, and Ni to below $10^{10}/cm^2$.[488] Dilute solutions of $HF–HNO_3$ or $HF–HNO_3–H_2O_2$ are found to be more effective than RCA at removing surface metal impurities such as Ca, Ni, Zn, and Al.[454] Treatment with a mixture of HNO_3 and diluted HF, which removes about 30 nm silicon, after RCA cleaning reduces significantly Fe, Ca, and Mg surface concentration.[631] SC1 cleaning followed by a very dilute acid $1:10^4$ of $HCl:H_2O$ produces better results regarding removal of metallic impurities and particles.[465] Using ultrapure water to prepare the RCA cleaning solutions leads to better results.[131] Cleaning with ozonized water and peroxide to remove particles and metals is shown to produce a clean surface with Cu concentration below $10^8/cm^2$.[99]

7.8.2. Defect Etching

Defect etching refers to the etching process that preferentially attacks the strained bonds of defects within a crystal. It is a simple and fast method of determining the

TABLE 7.7. Characteristics and Applications of Defect Etchants

Etchant[a]	Characteristics and applications	Refs.
Sirtl	3 min, reveals defects for (111) wafer, but not satisfactory for (100) wafer	340, 387, 992
Dash	several hours, yields deep etch pits on all orientations, sensitive to oxygen impurity	3191, 020
Secco	20 min without and 5 min with ultrasonic agitation, reveals different types of defects and dislocations of different orientations, relatively poorly defined circular etch pits, requires ultrasonic agitation to minimize artifacts	319, 340, 387, 455
Wright	5–20 min, well-defined shape and orientation-dependent etch features, smooth background surface, slow etch rate, sharp definition of defects from hot processing, relatively insensitive to dislocation during crystal growth	388, 389, 433, 652
Schimmel	5 min, comparable to Secco etch for (100) wafer, no need for ultrasonic agitation	340, 387
Seiter[b]	20–60 min, stacking faults and swirl defects on (100) planes	1023
Archer	1–3 min, a dilute Schimmel etch, enhances visibility of dislocation etch pits in very thin layer of lightly doped epitaxy on heavily doped substrate	375
Yang	2–5 min, well-defined etch features of a wide range of defects of different orientations and resistivities, an improved etch over earlier ones	387, 445
Sopori	30 s, reveals dislocation networks, twins, and grain boundaries of polysilicon	993
Mayer[c]	15–20 min, reveals striations in dislocation-free silicon	311
MEMC[d]	1 min, reveals dislocations and slips, nontoxic, a substitute for Sirtl or Wright etch	204
Kashiwagi[e]	2–60 min, reveals defects by strain field of small defect-energy and defects of polycrystalline materials	91
Troxell	5 s in EDP, reveals grain structure and orientation of polycrystalline silicon	393

[a]Unless otherwise indicated the composition is given in Table 7.1.
[b]9 parts of 120 g CrO_3 in 100 ml H_2O and 1 part of HF (49%).
[c]0.2–1 g/100 ml HF (48%) + drops of wetting agents.
[d]36 HF (48%) : 25 NHO_3 (70%) : 18 HAc (glacial) : 21 H_2O + 1 g $Cu(NO_3)_2 \cdot H_2O$ per mixed aicd.
[e]1 : 4 : 5 for HF (50%) : HNO_3 (61%) : CH_3CO_2H (glacial).

structural perfection of single crystals. The morphological features developed by defect etching have a characteristic shape and may occur at random or in arrays revealing crystalline imperfections such as dislocation, slip, lineage, and stacking faults. Defect etching has been widely used to evaluate dislocations and also to delineate process-induced defects in silicon wafers and epitaxial deposits.[375,387] In general, the etching features and operating conditions in different defect etching systems are well characterized but the etching processes that lead to the development of the defect features are not well understood. The techniques and procedures for defect etching of silicon crystal are well established and can be found in a series of ASTM Standards.[439–442]

Many different etchants have been developed for various purposes as shown in Table 7.7. By using proper etchants and procedures, different types of crystal defects can be evaluated: flow pattern defects,[246] stacking faults,[387,433,1023]

dislocations,[91,304,319,340,387,433,1020] dislocation network,[162,319,387] oxide precipitates,[445] swirl patterns,[387,433,1023] striations,[311,433] hillock defects,[652] epitaxial defects,[375] epitaxial alignment,[367] grain boundary,[91,319,455] twin band,[91] diamond saw damage,[391] *pn* junction,[398,399,410] metallic precipitates,[388,1173] and damaged layer of mechanically polished surface.[302]

Most defect etchants are mixtures of CrO_3 and HF.[319,340,387] The preferential etching of dislocations takes place only at a proper concentration ratio of CrO_3 and HF.[387] These etchants are easy to use and fast, taking only several minutes to reveal the defect etch features. Agitation is in general not required but it may improve the quality of etched features in some etchants, such as Wright etch,[433] Yang etch,[387] Secco etch.[319] Non-CrO_3 etchants are also used for defect etching. For example, HF–HNO_3–CH_3CO_2H-based etchant has been found to be highly sensitive for defects of polycrystalline materials.[91,993] Etching in a $CuSO_4$–HF solution under anodic bias reveals surface defects associated with dislocation networks.[162] Etching profile by staining in Cu^{2+}-containing acids at forward bias condition under illumination reveals *pn* junction and doping.[410,576] The copper preferentially is deposited on the *n* region, while the silicon preferentially dissolves on the *p* region.

The degree of differential etching at defects depends on the orientation of the crystal. In general, for diamond-type structures such as silicon it is much easier to reveal dislocations on the {111} planes than on other planes.[289,387] Some etchants, such as Sirtl etch, reveal sharply the defects on (111) planes but are not satisfactory for (100) planes.

The defect etching behavior of different silicon crystal planes has been related to the different surface potentials of the planes.[833] The surface energy of the low-index surfaces follows the order (111) < (110) < (100). The potential difference between a dislocation and its surrounding area is greater on (111) surfaces than on (100) surfaces, leading to a larger degree of preferential etching of the defects.

The etch pattern of dislocations is determined by the inclination of dislocations to the surface.[387] For dislocations lying nearly parallel to the surface, dislocation lines are observed. For dislocations lying at a steep inclination to the surface, etch pits result. The basic unit of an etch pit is generally bounded by the (111) planes intersecting the surface. The shape of a dislocation etch pit, which can be viewed as a superposition of the basic units etched at different intervals along a dislocation, is uniquely determined by the orientation of wafer surfaces and dislocation lines. Figure 7.61 schematically illustrates the shapes of etch pits developed on the three major surfaces.

For the formation of a dislocation etch pit it is necessary that the etching rate along the dislocation line be greater than the rate on the rest of the surface as shown in Fig. 7.1(c). The increased etching rate along the dislocation line is due to the strain field associated with the dislocation.[473,1022] Alternatively, the increased reactivity of dislocations may be due to the impurities preferentially segregated at dislocations. The increased reactivity of edge dislocations leading to the initiation and propagation of etch pits can be understood in terms of the chemical bonding and structure of the atoms along the dislocation line. The atoms along a dislocation are only triply bonded to the lattice and thus have dangling bonds. The terminal atom of an edge dislocation intersecting the surface may have only two dangling bonds. The sensitivity of an etchant to defect etching is thus determined by the etch rate at the defects relative to that of the

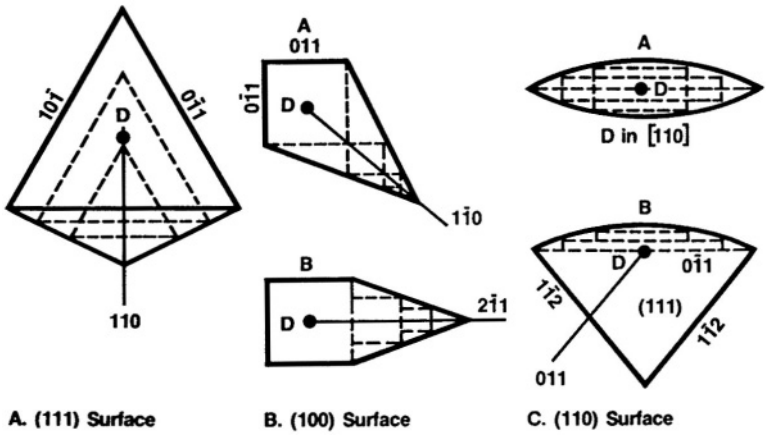

FIGURE 7.61. Schematic drawing of dislocation etch pit on (A, left) (111) surfaces, (B, center) (100) surfaces, and (C, right) (110) surfaces. D refers to the emergence of a dislocation to the surface. Solid line refers to the shape of an etch pit. Dashed line refers to the basic unit of an etch pit. After Yang.[387] (Reproduced by permission of The Electrochemical Society, Inc.)

surrounding area. Sharp etch pits are found to develop in etchants with a sensitivity factor of 1.5–2.[91]

Not all etch pits developed in etching solutions are related to crystal defects. For example, random and flat-bottomed etch pits are found to develop on dislocation-free silicon wafer in HNO_3–HF–CH_3COOH solutions.[168] Similar well-defined square and randomly distributed pits of several micrometers in size are found after immersion of (100) *p*-Si in a HNO_3–HF–CH_3COOH solution.[727] Large etch pits (80–300 μm in size), the surface of which is covered with a porous silicon layer, have been found to form on *p*-Si in quiescent concentrated HF solutions.[1007] The number of pits is greatly reduced in diluted solutions. This phenomenon can be attributed to the combined effect of porous silicon formation and pitting corrosion.

7.8.3. Material Removal

Etching is widely used as a process for material removal in silicon device fabrications. The important aspect of any etching process is the ability to control the amount of materials with sufficient spatial accuracy. The process and structural diversity in device fabrication necessitates diverse etching techniques—chemical or electrochemical, junction, anisotropicity, masking, and illumination—to provide uniform as well as selective etching, with lateral selectivity as well as in-depth selectivity. Figure 7.62 highlights the basic uniform and selective etching techniques for removing materials.

Uniform Material Removal. In the category of uniform etching the simplest method is immersing silicon samples in etchants such as KOH or HF–HNO_3 solutions as shown in Fig. 7.62(1).[103,149,331,450] It is normally used in applications such as damaged layer removal[450,490] and polishing[33,306] and in-depth doing profiling.[18,852] The etching is most commonly operated at the OCP but can be done under an anodic potential and/or illumination to add extra control. Etching with potential control requires an ohmic contact at the back side of the wafer in order to apply an anodic potential on the silicon

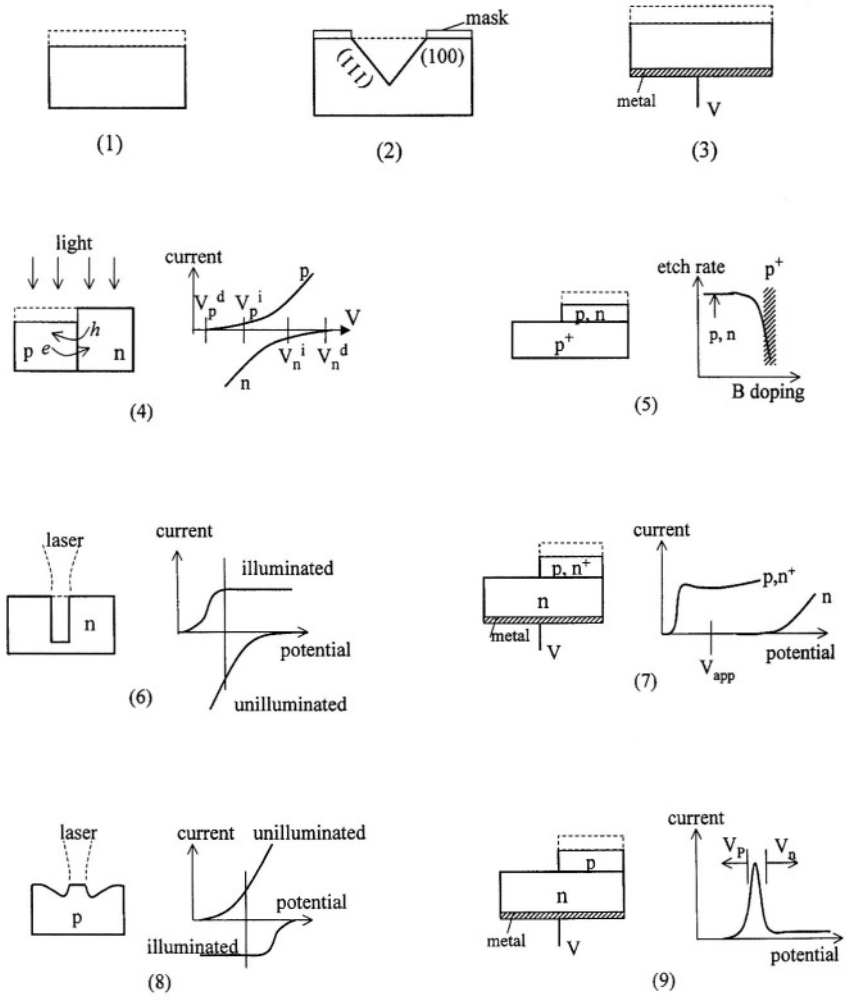

FIGURE 7.62. Schematic illustration of the different etching techniques for material removal. (1) Planar etching at OCP. (2) Anisotropic etching of masked surface. (3) Planar etching under an anodic bias. (4) Lateral selective etching of the p region of an illuminated pn junction. (5) Vertical selective etching using heavily doped material for etch stop. (6) Preferential etching of illuminated area on an n-type material. (7) Vertical selective etching of p or n^+ material under an anodic potential in the dark using the low etch rate of n-Si as etch stop. (8) Preferential etching of the nonilluminated area on an illuminated p-type material. (9) Vertical selective etching of p-Si of anodically biased pn junction using the passivity of n-Si as etch stop.

sample as shown in Fig. 7.62(3). Also, for uniform etching in fluoride-based solutions, the potential has to be in the current plateau region of an anodic i–V curve (see Fig. 5.1). Instead of applying an external current, anodic potential can be applied via galvanic action by depositing a metal on a part of the silicon surface.[1181]

Chemical etching of the silicon wafer in mixtures of HF and HNO_3 is used to remove surface work damage and stress from the slicing operation as well as to provide

a relatively nonporous and clean back side of the finished wafer.[471] It typically removes 0.5 to 1 mil of material from each side of the wafer. It has been reported that for the etching to remove the damaged layer, KOH solutions offer better results in terms of yield, flatness of back side, and metal contamination compared with $HF–HNO_3$ solutions.[490] A $HNO_3–HF–CH_3OOH–Br_2$ solution has been used to remove the damaged layer on mechanically polished surfaces.[302]

Chemomechanical polishing, which combines mechanical abrasion and chemical etching, is a basic processing technology for the production of flat, defect-free reflective surfaces. A widely used chemomechanical polishing technique for silicon uses an aqueous colloidal silica suspension.[213] The polishing proceeds by a combination of the reactions of silicon with the solution and the mechanical removal of the reaction products by the polishing pad and the abrasive fluid. Electropolishing has been proposed as an alternative technique to mechanical polishing for wafer polishing.[33,303,306]

Selective Material Removal. Selective etching can be realized by using masking, anisotropicity, *pn* junction, focused illumination, heavy boron doping, and potential control. All of these methods can be used for lateral selective etching, but only the methods that provide a boundary with a clear difference in the etch rates of the materials making the boundary, such as a *pn* junction or a junction between boron heavily doped and moderately doped materials, can be used for in-depth selective etching. Etching over a confined area on (100) substrate in an anisotropic solution results in the formation of a cavity as illustrated in Fig. 7.62(2). In the case of an illuminated *pn* junction as shown in Fig. 7.62(4), the photogenerated holes in the *n* region are flown to the *p* region resulting in dissolution of the silicon in the *p* region. When the illumination is confined in an area, the photoenhanced dissolution occurs either within the illuminated area or outside of the illuminated area depending on the material type.[422,600,758] For *n*-type material, illumination generates a selective etching which leads to the formation of a cavity at the illuminated area as shown in Fig. 7.62(6). On the other hand, for *p*-type material, illumination results in the formation of a column as shown in Fig. 7.62(8).

In-depth selective etching requires that the material to be removed have a much larger etch rate than the material beneath it so that etch stop occurs at the end of the etching. For etching alkaline solutions, heavily boron doped silicon can be used as the material for etch stop. This is based on the difference of several orders of magnitude in the etch rates between heavily doped and lowly doped materials. Etch stop can also be realized using the difference in the dissolution rates of *p*- and *n*-type silicon at anodic potentials in HF solutions as shown in Fig. 7.62(7). For example, in-depth selective etching of a *p*-type silicon can be realized by anodic polarization in HF solutions using *n*-type silicon for etch stop.

In-depth selective etching of silicon in alkaline solutions can also utilize the different passivation potentials between *p*- and *n*-type materials in alkaline solutions such as KOH,[152,511,536] EDP,[112] NH_4OH,[521,1004] hydrazine,[205,462448] and TMAH.[516] In this method, as shown in Fig. 7.62(9), an anodic voltage sufficient to cause passivation of *n*-Si is applied via an ohmic contact. Due to the potential drop in the reversely biased *pn* junction, the *p*-Si is maintained at a potential negative to the passivation potential and is etched. On complete removal of the *p*-Si, the junction disappears and the etch stops because the *n*-Si is passivated. A current peak, corresponding to the formation of the

TABLE 7.8. Examples of Silicon Structures that May Be Fabricated by Etching

Structure	Etchant	Method	Refs.
various	KOH, EDP	anisotropic etching, review	54, 531, 542
micromachining	various	review	851, 994
vertical trenches	KOH	(110) wafer	401, 401, 478
verticle walls on (100) wafer	KOH	pattern and etch from both sides of wafer	245
U and V grooves		different alignment on (110) wafer	184, 528
sharp convex edge	KOH	corner compensated masks	592, 593, 707, 989
membranes	KOH	etch stop by potential-dependent passivation	588
membranes	NaOH, NH_4OH	etch stop by p^+-Si	341, 711
membranes	EDP	etch stop by p^+ diffused layer	403, 526
high-aspect-ratio pillars	HF + alcohol	anodic etching plus back side illumination	782
ultrathin membranes	EDP	two-step etching with a p^+ etch stop layer	753
cantilever beams	EDP	p^+ on p substrate	356
cantilever beams	KOH	porous silicon sacrificial layer	502
cavity	EDP	etch of n layer of layered pn junction	399
buried cavity	KOH	fusion bonding and anodic etch stop	500
high-aspect-ratio grooves	CsOH	(110) wafer	132
2-nm quantum wires	KOH	shifted resist pattern	736
precision nozzles	EDP	review, (100) wafer	343
inkjet nozzles	EDP	p^+ rib masking	539
comb-drive actuator	EDP	etch stop by p^+ layer	509
wafer bonding	various	wafer thinning	382
T-shaped beam	KOH	masking	507
micromirrors	EDP	(100) wafer	538
deep trenches	TMAH	mechanical cut with etching refinement	15
deep trenches		focused laser	279
IC devices		pn junction	296
pyramids	KOH	etch of masked islands	503, 529, 530
(411)-faced pyramids	KOH	corner compensated masking	707
various shapes of mesa	KOH	mask design via theoretical modeling	590
sensors and actuators	HF	etch of sacrificial oxide layers	533, 664
suspended circuit	TMAH, KOH	biased pn junction	516, 581, 588
cavity in p-Si with n-Si bottom	TMAH	pn junction biased by a gold layer	591
deep holes and trenches	HF	focused laser etch	279, 758
deep holes	HBr	microscopically confined etchant layer	830
deep holes and trenches	HBr	microscopically confined etchant layer	830
differently shaped cavities	KOH	mask alignments	513
multilevel structure	KOH	multistep masking and maskless etching	504
freestanding beams	NH_4F + acetic acid	front patterned samples with back illumination	999

passive oxide film on the *n*-Si, occurs when the *pn* interface is reached. This current peak signals the onset of the etch stop. Extra control can be obtained by applying different potentials on the *p*-Si and *n*-Si regions with *p*-Si maintained at a value near the OCP and *n*-Si at a value positive of the passivation potential.[536] This prevents the unwanted passivation of the *p*-Si which can result from short-circuiting due to point defects and current leakage. Etching of *p*-Si can also be realized by selective passivation using an accumulation layer for etch stop instead of a *pn* junction.[463] Based on the same principle as in-depth selective etching, laterally selective etching can be obtained by biasing a laterally positioned *pn* junction because *p*- and *n*-Si have different passivation potentials.[521]

Another group of methods for selective etching utilizes the high reactivity of porous silicon.[502] Porous silicon can selectively be formed in a patterned area. The porous silicon can then be easily dissolved in a KOH solution leading to the selective dissolution of the patterned area. Also, straight hole array with high aspect ratios can be generated through formation of macropores by back illumination on *n*-Si.[12,763]

Locally confined etchant can also be used to preferentially etch small holes on silicon.[830,1018,1098] In this technique an active etchant is generated through a reduction reaction at the tip of a fine electrode which is positioned near the silicon surface. In situations where diffusion-controlled process limits the in-depth etch rate, deep etching can obtained using a centrifugal force.[82]

Many different structures can be micromachined on silicon through etching. Whereas IC technology usually employs planar processes, in micromechanics, sensors, and actuators, selective etching must be used to fabricate three-dimensional and mobile elements.[285,517] Two aspects are of particular important in the fabrication of structures by etching: etch stop and etch feature definition, both of which rely on the selective etching of materials on a patterned silicon surface.[851] Virtually all microstructures utilize at least one etch stop technique during the course of their fabrication. Etch feature definition, on the other hand, is mainly achieved through masking and anisotropic etching which makes anisotropic etching one of the key processes for the fabrication of three-dimensional micromechanical devices.[517,918]

Table 7.8 lists some of the silicon structures that may be fabricated through etching. The many etching characteristics of silicon and the numerous etching systems provide a large range of variation in etch rate. This range of rate variation, in combination with various etching techniques, provides many methods for selective removal of materials on silicon as illustrated in Fig. 7.62, allowing the fabrication of diverse structures on silicon. Also, process simulation models and software tools have been developed to assist design and fabrication of structures of specific geometries.[515,517,524,1006,1080]

This page intentionally left blank

8

Porous Silicon

8.1. INTRODUCTION

Porous silicon (PS) is a material that is formed by anodic dissolution of silicon in HF solutions. The formation of PS was first reported in the late 1950s in studies on electropolishing of silicon.[33,957] Since then, particularly after 1990 when luminescence of PS was discovered, numerous investigations have been undertaken. These investigations have revealed that PS has extremely rich morphological features with properties that are very different from those of silicon and the formation process of PS is a very complex function of many factors such as HF concentration, type of silicon, current density, and illumination intensity.

The amount of information on PS in the published literature is enormous and it is not possible to cover all aspects of PS in one chapter. Thus, the focus in this chapter is on the phenomena related to the properties of silicon, such as the formation of PS and the resulting morphology. The phenomena associated with the properties of PS and the applications of PS are only briefly mentioned at the end of the chapter. In particular, there is so much information related to the luminescence of PS that it would require a separate book to organize this body of information.

In this chapter, the conditions for the formation of PS, the relation between the formation conditions and PS morphology, and the mechanisms for the formation of PS and morphology are discussed. The various aspects of surface condition, nature of reactions, and reaction kinetics that are fundamentally involved in the anodic dissolution of silicon are discussed in Chapters 2–5.

8.2. FORMATION OF POROUS SILICON

8.2.1. Characteristics of i–V Curves

PS can either be formed by anodization in HF-containing solution under an anodic bias or by an electroless process. The formation condition can best be characterized by *i–V* curves. Figure 5.3 shows a typical plot of an *i–V* curve of silicon in HF solutions. At small anodic overpotentials the current increases exponentially with the electrode potential. As the potential is increased, the current exhibits a peak and then remains at

a relatively constant value. PS forms in the exponential region but not at potentials higher than that corresponding to the current peak, J_1. Electrochemical polishing occurs in this region. At potentials above the exponential region and below the potential of the current peak, PS formation also occurs, but the PS layer does not completely cover the sample surface.[2] The surface coverage of PS decreases as the potential approaches the peak value. Hydrogen evolution simultaneously occurs in the exponential region and its rate decreases with potential and almost ceases above the peak value. The exisistance of these different regions are similar for other fluoride-containing solutions of various compositions and pH values.[34,700,775,939]

In the exponential region where PS forms, the slope of the logarithmic current density versus potential plot, i.e., the Tafel plot, is typically about 60mV/decade for *p* type and heavily doped *n* types of silicon samples as shown in Table 5.3.

Successive *i–V* curves, measured on the same specimen (Fig. 8.1), are virtually the same except for the first one when the surface is transformed from smooth to porous.[2] Because each curve is subsequently obtained on the electrode with a thicker PS layer, it means that the reactions are independent of PS thickness, and are not controlled by mass transport. The small difference between the first and subsequent ones in Fig. 8.1 suggests that the active surface area is not drastically changed by the formation of PS, although the total surface area is much increased due to the growth of PS. Also, the interface capacitance is not modified by the presence of a PS layer with increasing PS thicknesses.[5] This means that the pore walls in PS are depleted of carriers and are not active so that it is only conductive at the pore tips where active reactions take place. However, the formation of PS transforms the surface morphology so that the electrode behavior is changed from that of the original condition as shown in Fig. 8.2.[1153] After 5min of polarization at $-0.1\,V_{sce}$ at which PS forms, the capacitive loop of the n^+ silicon in 1% HF is greatly reduced. Formation of PS, as will be discussed later, results in an increased effective area as well as in an increased kinetics due to the enhancement of the electric field by the curvature at the pore tips.

The typical characteristics of the *i–V* curves of *p*-Si of different doping levels and orientations are essentially identical except for a slightly higher current density of the

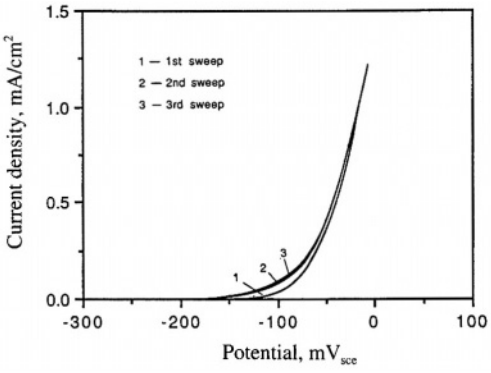

FIGURE 8.1. Successive *i–V* curves made on the same *p*-Si sample in 1% HF with a potential sweep rate of 2mV/s. After Zhang *et al.*[2] (Reproduced by permission of The Electrochemical Society, Inc.)

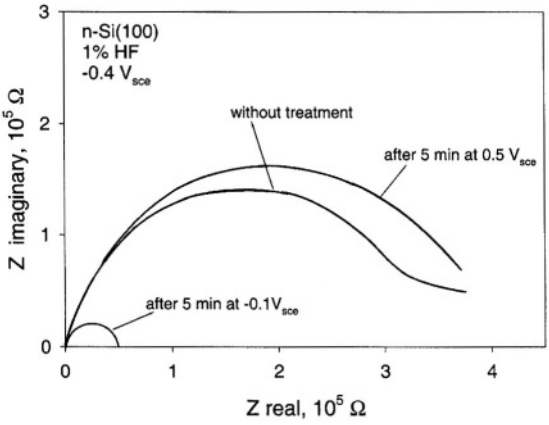

FIGURE 8.2. Complex impedance plot of n-Si(100), 2×10^{19}, in 1% HF at $-0.4\,V_{sce}$.[1153]

(100) orientation relative to that of the (111) orientation.[2,38] Figure 8.3 shows i–V curves of different types of Si in 1% HF solution. Except for a shift along the potential axis, which reflects the difference in the Fermi levels of these materials, the i–V curves of p type and heavily doped n types are largely identical.

The i–V curves on non-heavily doped n-Si are shown in Fig. 8.4. Unlike p-Si and heavily doped n-Si, a much larger anodic polarization is required to generate the dissolution reaction in the dark; the lower the doping level, the higher the applied potential for a given current density.[2] Also, the i–V curves may not show the clearly defined regions as on other types of Si, but depend on measurement procedures. As shown in Fig. 8.4 the i–V curve with a positive potential scanning rate is different from that with a negative scanning rate; different regions are revealed only on the curve measured at a certain negative scanning rate. As will be discussed later, it is the particular reaction and the morphology that give rise to the i–V characteristics shown in Fig. 8.4. Also, the current flow on n-Si is very sensitive to surface roughness.[9,42] Mechanical

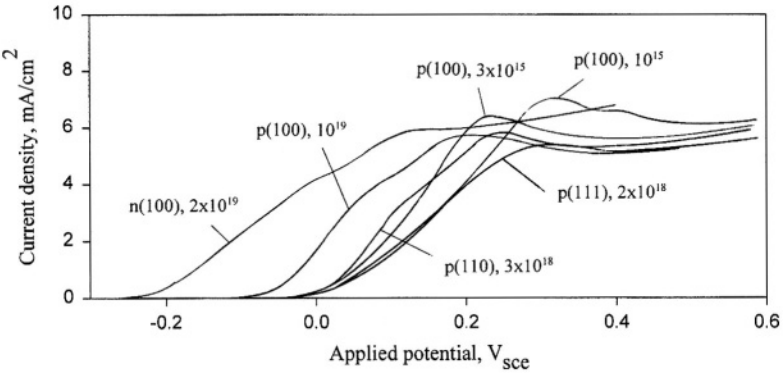

FIGURE 8.3. i–V curves of different silicon substrates in 1% HF.[1153]

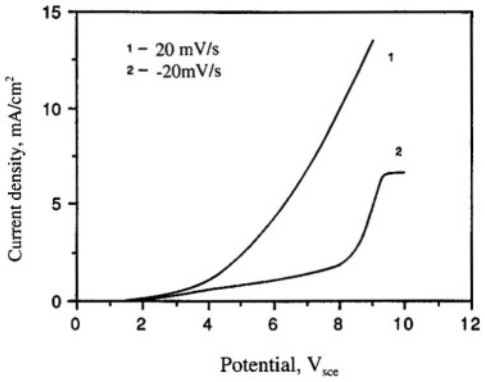

FIGURE 8.4. *i–V* curves of *n*-Si in 1% HF solution. After Zhang *et al.*[2] (Reproduced by permission of The Electrochemical Society, Inc.)

roughening or passing through an anodic current prior to PS formation will greatly increase the current density at lower potentials, at which the current density is very small without the surface roughening. The current rise occurs at a potential several volts lower on a rough surface than that on a smooth surface.

The *i–V* curve of *n*-Si under a high illumination intensity, when the reaction is no longer limited by the availability of photogenerated carriers, is identical to that for *p*-Si except for a shift along the potential axis. As for *p*-Si, formation of PS on *n*-Si occurs only below the critical current, J_1. The *i–V* relationship at a current density much lower than the saturation photocurrent density is similar to that observed on *p*-Si. When the saturation photocurrent density is lower than the critical current density, the current is limited by the saturation photocurrent.

The current at a given potential increases with HF concentration. The current density in the exponential region is linearly proportional to HF concentration, giving a reaction order of about 1, while in the electropolishing region the HF reaction order is about 1.35.[2] Also, the potential at peak current shifts to high values with increasing HF concentration. The *i–V* curves measured in concentrated HF solutions are very noisy due to the violent hydrogen evolution at high current densities in concentrated solutions. Unlike in diluted HF solutions, the current in concentrated HF solutions at high potential values depends on scanning rate and decreases on successive curves measured on the same sample, indicating the role of mass transport in the growing PS layer in these solutions.[1153]

8.2.2. Conditions for PS Formation and Electrochemical Polishing

Examination of the sample surfaces that are anodized at different potentials indicates that the potential corresponding to the maximum slope of the *i–V* curve is the upper limit for formation of a uniform PS layer. At potentials between the maximum slope and current peak, the porous layer may still form but the surface coverage is not uniform. Thus, the anodic behavior is characterized by three regions: PS formation, transition, and electropolishing.[2]

Plotting the current at the maximum slope and the peak current for different types of silicon as a function of HF concentration, the condition for occurrence of PS formation and electropolishing is obtained as shown in Fig. 8.5.[2] It is seen that the three regions in relation to current density and HF concentration are essentially independent of the silicon substrate doping type and concentration. This means that the differences in semiconducting properties of the silicon samples have little effect on the occurrence of these regions. The various parameters involved in PS formation such as potential, doping, and illumination affect the occurrence of different regions through their relation to the current density. Low current and high HF concentration favors PS formation whereas high current and low HF concentration favors polishing.

The occurrence of different regions during anodization of silicon in HF solutions is attributed to two competing reaction paths: direct dissolution of silicon and indirect dissolution through formation and dissolution of silicon oxide.[2] Formation of PS is only possible when the surface is not fully covered with an oxide film and direct electrochemical dissolution of silicon is possible. At low potentials, direct dissolution of silicon dominates and PS is readily formed. On the other hand, at potentials higher than the current peak, the entire surface is covered with an oxide film and the semiconducting properties are masked such that the dissolution is homogeneous across the surface and PS cannot be formed. Thus, the formation of an oxide film and its surface coverage determines the occurrence of these three regions. The existence of an oxide during PS formation and its increasing coverage with potential have been experimentally confirmed.[326]

The electropolishing region does not occur in anhydrous organic solutions due to the lack of water required for the formation of oxide film. Figure 8.6 shows that in anhydrous HF–MeCN solutions the current can increase with potential to a value of about $0.5\ A/cm^2$ without showing a peak current. The current increases linearly with potential due to the resistance in the solution and silicon substrate except for very small currents near the onset of anodic current where the current increases exponentially with

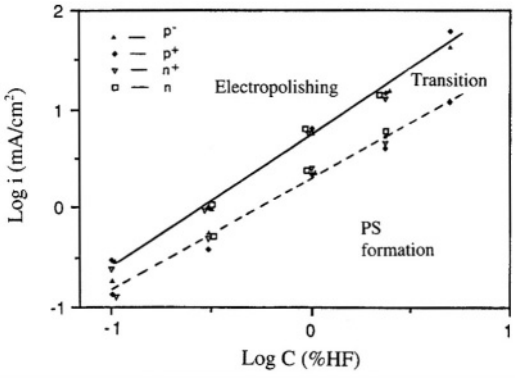

FIGURE 8.5. A plot of critical current densities as a function of HF concentration. Solid line is the peak current density; dashed line is the current density at the maximum slope shown in Fig. 5.3. After Zhang *et al.*[2] (Reproduced by permission of The Electrochemical Society, Inc.)

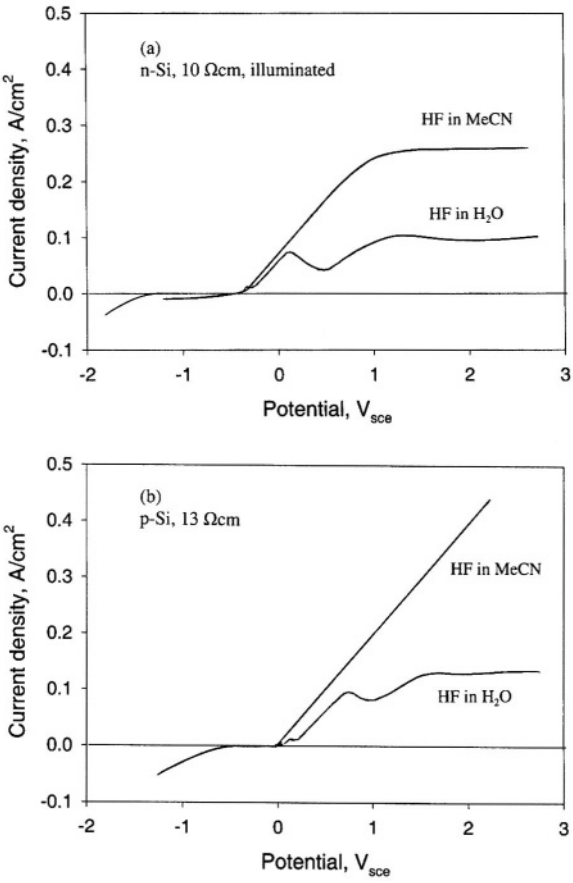

FIGURE 8.6. The *i–V* behavior of *p*-Si and *n*-Si (scan rate 0.5 V/s) illuminated with a 300 mW/cm^2 quartz halogen lamp in 2 M HF + 0.25 M TBAP in MeCN and in 2 M HF + 1 M NH_4F in H_2O. After Propst and Kohl.[248] (Reproduced by permission of The Electrochemical Society, Inc.)

potential. The characteristics of the *i–V* curves are independent of solution agitation and potential scanning rate indicating that mass transport in the electrolyte has very little effect. For *n*-Si the current is proportional to the light intensity and is only limited by the saturation photocurrent. The photon efficiency is about 4 indicating a current quadrupling effect; for every photon-generated electron, three electrons are injected from the states at the interface.

8.2.3. Effective Dissolution Valence and Hydrogen Evolution

As discussed in Chapter 5, the effective dissolution valence of silicon, *n*, can vary between 2 and 4 depending on the type of silicon, potential, and illumination intensity. In general, *n* increases with increasing anodic current density for all types of silicon substrates as shown in Fig. 5.21. The value of *n* sharply changes at the peak current

density, J_1. On the other hand, at a given current density, n increases with HF concentration. Also, the dissolution valence decreases with increasing PS layer thickness as shown in Fig. 8.7;[41] also, a dissolution valence as low as 0.5 is measured for thick PS films formed at low current densities. The low n values are due to the chemical dissolution of PS; the thicker the PS layer, the longer the sample is present in the electrolyte and the larger the amount of chemical dissolution. For p-Si, on which the PS has an extremely fine pore structure, the chemical dissolution during the growth of PS is significant and is responsible for the low n values below 2.

For p-Si in the PS formation region, n tends to increase with doping concentration particularly at high doping concentrations as shown in Fig. 8.8;[35,651] for n-Si the effect of doping concentration on dissolution valence is seen to depend on current density. It decreases with increasing illumination intensity as shown in Fig. 8.9. Substrate orientation has little effect on n as shown in Fig. 8.10.[1085]

Evolution of hydrogen gas occurs during the formation of PS. It is the result of the chemical reaction responsible for the effective dissolution valence of less than 4. Figure 8.11 shows that the amount of hydrogen gas is proportional to the time of anodization.[34] When the anodization is stopped, the hydrogen evolution still continues at a lower rate. *In situ* FTIR studies indicate that the H-termination of the silicon surface is preserved during PS formation on n-Si.[477,775,1123] The silicon atoms on the surface are

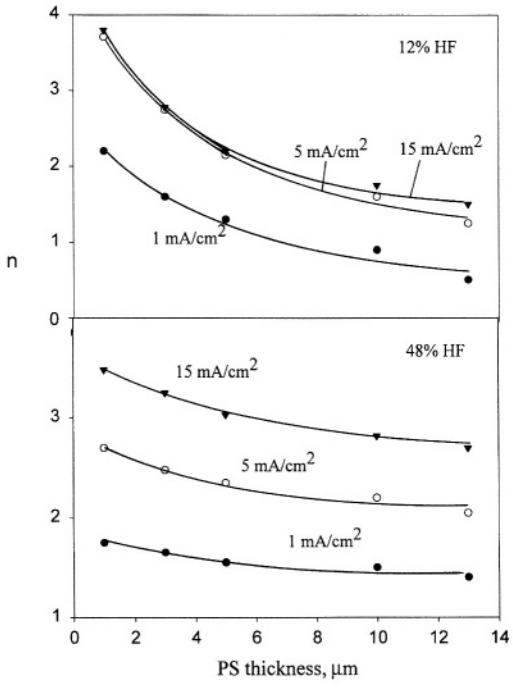

FIGURE 8.7. Dissolution valence of n-Si, 0.01 Ωcm, in 12 and 48% HF as a function of current density and PS thickness. After Parkhutik *et al.*[41]

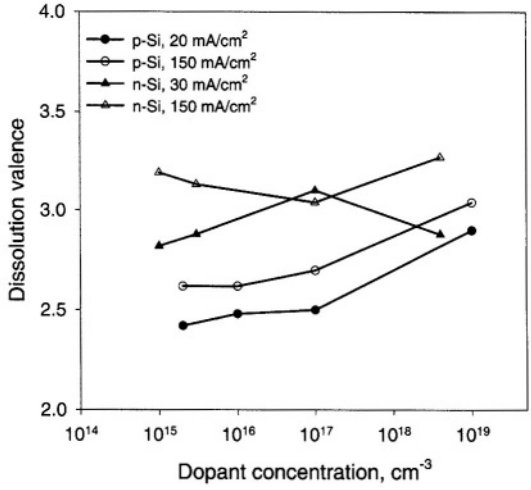

FIGURE 8.8. Dissolution valence versus dopant concentration. Illumination intensity is 26 mW/cm^2. After Arita.[651]

dynamically adsorbed by H and dissolved into the solution. The efficiency of hydrogen evolution and dissolution valence as a function of potential under various conditions is summarized in Fig. 5.23.

Due to the formation of hydrogen bubbles the space within the pores may not be fully filled by electrolyte. It has been found that for the PS formed on heavily doped *p*-type silicon in concentrated HF solution only slightly more than half of the pore volume is filled by the electrolyte.[40] The rest is occupied by the hydrogen gas generated during PS formation. However, it has been suggested by Lehmann and Foll[763] that the formation of hydrogen bubbles is likely to occur at the opening of the pores instead

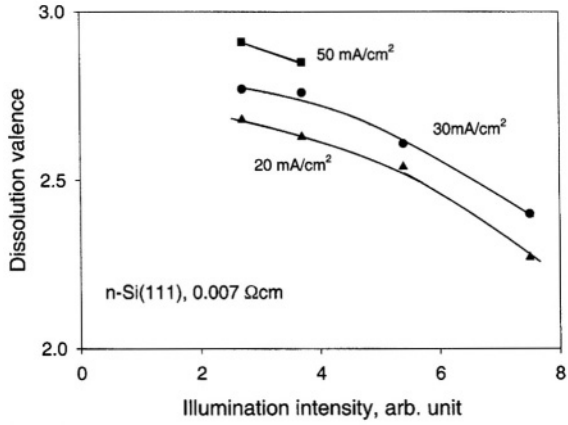

FIGURE 8.9. Dissolution valence of illuminated *n*-Si versus illumination intensity. After Arita.[651]

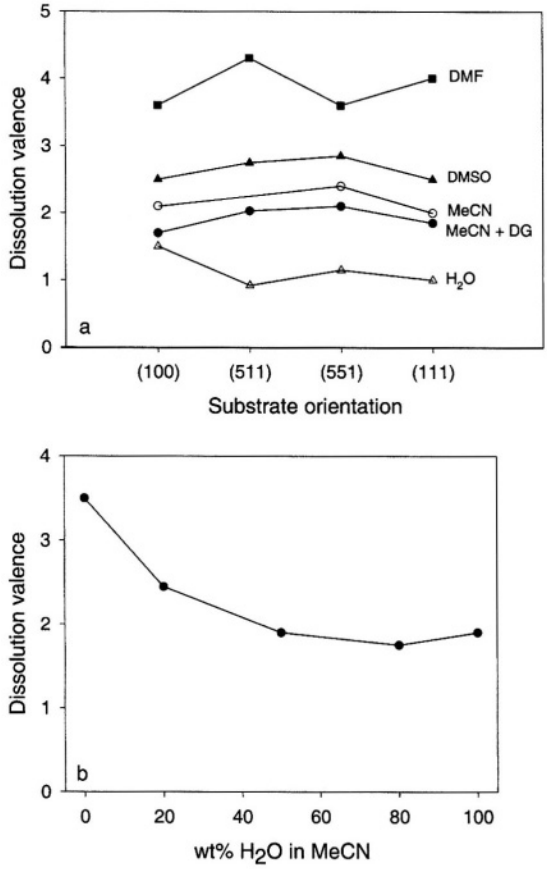

FIGURE 8.10. Dissolution valence in (a) different solvents and (b) water concentrations in MeCN. (Reprinted from Christophersen *et al.*[1085] © 2000, with permission from Elsevier Science.)

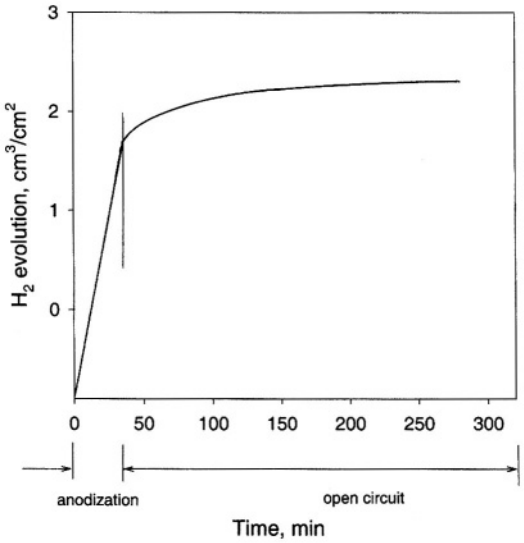

FIGURE 8.11. Hydrogen evolution versus time for a *p*-type (1 Ωcm) silicon electrode in 10N hydrofluoric acid during an afterpolarization. (Reprinted from Memming and Schwandt.[34] © 1966, with permission from Elsevier Science.)

of inside the pores, because if hydrogen bubbles were formed inside pores they would block the current path and stop the growth of the pore.

The formation of hydrogen does not occur in anhydrous organic solvents.[136,248,1085] Because of lack of hydrogen evolution the dissolution reactions are entirely electrochemical in nature with a dissolution valence of 4 at all current densities. Addition of water to the organic solvents reduces the dissolution valence as shown in Fig. 8.10.[1085]

8.2.4. Growth Rate of Porous Silicon

The growth rate of a PS layer can vary over a wide range depending on formation conditions as shown in Table 8.1. It can be as low as a few angstroms per second and as high as 4000 Å/s.[36,41] Such rates are well within the limits observed for planar etch rates of solid silicon and its oxides. The etch rates of silicon in $HF–HNO_3$ solutions of certain mixtures can be as high as 10^5 Å/s (see Table 7.1), and those of anodic oxides, according to Fig. 4.2, can be on the order of 1000 Å in concentrated HF solutions.

For *p*-Si the growth rate of PS at a given current density appears to increase linearly with HF concentration as shown in Fig. 8.12.[36,1128] For *n*-Si the growth rate also increases with HF concentration but the relation is not linear (Fig. 8.13).[12,1153] At a given HF concentration it increases linearly with increasing current density as shown in Fig. 8.14.[36] It also increases linearly with logarithmic dopant concentration (Fig. 8.15). The growth rate of PS on *n*-Si is more complicated. Figures 8.14 and 8.15 show that the growth rate on *n*-Si does not follow a linear function with current density nor with dopant concentration and under identical conditions the PS formed on *n*-Si type generally has a higher growth rate than that on *p*-Si. Also, the growth rate of PS on *n*-Si becomes relatively constant at current densities that are a significant fraction of the current peak J_1 as shown in Fig. 8.16.[12,763] The temperature of HF solutions generally has little influence on the growth rate of PS.[33,170] The formation of PS on *n*-type silicon in the dark does not occur below certain anodic potentials in the dark but can occur after roughening or formation of a thin PS layer under illumination.[36,40]

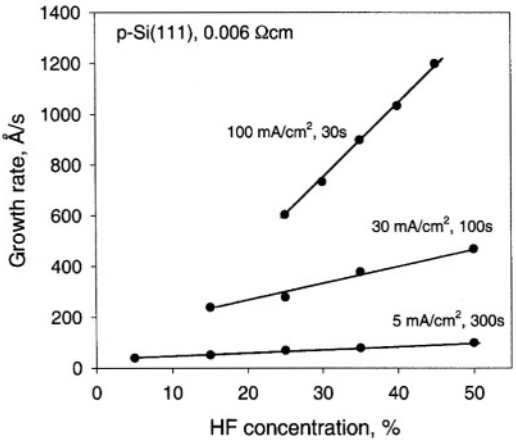

FIGURE 8.12. Effect of HF concentration on rate of PS formation. After Arita and Sunahama.[36] (Reproduced by permission of The Electrochemical Society, Inc.)

TABLE 8.1. Growth Rate of PS under Various Conditions

Silicon	[HF]	Current	Potential	Rate, Å/s	Ref.
***p*-Si**					
(100)					
1.5	30%	10		90	48
1.5	50%	10		100	48
1.5	50%	100		900	48
4	30	30		350	586
4	15:30	30		120	586
4	15:50 Triton[a]	30		400	586
5	10	3		10	1027
50	10	3		24	1027
50	10	10		55	1027
50	10	30		103	1027
100	25	20		150	952
1000	25	20		160	952
1000	25	20		260	952
(111)					
0.006	25%	5		70	36
0.006	25%	30		290	36
0.006	25%	100		600	36
0.006	50%	100		1200	36
0.006	50%	30		560	36
0.007	50%	100	0.3 V_{sce}	1400	40
0.007	50%	50	0.13 V_{sce}	750	40
0.007	50%	10	−0.1 V_{sce}	160	40
0.4	50%	25		270	366
1.6	50%	30		250	36
0.01	50%	100		1200	37
0.01	50%	30		500	37
0.1	24%	10		125	49
0.1	24%	40		375	49
(110)					
15	10	1		8.3, M[b]	1027
15	10	2		15	1027
***n*-Si**					
(100)					
10^{17}	1%	1.1	4	40	8
10^{17}	1%	4.2	6	55	8
10^{17}	2%	12	6	150	1153
10^{17}	5%	37	6	310	1153
10^{15}	10%	37, illu.	5	670	12
10^{15}	1%	1, illu.	5	25	12
10^{15}	3%	0.013	5	39	12
(111)					
5×10^{18}	12%	0.1		8	41
5×10^{18}	12%	1	0.33 V_{sce}	20	41
5×10^{18}	12%	5	0.75 V_{sce}	130	41
5×10^{18}	24%	1	0.30 V_{sce}	38	41
5×10^{18}	24%	5	0.70 V_{sce}	180	41
5×10^{18}	48%	1	0.28 V_{sce}	130	41
10^{17}	50%	150, illu.		4000	36
(110)					
0.82	10%	0.5		230	1153
0.82	10%	5	8–14	450	1153
0.82	10%	50		670	1153
3	4	4	1.5 V	49	1027

[a]Triton: soap solution.
[b]M: micropores

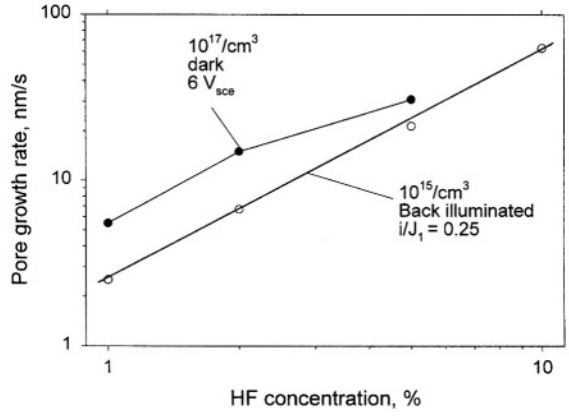

FIGURE 8.13. PS growth rate on *n*-Si as a function of HF.[12,1153]

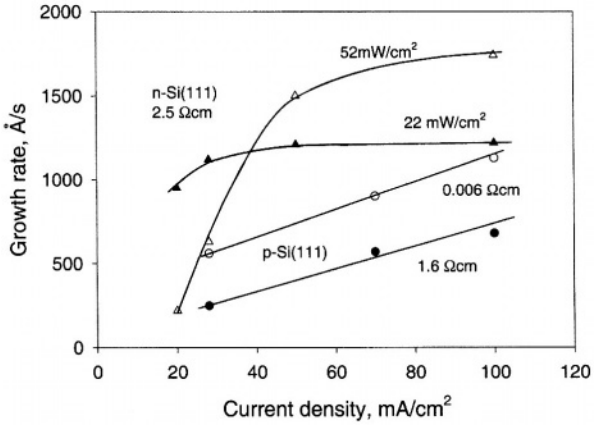

FIGURE 8.14. Effect of current density on rate of PS formation. After Arita and Sunahama.[36] (Reproduced by permission of The Electrochemical Society, Inc.)

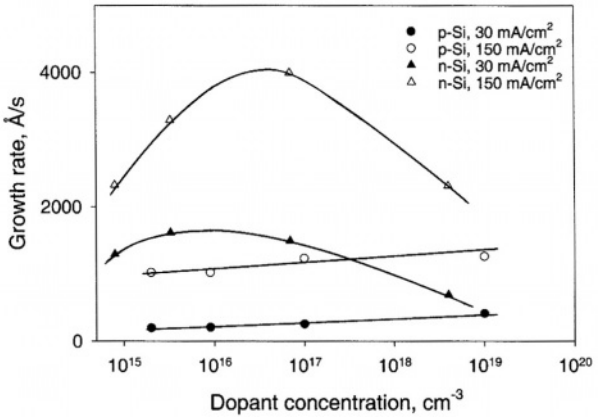

FIGURE 8.15. Effect of doping concentration on growth rate of PS. After Arita and Sunahama.[36] (Reproduced by permission of The Electrochemical Society, Inc.)

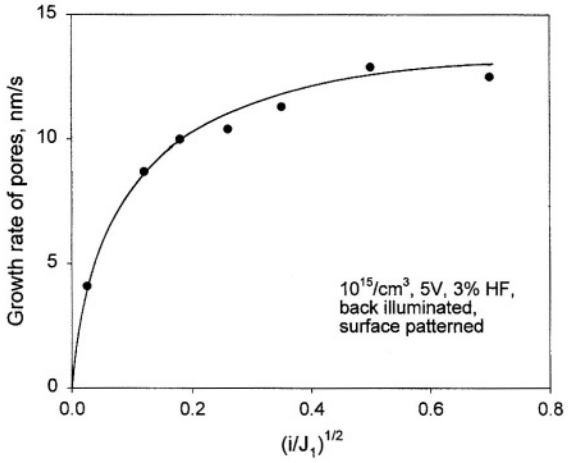

FIGURE 8.16. Growth rate of PS on n(100) as a function of the ratio of current to the peak current J_1 (see Fig. 5.1). (Reprinted from Lehmann.[12] © 1993, with permission from Elsevier Science.)

The current under a given potential is generally constant as a function of anodization time or of PS thickness.[40,41] Figure 8.17 shows that the PS growth on heavily doped n-Si is a linear function of time for thickness up to about 10 μm.[41] Such constant current and growth rate mean that the PS formed is uniform in thickness, a finding that agrees with the results from morphological investigations. At large thicknesses the growth may deviate from linearity. This occurs at different thicknesses under different conditions; it starts on a smaller PS thickness at high current densities in concentrated solutions.[41] The deviation from linearity, which indicates that either the effective area at the dissolution front is increased or the effective dissolution valence is increased, is due to the effect of diffusion in the electrolyte within the pores.[12,1133] PS growth rate is higher on (100) samples than on (111) samples.[1132]

8.2.5. Mass Transport

The exponential current–potential relationship in the PS formation region indicates that mass transport has little influence on PS formation. This is further confirmed by the fact the current during PS formation is essentially independent of the thickness of PS.[2,36,40] Also, the concentration of HF inside pores is found to be essentially the same as outside.[40] However, as the PS layer gets thicker, diffusion may start to limit the rate under high current densities. For example, Fig. 8.17 shows that the thickness of PS increases linearly with time under various current densities and potentials below 10 μm. At a certain thickness depending on HF concentration and current density, the growth slows down. It has been found that for a very thick PS layer (150 μm) there is a difference of about 20% in HF concentration at the tips of pores and the bulk solution.[12] The morphology of the PS formed under a diffusion-controlled situation will change with increasing thickness. Due to the depletion of HF at pore tips, the distribution of

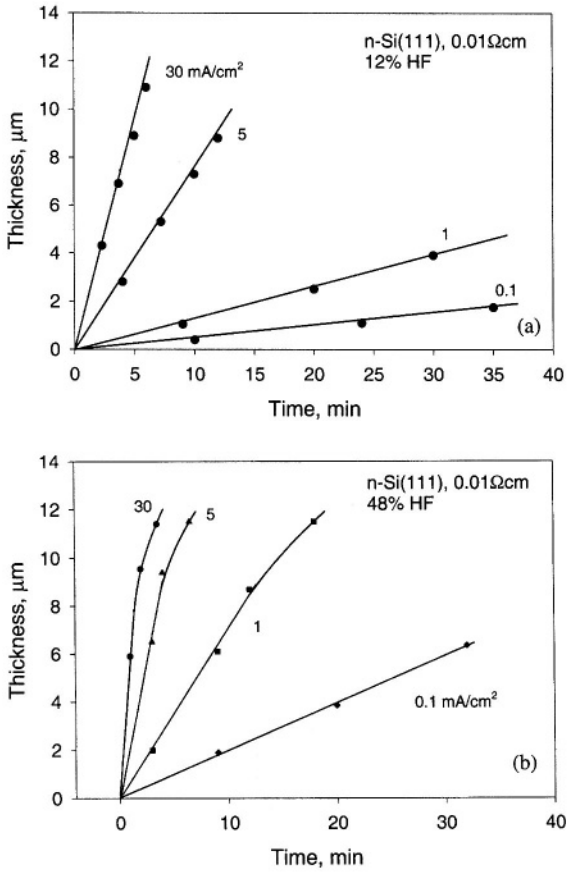

FIGURE 8.17. Kinetic dependence of the PS thickness on anodization time for (a) 12 wt % HF and (b) 48 wt % HF. After Parkhutik *et al.*[41]

the reactions, particularly the coverage of oxide at the pore bottom, is changed, which results in the change of morphology.[8]

Mass transport of uncharged species in an electrolyte occurs by either convection or diffusion. Given the conditions for PS formation, convection inside pores via physical stirring is only possible through the formation, growth, and movement of hydrogen bubbles. It has been reported that the pores during their growth are not fully filled with electrolyte, due most likely to the formation of hydrogen bubbles.[40] However, it has been argued that hydrogen bubbles may not be formed in the mass transport within pores because if they are formed inside pores they will block the pore and significantly reduce the rate of mass transport.[12]

In the potential range near the current peak before the electropolishing the current is limited primarily by the diffusion of HF from the bulk to the silicon/electrolyte interface.[33] In this region the coverage of PS on the electrode surface is no longer complete because oxide formation and dissolution proceed on a significant part of the surface.

At the current peak, the critical current at which the effect of mass transport reaches its maximum and the surface is covered with an oxide films, PS ceases to form. Although diffusion has a strong effect in the electropolishing region, the current is not fully limited by the diffusion process.[34,939]

8.2.6. Chemical Dissolution during PS Formation

During PS formation at an anodic potential, the tip of pores dissolves electrochemically. The pore wall areas that are sufficiently distant from the tips where no holes are available, dissolve only chemically and at a very low rate. The chemical dissolution does not depend on potential but on the time of immersion and the total surface area of the PS. Due to the large surface area of PS, a significant amount of material may be removed by the chemical dissolution during the formation period of PS. Figure 8.18 shows that the amount of chemical dissolution increases with immersion time in the HF solution and with decreasing HF concentration.[48] The dependence of the chemical dissolution on time has been found to follow the equation

$$W_{ch} = At^n \qquad (g/cm^3) \tag{8.1}$$

where t is time and A and n are constants depending on HF concentration and current density. For 40% HF and a current density of $40\,mA/cm^2$, the amount of chemical dissolution relative to that of electrochemical dissolution has been determined to be

$$W_{ch}/W_{ele} = 2.4 \times 10^{-3} t^{0.48} \tag{8.2}$$

This equation indicates that the amount of chemical dissolution relative to that of electrochemical dissolution increases with time. This is reasonable, as chemical dissolution is proportional to the surface area of PS which in turn increases with time while

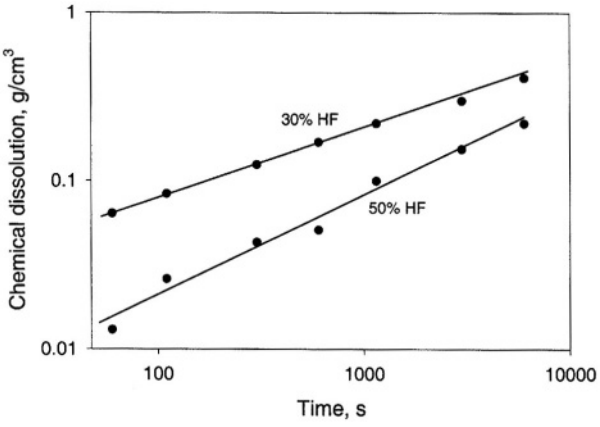

FIGURE 8.18. Relationship between amount of dissolved silicon and dipping time in HF solutions. The PS was formed in 40% HF at $50\,mA/cm^2$. After Unno *et al.*[48] (Reproduced by permission of The Electrochemical Society, Inc.)

electrochemical dissolution depends only on the surface area at the pore bottom that is independent of anodization time.

The values in Fig. 8.18 can be used to estimate the chemical dissolution rate on the surface of pore walls. For a PS with a density of 50% and a pore diameter of 3 nm, the absolute dissolution rate of PS equals the dissolution rate of PS ($g/cm^3 \cdot t$) divided by silicon density ($2.33\ g/cm^3$) and by specific area (cm^2/cm^3). The chemical dissolution rate is estimated to be about 6×10^{-4} Å/s, assuming the PS consists of straight cylindrical pores of equal diameter. The order of magnitude is in agreement with the planar etch rate of silicon in concentrated HF solutions (see Chapter 7). The real chemical dissolution rate of PS should be larger than that of a flat surface due to the large amount of lattice defects associated with PS. The chemical dissolution during PS formation is responsible for the dissolution valence lower than 2 (Fig. 8.7[41]) and the change of PS density with depth, particularly for lowly doped material.

8.3. MORPHOLOGY

8.3.1. General

Morphology, which is determined by the distribution of materials in space, is the least quantifiable aspect of a material. It is thus very difficult to characterize morphology of PS, which has extremely rich details with respect to the range of variations in pore size, shape, orientation, branch, interconnection, and distribution. Qualitatively, the diverse morphological features of PS reported in the literature can be summarized by Fig. 8.19 with respect to six different aspects: pore shape, pore orientation, shape of a pore bottom, fill of macropores, branching, and depth variation of a PS layer.

The condition for PS formation is determined by current density and HF concentration and is essentially independent of the condition of the silicon substrate as described in Section 8.2.2. The morphology of PS, on the other hand, is determined by all factors involved in anodization, particularly the factors related to the substrate. For example, doping concentration, which does not affect the nature of electrochemical reactions, is a principal factor determining the morphology of PS.

Thus, the morphology of PS can be roughly grouped, according to the type and concentration of doping, into four main categories: (1) moderately doped *p*-Si (10^{15}–10^{18}), (2) highly doped *p*-Si and *n*-Si ($>10^{19}$), (3) *n*-Si ($<10^{18}$), and (4) lowly doped *p*-Si ($<10^{15}$). The PS formed on moderately doped *p*-Si has extremely small pores ranging typically from 1 to 10 nm. The pores are highly interconnected as illustrated in Fig. 8.19(5f). For heavily doped *p* and *n* types, the pores have diameters typically ranging from 10 to 100nm. The pores show clear orientation and are less interconnected as illustrated in Fig. 8.19(5e). For *n*-Si, the pores, with a wide range of diameters from 10 nm to 10 μm, are generally straight and clearly separated as shown in Fig. 8.19(5a–d). For lowly doped *p*-Si, the PS can have two distinctive and continuous pore diameter distributions: large pores on the order of micrometers and small pores on the

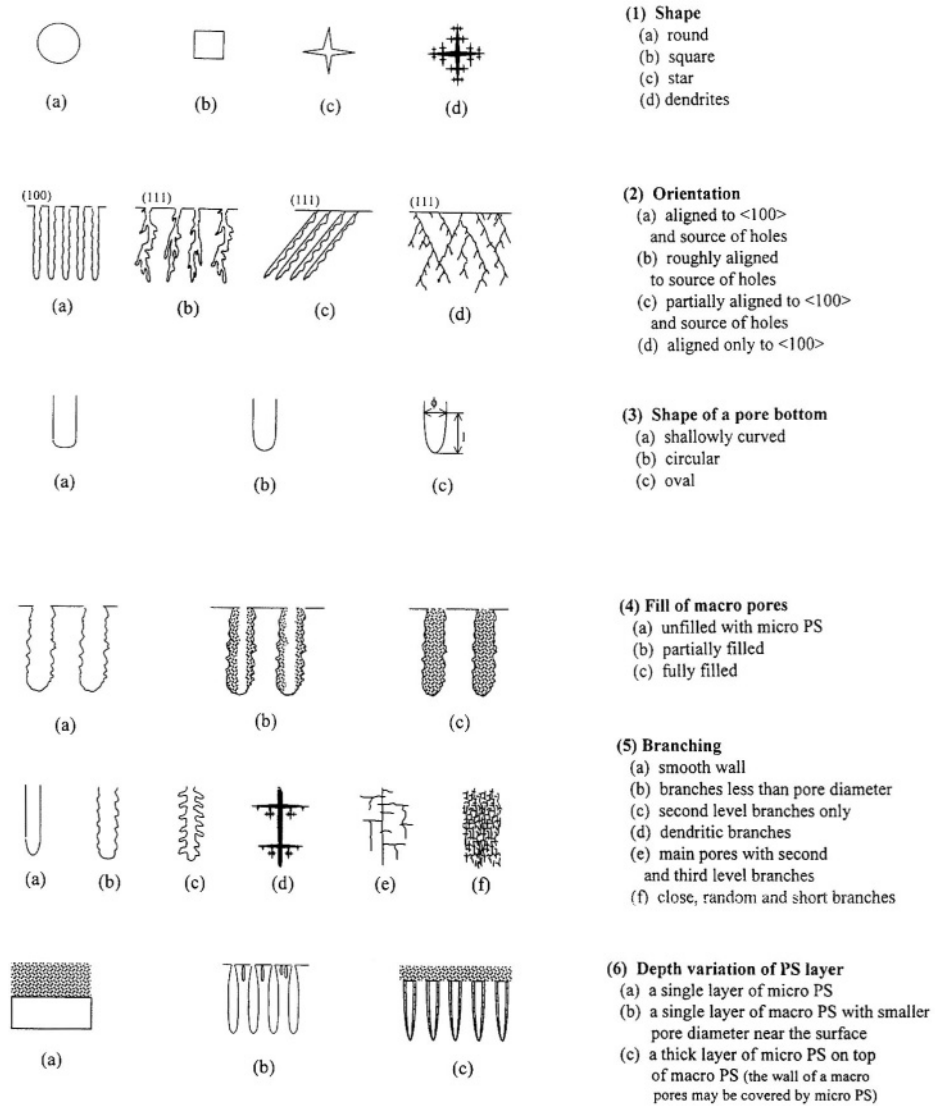

FIGURE 8.19. Schematic illustration of the morphological features of PS.

order of nanometers as shown in Fig. 8.19(6c). The large pores can be fully or partially filled by the small pores as shown in Fig. 8.19(4a–c).

The morphology of the PS formed on *n*-Si also strongly depends on illumination conditions, that is, intensity, frequency, and direction (front or back). Very different morphologies are produced by front versus back illumination. Back illumination generally produces straight pores, whereas front illumination typically produces a two-layer PS as shown Fig. 8.19(6c).

8.3.2. *Diameter and Interpore Spacing*

Among the morphological features, the average pore diameter of a PS, as a quantifiable and easily measurable parameter, is most commonly determined. Table 8.2 shows the pore diameter and interpore spacing reported for the PS formed under various conditions. Pores can be classified as micropore if the pore diameter is less than 2 nm, as mesopore if it is between 2 and 50 nm, and as macropore if it is larger than 50nm.[12] For simplicity, the pores discussed in this chapter are categorized as only micropores (less than 10nm) and macropores (larger than 50nm). Pores between 10 and 50 nm may be grouped into either micro- or macropores depending on the specific situation.

Effect of Doping. The diameter of pores and interpore spacing, under the same anodization condition, vary with doping type and concentration in a wide range, from about 1 nm to about 10 μm, about 4 orders of magnitude.[60,952,1084,1162] The PS formed on different substrates can be roughly grouped into four main categories according to doping concentration: (1) moderately doped *p*-Si (10^{15}–10^{18}), (2) highly doped p^+-Si and n^+-Si (>10^{19}), (3) *n*-Si (<10^{18}), and (4) lowly doped *p*-Si (<10^{15}). The PS formed on moderately doped *p*-Si has extremely small pores typically from 1 to 10nm. For heavily doped *p* and *n* types, the pores have diameters typically ranging from 10 to 100nm. For *n*-Si, the pores have a wide range of possible diameters from 10nm to 10 μm. For lowly doped *p*-Si, the PS can have two distinct distributions of pore diameters: large pores with a distribution of diameters on the order of micrometers and small pores on the order of nanometers. The effect of doping on pore diameter strongly depends on solution composition, potential, and illumination conditions.

For a given type of pores, pore diameter varies continuously with doping concentration in a continuum. Figure 8.20 shows that for *n*-Si the diameter of the pores increases with the sample resistivity at different current densities.[1084] In contrast, the pore diameter of *p*-Si of moderate or high doping concentrations decreases with increasing doping concentration. Macropores can also form on highly doped *n*-Si and lowly doped *p*-Si under certain conditions.[247,952,1139,1165]

Effect of Potential, Current, and HF Concentration. Pore diameter generally increases with increasing potential and current density.[8,47,50,1084] Figure 8.20 shows that the diameter of pores formed on both *p*-Si and *n*-Si increases with current density over a wide range of doping concentrations.[47,1084] Figure 8.21 shows the cross sectional morphology for lowly and highly doped *p*-Si.[35] Figures 8.22 and 8.23 show that the diameter of the pores formed on nisi increases with potential.[8] Also, the PS formed in or near the transition region according to the *i*–*V* curve tends to have relatively larger pores; macropores can form on highly doped *p*-Si.[2] They are also found on highly doped *n*-Si.[1139]

For a given substrate, the sensitivity of pore diameter to HF concentration strongly depends on the solvent.[247,1027] Figure 8.24 shows that pore diameter decreases with increasing HF concentration.[1086,1140] A wider range of variations in pore diameters can be obtained in organic solvents than in aqueous solutions. For example, it has been found that under the same conditions, macropores can form in organic solutions but may not in aqueous solutions.[1139]

TABLE 8.2. Pore Diameter, Interpore Spacing, and Pore Density of the PS Formed under Different Conditions[a]

Material, Ωcm	Solution, % HF	Current, mA/cm^2	Diameter, μm	Spacing, μm	PS density, %	Ref.
p						
(100)						
0.001	20	100	0.05	0.01		4
	49	10	0.009			60
0.005	20	100	0.03	0.015		624
0.006	33	50	0.005			156
	24 + 47% eth[b]	200	0.002	0.0015		762
0.01	40 + 2 g/l CrO_3	OCP	~0.04	~0.02		764
	10	10	0.0052		69	47
	25	10	0.0024		37	47
	25	80	0.004		49	47
	25	240	0.0047		63	47
	35	80	0.0024		38	47
	35	240	0.0033		50	47
	40	30	0.006	0.01	69	35
	20	30	0.012	0.015	49	35
	20	100	<0.001		21	35
	69	30	0.006	0.015		572
	49	30	0.012	0.02	23	572
	10	10	0.016			575
0.02	25 + 50% eth	30	0.05	0.02	40	647
0.55	50	100	0.006	0.005	40	647
1	49	30	0.003		41	572
10	49	10	0.001			60
13	2 M HF + MeCN[c]	7	1–2	2–3		248
18	46	1	0.002	0.002		226
20	3	2	1.5–3, MP[d]	1–3		1027
25	48	10	0.0025		64	35
	48	100	0.005		48	35
	20	100	<0.001		36	35
40	20	20	<0.003	<0.003		624
50	10	3	2.4–4, MP	1–2		1027
	10	10	4.5–7, MP	0.5–1.5		1027
	10	30	4.9–9, MP	0–1.5		1027
100	25	20	3–6, MP	0.5	90	952
224	2 M HF + MeCN	7	1–2	0.5–2		136
1000	25	20	5–7.5, MP	1–2	50	952
(111)						
10	50	20	0.004			640
	50:eth (1:3)	20	0.004			640
(110)						
0.01	49	2	0.005			60
0.4	24 + 47% eth	50	0.035	0.01		762
(110)						
0.03	10	10	0.006	0.006		59
15	10	2	1.5–2.5, MP	0.5–1		1027
n						
(100)						
0.002	1	4	0.05	0.05		1153
0.005	49	10	0.004			60

TABLE 8.2. *Continued*

Material, Ωcm	Solution, % HF	Current, mA/cm^2	Diameter, μm	Spacing, μm	PS density, %	Ref.
0.007	15	65	0.004			47
	15	130	0.007		57	47
0.01	5	0.1 V, 15 mA illu.	1–4	0–4		247
0.02	6 in TMAH[e]		0.5	0.1–0.5		1140
	8 in TMAH		0.05	0.1–0.3		1140
0.03	4	4	0.05	0.3–0.8		1139
0.1	49	80	0.06			575
	10	10	0.02			575
	1	4 V	0.08	0.2		8
	1	6 V	0.33	0.64		8
	1	8 V	0.44	0.2		8
	5	6 V	0.14	0.44		8
	49	10	0.007			60
	20	50	0.009	0.03		46
	10	10	0.02			60
	20:60, HF:eth	50 mA	0.08	0.1		4
	20	50 mA	0.1	0.1		4
1	2.5	0.5, 10 V, illu.B[f]	0.6	6.9		763
2.6	10:35, HF:eth	10 mA illu.	0.3	0.2–0.6		140
3	10:35, HF:eth	1.2 V, 5 mA illu.	0.33	1–2		10
	10:35, HF:eth	1 V, 10 mA illu.	0.1	1		10
5	49	100	0.3			60
	5	0.1 V, illu. 15 mA/cm^2	2–3.5	2–5		247
	6	3 V, 10 mA illu.B	2.5	5		12
	3	5 V, illu.B	0.3	1		12
	2.5	3 V, 5 mA illu.B	2.2	1.3		12
	5	–0.4 V, 12 mA illu.B	3.5	~0		12
	5	–0.2 V, 12 mA illu.B	3.5	3.5		12
	5	0 V_{Pt}, 12 mA illu.B	1.6	1.6		12
	5	2 V, 12 mA illu.B	1.6	1.6		12
10	20:60, HF:eth	50 mA	0.8	>0.5		4
20	2.5	1.5, 10 V, illu.B	2	5.5		763
80	2.5	1.33, 1 V, illu.B	10	20		763
(111)						
0.01	12–48	20	0.01			53
0.008	25:50, HF:eth	50	0.01	0.03		1084
2.5	50	30, 7 mW	1.5			36
	50	30, 54 mW	0.3			36
	50	90, 54 mW	1.7			651
(110)						
0.82	49	80	0.01	0.1		59
	2	5, 21 V	4	2		1153
	10	0.5	0.1	1		1153
	10	5, 45 → 8 V	0.3	1.2		1153
	10	50, → 13 V	3.5	4		1153
3	4	4, 1.5 V	2–4	1–2		1027

[a]Values are listed in ascending order of the resistivity of the silicon substrate.
[b]eth, ethanol.
[c]MeCN, acetonitrile.
[d]MP, macropores of two-layer PS.
[e]TMAH, tetramethylammoniumhydroxide.
[f]B, back side.

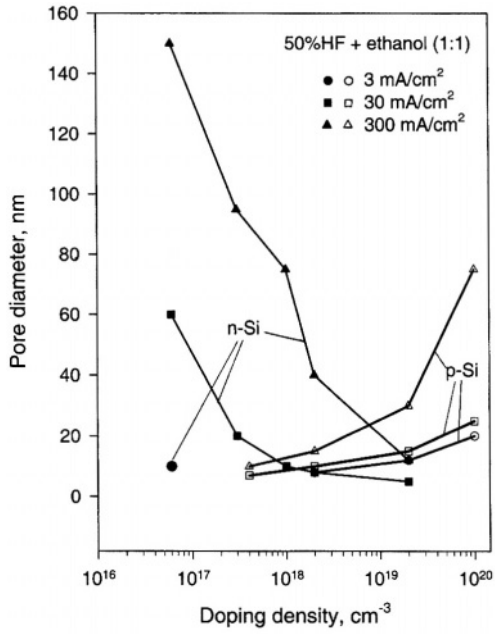

FIGURE 8.20. Pore diameter of the PS formed in 50% HF + ethanol (1:1) as a function of doping concentration and current density. Data from Ref.[1084]

Primary and Branched Pores. The branched pores are significantly smaller than the primary pores.[35,60,575,1126] The hierarchical pore structure has been found to be universal to the PS formed on all types of substrates.[575]

Pore Arrays. Straight large pores with smooth walls can be formed by back side illumination of *n*-Si of (100) orientation.[12,763,768] Using micropatterning for pore initiation sites (micro processed pits), regularly spaced pore arrays can be produced. Production of pore arrays of $2\,\mu m$ in diameter up to $400\,\mu m$ deep on a 6-inch wafer has been reported.[1169] Well-aligned pore arrays have not been obtained on [111] and [110] wafers due to the misalignment between the direction of pore growth and that of the hole source.[768]

Under given formation conditions, the pore diameter beyond the surface region reaches a certain size determined by the formation conditions (i.e., HF concentration, current density, potential, and doping concentration) and is generally constant with increasing depth. According to Lehmann and Grüning[768] as shown in Fig. 8.25, the smallest possible pore diameter for a regular pore array is about $0.3\,\mu m$, below which branching at the side of the pore bottom occurs. The largest pores are found to be about $20\,\mu m$, above which formation of straight and smooth pores becomes a problem due to hydrogen bubble formation. The diameter of the macropores formed on *n*-Si is proportional to $(i/J_1)^{1/2}$.[12] Because $J_1 \propto [\mathrm{HF}]^{1.3}$,

$$\Phi = Ai^{1/2}[HF]^{-1.3} \tag{8.3}$$

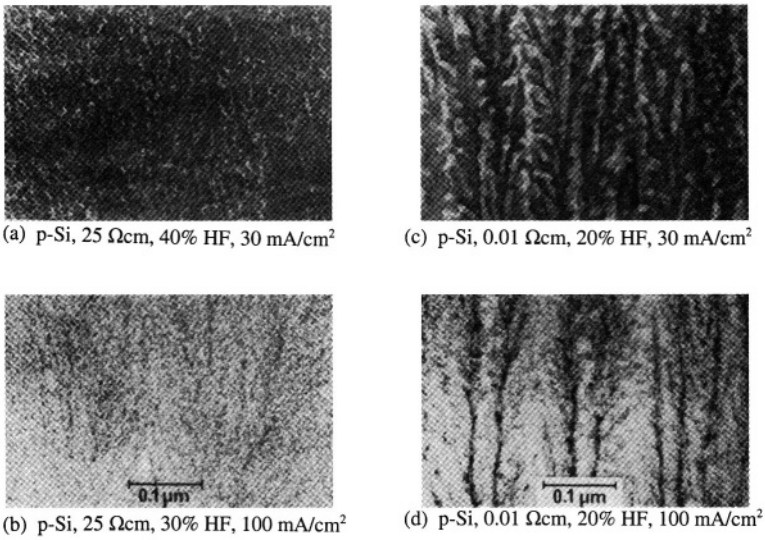

(a) p-Si, 25 Ωcm, 40% HF, 30 mA/cm^2

(c) p-Si, 0.01 Ωcm, 20% HF, 30 mA/cm^2

(b) p-Si, 25 Ωcm, 30% HF, 100 mA/cm^2

(d) p-Si, 0.01 Ωcm, 20% HF, 100 mA/cm^2

FIGURE 8.21. Cross sectional morphology of PS formed on *p*-Si (a) 25 Ωcm, 40% HF, 30 mA/cm^2 (b) 25 Ωcm, 30% HF, 100 mA/cm^2 (c) 0.01 Ωcm, 20% HF, 30 mA/cm^2 (d) 0.01 Ωcm, 20% HF, 100 mA/cm^2. (Reprinted from Beale *et al.*[35] © 1985, with permission from Elsevier Science.)

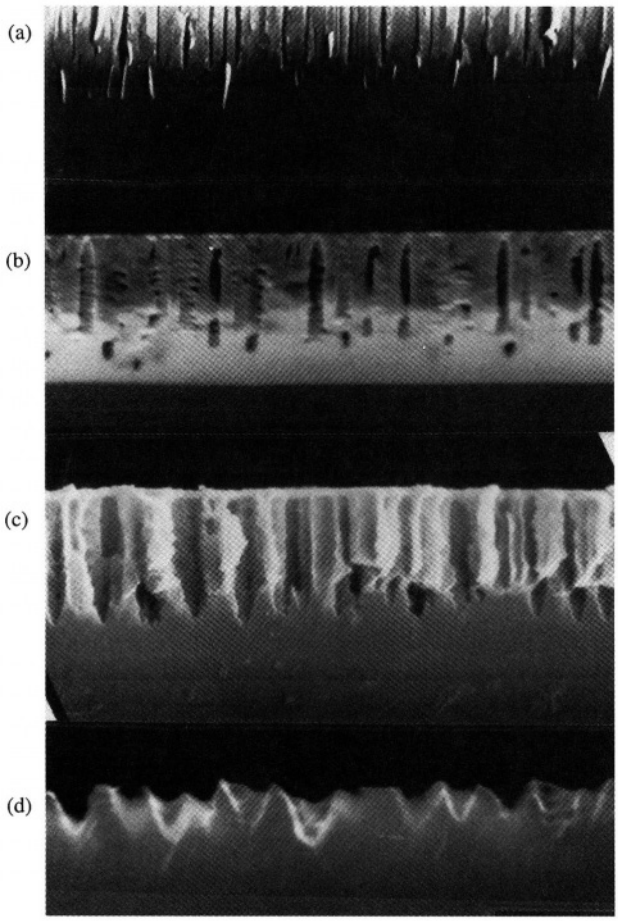

FIGURE 8.22. Cross-section morphology of PS layers formed in 1% HF solution at different potentials. After Zhang.[8] (Reproduced by permission of The Electrochemical Society, Inc.)

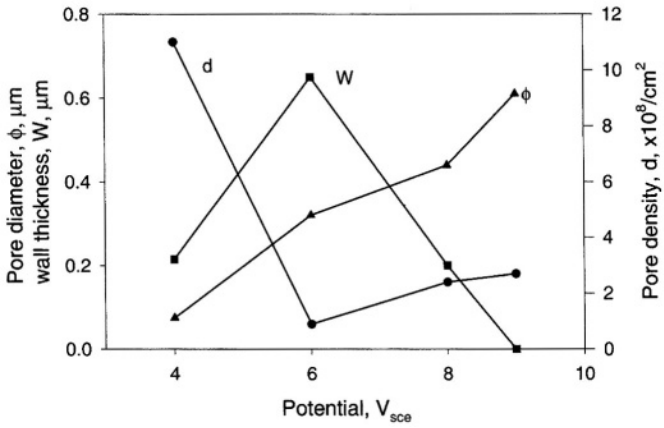

FIGURE 8.23. Average diameter (ϕ), wall thickness (W), and pore density (d), as a function of potential for the PS layers formed in 1% HF solution. After Zhang.[8] (Reproduced by permission of The Electrochemical Society, Inc.)

where A is a constant. Also, there is a power law relationship, $\Phi = N_d^{0.42}$, existing between pore diameter and doping concentration for the formation of stable pores (deep pores without pore branching or dying).

Variation from Surface to Bulk. The pores at the surface are smaller than those in the bulk of PS as, for example, shown in Fig. 8.26.[8,37,40] Such an increase in pore diameter from the surface to the bulk is due to the transition from pore initiation to steady growth. Also, the walls of macropores may be covered with a layer of micropores, i.e., two-layer PS, on illuminated n-Si or on very lowly doped p-Si. On illuminated n-Si samples, a micro PS layer exists on the surface of the large pores

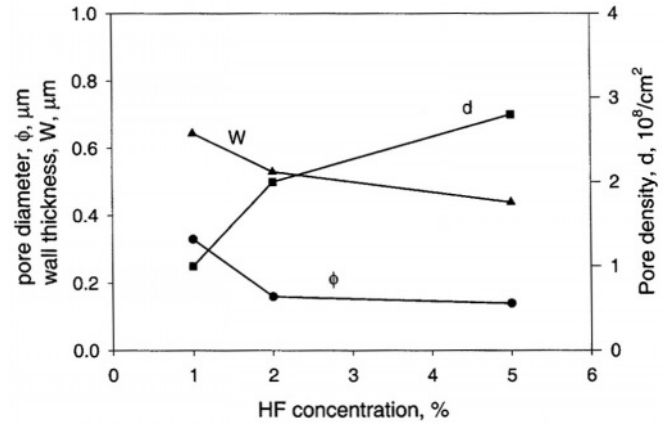

FIGURE 8.24. Pore diameter ϕ, wall thickness W, and pore density d at 6 V as a function of HF concentration. After Zhang.[8] (Reproduced by permission of The Electrochemical Society, Inc.)

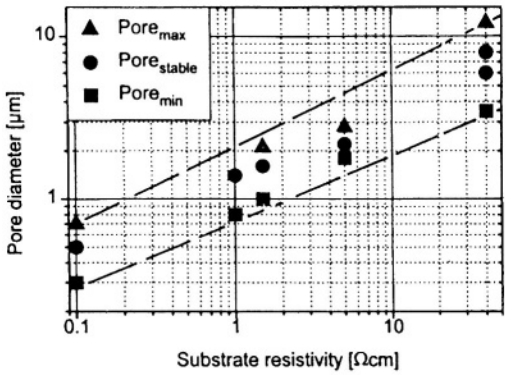

FIGURE 8.25. The relationship between pore diameter and *n*-type doping density of the silicon substrate for stable formation of macropore arrays. The upper and lower limits of stable pore formation are shown as a function of substrate resistivity (dashed lines). (Reprinted from Lehmann and Grüning.[768] © 1997, with permission from Elsevier Science.)

formed.[10,12,16] The pore diameter of this micro PS layer is less than 2nm and the thickness of this layer changes with illumination intensity and the amount of charge passed.[16] Also, the diameter of macropores on front-illuminated *n*-Si changes with the amount of charge passed.[763] The pore size and depth variation of PS on *n*-Si are very different for front- and back-illuminated samples. The diameter of pores on two-layer PS will be further discussed in Section 8.3.6.

For very deep pores the diameter may start to increase with a decreased growth rate due to the effect of the diffusion process in the pore electrolyte. The depth at which this occurs depends on current density and HF concentration. Figure 8.27 shows that the maximum depth of pores formed on back-illuminated *n*-Si without changing of

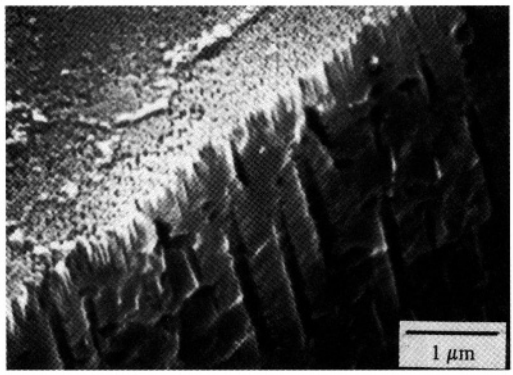

FIGURE 8.26. SEM photograph showing smaller pore diameter and large pore density near the surface than in the bulk in 5% HF at 6 V. After Zhang.[8] (Reproduced by permission of The Electrochemical Society, Inc.)

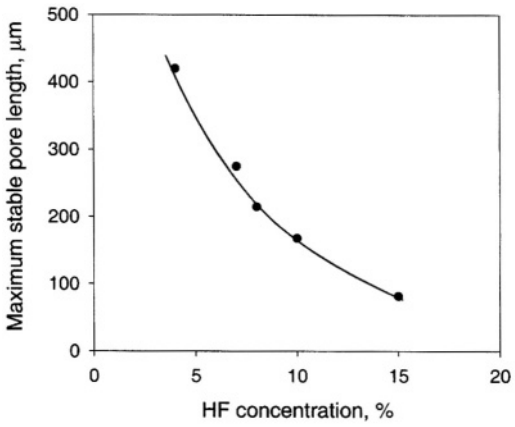

FIGURE 8.27. The maximum pore depth that can be achieved without a degeneration at the pore tips as a function of electrolyte concentration (with surfactant) for cylindrical pores. (Reprinted from Lehmann and Grüning.[768] © 1997, with permission from Elsevier Science.)

morphology decreases with increasing HF concentration.[768] Low HF concentration, low temperature, and low growth rate favors formation of deep uniform pores.

Interpore Spacing. The variation of interpore spacing or wall thickness is more complex than pore diameter and there is much less information on the correlation between wall thickness and formation conditions. Interpore spacing depends on the formation conditions such as applied potential and HF concentration rather differently than does pore diameter.[8,1084] In general, the walls are on the same order as or smaller than the pore diameter. The wall is thin in the PS of small pores but may also be thin in the PS of large pores. In particular, the interpore spacing depends on potential; it increases with potential at small currents but at a certain current it starts to decrease with increasing potential. When the spacing is reduced to zero, pores no longer form, and instead, shallow pits form as shown in Fig. 8.22(d).

Distribution of Pore Diameter. Pore diameters of the PS layer formed under a given set of conditions have a distinct distribution. Normal, log-normal, bimodal, fractal, and nonuniform distributions have been found for the PS formed under different conditions.[16,47,133,772,767,780,856]

Figure 8.28 shows the pore size distributions for the PS formed on highly doped *p*-Si at different current densities.[47] For the PS formed on heavily doped silicon, the pores at a given HF concentration have a narrower distribution at lower current; at a given current density, the distribution is narrower at lower HF concentrations. A bimodal distribution of pore diameter is generally associated with two-layer PS on lowly doped *p*-Si and illuminated *n*-Si. The PS formed on *p*-Si has also been found to have a bimodal distribution of particles sizes: small spherically shaped particles with a diameter of a few nanometers and large cylindrically shaped particles oriented with their axis perpendicular to the surface.[771,772] The distribution of pore size with multiple peaks may be attributed to the fact that PS may have a surface micropore layer and smaller branched pores.[133,780] Due to the hierarchical structure of the branched pores, the distribution of pore diameters for highly branched PS is found to be fractal-like.[60,575]

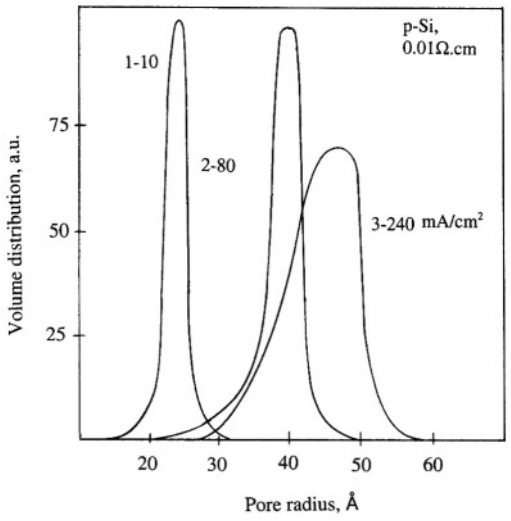

FIGURE 8.28. Pore size distribution for PS formed on heavily doped *p*-Si, 0.01 Ωcm in 25% HF at (1) 10, (2) 28, and (3) 240 mA/cm^2. After Herino *et al.*[47] (Reproduced by permission of The Electrochemical Society, Inc.)

Illumination during formation of PS on *p*-Si has been found to affect the distribution of pore diameter; it increases the amount of the smaller nanocrystals, while reducing the amount of larger crystals.[1124] For the PS formed under an illuminated substrate, the relative amount of small crystals is found to increase with reduction of light wavelength.[774]

Pore Density. The density of pores is determined by the diameter and pore spacing, and depends on any factors that have an effect on the diameter and spacing. Figure 8.29 is a summary by Lehmann *et al.*[1084] of pore density as a function of doping concentration. It shows that except for micro PS (less than 2nm in size) the density of pores increases with doping concentration. Generally, the density of pores increases with decreasing pore size.

The density of pores is generally higher near the surface than in the bulk.[8,1133] At the growing front of PS in the bulk, the pore density is independent of the initial surface condition. For example, for the bulk pores formed on *n*-Si with patterned initiation sites under back illumination the pores will merge or branch from the initially patterned pores depending on the specific conditions.[763]

Figure 8.24 shows that for the PS formed on *n*-Si in the dark pore density increases with increasing HF. Pore density also increases with increasing temperature.[1133] Figure 8.30 shows that for the PS formed on back-illuminated *n*-Si, the pore density in the transition phase increases with increasing potential for different doping levels; high potential favors nucleation of pores. Figure 8.31 shows that the stable growth-phase pore density increases with potential for highly doped material but decreases with potential for lowly doped. Such a dependence of pore density on doping can be explained using the data in Fig. 8.23, namely, the pore density decreases with increasing potential at low potentials due to increase of the space charge layer thick-

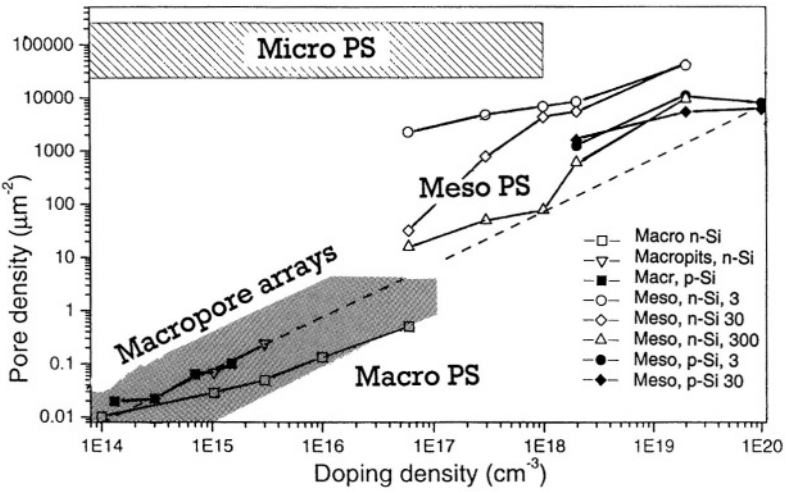

FIGURE 8.29. Pore density versus silicon electrode doping density for PS layers of different size regimes. The PS are formed in 6% HF or 1:1 mixture of 50% HF and methand. The mesopore formation current density (in mA/cm^2) is indicated in the legend. The pore density of micropores and mesopores was calculated from pore diameter and porosity. The dashed line shows the pore density of a triangular pore pattern with a pore pitch equal to twice the width of the space charge layer at 3 V. Note that only macropores on *n*-type substrates may show a pore spacing significantly exceeding the SCL width. The regime of stable macropore array formation is indicated by a dot pattern. (Reprinted from Lehmann *et al.*[1084] © 2000, with permission from Elsevier Science.)

ness but decreases with potential at high potentials due to the reduced wall thickness. The pore density decreases with potential (Fig. 8.31) because the PS on the more highly doped substrate was obtained near the transition region (see Fig. 5.3), where the wall thickness decreases with increasing potential. On the other hand, for the potential range it is not in the transition region for the lowly doped material and pore density decreases with increasing potential.

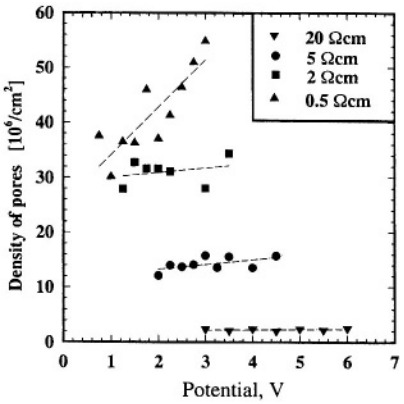

FIGURE 8.30. Density of pores in the redistribution phase as a function of etching potential and the doping level of the material. 5 mA/cm^2, 4% HF after Al Rifai *et al.*[1133] (Reproduced by permission of The Electrochemical Society, Inc.)

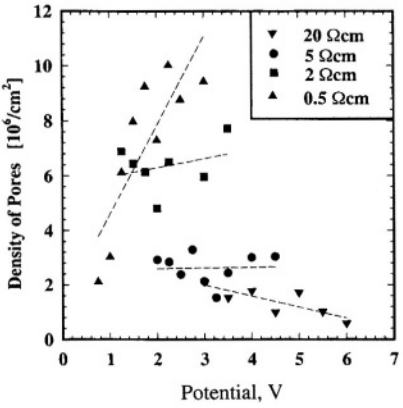

FIGURE 8.31. Density of pores in the stable growth phase as a function of etching potential and doping. The number of pores, as expected, decreases with potential for low-doped material but increases for high-doped material. 5 mA/cm^2, 4% HF after Al Rifai *et al.*[1133] (Reproduced by permission of The Electrochemical Society, Inc.)

8.3.3. Pore Orientation and Shape

The growth of individual pores, or the dissolution at pore tips, is anisotropic and thus depends on the orientation of the substrate. It is also determined by direction of the carrier source; pores tend to grow toward the carrier source. The relative effect of substrate orientation and direction of the carrier source on the orientation of pores is determined by the specific electrochemical reactions at the silicon/electrolyte interface at the pore bottoms under a given set of formation conditions.

The orientation of primary pores is in general in the <100> direction for all of the PS formed on (100) substrate.[36,60,1126] For PS with the dendritic structure shown in Fig. 8.32, pores propagate along the (100) direction even on(110)and(111)substrates.[154,763,1126]

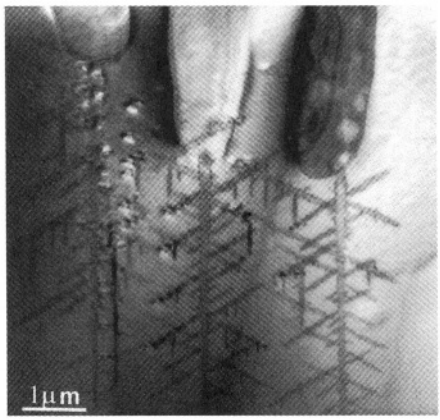

FIGURE 8.32. Dendritic PS morphology formed on n(100), 12 Ωcm in 4% HF at 4 mA/cm^2. After Jäger *et al.*[1126]

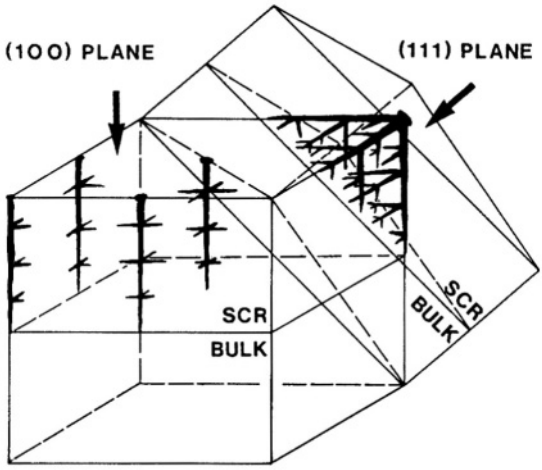

FIGURE 8.33. Schematic illustration of the growth direction of dendritic PS in relation to the crystal orientation of the silicon sample. After Lehmann and Foll.[763] (Reproduced by permission of The Electrochemical Society, Inc.)

Figure 8.33 schematically illustrates the dendritic pore growth along the <100> directions for both (100)- and (111)-oriented substrates.[763] The nondendritic branched pores formed on (100) substrate are not strictly perpendicular to the primary pores but deviate to various extents from the <100> direction toward the source of holes.[35,60,1083] Table 8.3 shows the orientation of the pores observed under different conditions.

Ronnebeck *et al.*[1083] found that the macropores formed on misoriented *n*(100) substrates (5 Ωcm, 2–5 mA/cm^2, 4% HF), from 15° to 35°, as well as on *n*(111) are oriented along the <100> direction when they are formed in the dark at high anodic potentials. However, when the samples are illuminated from the back, the pores formed on the (111) sample and the side pores formed on the 35° misoriented (100) sample are oriented along <113>. Figure 8.34 shows that the orientation of the main pores formed on the substrate 35° from the (100) surface is <100>, while that of the side pores is <113>. According to Ronnebeck *et al.,* crystal defects aligned in the <113> direction are a possible cause of the unusual pore orientation. In another study by the same group of researchers, the pores formed in dimethylforamide (DMF) are principally aligned in the (100) direction independent of the substrate orientation.[1138] Also, while macro pores may grow along the <113> direction on non-(100) substrates, the growth of the highly branched dendritic pores appears to be along the <100> direction independent of substrate orientation.[60,1126]

The dependence on substrate orientation for the macropores formed on *p*-Si is similar to that on *n*-Si.[1085,1138] The macropores formed on *p*-Si in anhydrous HF organic solutions are straight and well oriented along the <100> or <113> direction on substrates of different orientations, while those formed in solutions containing water tend to be perpendicular to the surface (less anisotropic effect) and are poorly aligned. According to Christophersen *et al.*,[1085,1138] the supply of oxygen and hydrogen in the solution are important to the anisotropic growth of pores based on their current burst theory (see next section); oxygen is necessary for smoothing the pore tips, whereas

TABLE 8.3. Orientation of Pores Found in Different PS Layers

Silicon	Solution	Current mA/cm^2	Orientation	Ref.
p				
(100)				
0.006	33%	50	⟨100⟩	156
0.01	10%	10	⟨100⟩	59
	HF + DMSO[a]		⟨100⟩	1085, 1126
(110)				
0.03	10%	10	⟨100⟩	59
15	10%	1	⟨100⟩ + ⟨110⟩, MP[c]	1027
	10%	2	⟨110⟩, MP	1027
(111)				
10	HF in MeCN[b]	10	⟨111⟩, MP	177
	HF + DMSO		⟨113⟩	1085
13	HF + MeCN	4	⟨113⟩	1126
n				
(100)				
0.1	20:60	50	⟨100⟩	4
0.1–10	20:60	50	⟨100⟩	46
0.01–200	2.5%	0.5–10, 1–10 V, illu.	⟨100⟩	763
10^{15}	5%	12, 0.2–2 V, illu.	⟨100⟩	12
1.2×10^{15}	5%	0.1 V, illu.	⟨100⟩, nanolayer	767
15° to (100), 5	4%	2–5, 1.5–5 V, back illu.	⟨100⟩	1083
35° to (100), 5	4%	2–5, 1.5–5 V, back illu	⟨100⟩, side pore ⟨113⟩	1083
	4%	2–5, 40–60 V	⟨100⟩	1083
(111)				
0.6–2.5	50%	30–150, illu.	⟨100⟩	36
0.09	49%	10	⟨100⟩	59
(110)				
0.82	49%	80	⟨100⟩	59
	10%	5	⟨100⟩	1153
5	4%	2–5, 1.5–5 V, back illu.	⟨113⟩	1083
	4%	2–5, 40–60 V	⟨100⟩	1083
(110)				
3	4%	4	⟨100⟩	1027

[a]DMSO, dimethylsulfoxide.
[b]HF in organic: 2 M HF + 0.25 M TBAP + 2.4 M H_2O in MeCN.
[c]MP, macropores of two-layer PS.

hydrogen is the decisive factor for the anisotropic growth and passivation of macropore side walls.

Large pores tend to have less anisotropic effect and grow more dominantly in the direction of carrier supply, namely, perpendicular to the surface. On the other hand, for pores of extremely small diameters, on the order of a few nanometers, the direction of individual pores is not well defined. The macropores formed on *p*-Si generally have smooth walls and an orientation toward the source of holes that is perpendicular to the surface even on (110) and (111) samples.[177,1027]

Depending on the orientation of the substrate and formation conditions, the cross section of individual pores may have different shapes as illustrated in Fig. 8.19(1),

which reflects the orientation-dependent dissolution nature of the reactions. The shape of the pores formed on (100) substrate is a square bounded by {011} planes with corners pointing to the <100> directions.[46,60] The shape of individual pores formed on *n*-Si tends to change from circular to square to starlike and to dendritelike with increasing potential.[763] Low formation voltage tends to favor circular shape and high voltage, starlike shape. Near-perfect square shape of pores can be obtained for the PS formed on *n*-Si at a certain current density, HF concentration, anodic bias, and illumination intensity. For macropores formed on lowly doped *p*-Si the shape of pores tends to be round at low current densities but tends to be square at high current densities on a (100) substrate and triangular on a (111) substrate.[177]

The bottom of pores is always curved, varying from a shallowly curved semicircle to an elongated cone depending on the formation conditions as pictured in Fig. 8.22.[8,10,12,763] Table 8.4 shows that the shape of pore bottoms, in terms of the ratio of the length to the diameter, can vary from as small as 0.3 for very shallow bottoms to as large as 5 for highly elongated bottoms. As will be discussed in Section 8.6, the curvature of the pore bottom is a principal factor in the reaction kinetics required for formation of PS and its morphology.

8.3.4. Pore Branching

As illustrated in Fig. 8.19(5), individual pores, depending on the formation conditions, may propagate straight in the preferred direction with very little branching or with formation of side pores. In general, the conditions that favor the formation of small pores

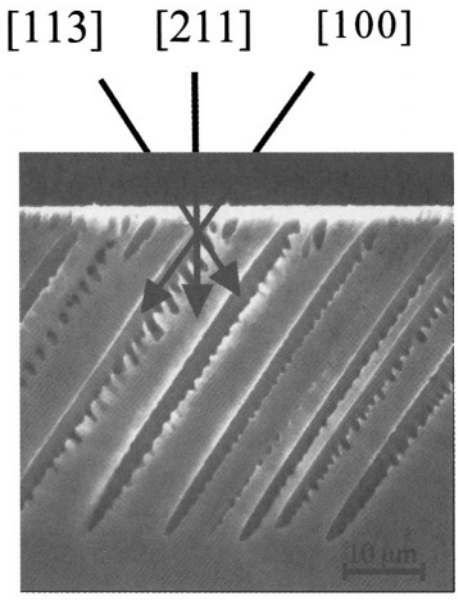

FIGURE 8.34. Preferential growth of pores *n*-Si misoriented 35° from (100) surface with back illumination. After Ronnebeck *et al.*[1083]

TABLE 8.4. Shape of Individual Pore Bottoms Observed for the PS Formed under Different Conditions

Material	Solution	i or V	Φ, μm	l/Φ[a]	Ref.
***n* (100)**					
$10^{15}/cm^3$	5% HF	$2\,V_{Pt}$, 12 mA/cm², B.illu.[b]	1.6	0.64	12
	5% HF	$0\,V_{Pt}$, 12 mA/cm², B.illu.	1.6	1.0	12
	5% HF	$-0.2\,V_{Pt}$, 12 mA/cm², B.illu.	3.7	0.85	12
$10^{17}/cm^3$	1% HF	$8\,V_{sce}$	0.43	1.8	8
	49% HF	80 mA/cm²	0.02	0.5	60
20 Ωcm	2.5% HF	$10\,V_{Pt}$, 1.5 mA/cm², B.illu.	2.0	4.0	763
80 Ωcm	2.5% HF	$1\,V_{Pt}$, 1.3 mA/cm²	10	0.93	763
0.4 Ωcm	2.5% HF	$14\,V_{Pt}$, 10 mA/cm², F.illu.	0.23	0.63	763
$3 \times 10^{17}/cm^3$	25:50, HF:eth	300 mA/cm²	0.1	1.4	1084
$6 \times 10^{16}/cm^3$	6% HF	30 mA/cm²	0.4	2.0	1084
$2 \times 10^{18}/cm^3$	6% HF	30 mA/cm²	0.2	0.3	1084
3 Ωcm	10:35, HF:eth	5 mA/cm², F.illu.	0.07	4.0	10
$10^{15}/cm^3$	5% HF	15 mA/cm², $0.1\,V_{sce}$, F.illu.	2.0	1.3	247
$4 \times 10^{18}/cm^3$	5% HF	15 mA/cm², F.illu.	0.25	1.0	247
3 Ωcm	12:25%, HF:eth	10 mA/cm², F.illu., high I_0	1.5	1.0	16
	12:25%, HF:eth	10 mA/cm², F.illu., low I_0	0.2	2.3	16
40 Ωcm	4% HF	5 mA/cm², 2 V, B.illu., 8-μm spacing	8.0	0.5	1027
	4% HF	1.6 mA/cm², 2 V,B.illu., 48-μm spacing	10	5.0	1027
n(111)					
5 Ωcm	4% HF	2–5 mA/cm², B.illu.	2.0	0.5	1083
n(110)					
3 Ωcm	4%HF	4 mA/cm², 1.5 V, B.illu.	3.6	0.8	1027
***p*(100)**					
10 cm³	25:50, HF:eth	300 mA/cm²	0.08	0.3	1084
50 Ωcm	10% HF	30 mA/cm²	7.5	0.8	1027
	10% HF	10 mA/cm²	6.3	0.6	1027
	10% HF	3 mA/cm²	5.0	0.4	1027
20 Ωcm	3% HF	2 mA/cm²	3.5	0.9	1027
50 Ωcm	10% HF	2 mA/cm², 16-μm spacing	13	0.7	1027
	10% HF	2 mA/cm², 8-μm spacing	6.5	0.7	1027
10 Ωcm	2 M HF + 2.4 M H_2O in MeCN	10 mA/cm²	1.5	0.4	177
224 Ωcm	2 M HF in MeCN	7 mA/cm²	1.3	2.0	136
13 Ωcm	2 M HF in MeCN	7 mA/cm², $2.25\,V_{sce}$	1.2	1.9	248
100 Ωcm	25% HF	20 mA/cm²	4.0	0.4	952
p(110)					
15 Ωcm	10% HF	1 mA/cm²	3.0	0.6	1027

[a] l/Φ, ratio of the length to the diameter of the curved pore bottom.
[b] B.illu., back side illuminated; F.illu, front side illuminated.

also favors branching. Thus, branching is increased with decreasing current density which generates smaller pores.[763]

The degree of branching and interpore connection, similar to pore diameter, depends strongly on doping concentration. The most highly connected PS is found in the PS of lowly doped *p* type and the micro PS of illuminated *n*-Si, on which the pores are extremely small, less than a few nanometers.[60] On the other hand, well-separated and straight pores are generally found on moderately or lowly doped *n*-Si. Under certain

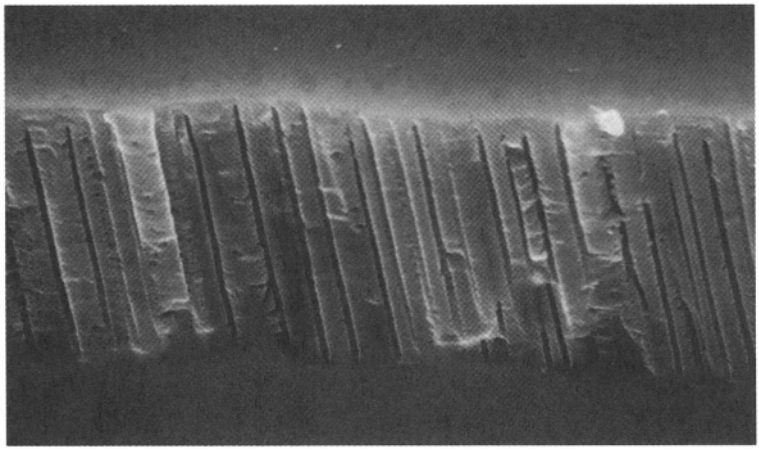

FIGURE 8.35. Straight pores with smooth wall formed on *n*-Si in the dark in 2% HF at 6 V.[1153]

conditions, perfectly straight pores with smooth walls can be formed on *n*-Si in the dark, as, for example, shown in Fig. 8.35.[1153] Also, on *n*-Si smooth and straight pores without branching can be obtained under back illumination using a surface-patterned substrate. On p^+ and n^+ samples, the pores grow perpendicular to the silicon surface with many secondary pores on the sides of these pores which sometimes results in branching.[35,572] The macropores formed on lowly doped *p-Si* generally have no side pores longer than the pore diameter.[136,177,1027]

The branches of the main pores are due principally to the tendency for anisotropic dissolution along the <100> direction. Like the main pores the branched pores are highly directional, propagating preferentially in the {100} planes and the long <100> directions.[46,60,763] Such directional branching can produce regularly spaced three-dimensional structures as shown in Fig. 8.36.[1153] The tendency to branch is stronger on (110) and (111)

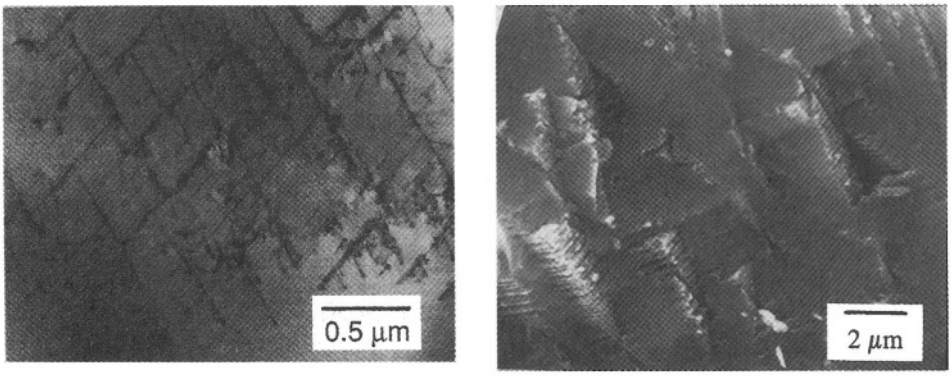

FIGURE 8.36. Three-dimensional porous structures generated by the formation of pores on an *n*(110) substrate. (a) 49% HF, 80 mA/cm^2 (b) 10% HF, 5 mA/cm^2. (Reprinted with permission from Smith *et al.*[60] © 1992, American Institute of Physics.)

substrates than on (100) because for substrates of non-(l00) orientations, no <100> direction coincides with the direction of the hole source. Due to the large tendency to branch, it is difficult to produce straight pores with smooth walls on (110) and (111) samples, even on the surface-patterned samples under back side illumination.[768]

8.3.5. Interface between PS and Silicon

The growth front of a PS layer (not individual pores) is always perpendicular to the surface of the substrate with back electrical contact. The growth front is planar, independent of the orientation of the silicon samples, because the growth of pores depends on the supply of carriers which are transported from the back of the sample. The interface between the PS layer and silicon substrate is essentially flat with a difference between high and low points within a few micrometers.

8.3.6. Depth Variation

The morphology of PS generally varies in the depth direction from the surface to the bulk. There are two types of depth variations: (1) The change of pore diameter near the original surface is gradual from the surface to the bulk where pore diameter is constant as shown in Fig. 8.19(6b); and (2) the change of pore diameter is abrupt from a surface layer to the bulk layer with a difference in diameter as large as three orders of magnitude as shown in Fig. 8.19(6c). The surface layer for the first type is formed due to the initiation of pores and their transition to steady-state growth. The second type is the two-layer PS with a micro PS on top of a macro PS. While two-layer PS forms only under certain conditions, the transition PS layer of varying thickness exists on the surface of all PS layers. Also, for two-layer PS the macropores may be filled to various extents by a micro PS layer as shown in Fig. 8.19(4). Layered PS structure due to the fluctuations in the substrate has also been observed.[779]

Transitional Layer. The transitional layer is formed only on the original sample surface and is associated with the nucleation of pores. It is present on top of the PS of all types of silicon.[8,36,40,763,1084,1133] The pores in the transitional layer are generally much smaller than those in the bulk. There is no clearly definable boundary separating the surface layer and the bulk, the pore sizes gradually changing to those of the bulk. The thickness of the surface layer is related to the size of pores; the smaller the pores, the thinner the surface layer.

For *n*-Si large the transition layer with smaller pores can be clearly seen as for example shown in Figs. 8.26 and 8.37.[8] The distributions of the pores in the transition layer and in the bulk stable growth layer are also different as shown in Fig. 8.38.[1133] On the other hand, for *p*-Si this surface layer is very thin (near zero) for some PS with extremely small pores. Figure 8.39 shows that the surface layer is a function of current.[40] Also, the thickness of this surface layer depends on dopant concentration as shown in Fig. 8.40. The thin transition layer on *p*-Si is denser than the bulk PS.[36,40]

The morphology of the transition layer, unlike the bulk morphology, depends sensitively on surface conditions, particularly surface roughness. For example, pores tend to form along a scratch.[60,154] For *n*-Si, which usually requires a large potential to generate current in the dark, the formation of PS can occur at much lower potentials if

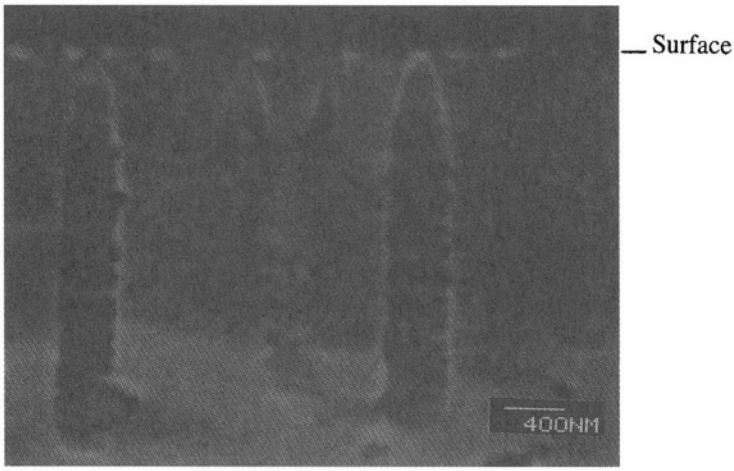

FIGURE 8.37. Variation of diameter of pores from the surface to the bulk, where it is constant, in 1% HF, 6 V, $n(100)$, $10^{17}/cm^3$. After Zhang.[8] (Reproduced by permission of The Electrochemical Society, Inc.)

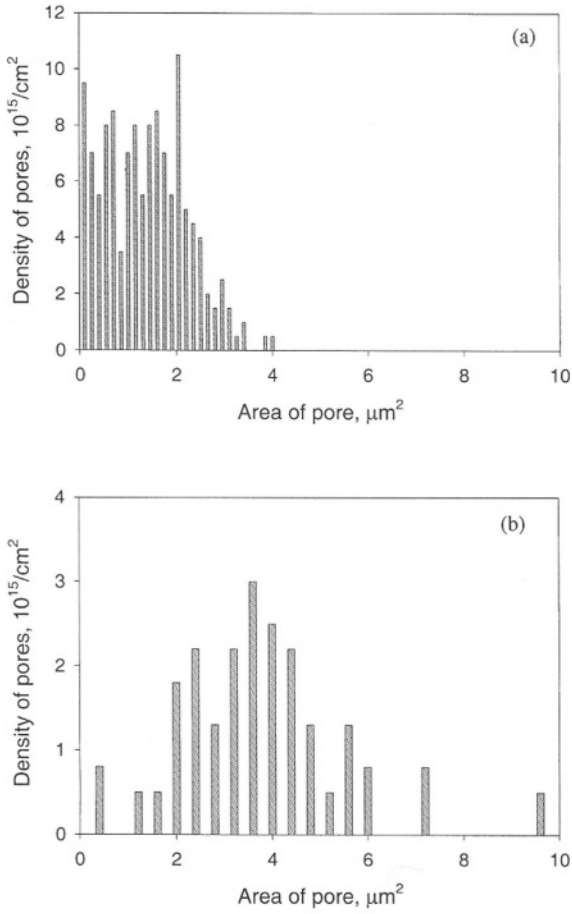

FIGURE 8.38. Histograms for the pore sizes and densities in (a) the nucleation phase and (b) the stable growth phase. After Al Rifai *et al.*[1133]

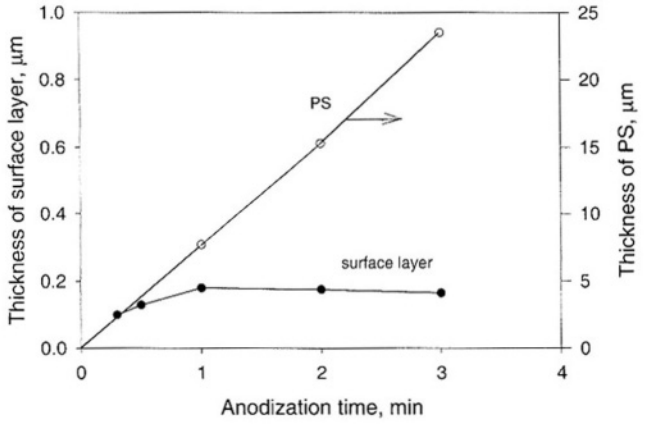

FIGURE 8.39. Thickness of the dense surface layer and PS versus anodization time as a function of anodic current density. P(111), 100 mA/cm^2, 50% HF After Unagami.[40] (Reproduced by permission of The Electrochemical Society, Inc.)

the surface is roughened first by mechanical grinding with sandpaper or by electrochemical polarization at a higher potential. A rough surface provides the sites with small radius of curvature for the initial preferential dissolution because electrochemical reactions on semiconductor surface are sensitive to surface curvature.[8] Different silicon materials show different sensitivity toward scratches of different sizes and sharpness.

A certain amount of uniform dissolution may occur prior to and during the initiation of pores. For example, as reported in one study, before the formation of the macropores on lowly doped p-Si(100) in anhydrous HF–MeCN solutions the entire surface is etched forming (111) facets of about 1 μm.[248] Pores then start to grow at the base of these facets. Once macropores are developed the surface etch rate is greatly reduced, by a factor of 4.

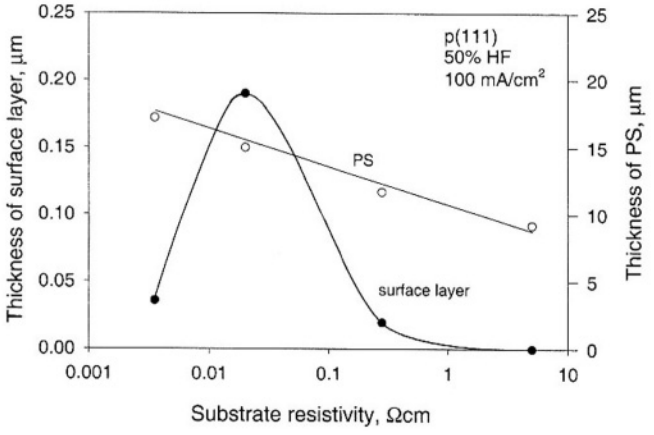

FIGURE 8.40. Dependence of thickness of the dense surface layer and PS on substrate resistivity [p(111), 50% HF, 100 mA/cm^2]. After Unagami.[40] (Reproduced by permission of The Electrochemical Society, Inc.)

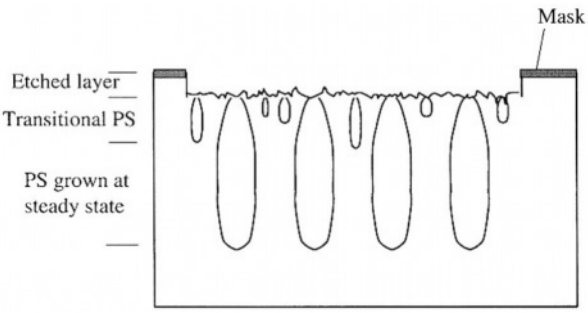

FIGURE 8.41. Schematic illustration of the regions on the sample after formation of a PS layer.

Thus, in general, the dissolution of silicon at an anodic current results in three regions of the silicon substrate which is exposed to the electrolyte as shown in Fig. 8.41. Such an etched layer prior to the initiation of pores is involved in all types of PS because the etching causes roughening of the surface, which is required for pore initiation. The etching phase is associated with the formation of macropores on both *n* and *p* types of silicon and with formation of micropores on *p*-Si.[794,1126] For example, for *n*-Si under back illumination initiation of macropores is preceded by an etching phase. As shown in Fig. 8.42, the thickness of the etched layer increases with increasing substrate resistivity.[1133] The pores are larger on the substrates of higher resistivity and a thicker etched layer is required to generate a higher degree of roughening for pores to initiate. On the other hand, the etched layer depends only very weakly on potential.

Two-Layer PS. Two-layer PS, with a micro PS layer on top of a macro PS layer, can form under certain conditions. For *n*-Si, formation of a two-layer PS is associated with front illumination, although it can also be formed with back illumination.[12,177,247,1027] For *p*-Si, two-layer PS is found to form on lowly doped substrates. For moderately or highly doped *p*-Si or for *n*-Si in the dark, formation of two-layer PS has not been observed.

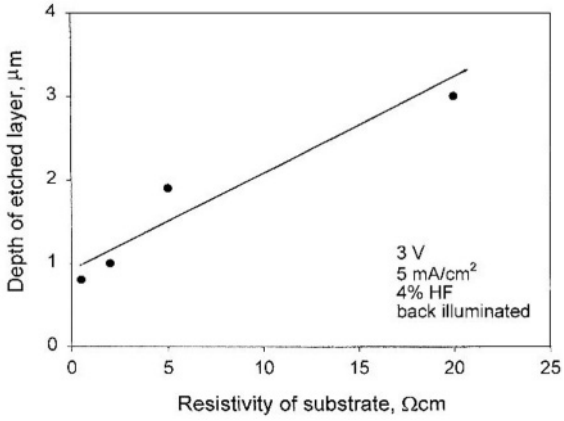

FIGURE 8.42. Etched layer thickness as a function of the substrate resistivity. (Reprinted from Al Rifai *et al.*[1133] © 2000, with permission from Elsevier Science.)

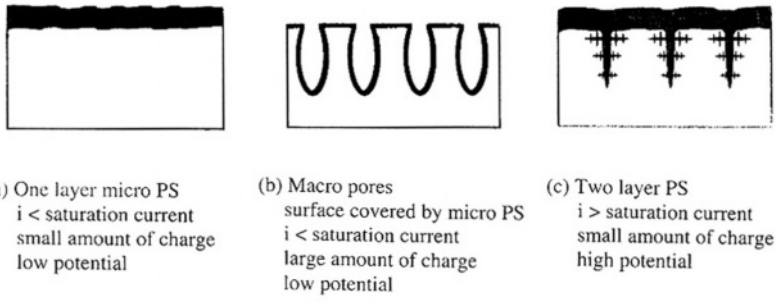

FIGURE 8.43. Three microstructural types observed in PS formed on illuminated *n*-Si. (a) Single-layer (SL), (b) double-layer (DL), and (c) large macropore (LMP) types. After Osaka *et al.*[16] (Reproduced by permission of The Electrochemical Society, Inc.)

Formation of PS of front-illuminated *n*-Si depends on the wavelength of the light; formation of large and deep pores does not occur with a white light at wavelength <800nm, but formation of cylindrical pores occurs at wavelength >867nm.[763] Unfiltered lamp radiation results in large pores covered with micro PS and its depth and shape depend on wavelength distribution. This phenomenon is due to the wavelength-dependent absorption depth; carriers that are generated deep in the bulk promote pore growth at the tips of macropores whereas near-surface generation results in the formation and dissolution of micro PS and lateral growth of the macropores.

The occurrence of the two-layer PS under front illumination depends on light intensity and the amount of charge passed as illustrated in Fig. 8.43.[16] There is a correlation between the occurrence of two-layer PS and the saturation photocurrent value.[10] Only a single micro PS layer forms at photocurrent densities below the photosaturation value whereas a two-layer PS forms at current densities above the saturation current as shown in Fig. 8.44. Also, a macro PS layer forms only after a certain amount of

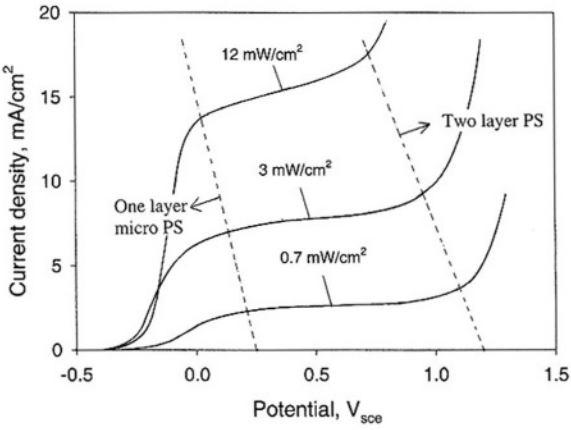

FIGURE 8.44. Voltammograms of *n*-Si electrodes in aqueous solution containing 10 wt % HF and 35 wt % C_2H_5OH at 5 mV/s under different light intensities. The illumination intensity was adjusted by changing the distance between the light source and the *n*-Si electrode. After Osaka *et al.*[10] (Reproduced by permission of The Electrochemical Society, Inc.)

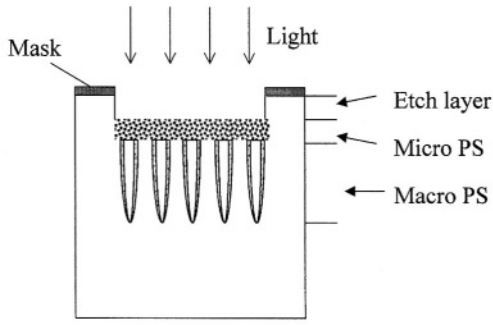

FIGURE 8.45. The three layers that result from formation of PS on illuminated *n*-Si sample: an etch layer, a micro PS layer, and a macro PS layer. The walls of the macropores may also be fully or partially covered with micro PS.

charge determined by the anodization conditions, which is the etch layer required for the initiation of macropores as discussed in the previous section.[247]

There is also an etched layer of Si on the surface of the anodized Si sample under illumination as illustrated in Fig. 8.45. This etched layer, which unlike that in the dark is required for the surface roughening for the initiation of pores, is mainly due to photocorrosion. As a result of the photoinduced dissolution the top surface of the PS layer recedes with time. The rate of dissolution depends on doping, HF concentration, current density, and illumination intensity. Figure 8.46 shows the variation of the three layers with the amount of charges passed; the etched layer on a highly doped sample is thicker than that on a lowly doped material. The thickness of the micro PS decreases while pore diameter and etched layer increase with increasing light intensity. Table 8.5 shows

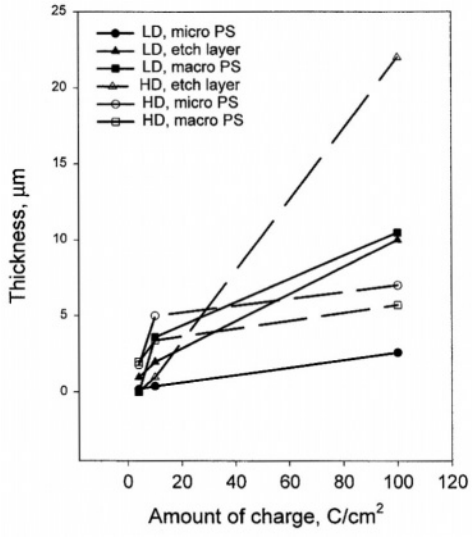

FIGURE 8.46. Variation of the thickness of the etch layer, micro PS, and macro PS on illuminated *n*(100) with the amount of charge passed. After Clement *et al.*[247] (Reproduced by permission of The Electrochemical Society, Inc.)

TABLE 8.5. Correlation between Formation Conditions and Structure of PS on Illuminated *n*-Si[a247]

	Nano PS thickness (μm)			Macropores (μm)		
Contition	Top	Wall	Depth of crater (μm)	ϕ	Depth	Wall
1.2×10^{15b}	1.25	0.2	3	2	4	2
4×10^{18b}	5	0.25	0.5	1	4	0.75
Charge passed	↗	↗	↗	↗	↗	~
Light intensity	↘	↘	↗	↗		

[a] *n*(100), 5% HF, 0.1 V_{sce}, white light from tungsten-halogen lamp.
[b] Amount of charge passed 10 C/cm^2.

an example of the effect of light intensity, HF concentration, and amount of charge passed on the thickness of the three layers.

The micro PS on top of the macro PS formed on *n*-Si under illumination can have a very complex structure. For example, it has been reported that the PS formed on *n*-Si has an irregular and square-shaped framework of pores with interconnected columns of 100–200 nm for lowly doped materials and 100–400 nm for highly doped materials.[767] Bounded to this rigid square-shaped framework and contained within is a finer structure with wirelike structures of sizes varying from 3 to 12 nm. Fractal morphology has been suggested to be associated with the micro PS.

The macropores formed on illuminated *n*-Si, once initiated, can increase in diameter with time without reaching a constant value as shown in Fig. 8.47.[247,763] Also, the diameter of the macropores formed under front illumination increases with increasing HF concentration as shown in Fig. 8.48, in contrast to the case of macropores formed in the dark (Fig. 8.24). The diameter of the macropores increases linearly with increas-

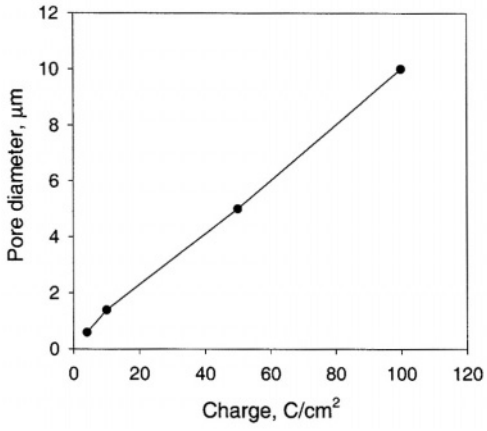

FIGURE 8.47. Variation of the thickness of the nanopore layer for different samples as a function of the amount of charge passed. After Clement *et al.*[247] (Reproduced by permission of The Electrochemical Society, Inc.)

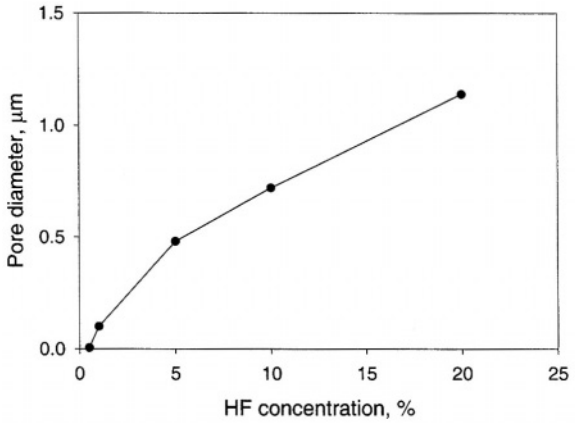

FIGURE 8.48. Variation of the average diameter of the macropores as a function of HF concentration for highly doped $n(100)$, charge passed $Q = 4\,C/cm^2$. After Clement *et al.*[247] (Reproduced by permission of The Electrochemical Society, Inc.)

ing light intensity at low light intensity up to $50\,mW/cm^2$ but changes little at higher intensities up to $400\,mW/cm^2$.

Two-layer PS on back-illuminated *n*-Si can also occur at low potentials (near the OCP) at a current density much lower than J_1 (the current peak of an *i–V* curve).[12] The top micro PS layer disappears with increasing potential (at a constant photocurrent density) and only macropores are formed with their surface covered with micro PS.

The PS formed on *p*-Si generally has micropores, but when the resistivity exceeds a certain value macropores can form underneath a layer of micropores.[177,952,1027] The resistivity at which this occurs depends on the solvent, HF concentration, and current density. In aqueous HF solutions macropores are found to occur on substrates of resistivity higher than $5\,\Omega cm$.[1027] On the other hand, macropores have been found to form on substrates with a lower resistivity of $1\,\Omega cm$ in 2M HF + DMF electrolyte.[177] The pore size of the top layer is similar to the single-layer PS formed on *p*-Si while that of the macropores is on the order of micrometers. The diameter of the macropores and the pore spacing increase with increasing doping concentration. Pore diameter may increase or decrease with increasing current depending on the solution composition, while interpore spacing decreases with increasing current.[177,1027] Presence of water in organic solvents tends to reduce the thickness of the micro PS layer. It has been found that a two-layer PS is formed on lowly doped *p*-Si in anhydrous HF–MeCN solutions, but addition of water results in the formation of only macropores without a top layer of micropores.[1085]

Fill of Pores. The macropores of two-layer PS may be completely filled with micropores or only partially filled depending on the solution composition.[1027,1085] When other conditions are the same, the macropores formed in organic solvents are more filled than those formed in aqueous solutions or mixtures of organic solvent and water. Addition of water to organic solutions reduces the extent of filling. Among organic solutions, according to Jäger *et al.*,[1126] the degree of filling of the macropores formed on *p*-Si depends on the oxidizing nature of the solutions: Macropores are filled with micro

PS in nonoxidizing electrolyte such as acetonitrile (MeCN), whereas they are not filled in oxidizing electrolytes such as DMF. However, it has been reported that the PS on *p*-Si (13 Ωcm) formed in anhydrous HF–MeCN solution has only the macropore layer with no nanometer PS covering the surface of the macropore walls and the sample surface.[248]

For the two-layer PS formed on front-illuminated *n*-Si, the degree of filling of the macropores depends on light intensity, on the amount of charge passed, as well as on the magnitude of the current relative to the saturation photocurrent.[10,16,247,767] The micro PS thickness increases with the amount of charge passed reaching a relative constant value as shown in Fig. 8.49 and it decreases with increasing light intensity.[247] The macropores formed on lowly doped *n*-Si under back illumination can also be filled by micro PS and the degree of filling decreases with increasing potential.[12]

8.3.7. Density and Specific Surface Area

The density of PS can be expressed as absolute density in units of grams per cubic centimeter or relative density (versus single-crystalline silicon) in units of percent. It can also be expressed as porosity which measures the amount of the open space with PS. Thus, the relative density plus porosity equals 1. In many studies the density of PS is determined by a simple gravimetric method of measuring the weight difference before and after anodization and the actual volume of PS.[32,36,48,50] It may also be determined by measuring the volume of liquid capillary absorbed in the pores.[50]

Porosity and density are most often used for characterization of PS in the literature due to their conveniently measurable nature. However, porosity is not a morphological parameter but a quantity, determined by the morphology. A given morphology has a definite density, but a given density may have different morphologies. Thus, porosity or density of PS alone does not specify the morphology of PS. Because

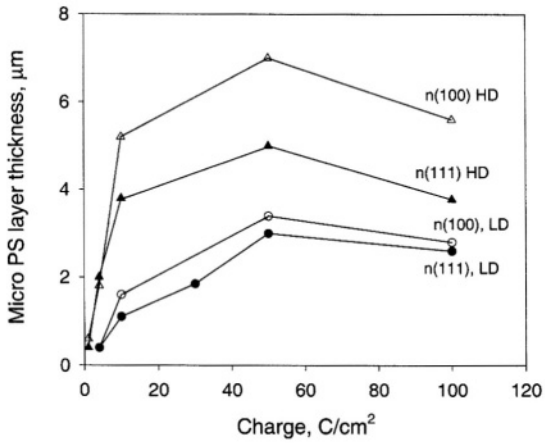

FIGURE 8.49. Variation of the thickness of the nanopore layer for different samples as a function of the amount of charge passed. After Clement *et al.*[247] (Reproduced by permission of The Electrochemical Society, Inc.)

porosity is a parameter that reflects the combined effect of pore diameter and interpore spacing, it may roughly be estimated from average pore size and interpore spacing. Also, while pore diameter and interpore spacing are the properties of individual pores, pore density and porosity are the properties of the PS layer. In essence, the physical and chemical properties of PS are not determined by porosity, although some properties can be correlated with porosity under specific conditions.

The following are some general observations on the effect of various factors on PS density.

1. PS density for both *p* and *n* types increases with increasing HF concentration (Figs. 8.50 and 8.51)[35,41,48]
2. The density of PS formed on *p*-Si decreases with increasing current density as shown in Fig. 8.50.[32,36,50] On the other hand, the density of PS formed on *n*-Si first increases with increasing current density, reaches a maximum, and then decreases as shown in Fig. 8.51.[32,35,36,41] The variation with current density is larger at lower HF concentrations.
3. PS density of *p*-type silicon increases with increasing dopant as shown in Fig. 8.52.[35,36,48] PS density of *n*-Si under front illumination increases with increasing dopant concentration, reaches a maximum at about $10^{16}/cm^3$, and then

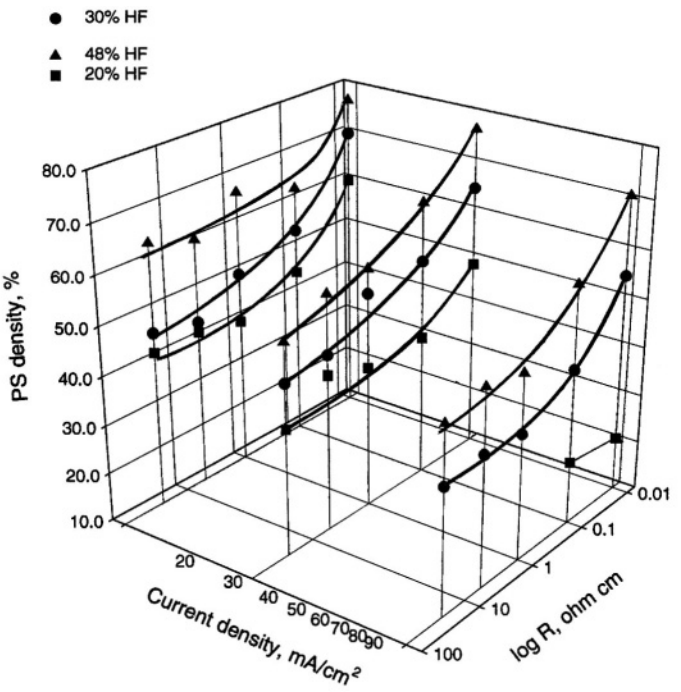

FIGURE 8.50. PS density of *p*-Si as a function of HF concentration, current density, and resistivity. Data from Ref.[35]

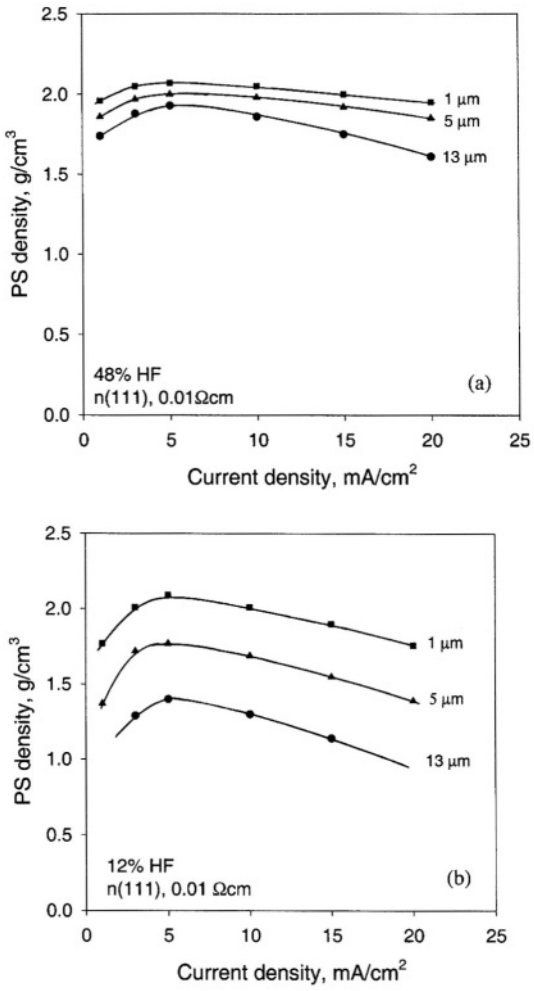

FIGURE 8.51. Dependence of the PS density on the anodic current density for various PS layer thicknesses. (a) 48 wt % HF; (b) 12 wt % HF. After Parkhutik *et al.*[41]

decreases (Fig. 8.52). As shown in Figs. 8.52 and 8.53, except for highly doped materials, *n* type generally has a higher PS density than *p* type.

4. PS density of *n*-Si decreases with increasing illumination intensity as shown in Fig. 8.53.[36]
5. For a given material the dependence of porosity on various factors is similar to that of pore diameter.
6. PS density tends to decrease with increasing anodization time or increasing PS thickness mainly due to chemical dissolution of PS (Fig. 8.51).[12,41,48,287,1133]

Specific surface area is the total physical area per unit volume (e.g., m^2/cm^3), and is a measure of the dispersion of the solid silicon in PS. In contrast to PS density, which is

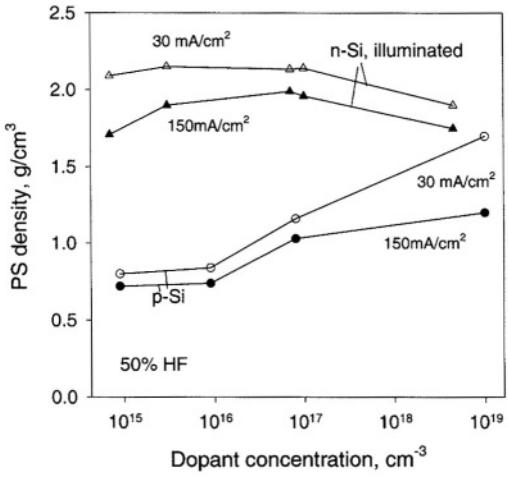

FIGURE 8.52. The effect of dopant concentration on the PS density. After Arita and Sunahama.[36] (Reproduced by permission of The Electrochemical Society, Inc.)

a measure of the total amount of solid in a unit volume, specific area defines how finely the solid is distributed. Because of the small diameter and interpore spacing, the specific area of PS can be extremely high as shown in Table 8.6.

Given the porosity and pore diameter, the specific area of a PS can be roughly estimated, assuming straight circular pores having an average diameter of Φ (cm):

$$A = 2 \times 10^{-4}\, p/\Phi \tag{8.4}$$

where A is the specific surface area (m^2/cm^3) and p is the porosity (%).

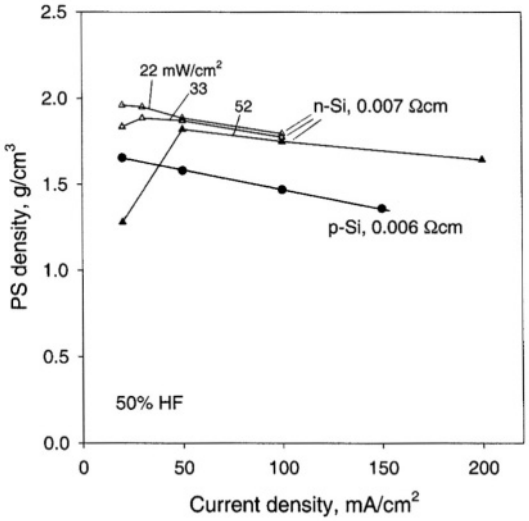

FIGURE 8.53. Effect of current density on the PS density. After Arita and Sunahama.[36] (Reproduced by permission of The Electrochemical Society, Inc.)

TABLE 8.6. Range of Pore Size, Porosity, and Specific Area of 0.01 Ωcm $p(100)$ silicon[47]

[HF], %	i, mA/cm^2	Pore size[a], nm	Porosity[b], %	Specific area, m^2/cm^3
10	10	3.6–7.0	69	200
25	10	1.8–2.8	37	230
	80	2.5–4.4	49	200
	240	3.2–6.4	63	230
35	80	1.7–3.8	38	210
	240	2.1–3.7	50	230

[a]Determined by N_2 adsorption isotherms.
[b]Determined by gravimetric method.

Similarly, pore density (number of pores per unit area) can be estimated as

$$n = p/(\pi\Phi^2) \tag{8.5}$$

As examples, according to the above equations for a PS with a density of 50% and for a pore diameter of 1 μm the specific area is 1 m^2/cm^3 and the pore density is 2.5×10^7/cm^2. For a pore diameter of 2 nm the specific area is 500 m^2/cm^3 and the pore density is 4×10^{12}/cm^2. PS with a specific surface area on the order of 200 m^2/cm^3 can be formed in a wide range of conditions.[35,47,772,1118] Specific area as high as 600–700 m^2/cm^3 can be associated with the PS formed on p-Si.[35,647,1103] This means that an increase on the order of 10^6 in surface area can result from the formation of PS on a solid silicon cube of 1 cm on each side (6 cm^2 in total surface area). Thus, PS exhibits a range of properties characteristic of the large surface area such as high chemical reactivity.

8.3.8. Composition

The composition of PS may deviate greatly from that of pure silicon due to the large surface area, which can be terminated by H, OH, O, or F (see Chapter 2). For macro PS, the ratio of surface silicon atoms to those in the bulk is small and the PS is largely composed of pure silicon with a small amount of adsorbed foreign species. On the other hand, for micro PS, the composition of the PS can be significantly different from the silicon substrate due to the huge surface area adsorbed by foreign species. As an example, assuming that the first layer of atoms on the surface has a thickness of 3 Å, a PS with a specific area of 100 m^2/cm^3 has 0.03 cm^3 of silicon atoms in the form of surface compounds. This represents 5% of the silicon atoms in the PS with a porosity of 40%. It accounts for as much as 50% of the silicon atoms for the PS with a specific area of 500 m^2/cm^3 and a porosity of 70%. Such a PS is essentially a surface of silicon compounds. This simple analysis is in general agreement with experimental observations. On the other hand, the PS formed on n-Si with doping levels from 10^{15}/cm^3 to 4×10^{18}/cm^3, which has large pores and relatively smaller specific area, is almost pure silicon with a small amount of fluorine, hydrogen, and oxygen.[42]

The atomic bonds in as-grown PS in HF solutions for both p and n types of silicon samples are found to consist of Si–H, Si–Si, and Si–O with a few percent fluoride

atoms.[36,1104] The PS formed on lowly doped *p*-Si in HF solution has a high concentration ($>>10^{20}/cm^3$) of H, C, O, and F.[6] The PS near the surface tends to be higher in O content and lower in H indicating that it is oxidized. A high concentration of hydrogen, between $10^{20}/cm^3$ and $10^{21}/cm^3$, is found to be incorporated into the walls of pores and into the bulk Si (from the tips) during PS formation.[794] Penetration depth is determined by the volume diffusion of hydrogen.[1108] Low pH favors hydrogen penetration. The hydrogen can exist in clustered states such as $(SiH_2)_2$ and monomer states such as SiH_2.[130] For the PS formed in HF–MeCN solutions the surface of PS is completely covered by hydride.[136,248] Newly formed mino PS is partially oxidized. It has been found that the extent of oxidation for the PS on lightly doped *p*-Si is on the order of 10% whereas it is much less on heavily doped materials, on the order of 1%.[35] Another study found that for highly doped *p*-Si, there is very little oxide content whereas about 50% of the PS is in the form of oxide for lowly doped *p*-Si.[176] The degree of oxidation of the silicon atoms in PS, in the form of SiO , depends on the region (on an *i–V* curve) it is formed.[770] Oxide content increases with potential approaching the electropolishing region. At the boundary of the PS formation region the oxygen is incorporated as a suboxide $SiO_{0.5}$ and SiO while in the transition region the oxygen is increased in the oxides as $SiO_{1.5}$ and SiO_2. It has been reported that oxygen in the form of oxide exists at the bottom of the pores on p^+ formed in 25% HF + 50% ethanol but not on *p*-Si.[762] The PS formed in the transition region (Fig. 8.5) is mostly composed of anodic silicon oxide.[770]

The amount of Si–O and Si–H bonding varies from the surface to the bulk of the PS. [794,1106] The relative amounts of oxidation states of the silicon atoms in the PS formed on both *p* and *n* types of silicon are affected by illumination and light wavelength.[1124] Also, the amount of oxidation of PS tends to vary with anodization time.[1103]

8.3.9. Crystallographic Structure

PS may be crystalline, polycrystalline, or amorphous depending on the type of silicon and formation conditions. In general, PS has the same single rystallographic structure as the substrate silicon except for the very fine micro PS in which the crystal structure can significantly deviate from the perfect silicon crystal lattice PS. The crystal structures of some PS formed under various conditions are listed in Table 8.7.

The difference in the crystallinity of PS of different morphological structures is shown in Fig. 8.54 as transmission electron diffraction (TED) patterns of PS formed on different silicon materials.[624] The crystalline structure deviates more from the perfect silicon crystalline structure as the PS structural dimension becomes smaller from sample a to d. The TED pattern in sample d for the PS on lowly doped *p*-Si shows significant electron scattering modification due to deviation from the perfect crystalline structure. Similar findings were reported in other studies: PS formed on heavily doped *p*-Si has the same single-crystalline structure as the substrate, whereas on lightly doped *p*-Si the Bragg spots are less defined and much diffuse electron scattering is observed.[35,36,566] It has been found that the PS formed on *p*-Si ($10\,\Omega$) in 50% HF has an amorphous layer of about $1\,\mu m$ on top of a polycrystalline layer of PS having a pore size of less than 3 nm.[640] Except for the top surface layer, which may also be amorphous or polycrystalline structures, the PS layers formed in the stable growing phase

TABLE 8.7. Crystallographic Characteristics of PS

Silicon	Solution HF	Current mA/cm^2	PS structure[a]		Ref.
			Surface	Bulk	
***p*(100)**					
1 Ωcm	24:49 (HF:Extra)	55		PC	68
1	50%	100	PC	SC	51
15	46%	1		AM	226
	46%, 0°C	1		PC	226
	45%	15		AM + PC	745
10	13:13 (HF:Extrand)	15	AM	AC	1060
***p*(111)**					
0.1	24%	10		SC	49
10	50%	20	AM	PC	640
	12:75 (HF:Extra)	20	AM	SC	640
0.006 Ωcm	50%	100 mA	SC	SC	36
1.5 Ωcm	50%	100 mA	SC		36
0.01 Ωcm	20%	30		SC	35
25 Ωcm	40%	30		SC	35
0.02	50%	100	PC + SC	SC	40
4×10^{18}	12–48%	1–80		SC	53
5	25%		AM	AM + SC	6
***n*(100)**					
1.2×10^{15}	5%	0.1 V, illu.	SC	SC	767
4×10^{18}	5%	0.1 V, illu.	SC	SC	767
***n*(111)**					
0.007 Ωcm	50%	100 mA, illu	SC	SC	36
0.007	50%	20 mA, high I_0	AM	PC	651
	50%	20 mA, low I_0	PC	SC	651
	50%	100 mA, low I_0	SC	SC	651
10^{15}–4×10^{18}/cm^3	5%	10 V	SC	SC	42

[a]SC, single crystalline; PC, polycrystalline; AM, amorphous.

generally are single crystalline (with some deviation from the substrate for very fine structures) over a wide range of thicknesses.[649,650]

For two-layer PS formed on illuminated *n*-Si the top micro PS may have very different crystal structures varying from amorphous to polycrystalline to distorted single-crystalline structure. For example, micro PS formed in 5% HF under illumination on *n*-Si with a doping range from 10^{15} to 10^{18}/cm^3 is single crystalline with the same orientation as the substrate.[247,767] On the other hand, amorphous structure is found in the micro PS formed on illuminated heavily doped *n*-Si.[640,651] The surface crystalline structure of the PS formed on *n*-Si under illumination varies from single crystalline to amorphous depending on the silicon resistivity and the condition of anodization as summarized in Fig. 8.55.[36]

Distortion of the crystalline structure of PS from that of substrate silicon is correlated with the size of the morphological structure and can be associated with a number of causes. The extent of change in lattice spacing depends on the type of PS formed. It has been found that the lattice spacing of the silicon atoms in PS is slightly larger than in the Si substrate and the expansion is about 0.04% for degenerately doped *p*-Si

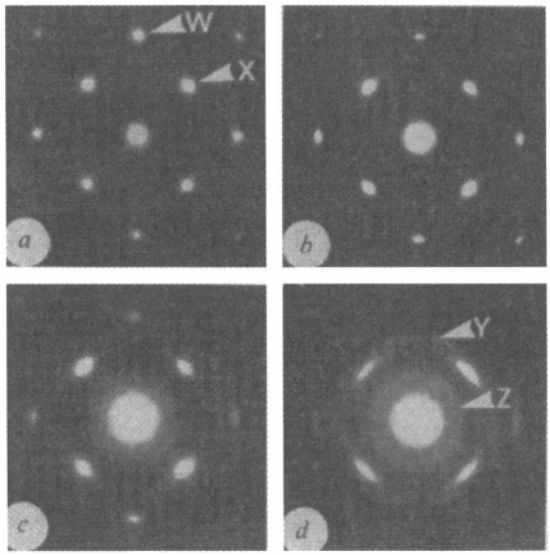

FIGURE 8.54. Transmission electron diffraction patterns given by PS of (100) samples: (a) p-Si, 0.005 Ωcm, 100 mA/cm^2, (b) p-Si, 0.02 Ωcm, 100 mA/cm^2, (c) n-Si, 0.012 Ωcm, 1.5 mA/cm^2, (d) 20 mA/cm^2, in 20% HF ethanol/H_2O mixture. After Cullis and Canham.[624]

and about 0.3% for nondegenerately doped p-Si.[647] It has been suggested that the lattice misorientation of the PS on moderately doped p-Si is due to the presence of compressive strain caused by the lattice expansion in the PS.[566,649,650] On the other hand, the increased lattice spacing is attributed to the adsorption of H atoms on the pore surface.[647] The larger distortion for the PS on nondegenerately doped p-Si is due to the larger surface area in order to accommodate more hydrogen atoms per volume of Si. Amor-

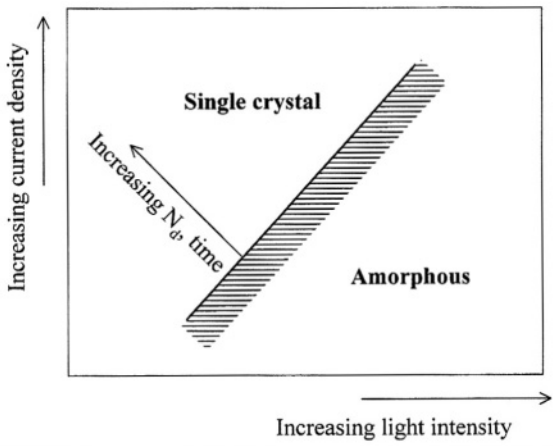

FIGURE 8.55. Effect of doping concentration, current density, time, and light intensity on the crystalline structure of PS formed on n-Si. After Arita and Sunahama.[36] (Reproduced by permission of The Electrochemical Society, Inc.)

phous PS of the very fine PS appears to be associated with oxidation. The as-grown PS on lowly doped *p*-Si, which may have various amounts of amorphous structure, can be oxidized to a great extent from 10 to 50%.[35,176,566]

8.3.10. Summary

The morphology of PS has extremely rich details as shown in Fig. 8.19, determined by the numerous factors involved in the anodization. Despite the enormous amount of research effort, the quantitative and, to some extent, qualitative correlation of the formation condition and morphology are still not clear. Generally, *p*-Si and *n*-Si have distinct differences in the correlation between the formation conditions and PS morphology. Among all formation conditions, doping concentration appears to show the most clear functional effect on morphology. For example, Fig. 8.57 shows the growth rate, dissolution valence, and porosity of the PS on *p*-Si and *n*-Si as a function of doping concentration and current density.[1084] Still, the correlations such those shown in Fig. 8.57, although covering a wide range of conditions, involve only a very limited region of the large multidimensional space of the conditions. For example, the correlations between doping concentration and morphology shown in Fig. 8.57 can be rather different in a different solution. They may also be different under illumination of different intensities and directions (i.e., front or back) and at different potentials. Nevertheless, as a rough generalization the various morphological aspects can be qualitatively correlated to the pore diameter of PS as shown in Fig. 8.56.

Some generalizations can be drawn about the structure and morphology of PS based on the information presented in the previous sections:

- Pore size ranges in orders of magnitude from about 1 nm to several micrometers.
- The distribution of pores is uniform laterally across the exposed silicon surface.

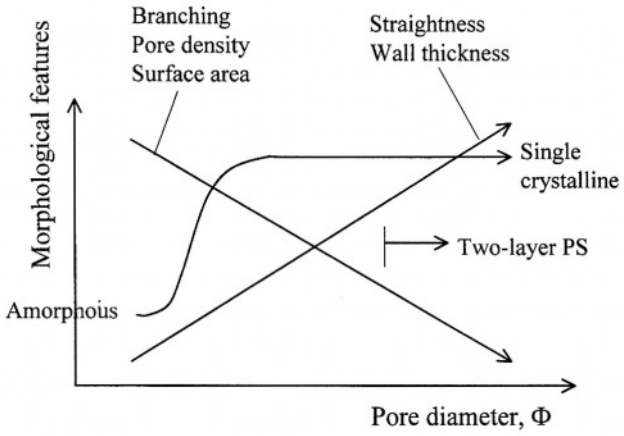

FIGURE 8.56. Tendency of morphological features as a function of pore diameter.

- The morphology of PS is uniform in the thickness direction except for a transition layer near the surface and two layer PS.
- Pore diameters are smaller in the transition layer near the surface than in the bulk of PS.
- Individual pores preferentially form along <100> direction, generally independent of the substrate orientation. Large primary pores tend to be perpendicular to the surface independent of the substrate orientation.
- The pore bottom is curved and the radius of curvature varies from the tip to the side wall with the smallest radius of curvature at the pore tip.
- The PS/silicon interface is flat and is parallel to the substrate surface.
- The surface of pore walls is rough at the atomic scale for all pores.
- Pore shape may be round, square, starlike, or dendritelike for the PS formed on (100) substrate.
- The bulk pore morphology (e.g., pore diameter and density) is independent of the initial surface conditions (e.g., defects, roughness) except for the surface where initiation sites are artificially introduced under conditions that independently control the current and potential (e.g., under back illumination)
- The degree of branching and interpore connection increases with decreasing pore diameter.
- Two-layer structure forms on front-illuminated *n*-Si and on high-resistivity *p*-Si; the top layer has microscopic pores (nanometer scale) while the bottom layer has macroscopic pores (micrometer scale).
- Back illumination tends to generate straight and nonbranched pores.
- Front illumination results in the formation of a micro PS and etching of the PS during its growth.
- The most significant factor determining pore diameter is doping type and concentration.
- Pore size increases with increasing current or potential, and decreases with increasing HF concentration.
- The pores in macro PS may be filled, or partially filled, or nonfilled by micro PS.
- Pores formed in non-aqueous HF solutions are smoother than those formed in aqueous HF solutions.
- Pores grow in the direction of carrier source, but are affected by the anisotropic nature of the dissolution processes.
- Branches on main pores are related to the anisotropic effect: Preferential dissolution is along the <100> direction.
- The effect of anisotropic dissolution on morphology decreases with increasing pore diameter; large pores tend to orient in a direction perpendicular to the surface and have less branching.
- The composition of macro PS is largely pure silicon; micro PS can have considerable amounts of hydrides, oxides, and other compounds depending on the conditions of anodization and posttreatment.
- Macro PS has the same single-crystalline structure and orientation as the substrate silicon. Micro PS, on the other hand, can have a wide range of variation in crystalline structure, from amorphous to polycrystalline to single

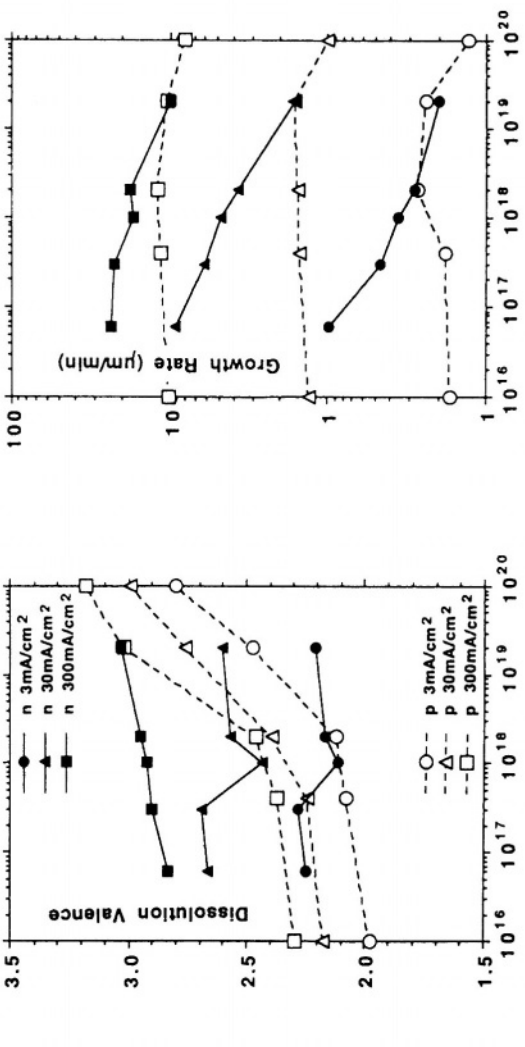

FIGURE 8.57. Values of dissolution valence, pore growth rate, and porosity of the PS formed in 50% HF in ethanol (1:1) at different current densities as a function of dopant concentration. (Reprinted from Lehmann *et al.*[1084] © 2000, with permission from Elsevier Science.)

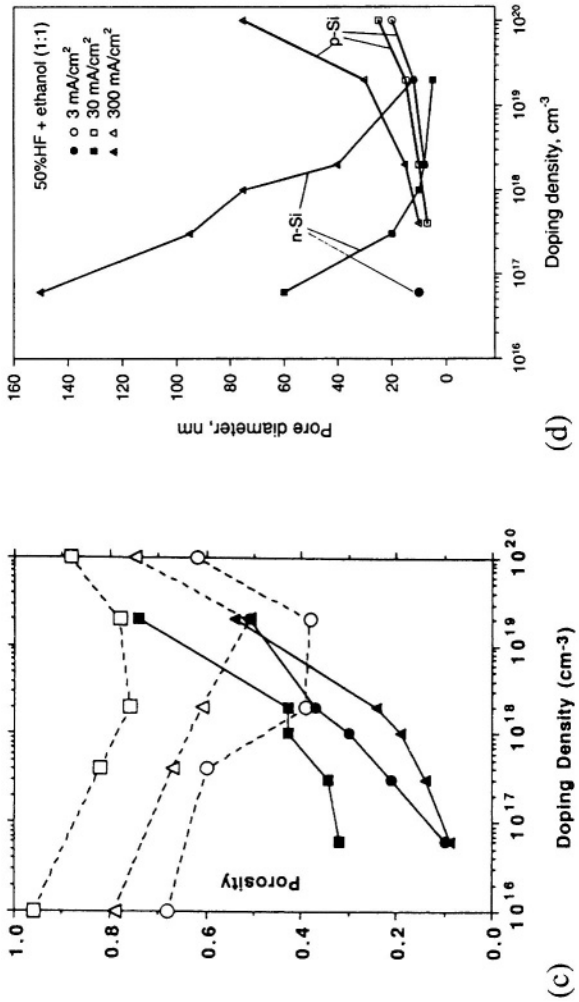

FIGURE 8.57. *Continued*

crystalline depending on the fitness of the PS structure and the degree of oxidation hydration.

8.4. PS FORMED AT OCP

PS can also be formed chemically without the application of a current by simply immersing a silicon sample in a HF solution containing some oxidation agents such as nitric acid or chromium oxide. The oxidants can be the redox couples, which do not deposit onto the surface after the reduction, or metal ions which deposit onto the surface after the reduction. The PS formed under such a condition are often referred to as stain films or chemical PS. As a characteristic feature, the OCP of the silicon during formation of chemical PS in the presence of an oxidant is several hundred millivolts more positive than without addition of an oxidation agent. The formation of chemical PS can further be modified by illumination.[658]

According to a study by Beale *et al.*,[764] chemical PS forms only below a certain concentration of oxidation agent; too high a concentration results in polishing of the surface. The PS formed at the OCP has a limited thickness depending on the substrate material as shown in Table 8.8. The film growth rate tends to decrease with time and eventually reach a limiting value. On *p*-Si the PS film is uniform and about 1 μm in thickness and is composed of single-crystalline material. The pores are a few tens of nanometers in size and oriented perpendicular to the direction of film growth. The limited thickness implies that a dissolution of the PS occurs during its growth. The steady-state thickness of a PS film therefore depends on the relative rates of formation and dissolution of PS. A formation rate of about 10 Å/s has been found in 1 HF:3 HNO_3:5 H_2O.[746]

Although the electrochemical nature of the processes involved in the formation of PS at open-circuit conditions (nonbiased) should be similar to that under anodic bias, there are several major differences in the formation conditions. The first is that at the OCP the driving force is provided by the oxidation agents, the reduction of which provides the anodic polarization of the electrode needed for silicon dissolution. Unlike the externally biased condition, the extent of polarization is limited by the oxidation power of the oxidation agents. The second is that the carrier supply at the open-circuit condition is localized and randomly oriented, while that at anodic potential is perpendicular to the surface. The anodic and cathodic sites in the chemical etching process must be in the vicinity of each other, and continuous alternations must occur between anodic and cathodic reactions on the surface at the pores tips.

TABLE 8.8. Thickness of the PS Films Formed under Open-Circuit Conditions[764]

	p type		*n* type	
Solution	0.01 Ωcm	1 Ωcm	0.005 Ωcm	1 Ωcm
2 g $NaNO_2$ in 100 ml 40% HF	>100 nm	<50 nm	>100 nm	<50 nm
0.2 g CrO_3 in 100 ml 40% HF	>100 nm	0	<50 nm	0

Formation rate and thickness of PS at the OCP can be altered by depositing a metal film on part of the exposed surface to form a galvanic cell.[312,1084] The dissolution rate of silicon is increased because the reduction of oxidants has a higher rate on the metal surface. For example, in the stain etching of $p(100)$ silicon with an Al film on the back side, the Al film reduces the incubation time for the start of the etching process.[769]

8.5. PS FORMED UNDER SPECIAL CONDITIONS

Different cell and electrode designs can be used for generation of PS of varying distribution and uniformity on the surface. For example, instead of back-side contact through a metallic coating which covers the entire wafer, the wafer sample can be clipped on one end which avoids the need for metallizing the back and PS can be formed on both sides. The lateral distribution of current is very uneven at the beginning of anodization but becomes more even later. As a result, the PS formed is thicker near the top than near the bottom of the wafer, and has a varying morphology from the top to the bottom of the wafer following the direction of the current flow.[6]

Another method is the use of two half-cells, in which Pt electrodes are immersed in each cell and a Si wafer is used to separate and isolate the cells.[436] In this design there is an electrolytic contact on the back and thus there is no need to metallize the back side of the wafer. The PS is found to be more uniform than the sample using back-side metal contact.

The different positions for the i–V curves of different silicon materials indicate that if a surface has different regions with different doping types or concentrations, selective PS formation can occur in the regions that are favorably doped.[35,185] Thus, when some regions of highly doped n-type wafer are ion amorphosed, formation of PS occurs only on the amorphosed regions and no PS forms on the crystalline regions.[35,1172]

Hydrogen bubbles sticking on the surface tend to prevent the formation of homogeneous PS.[36,50] The bubbles can be broken free and removed with an ultrasonic oscillator source. Also, surfactants can be added to the solution to reduce the amount of hydrogen bubbles adsorbed on the Si surface.[586,795] Water has a high surface tension; in inorganic solutions cations are known to increase the surface tension of solution and fluoride ions are rather effective in this process. During the formation of PS hydrogen gas is released so that if the surface tension is high the hydrogen gas is effectively trapped on the silicon surface in the form of bubbles which then mask the underlying surface preventing further dissolution of the surface. The presence of an organic material in an aqueous solution will result in a decrease of its surface tension. The amount of reduction depends on a number of factors such as the solubility of the organic solvent and the tendency of the organic material to adsorb preferentially at the water/air interface. Ethanol and acetic acid are known to decrease the surface tension. Under similar conditions the PS formed in the solution containing organic solvent such as ethanol appears to be more uniform and also less prone to side pore formation.[4,1084]

8.6. FORMATION MECHANISMS

8.6.1. Historical Development

Since the discovery of PS in the late 1050s, numerous theories have been proposed regarding the mechanisms of PS formation and the morphological features. Figures 8.58 and 8.59 detail the progress of research on PS over the last 50 years with respect to the discovery of major PS features and the theories proposed for various mechanistic aspects involved in PS formation and morphology. The parallel developments in the understanding of the fundamental electrochemical reactions of a silicon electrode in HF solutions are shown in Fig. 8.60.

Discovery of PS and the Initial Model. The formation of a solid surface layer (porous silicon) on a silicon electrode during dissolution in aqueous HF solution was first reported by Uhlir and Turner in the late 1950s.[33,957] In his study of electropolishing of silicon in HF solutions, Turner found that the solid surface film forms only below a critical current, J_1 (see Fig. 5.2). The effective dissolution valence in this current range was found to be about 2. At potentials more positive than the critical current, electropolishing occurs. Because the film (formed on *p*-Si) was found to be amorphous and contained fluoride, Turner suggested that the film could be a subfluoride $(SiF_2)_x$ grown on the surface during the anodic dissolution of silicon. In the mid-1960s, this film was found to consist mainly of polymerized silicon hydrides.[1134]

Based on a systematic study of the charge transfer kinetics of the silicon/electrolyte in HF solutions and the understanding that the anodic film was of amorphous

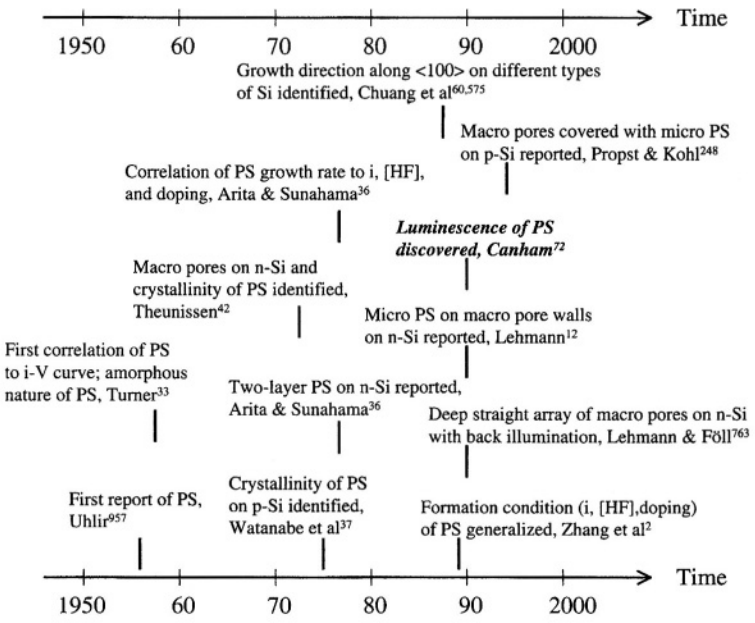

FIGURE 8.58. Progress in the discovery and characterization of PS features.

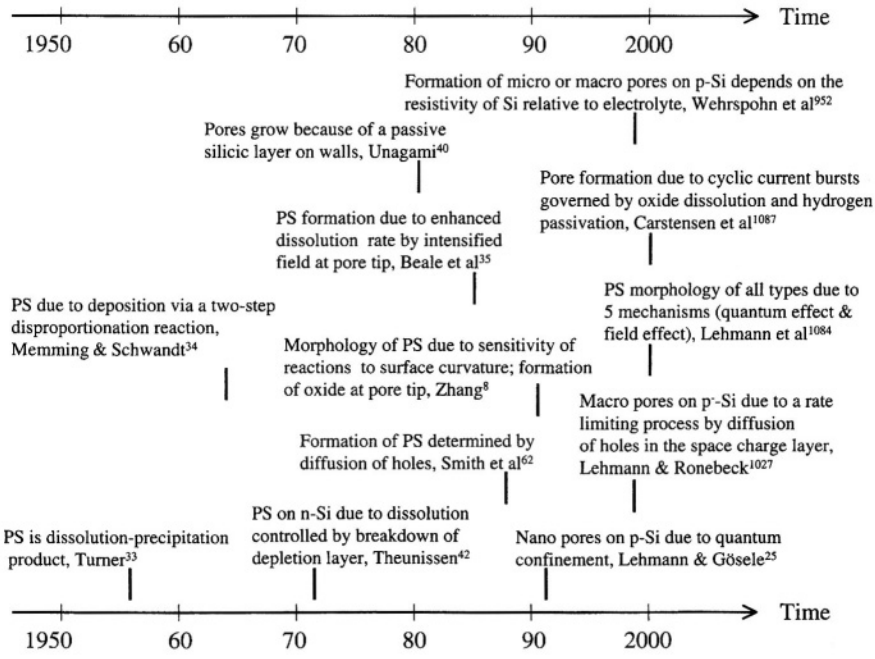

FIGURE 8.59. Progress of the theories on the formation mechanisms and morphology of PS.

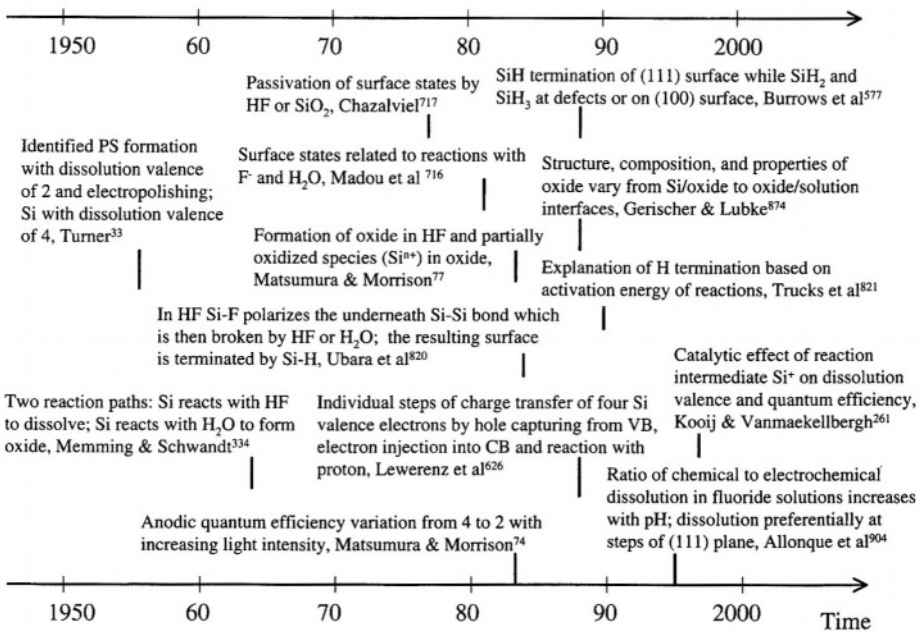

FIGURE 8.60. Progress of the research on the fundamental electrochemical reaction related to the formation of Si in HF solutions.

nature, Memming and Schwandt[34] proposed that the solid film that formed on the silicon surface during anodic dissolution was a dissolution/precipitation product ($Si^0_{amorphous}$) resulting from a two-step disproportionation reaction:

$$Si + 2HF + 2h \rightarrow SiF_2 + 2H^+ + (2 - \lambda)e$$

$$2SiF_2 \rightarrow Si^0_{amorphous} + SiF_4$$

Macropores on *n*-Si and the Barrier Breakdown Model. In the early 1970s, several studies found that the formation of etch pits and tunnels on *n*-Si occurs during anodization in HF solutions in the dark.[38,39,42,58] The size and number of these pits and tunnels change with doping density and potential.

Meek,[38,39] based on *i–V* curve and capacitance measurements, proposed that the large current observed on *n*-Si at an anodic potential in the dark is due to barrier breakdown. The breakdown is not due to a bulk mechanism but rather to interface tunneling from the states at the surface into the conduction band. Also, the breakdown is not uniform but localized causing the formation of the etch pits and tunnels.

In a systematic investigation of *i–V* characteristics and the morphology of the solid layer formed on *n*-Si, Theunissen[42] found that in the dark, deep etch tunnels can form on the substrates at a doping concentration higher than $2 \times 10^{16}/cm^3$. He also found that the structure of etch channels on *n*-Si is single crystalline, and thus concluded that the solid layer formed during anodization is the remaining substrate silicon left after anodic dissolution. It was also found that the channels have a rich texture which varies with formation conditions. Furthermore, the formation of channels is not related to crystal defects and the direction of the channels depends on the orientation of the substrate. Theunissen postulated that local breakdown of the depletion layer inside the semiconductor is responsible for the formation of etch channels. The breakdown of the barrier layer occurs when the maximum field at the silicon/electrolyte interface is larger than the critical breakdown field.

Characterization of PS and Growth Kinetics. A number of systematic studies were carried out to characterize the morphology and growth kinetics of PS from the mid-1970s to the early 1980s.[36,37,40,41,49] It was then established that the brown film formed on *p*-Si consists of very small pores, observable only under TEM, and has the same single-crystalline structure as the substrate. It thus is the substrate material remaining after anodic dissolution, such as the etch channels on *n*-Si. The growth rate of a PS layer for a given condition was found to be constant with increasing anodization time and the morphology is generally uniform with increasing thickness of PS. Thus, diffusion within the pores is not a rate-limiting process and the walls of the pores are not active. The dissolution reactions occur only on pore bottoms and are limited by the charge transfer process at the silicon/electrolyte interface. Decreased growth rate, which is accompanied by an increase of porosity, occurs for thick PS layers. A difference in the condition at the bottom of the deep pores from that of the shallow ones was suggested as the cause of this phenomenon.[49]

Depletion Layer and Field Intensification Model. By the mid-1980s the overall scope of the conditions for the formation of PS and of the various morphological features were largely identified, although many details of PS morphology and the

nature of the reactions would be revealed later (new morphological features at more refined scales are still reported today and will probably be the case for some time in the future).

Based on an extensive investigation of the anodic *i–V* relations, dissolution valence, and PS morphology on a large matrix of silicon substrates, Beale *et al.*[35] proposed a rather comprehensive model on the formation of PS. This was the first model that analyzed the *i–V* characteristics and correlated them with the current conduction mechanisms associated with silicon substrates of different types and doping concentrations.

Because the spacing between pores is always less than the width of the depletion layer and PS has a very high resistivity, Beale *et al.* proposed that the material in the PS is depleted of carriers and the presence of a depletion layer is responsible for current localization at pore tips where the field is intensified. This intensification of field is attributed to the small radius of curvature at the pore tips. For lowly doped *p*-Si the charge transfer is by thermionic emission and the small radius of curvature reduces the height of the Schottky barrier and thus increases the current density at the pore tips. For heavily doped materials the current flow inside the semiconductor is by a tunneling process and depends on the width of the depletion layer. In this case the small radius of curvature results in a decrease of the width of the depletion layer and increases the current density at pore tips. The initiation was considered to be associated with the surface inhomogeneities, which provide the initial localized high current density at small surface depressions.

The model of Beale *et al.* provided a deeper level of understanding of the current localization required for PS formation on different silicon substrates and pointed out the correlation between the relative dimension of pore size and the width of the depletion layer. Several concepts proposed in their model would be adopted and further developed in many of the later models such as those by Foll,[69] Zhang,[8] and Lehmann.[12,1084] However, because the model considered only the physical aspects of the semiconductor and none of the chemical reactions, it provided little insight for the change of pore size and other morphological features with current and HF concentration. Also, Beale's model assumed that the Fermi level of the semiconductor is pinned on the surface on the midgap which does not agree with the later experimental data.

Carrier Diffusion Model. Near the end of the 1980s Smith *et al.*[59,60,62] proposed a model with commuter simulation to describe the morphology of PS based on the hypothesis that the rate of pore growth is limited by diffusion of holes from the bulk of the silicon to the growing pore tip. The pore structure is determined by the intrinsic nature of the random walk and the magnitude of the diffusion length. A hole randomly walking toward the growing pore tips is more likely to contact those pores that are nearest to it, meaning the outer tips of pores have the highest probability of hole capture and growth. According to this model, the features of PS morphology are essentially determined by the hole diffusion length L which is a function of potential and dopant concentration. The interpore spacing is then on the order of two diffusion lengths, that is, $2L$. The PS density decreases with decreasing diffusion length along with an increasingly interconnected porous structure. To account for the variation in pore diameter and the transition from PS formation to electropolishing a sticking factor was introduced.

A hole needs to hit and stick to the surface to have a reaction at the active site. The pore tip was considered to be oxidized to a varying degree depending on the anodization conditions. The sticking factor is different along the surface of a pore tip which is partially covered with an oxide. When conditions are such that the sticking probability is much higher at the edge of the tip than in the middle, the dissolution process tends to result in electropolishing rather than PS formation.

Although the model simulated some of the morphological features of PS, it was too general to account for the different current conduction mechanisms for different types of silicon substrates. For example, for *n*-Si in the dark, the current is by electron injection into the conduction band from the surface, which cannot be explained by the carrier diffusion model. Also, there is no physical foundation for the sticking factor of carrier to the surface. Furthermore, the model did not consider the nature of the electrochemical reactions at the interface, which must be an important part of the formation mechanism.

Formation Condition of PS. A critical current density (the peak current of the *i–V* curve), below which PS forms and above which it does not, was identified by Turner's early study. However, it was not clear how accurate this current characterizes the formation condition and whether it is identical for different types of silicon substrates. Zhang *et al.*[2] in the late 1980s made a systematic study on the *i–V* curves of different silicon types and doping concentrations, current densities, and HF concentrations and on the electrode surface condition after anodization. The condition for PS formation on different substrates in the entire continuum of current and HF concentration was then established (Fig. 8.5). It was concluded that the conditions determining whether PS formation or electropolishing occurs is largely independent of the electronic properties of silicon such as doping type and concentration. It is the nature of the reactions that is responsible for the occurrence of the different regions of potential. The transition from PS formation to electropolishing was postulated to result from the two competing reactions between a direct dissolution of silicon through reacting with fluoride species and an indirect dissolution through oxide formation and dissolution. This hypothesis has been adopted in many of the later models on the formation mechanisms of PS.[12,859,1087,1135]

Quantum Confinement Model. To account for the formation of micropores of less than a few nanometers formed on *p*-Si, Lehmann and Gosele[71] in the early 1990s postulated that instead of the depletion layer, which is involved in macropores, quantum carrier confinement is responsible for the formation of the micropores on *p*-Si. The confinement occurs due to an increase in band-gap energy and energy barrier caused by the quantum size porous structure, which prevents the carriers from entering the wall regions of the PS as illustrated in Fig. 8.61.[25] Due to the quantum confinement the pore walls are depleted of carriers and thus do not dissolve during the anodization.

The quantum confinement model was extended by Frohnhoff *et al.*[133] to account for the wide distribution of pore diameters of the PS formed on *p*-Si. Tunneling of holes through silicon crystallites was proposed as a process also involved in the formation of the quantum size porous structure. The tunneling current oscillates with the crystallite size which was considered to be responsible for the uneven pore size distribution and for the stability of very small crystallites in the PS. The quantum confinement model

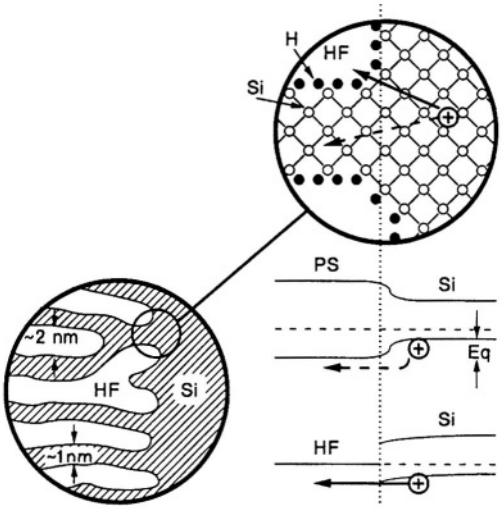

FIGURE 8.61. (Bottom left) Enlarged cross section of the PS/silicon interface. (Top) Chemical structure of the interface and two possible ways (dashed and solid arrow) for a hole to cross the interface. (Bottom right) Corresponding band diagram of the interface shown above and the two corresponding energy barriers for a hole penetrating into a wall (dashed arrow) or a pore tip (solid arrow) after Lehmann and Gosele[25] (© 1992, Reprinted by permission of John Wiley & Sons, Inc.)

has also been adopted by many groups to explain the many phenomena observed on PS such as current conduction and luminescence.[75,624,1156,1160]

The quantum confinement model reasonably explains the formation of crystallites of a few nanometers in size. However, it does not provide an explanation of what determines pore diameter. If quantum confinement, which is not related to doping type and concentration, were to occur, it should also occur on all types of silicon substrates. However, quantum size PS is not found in many types of PS, e.g., the PS formed on *n*-Si in the dark.

Surface Curvature Model. Based on the observation that the bottoms of pores are always curved, Zhang[8] in the early 1990s proposed a surface curvature model for the formation of PS on *n*-Si. It was postulated that the rate of reactions can be greatly increased on a curved surface because the surface curvature on the order of the width of the space charge layer or smaller reduces the effective width of the space charge layer and therefore greatly increases the interface tunneling current. Furthermore, Zhang recognized the variation of radius of curvature from the tip to the wall and pointed out its importance in determining the distributions of reactions (Si dissolution and oxide formation) and current density on the pore bottom. The dimension of pores and pore walls are determined by these distributions.

The model was considered to also be applicable for the PS formed on other types of silicon substrates. As a generalization, Zhang stated that it is the sensitivity of the semiconductor interface reactions to the curvature of the interface that enhances the preferential dissolution and leads to the formation of pores. For *p*-Si and heavily doped *n*-Si which have much thinner space charge layers than does *n*-Si, the radius of curvature must be small to affect the width of the space charge layer and, as a result, much

smaller pores are formed. This generalization is also applicable to the formation of porous structures on semiconductors other than silicon.

Formation of Uniformly Spaced Pore Array. Lehmann and Foll[763] in 1990 reported the formation of straight, smooth, and well-spaced macropore arrays on *n*-Si using back-side illumination and surface patterning. The major difference between back-side illumination and that in the dark is that the current is conducted through hole diffusion from the back under illumination whereas it is by electron tunneling (or breakdown) from the front surface in the dark. Also, unlike in the dark, the current and the potential under illumination can be independently controlled and thus a specific current can be obtained at different potentials. Using such a separated current and potential control plus surface patterning to define the number and spacing of the pores proved to be a versatile method for fabrication of deep pore arrays of well-defined pore diameters and interpore spacings.[763,770,1093] Among other morphological features, Lehmann and Foll found that as with the macropores generated in the dark the diameter of pores generated under backside illumination is closely correlated to the width of the space charge layer of the silicon material.

In further investigations Lehmann[12,850] found that the pores propagate at similar rates at different applied current densities. It was then postulated that all pore tips are limited by mass transfer in the electrolyte defined by J_1 (see Fig. 5.1) in the steady-state condition. It was further proposed that the relative rates of carrier transport in the silicon semiconductor and mass transport in the electrolyte determine the PS morphology of *n*-Si. At low current densities the reaction rate is limited by the transport of carrier to the pore tips and there is no accumulation of holes so that dissolution occurs only at pore tips while the pore walls do not dissolve because of the depletion of holes. At high current densities the reaction at pore tips is mass transport limited and holes accumulate at the pore tips and some of them move to the walls resulting in the dissolution of walls and larger pore diameters. When the concentration of holes in the walls is close to that at the pore tips, the condition for the preferential dissolution at pore tips disappears and PS ceases to form.

The rate of growth of macropores observed on *n*-Si is independent of current density when the current density at the tip equals J_1. The pore diameter was related by Lehmann[12] to the ratio of actual current density to peak current density

$$d = p(i/J_1)^{1/2} \tag{8.6}$$

where p is the spacing between two pores. Assuming an orthogonal pattern the wall thickness is then given as

$$w = p\left[1-(i/J_1)^{1/2}\right] \tag{8.7}$$

The above equations were found to be in good agreement with experimental data generated under back-side illumination and surface patterning. However, they are only phenomenological correlations of pore diameter and interpore spacing with current density, HF concentration (embedded in J_1), and doping concentration (embedded in p) under the specific condition. Equations (8.6) and (8.7) describe the pore diameter and spacing

only for the limited range in the continuum of these parameters. For example, it is not applicable for the pores formed at low current densities relative to the critical current, i.e., less than 10% of J_l when the growth rate of pores significantly increases with increasing current. Also, according to Lehmann's data the concentration reduction at the pore tip due to the diffusion effect is only about 20% at a PS thickness of 150 μm which indicates that diffusion has only a minor role in the rate-determining process. Processes other than diffusion must play a major role particularly for relatively shallow pores.

Formation of Two-Layer PS on Illuminated *n*-Si. Two-layer PS with a micro PS on top of a macro PS and on the walls of the individual macropores formed on illuminated *n*-Si had been reported in the late 1970s but was little investigated until the 1990s.[16,247,600,767] The micro PS may have a fractal-like geometry and can vary in the same layer in structure from amorphous to single crystalline and in diameter from a few to hundreds of nanometers.

Whereas the formation of a macro PS layer on *n*-Si under front illumination follows the same mechanism as the macro PS formed in the dark, the formation of micro PS is believe to be mainly due to the effect of the photogenerated carriers. Essentially, the dissolution reaction under illumination proceeds with a supply of photo holes which are generated near the surface and distributed uniformly in the porous structure. This results in a dissolution process different from that in the dark or back illumination and the formation of PS of extremely fine and randomly oriented structures.[4] According to Arita,[651] the anodic current under front illumination consists of three parts:

$$i = i_{\text{drift}} + i_{\text{diff}} + i_{\text{tunnel}} \tag{8.8}$$

where i_{drift}, i_{diff}, and i_{tunnel} are the drift current due to carriers generated in the depletion layer, the diffusion current due to minority carriers outside of the depletion layer, and the election tunneling current through the barrier into the conduction band. The drift current has a particularly strong effect on the crystalline structure of the PS:

$$i_{\text{drift}} \propto \mathrm{I_o}\alpha \exp(-\alpha x) \tag{8.9}$$

where I_o is the total flux of incident light, α is the light absorption coefficient, and x is the distance from the surface. The larger the contribution of the drift current, the stronger is the tendency to form amorphous PS because the amount of amorphous PS decreases with decreasing illumination intensity and with increasing PS thickness.

Alternatively, Clement *et al.*[247] proposed that the micro PS found under illumination could result from shattering of the macro PS into fine filaments due to residual stress. Dissolution-precipitation was also considered to be a possible mechanism for the formation of micro PS although it is inconsistent with the single-crystalline nature of the micro PS in many two-layer PS.

Theories on the Macro PS Formed on Lowly Doped *p*-Si. The formation of macro PS and two-layer PS on *p*-Si was first discovered by Kohl *et al.*[136,248] in the mid-1990s on lowly doped substrate in anhydrous organic HF solutions. Macropores on *p*-Si were later found to also form in aqueous solutions and the walls of the macropores are not always covered by a micro PS layer.[177,952,1058]

The formation of macro PS on *p*-Si was initially thought by Propst and Kohl[248] to relate to the chemistry of the organic solvents because some of the electrochemical reactions are fundamentally different from aqueous solutions, e.g., no hydrogen evolution occurred during PS formation. With the findings on the formation of macro PS in aqueous solutions, Wehrspohn *et al.*[1086,1061] provided a model based on an analysis of the resistance of the electrolyte, interface, and substrate and of the stability of current against perturbation. They suggested that a necessary condition for formation of macro PS on low-resistivity *p*-Si is that the resistivity of the substrate is higher than that of the electrolyte. The micro PS, which was considered to follow the same field intensification mechanism, acts as a precursor for the formation of macro PS.

The model of Wehrspohn *et al.* was soon proven to be invalid as macro PS was also found to occur in electrolytes having much higher resistance than the silicon substrate.[177,1027] Alternatively, Lehmann and Ronnebeck[1027] postulated that the formation of macro PS on lowly doped *p*-Si is due to the dominant effect of thermionic emission which is sensitive to barrier height rather than barrier width. However, this does not explain how the two PS layers with a difference of several orders of magnitude in pore size could be determined both at the same time by the space charge layer nor what governs the dimension of the macropores.

Miscellaneous Hypotheses. In many studies, the presence of a surface layer has been suggested to be essential for the formation of PS. For example, selective reaction of the hydrogen-bonded species has been suggested by Allongue *et al.* to be a necessary condition for the formation of PS.[794,1108] Similarly, surface roughening caused to the formation of surface hydrides and the associated dissolution of the silicon has been considered to be related to the formation of PS by Rappich and Lewerenz.[775] On the other hand, the observation of a very thin surface layer that is more dense than the bulk micro PS led Unagami[40] to suggest that the formation of PS is promoted by the deposition of a silicic acid on the pore walls which hinders the dissolution of the walls and results in the directional dissolution at the pore tips. Alternatively, Parkhutik *et al.*[41] suggested that a passive film composed of silicon fluoride and silicon oxide covers the wall and the bottom of the pores and that the formation of PS is similar to that of porous alumina where a barrier layer exists on the base of pores.

Some of the hypotheses have been highly mathematically developed. For example, a theoretical modeling based on charge transfer kinetics for PS morphology has been attempted by Jaguiro *et al.*[1170] Similar theoretical modeling considering the transport phenomena of carriers in the semiconductor, ions in the electrolyte, and surface tension has been proposed by Valance.[1056] A theory based principally on thermodynamical arguments has been offered by La Monica *et al.*[1163]

Integration of Models. An attempt has been made recently by Lehmann *et al.*[12,71,1027,1084] to unify the theories on the formation mechanisms of all types of PS. The fundamental assumption of the unified theory is that all of the surface of PS structure except for the pore tips is passivated due to the depletion of carriers. Different mechanisms are involved in the depletion zone between the pores: depletion by quantum confinement for the nano-scale pores and depletion by formation of the space charge layer for all other PS having a pore size larger than a few nanometers. As summarized in Fig. 8.62, the depletion by the space charge layer is further divided into four groups according to the size of pores in relation to the doping type and

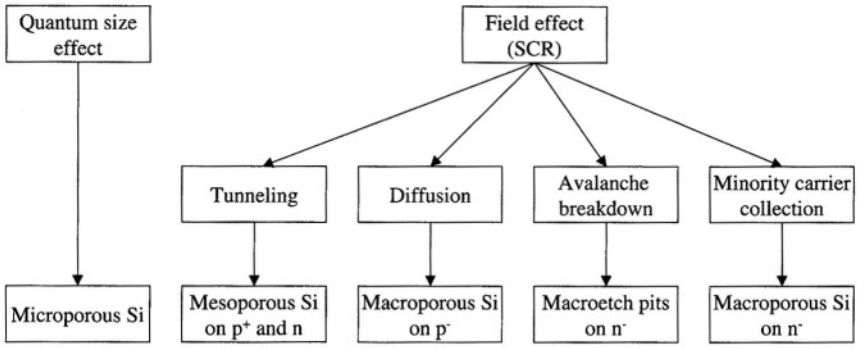

FIGURE 8.62. (Top row) Effects proposed to be responsible for pore wall passivation. (Middle row) Effects responsible for passivation breakdown at the pore tip. (Bottom row) The resulting kind of porous silicon structure together with substrate doping type. (Reprinted from Lehmann *et al.*[1084] © 2000, with permission from Elsevier Science.)

concentrations. The models for the formation mechanism of each of the groups have been described in the previous sections. (One may note that although the groups of theories organized in Fig. 8.62 seem to cover all mechanisms, they are disconnected and are not a coherent and integral body of theories.)

Current Burst Theory. The current burst theory of Foll *et al.*[1087,1135,1140,1141] has been developed most recently and is perhaps the most comprehensive model on the formation of different types of PS. This is so far the only model that considers, on the one hand, the relationships of morphological features to formation conditions, and on the other hand, to the specific electrochemical reactions under these conditions.

This model has a basic assumption that the electrochemical reactions involved in the dissolution of the silicon surface operate in microscopic units. These reaction units have a temporal and a spatial distribution in number and in the state of activity. The formation of pores is due to the synchronization of these operational units at certain time and geometrical scales. It is further assumed that the state of reactivity of these units oscillates by the same mechanism as the oscillation involved in the oxide formation–dissolution in HF at anodic potentials (see Section 5.10). Due to the nature of the oscillation the unit on any specific position of the electrode surface can be silent or burst into action resulting in an increase in current. More specifically, Foll *et al.* assumed the system to have the following features:

- Current flow is always spatially and temporally inhomogeneous, that is, it occurs by local current bursts.
- Current flow induces either direct dissolution or oxide formation and dissolution which always follows a current burst.
- The band bending of oxide-free surfaces cannot be changed by applied potential because the Fermi level is pinned in the midband gap due to the large surface state density. The surface tends to be terminated by hydrogen resulting in the passivation of the surface states and unpinning of the Fermi level. As a result of hydrogen termination and de-termination, the position of the Fermi level and thus the width of the space charge layer also oscillates with time.

- Because the hydrogen termination process takes a considerable amount of time, it is an important element contributing to the oscillation process.
- The rate of hydrogen termination varies with crystal orientation, is fastest on the (111) surface, and thus determines the probability of a current burst on surfaces of different orientations.

According to this model, as illustrated in Fig. 8.63 cycle of the processes occur involving active dissolution, oxide formation and dissolution, and hydrogen termination for a reaction unit on a growing pore bottom.[1087]

The current burst model is potentially powerful in providing explanations for many mechanistic and morphological aspects involved in the formation of PS. However, as recognized by Foll *et al.* themselves, it would be extremely difficult for such a unified model to be expressed in mathematical form because it has to include all of the conditional parameters and account for all of the observed phenomena. Fundamentally, all electrochemical behavior is in nature the statistical averages of the numerous stochastic events at a microscopic scale and could in theory be described by the oscillation of the reactions on some microscopic reaction units which are temporally and spatially distributed. Ideally, a single surface atom would be the smallest dimension of such a unit and the integration of the contribution of all of the atoms in time and space would then determine a specific phenomenon. In reality, it is not possible because one does not know with any certainty the reactivity functions of each individual atoms. The difficulty for the current burst model would be the establishment of the reactivity functions of the individual reaction units. Also, some of the assumptions used in this model are questionable. For example, there is no physical and chemical foundation for the assumption that the oxide covering the reaction unit is

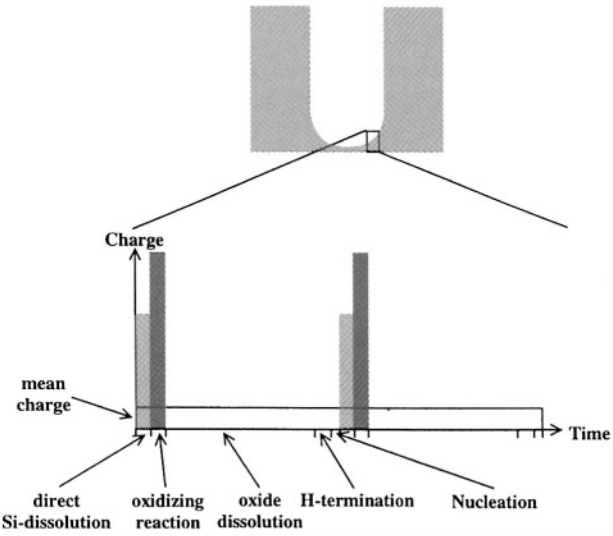

FIGURE 8.63. Schematic diagram of the charge density and time-consuming reactions at the Si/electrolyte interface. (Reprinted from Carstensen *et al.*[1087] © 2000, with permission from Elsevier Science.)

completely dissolved before formation of new oxide. Because the growth rate of the oxide film is limited by the film thickness, at a fixed potential, the growth rate of the oxide film will greatly increase with thinning of the film, which prevents the film from being completely dissolved by a chemical reaction process.

Advances in the Understanding of Electrochemical Reactions. Starting at the same time as the discovery of PS and particularly during the period from the late 1970s to the 1990s, a number of systematic studies have been made on the fundamental aspects of the electrochemistry of silicon in HF solutions as highlighted in Fig. 8.3. These studies revealed many important details regarding the electronic structure, nature of reactions and the carrier transfer kinetics of the silicon/electrolyte interface as discussed in detail in Chapters 2–5. Some of the key findings, which are relevant to the formation of PS in HF solutions, can be summarized in the following:

- In aqueous solutions silicon reacts spontaneously with water to form an oxide film which passivates the surface.
- The presence of HF results in the dissolution of silicon oxide and activates the surface to a variable extent depending on HF concentration and potential.
- The fluoride species such as HF and F^- also react directly with the bare silicon surface, and thus in aqueous HF solution, the dissolution of silicon atoms has two principal competing paths, one via the reaction with HF and the other with H_2O.
- Silicon, having four valence electrons, dissolves in multiple steps, each of which may occur at different energy levels and may proceed via the conduction band as well as the valence band depending on the condition of the Si/electrolyte interface.
- The surface of silicon during anodic dissolution is dynamically terminated by hydrogen and thus the dissolution of silicon atoms proceeds by first forming a Si–H bond.
- The replacement of the hydrogen by fluoride polarizes and weakens the Si–Si back bond and facilitates the subsequent attack on this bond by water or HF.
- The quantum efficiency of photoelectrochemical reactions may vary from 2 to 4, effective dissolution valence from 2 to 4, and efficiency of hydrogen evolution from 1 to near zero depending on light intensity and potential.
- Anodic oxide films formed under different kinetic conditions have drastically different structures, compositions, and properties (e.g., etch rate) and they change with time during the anodization.
- The applied anodic potential may mostly or partially drop in the space charge layer or in the Helmholtz layer depending on doping type and concentration as well as on the potential range.
- The rate of removal of surface silicon atoms by the electrochemical reactions is orientation dependent, lowest on (111) and higher on other orientations.

These reaction features must be involved in the formation of PS on silicon in HF. However, because of the great complexity of the anodic reactions on silicon in HF solutions on the one hand and of the extremely rich PS morphology on the other hand, the results from the two research domains, fundamental electrochemistry and PS formation mechanisms, have not been well integrated.

Summary. Many models have been proposed for the mechanisms involved in PS formation, but they generally have dealt only with limited aspects of this very complex system. No single theory is yet close to a globally quantitative description of the extremely rich and complex nature of the reactions and resulting morphological evolution of the silicon electrode surface involved in the formation of PS. Generally, some models can logically correlate certain theories in solid state and electrochemistry with some aspects of the phenomena but not with other aspects. Also, the morphology of PS has such a rich nature that every time a model is proposed to describe a set of features, further details that could not be predicted by the model are discovered. Given what has occurred in the last several decades during which there has been continuous discovery of new morphological features, it can be expected that new unexpected morphological features of PS may be discovered in the future. The situation about the formation mechanisms of PS is somewhat like the age-old tale about a group of blind people trying to describe an elephant, each provides a partial truth of the whole reality. We are still not at the stage where we can quantitatively model the mechanisms of PS formation and PS morphology with reasonable accuracy.

8.6.2. Analysis of the Mechanistic Aspects Involved in PS Formation

Any models attempting to describe the overall formation mechanism of PS must consider the fundamental electrochemical reactions in three essential aspects: (1) nature of reactions, reactants, products, intermediates, number of steps, and their sequences, (2) nature and rate of charge transport in the different physical phases at the silicon/electrolyte interface, and (3) spatial and temporal distributions of reactions and the cause of such distributions. Also, the models have to take into account every factors determining the PS morphology such as doping type and concentration, orientation of silicon, HF concentration, pH, illumination light wavelength and intensity, current density and potential.

The first and second aspects have been extensively investigated and reasonably well characterized as can be appreciated by the results described in Chapters 2–5. The third aspect, on the other hand, is still not well characterized due to its complexity. However, it is this aspect that determines the specific morphology of PS formed under given conditions. It is not yet clear how this aspect can be described with an integral model in accordance with the morphology of PS. Nevertheless, the spatial and temporal distributions of reactions are governed by the elements and events involved in the system. The following is an attempt to qualitatively sort out the physical schemes of these elements and events and their relative importance in the context of the overall system.

Effect of Radius of Curvature. The bottom of all pores is curved and the curvature of a semiconductor surface affects the field at the surface. For an interface with a spherical shape as illustrated in Fig. 8.64, the potential and field in the semiconductor can be calculated by solving Poisson's equation[8]:

$$V(x+r_0)=\frac{qN_B}{6\varepsilon}\left[(x+r_0)^2+\frac{2(x_d+r_0)^3}{x+r_0}-3(x_d+r_0)^2\right] \tag{8.10}$$

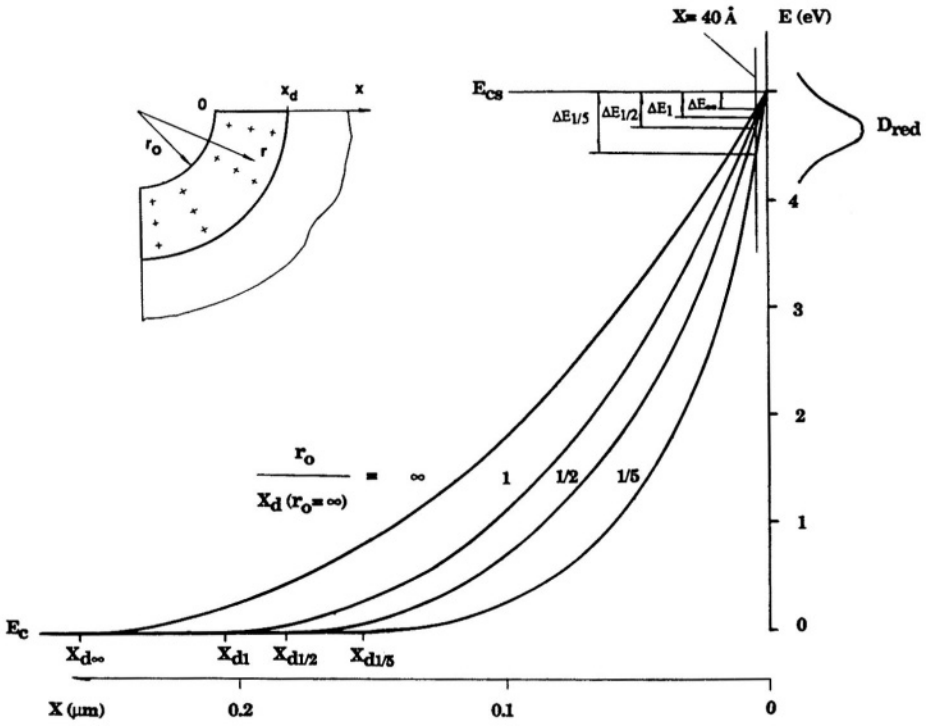

FIGURE 8.64. The energy band diagram (only the conduction band is shown) calculated from Eq. (8.10) for the silicon/electrolyte interface with a potential drop of 5 V and different radii of curvature. E_c is the conduction band edge in the bulk and E_{cs} is the conduction band edge at the surface. ΔE_∞, ΔE_1, $\Delta E_{1/2}$, and $\Delta E_{1/5}$ are the possible tunneling energy ranges for different radii of curvature. The distribution of occupied states at the interface, D_{red}, is also plotted. After Zhang.[8] (Reproduced by permission of The Electrochemical Society, Inc.)

and

$$\xi(x+r_0)=\frac{qN_B}{3\varepsilon}\left[-(x+r_0)+\frac{(r_0+x_d)^3}{(x+r_0)^2}\right] \tag{8.11}$$

where $r = x + r_0$, N_B is the ionized donor density, q is the electronic charge, r_0 is the radius of curvature of the interface, and x_d is the space charge layer width. According to Eq. (8.10) the field strength of a curved surface increases considerably when the radius of curvature is close to or smaller than the width of the space charge layer of a flat surface. Figure 8.64 shows the effect of radius of curvature on the energy band diagram with a potential drop of 5V across the space charge layer of an *n*-Si under an anodic bias. Clearly the potential drops more sharply for a smaller radius of curvature and the width of the space charge layer is considerably reduced. As a result, the field in the space charge layer is greatly increased, for example, the field is about 4 times higher for a curved surface with a radius of curvature of 1/5 $x_d(r_0 = \infty)$ than that for the

flat surface. For *n*-Si under anodic potentials the current conduction is by electron tunneling from the surface into the conduction band. Note that the steep band bending due to decreasing radius of curvature increases the number of energy levels for electron tunneling. In the case shown in Fig. 8.64 the available energy range for tunneling at a tunneling distance of 40 Å is about 180mV for a flat surface whereas it is about 470mV for a curved surface with a radius of curvature of $1/5\ x_d (r_0 = \infty)$.

Similar analysis can be made for other types of materials. Thus, as a generalization, the curvature of a surface causes field intensification, which results in a higher current than that on a flat surface. Although the detailed current flow mechanism can be different for different types of materials under different potential and illumination conditions, the effect of surface curvature on the field intensification at local areas is the same. The important point is that the order of magnitude for the radius of curvature that can cause a significant effect on field intensification is different for substrates having different widths of the space charge layer. Surface curvature determines the vector of the field, that is, magnitude and direction of the field near the surface and is a principal factor determining the dimensions of the pores.

Potential Drop in the Substrate. For a moderately or highly doped material the potential drop due to ohmic resistance in the substrate is very small. For example, for a substrate with a resistivity of $0.1\,\Omega\text{cm}$ ($\sim 10^{17}/\text{cm}^3$) the potential drop in the 0.1 mm thick substrate at a current density of $10\,\text{mA/cm}^2$ is 0.01mV, which is insignificant relative to a potential in the millivolt range that is required to significantly affect the rate of charge transfer process at the interface. However, when the resistivity is on the order of $10\,\Omega\text{cm}$ ($\sim 10^{15}/\text{cm}^3$) or larger the potential drop inside the substrate is in the millivolt range and starts to affect the distribution of the change of potential in the current path.

For a solid between two spherical surfaces shown in Fig. 8.65, the resistance can be described by

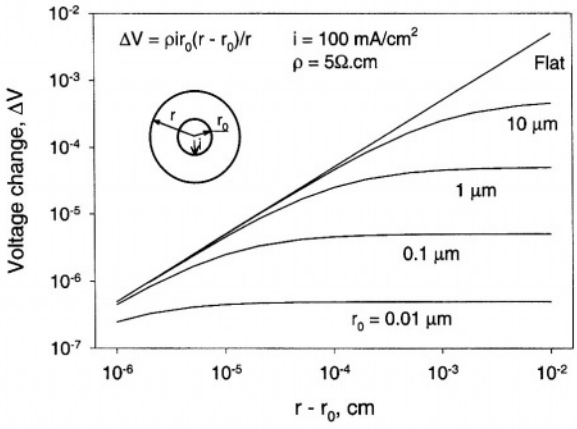

FIGURE 8.65. The change of voltage due to resistance of the material in the substrate of a hollow sphere as a function of radius of curvature of the inner sphere.

$$R = \rho(r - r_0)/(4\pi r_0 r) \tag{8.12}$$

where ρ is the resistivity of the material and r_0 and r are the diameters of the inner sphere and outer sphere, respectively. The potential drop, ΔV_R, for a current $I = i4\pi r_0^2$, where i is the current density on the inner surface, flowing through the solid is then described by

$$\Delta V_R = IR = \rho i r_0 (r - r_0)/r \tag{8.13}$$

Figure 8.65 shows that the potential drop in the material with a curved surface increases nonlinearly with increasing distance from the inner sphere and most of the potential drop occurs within a distance of a few times the diameter of the inner sphere. Also, for the same thickness of the solid the total potential drop increases with increasing radius of curvature of the inner sphere, reaching the maximum at an infinitely large radius of curvature, that is, a flat surface. The value of the potential drop is in the millivolt range for an inner diameter of $10\,\mu m$ under the conditions shown in Fig. 8.65. It will be larger if the current density or the resistivity is higher. Also, the results shown in Fig. 8.65 are for a spherical surface. In the case of curved pore bottoms, which are roughly semispherical, the potential drop from individual pore bottom into the solid must be significantly larger than that of an isolated sphere because the current flow from one pore overlaps those from neighboring pores.

The results of the above analysis suggest that the formation of macro PS on lowly doped materials can be associated with a nonlinear potential distribution in the solid of a curved surface due to the high resistivity of the solid. The formation of two-layer PS on *p*-Si indicates that there are two different physical layers in which the potential–current relations are sensitive to the radius of curvature. The space charge layer of *p*-Si is thin under an anodic potential and is associated with the formation of the micro PS. The nonlinear resistive effect of the substrate is responsible for that of the macro PS. Also, to have the same change of potential drop in the substrate, ΔV_R, at a given current density, the radius of curvature must be smaller for a material of larger resistivity according to Eq. (8.12). This means that the pore diameter decreases with increasing resistivity, which agrees with experimental results.[1027]

As a further deduction, the effect of high substrate resistivity should also occur in the case of lowly doped *n*-Si. However, the width of the space charge layer under an anodic potential, at which macro PS is formed, is on the same order of magnitude as the dimension of the resistive layer. The effect of the space charge layer and the resistive layer on the pore diameter are not distinguishable under normal conditions. If the conditions can be controlled such that the pores formed due to the effect of the space charge layer and those due to the effect of the resistive layer have a size difference of at least one order of magnitude, it would be possible to obtain PS with two distinct distributions of pore diameters on high-resistivity *n*-Si as illustrated in Fig. 8.66(a). Such a condition might exist at a low potential (small space charge layer thickness) on a back-illuminated substrate. Also, if this is true it should then be possible to obtain PS with three distinct distributions of pore diameters on a front-illuminated sample as illustrated in Fig. 8.66(b).

Anisotropic Effect. As discussed in Chapter 7, anisotropic etching occurs when the dissolution reactions depend on the concentration of the active surface species. In

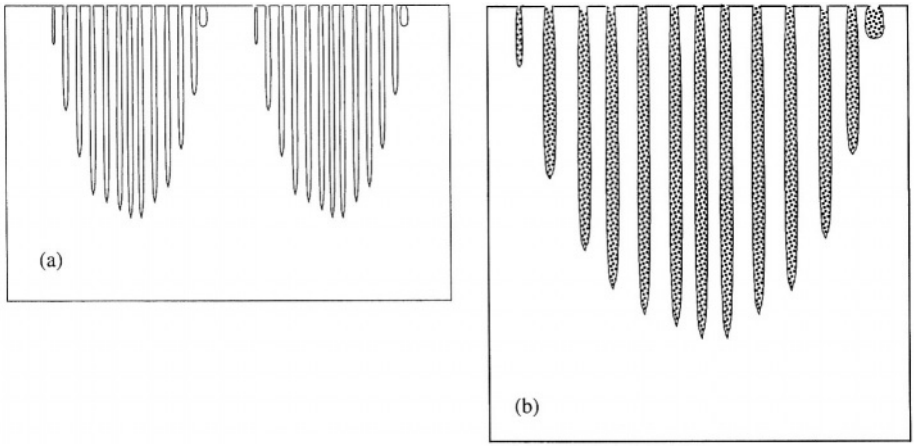

FIGURE 8.66. Schematic illustration of PS with (a) two, (The tips of the pores forms the contour of the larger pores) and (b) three distinct distributions of pore diameters the dots inside pores represent micro PS.

alkaline solutions, the active surface species are the atoms on the (111) steps which are likely to be bonded by two or three foreign species such as H, F, and OH and are thus most easily removed from the lattice in a reaction with the electrolyte. The fact that (100) is a preferentially attacked direction during PS formation indicates that the same mechanism as that involved in alkaline solutions may be involved in the anisotropic growth of pores. The difference between this case and that in alkaline solutions is that in HF solutions the removal of silicon atoms is an electrochemical reaction involving holes such that the rate of reaction depends on $[h]^*[Si_{active}]^*[A]$ whereas in alkaline solutions it depends only on $[Si_{active}]^*[A]$ (see Fig. 7.40). The rate of the electrochemical reaction is a function of the potential across the Helmholtz layer.

Simplistically, the effect of anisotropic dissolution on the growth of pores can be described by the difference in the current densities between the (100) and (111) orientations, $\Delta i_{<100>} = i_{<100>} - i_{<111>}$, and the current density on pore bottoms as shown in Fig. 8.67. Thus, at the tips of the main pores, the total current density is that due to carrier effect plus that due to lattice effect

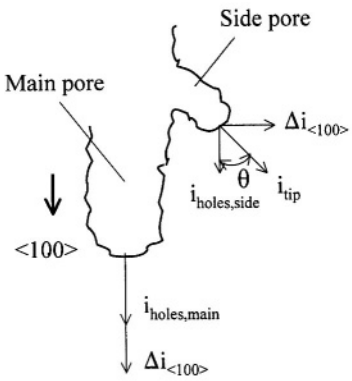

FIGURE 8.67. Schematic illustration of the current components at the tips of the main pores and side pores.

$$i_{t,main} = i_{hole,main} + \Delta i_{<100>} \tag{8.14}$$

while at the tips of the side pores the current density is

$$i_{t,side} = i_{hole,side}\cos\theta + \Delta i_{<100>}\sin\theta \tag{8.15}$$

That the growth rate of the side pores is generally much slower than that of the main pores may reflect the fact that carrier current of the side pores $i_{hole,side}$ is much smaller than $i_{hole,main}$ due to the unfavorable geometric location. Also, for the side pores the component due to carrier effect and that due to lattice effect do not overlap. Thus, side pores grow in an angle, $\tan\theta = \Delta i_{<100>}/i_{hole,side}$, from the growth direction of the main pores and only become normal to the main pores when $\Delta i_{<100>} >> i_{hole,side}$. Also, when $i_{hole,main} >> i_{hole,side}$ the side pores do not grow very long before they cease growing because the growing bottom of the main pore quickly moves the source of holes farther away from the side pore. There is little branching under such a condition.

Reactions on the Surfaces of Silicon and Silicon Oxide. As discussed in Chapter 5, there are two basic reactions, that is, direct dissolution of silicon and indirect dissolution through the formation and dissolution of silicon dioxide. The rates of both reactions increase with potential and proceed simultaneously on the surface of silicon. They compete with each other in rate and coverage of the surface area, and the relative surface coverage of the two reactions depends on the potential. At a low potential the surface coverage of oxide is zero when the rate of oxide formation is low compared with the dissolution rate of the oxide. On the other hand, the coverage is 1 and the entire surface is covered with an oxide film when the rate of oxide formation is much higher than the dissolution rate of oxide. Between the two extremes the surface is partially covered with oxide films at local places where the rate of oxide formation equals the oxide dissolution rate. At low potentials the oxide formation rate is low compared with the dissolution rate and the surface is not covered with an oxide film. Thus, depending on the radius of curvature the bottom of a pore may be covered with an oxide film of varying thickness as shown in Fig. 8.68.

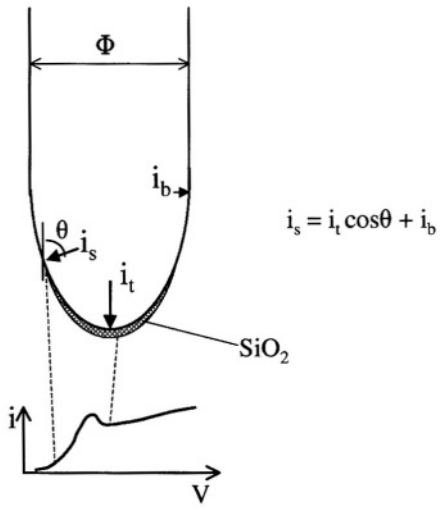

FIGURE 8.68. Schematic illustration of current variation and coverage of silicon oxide on the surface of a pore bottom.

Such reaction processes are responsible for the transition with increasing potential from PS formation to electropolishing as typically revealed in an i–V curve.[2] Once the whole surface is covered with an oxide film, further reaction can only proceed through the formation of oxide followed by its dissolution by HF and electropolishing rather than PS formation occurs. Increasing further the potential will only increase the oxide film thickness. On the other hand, increasing HF concentration will increase the dissolution rate of oxide (see Chapter 4). The presence of oxide on the silicon surface in the PS formation region and its increase with potential have been experimentally observed.[326]

When the surface is completely covered with an oxide film, dissolution becomes independent of the geometric factors that are responsible for the formation and directional growth of pores, such as surface curvature and orientation. Fundamentally, unlike silicon, which does not have an atomic structure identical in different directions, anodic silicon oxides are amorphous in nature and thus show intrinsically identical structure in all orientations. Also, on the oxide-covered surface the rate-determining step is no longer electrochemical but rather the chemical dissolution of the oxide.

Distribution of Reactions and Their Rates on Pore Bottoms. For a stably growing PS the reactions and rates are different on the pore walls and on the pore bottoms. Furthermore, they are different at different positions of a pore bottom due to the difference in the radius of curvature. The current is the largest at the pore tip because there the radius of curvature is the smallest. It decreases from the pore tip to the pore wall as the radius of curvature increases. On the other hand, because the reactions involved on a silicon surface in HF solution depend on the current density, for a given condition, direct dissolution of silicon dominates at a relatively low current range whereas oxide formation and dissolution dominate at a higher current range. Thus, oxide formation and dissolution tend to occur at the pore tips at a lower applied potential than at the side of the pore bottom. The distribution of the kinds of reactions along the pore bottom at different current densities is shown in Fig. 8.69.

For a pore to propagate under a steady state the current density on the side of the pore bottom, i_s, and that at the pore tip, i_t, as illustrated in Fig. 8.68 have the following relation:

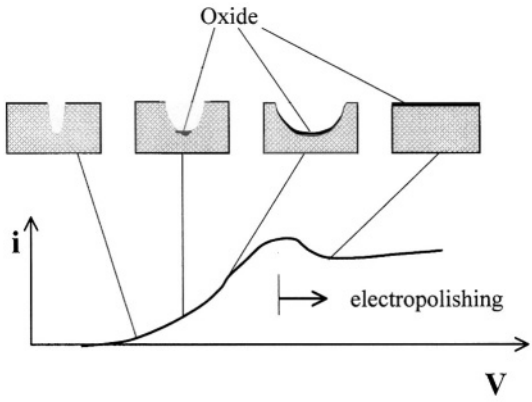

FIGURE 8.69. Schematic illustration of distribution of oxide along a pore bottom as a function of potential.

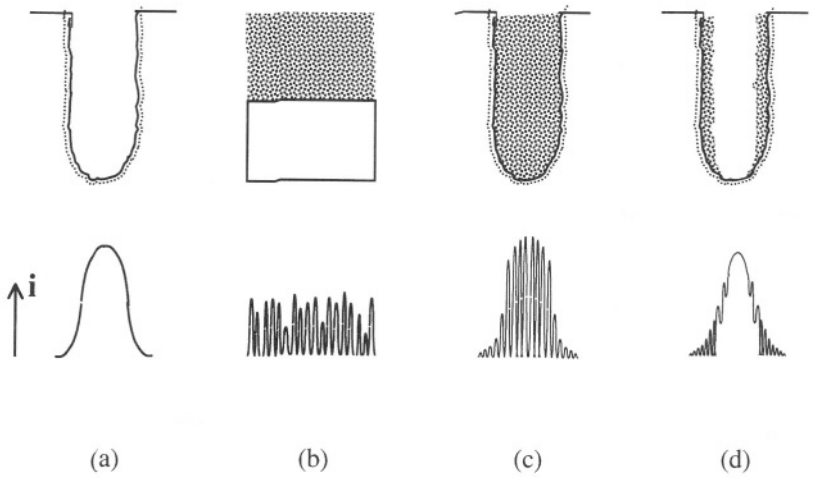

FIGURE 8.70. Schematic illustration of different types of PS and the current distributions along the illustrated dimension: (a) void macropore; (b) micro PS; (c) macropore filled with micro PS; (d) macropore partially filled with micro PS.

$$i_s = i_t \cos\theta + i_b \tag{8.16}$$

where i_b is the extra current mostly due to the anisotropic effect and is responsible for the formation of the side pores. The current density at different sites on the bottom depends on θ. It is the largest at the tip where $\theta = 0$, and is the smallest on the boundary of the bottom where $\theta = 90°$. Such a distribution of current density is provided by the distribution of radius of curvature along the pore bottom, which determines the field at the silicon surface and the nature of the reactions. For different HF concentrations and potentials the current density distribution on the pore bottom is different and so is the shape of the pore bottom. When the pore bottom is curved to such an extent that the current density distribution on the pore bottom for a given HF concentration and a given potential satisfies Eq. (8.16), pores will propagate stably.

For macropores in a stable growth condition, the distribution of current density on the surface of an individual pore bottom is bell-like and is constant with increasing depth as shown in Fig. 8.70(a). For micro PS, the pores tend to grow in a randomly fashion. The distribution of the current at the dissolution front of the PS is highly modulated across the surface as illustrated in Fig. 8.70(b). The distribution changes with time but at any given time there are areas on which the current is near zero (e.g. on the walls).

For two-layer PS, in which macropores can be filled or partially filled with micro PS, the current profiles are illustrated in Fig. 8.70(c,d). The bell-shaped distribution of the current responsible for the growth of the macropores consists of fine modulations of the current responsible for the growth of the micro PS. When the current densities are such that no oxide occurs on any area of the pore bottom, the macropore is fully filled with micro PS. When the current densities are such that oxide forms at the tip area, and no micro current modulation is possible on the oxide-covered surface, the formation of partially micro PS-filled macropores occurs. These different levels of current modulation are governed by the effects of curvature, orientation, and illumination.

Dissolution of PS. The dissolution of PS during PS formation may be due to two processes: a process in the dark and a process under illumination. Both are essentially corrosion processes by which the silicon in the PS is oxidized and dissolved with simultaneous reduction of the oxidizing species in the solution. The corrosion process is responsible for the formation of micro PS of certain thickness (stain film) as well as the dissolution of the existing PS. The material in the PS which is at a certain distance from the pore tips is little affected by the external bias due to the high resistivity of PS and is essentially at an open-circuit condition (OCP). This dissolution process, which is often referred to as chemical dissolution, is an electrochemical process because it involves charge transfer across the interface. The anodic and cathodic reactions in the microscopic corrosion cells depend on factors such as surface potential and carrier concentration on the surface which can be affected by illumination and the presence of oxidants in the solution.

Because the dissolution of silicon in HF solution requires holes according to reaction II in Fig. 5.68, the corrosion rate of silicon in HF solutions is very low due to the unavailability of holes at the OCP (see Chapter 7). But due to the large surface area of PS the amount of dissolution still has a significant effect on the density of PS (e.g., PS density decreases with increasing PS thickness as shown in Fig. 8.51). The presence of oxidants in the solution can greatly increase the corrosion rate of PS.

Illumination generates holes within the material of the PS and causes photocorrosion of the PS. Depending on the illumination intensity and time, the PS can be thinned to various extents by the photoinduced corrosion. This corrosion process is responsible for the etched crater between the initial surface and the surface of PS as shown in Fig. 8.45. It is also responsible for the fractal structure of the micro PS formed under illumination due to the different widths of the surface charge layer at which the holes are generated.

Potential Drops in Different Phases of the Current Path. There are five possible physical phases in the current path in which significant potential drops may occur as illustrated in Fig. 8.71. They are the substrate, the space charge layer, the Helmholtz layer, the surface oxide film, and the electrolyte. The overall change in the applied

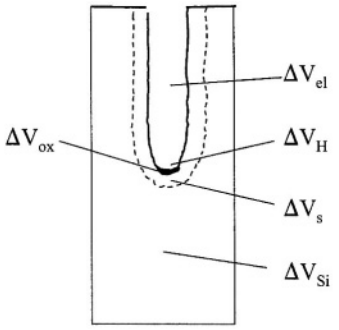

FIGURE 8.71. Schematic illustration of the potential drop along the current path in a pore. ΔV_{Si}, potential drop in silicon substrate; ΔV_s, potential drop in the space charge layer; ΔV_{ox}, potential drop in oxide; ΔV_H, potential drop in the Helmholtz layer; ΔV_{el}, potential drop in electrolyte.

$$\Delta V_{app} = \Delta V_{si} + \Delta V_s + \Delta V_{ox} + \Delta V_H + \Delta V_{el}$$

potential due to a change of current density in the current path is the sum of the potential drops in these phases:

$$\Delta V_{app} = \Delta V_{Si} + \Delta V_s + \Delta V_H + \Delta V_{ox} + \Delta V_{el} \tag{8.17}$$

As described above, the factors that cause change of the current distribution on the bottom of pores will affect the morphology of PS. Thus, the phases in the current path that have relatively large resistance will take large portions of the change in the applied potential and thus change the current distribution along the pore bottoms, affecting the morphology of PS. For a given condition, i.e., doping type and concentration, HF concentration, current density, potential, illumination intensity and direction, there is a certain distribution of the applied potential in the different phases of the current path.

The last term, ΔV_{el}, in Eq. (8.17) is the resistance of the electrolyte. It causes a potential drop that is linearly distributed in the electrolyte inside the pores and thus does not have an effect on the current distribution on the pore bottom although it takes a significant amount of in the applied potential. However, as will be discussed later, the potential drop in the electrolyte has an important effect in maintaining the flat growth front of the PS layer.

In the case when the substrate is moderately doped and the surface is free of oxide, the rates of reactions are determined by the resistance in the space charge layer and in the Helmholtz double layer. The reactions under these conditions have a great tendency to localize because the rates of charge transfer in both layers are sensitive to geometric factors. The reaction that is kinetically limited by the space charge layer is sensitive to the radius of curvature and that by the Helmholtz layer to the orientation of the surface. Depending on the relative effect of each layer, the curvature effect versus anisotropic effect can vary.

When the pore bottom is covered with an oxide, partially or fully, the change of applied potential occurs almost entirely in the oxide due to the very high resistance of the oxide. The rate of reactions is now limited by the chemical dissolution of the oxide on the oxide-covered area and when the entire pore bottom is covered with an oxide the rate of reaction is the same on the entire surface of the pore bottom. As a result, the bottom flattens and no PS forms. The change of oxide coverage on the pore bottom can also occur when diffusion of the electrolyte inside deep pores becomes the rate-limiting process. A decreased HF concentration at the pore bottom due to the diffusion effect can result in the formation of an oxide on the bottom of deep pores under conditions in which it does not occur in shallow pores.

In the case when the resistance of the substrate is high and a significant amount of potential is dropped in the substrate, the potential drop may not be uniform along a curved pore bottom due to the nonlinear potential distribution in the material surrounding the bottom. Formation of macro PS on lowly doped materials due to resistive effect becomes possible under such conditions.

Relativity of the Dimensions and Events. Formation of PS is due to preferential dissolution of a silicon surface; the rate is larger at some areas of the surface relative to others. Such relative rates with respect to the spatial position of the areas, on which these processes occur, are determined by the relative nature of the physical and

chemical dimensions and events. Specifically, the relative nature of the following aspects are important in determining the morphology of PS:

1. The phases that produce a *relatively large contribution* to the change of applied potential affect the current distribution along the pore bottom and thus affect the morphology of PS.
2. The effect of radius of curvature only becomes significant in affecting the width of the space charge layer when its value is on the same order or less *relative* to the width of the space charge layer.
3. It is the *relative depletion,* not the absolute depletion, that is important in determining the directional growth of pores (the walls of many types of PS are not depleted). The relative depletion is due to the *relatively fast advance* of the pore tips which allows very little time for reactions on the walls before the wall region becomes depleted.
4. The *relative magnitude of the current* in the direction of the carrier source to that in the direction of <100> affects the tendency to branch. The larger the former compared to the latter, the smaller is the tendency to branch.
5. The *relative dissolution rate* on the (100) surface to that on the (111) surface is a determining factor for the orientation of pores.
6. The *relative growth rate* of the side pores to that of the main pores affects the length of the side pores. The length of the side pores is short when their rate of growth is much smaller than that of the main pores because the relatively fast-growing main pores quickly deplete the carriers at the tips of the side pores.
7. The *relative change of the profile of* the pore bottom due to a given amount of dissolution caused by local current perturbation determines the straightness of pores. Assume that the amount of dissolution due to a current perturbation, Δi, is $\Delta m = A\Delta i^* t$ where A is a constant. This amount of dissolution may cause only a small change of the profile of the bottom of a large pore but can significantly change that of a small pore and thus alter the growth direction of the small pore as shown in Fig. 8.72. This is why the large pores are generally straighter than the small pores.
8. Related to point 7 is the scale of the regular morphological features in a PS *relative* to the size of the perturbation caused by the reaction processes which are stochastic near the atomic scale. The stochastic nature of these reactions affects the phenomena of larger scales through different factors in the solution, interface, and substrate, seen as inhomogeneities in the crystalline structure, temperature, concentration, and so on. This aspect of relative regularity at different scales is reflected in the dimensional distribution of the morphological features such as the size of pores and smoothness of the pore walls. As a result, the larger scale features of PS generally have more regular patterns than the smaller ones.

Pore Diameter and Interpore Spacing. Pore diameter and interpore spacing are the prominent morphological parameters which as discussed above are determined by two large groups of factors: those that affect the dimension of the space charge layer and those that affect the distribution of the reactions on the pore bottoms. The first group of

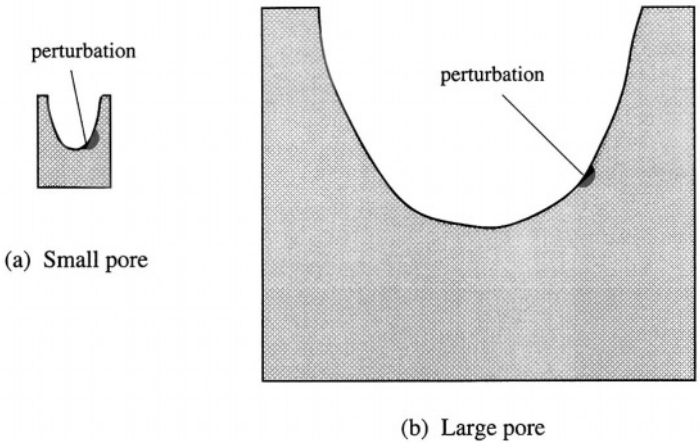

FIGURE 8.72. Schematic illustration of the effect of a given amount of local current perturbation on the profile of a small pore relative to a larger pore. The profile of the small pore is altered more than that of the larger pore.

factors include doping type and concentration, potential, and illumination direction and determine the overall range of pore diameters. The second group of factors include current density, HF concentration, illumination frequency, and intensity and determine the variation of pore diameter and interpore spacing. Eventually, the change of pore diameter, pore wall thickness, and transition from PS formation to electropolishing on silicon are determined by the change of the distributions of the reactions and their rates along the pore bottom by changing the shape of the curved pore bottom. Except for the macro PS on lowly doped *p*-Si, both pore diameter and wall thickness are largely determined by the width of the space charge layer. Pore diameter is determined by the radius of curvature which is on the same order of magnitude as the width of the space charge layer. Wall thickness is generally less than twice the space charge layer thickness so that the walls are depleted of carriers because of the overlapping of the two space charge layers. If the wall thickness is larger than twice the space charge layer, the walls are not depleted of carriers and dissolution can still occur and new pores can form along the wall and propagate into the wall. Under certain conditions such as back-side illumination and surface patterning, pore walls can be much larger than twice the space charge layer because of the large relative depletion of the carriers in the walls compared with carrier concentration at the pore tips as discussed in the preceding section.

The actual wall thickness depends on the relative dissolution rates between the edge of a pore bottom (see Fig. 8.68) and the tip, that is, between i_b and i_t. If i_b is comparable to i_t, significant dissolution occurs at the edge of the pore bottom before the pore tip propagates a distance away. This will result in a thin wall, or even no wall at all when i_b equals i_t. On the other hand, if i_b is very small compared to i_t, the pore tip will propagate relatively fast so that, before much dissolution occurs on the edge of the pore bottom, the edge has already moved into the wall region where the current is very small and the dissolution is virtually stopped. This will generate relatively thick walls (compared to pore size).

At a given anodic current density, the potential, which determines the width of the space charge layer, is different for different doping type and concentration due to different current conducting mechanisms. The combination of doping and potential thus provides a wide range of space charge layer widths and thus a wide range of pore diameters. Figure 8.73 schematically illustrates the space charge layer width for differently doped materials. For *n*-Si the space charge layer and thus the dimension of the pores increases with decreasing doping concentration and increasing potential. For *p*-Si, on the other hand, the application of an anodic potential reduces the width of the space charge layer which results in smaller pores. However, when the doping concentration is lower than a certain level, the effect of resistivity of the substrate becomes important and formation of macropores occurs. A micro PS layer can form on the surface of the macropores when the width of the space charge layer is also in effect. The band structure for such a case is illustrated in Fig. 8.73(a). This mechanism should also operate for lowly doped *n*-Si as illustrated in Fig. 8.73(d).

Under illumination, photocarriers are generated in the semiconductor from the surface to the depth of penetration determined by the wavelength of the light. The thickness of the space charge layer which has a field effect on the photocarriers then varies from almost zero to the full width of the space charge layer depending on where those carriers are generated. Correspondingly, the size of pores and wall thickness for the PS formed under illumination may vary from zero (i.e., corrosion of PS) to that comparable to the width of the space charge layer, resulting in a fractal-like structure.

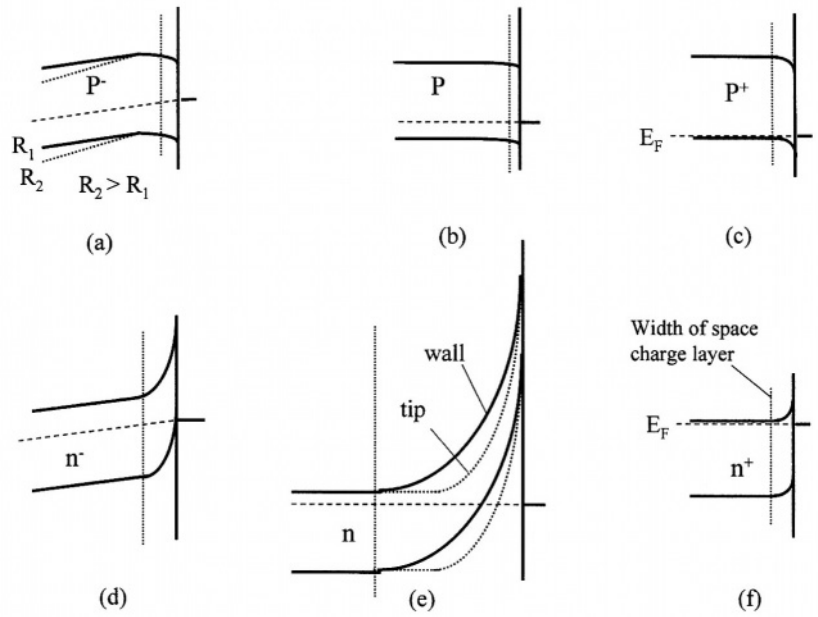

FIGURE 8.73. Band structures of different materials during PS formation under anodic polarization. (a) Lowly doped *p*-Si; (b) moderately doped *p*-Si; (c) heavily doped *p*-Si; (d) lowly doped *n*-Si; (e) moderately doped *n*-Si; (f) heavily doped *n*-Si; R is the resistance of the substrate.

When the current is larger than a certain value at which oxide starts to form at the tip of pores, increasing current density will increase the coverage of the oxide film on the pore bottom. In such a case the relative change in the current at the pore tip $\Delta i_t/i_t$ with an increase in the overall current, Δi, is less than that at the side of the pore bottom, $\Delta i_s/i_s$, that is, $\Delta i_t/i_t < \Delta i_s/i_s$. As a result, the pore bottom is flattened, which results in larger pores and thinner walls. On the other hand, when the current is relatively small so that the current density at the pore tips is still much less than that required for the formation of oxide, an increase in applied current density will cause a relatively larger change at the tip than on the side of the pore bottom (the slope of an i–V curve in this current range increases with increasing current density), that is, $\Delta i_t/i_t > \Delta i_s/i_s$. As a result, the pore bottom becomes sharper with increasing current density.

On the other hand, increasing the concentration of HF increases the dissolution rate of oxide, which in turn increases the sharpness of the pore bottom. As a result, the pores become smaller and the walls thicker.

Variation of Morphology from Surface to Bulk. Initiation of Pores. Formation of pores is a result of preferential dissolution of the silicon surface due to the sensitivity of the electrochemical reactions to the surface curvature. A silicon surface, no matter how well it is prepared, is not perfectly flat at the atomic scale, but has surface defects such as surface vacancies, steps, kink sites, and dopant atoms that constitute the intrinsic microroughness of the surface (see Chapter 7). The dissolution of the surface is thus not uniform but modulated at the atomic scale with higher rates at the defects and depressed sites. The microroughness of the surface will increase with the amount of dissolution due to the sensitivity of the reactions to surface curvature associated with the micro depressed sites. These sites, due to the higher dissolution rates, will evolve into pits and eventually into pores. It is generally observed that for two-layer PS on *p*-Si and illuminated *n*-Si, a certain thickness of micro PS or etching, which is required to generate the right radius of curvature, occurs prior to the initiation of the macropores.

The pores so initiated are very small in size but large in number due to the nature of surface defects. However, for PS formed under a steady state at a given anodization condition, the morphology has certain characteristics in terms of pore size, density, branching, and so on. Thus, the tiny pores initiated on the surface are not stable but tend to grow to the size required for a stable pore propagation. As the pores propagate into the bulk, some vanish and some grow gradually in size. The thickness of the initiation phase is comparable to the diameter of the pores grown at the steady state as shown for example in Fig. 8.37.[8] Thus, the initiation layer is very thin for micro PS and relatively thick for macro PS.

It is important to note that although surface defect sites are associated with the initiation of pores, they do not determine the density and dimension of the pores in the bulk PS. The bulk morphology of PS is determined by the property of semiconductors and anodization conditions. However, under certain conditions such as those for the formation of macropores on lowly doped materials, control of the initiation sites by surface patterning can to some extent change the PS morphology.

Flatness of the Growth Front of PS. The growth front of all types of PS is generally flat and parallel to the initial surface of the substrate, meaning that the pores, which may have a range of diameters and shapes, propagate at essentially the same rate.

As discussed in the section on the distribution of the applied potential in the different phases in the current path, the electrolyte inside a pore does not affect the current distribution on the pore bottom due to the even distribution of the potential along the length of the pores. However, it is the potential drop in the electrolyte phase that maintains the same growth rate for the different pores. For a pore of length l, the potential drop in the electrolyte with resistivity ρ inside the pore at an average current density i is $\Delta V_{el} = i*\rho*l$ which is independent of pore diameter and shape and depends only on one geometric factor, that is, the length of the pores. Assuming that one pore is significantly ahead of the rest of the pores, the current i in this pore will increase due to the reactions occurring on the side wall of the pore. This will then increase the potential drop, ΔV_{el}, which in turn will result in a reduction of the potential available for other phases in the current path. The reduction of the potential in other phases will then reduce the current density on the pore bottom and slow the growth of the advanced pore. Thus, due to such a process individual pores can only grow at the same rate and as a result, the growth front of a PS layer is flat at a scale larger than the diameter of pores.

Two-Layer PS. Two-layer PS with a micro PS on top of a macro PS layer is formed on lowly doped *p*-Si or illuminated *n*-Si. For lowly doped *p*-Si, two-layer PS can form when the conditions are such that the space charge layer and the resistive layer differ in dimension by several orders of magnitude and both are significantly involved in the rate-limiting process due to the effect of surface curvature on the current flow near the surface and in the substrate. For *n*-Si, two-layer PS can form on a front-illuminated substrate as long as the conditions exist for the formation of macropores. It may also form in the dark under conditions similar to those for the formation of two-layer PS on lowly doped *p*-Si.

Figure 8.74 illustrates the two-layer PS formed on illuminated *n*-Si. The photogenerated holes are located near the surface and flow in various directions depending on the direction of the field inside the crystallites of the PS. These photocarriers can

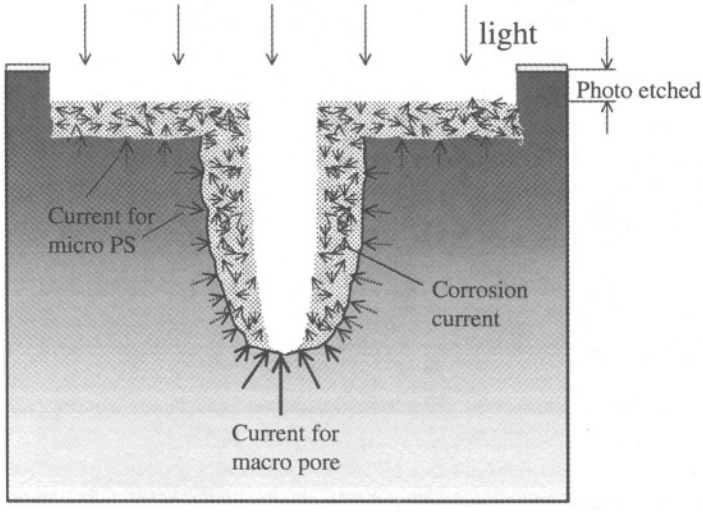

FIGURE 8.74. Schematic illustration of formation of a macropore partially filled with micro PS on *n*-Si under illumination. Shades represent the density of photo generated holes.

result in the dissolution of PS without the assistance of an applied anodic potential and are responsible for the etching of the PS layer, On the other hand, the photocarriers generated at different depths within the space charge layer are collected at the bottom surface of the macropores, resulting in the formation and growth of the micro PS. The holes that are generated beyond the space charge layer are mostly collected and react at the bottom of the macropores. Also, depending on the current density relative to that for the formation of oxide, the tip area may or may not be covered with an oxide film. When the entire pore bottom is not covered with any oxide, the macropores will be fully filled with micro PS. On the other hand, when the tip area of pores is covered with an oxide film, local micromodulation of current density due to photocarriers generated at different depths is not possible so that the macropores are only partially filled with micro PS as illustrated in Fig. 8.74.

8.6.3. Summary

PS displays a wide range of morphological variations. However, under a given condition, except for the transition layer near the surface, the pores are spatially uniformly distributed and the reactions occurring anywhere within PS during its growth can be represented by what occurs on the surface of a single pore–wall–pore unit. Thus, the formation of PS having specific morphological features is basically determined by the distribution of reactions and their rates along the surface of this unit.

Kinetically, the overall dissolution process consists of carrier transport in the semiconductor, electrochemical reactions at the interface, and mass transport of the reactants and reaction products in the electrolyte. Also, there are a number of reactions involved at the interface and these reactions consist of several steps and subreactions. At any given time the dissolution kinetics can be controlled by any one or several of these steps. The distribution of reactions along a pore bottom under a steady-state condition during pore propagation must be such that pore walls are relatively less active than the pore tip. Then, the dissolution reactions are concentrated at the pore tip resulting in the preferential dissolution and formation of pores. The formation of pores is the consequence of spatially and temporally distributed reactions.

The distribution of the reactions and their rates on the surface of a silicon electrode in HF solution are determined by at least the following processes: (1) Electrochemical reactions on a semiconductor surface are sensitive to surface curvature. The reaction rates at depressed sites which have smaller radii of coverture are larger than those of the surrounding area. Such sites may preexist due to the intrinsic random roughness of the surface or may be generated after a certain amount of dissolution which roughens the surface. (2) The reactivities of the atoms on the surface of different crystal orientations are intrinsically different (anisotropic nature). (3) In the entire current path the phases that cause significant potential changes due to current perturbation will affect the distribution of the current and reactions on a curved surface. (4) The reactions involved in silicon dissolution have two paths: Silicon may react with fluoride species and dissolve directly into the solution or may react with water to form oxide and dissolve indirectly. The direct dissolution is sensitive to surface geometrical factors such as surface curvature and orientation, but the indirect

dissolution through the formation and dissolution of oxide is insensitive to the surface geometrical factors. Formation of an oxide film masks the semiconductor properties of silicon.

The fundamental reason for the formation of pores is that the rate of electrochemical reactions on a semiconductor is sensitive to the radius of curvature of the surface. This sensitivity can either be associated with the width of the space charge layer or the resistance of the substrate. Thus, when the rate of the dissolution reactions depends on the width of the space charge layer, formation of pores can in principle occur in a semiconductor electrode, not just on silicon. The specific porous structures are governed by the relative significance in spatial and temporal scales among the geometric dimensions, reactions and their rates, physical regions of the current path, and so on. Because different dimensions, rates, regions, and so on may be significant in the formation process, the mechanistic details for the formation of each specific type of PS morphology vary with situations. As a global generalization, the conceptual analysis for the mechanisms involved in the formation of PS can be called the curvature-relativity model.

The types of PS can be categorized into three groups according to this model: (1) Space charge layer controlled; this includes all PS except for the macro PS formed on *p*-Si The diameter of the pores in this group is comparable to the width of the space charge layer. (2) Substrate resistance controlled; this includes the macro PS formed on lowly doped *p*-Si and possibly on lowly doped *n*-Si (a prediction). (3) Photocarrier controlled; this includes two-layer PS (micro PS for $\alpha^{-1} >$ SCL and macro PS for $\alpha^{-1} <$ SCL) and the micro PS structures resulting from photocorrosion.

Figure 8.75 summarizes PS features according to the formation conditions defined by the kinetics relative to current and HF concentration. The lines defining the regions are determined by the nature of the reactions and are independent of the doping type and concentration (see Fig. 8.5). One important factor governing the change of one region to another shown in Fig. 8.75 is the formation and coverage of an anodic oxide film on the surface. The coverage of oxide on the surface increases from zero in PS region A to only at pore tips in PS region B to part of the surface in the transition region to full coverage in the electropolishing region. The actual size of the pores under a given anodization condition is primarily determined by doping concentration. Most of the other morphological features can be phenomenologically correlated with pore diameter as illustrated in Fig. 8.56. The mechanisms responsible for these features are determined by the various factors involved in the formation processes discussed in Section 8.6.2. The characteristics of fundamental reaction processes and the rate-limiting steps in these reactions are given in Table 5.8.

A quantitative description of the diverse morphological features of PS requires the integration of the aspects discussed above as well as the fundamental reaction processes involved in silicon/electrolyte interface structure, anodic dissolution, and anodic oxide formation and dissolution as detailed in Chapters 2–5. Any mathematical formulation for the mechanisms of PS formation without such a global integration would be limited in the scope of its validity and in the power to explain details. In addition, a globally and microscopically accurate model would also require the full characterization of all of the morphological features of PS in relation to all of the

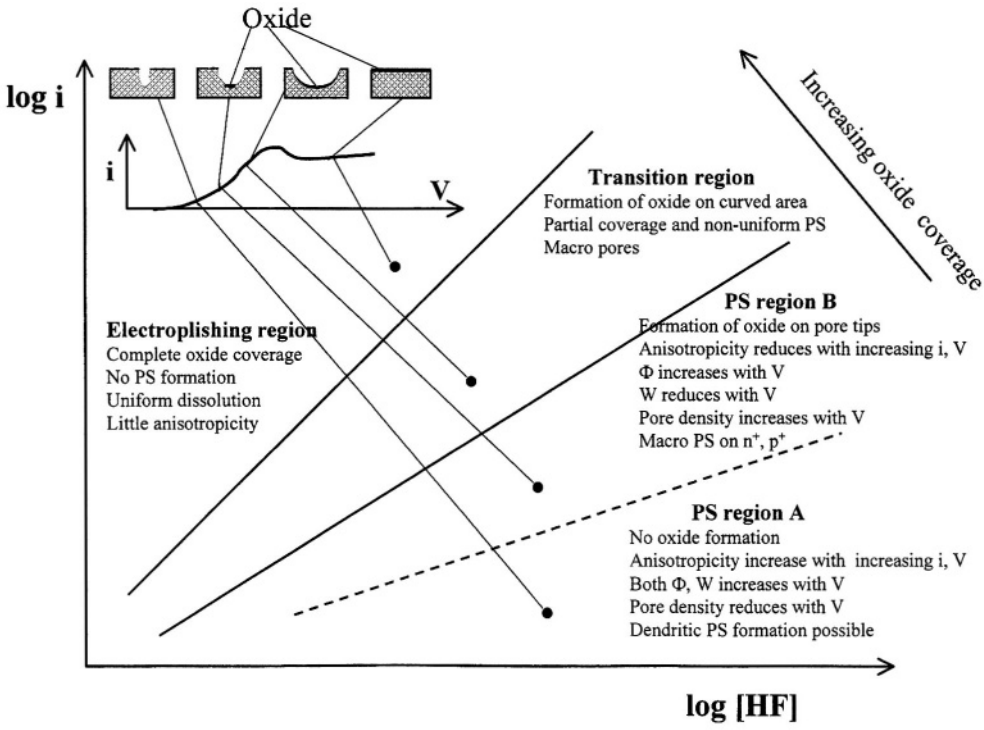

FIGURE 8.75. Conditions for the formation of various morphological features of PS.

formation conditions, which has not as yet been achieved according to the information gathered in this book.

8.7. PROPERTIES AND APPLICATIONS

As may be expected from the rich morphology, PS has a wide range of interesting properties, of which luminescence is most well known. Since its first report by Canham in 1990,[72] the phenomenon of luminescence has been intensely investigated due to the strong interest in the potential application of PS as an optoelectronic material. This research effort has generated a huge amount of results; some 1500 papers were published on PS in the 7 years following Canham's finding.[1107,1111] This body of information is not dealt with in detail in this book as the focus here is on the electrochemical properties of single-crystalline silicon, not those of PS which is essentially a different material. Table 8.8 lists examples of studies on the properties of PS so as to provide a rough idea of the scope of this research area. Detailed review of this body of information can be found in a number of articles.[870,1107,1073,1075,1161]

TABLE 8.8. Examples of Investigations on the Properties of Porous Silicon

Properties	Treatment and measurement	Refs.
Thermal	Oxidation, annealing, etc.	37, 51, 53, 171, 181, 639, 644
Electrical, metal contact	Conductivity, *i–V*, etc.	209, 845
Conductivity, liquid	Electrochemical methods	40, 798, 926
Mechanical	Stress, strain	3, 171, 257, 777
Etching rate	In HF	36, 47, 48
	In NaOH	36, 50
Deposition of polymer	Review	889, 924
	Miscellaneous	30, 188, 889, 1054, 1129, 1164
Deposition of metals	Review	1130
	Fe	783
	Cu	802
	Ni	365
	Tin oxide	31
	Epilayer of GaAs	159
Anodic oxidation	In KNO_3	210, 842, 1121
Capacitance	In liquids	926
Optical	Absorption, reflectance, etc.	71, 176, 870, 890, 1073, 1075, 1088
Electrochemical	*i–V*, E_{fb}, impedance, etc.	140, 209, 360, 611, 892, 926, 988
Luminescence	Review	292, 870, 1073, 1075, 1107, 1111
	Effect of redox couples, EL[a]	945, 969
	Decay of EL	255, 797
	Illumination during PS formation	10, 713
	HCl, EL	843
	In solutions of $SO_4^{2-} + S_2O_8^{2-}$, EL	63, 101, 140, 751, 803, 969, 1014, 1078, 1157, 1160
	Effect of metal deposits	730, 796, 803
	Infrared excitation	28
	Light intensity and wavelength, PS thickness	216, 366, 633, 868
	Doping, current density, solution composition	6, 28, 65, 66, 67, 72, 243, 255, 624, 1014
	In Na_2SO_4, PL	70
	Ambient atmosphere	255
	Wettability, EL	740
	Methoxylation of PS	128
	Effect of temperature	752
	Laterally anodized PS	6, 642, 757
	Double anodization in low or high HF	723
	Chemical PS	239, 250, 732, 746, 747, 749
	Effect of porosity	890
	Effect of annealing	65, 754
	Effect of NaOH treatment	423
	Effect of electron beam radiation	728
	PL during PS formation	578
	Transition of crystallinity by X rays, PL	864
	Effect of PS microstructure	67, 68, 92, 460, 640, 745, 748, 750, 759
	In boiling water	564, 739
	Thermal oxidation	64, 65, 66, 137, 565
	Ozone oxidation	737
	Plasma treatment	738

TABLE 8.8. *Continued*

Properties	Treatment and measurement	Refs.
	Water interaction with oxidized PS	267
	Effect of magnetic field during PS formation	721
	Distribution of oxygen in PS	762
	Aging effect	4, 72, 565, 734
	Anodization, PL	63, 222, 255
	$Si_{1-x}Ge_x$, x = 0–20%, PL	1122
	Poly Si, metallurgical-grade Si	250, 265, 804
	Effect of Oxidants in etching solution, PL	863
	Quantum effect	75, 624, 846, 1156, 1157, 1159

[a]EL, electroluminescence; PL, photoluminescence.

Ideas on the applications of PS in microelectronics, optoelectronics, solar cells, and sensors have continuously been generated since its discovery 50 years ago.[443,823,868,1161] For a similar reason as stated above for the properties of PS, detailed discussion of the applications of PS is not included here. Table 8.9 should serve to provide some relevant references for interested readers.

TABLE 8.9. Examples of the Possible Applications Proposed in the Literature

Applications	PS, process and structure	Refs.
Microchannels	p(111), arrays of curved pipes	1113
Macro porous wafer	n, back illumination	768, 1169
High-aspect pillars	n, back illumination, repeated oxidation and etching	782
Light-emitting diodes	Patterned pn junction	318
Micromachining	p^+, n^+, (111), (100), definition of etched profile	1132
	n, back illumination, porous membrane	1131
	Dubbed trenches	1137
	PS as an undercut sacrificial material	383
Capacitor	n, back illumination, arrays of macropores	1117
Nanopit array	n, AFM tip cathode	1101
Nanocomposite	Deposition of materials into PS, review	1130
Ion sensors	Na^+, oxidized PS on p-Si	997
Localized illumination	n, p, area differential doping	865
Field emission device	PS pixels or diodes	30, 72, 655
Dielectric isolation	Oxidized PS	56, 156, 179, 185, 190, 225
Thermal isolation	PS as a sacrificial processing material	503
Imaging	Variation of PS thickness	24
Biosensor	PS membrane	119
Solar cell coating	PS as an antireflection layer	189
Wafer defect reduction	PS layer as impurity getting center	233

This page intentionally left blank

9

Summary and Closing Remarks

9.1. COMPLEXITY

Silicon exhibits a diverse range of electrochemical phenomena, such as current oscillation, anisotropic etching, formation of porous silicon, etc. Each of these phenomena has extremely rich details that are governed by complex relationships between structures and properties of silicon electrodes on the one hand and between properties and experimental conditions on the other. The silicon/electrolyte interface is a complex system in which a great many variables are interacting with each other in a great many ways.[1182,1183]

The physical and chemical nature of the silicon/electrolyte interface, in terms of carrier type and density, charge distribution and transfer, surface reactions, evolution of surface geometry, etc., are determined by numerous variables as illustrated in Fig. 9.1. Each of these variables is a continuum of a wide dimensional range and its effect on the electrode properties involves time and micro-surface geometry. Thus, the possible conditions determined by the combinations of these variables are infinite, responsible for the diverse phenomena and complex details observed on silicon electrodes. The experimental results on silicon electrodes generated in the past decades have been overwhelming, but many phenomena on silicon electrodes are still not fully characterized due to their complex nature. Also, what occurred in the past indicates that the more is known about the system the more questions are generated. Thus, in a philosophical sense, the details of the system may never be completely revealed because every time a phenomenon is characterized at one temporal-spatial scale under a condition, further details with increasing complexity start to emerge at a finer scale or under a new condition.

The high degree of details that have already been characterized on silicon electrodes is associated with the great diversity of conditions that have been explored, the high sensitivity in experimental control and measurement, and the large number of investigations made in the past. In particular, many details could not be experimentally resolved without the high sensitivity in experimental control and measurement. To this end the most important control has been for the silicon substrate, which is conveniently available in single crystalline form of high quality to researchers of all fields. Such high degree of standardization and availability has been unique to silicon. No

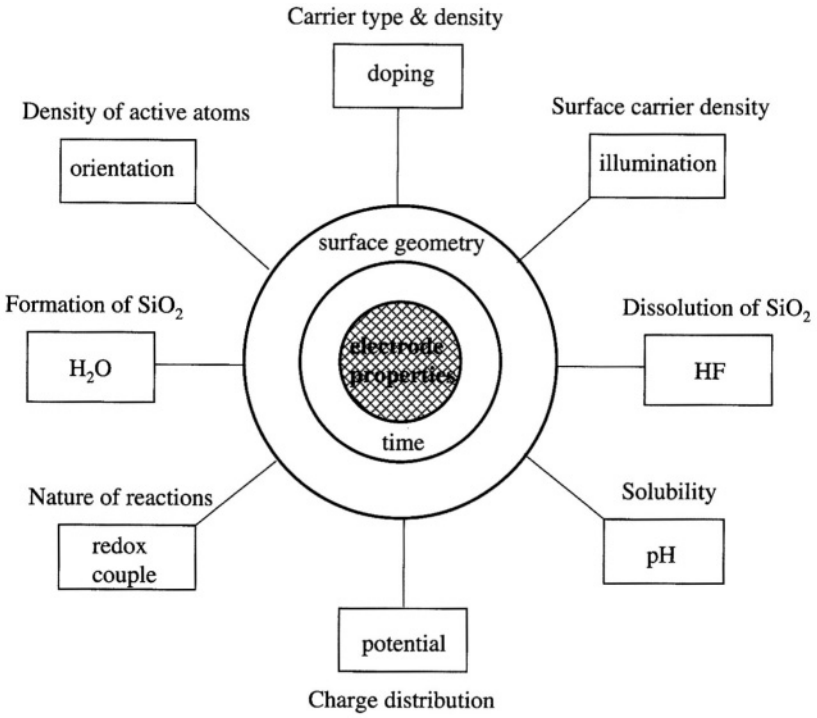

FIGURE 9.1. The major variables that affect the electrochemical properties of silicon electrodes.

other material has this advantage and accordingly none has been characterized to the same levels of details as silicon. In this, silicon is truly a model material, by which new phenomena and science are explored.

The complexity of the system implies that many phenomena are not directly explainable by the basic theories of semiconductor electrochemistry. The basic theories are developed for idealized situations, but the electrode behavior of a specific system is almost always deviated from the idealized situations in many different ways. Also, the complex details of each phenomenon are associated with all the processes at the silicon/electrolyte interface from a macro scale to the atomic scale such that the rich details are lost when simplifications are made in developing theories. Additionally, most theories are developed based on the data that are from a limited domain in the multidimensional space of numerous variables. As a result, in general such theories are valid only within this domain of the variable space but are inconsistent with the data outside this domain. In fact, the specific theories developed by different research groups on the various phenomena of silicon electrodes are often inconsistent with each other. In this respect, this book had the opportunity to have the space and scope to assemble the data and to review the discrete theories in a global perspective. In a number of cases, this exercise resulted in more complete physical schemes for the mechanisms of the electrode phenomena, such as current oscillation, growth of anodic oxide, anisotropic etching, and formation of porous silicon.

One problem in meaningful application of the basic electrochemical theories is related to surface states that may be associated with surface defects, interface states at silicon/oxide interface, adsorbed species, or reaction intermediates. They are often conveniently considered to be responsible for the results that are inconsistent with the basic theories. However, the understanding on the nature of surface states at the silicon/electrolyte interface is still poor; one is aware of some consequences of surface states but knows little of their origins and their specific roles in various electrode processes.

A closely related matter is the measurement and use of the flatband potential. The existing data show that for a silicon/electrolyte interface the flatband potential is specific to the given surface condition. Also, the flatband potential generally drifts due to the fact that the surface of silicon in electrolytes changes constantly with time. Also, it changes with application of potentials which is generally required for the determination of flatband potential. Therefore, any theory which assumes a fixed value of flatband potential will be limited in its scope of validity.

Another problem in application of the basic theories is associated with surface geometry. Most theories are developed to describe the relationships among the area-averaged quantities such as charge density, current density, and potentials assuming a uniform electrode surface. In fact, the silicon surface may not be uniform at the micrometer, nanometer, or atomic scales. There can be great variations in the distribution of reactions from extremely uniform, for example, in electropolishing, to extremely nonuniform, for example, in the formation of porous silicon.

There are two principal aspects with respect to the nature of an electrode surface: 1) the chemical nature in terms of the specific of events at the atomic scale and the kinetic quantities measured at a macroscopic scale which are the global average of the atomistic events; and 2) the physical nature in terms of surface geometry and its effect on the kinetics and its evolution during the reaction processes.

Surface lattice structure at the atomic scale and surface curvature at the nanometer to micrometer scale are two major geometric factors that affect the uniformity of the reactions on the surface and are responsible for the occurrence of anisotropic etching and formation of porous silicon. The difference in the reactivity of the atoms at different surface lattice structures is responsible for the anisotropic nature of reactions, while the electrochemical reactions that depend on the supply of charge carriers is sensitive to surface curvature. The carrier density at depressed sites which have smaller radii of curvature are larger than those of the surrounding area. Such sites may preexist due to the roughness of the surface or may be generated as a result of interaction between the electrode and electrolyte. The spatial distribution of electrochemical processes is determined by geometric factors such as surface lattice structure and curvature, the study of which can be called as geometric electrochemistry.

The overall electrode process consists of carrier transport in the semiconductor, electrochemical reactions at the interface, and mass transport of the reactants and reaction products in the electrolyte. There are a number of physical phases associated in the current path and the change of potential in each phase has a specific effect in relation to surface geometry. Also, a number of different reactions can occur simultaneously on the surface and compete in surface coverage and in reaction rate. Particularly, the anodic reactions of silicon in HF solutions have two parallel paths: silicon may react with fluoride species and dissolve directly or may react with water to form oxide.

The direct dissolution is sensitive to surface geometrical factors such as surface curvature and orientation, while the indirect dissolution through the formation and dissolution of oxide is insensitive to the surface geometrical factors. Formation of an oxide film, which generally shifts the rate limiting process to inside the oxide, masks the semiconductor properties of silicon.

9.2. SURFACE CONDITION

Silicon is a rather active element and unless in a vacuum its surface is never "clean" because of the adsorption by foreign species. In water and aqueous solutions, the surface of silicon can be terminated by various species including hydrogen, hydroxyl, fluorine, and oxide. The specific type of termination, in terms of structure and composition, depends on how the surface is prepared and cleaned. In non-HF aqueous solutions, the silicon surface is generally covered by an oxide film and in HF solutions the silicon surface tends to be terminated by hydrogen (in the form of hydrides). The formation of a surface hydride layer or oxide layer is responsible for the stability of silicon in aqueous solutions.

In HF solutions the surface coverage of hydrogen and oxide is a function of potential. As schematically illustrated in Fig. 6.7, the surface is fully covered by an oxide film at anodic potentials higher than the passivation potential, while it is fully covered by hydrogen at potentials more negative of the open circuit potential. From the open circuit potential to the passivation potential, the surface coverage of hydrogen gradually decreases as the coverage of oxide increases. Also, while at potentials near the open circuit potential and below the passivation potential the hydride or oxide layer is on the order of a monolayer, the hydride layer at the cathodic potentials and the oxide layer at potentials higher than the passivation potential is relatively thick. The difference in the kinetics for formation of a hydride layer and an oxide layer and in the stability of these two layers plays a critical role in the diverse phenomena observed on silicon electrodes.

The silicon surface may be hydrophobic or hydrophilic depending on whether it is terminated by hydroxyl or hydrogen groups. Also, surface impurities, in the form of metals, ceramic, and organic species can reach a surface atomic concentration higher than 0.1% at 1 ppm impurity concentration in the electrolytes. In addition, a silicon surface, even under the best prepared conditions, is not completely flat but has a certain degree of roughness. The roughness can be associated with vacancies, kinks, adatoms, steps, and terraces at the atomic scales and with pits, hillocks, scratches, deposits, etc., at a macro scale. Once in an electrolyte, the hydrophobicity and the roughness tend to change over time as electrode processes occur, which is the basis for the processes, such as cleaning, for surface preparation and control.

9.3. OXIDE FILM

Silicon oxide plays a particularly important role in the properties of silicon electrodes. In air the surface of silicon is always covered with a very thin oxide film, the thickness of which may vary from 5 to 20 Å depending on the preparation conditions.

In water after a sufficient time lapse the surface is always covered with a thin oxide film and the steady state thickness depends on the initial surface condition. The steady state thickness of the native oxide films formed on the silicon surface in water is similar to that formed in air. Water is essential for the formation of oxide on the silicon surface in different solutions, organic or inorganic. Oxide film does not form on the surface in water when the concentration of HF is higher than 10 ppm.

The native oxide can be thickened with application of an anodic potential. The rate of growth and final thickness at a given potential depends, among other factors, on solution composition. Holes from the valence band are responsible for the oxidation reaction for p-Si while injection of electrons into the conduction band is for n-Si. The oxidation reaction occurs at the silicon/oxide interface through several intermediate steps forming partially oxidized species which can act as interface states. The oxygen required to form the oxide structure is from the water, either residual or generated during anodization, in the electrolyte. The water molecules enter into the first layers of the oxide and dissociate into ionic species, such as O^{2-} and/or OH^{-}, which then migrate toward the silicon/oxide interface under the effect of the electrical field in the oxide.

As illustrated in Fig. 3.19, anodic oxide behaves like a doped semiconductor and is capable of conducting a large electronic current under anodizing conditions, which are responsible for the low ionic current efficiency due to side reactions. The side reaction is the oxidation of water in aqueous solution and is the oxidation of the solvent molecules in non-aqueous solutions. Photo emission may result from the charged carriers going through the energy steps at the oxide/electrolyte interfaces, silicon oxide interfaces, and localized states in the oxide during the oxidation process.

The oxide films formed by anodization have generally a loose structure containing a significant amount of water, hydroxyl ions and other species, which are present in the electrolyte. As-formed anodic oxides may contain SiO, SiOH and SiH groups, absorbed water, oxidation products of the solvent and ionic impurities to levels as high as $10^{21}/cm^3$. Due to the incorporation of OH and water, anodic oxides are generally non-stoichiometric with silicon deficient structures. Also, anodic oxide is not uniform but changes with distance from the Si/SiO_2 interface to SiO_2/electrolyte interface and tends to change with time, which plays a critical role in current oscillation.

The physical, chemical, and electrical properties of anodic silicon oxides are determined by this loose structure and the incorporation of foreign species. The electrical properties of anodically formed oxides is very poor in comparison with those of thermal oxides due to the high concentration of charges and states associated with the loose structure and high levels of impurities. Most notably, the etch rates of anodic oxides are generally many times higher than thermal oxide. Also, the silicon/oxide interface region has a high density of partially oxidized silicon atoms, which significantly contribute to interface charge. The reaction of these partially oxidized silicon atoms with hydrogen is also responsible for the small amount of hydrogen evolution and an oxidation valence of less than four in the passive region.

The role of oxide in the major phenomena of silicon electrodes in terms of surface coverage and rates of formation and dissolution can be qualitatively described by Fig. 9.2. Depending on the condition, the surface coverage of oxide may vary from zero to one. Under a condition when the formation rate for the first layer of oxide is larger than the dissolution rate the oxide will grow in thickness and full oxide coverage of the

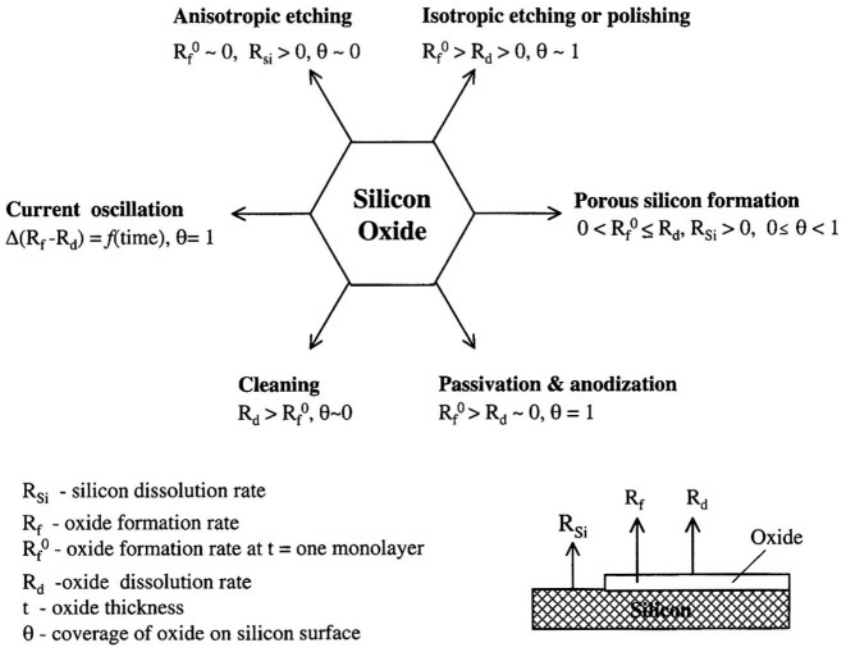

FIGURE 9.2. Conceptual illustration on the role of silicon oxide in different electrochemical phenomena of silicon in terms of surface coverage and rates of formation and dissolution.

surface results, which is the case at the potential higher than the passivation potential. When the formation rate of the first layer of oxide is smaller than the dissolution rate, the coverage is zero. This is the case in silicon surface cleaning in dilute HF solutions, where it is desirable to form a ceratin amount of oxide during the cleaning but the surface must be free of oxide at the end of cleaning. In the case of anisotropic etching in alkaline solutions, which has to occur on a bare silicon surface, the coverage is also near zero because oxide formation is not involved in the dissolution process. In contrast, for isotropic etching or electropolishing in HF solutions the presence of an oxide of certain thicknesses is necessary to mask the crystallographic character of the silicon surface. In the case of porous silicon formation in HF solutions, the active silicon surface may be covered by oxide to a varying degree depending on the specific condition. The walls of pores are free of oxide while the pore tips may or may not be free of oxide depending on current density. In the case of current oscillation on oxide covered surface in HF solutions, the surface is fully covered with oxide but the rates of formation and dissolution of oxide change with time.

9.4. SENSITIVITY TO CURVATURE

A particularly important property of silicon electrodes is the sensitivity of the rate of electrochemical reactions to the radius of curvature of the surface, i.e., the sensitiv-

ity to surface geometry. Since an electric field is present in the space charge layer near the surface of a semiconductor, the vector of the field varies with the radius of surface curvature. The surface concentration of charge carriers and the rate of carrier supply, which are determined by the field vector, are affected by surface curvature. The situation is different on a metal surface. There exists no such field inside the metal near the surface and all sites on a metal surface, whether it is curved not, are identical in this aspect.

Thus, on a perfectly flat semiconductor surface the concentration of charge carriers is uniform across the surface because the vector of the field at every spot of the entire surface is perpendicular to the surface and has the same magnitude. On a curved surface, on the other hand, the rate of carrier transport to the surface depends on the radius of curvature. Therefore, the rate of the electrochemical reactions, when is limited by the supply of charge carriers, is sensitive to the radius of surface curvature. This sensitivity, as an intrinsic property of semiconductors, determines the distribution of reactions on the surface and determines the geometric evolution of the surface when the reaction results in the change of surface morphology. Thus, it plays a critical role in the formation of pores in silicon and surface roughness. Also, it may be an important factor determining the breakdown of passive films of various metals and semiconductors.[1183] This property has generally been observed on semiconductors, for example, the formation of pores on the electrodes of Ge, InP, GaAs, SiC, etc.

Physically, the sensitivity of reactions to surface curvature can be associated with the space change layer or the resistance of the substrate. For moderately or highly doped materials, this sensitivity is only associated with the space change layer because the ohmic potential drop in the semiconductor substrate is very small. However, for lowly doped material a significant amount of potential can drop in the semiconductor to cause the current flow inside semiconductor to be also sensitive to the curvature of the surface. In this situation, the sensitivity is associated with both the width of space change layer and the resistivity of the substrate. The radius of curvature required for the occurrence of the sensitivity caused by space change layer is different from that by substrate resistivity. Therefore, under certain doping and polarization conditions, the current on the surface can have two different distributions associated with radii of curvature of different scales. Such current distribution can result in the formation of geometric structures of two different scales such as the formation two-layer porous silicon (see Fig. 8.70).

The distribution of chemical reactions which do not involve charge carriers in the semiconductor is not affected by surface curvature. Thus, formation of pores does not occur in KOH solutions where the dissolution of silicon is of almost 100% chemical nature. Also, the effect of surface curvature is little when the surface is covered with an oxide film which masks the semiconductor properties of silicon, e.g., during electropolishing in HF.

The sensitivity depends on the radius of curvature relative to the width of space charge layer. This effect can be measured by a normalized parameter $\lambda = x_d/r$, defined as relative curvature.[8,1183] At $\lambda = 1$, i.e., when the radius of curvature is in the order of the width of space change layer the electrochemical reactions will be significantly affected (see Fig. 8.64). Thus, for any electrochemical reactions that can cause the surface geometry to change, either a dissolution or deposition, the surface distribution

of current will be affected by the surface curvatures that have a radius close or smaller than the width of the space charge layer.

9.5. SENSITIVITY TO LATTICE STRUCTURE

The surface of a single crystalline silicon can have different reactivities depending on the orientation of the surface. This orientation dependent reactivity is determined by the bonding condition of the surface silicon atoms in the surface lattice structure which is different for surfaces of different orientations. Characteristically, for example, the atoms on (111) surface have three bonds connecting to the substrate lattice while those on (100) surface have only two. Also, the bonding of the surface silicon atoms to the species in the solution such as OH^- change the bond strength of the atoms to the substrate, and thus their reactivity, to varying extent. In addition, a real surface has atomic structures associated with roughness and defects, which deviate from the lattice structure of determined by the orientation. The atoms at these structures have different bonding conditions and different reactivity.

The reactivity of the surface can be described by the density of the active surface atoms as illustrated in Fig. 7.40. The density and distribution of surface active atoms determines the difference in the reactivity of different surfaces. Thus, the etching of silicon in KOH is anisotropic because the difference in the density of surface active atoms on (100) and (111) surfaces is large. On the other hand, the etching of silicon in $HF–HNO_3$ is largely isotropic because the density of surface active atoms is similar for surfaces of different orientations. In HF solutions, the surface has an intrinsic tendency to roughen due to the sensitivity of the electrochemical reactions to surface curvature. As a result, the surface which is rough at the atomic scale has no distinct crystallographic character and can be viewed as an amorphous surface, as illustrated in Fig. 9.3a. On the other hand, the surface shown in Fig. 9.3b is less rough and has a clear crystallographic character. It can be generalized that when the number atoms at kink sites, steps, and other defects is close to the density of surface atoms, the surface loses its crystallographic nature. Similarly, the reaction is also essentially isotropic in the case of electropolishing in HF solutions because the dissolution is through the formation and dissolution of silicon oxide which is amorphous in structure. The formation

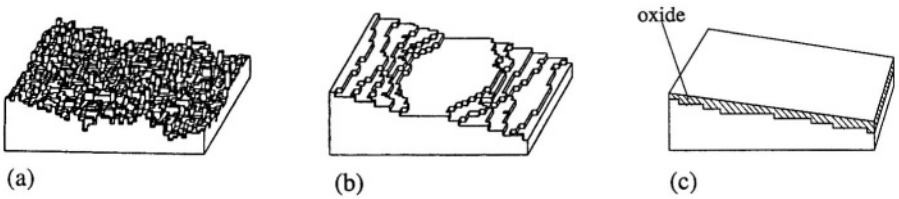

FIGURE 9.3. Schematic illustration of the conditions of surface lattice structure: (a) amorphous-like surface with no identity of orientation, (b) surface with kinds, steps and terraces characteristic of certain crystalline orientation, and (c) surface with no identity of the lattice structure of the crystal due to the coverage of an amorphous oxide film (a) and (b) after Jeong and Williams.[1074]

of an amorphous oxide film masks the crystallographic nature of the substrate as shown in Fig. 9.3c.

9.6. RELATIVITY

An important mechanistic aspect is the relative nature of the dimensions and events in space and in time. The electrochemical reaction processes can vary in quality and quantity in temporal and spatial scales of many orders of magnitude, which is responsible for the diverse phenomena observed on silicon electrodes. The understanding of the relative nature of dimensions and events are essential in mechanistic descriptions of this complex system. The following are the relative dimensions and events that are important in determining the electrode phenomena of silicon.

1. The amount of reaction with fluoride based species relative to that with water based species determines the relative surface coverage by hydride, hydroxide, and oxide, the reactivity of the surface and the crystallographic character of the surface.
2. The amount of chemical reactions relative to electrochemical reactions determines the amount of anodic hydrogen evolution and the value of effective dissolution valence.
3. The rate of oxide formation relative to dissolution of the oxide determines the surface coverage, thickness, and properties of oxide, occurrence of passivation and current oscillation as well as uniformity of anodic dissolution.
4. Rate of removal of atoms from kinks and steps relative to that from terraces determines the anisotropicity of reactions.
5. Atomic scale roughness in terms of the density of kinks sites and steps relative to surface atomic density determines effect of surface lattice structure on the rate of reactions; when the roughness is low relative to atomic density the reactions show a high degree of anisotropicity and when it is high the reactions tend to be isotropic.
6. The radius of surface curvature relative to the width of space charge layer determines the sensitivity of reactions to surface roughness, the distribution of reactions on the surface. It is the principal factor in the formation of pores in semiconductors and the porous morphology.
7. The wavelength of light relative to the width of the space charge layer affects the quantum efficiency of photocurrent, the vector of photocarrier flux on the surface, and is responsible for the fractal-like morphology of the micro PS in two-layer PS.
8. The relative distribution of potential change in different physical phases along the current path determines the rate determining processes and the role of each physical phase in the overall electrode phenomenon.

In addition to the ones listed above, there are other relative dimensions and events that are associated with specific phenomena, for example, relative carrier depletion in the directional growth of pores on a semiconductor electrode. Fundamentally, the relativity of these dimensions and events are associated with the relativity of

randomness of events at different temporal and spatial scales, that is, the duality of the stochastic nature of the microscopic and atomic events and the deterministic macroscopic phenomena. Such duality, as a general materials property, exhibits in all the phenomena on silicon electrodes. For examples, random removal of individual silicon atoms from the surface versus the predictable etching rate of the surface, the random locations of initiation of pores versus the deterministic direction of propagation of pores, the randomness of surface lattice structure at the atomic and near atomic scales versus the deterministic surface roughness at a macroscopic scale.

9.7. FUTURE RESEARCH INTERESTS

The amount of information on the electrochemical properties of silicon, as summarized in this book, is enormous owing to the research interests over the last five decades. The intensity of research on silicon electrodes is likely to continue in the foreseeable future for three major reasons.

The primary reason is the continued use of silicon as the mainstream material for future generations of electronic devices.[1041,1067,1190,1195] Many problems encountered in the diminishing device feature size are related to surface properties of silicon, such as surface roughness, which are determined by the numerous wet processes, such as cleaning. In addition, the increasing applications for sensors and actuators that are compatible with integrated circuits demands the fabrication of micro mechanical devices that are three-dimensional and moveable. Chemical etching of silicon with its large range of etch rates and selectivity with respect to orientation, doping type and concentration, and foreign materials, is one of the key processes for the fabrication of theses devices.[517,851,918] Also, there is a renewed interest in electrodeposition of metals such as copper for replacing aluminum as the conducting material for micro devices.[1192–1194] Furthermore, silicon technology will play an important role in molecular engineering and nano technology which will emerge as a dominant industry in the 21th century.[1184,1188,1191] Research on electrochemical properties of silicon is essential for understanding and development of wet processes that can control surface conditions and generate micro and nano surface structures, dissolved or deposited, of increasing complexity.

The second reason is due to the importance of silicon material in the advancement of solid state physics and material science. There is a huge existing knowledge base and high degree of standardization and availability associated with silicon as a material. Such knowledge base, standardization, and availability, which do not exist with any other material, are essential for large scale researches into deeper questions that cannot yet be asked for other materials. In fact, the current investigations on silicon electrodes routinely cover almost the whole dimensional range from the scale of the electrode to the atomic scale. New phenomena will be discovered and new knowledge will be generated at deeper levels and wider scopes on silicon electrodes. There are many topics that are of interest for further research, specifically, for example,

1. the chemical and electrochemical characters of hydrogen reaction
2. surface structural condition and kinetic processes for the formation of a silicon–oxygen network that passivate the surface

3. transformation of structure and properties of anodic oxides after their formation
4. the continuum from individual atomic events and large scale phenomena
5. solvation structure and process of silicon in solution
6. spatial distribution of reactions and evolution of surface geometry at different scales
7. chemical bonding and stability of the atoms at different surface lattice structures
8. difference between Si–OH and Si–F bonds in determining the chemical or electrochemical dissolution of the silicon atom
9. physical and chemical nature of different types of surface states
10. global kinetic theories that include all the essential elements and can account for different electrode phenomena.

The third reason is attributed to our innate interest in functional interfaces between the man-made non-living matters and the living matters, the most important of which is the human body. The information in the man-made world is stored and processed electronically while that in the human body is stored and processed chemically or electrochemically. The electrochemical processes must play an important role in enabling the technology for direct exchange of information between the two worlds. In this regard, silicon, which is already the dominant material for processing electronic information, seems to be a natural candidate as the electrode material on which such interfaces could be investigated and developed. The processes to deposit organic molecules such as amino acid and proteins on silicon that can functionally bond to cells and live tissues and the characterization for the electrochemical properties of these silicon/bio-material interfaces should be an interesting research area in the future.[1187–1189]

New interests and deeper questions, which may still be beyond the imagination at this time, will surely continue to emerge in the future. There are more interesting questions, on silicon electrodes to be researched now than before. In some ways, what has been accomplished is just a preparation for the greater research challenges that lay ahead, which must be atomistic in detail, complex in the relationships among phenomena and variables, and integral in scope to relate the events at the atomic scale with the phenomena at a macro scale.

This page intentionally left blank

References

1. H. Gerischer, The impact of semiconductor on the concepts of electrochemistry, *Electrochim. Acta* **35**, 1677, 1990.
2. X. G. Zhang, S. D. Collins, and R. L. Smith, Porous silicon formation and electrochemical polishing of silicon by anodic polarization in HF solutions, *J. Electrochem. Soc.* **136**, 1561, 1989.
3. M. D. Drory, P. C. Searson, and L. Liu, The mechanical properties of porous silicon membranes, *J. Mater. Sci. Lett.* **10**, 81, 1990.
4. P. C. Searson, J. M. Macaulay, and S. M. Prokes, The formation, morphology and optical properties of porous silicon structures, *J. Electrochem. Soc.* **139**, 3373, 1992.
5. I. Ronga, A. Bsiesy, F. Gaspard, F. Herino, M. Ligeon, and F. Muller, Electrical characterization of the silicon–electrolyte interface in the conditions of porous silicon formation, *J. Electrochem. Soc.* **138**, 1403, 1991.
6. K. H. Jung, S. Shih, D. L. Kwong, T. George, T. L. Lin, H. Y. Liu, and J. Zavada, Photoluminescence, structure, and composition of laterally anodized porous Si, *J. Electrochem. Soc.* **139**, 3363, 1992.
7. N. Koshida and K. Echizenya, Characterization studies of p-type porous Si and its photoelectrochemical activation, *J. Electrochem. Soc.* **138**, 837, 1991.
8. X. G. Zhang, Mechanism of pore formation on n-type silicon, *J. Electrochem. Soc.* **138**, 3750, 1991.
9. P. C. Searson and X. G. Zhang, The anodic dissolution of silicon in HF solutions, *J. Electrochem. Soc.* **137**, 2539, 1990.
10. T. Osaka, K. Ogasawara, M. Katsunuma, and T. Momma, Control of the structure of n-type silicon and its electroluminescence properties, *J. Electroanal. Chem.* **396**, 69, 1995.
11. H. Gerischer and M. Lubke, On the etching of silicon by oxidants in ammonium fluoride, *J. Electroanal. Chem.* **135**, 2782, 1988.
12. V. Lehmann, The physics of macro-pore formation in low doped n-type silicon, *J. Electroanal. Chem.* **140**, 2836, 1993.
13. K. McAndrew and P. Sukank, Nonuniform wet etching of silicon dioxide, *J. Electrochem. Soc.* **138**, 863, 1991.
14. P. M. M. C. Bressers, M. Plakman, and J. J. Kelly, Etching and electrochemistry of silicon in acidic bromine solutions, *J. Electronanal. Chem.* **406**, 131, 1996.
15. H. P. Kattelus, Wet refinement of dry etched trenches in silicon, *J. Electrochem. Soc.* **144**, 3188, 1997.
16. T. Osaka, K. Ogasawara, and S. Nakahara, Classification of the pore structure of n-type silicon and its microstructure, *J. Electrochem. Soc.* **144**, 3226, 1997.
17. M. Elwenspoek, On the mechanism of anisotropic etching of silicon, *J. Electrochem. Soc.* **140**, 2075, 1993.
18. E. Peiner and A. Schlachetzki, Anodic dissolution during electrochemical carrier concentration profiling of silicon, *J. Electrochem. Soc.* **139**, 552, 1992.
19. Y. H. Seo, K. S. Nahm, and K. B. Lee, Mechanistic study of silicon etching in $HF–KBrO_3–H_2O$ solution, *J. Electrochem. Soc.* **140**, 1453, 1992.
20. R. C. Anderson, R. S. Muller, and C. W. Tobias, Chemical surface modification of porous silicon, *J. Electrochem. Soc.* **140**, 1393, 1993.

21. E. S. Kooij, R. W. Despo, F. P. J. Mulders, and J. J. Kelly, Electrochemistry of porous and crystalline silicon electrodes in methylviologen solutions, *J. Electroanal. Chem.* **406**, 139, 1996.
22. P. Allongue, V. Costa-Kieling, and H. Gerischer, Etching in KOH solutions, *J. Electrochem. Soc,* **140**, 1018, 1993.
23. O. Tescheke and D. M. Soares, Isolated submicrometer filaments formed by silicon anodization in HF solutions, *J. Electrochem. Soc.* **143**, L100, 1996.
24. V. V. Doan and M. Sailor, Luminescence color image generation on porous silicon, *Science* **256**, 1791, 1992.
25. V. Lehmann and U. Gosele, Porous silicon: Quantum sponge structures grown via a self-adjusting etching process, *Adv. Mater.* **4**, 114, 1992.
26. M. Yamana, N. Kashiwazaki, A. Kinoshita, T. Nakano, M. Yamamoto, and C. W. Walton, Porous silicon oxide formation by the electrochemical treatment of a porous silicon layer, *J. Electrochem. Soc.* **137**, 2925, 1990.
27. J. L. Heinrich, C. L. Curtis, G. M. Credo, K. L. Kavanagh, and M. J. Sailor, Luminescent colloidal silicon suspensions from porous silicon, *Science* **255**, 66, 1992.
28. R. P. Chin, Y. R. Shen, and V. Petrova-Koch, Photoluminescence from porous silicon by infrared multiphoton excitation, *Science* **270**, 776, 1995.
29. J. S. Shor and A. D. Kurtz, Direct observation of porous SiC formed by anodization in HF, *Appl. Phys. Lett.* **62**, 2836, 1993.
30. L. Zhang, J. Coffer, Y. G. Rho, and R. F. Pinizzotto, Fabrication of a porous silicon diode possessing distinct red and orange electroluminescence regions, *J. Electrochem. Soc.* **143**, L42, 1996.
31. C. Ducso, N. Q. Khanh, Z. Horvath, I. Barsony, M. Utriainen, S. Lehto, M. Nieminen, and L. Niinisto, Deposition of tin oxide into porous silicon by atomic layer epitaxy, *J. Electrochem. Soc.* **143**, 683, 1996.
32. D. X. Bai, B. X. Liu, E. D. Lan, C. L. Ma, and J. Chai, Formation of porous silicon and its mechanism, *Cailiao Bohu* **29**, 3, 1996.
33. D. R. Turner, Electropolishing silicon in hydrofluoric acid solutions, *J. Electrochem. Soc.* **105**, 402, 1958.
34. R. Memming and G. Schwandt, Potential distribution and formation of surface states at the silicon–electrolyte interface, *Surf. Sci.* **4**, 109, 1966.
35. M. I. J. Beale, J. D. Benjamin, M. J. Uren, N. G. Chew, and A. G. Cullis, Dissolution reaction effect on porous-silicon density, *J. Cryst. Growth* **73**, 622, 1985.
36. Y. Arita and Y. Sunahama, Formation and properties of porous silicon film, *J. Electrochem. Soc.* **124**, 285, 1977.
37. Y. Watanabe, Y. Arita, T. Yokoyama, and Y. Lgarashi, Formation and properties of porous silicon and its application, *J. Electrochem. Soc.* **122**, 1315, 1975.
38. R. L. Meek, Anodic dissolution of N silicon, *J. Electrochem. Soc.* **118**, 437, 1971.
39. R. L. Meek, n+ silicon–electrolyte interface capacitance, *Surf. Sci.* **25**, 526, 1971.
40. T. Unagami, Formation mechanism of porous silicon layer by anodization in HF solution, *J. Electrochem. Soc.* **127**, 476, 1980.
41. V. P. Parkhutik, L. K. Glinenko, and V. A. Labunov, Kinetics and mechanism of porous layer growth during n-type silicon anodization in HF solution, *Surf. Technol,* **20**, 265, 1983.
42 M. J. J. Theunissen, Etch channel formation during anodic dissolution of n-type silicon in aqueous hydrofluoric acid, *J. Electrochem. Soc.* **119**, 351, 1972.
43. P. C. Searson and X. G. Zhang, The potential distribution at the silicon/electrolyte interface in HF solutions, *Electrochim. Acta* **36**, 499, 1991.
44. S. R. Morrison, *Electrochemistry of Semiconductor and Oxidized Metal Electrodes,* Plenum Press, New York, 1981.
45. R. S. Muller and T. I. Kamins, *Device Electronics for Integrated Circuits,* John Wiley & Sons, 1977.
46. P. C. Searson, J. M. Macaulay, and F. M. Ross, Pore morphology and the mechanism of pore formation in n-type silicon, *J. Appl. Phys.* **72**(1), 253, 1992.
47. R. Herino, G. Romchil, K. Boala, and C. Bertrand, Porosity and pore size distribution of porous silicon layers, *J. Electrochem. Soc.* **134**, 1994, 1987.
48. H. Unno, K. Imai, and S. Muramoto, Dissolution reaction effect on porous silicon density, *J. Electrochem. Soc.* **134**, 645, 1987.

49. V. Labunov, I. Baranov, and V. Bondarenko, Investigation of porous silicon formation during anodic treatment in aqueous HF, *Thin Solid Films* **64**, 479, 1979.
50. G. Bomchil, R. Herino, K. Barla, and J. C. Pfister, Pore size distribution in porous silicon studied by adsorption, *J. Electrochem. Soc.* **130**, 1611, 1983.
51. T. Uganami and M. Seki, Structure of porous silicon layer and heat treatment effect, *J. Electrochem. Soc.* **125**, 1339, 1978.
52. A. Y. C. Yu., Electron tunneling and contact resistance of metal–silicon contact barriers, *Solid-State Electron.* **13,** 239, 1970.
53. V. Labunov, V. Bondarenko, L. Glinenko, A. Dorofeev, and L. Tabulina, Heat treatment effect on porous silicon, *Thin Solid Films* **137**, 123, 1986.
54. K. E. Bean, Anisotropic etching of silicon, *IEEE Trans. Electron Devices* **25**, 1185, 1978.
55. C. Gui, M. Elwenspoek, J. G. E. Gardeniers, and P. V. Lambeck, Present and future role of chemical mechanical polishing in wafer bonding, *J. Electrochem. Soc.* **145**, 2204, 1998.
56. K. Imai and H. Unno, FIPOS (full isolation by porous oxidized silicon) technology and its application to LSI's, *IEEE Trans. Electron Devices* **31**, 297, 1984.
57. J. Judge, A study of the dissolution of SiO_2 in acidic fluoride solutions, *J. Electrochem. Soc.* **118**, 1772, 1971.
58. R. Meek, Electrochemically thinned n/n^+ epitaxial silicon—Method and applications, *J. Electrochem. Soc.* **118**, 1240, 1971.
59. S. F. Chuang, S. D. Collins, and R. L. Smith, preferential propagation of pores during the formation of porous silicon: A transmission electron microscopy study, *Appl. Phys. Lett.* **55**(7), 675, 1989.
60. R. L. Smith and S. D. Collins, Porous silicon formation mechanisms, *J. Appl. Phys.* **71**(8), R1, 1992.
61. R. Memming and G. Schwandt, Potential distribution and formation of surface states at the silicon–electrolyte interface, *Surf. Sci.* **5**, 97, 1966.
62. R. L. Smith, S. F. Chuang, and S. D. Collins, A theoretical model of the formation morphologies of porous silicon, *J. Electron. Mater.* **17**, 228, 1988.
63. P. M. M. Bressers, J. W. J. Knapen, and E. A. Meulenkamp, Visible light emission from a porous silicon/solution diode, *Appl. Phys. Lett.* **61**(1), 108, 1992.
64. A. Nakajima, T. Itakura, S. Watanabe, and N. Nakayama, Photoluminescence of porous Si, oxidized then deoxidized chemically, *Appl. Phys. Lett.* **61**(1), 46, 1992.
65. S. M. Prokes, J. A. Freitas, Jr., and P. C. Searson, Microluminescence depth profiles and annealling effects in porous silicon, *Appl. Phys. Lett.* **62**(26), 3295, 1992.
66. V. Petrova-Koch, T. Muschik, A. Kux, B. K. Meyer, and F. Koch, Rapid-thermal-oxidized porous Si—The superior photoluminescent Si, *Appl. Phys. Lett.* **61**(8), 943, 1992.
67. C. Tsai, K. H. Li, D. S. Kinoski, R. Z. Qian, T. C. Shu, J. T. Irby, S. K. Banerjee, A. F. Tasch, J. C. Campbell, B. K. Hance, and J. M. White, Correlation between silicon hydride species and the photoluminescence intensity of porous silicon, *Appl. Phys. Lett.* **60**(14), 1700, 1992.
68. M. W. Cole, Microstructure of visibly luminescent porous silicon, *Appl. Phys. Lett.* **60**(22), 2800, 1992.
69. H. Foll, Properties of silicon–electrolyte junction and their application to silicon characterization, *Appl. Phys. A* **53**, 8, 1991.
70. H. Gomyou and H. Morisaki, Effect of electrochemical treatments on the photoluminescence from porous silicon, *J. Electrochem. Soc.* **139**, L86, 1992.
71. V. Lehmann and U. Gosele, Porous silicon formation: A quantum wire effect, *Appl. Phys. Lett.* **58**(8), 856, 1991.
72. L. T. Canham, Silicon quantum wire array fabrication by electrochemical and chemical dissolution of wafers, *Appl. Phys. Lett.* **57**(10), 1046, 1990.
73. V. Lehmann and H. Foll, Minority carrier diffusion length mapping in silicon wafers using a Si-electrolyte-contact, *J. Electrochem. Soc.* **135**, 2831, 1988.
74. M. Matsumura and S. R. Morrison, Anodic properties of n-Si and n-Ge electrodes in HF solution under illumination and in the dark, *J. Electroanal. Chem.* **147**, 157, 1983.
75. C. Vanleugenhaghe, G. Valensi, and M. Pourbaix, Fluorine, in *Atlas of Electrochemical Equilibria in Aqueous Solutions,* M. Pourbaix (ed.), p. 579, National Association of Corrosion Engineers, Houston, 1974.

76. H. Massoud, Charge-transfer dipole moments at the Si–SiO interface, *J. Appl. Phys.* **63**, 2000, 1988.
77. M. Matsumura and S. R. Morrison, Photoanodic properties of an n-type of silicon electrode in aqueous solutions containing fluorides, *J. Electroanal. Chem.* **144**, 113, 1983.
78. M. S. Wrighton, J. M. Bolts, A. B. Bocarsly, M. C. Palazzotto, and E. G. Walton, Stabilization of n-type semiconductors to photoanodic dissolution: II–VI and III–V compound semiconductors and recent results for n-type silicon, *J. Vac. Sci. Technol.* **15**, 1429, 1978.
79. H. Gerischer, Charge transfer processes at semiconductor–electrolyte interfaces in connection with problems of catalysis, *Surf. Sci.* **18**, 97, 1969.
80. L. M. Peter, The semiconductor–electrolyte interface, in *Trends in Interfacial Electrochemistry,* A. F. Silva (ed.), Reidel, Dordrecht, 1984.
81. J. O. Bokris and S. U. M. Khan, On the evolution of concepts concerning events at the semiconductor/solution interface, *J. Electrochem. Soc.* **132**, 2648, 1985.
82. H. K. Kuiken and R. P. Tijburg, Centrifugal etching: A promising new tool to achieve deep etching, *J. Electrochem. Soc.* **130**, 1722, 1980.
83. J. N. Chazalviel and A. V. Rao, Optical absorption by surface states and atomic reorganization effects at the semiconductor/electrolyte interface, *J. Electrochem. Soc.* **134**, 1138, 1987.
84. F. Decker, B. Pettinger, and H. Gerischer, Hole injection and electroluminescence of n-GaAs in the presence of aqueous redox electrolytes, *J. Electrochem. Soc.* **130**, 1335, 1983.
85. H. Gerischer, On the role of electrons and holes in surface reaction on semiconductors, *Surf. Sci.* **13**, 265, 1969.
86. R. Memming, Processes at semiconductor electrodes, in *Comprehensive Treatise of Electrochemistry,* Vol. 7, B. E. Conway, J. O. Bockris, E. Yeager, S. U. M. Khan, and R. E. White (eds.), Plenum Press, New York, p. 529.
87. D. Laser and A. Bard, Semiconductor electrodes IV. Electrochemical behaviour of n and p type silicon electrodes in acetonitrile solutions, *J. Phys. Chem.* **80**, 459, 1976.
88. H. Preier, Surface carrier generation including tunnel transitions, *Surf. Sci.* **17**, 125, 1969.
89. E. D. Palik and R. T. Holm, Electric field modulated infrared internal reflection study of the silicon–electrolyte interface, *J. Appl. Phys.* **56**(1), 843, 1984.
90. K. Chandrasekaran, R. C. Kainthla, and J. O. Bockris, An impedance study of the silicon–solution interface under illumination, *Electrochim. Acta* **33**, 327, 1988.
91. Y. Kashiwagi, R. Shimokawa, and M. Yamanaka, Highly sensitive etchants for delineation of defects in single- and polycrystalline silicon materials, *J. Electrochem. Soc.* **143**, 4073, 1996.
92. Y. Suda, T. Koizumi, K. Obata, Y. Tezuka, S. Shin, and N. Koshida, Surface electronic structure and photoluminescence mechanism of porous silicon, *J. Electrochem. Soc.* **143**, 2502, 1996.
93. G. Oskam, J. C. Schmidt, P. M. Hoffmann, and P. C. Searson, Electrical properties of n-type (111) Si in aqueous $K_4Fe(CN)_6$ solution, *J. Electrochem. Soc.* **143**, 2531, 1996.
94. G. Oskam, J. C. Schmidt, and P. C. Searson, Electrical properties of n-type (111) Si in aqueous $K_4Fe(CN)_6$ solution. II. Intensity modulated photocurrent spectroscopy, *J. Electrochem. Soc.* **143**, 2538, 1996.
95. M. Matsumura and H. Fukidome, Enhanced etching rate of silicon in fluoride containing solutions at pH 6.4, *J. Electrochem. Soc.* **143**, 2683, 1996.
96. J. Jeon, S. Raghavan, H. G. Parks, J. Lowell, and L. Ali, Electrochemical investigation of copper contamination on silicon wafers from HF solutions, *J. Electrochem. Soc.* **143**, 2870, 1996.
97. A. Somachekhar and S. O'Brien, Etching films in aqueous 0.49% HF, *J. Electrochem. Soc.* **143**, 2885, 1996.
98. J. A. Bardwell, E. M. Allegreto, J. Phillips, M. Buchanan, and N. Draper, Influence of the initial electrochemical potential on the growth mechanism and properties of anodic oxides on (100) Si, *J. Electrochem. Soc.* **143**, 2931, 1996.
99. T. Ohmi, Total room temperature wet cleaning for Si substrate surface, *J. Electrochem. Soc.* **143**, 2957, 1996.
100. K. Asare, D. Wei, and K. K. Mishra, Dissolution windows for wet chemical processing of silicon and silicon dioxide: Potential–pH diagrams for the $Si–F–H_2O$ system, *J. Electrochem. Soc.* **143**, 749, 1996.
101. S. Billat, Electroluminescence of heavily doped p-type porous silicon under electrochemical oxidation in galvanostatic regime, *J. Electrochem. Soc.* **143**, 1055, 1996.

102. T. Homma, Properties of fluorinated silicon oxide films formed using fluorotriethoxysilane for interlayer dielectrics in multilevel interconnections, *J. Electrochem. Soc.* **143**, 1084, 1996.
103. B. Schwartz and H. Robbins, Chemical etching of silicon. III. A temperature study in the acid system, *J. Electrochem. Soc.* **108**, 365, 1961.
104. C. P. Wen and K. P. Weller, Preferential electrochemical etching of p^- silicon in an aqueous $HF–H_2–SO_4$ electrolyte, *J. Electrochem. Soc.* **119**, 547, 1972.
105. E. A. Lewis and E. A. Irene, The effect of surface orientation on silicon oxidation kinetics, *J. Electrochem. Soc.* **134**, 2333, 1987.
106. H. Barber, H. B. Lo, and J. E. Lones, Repeated removal of thin layers of silicon by anoidic oxidation, *J. Electrochem. Soc.* **123**, 1404, 1976.
107. E. F. Duffek, C. Mylroie, and E. A. Benjamini, Electrode reactions and mechanism of silicon anodization in N-methylacetamide, *J. Electrochem. Soc.* **111**, 1042, 1964.
108. E. D. Palik, O. J. Glembocki, and I. Heard, Jr., Study of bias-dependent etching of Si aqueous KOH, *J. Electrochem. Soc.* **134**, 404, 1987.
109. O. J. Glembocki, E. Stahlbush, and M. Tomkiewicz, Bias-dependent etching of silicon in aqueous KOH, *J. Electrochem. Soc.* **132**, 145, 1985.
110. W. Ryan, R. E. White, and S. L. Kelly, A mathematical model for the initial corrosion rate of a porous layer on a rotating disk electrode, *J. Electrochem. Soc.* **134**, 2154, 1987.
111. D. R. Turner, On the mechanism of chemically etching germanium and silicon, *J. Electrochem. Soc.* **107**, 810, 1960.
112. R. L. Gealer, H. K. Karsten, and S. M. Ward, The effect of an interfacial p–n junction on the electrochemical passivation of silicon in aqueous ethylenediamine–pyrocatechol, *J. Electrochem. Soc.* **135**, 1180, 1988.
113. T. C. Teng, An investigation of the application of porous silicon layer to the dielectric isolation of integrated circuits, *J. Electrochem. Soc.* **126**, 870, 1979.
114. E. D. Palik, V. M. Bermudez, and O. J. Glembocki, Ellipsometry study of orientation-dependent etching of silicon in aqueous KOH, *J. Electrochem. Soc.* **143**, 871, 1985.
115. W. A. Pliskin and R. P. Gnall, Evidence for oxidation growth at the oxide–silicon interface from controlled etch studies, *J. Electrochem. Soc.* **111**, 872, 1964.
116. B. Schwartz and H. Robbins, Chemical etching of silicon. IV. etching technology, *J. Electrochem. Soc.* **123**, 1903, 1976.
117. P. F. Schmidt and W. Michel, Anodic formation of oxide films on silicon, *J. Electrochem. Soc.* **104**, 230, 1957.
118. E. A. Irene, D. W. Dong, and R. J. Zeto, Residual stress, chemical etch rate, refractive index, and density measurements on SiO films prepared using high pressure oxygen, *J. Electrochem. Soc.* **127**, 396, 1980.
119. V. S. Y. Lin, A porous silicon-based optical interferometric biosensor, *Science* **278**, 840, 1997.
120. O. M. R. Chayan, J. J. Chen, and H. Y. Chien, Copper deposition on Hf etched silicon surface: Morphological and kinetic studies, *J. Electrochem. Soc.* **143**, 92, 1996.
121. J. S. Jeon, S. Raghavan, and J. P. Carrejo, Effect of temperature on the interaction of silicon with nonionic surfactants in alkaline solutions, *J. Electrochem. Soc.* **143**, 278, 1996.
122. V. Lemann, On the origin of electrochemical oscillations at silicon electrodes, *J. Electrochem. Soc.* **143**, 1313, 1996.
123. K. Osseo-Asare, Etching kinetics of silicon dioxide in aqueous fluoride solutions: A surface complexation model, *J. Electrochem. Soc.* **143**, 1339, 1996.
124. Q. B. Vu, D. A. Strieker, and P. M. Zavracky, Structure characteristics of (100) silicon anisotropically etched in aqueous KOH, *J. Electrochem. Soc.* **143**, 1372, 1996.
125. Y. Shiramizu, K. Watanabe, M. Tanaka, H. Aoki, and H. Kitajima, Removal of metal and organic contaminants from silicon substrate using electrolysis-ionized water containing ammonium chloride, *J. Electrochem. Soc.* **143**, 1632, 1996.
126. K. Ljungberg, U. Jansson, S. Bengtsson, and A. Soderbarg, Modification of silicon surface with H_2SO_4:H_2O_2HF and HNO_3:HF for wafer bonding applications, *J. Electrochem. Soc.* **143**, 1709, 1996.
127. P. M. M. C. Bressers, J. J. Kelly, J. G. E. Gardeniers, and M. Elwenspoek, Surface morphology of p-type (100) silicon etched in aqueous alkaline solution, *J. Electrochem. Soc.* **143**, 1744, 1996.

128. M. Warntjes, C. Vieillard, F. Ozanam, and J. N. Chazalviel, Electrochemical methoxylation of porous silicon surface, *J. Electrochem. Soc.* **142**, 4139, 1995.
129. L. C. Chen, M. Chen, C. Lien, and C. C. Wan, The band model and the etching mechanism of silicon in aqueous KOH, *J. Electrochem. Soc.* **142**, 170, 1995.
130. Y. Ogata, H. Niki, T. Satsuo, T. Sakka, and M. Iwasaki, Hydrogen in porous silicon: Vibrational analysis of SiH_x species, *J. Electrochem. Soc.* **142**, 195, 1995.
131. S. G. S. Filho, C. M. Hasenack, L. C. Salay, and P. Mertens, A less critical procedure for silicon wafer using diluted HF dip and boiling in isopropyl alcohol as final steps, *J. Electrochem. Soc.* **142**, 902, 1995.
132. S. Yao, J. Hesketh, and A. T. Macrander, Etching high aspect ratio (100) silicon grooves in CsOH, *J. Electrochem. Soc.* **142**, L23, 1995.
133. St. Frohnhoff, M. Marso, M. G. Berger, M. Thonossen, H. Luth, and H. Munder, An extended quantum model for porous silicon formation, *J. Electrochem. Soc.* **142**, 615, 1995.
134. J. S. Jeon, S. Raghavan, and R. P. Sperline, Behavior of polyethylene oxide based nonionic surfactants in silicon processing using alkaline solutions, *J. Electrochem. Soc.* **142**, 621, 1995.
135. K. K. Yoneshige, H. G. Parks, S. Raghavan, J. B. Hiskey, and P. J. Resnick, Deposition of copper from a buffered oxide etchant onto silicon wafers, *J. Electrochem. Soc.* **142**, 671, 1995.
136. M. M. Rieger and P. A. Kahl, Mechanism of (111) silicon etching in HF–acetonitrile, *J. Electrochem. Soc.* **142**, 1490, 1995.
137. Y. Ogata, H. Niki, T. Sakka, and M. Iwasaki, Oxidation of porous silicon under water vapor environment, *J. Electrochem. Soc.* **142**, 1595, 1995.
138. C. Spinella, V. Raineri, and S. U. Campisano, Selective etching of B-doped silicon: Mechanisms and two-dimensional delineation of concentration profiles, *J. Electrochem. Soc.* **142**, 1601, 1995.
139. P. Schmuki, H. Bohni, and J. A. Bardwell, In-situ characterization of anodic silicon oxide films by AC impedance measurements, *J. Electrochem. Soc.* **142**, 1705, 1995.
140. K. Ogasawara, T. Momma, and T. Osaka, Enhancement of electroluminescence from n-type porous silicon and its photoelectrochemical behavior, *J. Electrochem. Soc.* **142**, 1874, 1995.
141. J. G. Park and M. F. Pas, Effects of drying methods and wettability of silicon on the formation of water marks in semiconductor processing, *J. Electrochem. Soc.* **142**, 2028, 1995.
142. L. Torcheux, A. Mayeux, and M. Chemla, Electrochemical coupling effects on the corrosion of silicon samples in HF solutions, *J. Electrochem. Soc.* **142**, 2037, 1995.
143. C. Wisniewski, I. Denicolo, and I. A. Hummelgen, Electrochemically deposited cobalt thin films on p-type silicon and its characterization, *J. Electrochem. Soc.* **142**, 3889, 1995.
144. T. Aoyama, T. Yamazaki, and T. Ito, Nonuniformities in chemical oxides on silicon surfaces formed during wet chemical cleaning, *J. Electrochem. Soc.* **142**, 2280, 1995.
145. I. Teerlinck, P. W. Mertens, H. F. Schmidt, M. Meuris, and M. M. Heyns, Impact of the electrochemical properties of silicon wafer surfaces on coper outpluting from HF solutions, *J. Electrochem. Soc.* **142**, 3323, 1995.
146. V. Bertagna, C. Plougonven, F. Rouelle, and M. Chemla, p- and n-type silicon electrochemical properties in dilute hydrofluoric acid solutions, *J. Electrochem. Soc.* **142**, 3532, 1995.
147. J. B. Flynn, Saturation currents in germanium and silicon electrodes, *J. Electrochem. Soc.* **105**, 715, 1958.
148. A. S. Tenney and M. Ghezzo, Etch rates of doped oxides in solutions of buffered HF, *J. Electrochem. Soc.* **129**, 1091, 1973.
149. H. Robbins and B. Schwartz, Chemical etching of silicon. I. The system HF, HNO_3 and H_2O, *J. Electrochem. Soc.* **106**, 505, 1959.
150. H. Robbins and B. Schwartz, Chemical etching of silicon. II. The system HF, HNO_3 H_2O and $HC_2H_3O_2$, *J. Electrochem. Soc.* **107**, 108, 1960.
151. E. D. Palik, V. M. Bermudez, and O. J. Glembocki, Ellipsometric study of the etch-stop mechanism in heavily doped silicon, *J. Electrochem. Soc.* **133,** 135, 1985.
152. H. A. Waggener, Electrochemically controlled thinning of silicon, *Bell Syst. Tech. J.* **473**, 1970.
153. V. Harrap, Equal etch baths of Si_3N_4 and SiO_2 utilizing HF dilution and temperature dependence, in *Semiconductor Silicon,* H. R. Hoff and U. Burgess (eds.), p. 354, Electrochemical Society, Pennington 1973.

154. S. F. Chuang, S. D. Collins, and R. L. Smith, Preferred crystallographic directions of pore propagation in porous silicon layers, The Technical Digest of the Solid State Sensor and Actuator Workshop, Hilton Head Island, SC, June 6–9 (IEEE, New York), p. 151, 1988.
155. S. M. Sze and G. Gibbons, Avalanche breakdown voltages of abrupt and linearly graded p–n junctions in Ge, Si, GaAs, and GaP, *Appl. Phys. Lett.* **8**, 111, 1966.
156. H. Braumgart, R. C. Frye, F. Philipp, and H. J. Leamy, Dielectric isolation using porous silicon, *Mater. Res. Soc. Symp. Proc.* **33**, 63, 1984.
157. S. M. Sze and G. Gibbons, Effect of junction curvature on breakdown voltage in semiconductors, *Solid-State Electron.* **9**, 831, 1966.
158. R. Memming, Charge transfer kinetics at semiconductor electrodes, *Ber. Bunsenges. Phys. Chem.* **91**, 353, 1987.
159. T. L. Lin, L. Sadwick, K. L. Wang, Y. C. Kao, R. Hull, C. W. Nieh, D. N. Jamieson, and J. K. Liu, Growth and characterization of molecular beam epitaxial GaAs layers on porous silicon, *Appl. Phys. Lett.* **51**, 814, 1987.
160. E. A. Irene, An overview of the kinetics of oxidation of silicon: The very thin SiO_2 film growth regime, in *Passivity of Metals and Semiconductors,* M. Froment (ed.), p. 11, Elsevier Science, Amsterdam, 1983.
161. N. S. Lewis and A. B. Bocarsly, Silicon (Si) and germanium (Ge), in *Semiconductor Electrodes,* H. O. Finklea (ed.), p. 241, Amsterdam, Alsevier 1988.
162. P. H. Bellin and W. K. Zwicker, Observation of surface defects in electrolytically etched silicon by infrared microscopy, *J. Appl. Phys.* **42**, 1216, 1971.
163. Y. Arita, K. Kato, and T. Sudo, The n^+-IPOS scheme and its applications to IC's, *IEEE Trans. Electron Devices,* **24**, 456, 1977.
164. R. M. Candea, M. Kastner, R. Goodman, and N. Hickok, Photoelectrolysis of water: Si in salt water, *J. Appl. Phys.* **47**, 2724, 1976.
165. F. Herman, Electronic structure of the $Si–SiO_2$ interface, in *Insulating Films on Semiconductors,* M. Schulz and G. Pensl (eds.), p. 2, Springer-Verlag, Berlin, 1981.
166. C. R. Helms, Morphology of the $Si–SiO_2$ interface, in *Insulating Films on Semiconductors,* M. Schulz and G. Pensl (eds.), p. 18, Springer-Verlag, Berlin, 1981.
167. P. O. Hahn and M. Henzler, Influence of oxidation parameters on atomic roughness at the $Si–SiO_2$ interface, in *Insulating Films on Semiconductors,* M. Schulz and G. Pensl (eds.), p. 26, Springer-Verlag, Berlin, 1981.
168. R. B. Heimann, M. B. Ives, and P. Zaya, Influence of surface films on their development of pits during etching of silicon, *J. Cryst. Growth* **57**, 48, 1982.
169. F. D. Gealy and H. L. Tuller, Determination of electrically active defect profiles in semiconductors using a photoelectrochemical technique, in *MRS Symposium Proceedings,* R. Scegel, J. Weertman, and R. Sinclair (eds.), **82**, 151, 1987.
170. R. C. Frye, The formation of porous silicon and its applications to dielectric isolation, *Mater. Res. Soc. Symp. Proc.* **33**, 53, 1984.
171. K. Barla, R. Herino, and G. Bomchil, Stress in oxidized porous silicon layers, *J. Appl. Phys.* **59**, 439, 1986.
172. A. J. Bard, Semiconductor photoelectrochemical cells, in *Proceedings on Electrode Processes,* Vol. 80–3, p. 136, The Electrochemical Society Pennington, 1979.
173. H. N. Farrer and F. J. C. Rossotti, Proton–fluoride association in sodium perchlorate media, *J. Inorg. Nucl. Chem.* **26**, 1959, 1964.
174. M. T. Pham and J. Hueller, Ion implanted silicon–electrode interface, *J. Appl. Electrochem.* **7**, 531, 1977.
175. Y. J. Chabal, Hydride formation on the Si(100): H_2O surface, *Phys. Rev. B* **29**, 3677, 1984.
176. C. Pichering, M. I. J. Beal, and D. J. Robins (Optical properties of Porous silicon films), *Thin Solid Films* **125**, 157, 1984.
177. E. A. Ponomarev and C. Levy-Clement, Macropore formation on p-type Si in fluoride containing organic electrolytes, *Electrochem. Solid-State Lett.* **1**, 42, 1998.
178. Y. Nakato and H. Tsubomura, Remarkably high photovoltages generated at n-type silicon semiconductor electrodes coated with extremely small platinum islands, *Electrochem. Solid-State Lett.* **91**, 405, 1987.

179. R. P. Holmstrom and J. Y. Chi, Complete dielectric isolation by highly selective and self-stopping formation of oxidized porous silicon, *Appl. Phys. Lett.* **42**, 386, 1983.
180. W. Ranke and Y. R. Xing, Orientation dependent adsorption on a cylindrical silicon crystal, *Surf. Sci.* **157**, 339, 1985.
181. Y. Arita, K. Kuranari, and Y. Sunohara, Thermal behaviour of porous silicon, *Jpn. J. Appl. Phy.* **127**, 1655, 1976.
182. R. Memming, Surface recombination at higher injection levels, *Surf. Sci.* **1**, 88, 1964.
183. K. Moslavac and B. Lovrecek, The anodic passivation on silicon single crystals, *Electrochim, Acta* **14**, 373, 1969.
184. D. L. Kendall, On the etching of very narrow grooves in silicon, *Appl. Phys. Lett.* **26**, 195, 1975.
185. S. S. Tsao, D. R. Mayers, T. R. Guilinger, and M. J. Kelly, Selective porous formation in buried p^+ layers, *J. Appl. Phys.* **62**, 4182, 1987.
186. G. Mende, Detection of mobile ion during the anodic oxidation of silicon, *J. Electrochem. Soc.* **127**, 2085, 1980.
187. N. F. Mott, Transport of oxygen and water in oxide layer, in *Passivity of Metals and Semiconductors,* M. Froment (ed.), p. 1, Elsevier Science, Amsterdam, 1983.
188. W. Z. Zhou, J. M. Thomas, D. S. Shephard, B. F. G. Johnson, D. Ozkaya, T. Maschmeyer, R. G. Bell, and Q. F. Ge, Ordering of ruthenium cluster carbonyls in mesoporous silica, *Science* **280**, 705, 1998.
189. A. Prasad, S. Balakrishnan, S. K. Jain, and G. C. Jain, Porous silicon oxide anti-reflection coating for solar cells, *J. Electrochem. Soc.* **129**, 587, 1982.
190. S. S. Tsao, Porous silicon techniques for SOI structures, *IEEE Circuits Device,* 3, November 1987.
191. R. C. Kainthla, B. Zelenay, and J. O. Bockris, Protection of n-Si photoanode against photocorrosion in photoelectrochemical cell for water electrolysis, *J. Electrochem. Soc.* **133**, 248, 1986.
192. R. L. Smith, B. Kloeck, N. DeRooij, and S. D. Collins, The potential dependence of silicon anisotropic etching in KOH at 60°C, *J. Electroanal. Chem. Interfacial Electrochem.* **238**, 103, 1987.
193. S. S. Tsao, T. R. Guilinger, M. J. Kelly, and P. J. Clews, Multilevel porous silicon formation, *J. Electrochem. Soc.* **136**, 586, 1989.
194. F. Gaspard, A. Bsiesy, M. Ligeon, F. Muller, and R. Herino, Charge exchange mechanism responsible for p-type silicon dissolution during porous silicon formation, *J. Electrochem. Soc.* **136**, 3043, 1989.
195. J. E. A. M. van den Meerakker and J. H. C. van Vegchel, Silicon etching in CrO_3–HF solutions. I. High $[HF]/[CrO_3]$ regions, *J. Electrochem. Soc.* **136**, 1949, 1989.
196. J. E. A. M. van den Meerakker and J. H. C. van Vegchel, Silicon etching in CrO_3–HF solutions. II. Low $[HF]/[CrO_3]$ regions, *J. Electrochem. Soc.* **136**, 1954, 1989.
197. H. Doushita, M. Matsumura, and H. Tsubomura, Anomalous high photocurrents observed in p-type silicon electrodes having high electric resistances, *J. Electrochem. Soc.* **136**, 84, 1989.
198. J. Ruzyllo, A. M. Hoff, D. C. Frystak, and S. D. Hossain, Electrical evaluation of wet and dry cleaning procedures for silicon device fabrication, *J. Electrochem. Soc.* **136**, 1474, 1989.
199. M. T. Spilter and J. D. Cary, Photoelectrochemical analysis of doped hydrogenated amorphous silicon, *J. Electrochem. Soc.* **136**, 2295, 1989.
200. G. Gould and E. A. Irene, An in situ ellipsometry study of aqueous NH_4OH treatment of silicon, *J. Electrochem. Soc.* **136**, 1108, 1989.
201. K. Ghowsi and R. J. Gale, Theoretical model of the anodic oxidation growth kinetics of Si at constant voltage, *J. Electrochem. Soc.* **136**, 867, 1989.
202. T. Odenweller, On the theory of the semiconductor/electrolyte-interface (I), *J. Electrochem. Soc.* **137**, 2457, 1990.
203. W. Kern, The evolution of silicon wafer cleaning technology, *J. Electrochem. Soc.* **137**, 1887, 1990.
204. T. C. Chandler, MEMC etch—A chromium trioxide-free etchant for delineating dislocations and slip in silicon, *J. Electrochem. Soc.* **137**, 944, 1990.
205. Y. P. Xu and R. S. Huang, Anodic dissolution and passivation of silicon in hydrazine, *J. Electrochem. Soc.* **137**, 948, 1990.
206. H. Seidel, L. Csepregi, A. Heuberger, and H. Baumgartel, Anisotropic etching of crystalline silicon in alkaline solutions. I. Orientation dependence and behavior of passivation layer, *J. Electrochem. Soc.* **137**, 3612, 1990.

207. H. Seidel, L. Csepregi, A. Heuberger, and H. Baumgartel, Anisotropic etching of crystalline silicon in alkaline solutions. II Influence of dopants, *J. Electrochem. Soc,* **137**, 3626, 1990.
208. J. E. A. M. van den Meerakker and M. H. M. van den Straaten, A mechanistic study of etching in NH_3/H_2O_2 cleaning solutions, *J. Electrochem. Soc.* **137**, 1239, 1990.
209. R. C. Anderson, R. S. Muller, and C. W. Tobias, Investigations of the electrical properties of porous silicon, *J. Electrochem. Soc.* **138**, 3406, 1991.
210. A. Bsiesy, F. Gaspard, R. Herino, M. Ligeon, F. Muller, and J. C. Oberlin, Anodic oxidation of porous silicon layers formed on lightly p-doped substrates, *J. Electrochem. Soc.* **138**, 3450, 1991.
211. K. B. Albaugh, Electric phenomena during anodic bonding of silicon to sodium borosilicate glass, *J. Electrochem. Soc.* **138**, 3089, 1991.
212. S. S. Tsao, T. R. Guilinger, M. J. Kelly, V. S. Kaushik, and A. K. Datye, Porous silicon formation in $n^-/n^+/n^-$ doped structures, *J. Electrochem. Soc.* **138**, 1739, 1991.
213. W. L. C. M. Heyboer, G. A. C. M. Spierings, and J. E. A. M. van den Meerakker, Chemomechanical silicon polishing, *J. Electrochem. Soc.* **138**, 774, 1991.
214. V. Lehmann, K. Mitani, D. Feijoo, and U. Gosele, Implanted carbon: An effective etch-stop in silicon, *J. Electrochem. Soc.* **138**, L3, 1991.
215. A. V. Rao, F. Ozanam, and J. N. Chazalviel, In situ fourier-transform electromodulated infrared study of porous silicon formation: Evidence for solvent effects on the vibrational linewidths, *J. Electrochem. Soc.* **138**, 153, 1991.
216. H. Koyama and N. Koshida, Photoelectrochemical effects of surface modification of n-type Si with porous layer, *J. Electrochem. Soc.* **138**, 254, 1991.
217. U. S. Pahk, S. Chongsawangvirod, and E. A. Irene, In situ differential reflectance study of the etching of SiO_2 films, *J. Electrochem. Soc.* **138**, 308, 1991.
218. H. Proksche and G. Nagosen, The influence of NH_4F on the rates of undoped SiO_2 in buffered oxide etch, *J. Electrochem. Soc.* **138**, 521, 1991.
219. D. J. Godbey, A. H. Krist, K. D. Hobart, and M. E. Twigg, Selective removal of $Si_{1-x}Ge_x$ from (100) Si using $HNO_3$and HF, *J. Electrochem. Soc.* **139**, 2943, 1992.
220. T. Ohmi, T. Imaoka, I. Sugiyama, and T. Kezuka, Metallic impurities segregation at the interface between Si wafer and liquid during wet cleaning, *J. Electrochem. Soc.* **139**, 3317, 1992.
221. H. Linde and L. Austin, Wet silicon etching with aqueous amine gallates, *J. Electrochem. Soc.* **139**, 1170, 1992.
222. G. L. Schnable, W. Kern, and R. B. Comizzoli, Passivation coatings on silicon devices, *J. Electrochem. Soc.* **122**, 1092, 1975.
223. S. L. Yau, F. R. Fan, and A. J. Bard, In situ STM imaging of silicon (111) in HF under potential control, *J. Electrochem. Soc.* **139**, 2858, 1992.
224. K. Y. Lee, C. H. Chung, J. H. Han, S. W. Rhee, and S. H. Moon, Thermodynamic evaluation of equilibrium compositions in the Si–H–F system, *J. Electrochem. Soc.* **139**, 3539, 1992.
225. C. Oules, A. Halimaoui, J. L. Regolini, A. Perio, and G. Bomchil, Silicon on insulator structure obtained by epitaxial growth of silicon over porous silicon, *J. Electrochem. Soc.* **139**, 3595, 1992.
226. H. Ono, H. Gomyou, H. Morisaki, S. Nozaki, Y. Show, M. Shimasaki, M. Iwase, and T. Izumi, Effect of anodization temperature on photo luminscence from porous silicon, *J. Electrochem. Soc.* **140**, L180, 1993.
227. J. Rappich, H. J. Lewerenz, and H. Gerischer, The surface of Si(111) during etching in NaOH studied by FTIR spectroscopy in the ART technique, *J. Electrochem. Soc.* **140**, L187, 1993.
228. G. Mende, H. Flietner, and M. Deutscher, Optimization of anodic silicon oxide films for low temperature passivation of silicon surfaces, *J. Electrochem. Soc.* **140**, 188, 1993.
229. R. Ravi and C. G. Takoudis, Binding energies of H and Cl on Si(111), *J. Electrochem. Soc.* **140**, 195, 1993.
230. G. Zhou, Y. Nakanishi, and Y. Hatanaka, Light emission effect in anodic oxidation of Si, *J. Electrochem. Soc.* **140**, 1468, 1993.
231. M. Wong and R. A. Bowling, Silicon etch using vapor phase HF/H_2O and O_3, *J. Electrochem. Soc.* **140**, 567, 1993.
232. W. A. Pliskin and H. S. Lehman, Structural evaluation of silicon oxide films, *J. Electrochem. Soc.* **112**, 1013, 1965.

233. S. Y. Shieh and J. W. Evans, Some observations of the effect of porous silicon on oxidation-induced stacking faults, *J. Electrochem. Soc.* **140**, 1094, 1993.
234. P. Allongue, V. C. Kieling, and H. Gerischer, Etching of silicon in KOH solutions. I. In situ scanning tunneling microscopic investigation of n-Si(111), *J. Electrochem. Soc.* **140**, 1009, 1993.
235. P. J. Hesketh, C. Ju, S. Gowda, E. Zanoria, and S. Danyluk, Surface free energy model of silicon anisotropic etching, *J. Electrochem. Soc.* **140**, 1080, 1993.
236. R. R. C. Henderson, J. L. Coffer, and L. A. F. Sesler, The impact of sonication on the structure and properties of stain-etch porous silicon, *J. Electrochem. Soc.* **141**, L166, 1994.
237. H. Morinaga, M. Suyama, and T. Ohmi, Mechanism of metallic particles growth and metal-induced pittings on Si wafer surface in wet chemical processing, *J. Electrochem. Soc.* **141**, 2834, 1994.
238. S. Verhaverbeke, I. Teerlinck, C. Vinckier, G. Stevens, R. Cartuyvels, and M. M. Heyns, The etching mechanisms of SiO_2 in hydrofluoric acid, *J. Electrochem. Soc.* **141**, 2852, 1994.
239. H. Kikuyama, M. Waki, M. Miyashita, T. Yabune, and N. Miki, A study of the dissolution state and the SiO_2 etching reaction for HF solutions of extremely low concentration, *J. Electrochem. Soc.* **141**, 366, 1994.
240. V. I. Beklemishev, V. V. Levents, I.I. Makhonin, M. S. Minazhdinov, and I. V. Seletskaia, Examination of Si substitute surface after different chemical pretreatments by means of nulling ellipsometry, *J. Electrochem. Soc.* **141**, 554, 1994.
241. P. de Mierry, A. Etcheberry, R. Rizk, P. Etchegoin, and M. Aucouturier, Defects induced in p-type silicon by photocathodic changing of hydrogen, *J. Electrochem. Soc.* **141**, 1539, 1994.
242. L. Mouche, F. Tardif, and J. Derrien, Particle deposition on silicon wafers during wet processes, *J. Electrochem. Soc.* **141**, 1684, 1994.
243. E. A. Meulenkamp, T. J. Cleij, and J. J. Kelly, Electroluminescence and chemiluminescence of porous silicon in nonaqueous solution, *J. Electrochem. Soc.* **141**, 1157, 1994.
244. D. Landheer, J. A. Bardwell, and K. B. Clark, Electrical properties of thin anodic oxides formed on silicon in aqueous NH_4OH solutions, *J. Electrochem. Soc.* **141**, 1309, 1994.
245. P. M. Zavrocky, T. Earles, N. L. Pokrovskiy, J. A. Green, and B. E. Burns, Fabrication of vertical sidewalls by anisotropic etching of silicon (100) wafers, *J. Electrochem. Soc.* **141**, 3182, 1994.
246. W. Wijaranakula, Characterization of crystal originated defects in czochralski silicon using nonagitated Secco etching, *J. Electrochem. Soc.* **141**, 3273, 1994.
247. C. L. Clement, A. Lagoubi, and M. Tomkiewicz, Morphology of porous n-type silicon obtained by photoelectrochemical etching, *J. Electrochem. Soc.* **141**, 958, 1994.
248. E. K. Propst and P. A. Kohl, The electrochemical oxidation of silicon and formation of porous silicon in acetonitrile, *J. Electrochem. Soc.* **141**, 1006, 1994.
249. T. Wang, S. Surve, and P. J. Hesketh, Anisotropic etching of silicon in rubidium hydroxide, *J. Electrochem. Soc.* **141**, 2493, 1994.
250. A. J. Steckl, J. Xu, and H. C. Mogul, Crystallinity and photoluminescence in stain-etched porous silicon, *J. Electrochem. Soc.* **141**, 674, 1994.
251. C. A. Desmond, C. E. Hunt, and S. N. Farrens, The effects of process-induced defects on the chemical selectivity of highly doped boron etch stops in silicon, *J. Electrochem. Soc.* **141**, 178, 1994.
252. D. J. Monk, D. S. Soane, and R. T. Howe, Hydrofluoric acid etching of silicon dioxide sacrificial layers, *J. Electrochem. Soc.* **141**, 264, 1994.
253. P. Gorostiza, R. Diaz, F. Sanz, and J. R. Morante, Different behavior in the deposition of plenum from HF solutions on n^- and p^- type (100) Si substrates, *J. Electrochem. Soc.* **144**, 4119, 1997.
254. V. Bertagna, F. Rouelle, G. Revel, and M. Chemla, Electrochemical and radiochemical study of copper contamination mechanism from HF solutions onto silicon substrates, *J. Electrochem. Soc.* **144**, 4175, 1997.
255. S. Sen, J. Siejka, A. Savtchouk, and J. Lagowski, Assessment of conditions influencing Si electroluminescence, *J. Electrochem. Soc.* **144**, 2230, 1997.
256. L. F. O. Maritins, L. Seligman, S. G. S. Filho, P. C. T. D'Ajello, C. M. Hasenack, and A. A. Pasa, Electrochemical evidence of a copper-induced etching of n-type Si in dilute hydrofluoric acid solutions, *J. Electrochem. Soc.* **144**, L106, 1997.
257. T. Unagami, Intrinsic stress in porous silicon layers formed by anodization in HF solutions, *J. Electrochem. Soc.* **144**, 1835, 1997.

258. J. H. Wei and S. C. Lee, The structure change of liquid phase deposited silicon oxide, *J. Electrochem. Soc.* **144**, 1870, 1997.
259. B. C. Chung, G. A. Marshall, C. W. Pearce, and K. P. Yanders, The prevention of Si pitting in hydrofluoric acid cleaning by additions of hydrochloric acid, *J. Electrochem. Soc.* **144**, 652, 1997.
260. H. Fukidome, T. Ohno, and M. Matsumura, Analysis of silicon surface in connection with its unique electrochemical and etching behavior, *J. Electrochem. Soc.* **144**, 679, 1997.
261. E. S. Kooij and D. Vanmaekelbergh, Catalysis of pore initiation in the anodic dissolution of silicon in HF, *J. Electrochem. Soc.* **144**, 1296, 1997.
262. K. Usuda and K. Yamada, Atomic force microscopy observations of Si surfaces after rinsing in ultrapure water with low dissolved oxygen concentration, *J. Electrochem. Soc.* **144**, 3204, 1997.
263. P. Menna, Y. S. Tsuo, M. M. Al-Jassim, S. E. Asher, F. J. Pern, and T. F. Ciszek, Light emitting porous silicon from cast metallurgical-grade silicon, *J. Electrochem. Soc.* **144**, L115, 1997.
264. P. Gorostiza, P. Diaz, J. Servat, and F. Sanz, Atomic force microscopy study of the silicon doping influence on the stages of platinum electroless deposition, *J. Electrochem. Soc.* **144**, 909, 1997.
265. P. H. Chang, C. T. Huang, and J. S. Shie, On liquid phase deposition of silicon dioxide by boric acid addition, *J. Electrochem. Soc.* **144**, 1144, 1997.
266. F. Wang, Y. Shi, J. Liu, Y. Lu, S. Gu, and Y. Zheng, Highly selective chemical etching of Si vs. $Si_{1-x}Ge_x$ using NH_4OH solution, *J. Electrochem. Soc.* **144**, L37, 1997.
267. S. Zangooie, R. Bjorklund, and H. Arwin, Water interaction with thermal oxidation porous silicon layers, *J. Electrochem. Soc.* **144**, 4027, 1997.
268. B. Wang and R. J. Holbrook, Microindentation for fracture and stress corrosion cracking studies in single crystal silicon, *J. Electrochem. Soc.* **134**, 2254, 1987.
269. E. D. Palik, J. W. Faust, Jr., H. F. Gray, and R. F. Greene, Study of the etch-stop mechanism in silicon, *J. Electrochem. Soc.* **129**, 2052, 1982.
270. A. J. Bard, A. B. Bocarsly, F. R. F. Fan, E. G. Walton, and M. S. Wrighton, The concept of fermi level pinning at semiconductor/liquid junctions, *J. Am. Chem. Soc.* **102**, 3671, 1980.
271. R. E. Malpas, K. Itaya, and A. J. Bard, Semiconductor electrodes, 32. n and p GaAs, n and p Si, and n type TiO_2 in liquid ammonia, *J. Am. Chem. Soc.* **103**, 1625, 1981.
272. A. B. Bocarsly, D. C. Bookbinder, R. N. Dominey, N. S. Lewis, and M. S. Wrighton, Photoreduction at illuminated p-type semiconducting silicon photoelectrodes. Evidence for Fermi level pinning, *J. Am. Chem. Soc.* **102**, 3683, 1980.
273. R. de Gryse, W. P. Gomes, F. Cardon, and J. Vennik, On the interpretation of Mott–Schottky plots determined at semiconductor/electrolyte systems, *J. Electrochem. Soc.* **122**, 712, 1975.
274. K. Uosaki and H. Kita, Effects of the helmholtz layer capacitance on the potential distribution at semiconductor/electrolyte interface and the linearity of the Mott–Schottky plot, *J. Electrochem. Soc.* **130**, 895, 1983.
275. N. S. Lewis, A quantitative investigation of the open-circuit photovoltage at the semiconductor/liquid interface, *J. Electrochem. Soc.* **131**, 2496, 1984.
276. I. L. Abrahams, L. G. Casagrande, M. D. Rosenhblum, M. L. Rosenbluth, P. G. Santangelo, B. J. Tufts, and N. S. Lewis, Opportunities in semiconductor photoelectrochemistry, *New J. Chem.* **11**(2), 157, 1987.
277. R. Memming, Surface recombination at higher injection levels, *Surf. Sci.* **1**, 88, 1964.
278. H. C. Harten, The surface recombination on silicon contacting electrolyte, *J. Phys. Chem. Solids* **14**, 220, 1960.
279. R. M. Osgood, A review of laser chemical processing, *Mater. Res. Soc. Symp. Proc.* **74**, 75, 1987.
280. C. M. A. Ashruf, P. J. French, P. M. Sarro, P. M. M. C. Bressers, and J. J. Kelly, Electrochemical etch stop engineering for bulk micromachining, *Mechatronics* **8**, 595, 1998.
281. B. Quiniou, R. Scarmozzino, Z. Wu, and R. M. Osgood, Photoemission scanning microscopy of doped regions on semiconductor, *Appl. Phys. Lett.* **55**, 481, 1989.
282. V. Bertagna, F. Rouelle, and M. Chemla, A improved electrochemical cell for the characterization of silicon/electrolyte interfaces, *J. Appl. Electrochem.* **27**, 1179, 1997.
283. S. R. Morrison, Study of semiconductors using electrochemical techniques, *J. Vac. Sci. Technol.* **15**(4), 1417, 1978.
284. J. Reichman, The current–voltage characteristics of semiconductor-electrolyte junction photovoltaic cells, *Appl. Phys. Lett.* **36**(7), 574, 1980.

285. J. D. Olivas and S. Bolin, *Advancements in MEMS Materials and Processing Technology,* p. 38, JOM, 1998.
286. C. Serre, S. Barret, and R. Herino, Characterization of the electropolishing layer during anodic etching of p-type silicon in aqueous solutions, *J. Electrochem. Soc.* **141**, 2049, 1994.
287. G. D. Francia and A. Salerno, Electrical charge and HF concentration effect on porous silicon formation, *J. Electrochem. Soc.* **141**, 689, 1994.
288. D. J. Monk, D. S. Soane, and R. T. Howe, *Hydrofluoric Acid Etching of Silicon Dioxide Sacrificial Layers, J. Electrochemical Soc.* **141**, 270, 1994.
289. H. C. Gatos and M. C. Lavine, Chemical behaviour of semiconductors: Etching characteristics, in *Progress in Semiconductors,* Vol. 9, A. F. Gibon and R. E. Burgess (eds.), p. 1, Boca Raton, FL, CRC Press, 1965.
290. A. K. Vijh, Silicon, in *Encyclopedia of Electrochemistry of Elements,* Vol. V, A. J. Bard (ed.), p. 287, Dekker, New York, 1976.
291. R. L. Smith, B. Kloeck, and S. D. Collins, Kinetics of anodic passivation on <111> silicon in KOH, *J. Electrochem. Soc.* **135**, 2001, 1988.
292. S. S. Iyer and Y. H. Xie, Light emission from silicon, *Science* **260**, 40, 1993.
293. G. Li, E. A. Kneer, B. Vermeire, H. G. Parks, and S. Raghavan, A comparative electrochemical study of copper deposition onto silicon from dilute and buffered hydrofluoric acids, *J. Electrochem. Soc.* **145**, 241, 1998.
294. K. Kirah, A. Zekry, H. F. Ragaie, and W. F. Fikry, Modeling of the transient behaviour of anodic oxides formed in Si/HF electrolyte systems, *J. Electrochem. Soc.* **145**, 332, 1998.
295. X. Cheng, G. Li, E. A. Kneer, B. Vermeire, H. G. Parks, and S. Raghavan, Electrochemical impedance spectroscopy of copper deposition on silicon from dilute hydrofluoric acid solutions, *J. Electrochem. Soc.* **145**, 352, 1998.
296. M. J. J. Theunissen, J. A. Appels, and W. H. C. G. Verkuylen, Application of preferential electrochemical etching of silicon to semiconductor device technology, *J. Electrochem. Soc.* **117**, 959, 1970.
297. H. J. A. van Dijk and J. de Jonge, Preparation of thin silicon crystals by electrochemical thinning of epitaxially grown structures, *J. Electrochem. Soc.* **117**, 553, 1970.
298. T. I. Kamins, Diffusion in thin silicon films formed by electrochemical etching, *J. Electrochem. Soc.* **121**, 266, 1974.
299. T. B. Tripp, The anodic oxidation of silicon nitride films on silicon, *J. Electrochem. Soc.* **117**, 158, 1970.
300. A. G. Revesz, Anodic oxidation of silicon in KNO_3–N-methylacetamide, *J. Electrochem. Soc.* **114**, 629, 1967.
301. M. Croset, E. Petreanu, D. Samuel, G. Amsel, and J. P. Nadai, An ^{18}O study of the source of oxygen in the anodic oxidation of silicon and tantalum in some organic solvents, *J. Electrochem. Soc.* **118**, 717, 1971.
302. G. R. Booker and R. Stickler, Large-area "jet" electrolytic polishing of Ge and Si, *J. Electrochem. Soc.* **109**, 1167, 1962.
303. M. V. Sullivan, D. L. Klein, R. M. Finne, L. A. Pompliano, and G. A. Kolb, An electropolishing technique for germanium and silicon, *J. Electrochem. Soc.* **110**, 412, 1963.
304. J. Van Muylader, J. Besson, W. Kunz, and M. Pourbaix, Silicon, in *Atlas of Electrochemical Equilibria in Aqueous Solutions,* M. Pourbaix (ed.), p. 458, National Association of Corrosion Engineers, Houston, 1974.
305. C. R. Gomes and V. C. Kieling, Effect of solution composition in nickel electrodeposition on silicon surfaces, *Metal Finishing* p. 49, January 1998.
306. B. A. Unvala, D. B. Holt, and A. San, Jet polishing of semiconductors, *J. Electrochem. Soc.* **119**, 318, 1972.
307. C. M. Osburn and D. W. Ormond, Dielect breakdown in silicon dioxide films on silicon, *J. Electrochem. Soc.* **119**, 591, 1972.
308. C. M. Osburn and D. W. Ormond, Dielect breakdown in silicon dioxide films on silicon, *J. Electrochem. Soc.* **119**, 597, 1972.
309. C. M. Osburn and E. J. Weitzman, Electrical conduction and dielectric breakdown in silicon dioxide films on silicon, *J. Electrochem. Soc.* **119**, 603, 1972.

310. F. N. Schwettmann, R. J. Dexter, and D. F. Cole, Etch rate characterization of boron-implanted thermally grown SiO_2, *J. Electrochem. Soc.* **120**, 1566, 1973.
311. K. R. Mayer, A simplification of kamper's striation etch for silicon, *J. Electrochem. Soc.* **120**, 1780, 1973.
312. C. M. A. Ashruf, P. J. French, P. M. M. C. Bressers, and J. J. Kelly, Galvanic porous silicon formation without external contacts, *Sensors Actuators* **A74**, 118, 1999.
313. R. L. Meek, T. M. Buck, and C. F. Gibbon, Silicon surface contamination: Polishing and cleaning, *J. Electrochem. Soc.* **120**, 1241, 1973.
314. B. E. Deal, The current understanding of changes in the thermally oxidized silicon structure, *J. Electrochem. Soc.* **121**, 198c, 1974.
315. E. S. Kooij, M. Hamoumi, J. J. Kelly, and R. E. I. Schropp, Photoselective metal deposition on amorphous silicon p-i-n solar cells, *J. Electrochem. Soc.* **144**, L271, 1997.
316. F. P. Fehlner, Formation of ultrathin oxide films on silicon, *J. Electrochem. Soc.* **119**, 1723, 1972.
317. D. J. Silversmith, Nonuniform lateral ionic impurity distributions at $Si–SiO_2$ interfaces, *J. Electrochem. Soc.* **119**, 1589, 1972.
318. S. McGinnis, P. Sines, and B. Das, Pulsed current anodization: An effective method for fabricating patterned porous silicon p–n junction light emitting diodes, *Electrochem. Solid-State Lett.* **2**, 468, 1999.
319. F. S. Aragona, Dislocation etch for (100) planes in silicon, *J. Electrochem. Soc.* **119**, 948, 1972.
320. R. C. Henderson, Silicon cleaning with hydrogen peroxide solutions: A high energy electron diffraction and Auger electron spectroscopy study, *J. Electrochem. Soc.* **119**, 772, 1972.
321. M. Takigawa, T. Satoh, and K. Shono, Selective removal of BP from Si substrate, *J. Electrochem. Soc.* **122**, 824, 1975.
322. M. G. Yang and K. M. Koliwad, Auger electron spectroscopy of cleanup-related contamination on silicon surfaces, *J. Electrochem. Soc.* **122**, 675, 1975.
323. M. J. Declercq, L. Gerzberg, and J. D. Meindl, Optimization of the hydrazine–water solution for Anisotropic etching of silicon in integrated circuit technology, *J. Electrochem. Soc.* **122**, 545, 1975.
324. T. I. Kamins and B. E. Deal, Characteristics of $Si–SiO_2$ interfaces beneath thin silicon films defined by electrochemical etching, *J. Electrochem. Soc.* **122**, 557, 1975.
325. S. I. Raider, R. Flitsch, and M. J. Palmer, Oxide growth on etched silicon in air at room temperature, *J. Electrochem. Soc.* **122**, 413, 1975.
326. A. Belaidi, M. Safi, F. Ozanam, J. N. Chazalviel, and O. Gorochov, Surface chemistry during porous-silicon formation in dilute fluoride electrolytes, *J. Electrochem. Soc.* **46**, 2659, 1999.
327. H. Day, A. Christou, and D. J. Bressan, The retention of fluorine by silicon surfaces: Interaction with gold-refractory transistor metallizations, *J. Electrochem. Soc.* **121**, 790, 1974.
328. W. Van Gelder and V. E. Hauser, The etching of silicon nitride in phosphoric acid with silicon dioxide as a mask, *J. Electrochem. Soc.* **114**, 869, 1967.
329. A. F. Bogenschutz, W. Krusemark, K. H. Locheer, and W. Mussinger, Activation energies in the chemical etching of semiconductors in $HNO_3–HF–CH_3COOH$, *J. Electrochem. Soc.* **114**, 970, 1967.
330. J. J. Gannon and C. J. Nuese, A chemical etchant for the selective removal of GaAs through SiO_2 masks, *J. Electrochem. Soc.* **121**, 1215, 1974.
331. B. Schwartz and H. Robbins, Chemical etching of silicon. IV. Etching technology, *J. Electrochem. Soc.* **123**, 1903, 1976.
332. L. R. Plauger, Etching studies of diffusion source boron glass, *J. Electrochem. Soc.* **120**, 1428, 1973.
333. G. B. Larrabee, K. G. Heinen, and S. A. Harrell, Measurement of the retention of fluoride by silicon and silicon dioxide surfaces, *J. Electrochem. Soc.* **114**, 867, 1967.
334. R. M. Finne and D. L. Klein, A water–amine-complexing agent system for etching silicon, *J. Electrochem. Soc.* **114**, 965, 1967.
335. R. Lieberman and D. L. Klein, Temporary protection of silicon surfaces by iodine films, *J. Electrochem. Soc.* **113**, 956, 1966.
336. G. B. Larrabee, The contamination of semiconductor surfaces, *J. Electrochem. Soc.* **108**, 1130, 1961.
337. D. G. Schimmel and M. J. Elkind, An examination of the chemical staining of silicon, *J. Electrochem. Soc.* **125**, 152, 1978.
338. S. I. Raider and A. Berman, On the nature of fixed oxide charge, *J. Electrochem. Soc.* **125**, 629, 1978.
339. A. K. Sinha and T. E. Smith, Kinetics of the slow-trapping instability at the Si/SiO_2 interface, *J. Electrochem. Soc.* **125**, 743, 1978.

340. D. G. Schimmel, Defect etch for <100> silicon evaluation, *J. Electrochem. Soc.* **126**, 479, 1979.
341. I. Barycka, H. Teterycz, and Z. Znamirowski, Sodium hydroxide solution shows selective etching of boron-doped silicon, *J. Electrochem. Soc.* **126**, 345, 1979.
342. A. Reisman, M. Berkenblit, S. A. Chan, F. B. Kaufman, and D. C. Green, The controlled etching of silicon in catalyzed ethylenediamine–pyrocatechol–water solutions, *J. Electrochem. Soc.* **126**, 1406, 1979.
343. E. Bassous and E. F. Baran, The fabrication of high precision nozzles by the anisotropic etching of (100) silicon, *J. Electrochem. Soc.* **126**, 1321, 1979.
344. F. Pintchovski, J. B. Price, O. J. Tobin, J. Peavey, and K. Kobold, Thermal characteristics of the H_2SO_4–H_2O silicon wafer cleaning solution, *J. Electrochem. Soc.* **126**, 1428, 1979.
345. G. I. Parisi, S. E. Haszko, and G. A. Rozgonyi, Tapered windows in SiO_2: The effect of NH_4F:HF dilution and etching temperature, *J. Electrochem. Soc.* **124**, 917, 1977.
346. W. D. Mackintosh and H. H. Plattner, The identification of the mobile ion during the anodic oxidation of silicon, *J. Electrochem. Soc.* **124**, 396, 1977.
347. K. Lida, Polycrystalline aluminum oxide anodization on silicon, *J. Electrochem. Soc.* **124**, 614, 1977.
348. Y. Harada, K. Fushimi, S. Madokoro, H. Sawai, and S. Ushio, The characterization of via-filling technology with electroless plating method, *J. Electrochem. Soc.* **133**, 2428, 1986.
349. F. Shimura, TEM observation of pyramidal hillocks formed on (100) silicon wafers during chemical etching, *J. Electrochem. Soc.* **127**, 551, 1980.
350. A. Reisman, M. Berkenblit, C. J. Merz, A. K. Ray, and D. C. Green, Anomalous etch structure using ethylenediamine–pyrocatechol–water based etchants and their elimination, *J. Electrochem. Soc.* **127**, 1208, 1980.
351. Y. Avigal, D. Cahen, G. Hodes, J. Manassen, B. Vainas, and A. G. G. Gibson, Photoelectrochemistry of hydrogenated amorphous silicon (a-Si:H), *J. Electrochem. Soc.* **127**, 1209, 1980.
352. K. M. Sancier and V. Kapur, Silicon oxidation in fluoride solutions, *J. Electrochem. Soc.* **127**, 1848, 1980.
353. C. D. Sharpe and P. Lilley, The electrolyte–silicon interface: Anodic dissolution and concentration profiling, *J. Electrochem. Soc.* **127**, 1918, 1980.
354. D. L. Klein and D. J. D'Stefan, Controlled etching of silicon in the HF–HNO_3 system, *J. Electrochem. Soc.* **109**, 37, 1962.
355. L. K. White, Bilayer taper etching of field oxides and passivation layers, *J. Electrochem. Soc.* **132**, 1705, 1985.
356. R. D. Jolly and R. S. Muller, Miniature cantilever beams fabricated by anisotropic etching of silicon, *J. Electrochem. Soc.* **127**, 2750, 1980.
357. A. G. Revesz, On SiOH and SiH Groups in SiO_2 films on silicon, *J. Electrochem. Soc.* **124**, 1811, 1977.
358. H. J. Lewerenz and J. Stumper, In-situ conditioning at amorphous silicon/aqueous electrolyte junctions, *J. Electrochem. Soc.* **134**, 1877, 1987.
359. G. Gould and E. A. Irene, The influence of silicon surface cleaning procedures on silicon oxidation, *J. Electrochem. Soc.* **134**, 1031, 1987.
360. N. Koshida, M. Nagasu, and Y. Kiuchi, Impedance spectra of T type porous Si–electrolyte interface, *J. Electrochem. Soc.* **133**, 2283, 1986.
361. A. Ishizaka and Y. Shiraki, Low temperature surface cleaning and its application to silicon MBE, *J. Electrochem. Soc.* **133**, 666, 1986.
362. O. Chyan, S. I. Ho, and K. Rajechwar, Heterojunction photoelectrodes III, *J. Electrochem. Soc.* **133**, 531, 1986.
363. J. Gobet and H. Hannenberger, Electrodeposition of silicon from a nonaqueous solvent, *J. Electmchem. Soc.* **110**, 135, 1988,
364. H. Yoneyama, K. Wakamoto, and H. Tamura, Photoelectrochemical properties of polypyrrole-coated silicon electrodes, *J. Electrochem. Soc.* **132**, 2414, 1985.
365. R. Herino, P. Jan, and G. Bomchil, Nickel plating on porous silicon, *J. Electrochem. Soc.* **132**, 2513, 1985.
366. N. Koshida, M. Nagasu, T. Sakusabe, and Y. Kiuchi, The current characteristics of a photoelectrochemical cell using p-type porous Si, *J. Electrochem. Soc.* **132**, 346, 1985.

367. J. L. Hoyt, E. F. Crabbe, R. F. W. Pease, and J. F. Gibbons, Etching technique for characterization of epitaxial alignment of arsenic implanted polycrystalline silicon films on <100>, *J. Electrochem, Soc.* **135**, 1839, 1988.
368. G. Gould and E. A. Irene, An in situ study of aqueous HF treatment of silicon by contact angle measurement and ellipsometry, *J. Electrochem. Soc.* **135**, 1535, 1988.
369. A. H. El-Hoshy, Measurement of p-etch rates for boron-doped glass films, *J. Electrochem. Soc.* **117**, 1583, 1970.
370. H. Hasengawa, S. Arimoto, J. Nanjo, H. Yamamoto, and H. Ohno, Anodic oxidation of hydrogenated amorphous silicon and properties of oxide, *J. Electrochem. Soc.* **135**, 424, 1988.
371. A. Prasad, S. Balakrishman, S. K. Jain, and G. C. Jain, Porous silicon oxide anti-reflection coating for solar cells, *J. Electrochem. Soc.* **129**, 596, 1982.
372. H. J. Byker, V. E. Wood, and A. E. Austin, Photoelectrochemistry of n-p-type silicon in acetonitrile, *J. Electrochem. Soc.* **129**, 1982, 1982.
373. G. V. Amerongen, D. Guyomard, R. Heindl, M. Herlem, and J. L. Sculfort, Photoelectrochemical behavior of p-type Si single crystals in liquid ammonia and in liquid ammoniate of sodium iodide, *J. Electrochem. Soc.* **129**, 1998, 1982.
374. F. Sugimoto and S. Okamura, Adsorption behavior of organic contaminants on a silicon wafer surface, *J. Electrochem. Soc.* **46**, 2725, 1981.
375. V. D. Archer, Methods for defect evaluation of thin <100> orientated silicon epitaxial layers using a wet chemical etch, *J. Electrochem. Soc.* **129**, 2074, 1982.
376. C. M. Gronet, N. S. Lewis, G. W. Cogan, J. F. Gibbons, and G. R. Moddel, Correlation of the photoelectrochemistry of the amorphous hydrogenated silicon/methanol interface with bulk semiconductor properties, *J. Electrochem. Soc.* **131**, 2873, 1984.
377. G. Ghidini and F. W. Smith, Interaction of H_2O with Si(111) and (100), *J. Electrochem. Soc.* **131**, 2924, 1984.
378. J. W. Faust and E. D. Palik, *Study of the Orientation Dependent Etching and Initial Anodization of Si Aqueous KOH, J. Electrochem. Soc.* p. 1413, 1983.
379. E. D. Palik, H. F. Gray, and P. B. Klein, A Raman study of etching silicon in aqueous KOH, *J. Electrochem. Soc.* **130**, 956, 1983.
380. H. Nielsen and D. Hackleman, Some illumination on the mechanism of SiO_2 etching in HF solutions, *J. Electrochem. Soc.* **130**, 708, 1983.
381. S. T. Ann and W. A. Tiler, A stain technique for the study of two-dimensional dopant diffusion in silicon, *J. Electrochem. Soc.* **135**, 2370, 1988.
382. W. P. Maszara, Silicon-on-insulator by wafer bonding: Review, *J. Electrochem. Soc.* **138**, 341, 1991.
383. X. Z. Tu, Fabrication of silicon microstructures based on selective formation and etching of porous silicon, *J. Electrochem. Soc.* **135**, 2105, 1988.
384. L. Liou, W. G. Spitzer, and S. Prussin, Amorphous silicon produced by ion implantation—etching rate in HF solution and effect of annealing, *J. Electrochem. Soc.* **131**, 672, 1984.
385. D. J. Day, W. R. Middleton, T. W. Janes, J. C. White, and V. J. Mifsud, Passivation and maskless processing with anisotropic etches in silicon, *J. Electrochem. Soc.* **131**, 407, 1984.
386. N. F. Raley, Y. Sugiyama, and T. V. Duzer, (100) silicon etch-rate dependence on boron concentration in ethylenediamine–pyrocatechol-water solutions, *J. Electrochem. Soc.* **131**, 161, 1984.
387. K. H. Yang, An etch for delineation of defects in silicon, *J. Electrochem. Soc.* **131**, 1140, 1984.
388. C. J. Werkhoven, C. W. Bull-Lieuwma, B. J. H. Leunissen, and M. P. A. Viegers, Characterization of metallic precipitates in epitaxial Si by means of preferential etching and TEM, *J. Electrochem. Soc.* **131**, 1388, 1984.
389. G. Nagasubramenian, B. L. Wheeler, F. R. F. Fan, and A. Bard, Semiconductor electrodes, *J. Electrochem. Soc.* **129**, 1742, 1982.
390. W. M. Ayers, p-type amorphous silicon/liquid junction solar cell, *J. Electrochem. Soc.* **129**, 1644, 1982.
391. R. L. Meek and M. C. Huffstutler, Jr., ID-diamond sawing damage to germanium and silicon, *J. Electrochem. Soc.* **109**, 893, 1969.
392. R. Muller, Surface photovoltage studies of silicon electrolyte systems, *J. Electrochem. Soc.* **109**, 1195, 1962.
393. J. R. Troxell and J. L. Kenty, Silicon grain delineation using ethylenediamine pyrocatechol, *J. Electrochem. Soc.* **134**, 2369, 1987.

394. W. Haas, Silicon dioxide as dielectric in solid electrolyte capacitors, *J. Electrochem. Soc.* **109**, 109, 1962.
395. A. V. Rao and J. N. Chazalviel, Chemical trends in the electromodulated infrared vibrational spectroscopy of various silicon/electrolyte interfaces, *J. Electrochem. Soc.* **134**, 2777, 1987.
396. Y. Nakato, T. Ueda, Y. Egi, and H. Tsubomura, Decomposition potentials of crystalline silicon as related to the photocurrent stability of p–n junction silicon semiconductor electrodes, *J. Electrochem. Soc.* **134**, 353, 1987.
397. K. Watanabe, T. Tanigaki, and S. Wakayama, The properties of LPCVD SiO_2 film deposited by SiH_2Cl_2 and N_2O mixtures, *J. Electrochem. Soc.* **128**, 2630, 1981.
398. A. Bohg, Ethylene diamine–pyrocatechol–water mixture shows etching anomaly in boron-doped silicon, *J. Electrochem. Soc.* **118**, 401, 1971.
399. J. C. Greenwood, Ethylene diamine–catechol–water mixture shows preferential etching of p–n junction, *J. Electrochem. Soc.* **116**, 1325, 1969.
400. J. N. Chazalviel, Photocurrent spectroscopy of interface states at a semiconductor–electrolyte junction, *J. Electrochem. Soc.* **127**, 1822, 1980.
401. R. W. Ade and E. R. Fossum, Limitations of orientation dependent microstructure etching in silicon, *J. Electrochem. Soc.* **134**, 3192, 1987.
402. S. Holdcroft and B. L. Funt, The energies of electron transfer at the polypyrrole/silicon interface, *J. Electrochem. Soc.* **135**, 3106, 1988.
403. E. D. Palik, O. J. Glembocki, and R. E. Stahlbush, Fabrication and characterization of Si membranes, *J. Electrochem. Soc.* **135**, 3126, 1988.
404. M. J. Madou, W. P. Gomes, F. Fransen, and F. Cardon, Anodic oxidation of p-type silicon in methanol as compared to glycol, *J. Electrochem. Soc.* **129**, 2749, 1982.
405. T. Aoyama, T. Yamazaki, and T. Ito, Nonuniformities in chemical oxides on silicon surfaces formed during wet chemical cleaning, *J. Electrochem. Soc.* **143**, 2280, 1996.
406. D. K. Sohn, S. C. Park, S. W. Kang, and B. T. Ahn, A study of Cu metal deposition on amorphous Si films from Cu solutions for low-temperature crystallization of amorphous Si films, *J. Electrochem. Soc.* **144**, 3592, 1997.
407. G. J. Norga, M. Platero, K. A. Black, A. J. Reddy, J. Michel, and L. C. Kimerling, Mechanism of copper deposition on silicon from dilute hydrofluoric acid solution, *J. Electrochem. Soc.* **144**, 2801, 1997.
408. S. Cattarin, J. N. Chazalviel, C. D. Fonseca, F. Ozanam, L. M. Peter, G. Schlichthorl, and J. Stumper, In situ characterization of the p-Si/NH_4F interface during dissolution in the current oscillation regime, *J. Electrochem. Soc.* **145**, 498, 1998.
409. M. Niwano, T. Miura, and N. Miyamoto, Hydrogen exchange reaction on hydrogen-terminated (100) Si surface during storage in water, *J. Electrochem. Soc.* **145**, 659, 1998.
410. C. P. Wu, E. C. Douglas, C. W. Mueller, and R. Williams, Techniques for lapping and staining ion-implanted layers, *J. Electrochem. Soc.* **126**, 1982, 1979.
411. G. M. Rao, D. Elwell, and R. S. Feigelson, Electrowinning of silicon from K_2SiF_6–molten fluoride systems, *J. Electrochem. Soc.* **127**, 1940, 1980.
412. W. Kern and R. C. Heim, Chemical vapor deposition of silicate glasses for use with silicon devices, *J. Electrochem. Soc.* **117**, 568, 1970.
413. L. A. Harris and J. A. Hugo, Thin platinum films on silicon, *J. Electrochem. Soc.* **128**, 1203, 1981.
414. Y. Takeda, R. Kanno, O. Yamamoto, T. R. R. Mohan, C. H. Lee, and F. A. Kroger, Cathodic deposition of amorphous silicon from tetraethylorthosilicate in organic solvents, *J. Electrochem. Soc.* **128**, 1221, 1981.
415. F. R. Fan, B. L. Wheeler, and A. J. Bard, Semiconductor electrodes XXXIX, *J. Electrochem. Soc.* **128**, 2042, 1981.
416. Y. Nakato, Y. Iwakabe, M. Hiramoto, and H. Tsubomura, Tungsten or molybdenum coated p–n junction silicon electrodes for efficient and stable photoelectrochemical solar energy, *J. Electrochem. Soc.* **133**, 1203, 1986.
417. A. K. Agrawal and A. E. Austin, Electrodeposition of silicon from solutions of silicon halides in aprotic solvents, *J. Electrochem. Soc.* **128**, 2292, 1981.
418. R. Noufi, D. Tench, and L. F. Warren, Protection of semiconductor photoanodes with photoelectrochemically generated polypyrrole films, *J. Electrochem. Soc.* **128**, 2596, 1981.

419. C. H. Lee and F. A. Kroger, Cathodic deposition of amorphous alloys of silicon, carbon and fluorine, *J. Electrochem. Soc.* **129**, 936, 1982.
420. K. D. Beyer and R. H. Kastl, Impact of deionized water rinse on silicon surface cleaning, *J. Electrochem. Soc.* **129**, 1027, 1982.
421. L. Fornarini, F. Stirpe, and B. Scrosati, Electrochemical solar cells with layer-type semiconductor anodes. Nonaqueous electrolyte cells, *J. Electrochem. Soc.* **129**, 1155, 1982.
422. P. M. Sarro and A. W. van Herwaarden, Silicon cantilever beams fabricated by electrochemically controlled etching for sensor applications, *J. Electrochem. Soc.* **133**, 1724, 1986.
423. Y. Fukuda, W. Zhou, K. Furuya, and H. Suzuki, Photoluminescence change of as-prepared and aged porous silicon with NaOH treatment, *J. Electrochem. Soc.* **146**, 2697, 1999.
424. K. H. Beckmann and N. J. Harrick, Hydrides and hydroxyls in thin silicon dioxide films, *J. Electrochem. Soc.* **118**, 614, 1971.
425. D. M. Brown and P. R. Kennicott, Glass source B diffusion in Si and SiO_2, *J. Electrochem. Soc.* **118**, 293, 1971.
426. R. O. Schwenker, Etch rate characterization of borosilicate glasses as diffusion sources, *J. Electrochem. Soc.* **118**, 313, 1971.
427. P. F. Schmidt and J. D. Ashner, Tracer investigation of hydroxyls in SiO_2 films on silicon, *J. Electrochem. Soc.* **118**, 325, 1971.
428. J. Wong, Vapor deposition and properties of binary arsenosilicate glass films, *J. Electrochem. Soc.* **129**, 1071, 1972.
429. M. Ghezzo and D. M. Brown, Arsenic glass diffusion in Si and SiO_2, *J. Electrochem. Soc.* **120**, 110, 1973.
430. G. L. Kuhn and C. J. Rhee, Thin silicon film on insulating substrate, *J. Electrochem. Soc.* **120**, 1563, 1973.
431. E. H. Snow and B. E. Deal, Polarization phenomena and other properties of phosphosilicate glass films on silicon, *J. Electrochem. Soc.* **113**, 263, 1966.
432. W. D. Mackintosh and H. H. Plattner, The identification of the mobile ion during the anodic oxidation of silicon, *J. Electrochem. Soc.* **124**, 1950, 1977.
433. M. W. Jenkins, A new preferential etch for defects in silicon crystals, *J. Electrochem. Soc.* **124**, 757, 1977.
434. E. Bassous and E. F. Baran, The fabrication of high precision nozzles by the anisotropic etching of (100) silicon, *J. Electrochem. Soc.* **125**, 1231, 1978.
435. A. Reisman, M. Berkenblit, S. A. Chan, F. B. Kaufman, and D. C. Green, The controlled etching of silicon in catalyzed ethylenediamine–pyrocatechol–water solutions, *J. Electrochem. Soc.* **126**, 1407, 1979.
436. K. H. Jung, S. Shih, and D. L. Kwong, Developments in luminescent porous Si, *J. Electrochem. Soc.* **140**, 3046, 1993.
437. H. J. Lewerenz, T. Bitzer, M. Gruyters, and K. Jacobi, Electrolytic hydrogenation of silicon, *J. Electrochem. Soc.* **140**, L44, 1993.
438. E. Hsu, H. G. Parks, R. Craigin, S. Tomooka, J. S. Ramberg, and R. K. Lowry, Deposition characteristics of metal contaminants from HF-based process solutions onto silicon wafer surfaces, *J. Electrochem. Soc.* **139**, 3659, 1992.
439. Standard Test Method for Crystallographic Perfection of Silicon by Preferential Etch Techniques, ASTM Standard, F47-88, Annual Book of ASTM Standards, Vol.10.05, p.65, 1988.
440. Standard Test Method for Crystallographic Perfection of Silicon by Preferential Etch Techniques, ASTM Standard, F80-88a, Annual Book of ASTM Standards, Vol.10.05, p.130, 1988.
441. Standard Test Method for Crystallographic Perfection of Silicon by Preferential Etch Techniques, ASTM Standard, F110-88, Annual Book of ASTM Standards, Vol.10.05, p.117, 1988.
442. Standard Test Method for Crystallographic Perfection of Silicon by Preferential Etch Techniques, ASTM Standard, F154-88, Annual Book of ASTM Standards, Vol.10.05, p.220, 1988.
443. R. Herino, Porous silicon for microelectronics and optoelectronics, *Mater. Sci. Technol.* **13**, 965, 1997.
444. K. A. Jackson and A. F. Witt, Silicon: Preparation and properties, in *Encyclopaedia of Materials Science and Engineering,* p. 4427, Pergamon Press, Elmsford, NY, 1986.
445. K. S. Choe, On the improper use of Yang preferential etching in determining precipitates in crystalline silicon, *J. Electrochem. Soc.* **142**, 1647, 1995.

446. J. Rappich and H. J. Lewerenz, In situ Fourier transform infrared investigation on the electrolytic hydrogenation of n-silicon (111), *J. Electrochem. Soc.* **142**, 1233, 1995.
447. C. A. Deckert, Pattern etching of CVD Si_3N_4/SiO_2 composites in HF/glycerol mixtures, *J. Electrochem. Soc.* **127**, 2433, 1980.
448. M. Hirita, S. Suwazono, and H. Tanigawa, Diaphragm thickness control in silicon pressure sensors using an anode oxidation etch-stop, *J. Electrochem. Soc.* **134**, 2037, 1987.
449. J. A. Bardwell, K. B. Clark, D. F. Mitchell, D. A. Bisaillion, G. I. Sproule, B. MacDougall, and M. J. Graham, Growth and characterisation of room temperature anodic SiO_2 films, *J. Electrochem. Soc.* **140**, 2135, 1993.
450. H. Kasapbasioglu and P. J. Hesketh, Fabrication of a grooved single-crystal silicon X-ray analyser, *J. Electrochem. Soc.* **140**, 2319, 1993.
451. D. J. Monk, D. S. Soane, and R. T. Howe, Determination of the etching kinetics for the hydrofluoric acid/silicon dioxide system, *J. Electrochem. Soc.* **140**, 2339, 1993.
452. H. Kikuyama, M. Waki, I. Kawanabe, M. Miyashita, T. Yabune, and N. Miki, Etching rate and mechanism of doped oxide in buffered hydrogen fluoride solution, *J. Electrochem. Soc.* **139**, 2239, 1992.
453. M. L. Kniffin, T. E. Beerling, and C. R. Helms, The effectiveness of aqueous cleaning for the removal of evaporation iron and copper from silicon surfaces, *J. Electrochem. Soc.* **139**, 1195, 1992.
454. T. H. Park, Y. S. Ko, T. E. Shim, J. G. Lee, and Y. K. Kim, The cleaning effects of $HF–HNO_3–H_2O_2$ system, *J. Electrochem. Soc.* **142**, 571, 1995.
455. Z. Shi, Observation of K_2SiF_6 crystal growth during Secco etching of polycrystalline silicon, *J. Electmchem. Soc.* **142**, 2377, 1995.
456. C. H. Ting and M. Paunovic, Selective electroless metal deposition for integrated circuit, *J. Electmchem. Soc.* **136**, 456, 1989.
457. T. F. Hung, H. Wong, and Y. C. Cheng, A new design of anodic oxidation reactor for high-quality gate oxide preparation, *J. Electrochem. Soc.* **138**, 3747, 1991.
458. T. A. Kwa, P. J. French, R. F. Wolffenbuttel, P. M. Sarro, L. Hellemans, and J. Snauwaert, Anisotropically etched silicon mirrors for optical sensor applications, *J. Electrochem. Soc.* **142**, 1226, 1995.
459. P. F. Schmidt, T. W. O'Keeffe, J. Oroshnik, and A. E. Owen, Doped anodic oxide films for device fabrication in silicon, *J. Electrochem. Soc.* **112**, 800, 1965.
460. S. L. Tau, M. Arendt, A. J. Bard, B. Evans, C. Tsai, J. Sarathy, and J. C. Campbell, Study of the structure and chemical nature of porous Si and siloxene by STM, AFM, XPS and LIMA, *J. Electrochem. Soc.* **141**, 402, 1994.
461. T. Ohmi, T. Imaoka, T. Kekehiko, T. Kezuka, J. Takano, and M. Kogure, Degregation and removal of metallic impurity at interface of silicon and fluorine etchant, *J. Electrochem. Soc.* **140**, 811, 1993.
462. K. B. Sundaram and H. W. Chang, Electrochemical etching of silicon by hydrazine, *J. Electrochem. Soc.* **140**, 1592, 1993.
463. L. Smith and A. Soderbarg, Electrochemical etch stop obtained by accumulation of free carriers without p–n junction, *J. Electrochem. Soc.* **140**, 271, 1993.
464. H. Shimada, M. Onodera, S. Shimomura, K. Hirose, and T. Ohmi, Resistance-surfactant-free photoresist development process, *J. Electrochem. Soc.* **139**, 1721, 1992.
465. O. J. Anttila and M. V. Tilli, Metal contamination removal on silicon wafers using dilute acidic solutions, *J. Electrochem. Soc.* **139**, 1751, 1992.
466. J. Kato and Y. Maruo, Investigation of the charge observed in thermal oxide films originated from SC-1 precleaning, *J. Electrochem. Soc.* **139**, 1756, 1992.
467. O. J. Anttila, M. V. Tilli, M. Schekers, and C. L. Claeys, Effect of chemicals on metal contamination on silicon wafers, *J. Electrochem. Soc.* **139**, 1180, 1992.
468. M. Myamoto, N. Kita, S. Ishida, and T. Tatsuno, Prevention of microroughness generation on the silicon wafer surface in buffered hydrogen fluoride by a surfactant addition, *J. Electrochem. Soc.* **141**, 2899, 1994.
469. P. M. Dove and J. D. Rimstidt, Silica–water interactions, in *Silica—Physical Behaviour, Geochemistry and Materials Applications,* P. J. Heaney, C. T. Prewitt, and G. V. Gibbs (eds.), Review in Mineralogy, Vol.29, p.258, Mineralogical Society of America, Washington, D.C., 1994.
470. J. M. Olson and K. Carleton, Kinetics of silicon electrodeposition, in *Silicon Material Preparation and Economical Wafering Methods,* R. Lutwack and A. Morrison (eds.), p. 261, Noyes Publications, 1985.

471. Silicon wafer process technology: Slicing, etching, polishing, in *Semiconductor Silicon 1977,* H. R. Huff and E. Sirtl (eds.), p. 154, Electrochemical Society, Pennington, 1977.
472. F. Shimura, *Semiconductor Silicon Crystal Technology,* Academic Press, San Diego, 1990.
473. R. Heimann, Principles of chemical etching—The art and science of etching crystals, in *Silicon Chemical Etching,* J. Grabmaier (ed.), p. 174, Springer-Verlag, Berlin, 1982.
474. J. N. Chazalviel, Impedance studies at semiconductor electrodes: Classical and more exotic techniques, *Electrochim. Acta* **35**, 1545, 1990.
475. P. C. Searson and X. G. Zhang, The potential distribution at the silicon/electrode interface in HF solutions, *Electrochim, Acta* **36**, 499, 1991.
476. H. Bender, S. Verhaverbeke, and M. M. Heyns, Hydrogen passivation of HF-last cleaned (100) silicon surfaces investigated by multiple internal reflection infrared spectroscopy, *J. Electrochem. Soc.* **141**, 3128, 1994.
477. A. Venkateswara Rao, F. Ozanam, and J. N. Chazalviel, In situ Fourier-transform electromodulated infrared study of porous silicon formation: Evidence for solvent effects on the vibrational linewidths, *J. Electrochem. Soc.* **138**, 153, 1991.
478. D. L. Kendall, Vertical etching of silicon at very high aspect ratios, *Annu. Rev. Mater. Sci.* **9**, 373, 1979.
479. J. M. Aitken and E. A. Irene, Silicon dioxide films in semiconductor devices, in *Treatise on Materials Science and Technology,* Vol.26, p.1, Academic Press, New York, 1985.
480. J. A. Switzer, The n-silicon/thallium (111) oxide heterojunction photoelectrochemical solar cell, *J. Electrochem. Soc.* **133**, 722, 1986.
481. T. A. Skotheim and O. Inganas, Polymer solid electrolyte photoelectrochemical cells with n-Si-polypyrrole photoelectrodes, *J. Electrochem. Soc.* **132**, 2116, 1985.
482. T. Osaka, K. Ejiri, and N. Hirota, Photoelectrochemical behavior of iron oxide/n-Si heterojunction electrodes with an outer Pd layer, *J. Electrochem. Soc.* **131**, 1571, 1984.
483. F. R. Fan, T. V. Shea, and A. Bard, Semiconductor electrodes LIV, *J. Electrochem. Soc.* **131**, 828, 1984.
484. F. R. Fan, G. A. Hope, and A. Bard, Semiconductor electrodes XLVI, *J. Electrochem. Soc.* **129**, 1647, 1982.
485. R. E. Malpas, The electrochemistry and photoelectrochemistry of an aqueous ferrocene/ferricenium redox couple at platinum, n-silicon and n-indium phosphide electrodes, *J. Electrochem. Soc.* **129**, 1987, 1982.
486. J. N. Chazalviel, Electrochemical transfer via surface states: A new formulation for the semiconductor/electrolyte interface, *J. Electrochem. Soc.* **129**, 963, 1982.
487. G. S. Calabrese and M. S. Wrighton, Photoelectrochemical reduction of 2-t-butyl-9,10-anthraquinone at illuminated p-type Si: An approach to the photochemical synthesis of hydrogen peroxide, *J. Electrochem. Soc.* **128**, 1014, 1981.
488. M. Miyashita, T. Tusga, K. Makihara, and T. Ohmi, Dependence of surface microroughness of CZ, FZ and EPI wafers on wet chemical processing, *J. Electrochem. Soc.* **139**, 2133, 1992.
489. H. Fukidome, M. Matsumura, T. Komeda, K. Mamba, and Y. Nishika, In situ atomic force microscopy observation of dissolution process of Si(111) in oxygen-free water at room temperature, *Electrochem. Solid-State Lett.* **2**, 393, 1999.
490. L. D. Dyer, G. J. Grant, C. M. Tipton, and A. E. Stephens, A comparison of silicon wafer etching by KOH and acid solutions, *J. Electrochem. Soc.* **136**, 3016, 1989.
491. H. Proksche, G. Nagorsen, and D. Ross, The influence of NH_4F on the etch rates of undoped SiO_2 in buffered oxide etch, *J. Electrochem. Soc.* **139**, 521, 1992.
492. H. J. Lewerenz and T. Bitzer, Electrolytic hydrogenation of silicon, *J. Electrochem. Soc.* **139**, L21, 1992.
493. O. J. Anttila, M. V. Tilli, M. Schaekers, and C. L. Claeys, Effect of chemicals on metal contamination on silicon wafers, *J. Electrochem. Soc.* **139**, 1180, 1992.
494. J. Rappich, H. Jungblut, M. Aggour, and H. J. Lewerenz, Electrochemical smoothing of silicon (111), *J. Electrochem. Soc.* **141**, L99, 1994.
495. B. E. Deal, M. Sklar, A. S. Grove, and E. H. Snow, Characteristics of the surface-state charge (Q_{ss}) of thermally oxidized silicon, *J. Electrochem. Soc.* **114**, 266, 1967.
496. A. S. Grove, *Physics and Technology of Semiconductor Devices,* John Wiley & Sons, New York, 1967.
497. R. A. Street, *Hydrogenated Amorphous Silicon,* Cambridge University Press, London, 1991.

498. W. R. Runyan, *Silicon Semiconductor Technology,* Texas Instruments, 1965.
499. J. Derrien, F. Ringeisen, and M. Commande, Structure and growth kinetics of SiO_2 ultra thin film on Si(111) surface, in *Passivity of Metals and Semiconductors,* M. Froment (ed.), p. 447, Elsevier, Amsterdam, 1983.
500. J. M. Noworolski, E. Klaassen, J. Logan, K. Petersen, and N. I. Maluf, Fabrication of SOI wafers with buried cavities using silicon fusion bonding and electrochemical etchback, *Sensors Actuators A* **54**, 709, 1996.
501. G. Mayer and J. M. Kohler, Micromechanical compartments for biotechnological applications: Fabrication and investigation of liquid evaporation, *Sensors Actuators A* **60**, 202, 1997.
502. Th. Bischoff, G. Muller, W. Welser, and F. Koch, Frontside micromachining using porous-silicon sacrificial-layer technologies, *Sensors Actuators A* **60**, 228, 1997.
503. Cs. Ducso, E. Vazsonyi, M. Adam, I. Szabo, I. Barsony, and J. G. E. Gardeniers, Porous silicon bulk micromachining for thermally isolated membrane formation, *Sensors Actuators A* **60**, 235, 1997.
504. M. Bao, X. Li, S. Shen, and H. Chen, A novel micromachining technology for multilevel structures of silicon, *Sensors Actuators A* **63**, 217, 1997.
505. J. T. L. Thong, W. K. Choi, and C. W. Chong, TMAH etching of silicon and the interaction of etching parameters, *Sensors Actuators A* **63**, 243, 1997.
506. H. Linde, C. Whiting, and D. Benoit, Etch characteristics of various materials in ethanolamine etchants, *Sensors Actuators A* **63**, 251, 1997.
507. H. Chen, M. Bao, H. Zhu, and S. Shen, A piezoresistive accelerometer with a novel vertical beam structure, *Sensors Actuators A* **63**, 19, 1997.
508. V. P. Parkhutik and E. Matveeva, Observation of new oscillatory phenomena during the electrochemical anodization of silicon, *Electrochem. Solid-State Lett.* **2**, 371, 1999.
509. R. R. A. Syms, B. M. Hardcastle, and R. A. Lawes, Bulk micromachined silicon comb-drive electrostatic actuators with diode isolation, *Sensors Actuators A* **63**, 61, 1997.
510. B. E. Deal, The oxidation of silicon in dry oxygen, wet oxygen and steam, *J. Electrochem. Soc.* **110**, 527, 1963.
511. A. Gotz, J. Esteve, J. Bausells, S. Marco, J. Samitier, and J. R. Morante, Passivation analysis of micromechanical silicon structures obtained by electrochemical etch stop, *Sensors Actuators A* **37**, 744, 1993.
512. B. Garrido, J. Montserrat, and J. R. Morante, The role of chemical species in the passivation of <100> silicon surfaces by HF in water–ethanol solutions, *J. Electrochem. Soc.* **143**, 4059, 1996.
513. I. Barycka and I. Zubel, Silicon anisotropic etching in KOH–isopropanol etchant, *Sensors Actuators A* **48**, 229, 1995.
514. W. Ranke and Y. R. Xing, Orientation dependent adsorption on a cylindrical silicon crystal, *Surf. Sci.* **157**, 339, 1985.
515. H. Camon and Z. Moktadir, Atomic scale simulation of silicon etched in aqueous KOH solution, *Sensors Actuators A* **46**, 27, 1995.
516. M. C. Acero, J. Esteve, C. Burrer, and A. Gotz, Electrochemical etch-stop characteristics of TMAH:IPA solutions, *Sensors Actuators A* **46**, 22, 1997.
517. O. Than and S. Buttgenbach, Simulation, of anisotropic chemical etching of crystalline silicon using a cellular automata model, *Sensors Actuators A* **45**, 85, 1994.
518. O. Tabata, pH-controlled TMAH etchants for silicon micromachining, *Sensors Actuators A* **53**, 335, 1996.
519. H. G. Linde and L. W. Austin, Catalytic control of anisotropic silicon etching, *Sensors Actuators A* **49**, 181, 1995.
520. H. G. Linde and L. W. Austin, Helerocyclic catalysts for enhanced silicon oxidation and wet chemical etching, *Sensors Actuators A* **49**, 167, 1995.
521. L. C. Chen, M. Chen, T. H. Tsaur, C. Lien, and C. C. Wan, Selective etching of silicon in aqueous ammonia solution, *Sensors Actuators A* **49**, 115, 1995.
522. V. Bertagna, C. Plorgonven, F. Rouelle, and M. Chemla, Kinetics of electrochemical corrosion of silicon in dilute HF solutions, *J. Electroanal. Chem.* **422**, 115, 1997.
523. H.-U. Schreiber, Novel oxide planarization for integrated high-speed Si/SiGe heterojunction bipolar transistors, *IEEE Trans. Electron Devices* **43**(6), 1735, 1996.

524. N. A. Cade, R. A. Lee, and C. Patel, Wet etching of cusp structures for field-emission devices, *IEEE Trans. Electron Devices* **36**(11), 2709, 1989.
525. D. E. Aspenes and J. B. Theeten, Spectroscopic analysis of the interface between Si and its thermally grown oxide, *J. Electrochem. Soc.* **127**, 1359, 1980.
526. C. L. Huang and T. V. Duzer, Schottky diodes and other devices on thin silicon membranes, *IEEE Trans. Electron Devices* **23**(6), 579, 1976.
527. J. G. Hooley, The kinetics of the reaction of silica with group I hydroxides, *Can. J. Chem.* **39**, 1221, 1961.
528. E. S. Ammar and T. J. Rodgers, UMOS transistors on (110) silicon, *IEEE Trans. Electron Devices* **27**(5), 907, 1980.
529. R. A. Lee, C. Patel, H. A. Williams, and N. A. Cade, Semiconductor fabrication technology applied to micrometer valves, *IEEE Trans. Electron Devices* **36**(11), 2703, 1989.
530. H. H. Busta, R. R. Shadduck, and W. J. Orvis, Field emission from tungsten-clad silicon pyramids, *IEEE Trans. Electron Devices* **36**(11), 2679, 1989.
531. E. Bassous, Fabrication of novel three-dimensional microstructures by the anisotropic etching of (100) and (110) silicon, *IEEE Trans. Electron Devices* **25**, 1178, 1978.
532. S. J. Pearton, J. W. Corbett, and T. S. Shi, Hydrogen in crystalline semiconductors, *Appl. Phys. A* **43**, 153, 1987.
533. L. M. Roylance and J. B. Angell, A batch-fabricated silicon accelerometer, *IEEE Trans. Electron Devices* **26**(12), 1911, 1979.
534. A. Kamgar, S. J. Hillenius, R. M. Baker, S. Nakahara, and P. F. Bechtold, Gate oxide thinning at the active device/FOX boundary in submicrometer PBL isolation, *IEEE Trans. Electron Devices* **42**(12), 1995.
535. M. Aslam, B. E. Artz, S. L. Kaberline, and T. J. Prater, A comparison of cleaning procedures for removing potassium from wafers exposed to KOH, *IEEE Trans. Electron Devices* **40**(2), 292, 1993.
536. B. Kloeck, S. D. Collins, N. F. De Rooij, and R. L. Smith, Study of electrochemical etch-stop for high-precision thickness control of silicon membranes, *IEEE Trans. Electron Devices* **36**(4), 663, 1989.
537. T. Ohmi, M. Miyashita, M. Itano, T. Imaoka, and I. Kawanabe, Dependence of thin-oxide film quality on surface microroughness, *IEEE Trans. Electron Devices* **39**(3), 537, 1992.
538. Y.-H. Lee, B.-K. Ju, M.-H. Song, D.-H. Kim, T.-S. Hahn, and M.-H. Oh, White-light emitting thin-film electroluminescent device using micromachined structure, *IEEE Trans. Electron Devices* **44**(1), 39, 1997.
539. J. Chen and K. D. Wise, Nozzle array for inkjet printing, *IEEE Trans. Electron Devices* **44**, 1401, 1997.
540. S.-Y. Wu, A hybrid mass-interconnection method by electroplating, *IEEE Trans. Electron Devices* **25**(10), 1401&1201, 1978.
541. P. M. M. C. Bressers, S. A. S. P. Pagano, and J. J. Kelly, Ferricyanide reduction as a probe for the surface chemistry of silicon in aqueous alkaline solutions, *J. Electronanal. Chem.* **391**, 159, 1995.
542. D. B. Lee, Anisotropic etching of silicon, *J. Appl. Phys.* **40**(11), 4569, 1969.
543. L. D. Eske and D. W. Galipeau, Characterization of SiO_2 surface treatments using AFM contact angles and a novel dewpoint technique, *Colloids Surf.* **A154**, 33, 1999.
544. H. J. Lewerenz and M. Aggour, On the origin of photocurrent oscillation at Si electrodes, *J. Electroanal. Chem.* **351**, 159, 1993.
545. M. Aggour, M. Giersig, and H. J. Lewerenz, Interface condition of n-Si(111) during photocurrent oscillations in NH_4F solutions, *J. Electroanal. Chem.* **383**, 67, 1995.
546. S. Holdcroft, S. R. Morrison, and B. L. Funt, Electrocatalytic effects of redox polymer films on the reduction of O_2 on silicon semiconductors, *J. Electroanal. Chem.* **145**, 191, 1988.
547. J. Stumper and H.-J. Lewerenz, Dynamic interfacial processes at the amorphous silicon / aqueous electrolyte boundary, *J. Electroanal. Chem.* **274**, 11, 1989.
548. H. Kobayashi and H. Tsubomura, Theoretical and experimental studies on some new aspects of silicon–methanol photoelectrochemical cells, *J. Electroanal. Chem.* **272**, 37, 1989.
549. P. Akhter, A. Baig, and A. Mufti, Dissolution of Si(100) layers in NaOH aqueous solutions, *J. Phys. D* **22**, 1924, 1989.
550. H. Yoneyama, Y. Murao, and H. Tamura, Effect of attachment of trimethylchlorosilane and polymer adsorption on stability of silicon photoelectrodes in aqueous solutions, *J. Electroanal. Chem.* **108**, 87, 1980.

551. J.-N. Chazalviel and T. B. Truong, A quantitative study of Fermi level pinning at a semiconductor–electrolyte interface, *J. Electroanal. Chem.* **114**, 299, 1980.
552. J. A. Bruce and M. S. Wrighton, Study of textured n-type silicon photoanodes: electron microscopy, auger and electroanalytical characterization of chemically derivatized surfaces, *J. Electroanal. Chem,* **122**, 93, 1981.
553. A. B. Bocarsly, E. G. Walton, M. G. Bradley, and M. S. Wrighton, Two-electron oxidations at illuminated n-type semiconducting silicon electrodes, *J. Electroanal. Chem,* **100**, 283, 1979.
554. M. Morita, T. Ohmi, E. Hasegawa, M. Kawakami, and M. Ohwada, Growth of native oxide on a silicon surface, *J. Appl. Phys.* **68**(3), 1272, 1990.
555. D. Graf, M, Grundner, and R. Schulz, Oxidation of HF-treated Si wafer surfaces in air, *J. Appl. Phys.* **68**(10), 5155, 1990.
556. S. Bengtsson and L. Engstrom, Interface charge control of directly bonded silicon structures, *J. Appl. Phys.* **66**(3), 1231, 1989.
557. E. D. Palik, O. J. Glembocki, I. Heard, Jr., P. S. Burno, and L. Tenerz, Etching roughness for (100) silicon surfaces in aqueous KOH, *J. Appl. Phys.* **70**(6), 3291, 1991.
558. M. P. Valignat, M. Voue, G. Oshanin, and A. M. Cazabat, Structure and dynamics of thin liquid films on solid substrates, *Colloids Surf.* **A154**, 25, 1999.
559. M. Fuji, T. Takei, T. Watanabe, and M. Chikazawa, Wettability of fine silica powder surfaces modified with several normal alcohols, *Colloids Surf.* **A154**, 13, 1999.
560. D. Graf, M. Grundner, D. Muhlhoff, and M. Dellith, Influence of Cu on the native oxide growth of Si, *J. Appl. Phys.* **69**(11), 7620, 1991.
561. R. M. Candea, M. Kastner, R. Goodman, and N. Hickok, Photoelectrolysis of water: Si in salt water, *J. Appl. Phys.* **47**(6), 2724, 1976.
562. B. E. Deal and A. S. Grove, General relationship for the thermal oxidation of silicon, *J. Appl. Phys.* **36**(12), 3770, 1965.
563. T. Takahagi, I. Nagai, A. Ishitani, and H. Kuroda, The formation of hydrogen passivated silicon single-crystal surfaces using ultraviolet cleaning and HF etching, *J. Appl. Phys.* **64**(7), 3516, 1988.
564. K.-H. Li, C. Tsai, S. Shih, T. Hsu, D. L. Kwong, and J. C. Campbell, The photoluminescence spectra of porous silicon boiled in water, *J. Appl. Phys.* **72**(8), 3816, 1992.
565. S. M. Prokes, Study of the luminescence mechanism in porous silicon structures, *J. Appl. Phys.* **73**(1), 40, 1993.
566. I. M. Young, M. I. J. Beale, and J. D. Benjamin, X-ray double crystal diffraction study of porous silicon, *Appl. Phys. Lett.* **46**, 1134, 1985.
567. D. R. Lilliongton and W. G. Townsend, Effects of interfacial oxide layers on the performance of silicon Schottky-barrier solar cells, *Appl. Phys. Lett.* **28**(2), 97, 1976.
568. G. W. Cogan, C. M. Gronet, and J. F. Gibbons, 7.2% efficient polycrystalline silicon photoelectrode, *Appl Phys. Lett.* **44**(5), 539, 1984.
569. M. L. Rosenbluth, C. M. Lieber, and N. S. Lewis, 630-mV open circuit voltage, 12% efficient n-Si liquid junction, *Appl. Phys. Lett.* **45**(4), 423, 1984.
570. R. J. von Gutfeld and R. T. Hodgson, Laser enhanced etching in KOH, *Appl Phys. Lett.* **40**(4), 352, 1982.
571. C. H. Seager and D. S. Ginley, Passivation of grain boundaries in polycrystalline silicon, *Appl. Phys. Lett.* **34**(5), 337, 1979.
572. M. I. J. Beale, N. G. Chew, M. J. Uren, A. G. Cullis, and J. D. Benjamin, Microstructure and formation mechanism of porous silicon, *Appl. Phys. Lett.* **46**(1), 1095, 1985.
573. J. F. Gibbons, G. W. Cogan, C. M. Gronet, and N. S. Lewis, A 14% efficient nonaqueous semiconductor/liquid junction solar cell, *Appl Phys. Lett.* **45**(10), 1095, 1984.
574. G. S. Higashi, Y. J. Chabal, G. W. Trucks, and K. Raghavachari, Ideal hydrogen termination of the Si(111) surface, *Appl. Phys. Lett.* **56**(7), 656, 1990.
575. S.-F. Chuang, S. D. Collins, and R. L. Smith, Porous silicon microstructure as studied by transmission electron microscopy, *Appl. Phys. Lett.* **55**(15), 1540, 1989.
576. F. Subrahmanyan, H. Z. Massoud, and R. B. Fair, Experimental characterization of two-dimensional dopant profiles in silicon using chemical staining, *Appl. Phys. Lett.* **52**(25), 2145, 1988.
577. V. A. Burrows, Y. J. Chabal, G. S. Higashi, K. Raghavachari, and S. B. Christman, Infrared spectroscopy of Si (111) surfaces after HF treatment: Hydrogen termination and surface morphology, *Appl. Phys. Lett.* **53**(11), 998, 1988.

578. N. Chi, D. L. Philips, and K. Y. Chan, In situ photoluminescence characterization of porous silicon formation, *Thin Solid Films* **342**, 142, 1999.
579. M. Morita, T. Ohmi, E. Hasegawa, M. Kawakami, and K. Suma, Control factor of native oxide growth on silicon in air or in ultrapure water, *Appl. Phys. Lett.* **55**(6), 562, 1989.
580. D. Lapadatu and R. Puers, On the anodic passivation of silicon in aqueous KOH solutions, *Sensors Actuators A* **60**, 191, 1997.
581. E. H. Klaassen, R. J. Reay, C. Storment, and G. T. A. Kovacs, Micromachined thermally isolated circuits, *Sensors Actuators A* **58**, 43, 1997.
582. J. J. Kelly, E. S. Kooij, and D. Vanmaekelbergh, Generation and quenching of luminescence in n-type porous silicon/solution diodes: Role of adsorbed hydrogen, *Langmuir* **15**, 3666, 1999.
583. K. D. Legg, A. B. Ellis, J. M. Bolts, and M. S. Wrighton, n-type based Photoelectrochemical Cells: New ligand junction photo cells using a nonaqueous Ferricenium/Ferrocene electrolyte, *Proc. Natl. Acad. Sci. USA* **74**, 4116, 1977.
584. A. Kumar and N. S, Lewis, Short-wavelength spectral response properties of semiconductor/liquid junction, *J. Phys. Chem.* **94**, 6002, 1990.
585. M. X. Tan, C. N. Kenyon, and N. S. Lewis, Experimental measurement of quasi-Fermi levels at an illuminated semiconductor/liquild contact, *J. Phys. Chem.* **98**, 4959, 1994.
586. G. M. O'Halloran, M. Kuhl, P. J. Trimp, and P. J. French, The effect of additives on the adsorption properties of porous silicon, *Sensors Actuators A* **61**, 415, 1997.
587. P. E. Laibinis, C. E. Stanton, and N. S. Lewis, Measurement of barrier heights of semiconductor/liquid junctions using a transconductance method: Evidence for inversion at n-Si/CH_3OH-1,1′-dimethylferrocene$^{+/0}$ junctions, *J. Phys. Chem.* **98**, 8765, 1994.
588. D. Eichner and W. von Munch, A two-step electrochemical etch-stop to produce freestanding bulk-micromachined structures, *Sensors Actuators A* **60**, 103, 1997.
589. A. G. Revesz, The defect structure of grown silicon dioxide Films, *IEEE Trans. Electron Devices* **12**, 97, 1965.
590. C. R. Tellier and S. Durand, Micromachining of (hhl) silicon structures: Experiments and 3D simulation of etched shapes, *Sensors Actuators A* **60**, 168, 1997.
591. P. J. French, M. Nagao, and M. Esashi, Electrochemical etch-stop in TMAH without externally applied bias, *Sensors Actuators A* **56**, 279, 1996.
592. Q. Zhang, L. Liu, and Z. Li, A new approach to convex corner compensation for anisotropic etching, *Sensors Actuators A* **56**, 251, 1996.
593. X. Li, M. Bao, and S. Shen, Maskless etching of three-dimensional silicon structures in KOH, *Sensors Actuators A* **57**, 47, 1996.
594. E. Steinsland, M. Nese, A. Hanneborg, R. W. Bernstein, H. Sandn, and G. Kittilsland, Boron etch-stop in TMAH solutions, *Sensors Actuators A* **54**, 728, 1996.
595. J. E. A. M. van den Meerakker, The reduction of hydrogen peroxide at silicon in weak alkaline solutions, *Electrochim. Acta* **35**(8), 1267, 1990.
596. L. L. Ferry, Interfacial chemistry of p-silicon semiconductor liquid junctions, *Electrochim. Acta* **35**(2), 413, 1990.
597. G. Schlichthorl and H. Tributsch, Microwave photoelectrochemistry, *Electrochim. Acta* **37**(5), 919, 1992.
598. Y. Nakato and H. Tsubomura, Silicon photoelectrodes modified with ultrafine metal islands, *Electrochim. Acta* **37**(5), 897, 1992.
599. D. J. Blackwood, A. Borazio, R. Greef, L. M. Peter, and J. Stumper, Electrochemical and optical studies of silicon dissolution in ammonium fluoride solutions, *Electrochim. Acta* **37**(5), 889, 1992.
600. C. Levy-Clement, A. Lagoubi, R. Tenne, and M. Neumann-Spallart, Photoelectrochemical etching of silicon, *Electrochim. Acta* **37**(5), 877, 1992.
601. J.-N. Chazalviel, Ionic processes through the interfacial oxide in the anodic dissolution of silicon, *Electrochim. Acta* **37**(5), 865, 1992.
602. H. J. Lewerenz, Anodic oxides on silicon, *Electrochim. Acta* **37**(5), 847, 1992.
603. H. J. Lewerenz, J. Stumper, C. Pettenkofer, and R. Greef, Photoelectrochemically synthesised interfacial oxides on silicon: Composition and electronic properties, *Electrochim. Acta* **34**(12), 1729, 1989.
604. W. E. Spear and S. H. Baker, Electronic properties of metal–amorphous silicon barriers and junctions, *Electrochim. Acta* **34**(12), 1691, 1989.

605. G. Mende, F. Fenske, H. Flietner, M. Jeske, and J. W. Schultze, Localized anodic oxide films on Si: Preparation and properties, *Electrochim. Acta* **39**(8/9), 1259, 1994.
606. W. Kautek, N. Sorg, and J. Kruger, Femtosecond pulse laser second harmonic generation on semiconductor electrodes, *Electrochim. Acta* **39**(8/9), 1245, 1994.
607. A. Wolkenberg, Anodic polarization of silicon electrodes in water solutions of $NaNo_3$, *Electrochim. Acta* **21**, 1165, 1976.
608. D. Elwell and G. M. Rao, Mechanism of electrodeposition of silicon from K_2SiF_6-Flinak, *Electrochim. Acta* **27**(6), 673, 1982.
609. A. Q. Contractor and J. O. Bockris, Investigation of a protective conducting silica film on n-silicon, *Electrochim. Acta* **29**(10), 1427, 1984.
610. T. Osaka, H. Kitayama, and N. Hirota, Structural analysis of iron oxide coated n-silicon heterojunction photoanodes, *Electrochim. Acta* **29**(10), 1365, 1984.
611. V. P. Parkhutik, E. S. Matveeva, and R. Diaz Calleja, Impedance study of aging porous silicon films, *Electrochim. Acta* **41**(7/8), 1313, 1996.
612. S. Sternberg, I. Lingvay, and T. Visan, Behaviour of silicon electrodes in $LiCl–KCl–PbCl_2$ molten chlorides, *Electrochim. Acta* **30**(3), 283, 1985.
613. M. Szklarczyk, Short communication: Interaction of HCOOH with n-Si metalized electrode, *Electrochim. Acta* **32**(8), 1257, 1987.
614. J. Herrero and M. T. Gutierrez, Photoelectrochemical measurements of amorphous silicon thin films, *Electrochim. Acta* **36**(5/6), 915, 1991.
615. C. Zeyer and H. R. Gruniger, Surface treatment of Si by annealing and effect on Mott–Schottky plots, *Electrochim. Acta* **37**(15), 2791, 1992.
616. H. Tributsch, G. Schlichthorl, and L. Elstner, Microwave (Photo)electrochemistry: New insight into illuminated interfaces, *Electrochim. Acta* **38**(1), 141, 1993.
617. G. Gramaccioni, A. Selvaggi, and F. Galluzzi, Thin film multi-junction solar cell for water photoelectrolysis, *Electrochim. Acta* **38**(1), 111, 1993.
618. M. Szklarczyk, S. Smolinski, and J. Sobkowski, In situ radiotracer studies of HCOOH adsorption on n-Si(100) electrode, *Electrochim. Acta* **39**(11/12), 1903, 1994.
619. F. Ozanam, A. Djebri, and J.-N. Chazalviel, The hydrogenated silicon surface in organic electrolytes probed through *in situ* ir spectroscopy in the ATR geometry, *Electrochim. Acta* **41**(5), 687, 1996.
620. M. Nakamura, M.-B. Song, and M, Ito, Etching processing of Si(111) and Si(100) surfaces in an ammonium fluoride solution investigated by *in situ* ATR-IR, *Electrochim. Acta* **41**(5), 681, 1996.
621. J. Rappich and H. J. Lewerenz, *In situ* FTIR investigation of the electrochemical microstructuring of n-Si(111), *Electrochim. Acta* **41**(5), 675, 1996.
622. C. M. Gronet, N. S. Lewis, G. Cogan, and J. Gibbons, n-type silicon photoelectrochemistry in methanol: Design of a 10.1% efficient semiconductor/liquid junction solar cell, *Proc. Natl. Acad. Sci. USA* **80**, 1152, 1983.
623. C. M. Lieber, C. M. Gronet, and N. S. Lewis, Evidence against surface state limitations on efficiency of p-Si/CH_3CN junctions, *Nature* **307**, 533, 1984.
624. A. G. Cullis and L. T. Canham, Visible light emission due to quantum size effects in highly porous crystalline silicon, *Nature* **353**, 353, 1991.
625. K. D. Legg, A. B. Ellis, J. M. Bolts, and M. S. Wrighton, n-type Si-based photoelectrochemical cell: New liquid junction photocell using a nonaqueous ferricenium /ferrocene electrolyte, *Proc. Natl. Acad. Sci. USA* **74**, 4116, 1977.
626. L. M. Peter, J. Li, R. Peat, H. J. Lewerenz, and J. Stumper, Frequency response analysis of intensity modulated photocurrents at semiconductor electrodes, *Electrochim. Acta* **35**(10), 1657, 1990.
627. H. Gerischer, The impact of semiconductors on the concepts of electrochemistry, *Electrochim. Acta* **35**(11/12), 1677, 1990.
628. Y. Watanabe, Effects of annealing on oxygen depth profiles and chemical etching rates of thermally grown silicon oxides, *J. Electrochem. Soc.* **145**(4), 1306, 1998.
629. E. S. Kooij, K. Butter, and J. J. Kelly, Hole injection at the silicon/aqueous electrolyte interface: A possible mechanism for chemiluminescence from porous silicon, *J. Electrochem. Soc.* **145**(4), 1232, 1998.
630. D. Chopra, I.I. Suni, and A. A. Busnaina, Cu dissolution from Si(111) into an SC-1 process solution, *J. Electrochem. Soc.* **145**(4), L60, 1998.

631. R. Takizawa, T. Nakanishi, K. Honda, and A. Ohsawa, Ultraclean technique for silicon wafer surfaces with HNO_3–HF systems, *Jpn. J. Appl Phys.* L2210, 1988.
632. J. Haisma, G. A. C. M. Spierings, U. K. P. Biermann, and J. A. Pals, Silicon-on-insulator wafer bonding–wafer thinning technological evaluations, *Jpn. J. Appl. Phys.* 1426, 1989.
633. N. Koshida, H. Koyama, and Y. Kiuchi, Photoelectrochemical behavior of n-type porous-Si electrodes, *Jpn. J. Appl. Phys.* **25**, 1069, 1986.
634. T. Yasaka, K. Kanda, K. Sawara, S. Miyazaki, and M. Hirose, Chemical stability of HF-treated Si(111) surface, *Jpn. J. Appl. Phys.* **29**, 3567, 1991.
635. S. Watanabe, M. Shigeno, N. Nakayama, and T. Ito, Silicon-monohydride termination of silicon-111 surface formed by boiling water, *Jpn. J. Appl. Phys.* **29**, 3575, 1991.
636. O. Vatel, S. Verhaverbeke, H. Bender, M. Caymax, F. Chollet, B. Vermerire, P. Mertens, E. Andre, and M. Heyns, Atomic force microscopy and infrared spectroscopy studies of hydrogen baked Si surfaces, *Jpn. J. Appl. Phys.* **32**, L1489, 1993.
637. H. Morisake, H. Ono, H. Dohkoshi, K. Yazawa, A. Hiraki, M. Iwami, and T. Imura, Auger and X-ray analyses of iron-oxide-coated Si photoelectrodes, *Jpn. J. Appl. Phys.* **20**, 777, 1981.
638. N. Koshida and Y. Kiuchi, Observation of a long-life photoelectrochemical conversion with n-type porous-Si photoelectrodes, *Jpn. J. Appl. Phys.* **24**, 466, 1985.
639. Y. Kato, T. Ito, and A. Hiraki, Initial oxidation process of anodized porous silicon with hydrogen atoms chemisorbed on the inner surface, *Jpn. J. Appl. Phys.* **27**, L1406, 1988.
640. N. Noguchi, I. Suemune, M. Yamanishi, G. C. Hua, and N. Otsuka, Study of luminescent region in anodized porous silicons by photoluminescence imaging and their microstructures, *Jpn. J. Appl. Phys.* **31**, L490, 1992.
641. K. Sawara, T. Yasaka, S. Miyazaki, and M. Hirose, Atomic scale flatness of chemically cleaned silicon surfaces studied by infrared attenuated-total-reflection spectroscopy, *Jpn. J. Appl. Phys.* **31**, L931, 1992.
642. Y. Fujiwara, H. Nishitani, H. Nakata, and T. Ohyama, Structured photoluminescence spectrum in laterally anodized porous silicon, *Jpn. J. Appl. Phys.* **31**, L1763, 1992.
643. T. Matsuyama, M. Tanaka, S. Tsuda, S. Nakano, and Y. Kuwano, Improvement of n-type poly-Si film properties by solid phase crystallization method, *Jpn. J. Appl. Phys.* **32**, 3720, 1993.
644. T. Unagami, Oxidation of porous silicon and properties of its oxide film, *Jpn. J. Appl. Phys.* **19**, 231, 1980.
645. C. E. Krohn and J. C. Thompson, Photo-assisted electron injection at a semiconductor–NH_3, interface, *Chem. Phys. Lett.* **65**(1), 132, 1979.
646. D. Laser and A. J. Bard, Semiconductor electrodes photo-induced electrogenerated chemiluminescence and up-conversion at semiconductor electrodes, *Chem. Phys. Lett.* **34**(3), 605, 1975.
647. H. Sugiyama and O. Nittono, Microstructure and lattice distortion of anodized porous silicon layers, *J. Cryst. Growth* **103**, 156, 1990.
648. E. Yablonovitch, D. L. Allara, C. C. Chang, T. Gmitter, and T. B. Bright, Unusually low surface-recombination velocity on silicon and germanium surfaces, *Phys. Rev. Lett.* **57**, 249, 1986.
649. K. Barla, G. Bomchil, R. Herino, and J. C. Pfister, X-ray topographic characterization of porous silicon layers, *J. Cryst. Growth* **68**, 721, 1984.
650. K. Barla, R. Herino, G. Bomchil, and J. C. Pfister, Determination of lattice parameter and elastic properties of porous silicon by X-ray diffraction, *J. Cryst. Growth* **68**, 727, 1984.
651. Y. Arita, Formation and oxidation of porous silicon by anodic reaction, *J. Cryst. Growth* **45**, 383, 1978.
652. R. W. Series, K. G. Barraclough, and W. Bardsley, Quantitative determination of microdefect density in dislocation-free silicon by preferential chemical etching, *J. Cryst. Growth* **49**, 363, 1980.
653. M. Hao, H. Uchida, C. Shao, T. Soga, T. Jimbo, and M. Umeno, Porous GaAs formed by a two-step anodization process, *J. Cryst. Growth* **179**, 661, 1997.
654. E. Basaran, C. P. Parry, R. A. Kubiak, T. E. Whall, and E. H. C. Parker, Electrochemical capacitance–voltage depth profiling of heavily boron-doped silicon, *J. Cryst. Growth* **157**, 109, 1995.
655. D. Nicolaescu, V. Filip, and F. Okuyama, Proposal for a new self-focusing configuration involving porous silicon for field emission flat panel displays, *J. Vac. Sci. Technol.* **A15**(4), 2369, 1997.
656. A. Pasquarello, M. S. Hybertsen, and R. Car, First-principles study of Si 2p core-level shifts at water and hydrogen covered Si(001)2 × 1 surfaces, *J. Vac. Sci. Technol.* **B14**(4), 2809, 1996.

657. D. Schmidt, H. Niimi, B. J. Hinds, D. E. Aspnes, and G. Lucovsky, New approach to preparing smooth Si(100) surfaces: Characterization by spectroellipsometry and validation of Si/SiO_2 interface properties in metal-oxide-semiconductor devices, *J. Vac. Sci. Technol.* **B14**(4), 2812, 1996.
658. L. A. Jones, O. Yukseker, and D. F. Thomas, Dependence of photochemically etched porous silicon formation on photoetching wavelength and power, *J. Vac. Sci. Technol.* **A14**(3), 1505, 1996.
659. H. Sugimura and N. Nakagiri, Scanning probe anodization: Patterning of hydrogen-terminated silicon surfaces for the nanofabrication of gold structures by electroless plating, *J. Vac. Sci. Technol.* **B13**(5), 1933, 1995.
660. L. A. Nagahara, T. Ohmori, K. Hashimoto, and A. Fujishima, Effects of HF solution in the electroless deposition process on silicon surfaces, *J. Vac. Sci. Technol.* **A11**, 763, 1993.
661. C. R. Helms and B. E. Deal, Mechanisms of the HF/H_2O vapor phase etching of SiO_2, *J. Vac. Sci. Technol.* **A10**(4), 806, 1992.
662. Y. J. Chabal, G. S. Higashi, K. Raghavachari, and V. A. Burrows, Infrared spectroscopy of Si(111) and Si(100) surfaces after HF treatment: Hydrogen termination and surface morphology, *J. Vac. Sci. Technol.* **A7**, 2107, 1988.
663. D. Graf, M. Grundner, and R. Chulz, Reaction of water with hydrofluoric acid treated silicon(111) and (100) surfaces, *J. Vac. Sci. Technol.* **A7**(3), 808, 1989.
664. R. T. Howe, Surface micromachining for microsensors and microactuators, *J. Vac. Sci. Technol.* **B6**(6), 1809, 1988.
665. B. F. Philips, D. C. Burkman, W. R. Schmidt, and C. A. Peterson, The impact of surface analysis technology on the development of semiconductor wafer cleaning processes, *J. Vac. Sci. Technol.* **A1**(2), 646, 1983.
666. Y. Nakato and H. Tsubomura, Structures and functions of thin metal layers on semiconductor electrodes, *J. Photochem.* **29**, 257, 1985.
667. S. B. Felch and J. S. Sonico, A wet etch for polysilicon with high selectivity to photoresist, *Solid State Technol.* 47, September 1986.
668. J. A. Amick, Cleanliness and the cleaning of silicon wafers, *Solid State Technol.* 33, November 1976.
669. D. Tolliver, LSI wafer cleaning techniques, *Solid State Technol.* 33, November 1975.
670. C. R. Tellier, Some results on chemical etching of AT-cut quartz wafers in ammonium bifluoride solutions, *J. Mater. Sci.* **17**, 1348, 1982.
671. J. K. Vondeling, Fluoride-based etchants for quartz, *J. Mater. Sci.* **18**, 304, 1983.
672. C. R. Tellier and A. Brahim-Bounab, Anisotropic etching of silicon crystals in KOH solution—Part I. Experimental etched shapes and determination of the dissolution slowness surface, *J. Mater. Sci.* **29**, 5953, 1994.
673. C. R. Tellier and A. Brahim-Bounab, Anisotropic etching of silicon crystals in KOH solution—Part II. Theoretical two-dimensional etched shapes: Discussion of the adequation of the dissolution slowness surface, *J. Mater. Sci.* **29**, 6354, 1994.
674. G. Mende, J. Finster, D. Flamm, and D. Schulze, Oxidation of etched silicon in air at Room temperature: Measurements with ultrasoft X-ray photoelectron spectroscopy (ESCA) and neutron activation analysis, *Surf. Sci.* **128**, p. 169, 1983.
675. H. Kobayashi, J. Ono, T. Ishida, M. Okamoto, H. Kawanaka, and H. Tsubomura, Mechanism of photocurrent and photovoltage in solar cells using n-silicon electrodes in non-aqueous solutions, *J. Electroanal. Chem.* **312**, 57, 1991.
676. J. Stumper, R. Greef, and L. M. Peter, Current oscillations during anodic dissolution of p-Si in ammonium fluoride: An investigation using ring disc voltammetry and ellipsometry, *J. Electroanal. Chem.* **310**, 445, 1991.
677. S. Yamamura and H. Kojima, The photovoltaic effect of an insulating polymer-hybridized p-Si solar cell, *J. Electroanal. Chem.* **241**, 379, 1988.
678. R. Keita and L. Nadjo, Electrochemistry and photoelectrochemistry of sodium 9,10-anthraquinone-2,6-disulfonate in aqueous media, application to rechargeable solar cells and to the synthesis of hydrogen peroxide, *J. Electroanal. Chem.* **163**, 171, 1984.
679. R. E. Malpas and B. Rushby, The stability of two-layer ferrocene/polypyrrole-coated n-Si electrodes in aqueous photoelectrochemical photovoltaic cells, *J. Electroanal. Chem.* **157**, 387, 1983.
680. Y. Nakato, H. Yano, S. Nishiura, T. Ueda, and H. Tsubomura, Hydrogen photoevolution at p-type silicon electrodes coated with discontinuous metal layers, *J. Electroanal Chem.* **228**, 97, 1987.

681. M. G. Bradley, T. Tysak, and N. Vlachopoulos, Stabilization of n-Si to photoanodic decomposition by $[Bu_4N]$ $[Ni(S_2C_2Ph_2)_2]$ and $[Fe(-C_5H_5)(CO)]_4$, *J. Electroanal. Chem.* **160**, 345, 1984.
682. R. Malpas, F. R. Mayers, and A. G. Osborne, The chemical modification of small band gap semiconductor electrodes using chromium–carboxylic acid complexes of redox couples, *J. Electroanal. Chem.* **153**, 97, 1983.
683. B. Keita, I. Kawenoki, J. Kossanyi, D. Garreau, and L. Nadjo, Surface band energy shifts of a p-type Si electrode in the presence of redox couples, study of anthraquinone derivatives in the dark and under illumination, *J. Electroanal. Chem.* **145**, 293, 1983.
684. B. Keita, I. Kawenoki, J. Kossanyi, and L. Nadjo, Reduction of anthraquinone derivatives at n-type and p-type silicon electrodes, *J. Electroanal. Chem.* **145**, 311, 1983.
685. M. Handschuh, W. Lorenz, C. Adgerter, and T. Katterle, Determination of the kinetics of photoelectrochemical processes with minority carriers from photocurrent onset potential on semiconductor electrodes, *J. Electroanal. Chem.* **144**, 99, 1983.
686. J.-N. Chazalviel, Surface methoxylation as the key factor for the good performance of n-Si/methanol photoelectrochemical cells, *J. Electroanal. Chem.* **233**, 37, 1987.
687. M. G. Bradley and T. Tysak, p-type silicon based photoelectrochemical cells for optical energy conversion: Electrochemistry of tetra-azomacrocyclic metal complexes at illuminated p-type silicon semiconducting electrodes, *J. Electroanal. Chem.* **135**, 153, 1982.
688. M. Szklarczyk, J. Sobkowski, and J. Pacocha, Adsorption and reduction of formic acid on p-type silicon electrodes, *J. Electroanal. Chem.* **215**, 307, 1986.
689. C. R. Cabrera and H. D. Abruna, Electrocatalysis of CO_2 reduction at surface modified metallic and semiconducting electrodes, *J. Electroanal. Chem.* **209**, 101, 1986.
690. J. L. Dort, J. Joseph, J. R. Martin, and P. Clechet, pH dependence of the Si/SiO_2 interface state density for EOS systems, quasi-static and AC conductance methods, *J. Electroanal. Chem.* **193**, 75, 1985.
691. R. Keita and L. Nadjo, Activation of electrode surfaces, electrocatalysis of the photoelectrochemical interaction of hydrogen at p-type Si, *J. Electroanal. Chem.* **199**, 229, 1986.
692. F. Ozanam and J.-N. Chazalviel, In-situ infrared vibrational study of the early stages of silicon oxidation at the interface with a non-aqueous electrolyte, *J. Electroanal. Chem.* **269**, 251, 1989.
693. J.-N. Chazalviel, F. Ozanam, M. Etman, F. Paolucci, L. M. Peter, and J. Stumper, The p-Si/fluoride interface in the anodic region: Damped and/or sustained oscillations, *J. Electroanal. Chem.* **327**, 343, 1992.
694. L. A. Nagahara, T. Ohmori, K. Hashimoto, and A. Fujishima, The influence of hydrofluoric acid concentration on electroless copper deposition onto silicon, *J. Electroanal. Chem.* **333**, 363, 1992.
695. J. Stumper and L. M. Peter, A rotating ring-disc study of the photodissolution of n-Si in ammonium fluoride solutions, *J. Electroanal. Chem.* **309**, 325, 1991.
696. A. P. Abbott, S. A. Campbell, J. Satherley, and D. J. Schiffrin, Anisotropic etching of silicon at high pressure, *J. Electroanal. Chem.* **348**, 473, 1993.
697. S. A. Campbell, D. J. Schiffrin, and P. J. Tufton, Chemical and electrochemical anisotropic dissolution of silicon in ethylenediamine + pyrocatechol + water media, *J. Electroanal. Chem.* **344**, 211, 1993.
698. L. M. Peter, D. J. Blackwood, and S. Pons, Photocorrosion of n-Si in ammonium fluoride solutions: An investigation by in-situ Fourier transform infrared spectroscopy, *J. Electroanal. Chem.* **294**, 111, 1990.
699. H. Kobayashi, A. Chigami, N. Takeda, and H. Tsubomura, High photovoltages arising from n-silicon/methanol junctions studied by the temperature dependence of open-circuit photovoltages, *J. Electroanal. Chem.* **287**, 239, 1990.
700. M. J. Eddowes, Anodic dissolution of p- and n-type silicon kinetic study of the chemical mechanism, *J. Electroanal. Chem.* **280**, 297, 1990.
701. Y. J. Chabal and S. B. Christman, Evidence of dissociation of water on the Si(100) 2 × 1 surface, *Phys. Rev. B* **29**(12), 6974, 1984.
702. F. J. Himpsel, F. R. McFeely, A. Taleb-Ibrahimi, and J. A. Yarmoff, Microscopic structure of the SiO_2/Si interface, *Phys. Rev. B* **38**(9), 6084, 1988.
703. Y. J. Chabal, Hydrogen vibration on Si(111) 7 × 7: Evidence for a unique chemisorption site, *Phys. Rev. Lett.* **50**(23), 1850, 1983.
704. L. M. Peter, D. J. Blackwood, and S. Pons, In situ characterization of the illuminated silicon–electrolyte interface by Fourier-transform infrared spectroscopy, *Phys. Rev. Lett.* **62**(3), 308, 1989.

705. E. Yablonovitch, D. L. Allara, C. C. Chang, T. Gmitter, and T. B. Bright, Unusually low surface-recombination velocity on silicon and germanium surfaces, *Phys. Rev. Lett.* **57**(2), 14, 1986.
706. U. Schnakenberg, W. Benecke, B. Lochel, S. Ullerich, and P. Lange, NH_4OH-based etchants for silicon micromachining: Influence of additives and stability of passivation layers, *Sensors Actuators A* **25–27**, 1, 1991.
707. H. L. Offereins, K. Kuhl, and H. Sandmaier, Methods for the fabrication of convex corners in anisotropic etching of (100) silicon in aqueous KOH, *Sensors Actuators A* **25–27**, 9, 1991.
708. M. Mehregany and S. D. Senturia, Anisotropic etching of silicon in hydrazine, *Sensors Actuators* **13**, 375, 1988.
709. H. S. Fogler, K. Lund, and C. C. McCune, Acidization III—The kinetics of the dissolution of sodium and potassium feldspar in HF/HC1 acid mixtures, *Chem. Eng. Sci.* **30**, 1325, 1975.
710. H. Tsubomura, Y. Nakato, M. Hiramoto, and H. Yano, Metal oxide coated p–n junction silicon electrodes for photoelectrochemical solar energy conversion, *Can. J. Chem.* **63**, 1759, 1985.
711. U. Schnakenberg, W. Benecke, and B. Lochel, NH_4OH-based etchants for silicon micromachining, *Sensors Actuators A* **21–23**, 1031, 1990.
712. N. S. Lewis, A. B. Bocarsly, and M. S. Wrighton, Heterogeneous electron transfer at designed semiconductor/liquid interfaces. Rate of reduction of surface-confined ferricenium centers by solution reagents, *J. Phys. Chem.* **84**, 2033, 1980.
713. C. Tsai, K.-H. Li, J. C. Campbell, B. K. Hance, M. F. Arendt, J. M. White, S.-L. Yau, and A. J. Bard, Effects of illumination during anodization of porous silicon, *J. Electron. Mater.* **21**(10), 1992.
714. M. Croset and D. Dieumegard, Quantitative secondary ion mass spectrometry analysis of oxygen isotopes and other light elements in silicon oxide films, *Corros. Sci.* **16**, 703, 1976.
715. G. Willeke and K. Kellermann, Crystalline silicon etching in quiescent concentrated aqueous HF solutions, *Semicond. Sci. Technol.* **11**, 415, 1996.
716. M. J. Madou, B. H. Loo, K. W. Frese, and S. R. Morrison, Bulk and surface characterization of the silicon electrode, *Surf. Sci.* **108**, 135, 1981.
717. J.-N. Chazalviel, Schottky barrier height and reverse current of the n-Si–electrolyte junction, *Surf. Sci.* 204, 1979.
718. N. Cabrera and N. F. Mott, *Rep. Prog. Phys.* **12**, 163, 1948.
719. F. Rochet, M. Froment, C. D'anterroches, H. Roulet, G. Dufour, and R. Calsou, Epitaxial silica on stepped Si(001) surfaces, *Solid-State Electron.* **33**, 135, 1990.
720. S. K. Ghandhi, *VLSI Fabrication Principles,* John Willey & Sons, New York, 1983.
721. T. Nakagawa, H. Koyama, and N. Koshida, Control of structure and optical anisotropy in porous Si by magnetic-field assisted anodization, *Appl. Phys. Lett.* **69**(21), 3206, 1996.
722. V. P. Parkhutik, J. M. Albella, J. M. Martinez-Duart, J. M. Gomez-Rodriguez, A. M. Baro, and V. I. Shershulsky, Different types of pore structure in porous silicon, *Appl. Phys. Lett.* **62**(4), 366, 1993.
723. L. Jia, S. L. Zang, S. P. Wong, I. H. Wilson, S. K. Hark, Z. F. Liu, and S. M. Cai, Evidence for the quatum confined electrochemistry model of the formation mechanism of p-type porous silicon, *Appl. Phys. Lett.* **69**(22), 3399, 1996.
724. Y. Kang and J. Jorae, Dissolution mechanism for p-Si during porous silicon formation, *J. Electrochem. Soc.* **144**(9), 3104, 1997.
725. J. C. Jackson, T. Robinson, O. Oralkan, and D. J. Dumin, Differentiation between electric breakdowns and dielectric breakdown in thin silicon oxides, *J. Electrochem. Soc.* **145**(3), 1033, 1998.
726. M. Niwano, Y. Kimura, and N. Miyamoto, In situ infrared study of chemical state of Si surface in etching solution, *Appl. Phys. Lett.* **65**(13), 1692, 1994.
727. Y.-P. Zhao, Y.-J. Wu, H.-N. Yang, G.-C. Wang, and T.-M. Lu, In situ real-time study of chemical etching process of Si(100) using light scattering, *Appl. Phys. Lett.* **69**(2), 221, 1996.
728. J.-L. Maurice, A. Riviere, A. Alapini, and C. Levy-Clement, Electron beam irradiation of n-type porous silicon obtained by photoelectrochemical etching, *Appl. Phys. Lett.* **66**(13), 1665, 1995.
729. D. A. Redman, D. M. Follstaedt, T. R. Guilinger, and M. J. Kelly, Photoluminescence and passivation of silicon nanostructures, *Appl. Phys. Lett.* **65**(19), 2386, 1994.
730. D. Andsager, J. Hilliard, and M. H. Nayfeh, Behaviour of porous silicon emission spectra during quenching by immersion in metal ion solutions, *Appl. Phys. Lett.* **64**(9), 1141, 1994.
731. A. G. Nassiopoulos, S. Grigoropoulos, and D. Papadimitriou, Electroluminescent device based on silicon nanopillars, *Appl. Phys. Lett.* **69**(15), 2267, 1996.

732. M. J. Winton, S. D. Russell, J. A. Wolk, and R. Gronsky, Processing independent photoluminescence response of chemically etched porous silicon, *Appl. Phys, Lett.* **69**(26), 4026, 1996.
733. M.-J. Jeng and J.-G. Hwu, Enhanced nitrogen incorporation and improved breakdown endurance in nitrided gate oxides prepared by anodic oxidation followed by rapid thermal nitridation in N_2O, *Appl. Phys. Lett.* **69**(25), 3875, 1996.
734. H. Miauno, H. Koyama, and N. Koshida, Oxide-free blue photoluminescence from photochemically etched porous silicon, *Appl. Phys. Lett.* **69**(25), 3779, 1996.
735. M. Tajima, S. Ibuka, H. Aga, and T. Abe, Characterization of bond and etch-back silicon-on-insulator wafers by photoluminescence under ultraviolet excitation, *Appl. Phys. Lett.* **70**(2), 231, 1997.
736. H. Namatsu, K. Kurihara, M. Nagase, and T. Makino, Fabrication of 2-nm-wide silicon quantum wires through a combination of a partially-shifted resist pattern and orientation-dependent etching, *Appl. Phys. Lett.* **70**(5), 619, 1997.
737. L. Jia, S. P. Wong, I. H. Wilson, S. K. Hark, S. L. Zhang, Z. F. Liu, and S. M. Cai, Photoluminescence of ozone oxidized and HF etched porous silicon and the multiple source quantum well model, *Appl. Phys. Lett.* **71**(10), 1391, 1997.
738. Y. Xiao, M. J. Heben, J. M. McCullough, Y. S. Tsuo, J. I. Pankove, and S. K. Deb, Enhancement and stabilization of porous silicon photoluminescence by oxygen incorporation with a remote-plasma treatment, *Appl. Phys. Lett.* **62**(10), 1152, 1993.
739. X. Y. Hou, G. Shi, W. Wang, F. L. Zhang, P. H. Hao, D. M. Huang, and X. Wang, Large blue shift of light emitting porous silicon by boiling water treatment, *Appl. Phys. Lett.* **62**(10), 1097, 1993.
740. A. Halimaoui, Influence of wettability on anodic bias induced electroluminescence in porous silicon, *Appl. Phys. Lett.* **63**(9), 1264, 1993.
741. J. W. H. Maes, J. Caro, C. C. G. Visser, T. Sijlstra, E. W. J. M. van der Drift, S. Radelaar, F. D. Tichelaar, and E. J. M. Fakkeldij, Novel post-etching treatment of small windows in oxide for selective epitaxial growth, *Appl. Phys. Lett.* **70**(8), 973, 1997.
742. G. Polisski, B. Averboukh, K. Kovalev, and F. Koch, Control of silicon nanocrystallite shape asymmetry and orientation anisotropy by light-assisted anodization, *Appl. Phys. Lett.* **70**(9), 1116, 1997.
743. T. Bitzer, M. Gruyters, H. J. Lewerenz, and K. Jacobi, Electrochemically prepared Si(111) 1 × 1-H *surface, Appl. Phys. Lett.* **63**(3), 397, 1993.
744. S.-L. Zhang, K. Ho, Y. Hou, B. Qian, P. Diao, and S. Cai, Steplike behaviour of photoluminescence peak energy and formation of p-type porous silicon, *Appl. Phys. Lett.* **62**(6), 642, 1993.
745. J. M. Perez, J. Villalobos, P. McNeill, J. Prasad, R. Cheek, J. Kelber, J. P. Estrera, P. D. Stevens, and R. Glosser, Direct evidence for the amorphous silicon phase in visible photoluminescent porous silicon, *Appl. Phys. Lett.* **61**(5), 563, 1992.
746. S. Shih, K. H. Jung, T. Y. Hsieh, J. Sarathy, J. C. Campbell, and D. L. Kwong, Photoluminescence and formation mechanism of chemically etched silicon, *Appl. Phys. Lett.* **60**(15), 1863, 1992.
747. J. Sarathy, S. Shih, K. Jung, C. Tsai, K.-H. Li, D.-L. Kwong, J. C. Campbell, S.-L. Yau, and A. J. Bard, Demonstration of photoluminescence in nonanodized silicon, *Appl. Phys. Lett.* **60**(13), 1532, 1992.
748. R. P. Vasquez, R. W. Fathauer, T. George, A. Ksendzov, and T. L. Lin, Electronic structure of light-emitting porous Si, *Appl. Phys. Lett.* **60**(8), 1004, 1992.
749. R. W. Fathauer, T. George, A. Ksendzov, and R. P. Vasquez, Visible luminescence from silicon wafers subjected to stain etches, *Appl. Phys. Lett.* **60**(8), 995, 1992.
750. T. George, M. S. Anderson, W. T. Pike, T. L. Lin, R. W. Fathauer, K. H. Jung, and D. L. Kwong, Microstructural investigations of light-emitting porous Si layers, *Appl. Phys. Lett.* **60**(19), 2359, 1992.
751. L. T. Canham, W. Y. Leong, M. I. J. Beale, T. I. Cox, and L. Taylor, Efficient visible electroluminescence from highly porous silicon under cathodic bias, *Appl. Phys. Lett.* **61**(21), 2563, 1992.
752. C. H. Perry, F. Lu, F. Namavar, N. M. Kalkhoran, and R. A. Soref, Photoluminescence spectra from porous silicon (111) microstructures: Temperature and magnetic-field effects, *Appl. Phys. Lett.* **60**(25), 3117, 1992.
753. W. M. van Fuffelen, M. J. de Boer, and T. M. Klapwijk, Ultrathin silicon membranes to study supercurrent transport in crystalline semiconductors, *Appl. Phys. Lett.* **58**(21), 2438, 1991.
754. C. Tsai, K.-H. Li, J. Sarathy, S. Shih, J. C. Campbell, B. K. Hance, and J. M. White, Thermal treatment studies of the photoluminescence intensity of porous silicon, *Appl. Phys. Lett.* **59**(22), 2814, 1991.

755. S. Gardelis, J. S. Rimmer, P. Dawson, B. Hamilton, R. A. Kubiak, T. E. Whall, and E. H. C. Parker, Evidence for quantum confinement in the photoluminescence of porous Si and SiGe, *Appl. Phys. Lett.* **59**(17), 2118, 1991.
756. C. Y. Mak, B. Miller, L. C. Feldman, B. E. Weir, G. S. Higashi, E. A. Fitzgerald, T. Boone, C. J. Doherty, and R. B. van Dover, Selective electroless copper metallization of palladium silicide on silicon substrates, *Appl. Phys. Lett.* **59**(26), 3449, 1991.
757. K. H. Jung, S. Shih, T. Y. Ksieh, D. L. Kwong, and T. L. Lin, Intense photoluminescence from laterally anodized porous Si, *Appl. Phys. Lett.* **59**(25), 3264, 1991.
758. P. Lim, J. R. Brock, and I. Trachtenberg, Laset-induced etching of silicon in hydrofluoric acid, *Appl. Phys. Lett.* **60**(6), 1992.
759. R. Tsu, H. Shen, and M. Dutta, Correlation of Raman and photoluminescence spectra of porous silicon, *Appl. Phys. Lett.* **60**(1), 112, 1992.
760. T. Aoyama, T. Yamazaki, and T. Ito, Nonuniformities of native oxides on Si(001) surfaces formed during wet chemical cleaning, *Appl. Phys. Lett.* **61**(1), 102, 1992.
761. R. E. Hummel and S.-S. Chang, Novel technique for preparing porous silicon, *Appl. Phys. Lett.* **61**(16), 1965, 1992.
762. O. Teschke, Spatial distribution of oxygen in luminescent porous silicon films, *Appl. Phys. Lett.* **64**(16), 1986, 1994.
763. V. Lehmann and H. Foll, Formation mechanism and properties of electrochemically etched trenches in n-type silicon, *J. Electrochem. Soc.* **137**, 653, 1990.
764. M. I. J. Beale, J. D. Benjamin, M. J. Uren, N. G. Chew, and A. G. Cullis, The formation of porous silicon by chemical stain etches, *Appl. Phys. Lett.* **408**, 1986.
765. N. Miki, M. Maeno, and T. Ohmi, Conductivity and dissolution equilibrium of extemely anhydrous hydrogen fluoride, *J. Electrochem. Soc.* **137**, 790, 1990.
766. J. L. Gole, F. P. Dudel, L. Seals, M. Reider, P. Kohl, and L. A. Bottomley, On the correlation of aqueous and nonaqueous in situ and ex situ photoluminescent emissions from porous silicon, *J. Electrochem. Soc.* **145**, 3284, 1998.
767. A. A. Yaron, S. Bastide, J. L. Maurice, and C. L. Clément, Morphology of porous n-type silicon obtained by photoelectrochemical etching II, *J. Lumin.* **57**, 67, 1993.
768. V. Lehmann and U. Grüning, The limits of macropore array fabrication, *Thin Solid Films* **297**, 13, 1997.
769. D. Dimova-Malinovska, M. Sendova-Vassileva, N. Tzenov, and M. Kamenova, Preparation of thin porous silicon by stain etching, *Thin Solid Films* **297**, 9, 1997.
770. M. Bertolotti, F. Carassiti, E. Fazio, A. Ferrari, S. La Monica, S. Lazarouk, G. Liakhou, G. Maliello, E. Proverbio, and L. Schirone, Porous silicon obtained by anodization in the transition regime, *Thin Solid Films* **253**, 152, 1995.
771. H. Münder, C. Andrzejak, M. G. Berger, U. Klemradt, H. Lüth, R. Herino, and M. Ligeon, A detailed Raman study of porous silicon, *Thin Solid Films* **221**, 27, 1992.
772. M. Binder, T. Edelmann, T. H. Metzger, G. Mauckner, G. Goerigk, and J. Peisl, Bimodal size distribution in p^- porous silicon studied by small angle X-ray scattering, *Thin Solid Films* 276, 65, 1996.
773. L. M. Peter, D. J. Riley, and R. I. Wielgosz, An in-situ method of monitoring the surface area of porous silicon, *Thin Solid Films* **276**, 61, 1996.
774. M. Thönisson, M. G. Berger, R. Arens-Fisher, O. Glück, M. Krüger, and H. Lüth, Illumination-assisted formation of porous silicon, *Thin Solid Films* **276**, 21, 1996.
775. J. Rappich and H. J. Lewerenz, Photo and potential controlled nano porous silicon formation on N silicon: An in-situ FTIR investigation, *Thin Solid Films* **276**, 25, 1996.
776. G. Mende and E. Hensel, The electrophysical properties of anodically grown silicon oxide film, *Thin Solid Films* **168**, 51, 1989.
777. D. Bellet and G. Dolino, X-ray diffraction studies of porous silicon, *Thin Solid Films* **276**, 1, 1996.
778. E. C. C. Yeh, M. S. Chiou, and K. Y. J. Hsu, Computer simulation of percolated porous Si structure and its application to electrical conductivity simulation, *Thin Solid Films* **297**, 88, 1997.
779. A. Bruska, E. V. Astrova, U. Falke, T. Raschke, Ch. Radehaus, and M. Hietschold, Evidence of anisotropic structures of free-standing porous silicon films, *Thin Solid Films* **297**, 79, 1997.
780. S. Billat, M. Thonissen, R. Arens-Fischer, M. G. Berger, M. Kruger, and H. Luth, Influence of etch stops on the microstructure of porous silicon layers, *Thin Solid Films* **297**, 22, 1997.

781. R. B. Wehrspohn, J.-N. Chazalviel, F. Ozanam, and I. Solomon, Electrochemistry and photoluminescence of porous amorphous silicon, *Thin Solid Films* **297**, 5, 1997.
782. H. W. Lau, G. J. Parker, and R. Greef, High aspect ratio silicon pillars fabricated by electrochemical etching and oxidation of macroporous silicon, *Thin Solid Films* **276**, 29, 1996.
783. F. Ronkel, J. W. Schultze, and R. Arens-Fischer, Electrical contact to porous silicon by electrodeposition of iron, *Thin Solid Films* **276**, 40, 1996.
784. C. Pavelescu, C. Cobianu, L. Condriuc, and E. Segal, Etch rate behaviour of SiO_2 films chemically vapour deposited from silane, oxygen and nitrogen gas mixtures at low temperatures, *Thin Solid Films* **114**, 291, 1984.
785. S. S. Cohen, Contact resistance and methods for its determination, *Thin Solid Films* **104**, 361, 1983.
786. L. K. White, Etch rates of SiO_2 films in deuterated acidic fluorides, *Thin Solid Films* **79**, L73, 1981.
787. G. Mende, Uber den Einflub der Ionenimplantation auf die Geschwindigkeit der Anodischen Siliziumoxydation, *Thin Solid Films* **78**, 335, 1981.
788. E. Guerrero, G. Tobolka, and A. Baghai, Calibration for the anodic oxidation of silicon, *Thin Solid Films* **76**, 237, 1981.
789. L. A. Nagahara, T. Ohmori, K. Hashimoto, and A. Fujishima, The influence of hydrofluoric acid concentration on electroless copper deposition onto silicon, *J. Electroanal. Chem.* **333**, 363, 1992.
790. G. Mende, Uber die Selektive Anodische Oxydation von n-Silizium, *Thin Solid Films* **55**, 427, 1978.
791. Y. Nakato, K. Ueda, H. Yano, and H. Tsubomura, Effect of microscopic discontinuity of metal overlayers on the photovoltages in metal-coated semiconductor-liquid photoelectrochemical cells for efficient solar energy conversion, *J. Phys. Chem.* **92**, 2316, 1988.
792. R. A. Haken, I. M. Baker, and J. D. E. Beynon, An investigation into the dependence of the chemically-etched edge profiles of silicon dioxide films on etchant concentration and temperature, *Thin Solid Films* **18**, S3, 1973.
793. R. Nannoni and M. J. Musselin, Anodic oxidation of silicon effects of water on oxide properties, *Thin Solid Films* **6**, 397, 1970.
794. P. Allongue, C. H. de Villeneuve, M. C. Bernard, J. E. Peou, A. Boutry-Forveille, and C. Levy-Clement, Relationship between porous silicon formation and hydrogen incorporation, *Thin Solid Films* **297**, 1, 1997.
795. G. Sotgiu, L. Schirone, and F. Rallo, On the use of surfactants in the electrochemical preparation of porous silicon, *Thin Solid Films* **297**, 18, 1997.
796. P. Steiner, A. Wiedenhofer, F. Kozlowski, and W. Lang, Influence of different metallic contacts on porous silicon electroluminescence, *Thin Solid Films* **276**, 159, 1996.
797. F. Kozlowski, C. Sailer, P. Steiner, B. Knoll, and W. Lang, Time-resolved electroluminescence of porous silicon, *Thin Solid Films* **276**, 164, 1996.
798. B. Gelloz, A. Bsiesy, F. Gaspard, and F. Muller, Conduction in porous silicon contacted by a liquid phase, *Thin Solid Films* **276**, 175, 1996.
799. Th. Dittrich, I. Sieber, S. Rauscher, and J. Rappich, Preparation of thin nanoporous silicon layers on n- and p-Si, *Thin Solid Films* **276**, 200, 1996.
800. D. J. Monk, D. S. Soane, and R. T. Howe, A review of the chemical reaction mechanism and kinetics for hydrofluoric acid etching of silicon dioxide for surface micromachining applications, *Thin Solid Films* **232**, 1, 1993.
801. V. Lehmann, F. Hofmann, F. Moller, and U. Gruning, Resistivity of porous silicon: A surface effect, *Thin Solid Films* **255**, 20, 1995.
802. M. Jeske, J. W. Schultze, M. Thonissen, and H. Munder, Electrodeposition of metals into porous silicon, *Thin Solid Films* **255**, 63, 1995.
803. A. Bsiesy, F. Gaspard, R. Herino, M. Ligeon, F. Muller, R. Romestain, and J. C. Vial, Voltage-induced modifications of porous silicon luminescence, *Thin Solid Films* **255**, 80, 1995.
804. P. Joubert, A. Abouliatim, P. Guyader, D. Briand, B. Lambert, and M. Guendouz, Growth and luminescence of n-type porous polycrystalline silicon, *Thin Solid Films* **255**, 96, 1995.
805. I. Haller, Y. H. Lee, J. J. Nocera, Jr., and M. A. Jaso, Selective wet and dry etching of hydrogenated amorphous silicon and related materials, *J. Electrochem. Soc.* **135**(8), 2042, 1988.
806. H. Nagayama, H. Honda, and H. Kawahara, A new process for silica coating, *J. Electrochem. Soc.* **135**(8), 2013, 1988.

807. S. Watanabe, N. Nakayama, and T. Ito, Homogeneous hydrogen-terminated Si(111) surface formed using aqueous HF solution and water, *Appl. Phys. Lett.* **59**(12), 1458, 1991.
808. G. Oskam, P. M. Hoffmann, and P. C. Searson, In situ measurements of interface states at silicon surfaces in fluoride solutions, *Phys. Rev. Lett.* **76**(9), 1521, 1996.
809. R. Schmid, P. L. Huesmann, and W. S. Johnson, Thermodynamically uphill reduction of a surface-confined N, N′-dialkyl-4, 4′-bipyridinium derivative on illuminated p-type silicon surfaces, *J. Am. Chem. Soc.* **102**, 5125, 1980.
810. R. Noufi, A. J. Frank, and A. J. Nozik, Stabilization of n-type silicon photoelectrodes to surface oxidation in aqueous electrolyte solution and mediation of oxidation reaction by surface-attached organic conducting polymer, *J. Am. Chem. Soc.* **103**, 1849, 1981.
811. Y. Nakato, K. Ueda, and H. Tsubomura, Novel approch to efficient photoelectrochemical solar cells using electrolyte/discontinuous metal/semiconductor junction, *J. Phys. Chem.* **90**, 2090, 1986.
8!2. R. N. Dominey, N. S. Lewis, J. A. Bruce, D. C. Bookbinder, and M. S. Wrighton, Improvement of photoelectrochemical hydrogen generation by surface modification of p-type silicon semiconductor photocathodes, *J. Am. Chem. Soc.* **104**(2), 467, 1982.
813. G. S. Calabrese, M.-S. Lin, J. Dresner, and M. S. Wrighton, Photoelectrochemical cells based on amorphous hydrogenated silicon thin film electrodes and the behavior of photoconductor electrode materials, *J. Am. Chem. Soc.* **104**, 2412, 1982.
814. G. Hodes, L. Thompson, J. DuBow, and K. Rajeshwar, Heterojunction silicon/indium tin oxide photoelectrodes: Development of stable systems in aqueous electrolytes and their applicability to solar energy conversion and storage, *J. Am. Chem. Soc.* **105**, 324, 1983.
815. U. T. Mueller-Westerhoff and A. Nazzal, Ferrocenophanes as effective catalysts in the photoelectrochemical hydrogen evolution from acidic aqueous media, *J. Am. Chem. Soc.* **106**, 5381, 1984.
816. D. L. DuBois and J. A. Turner, Preparation and spectroelectrochemical characterization of silicon electrodes modified with molybdenum dinitrogen complexes, *J. Am. Chem. Soc.* **104**, 4989, 1982.
817. F.-R. F. Fan, R. G. Keil, and A. J. Bard, Semiconductor electrodes. 48. Photooxidation of halides and water on n-silicon protected with silicide layers, *J. Am. Chem. Soc.* **105**, 220, 1983.
818. R. A. Simon, A. J. Ricco, and M. S. Wrighton, Synthesis and characterization of a new surface derivatizing reagent to promote the adhesion of polypyrrole films to n-type silicon photoanodes: N-(3-(trimethoxysilyl)propyl)pyrrole, *J. Am. Chem. Soc.* **104**, 2031, 1982.
819. P. Jakob and Y. J. Chabal, Chemical etching of vicinal Si(111): Dependence of the surface structure and the hydrogen termination on the pH of the etching solutions, *J. Chem. Phys.* **95**(4), 2897, 1991.
820. H. Ubara, T. Imura, and A. Hiraki, Formation of Si–H bonds on the surface of microcrystalline silicon covered with SiO_x by HF treatment, *Solid State Commun.* **50**(7), 673, 1984.
821. G. W. Trucks, K. Raghavachari, G. S. Higashi, and Y. J. Chabal, Mechanism of HF etching of silicon surfaces: A theoretical understanding of hydrogen passivation, *Phys. Rev. Lett.* **65**(4), 504, 1990.
822. G. W. Trucks, K. Raghavachari, G. S. Higashi, and Y. J. Chabal, Comment on mechanism of HF etching of silicon surfaces: A theoretical understanding of hydrogen passivation, *Phys. Rev. Lett.* **66**(12), 1647, 1991.
823. R. T. Collins, P. M. Fauchet, and M. A. Tischler, Porous silicon: From luminescence to LEDs, *Phys. Today,* 24, January 1997.
824. P. A. Giguere and S. Turrell, The nature of hydrofluoric acid. A spectroscopic study of the proton-transfer complex $H_3O^+ \cdot F$, *J. Am. Chem. Soc.* **102**, 5473, 1980.
825. A. B. Bocarsly, E. G. Walton, and M. S. Wrighton, Use of chemically derivatized n-type silicon photoelectrodes in aqueous media. Photooxidation of iodide, hexacyanoiron (II), and hexaammineruthenium (II) at ferrocene-derivatized photoanodes, *J. Am. Chem. Soc.* **102**, 3390, 1980.
826. D. C. Bookbinder, N. S. Lewis, M. G. Bradley, A. B. Bocarsly, and M. S. Wrighton, Photoelectrochemical reduction of N, N′-dimethyI-4, 4′-bipyridinium in aqueous media at p-type silicon: Sustained photogeneration of a species capable of evolving hydrogen, *J. Am. Chem. Soc.* **101**, 7721, 1979.
827. J. M. Bolts, A. B. Bocarsly, M. C. Palazzotto, E. G. Walton, N. S. Lewis, and M. S. Wrighton, Chemically derivatized n-type silicon photoelectrodes. Stabilization to surface corrosion in aqueous electrolyte solutions and mediation of oxidation reactions by surface-attached electroactive ferrocene reagents, *J. Am. Chem. Soc.* **101**, 1378, 1979.

828. M. S. Wrighton, R. G. Austin, A. B. Bocarsly, J. M. Bolts, O. Haas, K. D. Legg, L. Nadjo, and M. C. Palazzotto, Design and study of a photosensitive interface: A derivatized n-type silicon photoelectrode, *J. Am. Chem. Soc.* **100**, 1602, 1978.
829. M. Szklarczyk and J. O. Bockris, Photoelectrocatalysis and electrocatalysis on p-silicon, *J. Phys. Chem.* **88**, 1808, 1984.
830. Y. Zu, L. Xie, B. Mao, and Z. Tian, Studies on silicon etching using the confined etchant layer technique, *Electrochim. Acta* **43**(12–13), 1683, 1998.
831. B. Rashkova, B. Guel, R. T. Potzschke, G. Staikov, and W. J. Lorenz, Electrodeposition of Pb on n-Si(111), *Electrochim. Acta* **43**(19–20), 3021, 1998.
832. M. V. Sullivan, D. L. Klein, R. M. Finne, L. A. Pompliano, and G. A. Kolb, An electropolishing technique for germanium and silicon, *J. Electrochem. Soc.* **110**(5), 412, 1963.
833. R. J. Jaccodine, Surface energy of germanium and silicon, *J. Electrochem. Soc.* **110**(6), 524, 1963.
834. P. Allongue, C. H. de Villeneuve, J. Pinson, F. Ozanam, J.-N. Chazalviel, and X. Wallart, Organic monolayers on Si(111) by electrochemical method, *Electrochim. Acta* **43**(19–20), 2791, 1998.
835. M. Croset and D. Dieumegard, Anodic oxidation of silicon in organic baths containing fluorine, *J. Electrochem. Soc.* **120**(4), 526, 1973.
836. R. Dreiner, A-C properties of anodic oxide films on silicon, *J. Electrochem. Soc.* **113**(11), 1210, 1966.
837. S. J. Silverman and D. R. Benn, Junction delineation in silicon by gold chemiplating, *J. Electrochem. Soc.* **105**(3), 170, 1958.
838. T. M. Buck and F. S. McKim, Effects of certain chemical treatments and ambient atmospheres on surface properties of silicon, *J. Electrochem. Soc.* **105**(12), 709, 1958.
839. J. B. Flynn, Saturation currents in germanium and silicon electrodes, *J. Electrochem. Soc.* **105**(12), 715, 1958.
840. M. V. Sullivan and J. H. Eigler, Electroless nickel plating for making ohmic contacts to silicon, *J. Electrochem. Soc.* **104**(4), 226, 1957.
841. G. Oskam, P. M. Hoffmann, J. C. Schmidt, and P. C. Searson, Energetics and kinetics of surface states at n-type silicon surfaces in aqueous fluoride solutions, *J. Phys. Chem.* **100**(5), 1801, 1996.
842. A. Grosman, M. Chamarro, V. Morazzani, C. Ortega, S. Rigo, J. Siejka, and H. J. von Bardeleben, Study of anodic oxidation of porous silicon: Relation between growth and physical properties, *J. Lumin.* **57**, 13, 1993.
843. H. Kaneko, P. J. French, and R. F. Wolffenbuttel, Photo- and electro-luminescence from porous Si, *J. Lumin.* **57**, 101, 1993.
844. E. Galun, R. Tenne, A. Lagoubi, and C. Levy-Clement, Room temperature photoluminescence of photoelectrochemically etched n-type Si, *J. Lumin.* **57**, 125, 1993.
845. M. B. Chorin, F. Moller, and F. Koch, AC conductivity in porous silicon, *J. Lumin.* **57**, 159, 1993.
846. F. Kozlowski, P. Steiner, and W. Lang, A model for the electroluminescence of porous n-silicon, *J. Lumin.* **57**, 163, 1993.
847. Y. Nakato, J. G. Jia, M. Ishida, K. Morisawa, M. Fujitani, H. Hinogami, and S. Yae, Efficient solar-to-chemical conversion by one chip of n-type silicon with surface asymmetry, *Electrochem. Solid-State Lett.* **1**(2), 71, 1998.
848. G. Oskam, J. G. Long, A. Natarajan, and P. C. Searson, Electrochemical deposition of metals onto silicon, *J. Phys. D* **31**, 1927, 1998.
849. E. A. Speers and J. R. Cahoon, Deposition of silica films using electrochemical procedures, *J. Electrochem. Soc.* **145**(6), 1812, 1998.
850. V. Lehmann, The physics of macroporous silicon formation, *Thin Solid Films* **255**, 1, 1995.
851. S. D. Collins, Etch stop techniques for micromachining, *J. Electrochem. Soc.* **144**(6), 2242, 1997.
852. R. Kinder, Electrochemical C-V profiling of silicon structure, *Phys. Status Solidi* **164**, 785, 1997.
853. W. M. Siu and R. S. C. Cobbold, Basic properties of the electrolyte–SiO_2–Si system: Physical and theoretical aspects, *IEEE Trans. Electron Devices* **26**(11), 1805, 1979.
854. V. Bertagna, F. Rouelle, and M. Chemla, An improved electrochemical cell for the characterization of silicon/electrolyte interfaces, *J. Appl. Electrochem.* **27**, 1179, 1997.
855. S. Cattarin, F. Decker, and D. Dini, Anodic silicon dissolution in acidic fluoride electrolyte. A probe beam deflection investigation, *J. Phys. Chem. B* **102**, 4779, 1998.
856. R. Houbertz, U. Memmert, and R. J. Behm, Morphology of anodically etched Si(111) surfaces: A structural comparison of NH_4F versus HF etching, *J. Vac. Sci. Technol. B* **12**(6), 3145, 1994.

857. B. Hamilton, Porous silicon, *Semicond. Sci. Technol.* **10**, 1187, 1995.
858. Y. Kang and J. Jorne, Photoelectrochemical dissolution of n-type silicon, *Electrochim. Acta* **43**(16–17), 2389, 1998.
859. H. You, Z. Nagy, and K. Huang, X-ray scattering study of porous silicon growth during anodic dissolution, *Phys. Rev. Lett.* **78**(7), 1367, 1997.
860. M. Aggour, M. Diersig, and H. J. Lewerenz, Interface Condition of n-Si(111) during photocurrent oscillations in NH_4F solutions, *J. Electroanal. Chem.* **383**, 67, 1995.
861. H. H. Hassan, B. Fotouhi, J.-L. Sculfort, S. S. Abdel-Rehiem, M. Etman, F. Oxanam, and J.-N. Chazalviel, Effect of alkali-metal and some quaternary-ammonium cations on the anodic dissolution of p-Si in fluoride media, *J. Electroanal. Chem.* **407**, 105, 1996.
862. D. Dini, S. Cattarin, and F. Decker, Probe beam deflection study of p-Si electrodissolution in acidic fluoride medium in the oscillating regimes, *J. Electroanal. Chem.* **446**, 7, 1998.
863. M. T. Kelly, J. K. M. Chun, and A. B. Bocarsly, High efficiency chemical etchant for the formation of luminescent porous silicon, *Appl. Phys. Lett.* **64**(13), 1693, 1994.
864. R. R. Kunz, P. M. Nitishin, H. R. Clark, M. Rothschild, and B. Ahern, Observation of a nanocrystalline-to-amorphous phase transition in luminescent porous silicon, *Appl. Phys. Lett.* **67**(12), 1766, 1995.
865. A. J. Steckl, J. Xu, H. C. Mogul, and S. Mogren, Doping-induced selective area photoluminescence in porous silicon, *Appl. Phys. Lett.* **62**(16), 1982, 1993.
866. J. Rappich, M. Aggour, S. Rauscher, H. J. Lewerenz, and H. Jungblut, Electrochemical surface conditioning of n-Si(111), *Surf. Sci.* **335**, 160, 1995.
867. A. J. Nozik, Photoelectrochemistry: Applications to solar energy conversion, *Annu Rev. Phys. Chem.* **29**, 189, 1978.
868. G. Bomchil, A. Halimaoui, I. Sagnes, P. A. Badoz, I. Berbezier, P. Perret, B. Lambert, G. Vincent, L. Garchery, and J. L. Regolini, Porous silicon: Material properties, visible photo- and electroluminescence, *Appl. Surf. Sci.* **65/66**, 394, 1993.
869. R. M. Candea, M. Kastner, R. Goodman, and N. Hickok, Photoelectrolysis of water: Si in salt water, *J. Appl. Phys.* **47**(6), 2724, 1976.
870. S. M. Prokes, Surface and optical properties of porous silicon, *J. Mater. Res.* **11**(2), 305, 1996.
871. W. Kern, Chemical etching of silicon, germanium, gallium arsenide, and gallium phosphide, *RCA Rev.* **39**, 278, 1978.
872. W. Kern, Wet-chemical etching of SiO_2 and PSG films, and an etching-induced defect in glass-passivated integrated circuits, *RCA Rev.* **47**, 186, 1986.
873. H. Gerischer and M. Lubke, The electrochemical behaviour of n-type silicon (111)-surfaces in fluoride containing aqueous electrolytes, *Ber. Bunsenges. Phys. Chem.* **91**, 394, 1987.
874. H. Gerischer and M. Lubke, Electrolytic growth and dissolution of oxide layers on silicon in aqueous solutions of fluorides, *Ber. Bunsenges. Phys. Chem.* **92**, 576, 1988.
875. Y. Nakato, S. Tonomura, and H. Tsubomura, The catalytic effect of electrodeposited metals on the photo-reduction of water at p-type semiconductors, *Ber. Bunsenges.* **80**(12), 1289, 1976.
876. R. Memming and F. Mollers, Two-step redox processes with quinones at semiconductor electrodes, *Ber. Bunsenges.* **76**(7), 609, 1972.
877. N. S. Lewis, A. B. Bocarsly, and M. S. Wrighton, Heterogeneous electron transfer at designed semiconductor/liquid interfaces. Rate of reduction of surface-confined ferricenium centers by solution reagents, *J. Phys. Chem.* **84**, 2033, 1980.
878. J. A. Bruce, T. Murahashl, and M. S. Wrighton, Synthesis and characterization of structured interfaces for hydrogen generation. Study of an N, N′-dialkyl-4, 4′-bipyridinium redox polymer/palladium catalyst system, *J. Phys. Chem.* **86**, 1552, 1982.
879. P. Leempoel, M. Castro-Acuna, F. F. Fan, and A. J. Bard, Semiconductor electrodes. 43. The effect of light intensity and iodine doping on the stabilization of n-silicon by phthalocyanine films, *J. Phys. Chem.* **86**, 1396, 1982.
880. K. W. Frese, Jr., Simple method for estimating energy levels of solids, *J. Vac. Sci. Technol* **16**(4), 1042, 1979.
881. B. Semmens and A. B. Meggy, The reaction of kaolin with fluorides, *J. Appl. Chem.* **16**, 122, 1966.
882. D. L. DuBois, Modification of silicon and carbon electrodes with methacrylamide polymers containing covalently attached molybdenum dinitrogen complexes, *Inorg. Chem.* **23**, 2047, 1984.

883. W. Kern, Radiochemical study of semiconductor surface contamination II. Deposition of trace impurities on silicon and silica, *RCA Rev.* 234, 1970.
884. W. Kern and D. A. Puotinen, Cleaning solutions based on hydrogen peroxide for use in silicon semiconductor technology, *RCA Rev.* 186, June 1970.
885. W. Kern, A technique for measuring etch rates of dielectric films, *RCA Rev.* 557, December 1968.
886. J. A. Bruce and M. S. Wrighton, Modified p-type Si photocathodes for photochemical hydrogen generation: Surface texturing, molecular derivatizing reagents, and nobel metal catalysts for multielectron processes, *Isr. J. Chem.* **22**, 184, 1982.
887. E. Kondoh, M. R. Baklanov, F. Jonckx, and K. Maex, Characterisation of HF-last cleaning of ion-implanted Si surfaces, *Mater. Sci. Semicond. Process.* **1**, 107, 1998.
888. P. T. Michaud and D. Babic, A Raman study of etching silicon in aqueous tetramethylammonium hydroxide, *J. Electrochem. Soc.* **145**(11), 4040, 1998.
889. W. Feng and B. Miller, Fullerene monolayer-modified porous Si. Synthesis and photoelectrochemistry, *Electrochem. Solid-State Lett.* **1**(4), 172, 1998.
890. D. Xu, G. Guo, L. Gui, Y. Tang, B. Zhang, and G. Qin, Preparation and characterization of freestanding porous silicon films with high porosities, *Electrochem. Solid-State Lett.* **1**(5), 227, 1998.
891. E. Propst and P. A. Kohl, The photoelectrochemical oxidation of n-Si in anhydrous HF-acetonitrile, *J. Electrochem. Soc.* **140**(5), L78, 1993.
892. R. Guerrero-Lemus, J. D. Moreno, J. M. Martinez-Duart, M. L. Marcos, J. Gonzalez-Velasco, and P. Gomez, Properties of porous silicon layers studied by voltammetric oxidation, *J. Appl. Phys.* **79**(6), 3224, 1996.
893. T. K. Sham and I. Coulthard, Porous silicon: A peculiar substance with remarkable properties, *Can. Chem. News* 13, February 1998.
894. L. H. Jones and R. A. Penneman, Infrared absorption spectra of aqueous HF_2^-, DF_2^-, and HF, *J. Chem. Phys.* **22**(25), 781, 1954.
895. P. Jakob and Y. J. Chabal, Chemical etching of vicinal Si(111): Dependence of the surface structure and the hydrogen termination on the pH of the etching solutions, *J. Chem. Phys.* **95**(4), 2897, 1991.
896. M. J. S. Dewar, J. Friedheim, G. Grady, E. F. Healy, and J. J. P. Stewart, Revised MNDO parameters for silicon, *Organometallics* **5**(2), 375, 1986.
897. G. S. Wirth and J. M. Gieskes, The initial kinetics of the dissolution of vitreous silica in aqueous media, *J. Colloid Interface Sci.* **68**(3), 492, 1979.
898. P. M. Dove and S. F. Elston, Dissolution kinetics of quartz in sodium chloride solutions: Analysis of existing data and a rate model for 25C, *Geochim. Cosmochim. Acta* **56**, 4147, 1992.
899. J. D. Rimstidt and H. L. Barnes, The kinetics of silica–water reactions, *Geochim. Cosmochim. Acta* **44**, 1683, 1980.
900. G. W. Trucks, K. Raghavachari, G. S. Higashi, and Y. J. Chabal, Mechanism of HF etching of silicon surfaces: A theoretical understanding of hydrogen passivation, *Phys. Rev. Lett.* **65**(4), 504, 1990.
901. P. De Mierry, D. Ballutaud, and M. Aucouturier, Effect of surface preparations on electrical and chemical surface properties of p-type silicon, *J. Electrochem. Soc.* **137**, 2966, 1990.
902. L. Bousse and P. Bergveld, On the impedance of the silicon dioxide/electrolyte interface, *J. Electroanal. Chem.* **152**, 25, 1983.
903. L. Bousse, N. F. De Rooji, and P. Bergveld, Operation of chemical sensitive field-effect sensors as a function of the insulator–electrolyte interface, *IEEE Trans. Electron Devices* **30**, 1263, 1983.
904. P. Allongue, V. Kieling, and H. Gerischer, Etching mechanism and atomic structure of H-Si(111) surfaces prepared in NH_4F, *Electrochim. Acta* **40**, 1353, 1995.
905. H. A. Waggener, Electrochemically controlled thinning of silicon, *Bell Syst. Tech. J.* 473, March 1970.
906. M. Grundner and H. Jacob, Investigations on hydrophilic and hydrophobic silicon (100) wafer surfaces by X-ray photoelectron and high-resolution electron energy loss-spectroscopy, *Appl. Phys. A* **39**, 73, 1986.
907. L. M. Peter, D. J. Blackwood, and S. Pons, In situ characterization of the illuminated silicon–electrolyte interface by fourier-transform infrared spectroscopy, *Phys. Rev. Lett.* **62**(3), 308, 1989.
908. H. J. Lewerenz, J. Stumper, and L. M. Peter, Deconvolution of charge injection steps in quantum yield multiplication on silicon, *Phys. Rev. Lett.* **61**(17), 1989, 1988.
909. J. Stumper, H. J. Lewerenz, and C. Pettenkofer, X-ray photoemission spectroscopy analysis of Si(111) under photocurrent-doubling conditions, *Phys. Rev. B* **41**(3), 1592, 1990.

910. A. A. Blumberg and S. C. Stavrinou, Tabulated functions for heterogeneous reaction rates: The attack of vitreous silica by hydrofluoric acid, *J. Am. Chem. Soc.* **64**, 1438, 1960.
911. J. R. Ligenza, Effect of crystal orientation on oxidation rates of silicon in high pressure steam **65**, 2011, 1961.
912. C. Pavelescu, C. Cobianu, and E. Segal, Etch rate of low-temperature chemically vapor deposited SiO_2 films in p-etch solution: The effect of deposition conditions, *J. Mater. Sci. Lett.* **4**, 1280, 1985.
913. R. Memming, Surface recombination at higher injection levels, *Surf. Sci.* **1**, 88, 1964.
914. G. F. Cerofolini, A study of the ionic route for hydrogen terminations resulting after SiO_2 etching by concentrated aqueous solutions of HF, *Appl. Surf. Sci.* **133**, 108, 1998.
915. H. Ochs, D. Bublak, U. Wild, M. Muhler, and B. O. Kolbesen, Depth distribution of zinc adsorbed on silicon surfaces out of alkaline aqueous solutions, *Appl. Surf. Sci.* **133**, 73, 1998.
916. W. E. Kline and H. S. Fogler, Dissolution kinetics: Catalysis by salts, *J. Colloid Interface Sci.* **82**(1), 103, 1981.
917. R. Memming, Solar energy conversion by photoelectrochemical processes, *Electrochim. Acta* **25**, 77, 1980.
918. K. E. Petersen, Silicon as a mechanical material, *Proc. IEEE* **70**(5), 420, 1982.
919. E. F. Duffek, E. A. Benjamini, and C. Mylroie, The anodic oxidation of silicon in ethylene glycol solutions, *Electrochem. Tech.* **3**(3–4), 75, 1965.
920. L. M. Peter, D. J. Blackwood, and S. Pons, Photocorrosion of n-Si in ammonium fluoride solutions: An investigation by in-situ Fourier transform infrared spectroscopy, *J. Electroanal. Chem.* **294**, 111, 1990.
921. L. M. Peter, A. M. Borazio, H. J. Lewerenz, and J. Stumper, Photocurrent multiplication during photodissolution of n-Si in NH_4F. Deconvolution of electron injection steps by intensity modulated photocurrent spectroscopy, *J. Electroanal. Chem.* **290**, 229, 1990.
922. L. J. Warren, The measurement of pH in acid fluoride solutions and evidence for the existence of $(HF)_2$, *Anal. Chim. Acta* **53**, 199, 1971.
923. H. Gerischer and W. Mindt, The mechanisms of the decomposition of semiconductors by electrochemical oxidation and reduction, *Electrochim. Acta* **13**, 1329, 1968.
924. J. W. Schultze and K. G. Jung, Regular nanostructured systems formed electrochemically: Deposition of electroactive polybithiophene into porous silicon, *Electrochim. Acta* **40**(10), 1369, 1995.
925. R. M. Hurd and N. Hackerman, Passivity phenomena at the silicon/electrolyte interface, *Electrochim. Acta* **9**, 1633, 1964.
926. B. Gelloz and A. Bsiesy, Carrier transport mechanisms in porous silicon in contact with a liquid phase: A diffusion process, *Appl. Surf. Sci.* **135**, 15, 1998.
927. B. D. Chase and D. B. Holt, Jet polishing of semiconductors. II. Electrochemically formed tunnels in GaP, *J. Electrochem. Soc.* **119**(3), 314, 1972.
928. C. Messmer and J. C. Bilello, The surface energy of Si, GaAs, and GaP, *J. Appl. Phys.* **52**(7), 4623, 1981.
929. A. V. Rao, J.-N. Chazalviel, and F. Ozanam, Infrared-reflection spectroscopy, *J. Appl Phys.* **60**(2), 696, 1986.
930. L. Bousse, S. Mostarshed, B. V. D. Shoot, N. F. De Rooij, P. Gimmel, and W. Gopel, Zeta potential measurements of TaO and SiO thin films, *J. Colloid Interface Sci.* **147**(1), 22, 1991.
931. P. Allongue, C. H. de Villeneuve, J. Pinson, F. Ozanam, J.-N. Chazalviel, and X. Wallart, Organic monolayers on Si(111) by electrochemical method, *Electrochim. Acta* **43**(19–20), 2791, 1998.
932. J.-N. Chazalviel, Impedance studies at semiconductor electrodes: Classical and more exotic techniques, *Electrochim. Acta* **35**(10), 1545, 1990.
933. F. Ozanam, C. da Fonseca, A. V. Rao, and J.-N. Chazalviel, In situ spectroelectrochemical study of the anodic dissolution of silicon by potential-difference and electromodulated FT-IR spectroscopy, *Appl. Spectrosc.* **51**(4), 519, 1997.
934. F. Ozanam and J.-N. Chazalviel, In-situ infrared vibrational study of the early stages of silicon oxidation at the interface with a non-aqueous electrolyte, *J. Electroanal. Chem.* **269**, 251, 1989.
935. J.-N. Chazalviel and T. B. Truong, An experimental study of the n-Si/acetonitrile interface: Fermi level pinning and surface states investigation, *J. Am. Chem. Soc.* **103**, 7447, 1981.
936. H. H. Hassan, J.-N. Chazalviel, M. Neumann-Spallart, F. Ozanam, and M. Etman, Chemical limitations to the anodic dissolution of p-Si in fluoride media, *J. Electroanal. Chem.* **381**, 211, 1995.

937. H. H. Hassan, J. L. Sculfort, M. Etman, F. Ozanam, and J.-N. Chavalviel, Kinetic and diffusional limitations to the anodic dissolution of p-Si in fluoride media, *J. Electroanal. Chem.* **380**, 55, 1995.
938. M. Etman, M. Neumann-Spallart, J.-N. Chazalviel, and F. Ozanam, Kinetic and diffusional current contributions in the anodic dissolution of p-Si immersed in fluoride electrolytes, *J. Electroanal. Chem.* **301**, 259, 1991.
939. J.-N. Chazalviel, M. Etman, and F. Ozanam, A voltammetric study of the anodic dissolution of p-Si in fluoride electrolytes, *J. Electroanal. Chem.* **297**, 533, 1991.
940. A. Belaidi, J.-N. Chazalviel, F. Ozanam, 0. Gorochov, A. Chari, B. Fotouhi, and M. Etman, Silicon surface states and subsurface hydrogen, *J. Electroanal. Chem.* **444**, 55, 1998.
941. A. Tardella and J.-N. Chazalviel, Highly accumulated electron layer at a semiconductor/electrolyte interface, *Phys. Rev. B* **32**(4), 2439, 1985.
942. J.-N. Chazalviel and M. Stefenel, Surface states induced by metal atoms at the Si/electrolyte interface, *Surf. Sci.* **134**, 865, 1983.
943. G. A. Parks, The isoelectric points of solid oxides, solid hydroxides, and aqueous hydroxo complex systems, *Chem. Rev.* **177**, 1965.
944. E. S. Kooij, S. M. Noordhoek, and J. J. Kelly, Reduction of peroxodisulfate at porous and crystalline silicon electrodes: An anomaly, *J. Phys. Chem.* **100**, 10754, 1996.
945. E. A. Meulenkamp, P. M. M. C. Bressers, and J. J. Kelly, Visible chemiluminescence and electroluminescence of porous silicon, *Appl. Surf. Sci.* **64**, 283, 1993.
946. W. M. Mullins and B. L. Averbach, Surface properties of silicon and aluminum oxide powders, *Surf. Sci.* **206**, 41, 1988.
947. J.-N. Chazalviel, Electrochemical transfer via surface states: A new formulation for the semiconductor/electrolyte interface, *J. Electrochem. Soc.* **129**(5), 963, 1982.
948. F. Ozanam and J.-N. Chazalviel, In-situ infrared characterization of the electrochemical dissolution of silicon in a fluoride electrolyte, *J. Electron Spectrosc. Relat. Phenom.* **64–65**, 395, 1993.
949. J.-N. Chazalviel and F. Ozanam, A theory for the resonant response of an electrochemical system: Self-oscillating domains, hidden oscillation, and synchronization impedance, *J. Electrochem. Soc.* **139**(9), 2501, 1992.
950. J.-N. Chazalviel, C. da Fonseca, and F. Ozanam, In situ infrared study of the oscillating anodic dissolution of silicon in fluoride electrolytes, *J. Electrochem. Soc.* **145**(3), 964, 1998.
951. F. Ozanam, J.-N. Chazalviel, A. Radi, and M. Etman, Resonant and nonresonant behavior of the anodic dissolution of silicon in fluoride media: An impedance study, *J. Electrochem. Soc.* **139**(9), 2491, 1992.
952. R. B. Wehrspohn, J.-N. Chazalviel, and F. Ozanam, macropore formation in highly resistive p-type crystalline silicon, *J. Electrochem. Soc.* **145**(8), 2958, 1998.
953. M. A. Butler and D. S. Ginley, Prediction of flatband potentials at semiconductor–electrolyte interfaces from atomic electronegativities, *J. Electrochem. Soc.* **125**(2), 228, 1978.
954. D. Vanmeakelbergh and P. C. Searson, On the electrical impedance due to the anodic dissolution of silicon in HF solutions, *J. Electrochem. Soc.* **141**(3), 697, 1994.
955. M. J. Madou, K. W. Freese, Jr., and S. R. Morrison, Photoelectrochemical corrosion as influenced by an oxide layer, *J. Phys. Chem.* **84**, 3423, 1984.
956. K. D. Legg, A. B. Ellis, J. M. Bolts, and M. S. Wrighton, n-type Si-based photoelectrochemical cell: New liquid junction photocell using a nonaqueous ferricenium/ferrocene electrolyte, *Proc. Natl. Acad. Sci. USA* **74**, 4116, 1977.
957. A. Uhlir, Jr., Electrolytic shaping of germanium and silicon, *Bell Syst. Tech. J.* **333**, March 1956.
958. K. Srinivasan and G. A. Rechnitz, Activity measurements with a fluoride-selective membrane electrode, *Anal. Chem.* **40**(3), 509, 1968.
959. I. Bergman and M. S. Paterson, Silica powders of respirable size. I. Preliminary studies of dissolution rates in dilute sodium hydroxide, *J. Appl. Chem.* **369**, 1961.
960. B. H. Loo, K. W. Freese, Jr., and S. R. Morrison, The influence of surface oxide films on the stabilization of photoelectrode, *Surf. Sci.* **109**, 75, 1981.
961. L. Young and F. G. R. Zobel, An ellipsometric study of steady-state high field ionic conduction in anodic oxide films on tantalum, niobium and silicon, *J. Electrochem. Soc.* **113**, 277, 1966.
962. Y. V. Pleskov and Y. Y. Gurevich, *Semiconductor Photoelectrochemistry,* Consultants Bureau, New York, 1986.

963. A. J. Bard and L. R. Faulkner, *Electrochemical Methods—Fundamentals and Applications,* John Wiley & Sons, New York, 1980.
964. S. M. Sze, *Physics of Semiconductor Devices,* John Wiley & Sons, New York, 1981.
965. P. C. Searson, D. D. Macdonald and L. M. Peter, Frequency domain analysis of photoprocesses at illuminated semiconductor electrodes by transient transformation, *J. Electrochem. Soc.* **139**, 2538, 1992.
966. P. C. Searson, S. M. Prokes, and O. J. Glembocki, Luminescence at the porous silicon/electrolyte interface, *J. Electrochem. Soc.* **140**, 3327, 1993.
967. R. T. Potzschke, G. Staikov, W. J. Lorenz, and W. Wiesbeck, Electrochemical nanostructuring of n-Si(111) single-crystal faces, *J. Electrochem. Soc.* **146**, 141, 1999.
968. V. Bertagna, R. Erre, F. Rouelle, and M. Chemla, Corrosion rate of n- and p-silicon substrates in HF, HF + HC1 and HF + NH_4F aqueous solutions, *J. Electrochem. Soc.* **146**, 83, 1999.
969. E. S. Kooij, Silicon: Electrochemistry and luminescence, Ph.D. thesis, Universitiet Utrecht, 1997.
970. X. G. Zhang, *Corrosion and Electrochemistry of Zinc,* Plenum Press, New York, 1996.
971. R. Srinivasan and I.I. Suni, Kinetic analysis of Au deposition from aqueous HF onto Si(111) by surface second harmonic generation, *J. Electrochem. Soc.* **146**, 570, 1999.
972. L. M. Loewenstein, F. Charpin, and P. W. Mertens, Competitive adsorption of metal ions onto hydrophilic silicon surfaces from aqueous solutions, *J. Electrochem. Soc.* **146**, 719, 1999.
973. *Merck Index,* 11th ed., Merck & Co., Rahway, NJ, 1989.
974. *CRC Handbook of Chemistry and Physics,* 68th ed., CRC Press, Boca Raton, FL, 1988.
975. Y. Mori, K. Uemura, and K. Shimanoe, Adsorption species of transtion metal ions on silicon wafer in SC-1 solution, *J. Electrochem. Soc.* **142**, 3104, 1995.
976. L. Mouche, F. Tardif, and J. Derrien, Mechanisms of metallic impurity deposition on silicon substrates dipped in cleaning solution, *J. Electrochem. Soc.* **142**, 2395, 1995.
977. L. M. Loewenstein and P. W. Mertens, Adsorption of metal ions onto hydrophilic silicon surfaces from aqueous solution: Effect of pH, *J. Electrochem. Soc.* **145**, 2841, 1998.
978. M. Miyamoto, T. Tatsuno, and Y. Ohta, Advanced ultrapure water by HF addition, *J. Electrochem. Soc.* **140**, 2546, 1993.
979. J. P. John and J. McDonald, Spray etching of silicon in the $HNO_3/HF/H_2O$ system, *J. Electrochem. Soc.* **145**, 2622, 1998.
980. J. A. Kerr, *CRC Handbook of Chemistry and Physics,* 68th ed., CRC Press, Boca Raton, FL, 1988.
981. E. S. Kooij, K. Butter, and J. J. Kelly, Silicon etching in HNO_3/HF solution: Charge balance for the oxidation reaction, *Electrochem. Solid State Lett.* **2**, 178, 1999.
982. K. T. Lee and S. Raghvan, Etch rate of silicon and silicon dioxide in ammonia–peroxide solutions measured by quartz crystal microbalance technique, *Electrochem. Solid State Lett.* **2**, 172, 1999.
983. S. Chandra and J. Singh, Capacitance–voltage measurement technique as a tool for in situ characterization of electrochemical etching of silicon, *J. Electrochem. Soc.* **146**, 1206, 1999.
984. O. J. Glembocki, E. D. Palik, G. R. de Guel, and D. L. Kendall, Hydration model for the molarity dependence of the etch rate of Si in aqueous alkali hydroxides, *J. Electrochem. Soc.* **138**, 1055, 1991.
985. S. M. Hu and D. R. Kerr, Observation of etching of n-type silicon in aqueous HF solutions, *J. Electrochem. Soc.* **114**, 414, 1967.
986. S. R. Morrison, F. V. Kerchove, and W. P. Gomes, Hole injection into dislocations in p-silicon electrodes, *Ber. Bunsenges. Phys. Chem.* **95**, 165, 1991.
987. J. Carstensen, R. Prange, and H. Foll, A model for current voltage oscillations at the silicon electrode and comparison with experimental results, *J. Electrochem. Soc.* **146**, 1134, 1999.
988. N. Koshida and K. Echizenya, Characterization studies of p-type porous Si and its photoelectrochemical activation, *J. Electrochem. Soc.* **138**, 837, 1991.
989. G. K. Mayer, H. L. Offereins, H. Sandamaier, and K. Kuhl, Fabrication of non-underetched convex corners inanisotropic etching of (100)-silicon in aqueous KOH with respect to novel micromechanical elements, *J. Electrochem. Soc.* **137**, 3947, 1990.
990. G. Osakam, P. M. Vereecken, and P. C. Searson, Electrochemical deposition of copper on n-Si/TiN, *J. Electrochem. Soc.* **146**, 1436, 1999.
991. M. Buberto, X. G. Zhang, R. Scarmozzino, A. E. Willner, D. V. Podlesnik, and R. M. Osgood, The laser-controlled micrometer-scale photoelectrochemical etching of III-V semiconductors, *J. Electrochem. Soc.* **138**, 1174, 1991.
992. E. Sirtl and A. Adler, *Z. Metallk.* **52**, 529, 1961.

993. B. L. Sopori, A new etch for polycrystalline silicon, *J. Electrochem. Soc.* **131**, 667, 1984.
994. K. C. Lee, The fabrication of thin, Freestanding, single-crystal, semiconductor membranes, *J. Electrochem. Soc.* **137**, 2556, 1990.
995. B. C. S. Chu, C. N. Chen, and J. S. Shie, Micromachining on (111)-oriented silicon, *Sensors Actuators* **75**, 271, 1999.
996. Y. Nemirovsky and A. El-Bahar, The non equilibrium band model of silicon in TMAH and in anisotropic electrochemical alkaline etching solutions, *Sensors Actuators* **75**, 205, 1999.
997. M. B. Ali, R. Mika, H. B. Ouada, R. M. Ghaieth, and H. Maaref, Porous silicon as substrate for ion sensors, *Sensors Actuators* **74**, 123, 1999.
998. C. M. A. Ashruf, P. J. French, P. M. M. C. Bressers, and J. J. Kelly, Galvanic porous silicon formation without external contacts, *Sensors Actuators* **74**, 118, 1999.
999. H. Ohji and P. J. French, Single step electrochemical etching in ammonium fluoride, *Sensors Actuators* **74**, 109, 1999.
1000. R. Divan, N, Moldovan, and H, Camon, Roughening and smoothing dynamics during KOH silicon etching, *Sensors Actuators* **74**, 18, 1999.
1001. K. Sato, M. Shikita, T. Yamashiro, K. Asaumi, Y. Iriye, and M. Yamamoto, Anisotropic etching rates of single-crystal silicon for TMAH water solution as a function of crystallographic orientation, *Sensors Actuators* **73**, 131, 1999.
1002. K. Sato, M. Shikida, T. Yamashiro, M. Tsunekawa, and S. Ito, Roughening of single-crystal silicon surface etched by KOH water solution, *Sensors Actuators* **73**, 122, 1999.
1003. B. Nikpour, L. M. Landsberger, T. J. Hubbard, M. Kahrizi, and A. Iftimie, Concave corner compensation between vertical (010)–(001) planes anisotropically etched in Si(100), *Sensors Actuators* **A66**, 299, 1998.
1004. H. Nojiri and M. Uchiyama, Bias-dependent etching of silicon in aqueous ammonia, *Sensors Actuators* **A34**, 167, 1992.
1005. O. Tabata, R. Asahi, H. Funabashi, K. Shimaoka, and S. Sugiyama, Anisotropic etching of silicon in TMAH solutions, *Sensors Actuators* **A34**, 51, 1992.
1006. R. A. Buser and N. F. de Rooij, ASEP*: A CAD program for silicon anisotropic etching, *Sensors Actuators* **28**, 71, 1991.
1007. K. Kellermann and G. Wileke, Observation of silicon etch pit formation in quiescent concentrated aqueous HF solutions, *Mater. Lett.* **19**, 7, 1994.
1008. D. Kendall, A new theory for the anisotropic etching of silicon and some underdeveloped chemical micromachining concepts, *J. Vac. Sci. Technol.* **A8**, 3598, 1990.
1009. R. B. Heimann, Kinetics of dissolution of silcion in CrO_3–HF–H_2O solutions, *J. Mater. Sci.* **19**, 1314, 1984.
1010. E. Herr and H. Baltes, KOH etching of high-index crystal planes in silicon, *Sensors Actuators* **31**, 283, 1992.
1011. H. Kobayashi, J. Ryuta, T. Shingouyi, and Y. Shimanuki, Study of Si etch rate in various composition of SC1 solution, *Jpn. J. Appl. Phys.* **32**, L45, 1993.
1012. A. Merlos, M. Acero, M. H. Bao, J. Bausells, and J. Esteve, TMAH/IPA anisotropic etching characteristics, *Sensors Actuators* **37–38**, 737, 1993.
1013. H. Kaigawa, K. Yamamoto, and Y. Shigematsu, Etching of thermally grown SiO_2 by NH_4OH in mixture of NH_4OH and H_2O_2 cleaning solution, *Jpn. J. Appl. Phys.* **33**, 4080, 1994.
1014. H. S. Park, T. S. Kang, and K. J. Kim, Influence of etching current density on visible electroluminescence from porous n-Si under cathodic bias, *J. Electrochem. Soc.* **146**, 1991, 1999.
1015. J. C. Flake, M. M. Rieger, G. M. Schmid, and P. A. Kohl, Electrochemical etching of silicon in nonaqueous electrolytes containing hydrogen fluoride or fluoroborate, *J. Electrochem. Soc.* **146**, 1960, 1999.
1016. G. J. Norga, M. Platero, K. A. Black, A. J. Raddy, J. Michel, and L. C. Kimerling, Detection of metallic contaminants on silicon by surface sensitive minority carrier lifetime measurements, *J. Electrochem. Soc.* **146**, 2602, 1998.
1017. J. Ryuta, T. Yoshimi, H. Kondo, H. Okuda, and Y. Shimanuki, Adsorption and desorption of metallic impurities on Si wafer surface in SC1 solution, *Jpn. J. Appl. Phys.* **31**, 2338, 1992.
1018. S. Meltzer and D. Mandler, Study of silicon etching in HBr solutions using a scanning electrochemical microscope, *J. Chem. Soc. Faraday Trans.* **91**, 1019, 1995.

1019. D. F. Weirauch, Correlation of the anisotropic etching of single-crystal silicon sphere and wafers, *J. Appl. Phys.* **46**, 1478, 1975.
1020. W. C. Dash, Copper precipitation on dislocation in silicon, *J. Appl. Phys.* **27**, 1193, 1956.
1021. T. L. Chu and J. R. Gavaler, Dissolution of silicon and junction delineation in silicon by the CrO_3–HF–H_2O system, *Electrochim. Acta* **10**, 1141, 1965.
1022. K. Sangwal, *Etching of Crystals,* Elsevier Science, New York, 1987.
1023. H. Seiter, Integrational etching methods, in *Semiconductor Silicon 1977,* H. R. Huff and E. Sirtl (eds.), p. 187, Electrochemical Society, Pennington, 1977.
1024. W. K. Zwicker and S. K. Kurtz, Anisotropic etching of silicon using electrochemical displacement reactions, in *Semiconductor Silicon,* H. R. Huff and R. R. Burgess (eds.), p. 315, Electrochemical Society, Pennington, 1973.
1025. H. Muraoka, T. Ohashi, and Y. Sumitomo, Controlled preferential etching technology, in *Semiconductor Silicon,* H. R. Huff and R. R. Burgess (eds.), p. 327, Electrochemical Society, Pennington, 1973.
1026. J. B. Price, Anisotropic etching of silicon with KOH–H_2O–isopropyl alcohol, in *Semiconductor Silicon,* H. R. Huff and R. R. Burgess (eds.), p. 339, Electrochemical Society, Pennington, 1973.
1027. V. Lehmann and S. Ronnebeck, The physics of macropore formation in low-doped p-type silicon, *J. Electrochem. Soc.* **146**, 2968, 1999.
1028. R. P. Chang, Plasma oxidation of semiconductor and metal surfaces, in *Passivity of Metals and Semiconductors,* M. Froment (ed.), p. 437, Elsevier, Amsterdam, 1983.
1029. B. Agius, M. Froment, and S. R. Rochet, Oxygen transport studied by ^{18}O labeling in thin thermal silicon oxide films in connection with their structural characteristics, in *Passivity of Metals and Semiconductors,* M. Froment (ed.), p. 453, Elsevier, Amsterdam, 1983.
1030. T. Sugano, Passivation of semiconductors, *Solid-State Electron.* **33**, 21, 1990.
1031. A. Namiki, XPS study on early stages of oxidation by atomic oxygen in silicon surfaces, *Solid-State Electron.* **33**, 107, 1990.
1032. Y. Nagasawa and H. Ishida, Backbond oxidation of hydrogen passivated silicon surface, *Solid-State Electron.* **33**, 129, 1990.
1033. M. Seo, K. Aotsuka, and N. Sato, Study on electroluminescence from Si during anodic oxidation, *Solid-State Electron.* **33**, 167, 1990.
1034. K. E. Heusler, Fundamental aspects of the passivation of metals and semiconductors, *Mater. Sci. Forum* **185–188**, 9, 1995.
1035. H. Flietner, Passivity and electronic properties of the silicon/silicon dioxide interface, *Mater. Sci. Forum* **185–188**, 73, 1995.
1036. J. Rappich and H. J. Lewerenz, Electrochemical and electronic passivation by hydrogenation of n-Si(111), *Mater. Sci. Forum* **185**, 83, 1995.
1037. S. Scharf, M. Schmidt, and D. Braunig, Influence of tunneling on trapping kinetics in thin layers, *Mater. Sci. Forum* **185–188**, 91, 1995.
1038. V. Uritsky, Role of electron/hole processes in the initial stage of silicon anodization, *Mater. Sci. Forum* **185–188**, 115, 1995.
1039. O. Najmi, I. Montero, L. Galan, and J. M. Albella, Study of the silicon oxide transportation during the breakdown process, *Mater. Sci. Forum.* **185–188**, 535, 1995.
1040. N. Fukuchi, Future outlooks for technology development in new materials business, Nippon Steel Technology Report No. 73, April 1997.
1041. C. M. Hu, Silicon nanoelectronics for the 21st century, *Nanotechnology* **10**, 113, 1999.
1042. G. Bub, M. I. Schoning, H. Luth, and J. W. Schultze, Modifications and characterization of a silicon-based microelectronic array, *Electrochim. Acta* **44**, 3899, 1999.
1043. N. Takano, N. Hosoda, T. Yamada, and T. Osaka, Effect of oxidized silicon surface on chemical deposition of nickel on n-type silicon wafer, *Electrochim. Acta* **44**, 3743, 1999.
1044. K. Morisawa, M. Ishida, S. Yae, and Y. Nakato, Electrochemical metal deposition on atomically nearly-flat silicon surfaces accompanied by nano-hole formation, *Electrochim. Acta* **44**, 3725, 1999.
1045. M. Grundner and H. Jacob, Investigation on hydrophilic and hydrophobic silicon (100) wafer surfaces by X-ray photoelectron and high-resolution electron energy loss-spectroscopy, *Appl. Phys.* **A39**, 73, 1986.
1046. K. Honda, A. Ohsawa, and N. Toyokura, Silicon surface roughness—structural observation by reflection electron microscopy, *Appl. Phys. Lett.* **48**, 779, 1986.

1047. V. Bertagna, C. Plougonven, F. Rouelle, and M. Chemla, Kinetics of electrochemical corrosion of silicon wafers in dilute HF solutions, *J. Electroanal Chem.* **422**, 115, 1997.
1048. P. Gorostiza, R. Diaz, M. A. Kulandainathan, F. Sanz, and J. R. Morante, Simultaneous platinum deposition and formation of a photoluminescent porous silicon layer, *J. Electroanal. Chem.* **469**, 48, 1999.
1049. P. J. Jorgensen, Effect of an electric field on silicon oxidation, *J. Chem. Phys.* **37**, 874, 1962.
1050. R. Heimann, Dissolution forms of single crystal spheres of quartz in acid alkali fluoride melts, *J. Cryst. Growth* **18**, 61, 1973.
1051. R. Heimann, Relation between equilibrium form and dissolution form of β-tin, *J. Cryst. Growth* **21**, 315, 1974.
1052. R. Heimann, W. Franke, and R. Lacmann, Dissolution forms of single crystal spheres of rutile, *J. Cryst. Growth* **13/14**, 202, 1971.
1053. R. Heimann, W. Franke, and R. Lacmann, Dissolution forms of single crystal spheres. IV. Dissolution of MgO, *J. Cryst. Growth* **28**, 151, 1975.
1054. L. Monastryrskii, T. Lesiv, and I. Olenych, Composition and properties of thin films on porous silicon surface, *Thin Solid Films* **343**, 335, 1999.
1055. E. Pincik, P. Bartos, M. Jergel, C. Falcony, J. Bartos, M. Kucera, and J. Kakos, The metastability of porous silicon/crystalline silicon structure, *Thin Solid Films* **343**, 277, 1999.
1056. A. Valance, Theoretical model for early stages of porous silicon formation from n- and p-Types silicon substrate, *Phys. Rev. B* **55**, 9706, 1997.
1057. H. Li, X. Huang, L. Chen, Z. G. Wu, and Y. Liang, A high capacity nano-Si composite anode material for lithium rechargeable batteries, *Electrochem. Solid-State Lett.* **2**, 547, 1999.
1058. S. Cattarin, E. Pantano, and F. Decker, Investigation by electrochemical and deflectometric techniques of silicon dissolution and passivation in alkali, *Electrochem. Commun.* **1**, 483, 1999.
1059. Z. Irena and B. Irena, Silicon anisotropic etching in alkaline solutions. I. The geometric description of figures developed under etching Si(100) in various solutions, *Sensors Actuators* **A70**, 250, 1998.
1060. M. L. Ciurea, V. Iancu, V. S. Teodorescu, L. C. Nistor, and M. G. Blanchin, Microstructural aspects related to carrier transport properties of nanocrystalline porous silicon films, *J. Electrochem. Soc.* **146**(9), 3516, 1999.
1061. R. B. Wehrspohn, F. Ozanam, and J.-N. Chazalviel, Nano- and macropore formation in p-type silicon, *J. Electrochem. Soc.* **146**(9), 3309, 1999.
1062. E. Konodoh, M. R. Baklanov, F. Jonckx, and K. Maex, Characterization of HF—last cleaning of ion-implanted Si surfaces, *Mater. Sci. Semicond. Process.* **1**, 107, 1998.
1063. T. Akermark, L. G. Gosset, J.-J. Ganem, I. Trimaille, and S. Rigo, Loss of oxygen at the $Si–SiO_2$ interface during dry oxidation of silicon, *J. Electrochem. Soc.* **146**(9), 3389, 1999.
1064. I.I. Suni, G. W. Gale, and A. A. Busnaina, Dissolution kinetics for atomic, molecular, and ionic contamination from silicon wafers during aqueous processing, *J. Electrochem. Soc.* **146**(9), 3522, 1999.
1065. R. B. Wehrspohn, F. Ozanam, and J.-N. Chazalviel, Nano- and macropore formation in p-type silicon, *J. Electrochem. Soc.* **146**(9), 3309, 1999.
1066. G. K. Hubler, Comparison of vacuum deposition techniques, *Pulsed Laser Deposition Thin Films* **327–55**, 327, 1994.
1067. Semiconductor processing—A second electronics revolution? *Mater. Today* 13, 1997.
1068. H. Hasegawa, Passivation and control of semiconductor interfaces by interface control layers, *Mater. Sci. Forum* **185–188**, 23, 1995.
1069. G. K. Celler, D. L. Barr, and J. M. Rosamilia, Etching of silicon by the RCA standard clean 1, *Electrochem. Solid-State Lett.* **3**(1), 47, 2000.
1070. S.-W. Lee, I. H. Cho, S. H. Park, H. G. Choi, N.-G. Kim, J.-W. Jung, H.-K. Kim, and S. B. Han, Novel dual gate oxide process with improved gate oxide integrity reliability, *Electrochem. Solid-State Lett.* **3**(1), 56, 2000.
1071. M. M. Rieger, J. C. Flake, and P. A. Kohi, Alternatives to hydrogen fluoride for photoelectrochemical etching of silicon, *J. Electrochem. Soc.* **146**(12), 4485, 1999.
1072. M. S. Kulkarni and H. F. Erk, Acid-based etching of silicon wafers: Mass-transfer and kinetic effects, *J. Electrochem. Soc.* **147**(1), 176, 2000.
1073. W. Theiß, Optical properties of porous silicon, *Surf. Sci. Rep.* **29**, 91, 1997.
1074. H.-C. Jeong and E. D. Williams, Steps on surfaces: Experiment and theory, *Surf. Sci. Rep.* **34**, 171, 1999.

1075. D. Kovalev, H. Heckler, G. Polisski, and F. Koch, Optical properties of Si nanocrystals, *Phys. Status Solidi B* **215**, 871, 1999.
1076. K. Oura, V. G. Lifshits, A. A. Saranin, A. V. Zotov, and M. Katayama, Hydrogen interaction with clean and modified silicon surfaces, *Surf. Sci. Rep.* **35**, 1, 1999.
1077. F. N. Dzegilenko, D. Srovastava, and A. Saini, Nanoscale etching and indentation of a silicon (001) surface with carbon nanotube tips, *Nanotechnology* **10,** 253, 1999.
1078. H. Noguchi, T. Kondo, K. Murakoshi, and K. Uosaki, Visible electroluminescence from n-type porous silicon/electrolyte solution interfaces: Time—dependent electroluminescence spectra, *J. Electrochem. Soc.* **146**(11), 4166, 1999.
1079. E. K. Wilson, Theoretical eye on materials, *C & EN, Chemical & Engineering News* 29, 31, 34, September 27, 1999.
1080. U. Heim, Some aspects of the mechanism of the wet anisotropic etching of crystals and their consequences for a process simulation, *Sensors Actuators* **A64,** 191, 1998.
1081. Y. Matsumoto, T. Shimada, and M. Ishida, Novel prevention method of stiction using silicon anodization for SOI structure, *Sensors Actuators* **A72**, 153, 1999.
1082. I. Zubel, Silicon anisotropic etching in alkaline solutions. II. On the influence of anisotropy on the smoothness of etched surfaces, *Sensors Actuators* **A70**, 260, 1998.
1083. S. Ronnebeck, J. Carstensen, S. Ottow, and H. Foll, Crystal orientation dependence of macropore growth in n-type silicon, *Electrochem. Solid-State Lett.* **2**, 126, 2000.
1084. V. Lehmann, R. Stengl, and A. Luigart, On the morphology and the electrochemical formation mechanism of mesoporous silicon, *Mater. Sci. Eng.* **B69,** 11, 2000.
1085. M. Christophersen, J. Carstensen, A. Feuerhake, and H. Foll, Crystal orientation and electrolyte dependence for macropore nucleation and stable growth on p-type Si, *Mater. Sci. Eng.* **B69–70,** 194, 2000.
1086. J.-N. Chazalviel, R. B. Wehrspohn, and F. Ozanam, Electrochemical preparation of porous semiconductors: From phenomenology to understanding, *Mater. Sci. Eng.* **B69–70,** 1, 2000.
1087. J. Carstensen, M. Christophersen, and H. Foll, Pore formation mechanisms for the Si–HF system, *Mater. Sci. Eng.* **B69–70,** 23, 2000.
1088. G. Amato, L. Boarino, A. M. Rossi, G. Lerondel, and A. Parisini, Low dimensional porous silicon superlattices, *Mater. Sci. Eng.* **B69,** 48, 1999.
1089. K. Sakaino, Y. Kawabata, and S. Adachi, Etching characteristics of Si(100) surfaces in an aqueous NaOH solution, *J. Electrochem. Soc.* **147**(4), 1530, 2000.
1090. M. Niwano, Y. Kondo, and Y. Kimura, In situ infrared observation of etching and oxidation processes on Si surfaces in NH_4F solution, *J. Electrochem. Soc.* **147**(4), 1555, 2000.
1091. F. De Smedt, C. Vinckier, I. Cornelissen, S. De Gendt, and M. Heyns, A detailed study on the growth of thin oxide layers on silicon using ozonated solutions, *J. Electrochem. Soc.* **147**(3), 1124, 2000.
1092. P. Gorostiza, M. A. Kulandainathan, R. Díaz, F. Sanz, P. Allongue, and J. R. Morante, Charge exchange processes during the open-circuit deposition of nickel on silicon from fluoride solutions, *J. Electrochem. Soc.* **147**(3), 1026, 2000.
1093. S. Ottow, V. Lehmann, and H. Foll, Processing of three-dimensional microstructures using macroporous n-type silicon, *J. Electrochem. Soc.* **143**(1), 385, 1996.
1094. T. Dittrich, I. Sieber, S. Rauscher, and J. Rappich, Preparation of thin nanoporous silicon layers on n- and p-Si, *Thin Solid Films* **276**, 200, 1996.
1095. P. Allongue, C. H. de Villeneuve, M. C. Bernard, J. E. Péou, A. Boutry-Forveille, and C. Lévy-Clément, Relationship between porous silicon formation and hydrogen incorporation, *Thin Solid Films* **297**, 1, 1997.
1096. R. B. Wehrspohn, J.-N. Chazalviel, F. Ozanam, and I. Solomon, Electrochemistry and photoluminescence of porous amorphous silicon, *Thin Solid Films* **297**, 5, 1997.
1097. D. Dimova-Malinovska, M. Sendova-Vassileva, N. Tzenov, and M. Kamenova, Preparation of thin porous silicon layers by stain etching, *Thin Solid Films* **297**, 9, 1997.
1098. S. Meltzer and D. Mandler, Study of silicon etching in HBr solutions using a scanning electrochemical microscope, *J. Chem. Soc. Faraday Trans.* **91**(6), 1019, 1995.
1099. M. R. Linford and C. E. D. Chidsey, Alkyl monolayers covalently bonded to silicon surfaces, *J. Am. Chem. Soc.* **115**, 12631, 1993.

1100. O. Nast, S. Rauscher, H. Jungblut, and H.-J. Lewerenz, Micromorphology changes of silicon oxide on Si(111) during current oscillations: A comparative in situ AFM and FTIR study, *J. Electroanal. Chem.* **422**, 169, 1998.
1101. W.-C. Moon, T. Yoshinobu, and H. Iwasaki, Fabrication of nanopit arrays on Si(111), *Jpn. J. Appl. Phys.* **38**, 483, 1999.
1102. V. Lehmann, F. Hofmann, F. Möller, and U. Grüning, Resistivity of porous silicon: A surface effect, *Thin Solid Films* **255**, 20, 1995.
1103. M. Schoisswohl, H. J. von Bardeleben, V. Morazzani, A. Grosman, C. Ortega, St. Frohnhoff, M. G. Berger, and H. Münder, Analysis of the surface structure in porous Si, *Thin Solid Films* **255**, 123, 1995.
1104. S. C. Bayliss, D. A. Hutt, Q. Zhang, P. Harris, N. J. Phillips, and A. Smith, Structural study of porous silicon, *Thin Solid Films* **255**, 128, 1995.
1105. M. Bertolotti, F. Carassiti, E. Fazio, Ferrari, S. La Monica, S. Lazarouk, G. Liakhou, G. Maiello, E. Proverbio, and L. Schirone, Porous silicon obtained by anodization in the transition regime, *Thin Solid Films* **253**, 152, 1995.
1106. W. Theiá, M. Wernke, and V. Offermann, Depth profiling of porous silicon layers by attenuated total reflection spectroscopy, *Thin Solid Films* **255**, 181, 1995.
1107. U. Gösele and V. Lehmann, Light-emitting porous silicon, *Mater. Chem. Phys.* **40**, 253, 1995.
1108. P. Allongue, C. H. de Villeneuve, L. Pinsard, and M. C. Bernard, Evidence for hydrogen incorporation during porous silicon formation, *Appl. Phys. Lett.* **67**(7), 941, 1995.
1109. J. Kasparian, M. Elwenspoek, and P. Allongue, Digital computation and in situ STM approach of silicon anisotropic etching, *Surf. Sci.* **388**, 50, 1997.
1110. A. Fidélis, F. Ozanam, and J.-N. Chazalviel, Fully methylated, atomically flat (111) silicon surface, *Surf. Sci.* **444**, L7, 2000.
1111. P. D. J. Calcott, The mechanism of light emission from porous silicon: Where are we 7 years on? *Mater. Sci. Eng.* **B51**, 132, 1998.
1112. P. Allongue, C. H. de Villeneuve, J. Pinson, F. Ozanam, J.-N. Chazalviel, and X. Wallart, Organic monolayers on Si(111) by electrochemical method, *Electrochim. Acta* **43**(19–20), 2791, 1998.
1113. M. C. dos Santos and O. Teschke, Aligned pipe arrays formation by silicon anodic etching, *J. Vac. Sci. Technol.* **B16**(4), 2105, 1998.
1114. P. Allongue, V. Kieling, and H. Gerischer, Atomic structure of Si surfaces etched in Triton/NaOH solutions, *J. Phys. Chem.* **99**, 9472, 1995.
1115. C. H. de Villeneuve, J. Pinson, M. C. Bernard, and P. Allongue, Electrochemical formation of close-packed phenyl layers on Si(111), *J. Phys. Chem.* **B101**, 2415, 1997.
1116. H. J. Lewerenz, Spatial and temporal oscillation at Si(111) electrodes in aqueous fluoride-containing solution, *J. Phys. Chem.* **B101**, 2421, 1997.
1117. V. Lehmann, W. Hönlein, H. Reisinge, A. Spitzer, H. Wendt, and J. Wilier, A novel capacitor technology based on porous silicon, *Thin Solid Films* **276**, 138, 1996.
1118. L. M. Peter, D. J. Riley, and R. I. Wielgosz, An in-situ method of monitoring the surface area of porous silicon, *Thin Solid Films* **276**, 61, 1996.
1119. M. Binder, T. Edelmann, T. H. Metzger, G. Mauckner, G. Goerigk, and J. Peisl, Bimodal size distribution in p—porous silicon studied by small angle X-ray scattering, *Thin Solid Films* **276**, 65, 1996.
1120. D. Buttard, D. Bellet, and T. Baumbach, X-ray diffraction investigation of porous silicon superlattices, *Thin Solid Films* **276**, 69, 1996.
1121. J. L. Cantin, M. Schoisswohl, A. Grosman, S. Lebib, C. Ortega, H. J. von Bardeleben, É. Vazsonyi, G. Jalsovszky, and J. Erostyak, Anodic oxidation of p^- and p^+-type porous silicon: Surface structural transformations and oxide formation, *Thin Solid Films* **276**, 76, 1996.
1122. M. Schoisswohl, J. L. Cantin, M. Chamarro, H. J. von Bardeleben, T. Morgenstern, E. Bugiel, W. Kissinger, and R. C. Andreu, Defects and visible photoluminescence in porous $Si_{1-x}Ge_x$, *Thin Solid Films* **276**, 92, 1996.
1123. J. Rappich and H. J. Lewerenz, Photo- and Potential-controlled nanoporous silicon formation on n-Si(111): An in-situ FTIR investigation, *Thin Solid Films* **276**, 25, 1996.
1124. M. Thönissen, M. G. Berger, R. Arens-Fischer, O. Glüger, and H. Lüth, Illumination-assisted formation of porous silicon, *Thin Solid Films* **276**, 21, 1996.

1125. D. Bellet and G. Dolino, X-ray diffraction studies of porous silicon, *Thin Solid Films* **276**, 1, 1996.
1126. C. Jäger, B. Finkenberger, W. Jäger, M. Christophersen, J. Carstensen, and H. Föll, Transmission electron microscopy investigations of the formation of macropores in n- and p-Si(001)/(111), *Mater. Sci. Eng.* **B69–70**, 199, 2000.
1127. G. Hasse, J. Carstensen, G. Popkirov, and H. Föll, Current transient analysis of the oxidizing process in the complete anodic regime of the Si-HF system, *Mater. Sci. Eng.* **B69–70**, 188, 2000.
1128. L. Koker and K. W. Kolasinski, Applications of a novel method for determining the rate of production of photochemical porous silicon, *Mater. Sci. Eng.* **B69–70**, 132, 2000.
1129. M. Gros-Jean, R. Herino, J.-N. Chazalviel, F. Ozanam, and D. Lincot, Formation and characterization of CdS/methyl-grafted porous silicon junctions, *Mater. Sci. Eng.* **B69–70**, 77, 2000.
1130. R. Hérino, Nanocomposite materials from porous silicon, *Mater. Sci. Eng.* **B69–70**, 70, 2000.
1131. A. M. Rossi, G. Amato, L. Boarino, and C. Novero, Realization of membranes for atomic beam collimator by macropore micromachining technique (MMT), *Mater. Sci. Eng.* **B69–70**, 66, 2000.
1132. M. Guendouz, P. Joubert, and M. Sarret, Effect of crystallographic directions on porous silicon formation on patterned substrates, *Mater. Sci. Eng.* **B69–70**, 43, 2000.
1133. M. H. Al Rifai, M. Christopherson, S. Ottow, J. Carstensen, and H. Foll, Dependence of macropore formation in n-Si on potential, temperature, and doping, *J. Electrochem. Soc.* **147**, 627, 2000.
1134. K. H. Beckmann, Investigation of the chemical properties of stain films on silicon by means of infrared spectroscopy, *Surf. Sci.* **3**, 314, 1965.
1135. H. Foll, J. Carstensen, M. Christophersen, and G. Hasse, A new view of silicon electrochemistry, *Phys. Status Solidi,* **(a)182**, 1, p. 7, 2000.
1136. J. Carstensen, R. Prange, and H. Foll, A model for current voltage oscillation at the silicon electrode and comparison with experimental results, *J. Electrochem. Soc.* **146**, 1134, 1999.
1137. M. Christophersen, P. Merz, J. Quenzer, J. Carstensen, and H. Foll, A new method of silicon microstructuring with electrochemical etching, *Phys. Status Solidi,* **(a)182**, 1, p. 561, 2000.
1138. M. Christophersen, J. Carstensen, and H. Föll, Crystal orientation dependence of macropore formation p- and n-type silicon in organic electrolytes, *Phys. Status Solidi,* **(a)182**, 1, p. 103, 2000.
1139. M. Christophersen, J. Carstensen, and H. Föll, Macropore formation of highly doped n-type silicon, *Phys. Status Solidi,* **(a)182**, 1, p. 45, 2000.
1140. J. Carstensen, M. Christophersen, and H. Föll, Parameter dependence of pore formation in silicon within a model of local current burst, *Phys. Status Solidi,* **(a)182**, 1, p. 63, 2000.
1141. G. Hasse, M. Christophersen, J. Carstensen, and H. Föll, New insights into Si electrochemistry and pore growth by transient measurements and impedance spectroscopy, *Phys. Status Solidi,* **(a)182**, 1, p. 23, 2000.
1142. J. Carstensen, R. Prange, and H. Föll, A model for current oscillation in the Si-HF system based on a quantitative analysis of current transients, *Appl. Phys.* **A67**, 459, 1998.
1143. P. Gorostiza, M. A. Kulandainathan, R. Dian, F. Sanz, P. Allongue, and J. R. Morante, Charge exchange processes during the open-circuit deposition of nickel on silicon from fluoride solutions, *J. Electrochem. Soc.* **147**, 1026, 2000.
1144. A. J. Nijdam, E. Van Veenendaal, J. G. E. Gardeniers, A. P. M. Kentgens, G. H. Nachtegaal, and M. Elwenspoek, Si-nuclear magnetic resonance on the etching products of silicon in potassium hydroxide solutions, *J. Electrochem. Soc.* **147**, 2195, 2000.
1145. G. Oskam and P. C. Searson, Electrochemistry of gold deposition on n-Si(100), *J. Electrochem. Soc.* 147, 2199, 2000.
1146. H. Habuka, M. Shimada, and K. Okuyama, Rate theory of multicomponent adsorption of organic species on silicon wafer surface, *J. Electrochem. Soc.* **147**, 2319, 2000.
1147. F. Katsuki, K. Kamei, A. Saguchi, W. Takahashi, and J. Watanabe, AFM studies on the difference in wear behavior between Si and SiO_2 in KOH solution, *J. Electrochem. Soc.* **147**, 2328, 2000.
1148. M. Stern, A method for determining corrosion rates from linear polarization data, *Corrosion* **14**, 440t, 1958.
1149. M. Stern and A. L. Geary, Electrochemical polarization—Part I. A theoretical analysis of the shape of polarization curves, *J. Electrochem. Soc.* **104**, 56, 1957.
1150. G. A. Parks, Surface and interfacial free energies of quartz, *J. Geogr. Res.* **89**, 3997, 1984.
1151. A. K. Vijh, Silicon, in *Encyclopedia of Electrochemistry of the Elements,* A. J. Bard (ed.), p. 287, Dekker, New York, 1976.

1152. M. L. W. van der Zwan, J. A. Bardwell, G. I. Sproule, and M. J. Craham, Mechanism of the growth of native oxide on hydrogen passivated silicon surfaces, *Appl. Phys. Lett.* **64**, 446, 1994.
1153. X. G. Zhang, unpublished.
1154. H. Gerischer, The role of semiconductor structure and surface properties in photoelectrochemical processes, *J. Electroanal. Chem.* **150**, 553, 1983.
1155. H. Kita, Periodic variation of exchange current density of hydrogen electrode reaction with atomic number and reaction mechanism, *J. Electrochem. Soc.* **113**, 1095, 1966.
1156. J. Li, S. Cai, and S. Zhang, Constant and steplike behavior of the cross-section dimension of Si quantum wires and quantum confinement effect in porous silicon formation, *Chin. Sci. Bull.* **41**(24), 2060, 1996.
1157. R. Wang, J. Li, Y. Chen, M. Tang, Y. Wang, S. Cai, and Z. Liu, Quantum confinement effect in electroluminescent porous silicon, *Sci. China* **41**(4), 337, 1998.
1158. S. Ottow, G. S. Popkirov, and H. Föll, Determination of flat-band potentials of silicon electrodes in HF by means of AC resistance measurements, *J. Electroanal. Chem.* **455**, 29, 1998.
1159. S.-L. Zhang, K.-S. Ho, Y. Hou, B. Qian, P. Diao, and S. Cai, The steplike behavior of photoluminescence peak energy and formation of p-type porous silicon, *Appl. Phys. Lett.* **62**(6), 1, 1993.
1160. R. Q. Wang, J. J. Li, S. M. Cai, Z. F. Liu, and S. L. Zhang, Two-peak electroluminescence of porous silicon in persulphate solution, *Appl. Phys. Lett.* **72**(8), 924, 1998.
1161. P. Schmuki, D. J. Lockwood, H. Isaacs, and A. Bsiesy, Proceedings of the International Symposium on Pits and Pores: Formation, properties, and significance for advanced luminescent materials, *Electrochem. Soc. Pro.* **97**(7), 26, 1997.
1162. V. Lehmann, A. Luigart, and V. Corbel, On the morphology and the electrochemical formation mechanism of mesoporous silicon, *Electrochem. Soc. Proc.* **97**(7), 132, 1997.
1163. S. La Monica, P. Jaguiro, and A. Ferrari, A thermodynamical explanation for pore growing stability in porous silicon, *Electrochem. Soc. Proc.* **97**(7), 140, 1997.
1164. T. Dubois, F. Ozanam, and J.-N. Chazalviel, Stabilization of the porous silicon surface by grafting of organic groups: Direct electrochemical methylation, *Electrochem. Soc. Proc.* **97**(7), 296, 1997.
1165. E. A. Ponomarev and C. Levy-Clement, Macroporous layer formation during electrochemical oxidation of p-Si in non-aqueous solutions, *Electrochem. Soc. Proc.* **97**(7), 319, 1997.
1166. T. Akermark, Molecular or atomic oxygen as the transported species in oxidation of silicon, *J. Electrochem. Soc.* **147**(5), 1882, 2000.
1167. P. M. Hoffmann, A. Radisic, and P. C. Searson, Growth kinetics for copper deposition on Si(100) from pyrophosphate solution, *J. Electrochem. Soc.* **147**(7), 2576, 2000.
1168. K. Kondo, A. Shigishi, and Z. Tanaka, Electrodeposition of Zinc–SiO_2 composite, *J. Electrochem. Soc.* **147**(7), 2611, 2000.
1169. J. E. A. M. van den Meerakker, R. J. G. Elfrink, F. Roozeboom, and J. F. C. M. Verhoeven, Etching of deep macropores in 6 in. Si wafers, *J. Electrochem. Soc.* **147**(7), 2757, 2000.
1170. P. Jaguiro, S. La Monica, S. Lazarouk, and A. Ferrari, Theoretical model of porous silicon formation, *Electrochem. Soc. Proc.* **97**(7), 296, 1997.
1171. P. M. Hoffmann, I. E. Vermeir, and P. Searson, Electrochemical etching of n-type silicon in fluoride solutions, *J. Electrochem. Soc.* **147**, 2999, 2000.
1172. A. Speigel, L. E. Erickson, and P. Schmuki, Selective growth of porous silicon on focused ion beam patterns, *J. Electrochem. Soc.* **147**, 2993, 2000.
1173. R. Chmolke, G. Puppe, and H. Piontek, Characterization of silicon wafer back sides with thermal oxide layers by copper deposition, *J. Electrochem. Soc.* **147**, 2999, 2000.
1174. R. Boukherroub, S. Morin, P. Sharpe, D. M. Wayner, and P. Allongue, Insights into the formation mechanisms of Si-OR monolayers from the thermal reactions of alcohols and aldehydes with Si(111)-H, *Langmuir* **16**, 7429, 2000.
1175. J. E. Bateman, R. D. Eagling, B. R. Horrocks, and A. Houlton, A deuterium labeling, FTIR, and ab initio investigation of the solution-phase thermal reactions of alcohols and alkenes with hydrogen-terminated silicon surfaces, *J. Phys. Chem. B* **104**, 5557, 2000.
1176. C. Spinella and G. D'Arrigo, Electrochemical etching of silicon: A powerful tool for delineating junction profiles in silicon devices by transmission electron microscopy, *J. Vac. Sci. Technol. B* **18**, 576, 2000.
1177. J. Grzanna, H. Jungblut, and H.-J. Lewerenz, A model for electrochemical oscillations at the Si/electrolyte contact, part II. Simulations and experimental results, *J. Electroanal. Chem.* **486**, 190, 2000.

1178. J. Grzanna, H. Jungblut, and H.-J. Lewerenz, A model for electrochemical oscillations at the Si/electrolyte contact, part I. Theoretical development, *J. Electroanal. Chem.* **486**, 181, 2000.
1179. I. Frature, S. Cattarin, M. Musiani, and B. Tribollet, Electrodissolution of Ti and p-Si in acidic fluoride media: Formation ratio of oxide layers from electrochemical impedance spectroscopy, *J. Electroanal. Chem.* **482**, 202, 2000.
1180. S. Cattarin, L. Frateur, M. Musiani, and B. Tribollet, Electrodissolution of p-Si in acidic fluoride media: Modeling of the steady state, *J. Electrochem. Soc.* **147**, 3277, 2000.
1181. X. H. Xia, C. M. A. Ashruf, P. J. French, and J. J. Kelly, Galvanic cell formation in silicon/metal contacts: The effect on silicon surface morphology, *Chem. Mater.* **12**, 1671, 2000.
1182. Z. Sardar and I. Abrams, *Introducing Chaos,* Totem Books, New York, 1999.
1183. R. J. Forster, Hopping Across Interfaces: Heterogeneous Electron Transfer Dynamics, *Interface* **9**(4) 24, 2000.
1184. B. C. Crandall, *Nanotechnology,* B. C. Crandell (ed.), The MIT Press, Cambridge, 1999.
1185. X. G. Zhang, "Surface Curvature and Passivation Breakdown", in the proceedings of the Passivity symposium, B. Ives, J. L. Luo, and Sumoki (eds.), Jasper, Canada, The Electrochemical Society, 2001.
1186. S. Langa, I. M. Tiginyanu, J. Carstensen, M. Christopherson, and H. Foll, Formation of Porous Layers with Different Morphologies during Anodic Etching of n-InP, *Electrochemical and Solid State Letters* **3**(11), 514, 2000.
1187. M. Jacoly, Semiconductors Meet Organics, *Chemical & Engineering News,* 32, April, 2000.
1188. R. Dagani, Building From the Bottom Up, *Chemical & Engineering News,* 27, October, 2000.
1189. R. F. Service, Neurons and Silicon Intimate, *Science* **284**, 578, 23 April, 1999.
1190. C. Bruckner-Lea, G. K. Celler, R. G. Kelly, J. Lessard, R. D. McConnell, K. Niki, and K. Rajeshwar, Technology in the Next Century, *Interface* **9**, 20, Spring, 2000.
1191. R. Dagani, NanoSpace 2000: Melding Two Worlds, *Chemical & Engineering News,* 39, February, 2000.
1192. S. W. Lim, R. T. Mo, P. A. Pianetta, and C. E. D. Chidsey, Effect of Silicon Surface Termination on Copper Deposition in Deionized Water, *J. Electrochem. Soc.* 148, C16, 2001.
1193. M. V. t. Kortenaar, J. M. de Goeij, Z. I. Kolar, G. Frens, P. J. Lusse, M. R. Zuiddam, and E. van der Drift, Electroless Silver Deposition in 100nm Silicon Structures, *J. Electrochem. Soc.* **148**, C28, 2001.
1194. Z. Chen, S. M. Lee, and R. K. Singh, Increased Copper Outplating from Dilute HF Solutions on Microstructurally Modified Silicon Surfaces, *J. Electrochem. Soc.* **147**, 3889, 2000.
1195. E. K. Wilson, Quantum Computers, *Chemical & Engineering News,* 35, November, 2000.

Index